Biomorphs: morphology, chemistry, and implications for the identification of early life

Anna Carnerup

A thesis submitted for the degree of
Doctor of Philosophy at
The Australian National University

January 2007

Except where otherwise indicated, this thesis is my own original work.

Anna Carnerup
10 January 2007

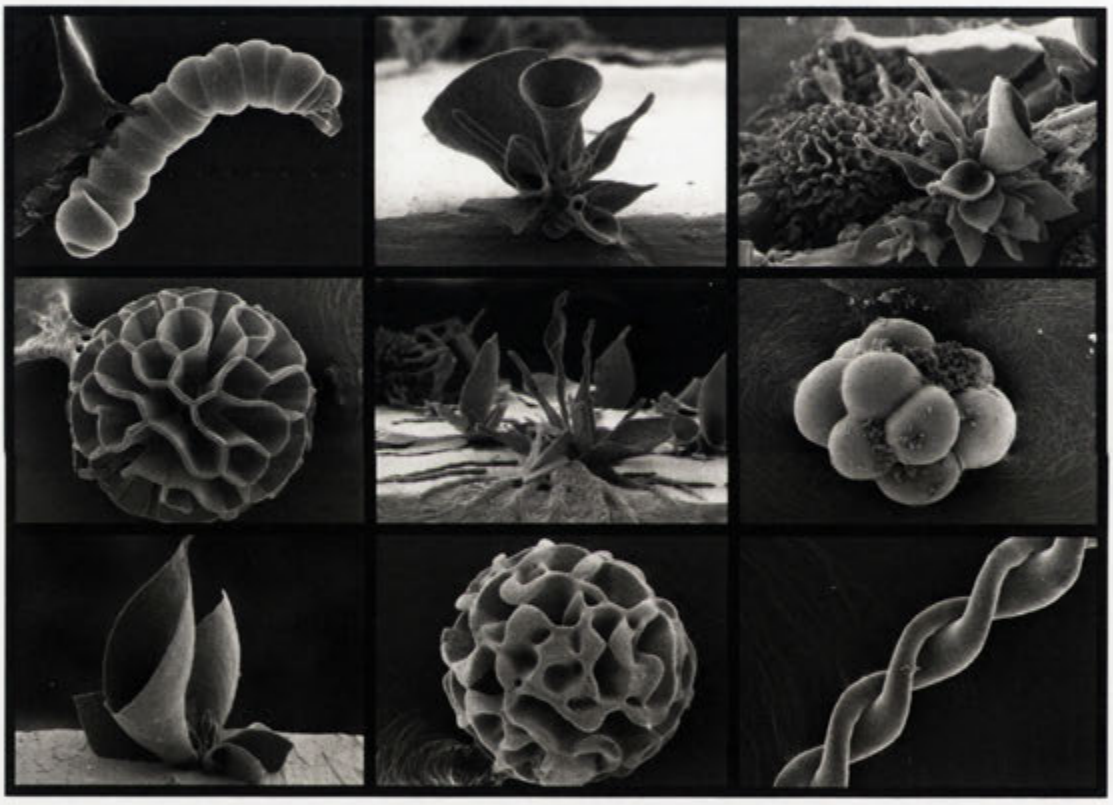

Acknowledgements

This thesis is the product of countless hours of sitting in labs, or with large machines, caring for and fostering biomorphs. Being a custodian of biomorphs requires some patience. However, if my custodial role has come to any good, it is because of the caring of others. I have many people to thank for their intellectual and personal support during the creation of this dissertation. The origins of this thesis, not unlike the origins of life, are easily obscured. This journey began not in Canberra, but in southern Sweden and I thank Barry Ninham and Zoltan Blum for encouraging me to visit the ANU. During my visit I was welcomed, challenged, and overwhelmed by the world of biomorphs. This was the first sprout of life for the thesis. The unique mix of intellectual synergies with ongoing socialising within the Department of Applied Mathematics provided an environment in which early life for ideas about biomorphs could flourish. All environments requiring a structuring principle, or principals, and my heartfelt thanks go to my supervisors. I must thank three people in particular for playing guiding and supporting roles in the life of this dissertation: Stephen, Ankie, and Andy.

Stephen Hyde is a mastermind. His capacity to see across disciplines and fields, and use his keen mind for insight into my little micrometer world, has me amazed from beginning to end. Ann-Kristin Larsson has taken me from 'crayons to perfume' in teaching me crystallography, electron microscopy, and the science of the nanoworld. She has also been a supportive friend and a supplier of frequent BBQs. Andrew Christy deserves all the medals any college of sciences can boast. His scientific agility, prowess, and scholarly patience has been a great source of information and comfort, especially with geological instrumentation and analysis.

Now that the conductors have been thanked, I must also thank a number of people who provided backstage support in this production. Without the help of technicians, staff and experts in the field this thesis would never have been completed. The range of experimental techniques learnt in the process is a joy to my thesis and a bore to my friends. Staff at the Electron Microscopy Unit at ANU showed constant support and interest in the project, and also let me use their large machines night after night. I also thank Ulrike Troitzsch for help with sample preparation and her analytical experience in XRD and XRF. My particular thanks goes to Sally Stowe and Frank Brink for their unlimited help with microscopy issues. My thanks also to Richard

Webster at the Research School of Chemistry at ANU for his help and unlimited use of the ReactIR machine. I am also pleased to thank David Dunstan at the Department of Chemical and Biomolecular Engineering, the University of Melbourne, for the use and help with dynamic light scattering. I also thank Peta Davies at the NMR facility of the Research School of Chemistry at ANU, for help with NMR issues. My sincerest appreciation also goes to John Fitzgerald and Harri Kokkonen at RSES, for the preparation of thin sections of biomorphs and guidance on TEM analysis. Dr. Vincent Otieno-Alego, now at Federal Police, also receives my gratitude for his assistance with Raman spectroscopy experiments conducted at University of Canberra. Cathy Gillespie at John Curtin School of Medical Research for Fluorescence microscopy provided valuable assistance with fluorescence microscopy. Matthias Kellermeier and Alina Voinescu helped with sample preparation of biomorphs during their visits to the ANU from Regensburg. Across distant shores, Juan Manuel García-Ruiz encouraged me to delve into the world of biomorphs. My heartfelt gratitude also goes to Desmond Morris for his kind permission to reproduce his art in this dissertation.

Within the Department of Applied Mathematics lurk colleagues, friends, and fellow night creatures, who provided essential feedback on the dissertation. Should Australia ever need a Batman, equipped with Batcave and scientific know-how, they may call upon Tim Senden. This ginger-nut superbrain provided the kind of scientific knowledge that could not only confound any villian in Gotham City, but greatly progressed my thesis. May he never turn to evil. Along with Tim, Arthur Sakellariou and Tim Sawkins provided vital X-ray CT expertise and built a new stage for small samples. In addition to his role as local celebrity, Vince Craig spared time for valuable discussions on silica and CTAB chemistry, as well as colloidal matters. Vince also deserves thanks for providing me with an uncluttered environment in which to slay the beast that is a dissertation. In addition to Tim and Vince, I thank Jochen Brocks for reading and commenting on draft chapters. Other friends and colleagues in Applied Mathematics, and the research school, provided more holistic support. My thanks to Vanessa Robins, Karlos Claxton, Gerd Schroeder, Joanne Harrison, and Christine Henry for keeping me fed and watered.

It would be remiss of me not to thank my wonderful husband, Len Seabrooke, who kept me laughing and commuted between Copenhagen and Canberra during the final legs of the dissertation. Apparently the seafood bar in Terminal 4 at Heathrow is not bad. Although I call this man 'blåbär', he is more than proficient in looking after me. I also thank my family in Sverige, Australia, and France. My love to them all.

Anna Carnerup, Canberra, December 2006.

Abstract

This dissertation is concerned with the morphogenesis of self-assembled silica-carbonate composite materials, referred to here as *biomorphs*. The synthesis of these materials involves very simple precursors; an alkaline barium-rich sodium silicate solution. The absorption of carbon dioxide from the air promotes precipitation of these complex materials within hours. Biomorphs are self-assembled composite structures, composed of nano-crystalline barium carbonate and amorphous silicate. A characteristic of these aggregates is their hierarchical structure at different length scales. On the nano-scale, they consist of elongated silica coated carbonate crystallites exhibiting orientational ordering. Although this ordering varies between morphologies, in most cases the witherite *c*-axis is aligned along the growth direction of the aggregate. The exceptions include 'bands' and 'palm trees', morphologies synthesised at elevated temperatures, in which the *c*-axis is perpendicular to the growth direction. Palm trees are, in contrast to other morphologies analysed, not polycrystalline, and are therefore a special case of carbonate growth in the presence of silicate. Helical morphologies are in most cases surrounded by a nm-thick silica skin, which is retained as a hollow cast after dissolution of the carbonate entity. On the micron-scale, a wide variety of morphologies are observed depending on reaction conditions. This dissertation examines their morphogenesis, and the effect of synthesis conditions on morphologies, by employing a range of techniques; particularly electron microscopy and crystallographic analysis. Detailed analysis of the biomorphs result by varying temperature, pH, sodium silicate and barium chloride concentration is outlined. The morphological change observed with a change in reaction conditions suggests that the formation of these complex morphologies is believed to be coupled to both crystallographic and reaction-diffusion relationships. Silica effectively poisons the growth of witherite, which results in nano-sized crystals encapsulated in silica and epitaxial relationships between the carbonate crystallites results in partial orientational ordering among the crystals

Biomorphs demonstrate that inorganic abiotic materials are not only restricted to classical crystallographic morphologies with angular facets, but can display a wide range of curved, helical intricate morphologies which are normally considered to be exclusive to the biological world. In all cases the biomorphs studied here are composed of nanocrystalline barium carbonate when a sufficient amount of sodium

silicate is present in the solution.

The very life-like morphologies exhibited by biomorphs have further implications to the identification of the earliest of life forms. With the aim of testing the criteria for the identification of early life, this dissertation examines biomorphs as potential pseudofossils. Biomorphs may display both chemical and morphological resemblance to some of the oldest microfossils on Earth and, as such, raise a number of problems in how we distinguish abiotic from biotic material; obviously a crucial element in the identification of fossilised microorganisms. Abiotic fossil-like biomorphs, with a kerogenous exterior, are produced from the adsorption and condensation of simple hydrocarbons. Such kerogenous biomorphs fulfil all currently accepted criteria for ancient microfossil identification. Geochemical investigations of a carbonate-chert rock from the Dresser formation, dating from the Archean, indicates that the chemical conditions giving rise to biomorphs could have been unavoidable in Archean times. As such, one can argue that biomorphs confuse the distinction between *bona fide* microfossils and abiogenic artifacts. However, if it can be shown that the prevailing geochemical conditions of microfossil localities are not consistent with the requirements for biomorph precipitation (high pH, barium, strontium, or calcium-rich siliceous environment), then biomorphs can be excluded as pseudofossils.

Publications

A.E. Voinescu, M. Kellermeier, A.M. Carnerup, A.-K. Larsson, D. Touraud, W. Kunz, L. Kienle, A. Pfitzner, and S.T. Hyde. *Submitted.* Self-assembled silica-calcium carbonate biomorphs.

A.E. Voinescu, M. Kellermeier, A.M. Carnerup, A.-K. Larsson, D. Touraud, S.T. Hyde, and W. Kunz. *Submitted.* Co-precipitation of silica and alkaline-earth carbonates using TEOS as silica source.

A.M. Carnerup, A.G. Christy, J.M. García-Ruiz, S.T. Hyde and A-K. Larsson. 2006. The record of early life: in search of biosignatures. In: Life as We Know It. Cellular Origin, Life in Extreme Habitats and Astrobiology series, edited by Joseph Seckbach, Kluwer Academic Publishers.

S.T. Hyde, A.M. Carnerup, A-K Larsson, A.G. Christy and J.M. García-Ruiz. 2004. Self-assembly of carbonate-silica colloids: between living and non-living form, Physica A 339, 24-33.

A.M. Carnerup, S.T. Hyde, A-K. Larsson, A.G. Christy and J.M. García-Ruiz. 2004 Silica-carbonate biomorphs and the implications for identification of microfossils. In: Life in the Universe. Cellular Origin, Life in Extreme Habitats and Astrobiology series vol. 7, pp. 221-222. Edited by Joseph Seckbach, Kluwer Academic Publishers.

J.M. García-Ruiz, S.T. Hyde, A.M. Carnerup, A.G. Christy, N.J. Welham and M.J. van Kranendonk. 2003. Self-assembled silica-carbonate structures and implications for detection of ancient microfossils, Science 302:1194.

J.M García-Ruiz, A Carnerup, A.G. Christy, N.J. Welham and S.T. Hyde. 2002. Morphology: An ambiguous indicator of biogenicity, Astrobiology 2:253.

Contents

Chapter 1

Introduction

1.1 Abiotic vs. biotic morphology

The elaborate skeletal structural designs displayed in many biominerals have long fascinated both the everyday shell collector as well as the research community. In the year 1872, Pieter Harting (1812-1885) published a landmark paper (Harting, 1872a), which would become one of the first of many in the emerging science of *biomineralisation*. Harting realised that the ability of an organism to produce intricate functional structures lies in the intimate interaction between organic and inorganic matter. By combining inorganic salts (calcium, magnesium salts, and carbonates, phosphates) with biological organic matter, such as blood, albumin, and chopped oyster meat, a great variety of structures were produced. Harting named these calcium carbonate-based abiological precipitates *calcospherites*, structures that indeed look very similar to certain biominerals (see Figure 1.1 A) (Harting, 1872a; Olivier et al., 1995). Harting's calcospherites were indeed abiotic, but nevertheless precipitated in the presence of biotic organic matter. It soon became clear that organic material is not necessary for producing life-like structures. In the late 19th century, Alfonso L. Herrera (1868-1942) and others, studied specifically alkaline earth carbonates and phosphates precipitated in silica as an experimental model for the origin of life. As in Harting's experiments, but without the influence of organic matter, Herrera observed an amazing morphological variety among the precipitates produced, a system very similar to the one analysed in this dissertation (see Figure 1.1 B) (Herrera, 1912). Moore and Evans (1915), and Moore (1915) also observed peculiar structures that grew from metastable colloidal solutions containing silica with and without colloidal ferric hydrate. These precipitates show filamentous morphologies, that in some cases branch and form a three-dimensional network of interlinked fibers. The very life-like character of these abiotic structures convinced histologists at the time that cotton filaments had contaminated the solution. However, chemical examination of the structures proved they were not made of organic material (Moore and Evans, 1915). This serves as an early

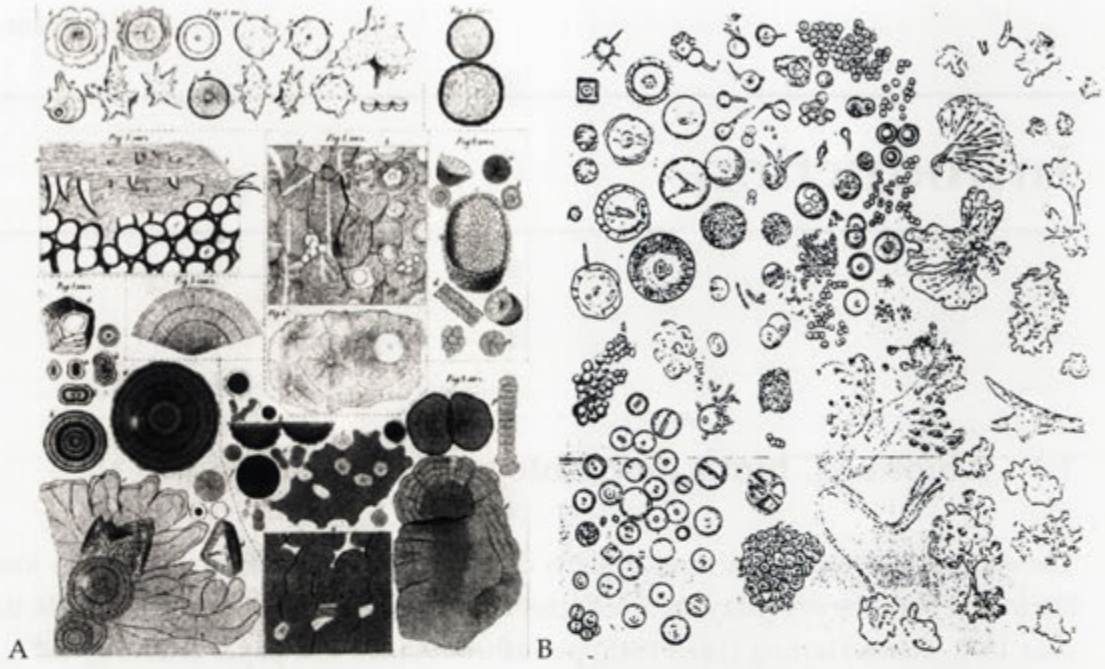

Figure 1.1: P. Harting's drawings of calcospherites (A) and A. Herrera's drawings of unusual calcium and barium carbonates and phosphates grown in concentrated silica solutions (B). Adapted from Harting (1872b) and Herrera (1912).

example of the difficulty in establishing the origin of a structure based on morphology alone. Even though it is not always explicitly stated, there is a common misconception that inorganic matter always adopts facetted and euhedral morphologies (García-Ruiz et al., 2002). However, inorganic abiological structures can display morphologies very similar to biological counterparts, and the distinction between inanimate and animate structures is therefore not so clear. The ability to differentiate between biological and abiological matter is especially crucial within the field of palaeontology, where fossils are identified largely based on comparative morphology and chemistry of the structure (see Chapter 5). It is then interesting to note, that even though it was realised early on that morphological identification can be dubious, it is still one of the main tools for identifying fossils, especially of microorganisms. Identification is made more difficult by the fact that the carbonaceous chemistry of such microstructures can be mimicked by inorganic reactions indifferent to the presence of biology. This was also realised very early on. Moore and Webster (1913) showed experimentally that simple organics can be produced from inorganic precursors, in this case from dilute solutions of ferric or uranic hydroxides using sunlight as energy source. Moore, and coauthors, had then shown that both complex morphology and organic chemistry is not indicative of life, and this was at the beginning of the 20th century! Unfortunately, this

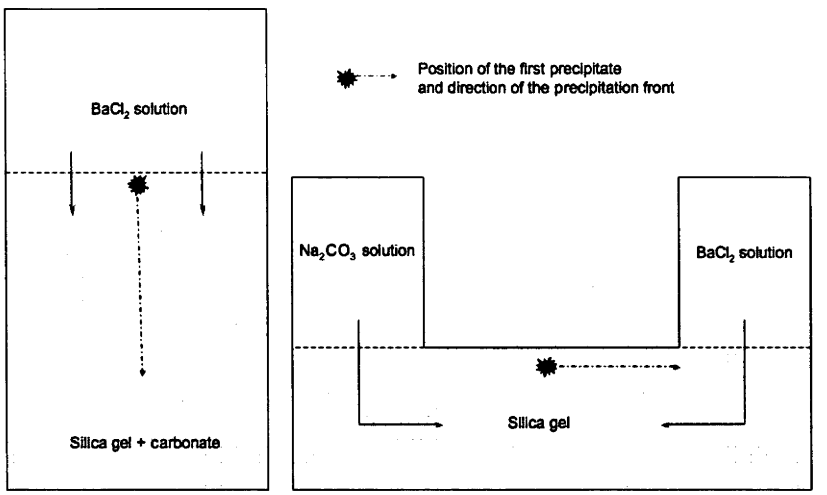

Figure 1.2: Design of cells used for silica gel experiments producing biomorphs.

knowledge seems to have been largely forgotten within the palaeontology community until recently, when Archean microfossils, claimed to be the earliest traces of life, as well as reports of microfossils found in a martian meteorite, were up for scrutiny. The earliest traces of life, enclosed in ancient sediments, are most often characterised as remnants of living organisms based on comparative morphology to modern biota. In particular ancient rocks, where the chemical and geological history is not obvious, such identification tools are problematic.

The close morphological resemblance of abiotic inorganic precipitates to ancient microfossils is at the heart of this dissertation. Self-assembled silica-carbonate structures, called biomorphs, show great morphological diversity depending on the reaction conditions used during synthesis (see front page of this dissertation for examples of biomorphs). These structures serve as a modern example of how difficult it can be to distinguish between a bona fide microfossil and abiotic structures. From the material science point of view, these self-assembled silica-carbonate structures are fascinating as they can serve as a laboratory model for biomimetic chemistry; chemistry, inspired by biomineralisation, to synthesise new ceramics and materials with hierarchical structure and complex form.

1.2 Biomorphs: A brief review

What are biomorphs? For the purpose of this study, biomorphs are self-assembled silica-carbonate composite structures that display a wide range of life-like morphologies depending on reaction conditions.

In the late 1970s, during his doctoral studies, Juan Manuel García-Ruiz discovered

Euhedral spikes, radiating from a central core	Spikes with irregular branch lengths with 'paraboloidal' structures at the tips	Spikes with fine branching at the tips	Complex morphologies including sheets and helical aggregates
< 8.5	8.5	9.0	9.5, 10 < **pH**

Figure 1.3: The change in morphology with pH observed for gel grown biomorphs (Baird et al., 1992).

these peculiar carbonate aggregates grown in silica gels, similar to the ones described by Herrera almost 70 years earlier (Baird et al., 1992). Again, an amazing morphological variety was observed in these gels. Twisted ribbons, worms, sheets, and globular structures, to name a few, were encountered in this system (García-Ruiz and Amarós, 1981). The precipitation technique used to synthesise biomorphs is envisioned in Figure 1.2, where counter diffusion of an alkaline earth metal (Ca, Ba or Sr) solution with a carbonate solution through a silica gel give rise to biomorphic aggregates (García-Ruiz and Moreno, 1985). As the diffusion progress through the gel, pH is locally reduced and precipitation of different silica-carbonate biomorphs take place at different locations throughout the gel. However, biomorphs can also be precipitated in alkaline barium- or strontium-rich silica solution, where the absorption of carbon dioxide from the air promotes the carbonate precipitation (García-Ruiz, 1998, 2000). This technique will be used throughout this dissertation.

A characteristic of biomorphic aggregates is their hierarchal arrangement at different length scales. On the micron scale, widely different morphologies can be produced depending on the reaction conditions. In the barium or strontium carbonate case, using a 0.5 M $BaCl_2$ or $SrCl_2$ solution at pH >10.2 in a silica gel, some of the aggregates show twisted, braid-like morphologies that can grow up to millimetres in length. It was originally observed that only left-handed twisted structures developed during growth (García-Ruiz and Amarós, 1981), however, later equal numbers of right- and left-handed twisted structures were acknowledged. Baird et al. (1992) investigated the effect of pH, ionic strength, and gel-media (agarose, silica, and silica-agarose) on morphogenesis of the aggregates, using agarose made nominally with 0.5 M $BaCl_2$. In all experiments conducted, the first precipitates were observed within 3 hours, and continued to grow for up to 5 days. Generally, larger and more elongated aggregates were formed in the direction away from the interface between the gel and the $BaCl_2$. In agarose gel, dendritic $BaCO_3$ grew at pH below 9.5, whereas higher pH resulted in

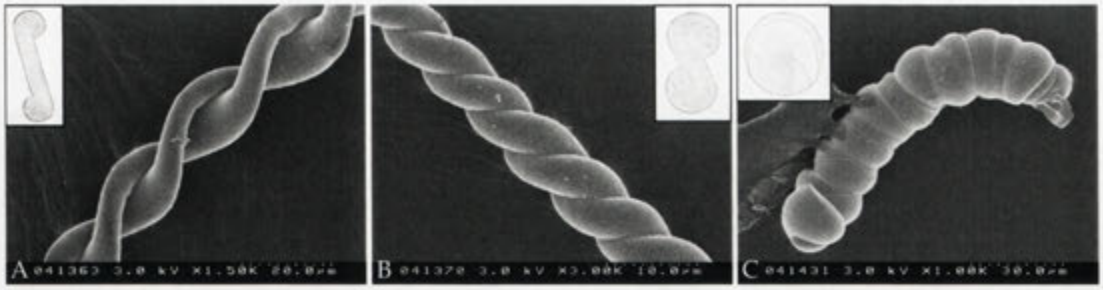

Figure 1.4: FESEM images of the three principle twisted aggregates; Twisted ribbons (A), double helix (B), and worm (C). Insets show very basic sketches of the cross-section. Note: the sketches are not drawn on a relative scale.

spherulitic $BaCO_3$. The reason for this morphological change was assigned to elevated concentrations of carbonate ions at this pH. In gels prepared with silica, regardless whether it was mixed with agarose or not, spectacular biomorphic morphologies, typical for silica-gels, were observed. The morphological change observed with change in pH in this system can be seen in Figure 1.3. It is noted that complex biomorphic aggregates are only obtained at high pH. Sheets and spirals often grow from a globular starting point, sometimes from the same aggregate, however, spirals were also observed growing from the tip of sheets (Baird et al., 1992). The sheets can vary in curvature, from trumpet-like to flat, although, the somewhat saddle-shaped sheets are most commonly observed. Most sheets are heart-shaped, and grow radially outward from the rim of the sheet. In some instances this rim curls around on itself, and when two such 'lips' curl in opposite directions, a twisted ribbon can grow outward from the meeting point of these lips (García-Ruiz et al., 2002). Three types of twisted structures have been observed, which can be classified according to the size of the lip-curling, and the extent of overlapping of successive twists (see Figure 1.4). Twisted ribbons are characterised by a small degree of lip-curling, whereas double helices have larger lips, and look like tightly wound ropes. In worms, on the other hand, no typical scrolling is observed, and a single helix is seen with a large degree of overlapping between successive layers (García-Ruiz et al., 2002). The degree of overlap can vary within a single twisted aggregate (García-Ruiz and Amarós, 1981), and at times a continuous development from twisted ribbon to double helix to worm can be seen (García-Ruiz et al., 2002).

Additives, such as ethylene glycol, did not have any effect at all on the morphology produced, sodium chloride however did. Addition of NaCl, or more specifically, using HCl to lower the pH before gelling instead of an ion exchange resin, facilitated the precipitation of complex morphologies at lower pH, where normally only dendritic structures are observed (Baird et al., 1992). For instance, García-Ruiz and Moreno (1997) showed that twisted ribbons could be grown in silica gels at pH 9.5,

and a constant average growth rate of 20-50 μm per minute was observed for such filaments. Increasing the temperature to 55 °C resulted in longer and thinner filamentous structures compared to room temperature. Several twisted ribbons, around 1 μm in diameter, emerged from a central cluster and grew, from a central point, up to 10 mm in length. The temperature dependence on the size of the twisted ribbons was suggested to be associated with a lower concentration of dissolved carbonate and a faster silicate polymerisation at higher temperature (García-Ruiz and Moreno, 1997). Increasing the carbonate concentration results in longer (up to 50 mm) and wider (> 0.2 mm) filaments, structures that has a double twist and coils around itself (García-Ruiz and Moreno, 1985). Reyes-Grajeda et al. (2002) showed that the addition of L-aminoacids also have an effect on the morphology produced.

On the nano-scale, these amazing aggregates consist of nanometer sized elongated carbonate crystals that show strong orientational ordering within a silica matrix. These rod-like crystals are stacked in a twisted way to build up the polycrystalline interior of the aggregate, that is then covered by an outer silica skin. Viewed under crossed polarisers, these sheets show contours of birefringence colours (Maltese crosses) indicative of a high degree of orientational ordering of the crystallites, such that the fast axis (c-axis) radiate outward from the centre of the sheet. This observation has been confirmed with SEM analysis of these sheets, showing that they are composed of crystals radiating from the centre of the aggregate, aligned parallel to the c-axis (García-Ruiz and Moreno, 1985; Baird et al., 1992). By dissolution of the carbonate entity with a weak acid, the silica skin can easily be seen as a perfect hollow cast of the original structure (García-Ruiz and Amarós, 1981).

Terada et al. (2003) investigated strontium carbonate biomorphs grown in silica gel with various carbonate concentrations (0.001-1.0 M) and pH (7.0-10.5), using a 1.0 M strontium chloride solution, and hydrochloric acid to gel the silica sol. Again, it was shown that the morphology changed depending on pH. At pH between 7.5 and 10.0, spherical aggregates consisting of pseudo-hexagonal aragonite-type clusters, that at the higher pH end also displayed platy fibrous subunits. At pH 10.5 petals, consisting of intertwined sheets, which often showed helical morphologies at the top of these sheets, were formed. The morphological evolution recorded with time can be seen in Figure 1.5, where the first precipitate showed dumbbell-like morphologies that with time closed up into spherical aggregates. Further growth resulted in pitted aggregates, and preferential growth at the tip of the 'veins' resulted in petals with sheet-like morphology. In the final stages of growth helical morphologies were produced at the tip of the petals. These petal-like aggregates were found in silica gels containing relatively low carbonate concentrations between 0.001-0.1 M. Using higher concentrations (1.0 M) produced dendritic and dense-branching morphologies. It was shown by TEM

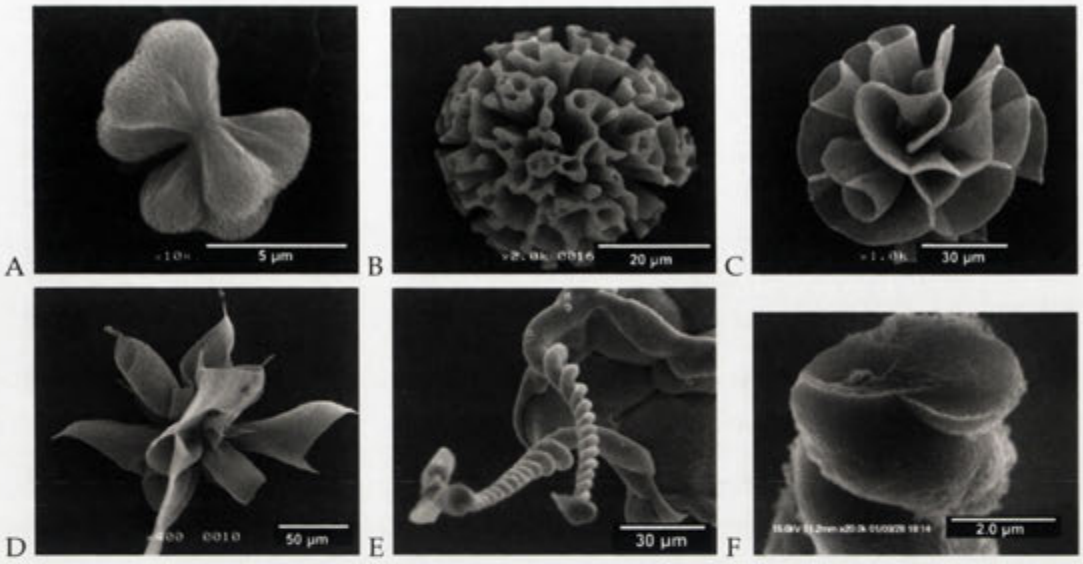

Figure 1.5: SEM images showing the morphological evolution of strontium carbonate biomorphs grown in silica gel at pH 10.5 with time; A 0.5 h; B 2 h; C 6 h; and D 9 h. helical morphologies often grew from the tip of the petals (E), and acid treatment of such an aggregate leaves the 3-D silica structure intact (F). Adapted after Terada et al. (2003).

analysis, that the sheets of the petals consist of elongated subunits with a diameter between 40-60 nm, which in turn have crystalline carbonate centres, 10-20 nm in diameter, aligned along the *c*-axis. Each individual carbonate crystallite was covered in an amorphous phase. Furthermore, it was shown that the *c*-axis and possibly also the *b*-axis were parallel to the surface of the sheets. Analysis of the change in subunit size and aggregate composition with pH showed that subunit diameter decreased, and was followed by an increase in Si/Sr atomic ratio, with an increase in pH. These changes occurred rapidly around pH 10, where these complex morphologies grow. For instance, at pH 10.5 the subunits had a diameter of between 40-60 nm as mentioned before, and the aggregate a Si/Sr atomic ratio of around 0.55, whereas at pH 10, the size were just slightly larger, ~ 70 nm, and the Si/Sr atomic ratio was reduced to around 0.1. In contrast to earlier reports (García-Ruiz and Amarós, 1981; García-Ruiz and Moreno, 1985; Baird et al., 1992; García-Ruiz, 1998), the twisted aggregates showed, upon dissolution of the crystalline carbonate entity, a gel-like silica structure that retained the 3-D morphology of the aggregate, but was devoid of an outer colloidal silica skin (see Figure 1.5 F).

Calcium carbonate biomorphs show quite different morphologies compared to their barium or strontium counterparts. At a pH of 10 and $CaCl_2$ of 0.5 M, aggregates with *sheaf of wheat* morphologies are obtained (see Figure 1.6 A), as well as finger-like structures (García-Ruiz and Moreno, 1985; Dominguez Bella and García-Ruiz, 1986,

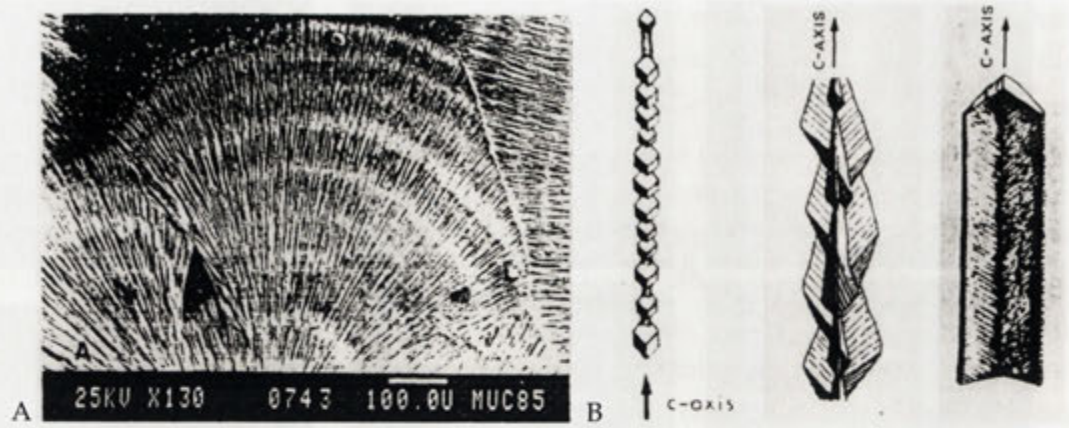

Figure 1.6: SEM image of a $CaCO_3$ biomorphs with banded sheaf of wheat morphology (A). Different kind of fibre design observed in banded (far left) and non-banded sheaf of wheat aggregates. Adapted from Dominguez Bella and García-Ruiz (1986).

1987). In the sheaf of wheat structures, three different textural crystal arrangement have been found; structures with concentric banding, and structures without banding that can adopt two different fibre types. The banding of some structures is due to the presence of radially arranged micro-sheaf of wheat particles, composed of calcite rhombohedra with the *c*-axis aligned along the fibre length (see Figure 1.6 B). The presence of calcite crystals without physical contact in these fibres suggests a silica-mediated growth. It has also been shown that these banded structures have a growth rate between 33.4 and 111 μm/day, which is very much higher than single crystals of calcite precipitated in a tetramethoxysilane gel. It was therefore suggested that the silicate has a catalytic effect on nucleation and growth, which affects the final morphology of the aggregate (Dominguez Bella and García-Ruiz, 1987). The sheaf of wheat structures without banding, on the other hand, are also built up by fibres but with a quite different morphology and arrangement of crystals. In this case, the fibres possess a 3-fold symmetry element, where each 'rib' contains calcite crystals arranged along the *c*-axis (see Figure1.6 B).

Imai et al. (2002) and Imai et al. (2003) found quite different $CaCO_3$ morphologies prepared with 1.0 M $CaCl_2$ in gels with $[Na_2CO_3]$ ranging from 0.001-1.0M. At low pH (~ 8), rhombohedral calcite was the main product, however, clusters of pseudo-hexagonal aragonite crystals were also precipitated. With an increase in pH, the aragonite aggregates became more and more complex, displaying porous and coral-like morphology at pH 10.5 (see Figure 1.7 A-D). These porous structures were composed of platy aragonite subunits, estimated to be around 30-80 nm in size from XRD patterns. It was also shown that the morphological change that occurred with

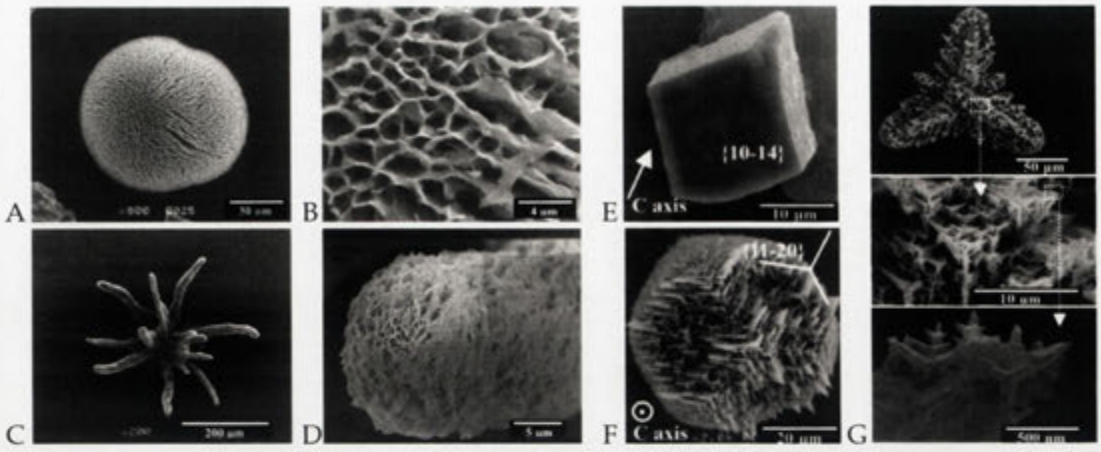

Figure 1.7: SEM images of $CaCO_3$ biomorphs with coral-like morphology (A, C), produced at pH 10.5. Images B and D show the porous and platy nature of the aragonite biomorphs in A and C respectively. Adapted from Imai et al. (2002). SEM images of the morphological evolution of calcitic three-pointed stars, from classical rhombohedral calcite observed after 1h (E), to a roughening of the {11-40} surface by growing edges perpendicular to the *c*-axis, and parallel to the {11-20} planes, observed after 12h (F), to large three-pointed stars, observed after 72 h (G). The fractal-like hierarchical behaviour of the calcitic stars is seen in G, where the overall morphology is composed of smaller, 1-5 μm stars, which in turn are composed of even smaller, 0.1-0.5 μm, stars. Adapted from Imai et al. (2003).

an increase in pH also resulted in smaller subunits with a higher silicon content. By dissolving the $CaCO_3$ content with 0.1 M HCl, the full 3-D morphology of the silica within the aggregate was revealed. Surprisingly no outer silica membrane was observed. The precipitation of these aragonite structures were accompanied by a large amount of calcite. However, using aragonite needles as crystallisation seeds, only the porous aragonite structures were produced. Interestingly, the calcite produced was also affected by the presence of silicate. Imai et al. (2003) described the progressive evolution of calcite rhombohedra to three-pointed stars (see Figure 1.7 E-G) as an effect of the increased silicate to carbonate ratio during crystal growth. At the early stages of growth, when the carbonate concentration was high, calcite rhombohedra formed, displaying classical {10-14} faces. As the carbonate concentration decreased during growth, the presence of silicate anions showed increasingly suppressive growth on the {11-20} planes, inducing the morphological evolution of three-ponted stars. Although, silicon was detected on the surface of these structures, no silicate encapsulation of the calcite crystals was observed, as was the case with the porous aragonite structures produced in the same experiment.

Compared to gel-derived biomorphs, relatively little has been written about such aggregates grown in silica solution. It has been noted that the same morphological

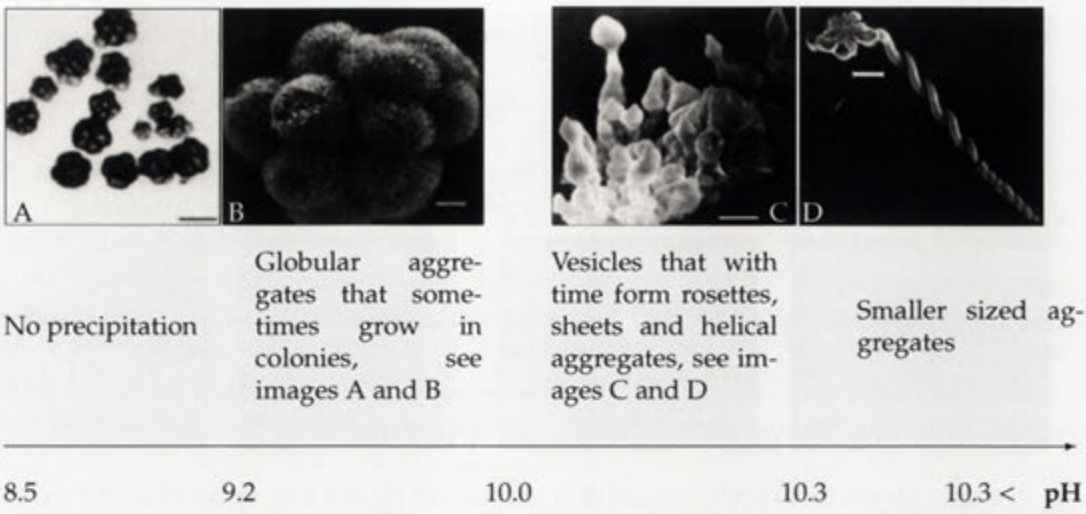

Figure 1.8: The change in morphology with pH observed for sol grown biomorphs. Scale bar in A 50 μm, B 5 μm, C 10 μm, and D 20 μm (García-Ruiz, 1998).

sequence can be obtained in the two systems. In the gel, larger morphological variety is observed in a single experiment as the diffusion of the metal chloride through the gel gradually changes the reactions conditions. In the sol based system, the morphologies observed can be traced in a line across the gel (García-Ruiz, 2000).

Changing the pH in silica sol-based experiments also gave rise to different morphologies (see Figure 1.8) (García-Ruiz, 1998, 2000). Using a 250 ppm silica solution García-Ruiz (1998) systematically analysed the change in morphology with pH, although, no specific $BaCl_2$ concentration was given. At pH below 9.5 no precipitation was observed, due to the low carbonate concentration in equilibrium with the atmosphere. However, at higher pH between 9.2-10.0, globular aggregates consisting of radiating crystals from a single crystal core, are observed. Between pH 10.0 and 10.3 large vesicles developed, with time, into 'encapsulations', rosettes, sheets and helical aggregates. These aggregates were described as hollow, having a wall of tenths of microns thick which in turn was characterised by a silica rich inner part, and carbonate rich phase on the outside. At even higher pH precipitation is observed within 5 minutes, yielding the very same morphologies having, but with a much smaller size of around 5 μm. It was also indicated that increasing the silica concentration would result in the same morphological evolution, but at slightly lower pH (García-Ruiz, 1998).

Mechanism of biomorph formation?

Since the 'rediscovery' of these strange and beautiful structures by Juan Manuel García-Ruiz in the 70s, the morphological origin of such spectacular growths has been, to say the least, puzzling. Essentially two models have been proposed for the formation of the complex morphologies observed in silica-carbonate systems. The first one, referred to as the 'top-down' model, suggests that the overall morphology is derived from the presence of the outer silica skin, that in turn determines the structural ordering of the carbonate crystallites within. The second one, referred to as the 'bottom-up' model, describes the 3-D morphology as originating from the self-assembly of the silica encapsulated carbonate crystallites (Hyde et al., 2004). In both cases, the formation of biomorphs is a result of a close interaction between silica and carbonate precipitation.

The top-down model has primarily been advocated in the early work by García-Ruiz and coauthors, as a silica skin was apparent on their precipitates. García-Ruiz and Amarós (1981) argued that the sheer presence of this membrane, easily seen upon dissolution of the carbonate interior, was indicative of the power of this membrane to control the crystallites' ordering, and therefore the global morphology. It was further suggested that the skin was formed by the catalytic effect of carbonate groups on metal silicate hydration, which induce the arrangement of the simultaneously growing carbonate crystals (García-Ruiz and Moreno, 1985). Baird et al. (1992) also noted that the tip of the growing helical aggregates is devoid of silica , and came to the conclusion that the development of the twist could be accounted for by the induced strain between the skin and its interior.

The chemical similarity between chemical gardens (see Section 2.3.3) and biomorphs led García-Ruiz and Moreno (1985) to suggest that the same formation mechanism must be in place, i.e. an osmotic pressure driven chemical reaction. As it has been noted that, in some cases, twisted aggregates can grow from the gel into the overlying $BaCl_2$ solution, sustaining constant geometrical morphology, this was interpreted as an indication that the growth of these aggregates is not due to the formation of dissipative structures caused by fluid instabilities (García-Ruiz and Moreno, 1997; Hyde et al., 2004).

Imai et al. (2002) and Terada et al. (2003) proposed a very different formation mechanism for biomorphic growth, as no external silicate membranes were ever observed in their systems. Terada et al. (2003) suggested that the complex morphologies arise as a consequence of the high solubility of silica at high pH, which are enabled to absorb on preferentially high anionic sites instead of carbonate anions, when silicate ions are the most dominant species of the two. That is to say, the morphology is controlled by the silicate to carbonate molar ratio. They identified three possible modes

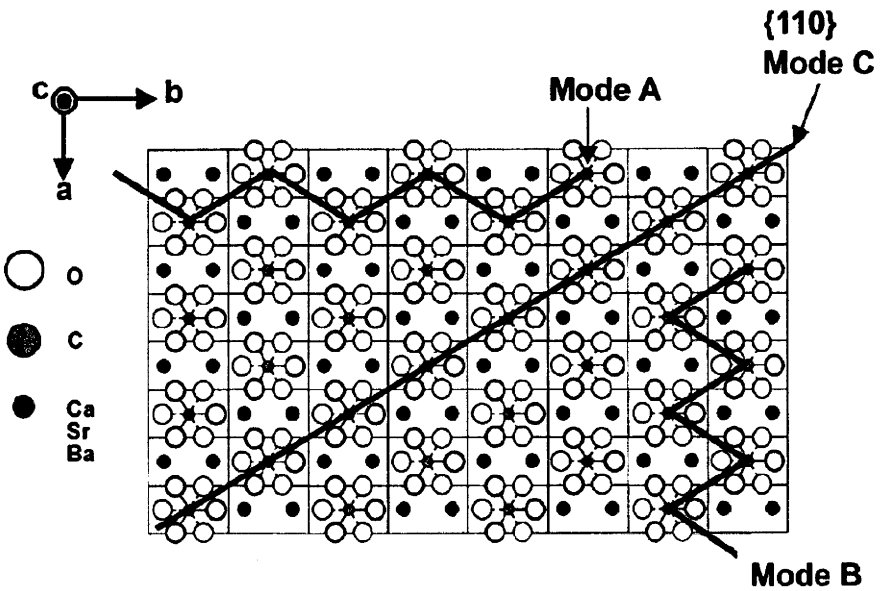

Figure 1.9: Schematic drawing of the aragonite-type (001) plane, showing three modes having high anionic sites, where silicate can absorb. Adapted from Terada et al. (2003).

of adsorption of silicate, envisioned in Figure 1.9. Mode C, which involves linearly arranged carbonate ions on the {110} planes, was determined to be the preferred mode of adsorption, since the other two are stressed as they adopt a zig-zag fit. However, depending on the carbonate in question, Modes A and B can be more or less probable to adsorb soluble silicate. As the *a*/*b*-axes ratio varies between the aragonite-type carbonates ($CaCO_3$ 0.622, $BaCO_3$ 0.597, $SrCO_3$ 0.607), it indicates that in $BaCO_3$ and $SrCO_3$ Mode B is more stressed, and Mode A less so, compared to the $CaCO_3$ case. For $BaCO_3$ and $SrCO_3$ then, Modes A and C are active, and adsorption of silicate at these sites induce polymerisation through dehydration reactions, thereby suppressing the growth in the *a*-direction while some growth along the *b*-direction was envisioned. This was the case observed for the $SrCO_3$ sheet-like structures, where the *c*-axis was elongated and the *b*-axis was parallel to the growth direction of the sheets. The overall morphology of the aggregates was attributed to instabilities on the growing surface of the initial spherulites, in which pitting of the surface occurred. The growth of the sheets were envisioned as *a self-catalytic mechanism in a diffusion field*, from which the sheets adapted their thickness from the width of the pits on the surface (Terada et al., 2003). A similar mechanism was thought to have caused the formation of the porous coral-like aragonite aggregates. In the $CaCO_3$ case, silicate anions preferentially adsorb to {110} planes (Mode A in Figure 1.9) and thereby inhibit growth, resulting in elongated crystals along the {110} and *c*-axis directions. Completely silica-covered

crystals then show platy appearance, with random branching, that self-assemble to produce the final 3-D porous structure (Imai et al., 2002).

Data collected during this dissertation allows more refined consideration for or against competing models of formation.

Naturally produced biomorphs and relations to early life detection?

As was mentioned earlier (see Section 1.1), non-facetted morphology is not exclusive to life. Or as García-Ruiz (1994) put it:

> 'The existence of these kinds of inorganic precipitates clearly shows that the distinction between "inorganic and organic symmetry" cannot be considered to have a sound basis.'

García-Ruiz (1994) further pointed out the morphological similarity between biomorphs and microfossils, and concluded that these kind of abiological structures should be taken into account when deducing the origin of a microfossil-like structure. Geochemically, all that is needed to produce biomorphs is an alkaline silica rich environment (gel or sol) and a source of barium, strontium, or calcium. These conditions are quite rare on modern Earth, but were possibly wide-spread in Precambrian times (see Chapter 5). Naturally produced biomorphs could therefore have been inevitable, and would be preserved in chert, just as microfossils most commonly are. Even though no accounts of naturally produced barium or strontium carbonate biomorphs exist, some indication of silica-modified carbonate precipitates are known in the form of calcite herringbone textures. Calcite herringbone is a chemical precipitate similar in texture to the sheaf of wheat structures described in previous section (see Figure 1.6), and were apparently common in Archean times (Sumner and Grotzinger, 1996b,a).

'Biomorph': its origin and use

Since there has been some commotion over the use of the term *biomorph* for these silica-carbonate aggregates (Hofmann, 2004), it is appropriate to give an explanation for why this is. Juan Manuel García-Ruiz named these growths 'biomorphs'[1] after Richard Dawkins work, due to their life-like morphology. Dawkins used the term in his book 'The Blind Watchmaker' to describe life-like structures developed by his computer sofware (Dawkins, 1988). These structures represent the simulation of evolution, where the user plays the role of natural selection, on a set of 16 genes applied to stick models. Indeed, various insects, trees and other life-like structures

[1]Biomorphs were, however, previously called *induced morphology crystal aggregates* (IMCAs), but will hereafter be termed biomorphs (García-Ruiz, 1994).

can be produced (Dawkins, 1988). The word 'biomorph' (from Greek *Bios* life + *Morphe* form) was, according to Dawkins, first coined by author and artist Desmond Morris who used this word to describe life-like shapes in his surrealist paintings. They are called biomorphs because they are 'biological in concept, but not representing a specific animal'. According to Morris the structures evolve in his mind and it is possible to follow their development in successive paintings (see Fig 1.10) (Morris, 1987). Although Dawkins claims that Morris coined the word, it appears in earlier publications. In 1895 A.C. Haddon describes the term as follows (Haddon, 1895):

> 'The biomorph is the representation of anything living in contradistiction to the skeuomorph, which...is the representation of anything made, or of the physicomorph which is the representation of an object or operation in the physical world.'

The Oxford English Dictionary[2] describes biomorph as 'a decorative form representing a living object'. A similar definition of the word biomorph is given on two other web-based dictionaries[3] as;

> 'A nonrepresentational form or pattern that resembles a living organism in shape or appearance'

A definition of the adjective biomorphic is given on Britannica Online as 'resembling or suggesting the forms of living organisms'[4]. So, biomorphs per se are viewed as 'resemblances of biological form'.

There has been some dispute over the use of the term biomorph applied to the silica-carbonate structures. Hofmann (2004) suggested the term 'abiomorphs' for abiotic precipitates resembling biological morphologies, but failed to give a reason for this terminology change. Since the word biomorph has solely been used to describe non-living creations with morphologies similar to biological forms there is, in my opinion, no reason to stop using biomorph as a name for our silica-carbonate aggregates.

1.3 Organisation of this dissertation

This dissertation investigates the morphogenesis of biomorphs using the sol-based synthesis under different initial conditions. The aim is to acquire further experimental

[2] dictionary.oed.com/cgi/entry/50022354?single=1&query_type=word&queryword=biomorph&first=1&max_to_show=10, Urldate: 2005-08-18

[3] www.thefreedictionary.com/biomorph, www.answerbag.com/t_view.php/428}, Urldate: 2005-08-18

[4] www.britannica.com/dictionary?book=Dictionary&va=biomorphic&query=biomorphic, Urldate: 2005-08-18

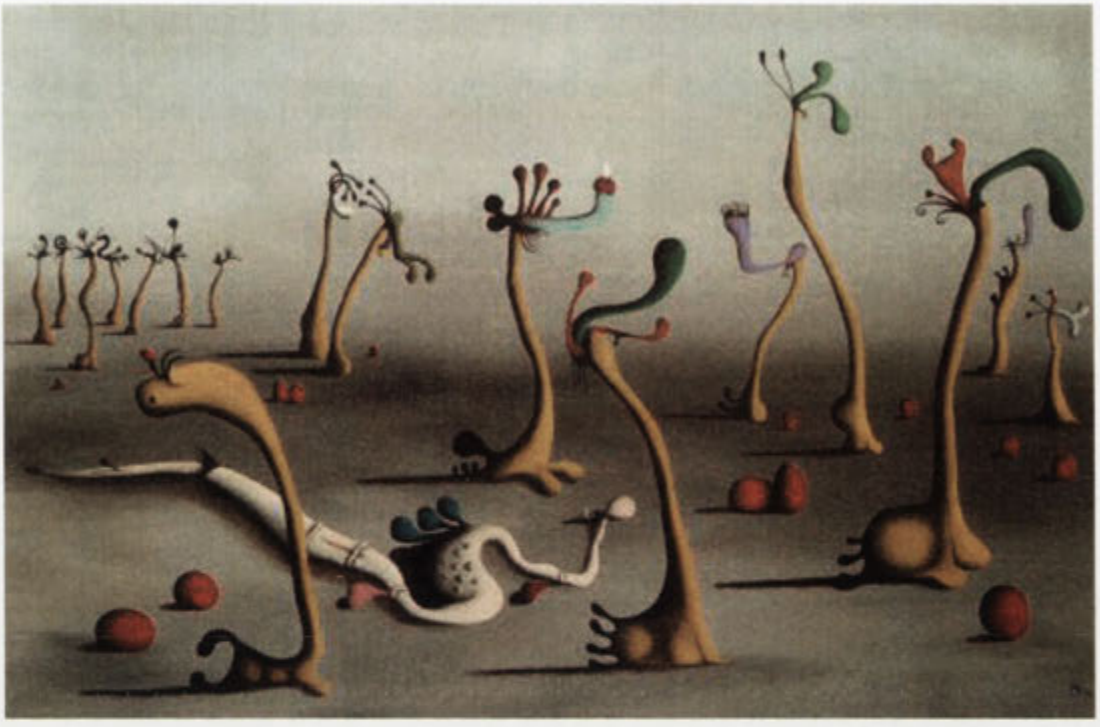

Figure 1.10: Desmond Morris' surrealist painting of biomorphs *Disturbance in the colony*. Adapted, with permission from the artist, from `www.desmond-morris.com/index.php`.

evidence of how such variations arises, which could aid the development of formation mechanisms, or support the ones described in this chapter. This dissertation is also concerned with questions regarding how such life-like structures can influence the identification of ancient microfossils. Is it possible to distinguish between bona fide Archean microfossils and silica-carbonate biomorphs?

The thesis essentially consists of two parts; Chapters 2 - 4 are concerned with the theory and characterisation of biomorphs, whereas Chapters 5 and 6 investigate the morphological and chemical similarity of biomorphs to some of the world's most ancient microfossils.

In Chapter 2 a review of carbonate and silica chemistry is given, where the crystallinity, solubility, and precipitation of such materials are discussed. Specifically, the interference of foreign substances on the morphogenesis is of most particular interest in relation to biomorphs. Self-assembly theory is briefly encountered, as well as biomineralisation.

Chapter 3 presents experimental results of the various morphologies that arise from different synthesis conditions. Chapter 4 presents a discussion on different models that can account for such morphological variety.

In Chapter 5 the Archean environment, in terms of ocean and atmosphere com-

position, is discussed. The nature and identification techniques used to characterise early life is also presented, which will be compared to biomorphs in Chapter 6.

Conclusions and suggestion for further work are presented in Chapter 7.

Chapter 2

Self-assembly in silicate-carbonate systems

2.1 Introduction

This chapter includes an overview of crystal structure and formation of the common carbonates, especially witherite, strontianite and the calcium carbonates. Silica chemistry is also discussed with particular focus on polymerisation and colloidal chemistry. This chapter also outlines self-assembly in general, and its relation to biomineralisation and biomorph precipitation. This will provide valuable information in subsequent chapters when trying to determine the origin of the morphology of biomorphs and theories of their formation.

2.2 Carbonate chemistry

As carbonate chemistry is an intricate part of precipitation of biomorphs, this section will give an introduction to carbonate crystal structure, dissolution and precipitation behaviour. Chapters 5 and 6 will discuss geochemical scenarios for biomorph precipitation, and relate to the geochemical analysis of an Archean carbonate-chert rock. The modification of crystal habit by the use of additives will also be reviewed.

2.2.1 Crystal structures of calcium carbonates

The crystal structures of the common MCO_3 carbonate minerals belong to the calcite-, aragonite- and dolomite-type (Chang et al., 1998), and each of these structures will be presented in this section. Calcium carbonate has several crystalline polymorphs, but calcite, aragonite and vaterite are the only ones that occur naturally (Carlson, 1983). Amorphous calcium carbonate is also known in biological and synthetic systems, where it most often acts as a precursor for crystallisation (Aizenberg et al.,

Name	Formula	Specific gravity	Cell dimensions (Å)	
			a	*c*
Calcite	$CaCO_3$	2.71	4.989	17.061
Magnesite	$MgCO_3$	3.00	4.632	15.012
Siderite	$FeCO_3$	3.97	4.691	15.379
Rhodochrosite	$MnCO_3$	3.70	4.768	15.635
Smithsonite	$ZnCO_3$	4.43	4.652	15.025
Otavite	$CdCO_3$	4.96	4.923	16.787
Gaspéite	$NiCO_3$	4.39	4.608	14.805

Table 2.1: The calcite-type carbonate minerals and their crystallographic data. Adapted after Chang et al. (1998)

1996). Most biomorphs studied in this thesis contain crystalline barium carbonate (witherite)(identified using electron diffraction in Chapter 3). This material is isostructural with the aragonite form of $CaCO_3$. The dolomite-type carbonates, which occur in the Pilbara cherts (Chapter 6) are also discussed below. Furthermore, the origin and depositional environments of all these carbonates are also mentioned.

Calcite

The calcite structure belongs to the rhombohedral carbonates (space group $R\bar{3}c$), which can be described using both the rhombohedral and hexagonal crystal axes. As the hexagonal system is now standard, this system will be used here to describe the calcite structure. The unit cell contains 6 $CaCO_3$ units and is a rhombohedrally-centered hexagonal unit cell with the *a*-axis being 4.99 Å and the *c*-axis 17.06 Å (Reeder, 1983). As can be seen in Figure 2.1 A, layers of Ca atoms alternate with layers of carbonate groups along the *c*-axis. The calcium atoms are in a rhombohedrally compressed version of a cubic closed-packed array, so Ca atoms can be represented as a stacking of hexagonal layers with three possible offsets, in the sequence ABCABC etc (see Figure 2.1 A). All carbonate groups within each layer have the same orientation, but going from one carbonate layer to the next, the groups are rotated 180°. This crystal structure allows calcium atoms to coordinate to 6 oxygen atoms, all from different carbonate groups (see Figure 2.1 F). Each oxygen atom is coordinated to two calcium atoms and one carbon atom. One way to visualise the calcite structure is the construction of an octahedron with one calcium atom at each vertex (see Figure 2.1 B and E). Then, each of the octahedra contain one carbonate group. In Table 2.1 a list of the other metal carbonates that crystallise with the calcite-type structure is given.

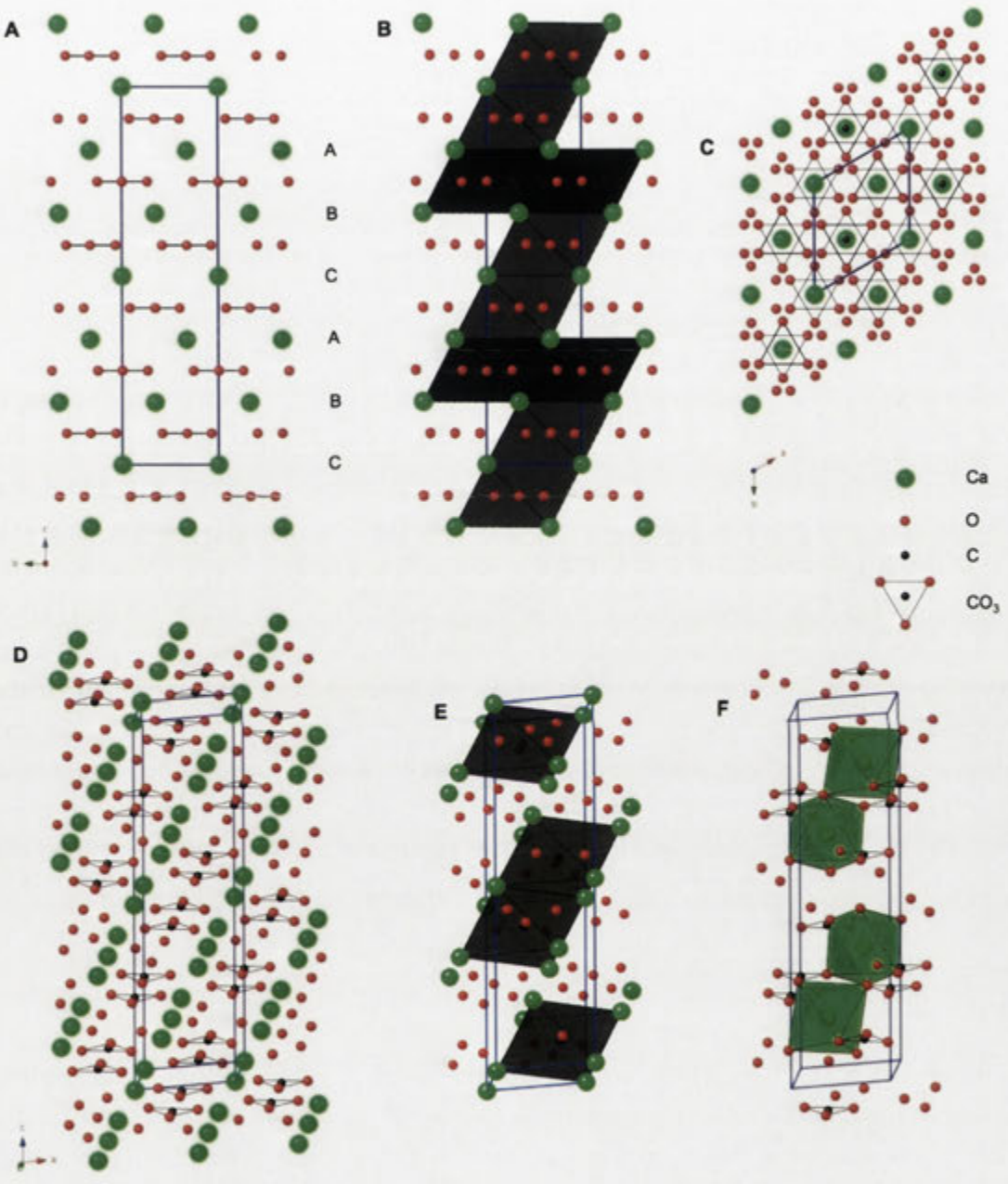

Figure 2.1: The crystal structure of calcite viewed along the <100> (A-B), [001] (C) and [0.237 2.398 0.125] (D-F) directions. Black octahedra in B and E contain one carbonate group each, and these polyhedra are sometimes used to describe the crystal structure of calcite. Green octahedra in F shows the 6-fold coordination of calcium atoms. Models were made with CrystalMaker software, using crystallographic data from the CrystalMaker Library.

Name	Formula	Specific gravity	Cell dimensions (Å)		
			a	*b*	*c*
Aragonite	$CaCO_3$	2.95	4.960	7.964	5.738
Strontianite	$SrCO_3$	3.7	5.090	8.358	5.997
Witherite	$BaCO_3$	4.3	5.312	8.896	6.428
Cerussite	$PbCO_3$	6.55	5.180	8.492	6.134

Table 2.2: The aragonite-type carbonate minerals and their crystallographic data. Adapted after Chang et al. (1998)

Aragonite

The second most common polymorph of calcium carbonate is aragonite, which is stable only at high pressures (~$3.5{\cdot}10^8$ Pa) at room temperature (Alam et al., 1990), or elevated temperatures. The space group for the aragonite structure is *Pmcn*; the structure can be described as successive layers stacked on each other along the *a*-axis in the following way; $AC_1BC_2AC_1BC_2$ etc, where A and B are layers with hexagonally closed packed Ca^{2+} atoms, and C are the CO_3^{2-} (Speer, 1983). As can be seen in Figure 2.2 A, there are two separate layers of carbonate groups (C_1 and C_2). As with calcite, one can construct octahedra with one calcium atom at each vertex to explain the crystal structure of aragonite. It can then be noted that each octahedron contains one carbonate group, which is placed at different heights in neighbouring octahedra, and the direction of the octahedra alters between successive layers. This structure gives rise to Ca atoms that are coordinated to 9 oxygen atoms from 6 different carbonate groups (see Figure 2.2 E). Aragonite and isostructural carbonates are listed in Table 2.2.

Vaterite

The least stable natural crystalline $CaCO_3$ polymorph is vaterite. Both orthorhombic and hexagonal cells have been reported for vaterite (Carlson, 1983; Dupont et al., 1997). The reason for this discrepancy is most likely due to the difficulty in producing large stable crystals for diffraction work. Vaterite is often polycrystalline and forms spherical aggregates composed of nanosized crystals. However, recently a method for stabilising the vaterite structure using polymers produced hexagonal platelets that showed very good crystallinity (Dupont et al., 1997). The orthorhomic vaterite crystal structure with an *a*-axis of 4.13, *b*-axis 7.15, and the *c*-axis 8.48 Å can be seen in Figure 2.3 (Meyer, 1960). In contrast to the other carbonate crystal types, the carbonate groups lie parallel to the *c*-axis, and each calcium atom is coordinated to 8 oxygens.

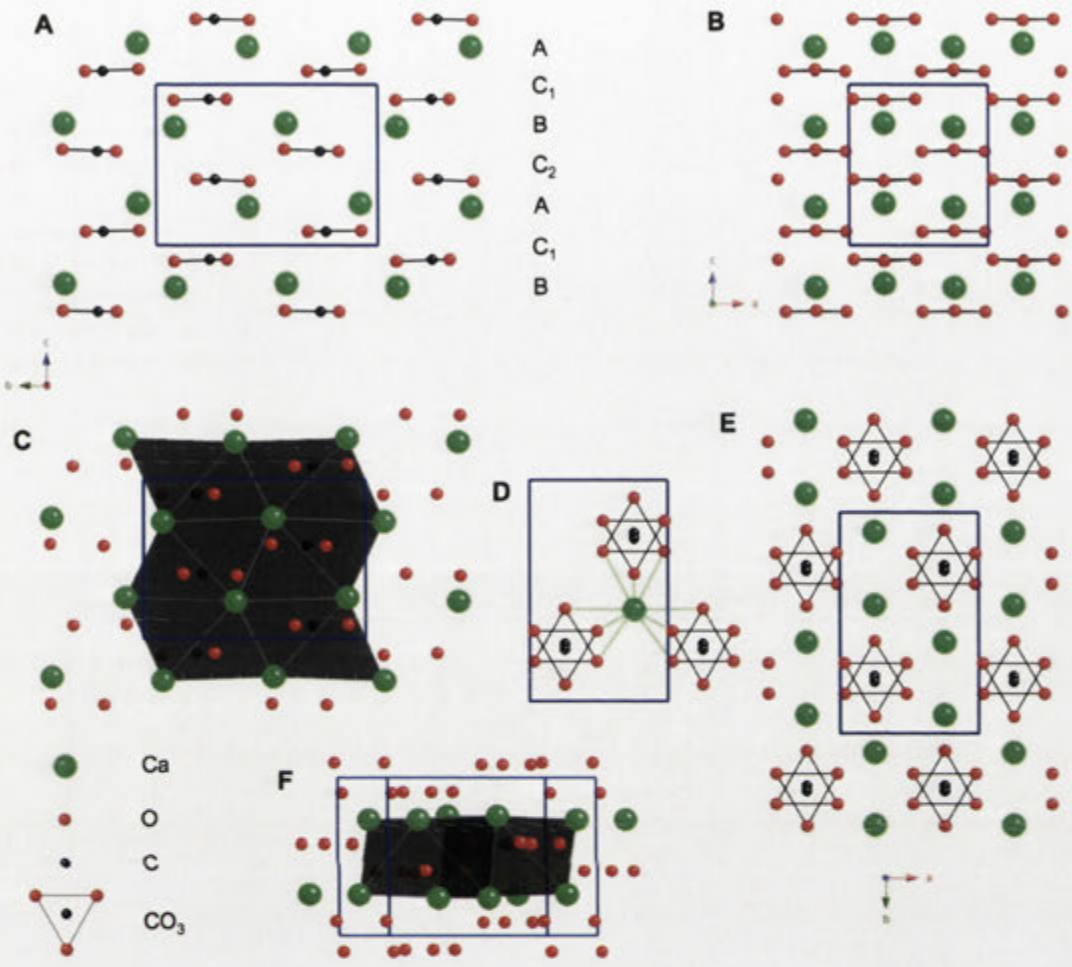

Figure 2.2: The crystal structure of aragonite viewed along the [100] (A, C), [010] (B), and [001] (E) directions. Black octahedra in C and F contain one carbonate group each, placed at different heights in neighbouring octahedra. In D and E Ca is shown to be coordinated to 9 oxygen atoms from 6 different carbonate groups. Models were made with CrystalMaker, using crystallographic data from the CrystalMaker Library.

Dolomite

There are many carbonate minerals based on the calcite-type structure containing more than one type of cation, of which dolomite will be discussed in this section. The dolomite structure is closely related to that of calcite; every other layer of Ca atoms is substituted by Mg atoms (see Figure 2.4). The space group is $R\bar{3}$, and the unit cell contains $3(CaMg(CO_3)_2)$ (Reeder, 1983). Each cation is coordinated to 6 oxygens from different carbonate groups, and each oxygen is coordinated to one Mg and one Ca cation. Carbonates other than dolomite that have the same crystallographic structure and belong to this group are ankerite, kutnahorite, and minrecordite (see Table 2.3).

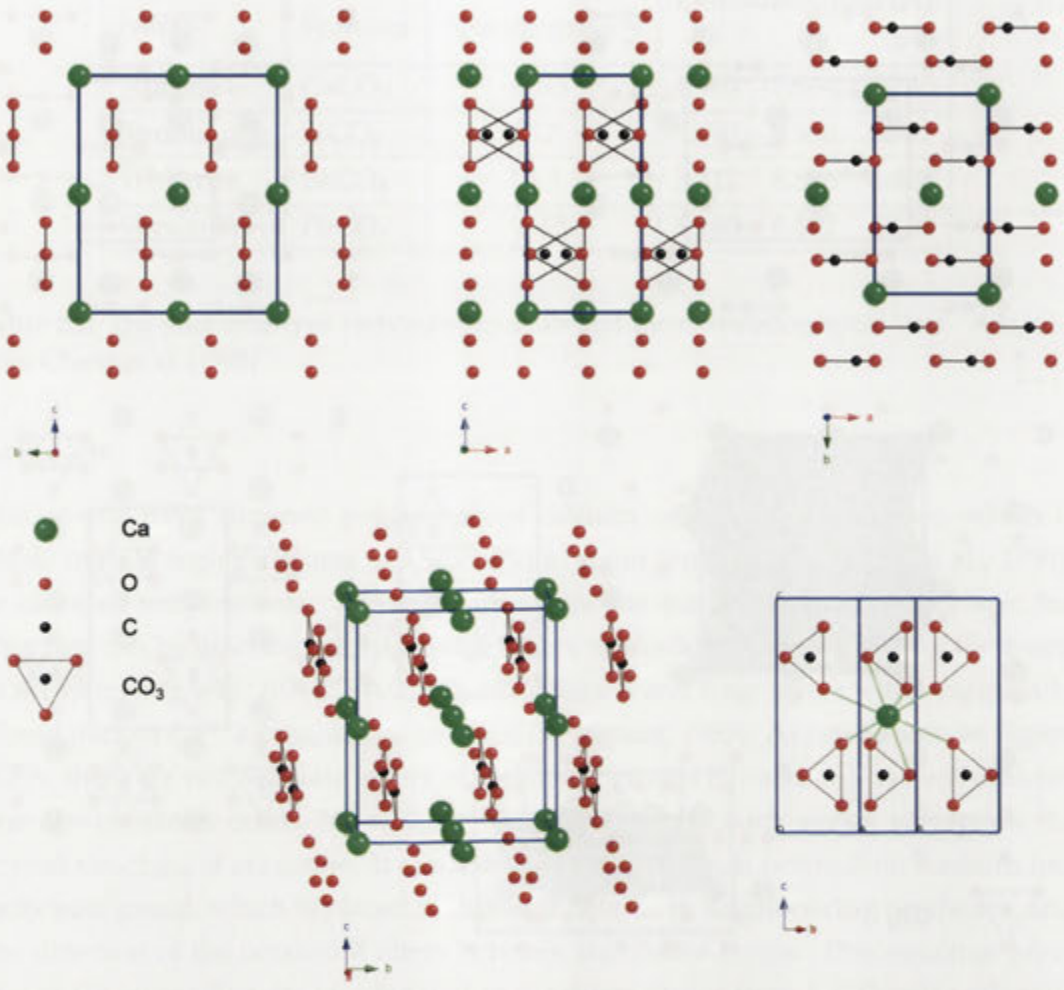

Figure 2.3: The crystal structure of vaterite viewed along the [100], [010], [001] and [2.144 -0.12 0.185] directions. In the bottom right corner one Ca atom is shown to be coordinated to 8 oxygen atoms from 6 different carbonate groups. Models were made with CrystalMaker, using crystallographic data from ICSD (code 27827, reference Meyer (1960)).

These carbonates are all double metal carbonates. There are also other carbonates with more than one type of cation that do not belong to the dolomite group, such as norsethite ($BaMg(CO_3)_2$), and alstonite ($BaCa(CO_3)_2$).

It is interesting to note that biomorphs have so far only been produced with carbonates having the aragonite crystal structure, which suggests that structure-specific factors may be responsible in part for the morphologies seen in this system. In Chapter 4 further discussion regarding the theories of biomorph formation is given.

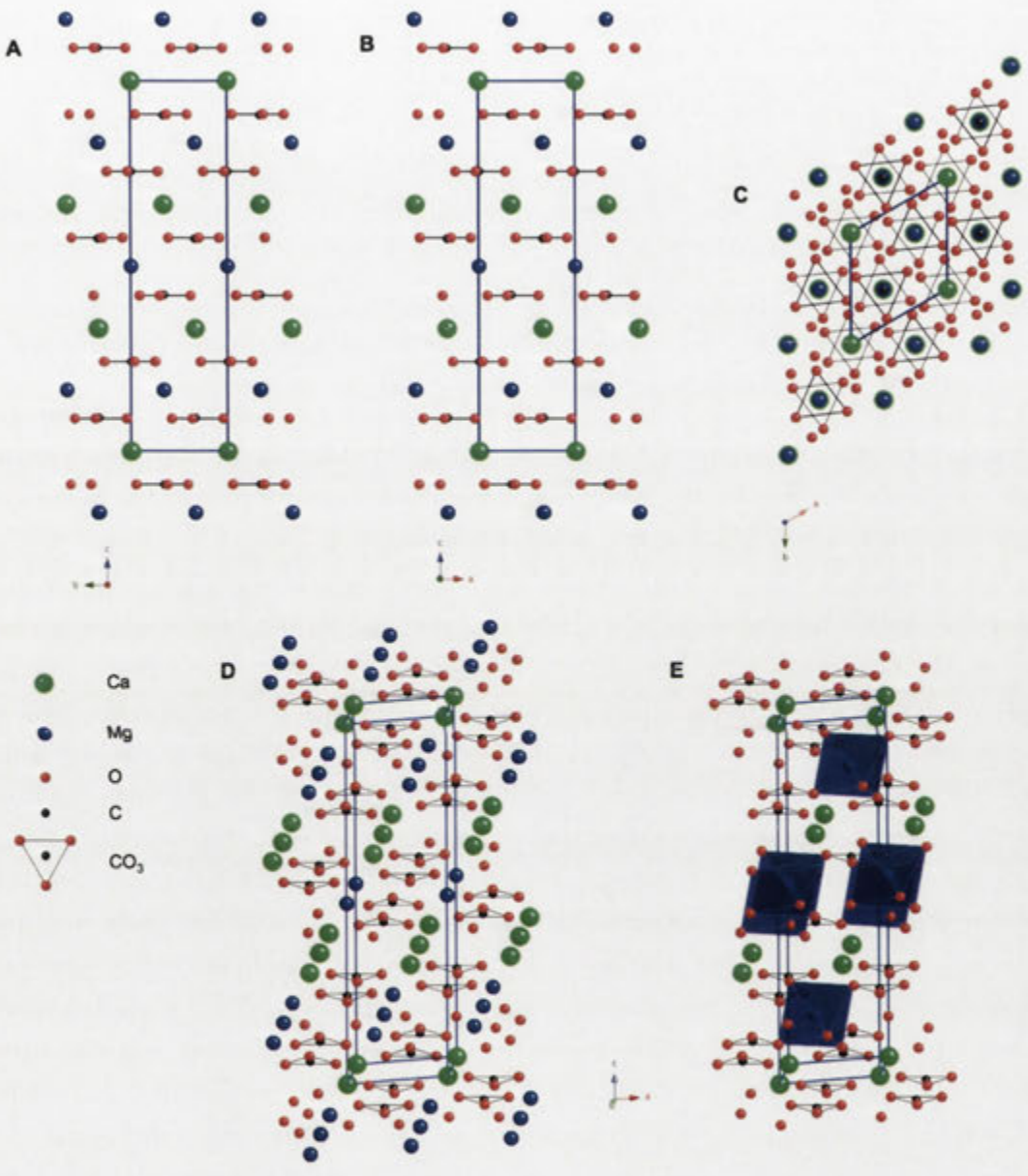

Figure 2.4: The crystal structure of dolomite viewed along the [100], [010], [001] and [1.8 2.5 0.2] directions. Each projection contains four unit cells marked with white lines. Each unit cell contain $3CaMg(CO_3)_2$. The polyhedra in the bottom right corner shows the 6-fold coordination of Mg atom to 6 oxygen atoms, each from different carbonate groups. Models were made with CrystalMaker (Palmer, 2005).

Name	Formula	Specific gravity	Cell dimensions (Å)	
			a	*b*
Dolomite	$CaMg(CO_3)_2$	2.85	4.807	16.003
Ankerite	$Ca(Mg, Fe)(CO_3)_2$	3.01	4.411	16.042
Kutnahorite	$CaMn(CO_3)_2$	3.12	4.873	16.349
Minrecordite	$CaZn(CO_3)_2$	3.45	4.818	16.029

Table 2.3: The dolomite-type carbonate minerals and their crystallographic data. Adapted after Chang et al. (1998)

2.2.2 Polymorphism and solid solutions among the common carbonates

In addition to the naturally occuring calcium carbonate polymorphs, calcite, aragonite, and vaterite, a variety of polymorphs can be synthesised at high temperature and pressures (see Figure 2.5). However, these phases are not relevant to biomorph formation and will not be discussed any further here.

Aragonite is a high pressure phase, and is metastable at room temperature and pressure, where it transforms into calcite (see Figure 2.5). The transformations between calcite and aragonite can occur in both the solid state and via dissolution/re-precipitation reactions in the aqueous phase. Other factors govern this transition as well. For example, calcite is known to undergo a transition to aragonite at high temperature and pressures, during grinding (Burns and Bredig, 1956; Dachille and Roy, 1960), and during exposure to short pulses of CO_2 laser beam (Alam et al., 1990). Aragonite can, however, be synthesised at low temperature and pressures when such a transition is inhibited by specific additives (see Section 2.2.4.2). Similarly, vaterite, which has low density, is metastable with respect to both aragonite and calcite, but can be synthesised at high temperature when transformation to the more stable phases is inhibited (Carlson, 1983). The reason for the wide variety of calcium carbonate polymorphs is the size of the calcium ion. As was described in Section 2.2.1, calcite has 6-fold coordinated calcium ions, whereas in aragonite they are coordinated to 9 oxygen atoms each. The size of the calcium ion is at the larger end for the calcite-type structure, and at the lower limit for the aragonite-type structure.

The preference for the calcite-type structure for carbonates with smaller cations than Ca^{2+} over the aragonite-type structure is due to the size of the cation. Small cations, such as Mg, are too small to bond stably to 9 oxygens. Conversely, large cations,such as Ba, are too large to fit in the 6-coordinated state the calcite structure (Reeder, 1983). The large size of the barium, strontium and lead cations in single carbonates therefore forces the carbonate to adopt the orthorhombic crystal structure.

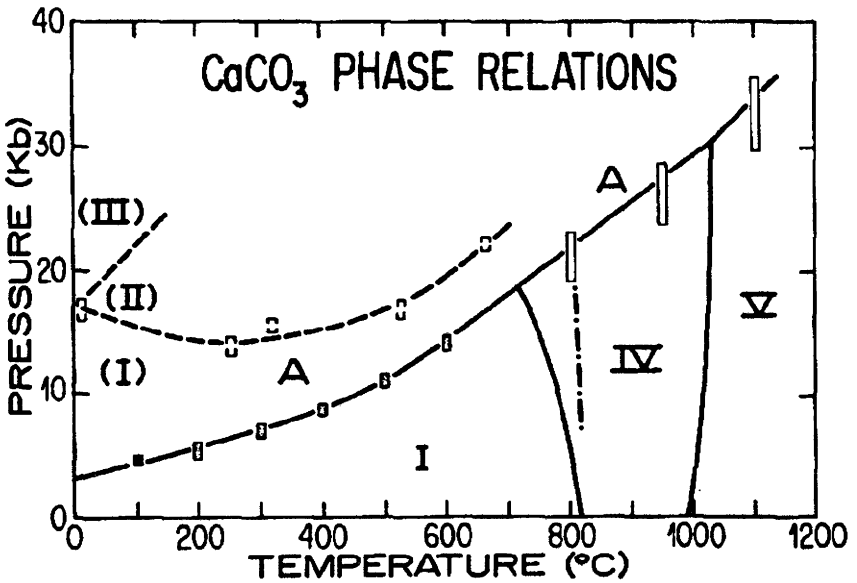

Figure 2.5: Phase relations between the calcium carbonate polymorphs. Metastable equilibria are represented by dashed lines, A stands for aragonite and I-V represent calcite and different calcite-like modifications. Diagram adapted from Carlson (1980).

Both $BaCO_3$ and $SrCO_3$ also have rhombohedral and cubic polymorphs, but these only form at very high temperature and pressures and will therefore not be further discussed (Weinbruch et al., 1992; Chang et al., 1998).

Classical crystal habit

The equilibrium shape of crystals is governed by the individual growth rates of different crystallographic faces. The most slowly growing faces develop the largest faces, a phenomenon related to the surface free energy and therefore the packing of the atoms at this interface. Generally, the most energetically favourable faces have densely packed atoms (low Miller indices), and the developing habit always has the same symmetry as the unit cell (Hartman, 1973; Mann, 2001). Common crystal morphologies of calcite and aragonite are respectively rhombohedral and needle-like.

Calcite crystals can adopt a wide range of morphologies; more than 300 crystal forms have been identified. The two most common crystal habits are the rhombohedral, which give rise to blocky crystals whith noticeable rhombohedral faces, and the prismatic-scalenohedral, which produce crystals with prismatic- and scalenohedral faces, crystals that are often referred to as 'dog-tooth spar' (Chang et al., 1998).

As with calcite, aragonite can form a great variety of crystal morphologies. The most common needle-like habit contains pseudo-hexagonal columns that are produced by twinning, discussed below (Chang et al., 1998). Strontium carbonate (strontianite)

commonly occurs as needle-like and fibrous crystals, which are elongated along the *c*-axis, and columnar crystals that are often cyclically twinned like aragonite and witherite. As has been mentioned previously, vaterite tends to form polycrystalline spherical aggregates, however other morphologies have been reported. Examples of aragonite needles, rhombohedral calcite, and a flower-like type of vaterite can be seen in Figure 2.10.

Twinning

During the crystallisation of orthorhombic carbonates, twinning often occurs on the (110) plane, i.e. the orientational order of the carbonate groups changes within a layer. Twinning in aragonite gives rise to a 60° rotation of the crystal *a*- and *b*-axes (see Figure 2.6 A). This often results in cyclic twins, or trillings, that have a pseudo-hexagonal morphology (Speer, 1983). Witherite occurs as white or grey, to brown or green crystals that are always twinned on {110}, which give rise to a bipyramid pseudo-hexagonal crystal morphology (see Figure 2.6 B) (Chang et al., 1998). Faces present are {010}, {021}, and {012}. An interpretation of the crystal habit of witherite and the faces present can be seen in Figure 2.6. It is clear from the high frequency of twinning that twinning boundary energies are very low in this structure.

Solid solutions

Depending on the conditions of the crystallising medium, the compositions of the precipitated carbonates can vary. The degree of solubility between the common carbonates largely depend on crystallographic relationships and the temperature and pressure of the system. In this section some of the common solid solutions are described, which will relate to the geochemical analyses presented in Chapter 6, as well as to biomorph synthesis experiments described in Chapter 3.

End-member carbonates that have a calcite-type structure include those of Mg, Fe, Cd, Mn, Zn, Co and Ni, which all have a smaller unit cell than calcite (see Table 2.1) (Reeder, 1983). Solid solution of these carbonates are more or less restricted depending on the size difference between the cations. Generally, smaller size differences give larger miscibility. Carbonates with cations larger than Ca are forced into the aragonite structure.

The most common ions that can substitute for calcium in calcite include magnesium, manganese, and ferrous iron. Magnesian calcites with up to 30 mol% $MgCO_3$ in skeletons of marine organisms and carbonate cements have been reported, and calcite containing 48 mol% magnesium has been found in deep-sea sediments. However, calcite with more than ~4% Mg is known to be metastable at low temperatures (see Figure

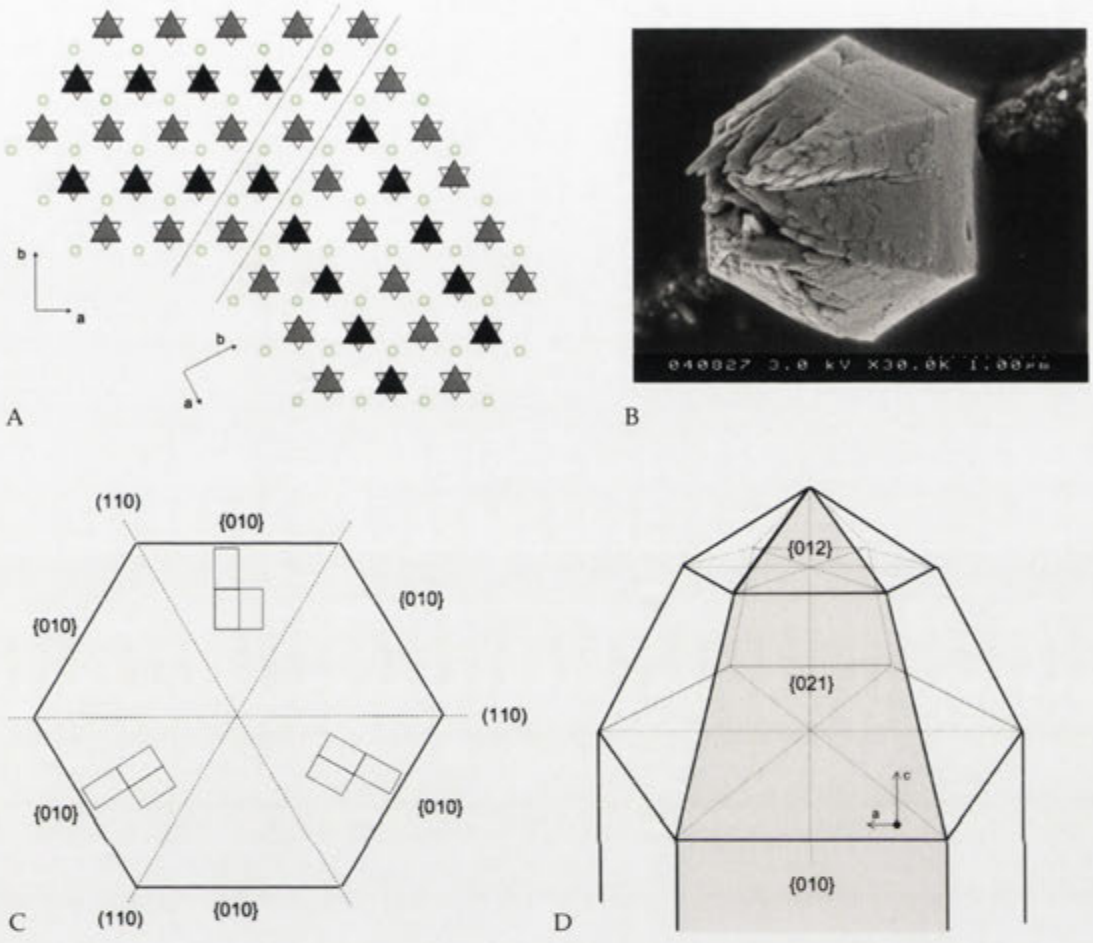

Figure 2.6: Schematic model of the (110) twinning which is very common in aragonite-type carbonates (A). The green circles represent calcium ions, and the different shades of grey represent carbonate groups at different heights (compare Fig 2.2 A). A witherite cyclic twin, displaying pseudohexagonal crystal structure (B).. In C and D the crystal faces on a schematic columnar crystal of witherite can be seen. Note that the crystal faces in C and D are not drawn to relative scale. A is redrawn from (Speer, 1983)

2.7). The Mg concentration in magnesian calcites is related to temperature, as well as Mg^{2+}/Ca^{2+} ratio and the CO_3^{2-} concentration of the associated water (Mackenzie et al., 1983). In the $CaCO_3$ – $FeCO_3$ system, no pure end-member $CaFe(CO_3)_2$ compound exists, and this system therefor shows limited solubility between the end members. Solid solutions with Fe>Mg are common, however. Natural calcite commonly contain 2-3 % ferrous iron, however, higher concentrations, up to 12 %, have been reported for specific geological locations (See Figure 2.7). Barium and strontium can also be incorporated into calcite, but only at very small amounts (ppm range) (Chang et al., 1998).

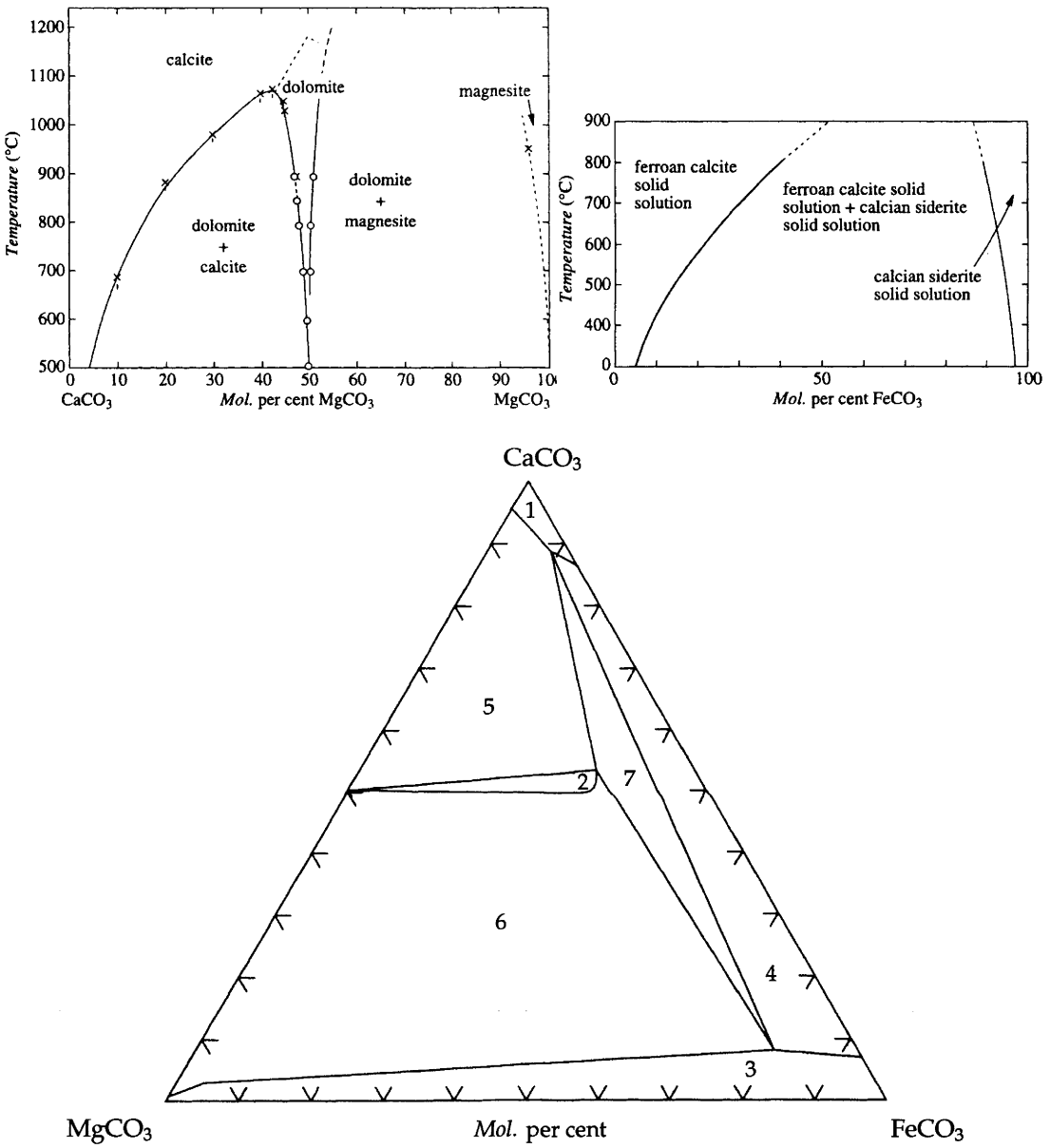

Figure 2.7: Phase diagrams of solid solutions within the $CaCO_3$-$MgCO_3$-$FeCO_3$ system. The experimentally solved binary system from calcite to magnesite shows limited solubility of Mg in calcite, and vice versa, and solubility increases with temperature (top left). Increasing temperature also increases Fe solubility in calcite (top right). The ternary phase diagram of Mg, Ca, and Fe containing carbonates at 450 °C is composed of seven different fields, differentiated by the presence of various phases: 1) calcite solid solution; 2) dolomite solid solution; 3) magnesite-siderite solid solution; 4) calcite solid solution + magnesite-siderite solid solution; 5) calcite solid solution + dolomite solid solution; 6) dolomite solid solution + magnesite-siderite solid solution; 7) calcite solid solution + dolomite solid solution + magnesite-siderite solid solution. Adapter from Chang et al. (1998).

Natural witherite containing up to 11 mol% Sr have been reported (Baldasari and Speer, 1979), and a complete solid solution between witherite and strontianite does occur at very high temperatures (above ~ 400°C) (Chang, 1965; Chang et al., 1998). Ca and Mg can also substitute for Ba, but only in very small amounts. Chang (1965) showed the phase relations between $BaCO_3$ – $SrCO_3$, $SrCO_3$ – $CaCO_3$ and $BaCO_3$ – $CaCO_3$. At 400°C $BaCO_3$ can incorporate ~ 3.5 mol% Ca, but no significant Ba exists in $CaCO_3$ below 600°C. However, above 850°C a complete solid solution series exists in a disordered rhombohedral form between $CaCO_3$ and $BaCO_3$. Pb does not substitute for Ba in witherite at ambient conditions, but at very high temperatures it has been experimentally shown that cerussite and witherite form a solid solution (Boström et al., 1969; Chang and Brice, 1972; Chang et al., 1998). Several double carbonates with Ba occur, such as barytocalcite ($CaBa(CO_3)_2$), alstonite ($CaBa(CO_3)_2$), paralstonite ($CaBa(CO_3)_2$), and norsethite ($MgBa(CO_3)_2$). Substitutions for strontium in strontianite include Ca, Ba and Pb. Natural strontianite can contain up to 10 wt% Ca, and at high temperature and pressures the $CaCO_3$ – $SrCO_3$ system forms a complete solid solution. Pb and Ba may also substitute for strontium but to a much lesser degree than Ca (Chang et al., 1998). As was mentioned before, a complete solid solution system exists between $BaCO_3$ – $SrCO_3$ at elevated temperatures. Furthermore, at 15 kbar and 550 °C, a complete solid solution exist between $BaCO_3$, $SrCO_3$, and $CaCO_3$ in the aragonite structure (Chang et al., 1998).

Dolomite rarely occurs as pure $CaMg(CO_3)_2$ (Warren, 2000), and the Mg cation can be substituted for Fe, Mn and Zn. Dolomite forms a complete solution into the ankerite field. As was mentioned earlier, end-member $CaFe(CO_3)_2$ has so far not been found in nature nor has it ever been experimentally produced (Chang et al., 1998).

2.2.3 Geological occurrences of carbonates

The natural carbonates show a large variation in composition, age and place of occurrence. Sedimentary carbonates account for 20 to 25 % of all sedimentary rocks (Boggs Jr., 2001). The most common natural carbonates are calcite and dolomite ($(Ca,Mg)(CO_3)_2$); they account for more than 90 % of all naturally produced carbonates (Reeder, 1983). Rocks that are mostly composed of calcite is referred to as limestones, and rocks with predominantly dolomite are confusingly called dolomite (or sometimes dolostones).

Calcite occurs in all three main rock types; sedimentary, metamorphic, and igneous rocks. Furthermore, it can also be found in hydrothermal deposits (Chang et al., 1998). Sedimentary calcite comprises both biologically produced materials, such as shells of marine organisms, and abiological calcite precipitated from solution. Calcitic

biominerals will be discussed in Section 2.4. Sedimentary calcite occurs as fine grains in marl and calcareous shale, cementing material in detrital sediments, as stalagmites and stalactites in caves, and sometimes as large crystals in vugs and geodes. Large calcareous 'towers' can precipitate form hot springs and streams, as well as alkaline lakes (Chang et al., 1998; Kazmierczak et al., 2004). Natural calcite is normally quite pure, but substitution of calcium by magnesium, manganese and ferrous iron is relatively common. This is the case for calcite occurring in the 'zebra-rock' for which analytical data is presented in Chapter 6. Although the presence of strontium and barium in calcite is rare, calcite occurring in igneous rocks (carbonatite) are enriched in strontium and barium.

Aragonite is the most common natural carbonate among the aragonite-structure minerals (Speer, 1983). This is because aragonite is a common biomineral in many invertebrates. In addition, aragonite occurs in recent marine sediments as needles or ooliths (spherical forms with a radial internal structure), and is also present in many evaporites and also in high pressure (blueschist facies) metamorphic rocks (Speer, 1983; Chang et al., 1998). Extensive aragonite precipitation has been proposed to have occurred in the 1.9-billion-year-old Rocknest Formation, Canada, as well preserved primary fabrics are preserved in these rocks. The aragonite was later replaced with dolomite and silica (Grotzinger and Reed, 1983). Most orthorhombic carbonates are formed as replacement minerals formed in low/temperature pressure fluids in sedimentary, metamorphic, and igneous rocks as well as ore deposits (Reeder, 1983).

Witherite generally occur as a relatively pure form of $BaCO_3$, but significant substitution of Sr can occur. Witherite is an uncommon mineral, but the second most common barium mineral after barite ($BaSO_4$). It occurs as deposits in low-temperature hydrothermal veins, and often in association with barite. It is generally believed that witherite is produced by alteration of barite with carbonated waters (Baldasari and Speer, 1979; Chang et al., 1998).

Strontianite commonly occurs as a low-temperature hydrothermal mineral in veins, cavities and concretions in calcarous clays and limestones. It is often associated with celestite $SrSO_4$, barite $BaSO_4$, calcite or gypsum ($CaSO_4 \cdot 2H_2O$) (Chang et al., 1998). In many cases it can be seen that the strontianite was formed as a alteration product of celestite. Suárez-Ordũna et al. (2004) experimentally showed that natural celestite will convert to strontianite under alkaline hydrothermal conditions with the concomitant release of Ba originally present in the celestite. The overall morphology of the crystal did not change during this treatment, but a new porous texture developed in response to the crystallographic dimensional change.

Dolomite is quite a rare mineral in modern rocks, a fact that has bewildered scientists for decades, as the surface waters are supersaturated with respect to dolomite.

However, dolomite is a common constituent of ancient rocks (Baker and Kastner, 1981; Arvidson and Mackenzie, 1999). Dolomite can form as a primary mineral, a secondary replacement, or as a hydrothermal/metamorphic mineral, but very rarely occurs as the ideal composition $CaMg(CO_3)_2$. Known compositions range from $Ca_{0.96}Mg_{1.04}(CO_3)_2$ to $Ca_{1.16}Mg_{0.94}(CO_3)_2$, and often contain Fe, Mn, and Zn (Warren, 2000). However, most of the dolomite present in the geological record is generally believed to have formed from diagenic replacement of limestone, through process(es) termed dolomitisation. Several different models have been proposed to explain the dolomitisation process, but the mechanism is still not completely understood. Generally, it is believed that dolomite evolves as magnesium rich pore fluids re-equilibriate with the parent rock through dissolution/precipitation reactions. Dolomitisation is seen as a potentially continuous process that is only limited by the fluid flow in the rock matrix (Warren, 2000).

It should be noted that much of the present day calcite and aragonite is in fact biogenic. Broken pieces of these biominerals form clasts in sedimentary rocks. They also occur in biologically mediated sedimentary structures, called stromatolites (see Section 5.3.4).

2.2.4 Precipitation and growth of carbonates

This section will discuss the conditions that allow for carbonate dissolution and precipitation, as well as crystal morphogenesis under different conditions. Carbonates can be precipitated by both biological and abiological physio-chemical processes (Braithwaite, 2005). As biogenically produced carbonates will be discussed in Section 2.4, only the abiogenic ones will be discussed here. The precipitation and growth behaviour of carbonates are functions of the aqueous carbonate chemistry. The equilibrium reactions controlling the types of carbonate ions present will first be discussed, followed by a section on the precipitation and dissolution of carbonates. In addition, examples of precipitated carbonates under varying conditions will serve as examples of how morphology, chemistry, and crystal growth are intertwined in regards to size and shape of the crystals formed. Combined, it is hoped that these sections will provide a base for elucidating biomorph morphogenesis.

2.2.4.1 The carbonate system

Atmospheric carbon dioxide dissolves in water, forming aqueous carbonate species as it is combined with H_2O. Carbon dioxide exists in three different forms in aqueous systems; as aqueous carbon dioxide ($CO_2(aq)$), as bicarbonate ions (HCO_3^-) and as

carbonate ions (CO_3^{2-}), related by the equilibria:

$$CO_2(aq) + H_2O \rightleftharpoons H_2CO_3 \rightleftharpoons HCO_3^- + H^+ \rightleftharpoons CO_3^{2-} + 2H^+ \tag{2.1}$$

The concentration of H_2CO_3 is very low compared to $CO_2(aq)$ ($[CO_2(aq)] \sim 650[H_2CO_3]$ at 25°C) so these neutral species are normally denoted by CO_2 (see Equation 2.2). The concentration of dissolved CO_2 is given by Henry's law, $[CO_2] = K_0(T,S) \cdot p_{CO_2}$), which states that the concentration of a soluble gas in solution is directly proportional to the partial pressure of the gas above the solution. $K_0(T,S)$ is the temperature and salinity dependent solubility coefficient of CO_2 in seawater. An increase in temperature results in a decrease in $K_0(T,S)$ at constant salinity, and a decrease in salinity at constant temperature will cause an increase in $K_0(T,S)$: thus CO_2 is more soluble at low temperatures and salinities. For instance, $K_0(25°C,S=35)=0.0284$, whereas $K_0(25°C,S=0)=0.0341$ (see Equation A.3) (Zeebe and Wolf-Gladrow, 2001).

$$CO_2 + H_2O \overset{K_1}{\rightleftharpoons} HCO_3^- + H^+ \overset{K_2}{\rightleftharpoons} CO_3^{2-} + 2H^+ \tag{2.2}$$

In Equation 2.2, K_1 and K_2 represent the thermodynamic equilibrium constants and are normally referred to as the first and second dissociation constants of carbonic acid. These constants related to the activities of the chemical species:

$$K_1 = \frac{\{HCO_3^-\}\{H^+\}}{\{CO_2\}} \tag{2.3}$$

$$K_2 = \frac{\{CO_3^{2-}\}\{H^+\}}{\{HCO_3^-\}} \tag{2.4}$$

where the activities of a given chemical species $\{CO_3^{2-}\}$ is related to its concentration $[CO_3^{2-}]$ as $\{CO_3^{2-}\} = \gamma_{CO_3^{2-}}[CO_3^{2-}]$. The term $\gamma_{CO_3^{2-}}$ is the activity coefficient of the carbonate ion, which can be approximated using the extended Debye-Hückel equation (see Equation A.1). For example, at low ionic strengths (0.1 mM), $\gamma_{CO_3^{2-}} = 0.96$, whereas at an ionic strength of 50 mM $\gamma_{CO_3^{2-}} = 0.46$. In diluted systems one can use the stoichimetric equilibrium constants, denoted by * as K_1^* and K_2^*, which are related to the concentration of the individual chemical species:

$$K_1^* = \frac{[HCO_3^-][H^+]}{[CO_2]} \tag{2.5}$$

$$K_2^* = \frac{[CO_3^{2-}][H^+]}{[HCO_3^-]} \tag{2.6}$$

T°C	S	P (atm)	pK_1^*	pK_2^*
25	35	1	5.86	8.92
25	0	1	6.35	10.33
0	35	1	6.11	9.38
0	35	300	5.96	9.29

Table 2.4: Values of the stoichiometric equilibrium constants for carbonate system at various temperatures and salinities. Adapted after Zeebe and Wolf-Gladrow (2001).

The stoichiometric equilibrium constants K_1^* and K_2^* are dependent on temperature (T), pressure (P) and salinity (S). A decrease in either temperature or salinity results in an decrease in the equilibrium constants, whereas the opposite applies to an increase in pressure (see Table 2.4). Another important quantity for carbonate systems the total dissolved inorganic carbon (C_T) which is defined as:

$$C_T = [CO_2] + [HCO_3^-] + [CO_3^{2-}] \tag{2.7}$$

Two models that are commonly used to characterise the carbonate system are the 'closed' and the 'open' systems. In the closed system the solution is closed to the atmosphere and aqueous CO_2 is treated as a non-volatile species, i.e. the system is characterised by a constant C_T. By plotting the logarithm of concentrations of the individual carbonate species against pH at constant C_T, a so called Bjerrum plot is obtained (see Figure 2.8 A, and Appendix A.1.1). In Figure 2.8 A it is evident that CO_3^{2-} is the dominant carbonate species at high pH, i.e. above pK_2^*. Furthermore, the shape of the Bjerrum plot is independent of C_T. However, the plot will move down vertically with decreasing C_T (pK_1^* and pK_2^* are constant). As the equilibrium constants are dependent on temperature, salinity, and pressure, the Bjerrum plot will shift horizontally with a change in these parameters. pK_2^* is more sensitive to such changes than pK_1^*, so the equivalence points (pH=pK) will shift relative to each other (Zeebe and Wolf-Gladrow, 2001). The closed system is useful when considering a system that does not equilibrate with the atmosphere, such as during acid-base titrations of a water sample in the laboratory or water in groundwater systems (Stumm and Morgan, 1996).

In the open system, the solution is allowed to equilibrate with a constant p_{CO_2} (atmospheric p_{CO_2} is 365 μatm). At equilibrium, $[CO_2]$ is independent of pH as it is only determined by p_{CO_2}. Then, the logarithmic concentrations of the other carbonate species are linear with respect to pH (see Figure 2.8 B, and Apeendix A.1.2). As can be seen in Figure 2.8 B, systems in equilibrium with the atmosphere at high pH accommodate higher C_T than at low pH, as the carbonate equilibria reactions are shifted

to the right (see Equation 2.2). The open system is useful when considering aqueous systems in contact with the atmosphere (Stumm and Morgan, 1996). Biomorph precipitation experiments are such systems. An alkaline solution open to equilibriate with atmospheric CO_2 will absorb CO_2, thereby lowering the pH, till equilibrium conditions are reached. In the presence of Ca^{2+}, or other cations that can precipitate as carbonates, CO_2 will continue to absorb into the solution till it has reached supersaturation and solid carbonate will precipitate. This is the case for biomorph precipitation experiments, as the reaction mixture contains $BaCl_2$ and silica at high pH. Continuous absorption of CO_2 from the air produces CO_3^{2-} and HCO_3^- at high pH, $CO_2 + OH^- \rightarrow HCO_3^- \rightarrow CO_3^2 - +H^+$ (Pinsent et al., 1956), and throughout the experiment pH is lowered as more and more CO_2 is absorbed. Eventually, supersaturation is reached and barium carbonate precipitates.

2.2.4.2 Dissolution and precipitation of carbonates

This section will discuss the factors controlling dissolution and precipitation of calcite, aragonite, vaterite, witherite, and strontianite.

The solubility equilibrium of calcium carbonate, its stoichiometric solubility product, K^*_{sp}, and the saturation state are defined as:

$$CaCO_3(s) \rightleftharpoons Ca^{2+} + CO_3^- \tag{2.8}$$

$$K^*_{sp} = [Ca^{2+}]_{sat} \cdot [CO_3^{2-}]_{sat} \tag{2.9}$$

$$pK_{sp} = pK^*_{sp} - \log(\gamma_{Ca^{2+}} \cdot \gamma_{CO_3^{2-}}) \tag{2.10}$$

$$\Omega = \frac{[Ca^{2+}] \cdot [CO_3^{2-}]}{K_{sp}} \tag{2.11}$$

As discussed in previous section, for exact calculations the activities should be used instead of concentrations as displayed in Equation 2.8, 2.9, and 2.11. Again, this is due to ion pairing in solutions with high ionic strength. The relationship between pK^*_{sp} and pK_{sp} can be seen in Equation 2.10. The concentrations used in the stoichiometric solubility products are the total concentrations, i.e. both 'free' and 'ion-paired' ions. The saturation state Ω defines a specific situation as undersaturated if $\Omega < 1$, which will lead to dissolution of the mineral, and supersaturated if $\Omega > 1$, which will lead to precipitation if all conditions permit. Some degree of supersaturation is needed for nucleation to occur. The degree of saturation is one of the main factors controlling the rate of reaction. Generally, the rate of dissolution or precipitation is faster with the system is far from equilibrium (Morse, 1983). Furthermore, the rate of precipitation exerts a strong influence on which $CaCO_3$ is produced. High precipitation rates favours

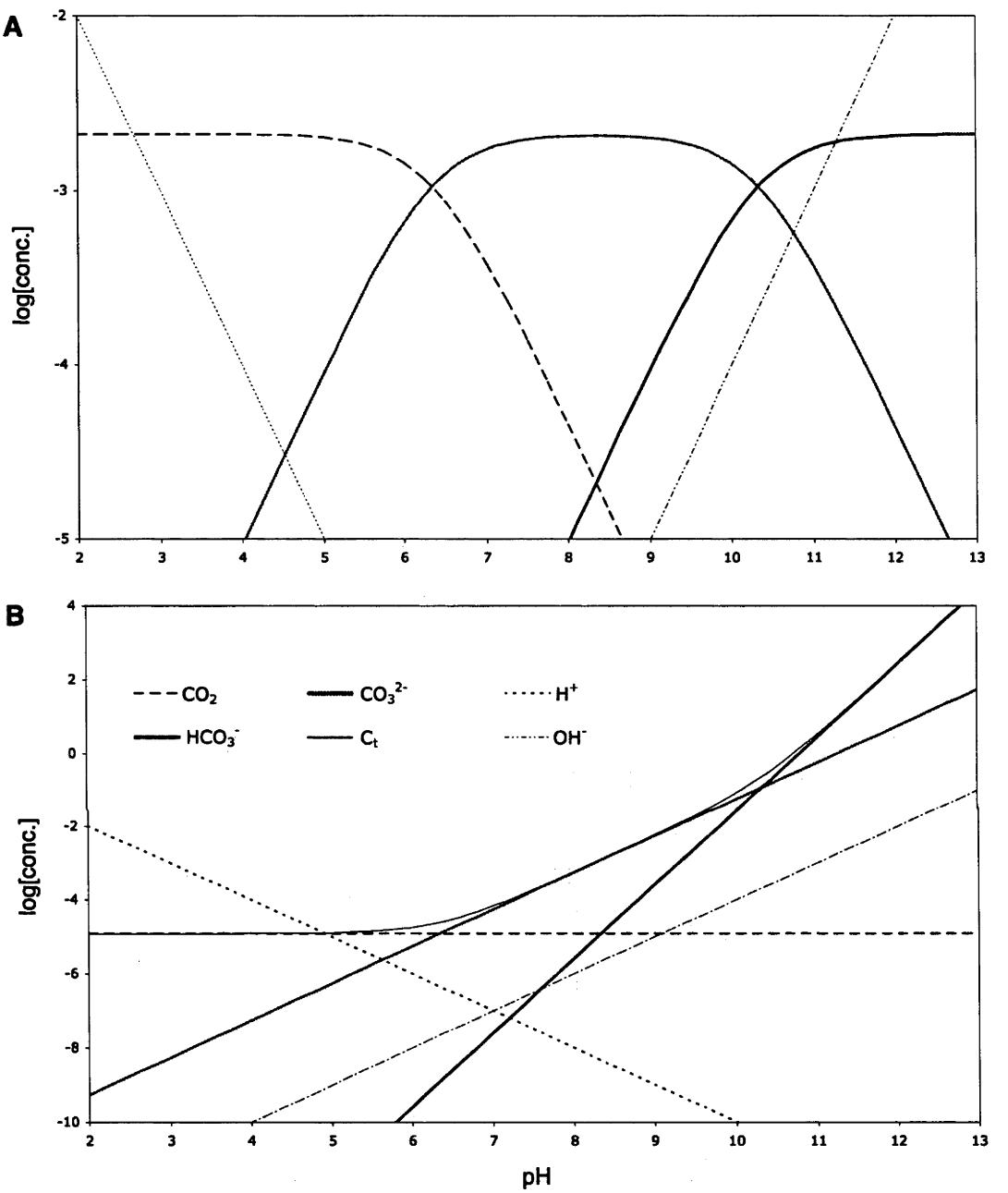

Figure 2.8: Two models, closed (A) and open (B) systems, that graphically characterise the aqueous carbonate system. For a detailed description of the construction of such graphs, see Appendix A.

the formation of aragonite, even though calcite is the most thermodynamically stable phase. Specifically, if the flux of CO_3^{2-} is high, aragonite will be the favoured $CaCO_3$ phase (Meldrum and Hyde, 2001). The solubility product is dependent on temperature, salinity, and pressure, as other equilibrium constants are. All orthorhombic

carbonates show decreased solubility at higher temperatures (Helz and Holland, 1965; Busenberg and Plummer, 1986) (see Figure 2.9 A, Appendix A.2 with Table A.1).

The solubility product of calcite has been determined under a variety of conditions, including variation in temperature, pressure, and in the presence of other ionic species (Miller, 1952; Ellis, 1959; Segnit et al., 1962; Plummer and Busenberg, 1982; Millero et al., 1984). The solubility of calcite decreases at higher temperatures and constant pressure (see Figure 2.9 A). An increase in p_{CO_2} results in an decrease in calcite solubility, as higher $[CO_3^{2-}]$ is established at equilibrium. The effect of other ionic species on the solubility of calcite has shown to increase the solubility, even though CO_2 is less soluble in solutions with high ionic strength. Miller (1952) presumed that this phenomenon could be explained by the 'salting-in' effect described by the Debye-Hückel theory. The activity coefficient will decrease with an increase in ionic strength (see Equation A.1 and A.2), leading to a higher required concentration at equilibrium. The presence of additional electrolytes decrease the number of collisions on the crystal surface that lead to solubilised ionic species, so an increase in concentration is necessary to maintain equilibrium. However, the type of salt used is of great importance to this behaviour. The solubility of calcite in a closed system with various amount of CO_2 has also shown to increase with a decrease in pH (see De Visscher and Vanderdeelen (2003) and references therein).

In contrast to calcium carbonates, studies of the solubility of barium and strontium carbonate is not as frequent in the literature. Busenberg and Plummer (1986) were the first to determine the temperature dependance of the solubility product of $BaCO_3$. As in the case of calcium carbonates, it is important to include the ion pairs $BaHCO_3^+$ and $BaCO_3^0$ when characterising the aqueous model of $BaCO_3$. Helz and Holland (1965) determined the solubility of strontianite at 50, 100 and 200 °C at pCO_2 between 1 and 50 atm. They found that strontianite is more soluble at higher pressures at constant temperature, but the solubility decreases at higher temperatures at constant pressure. So cooling of a solution in equilibrium with stronitianite at constant pressure will dissolve the mineral (Helz and Holland, 1965). In Figure 2.9 A the thermodynamic solubility products for calcite, aragonite, vaterite, witherite and stronitanite are plotted against temperature. Strontianite is the least soluble carbonate of the ones analysed in this figure, and witherite is comparatively much more soluble than strontianite in water. Aragonite, on the other hand, is more soluble than calcite, which is believed to aid the aragonite to calcite transformation. Vaterite, which is unstable at room temperature and pressure, is the most soluble calcium carbonate polymorph. Even though calcite is the only thermodynamically stable calcium carbonate phase at room temperature and pressure, aragonite and vaterite can be precipitated from aqueous solutions under these conditions if calcite precipitation is sufficiently slow.

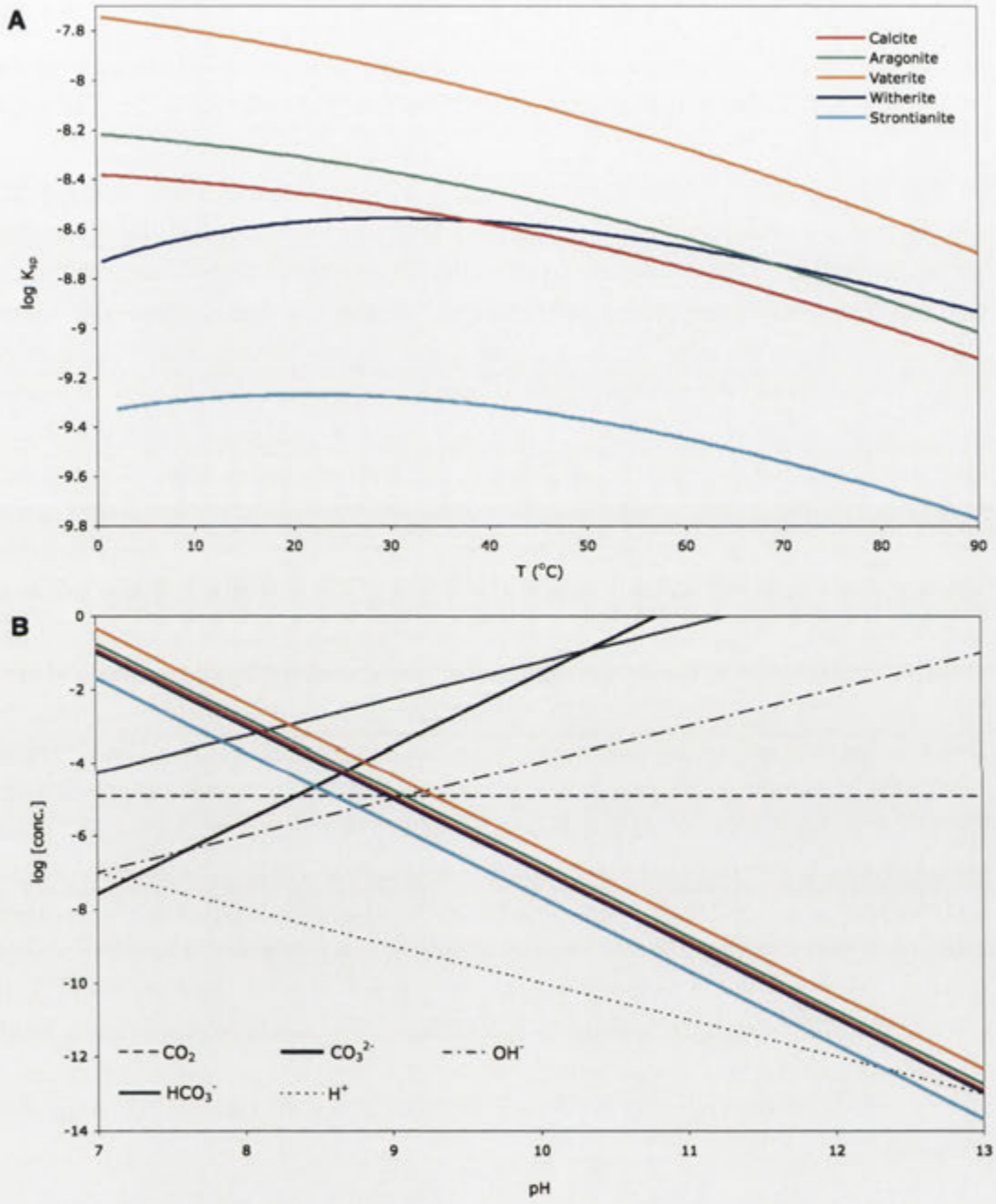

Figure 2.9: The solubility of witherite, strontianite, calcite, aragonite, and vaterite as a function of temperature (A). The solubility equations used to plot this graph were taken from Plummer and Busenberg (1982) for the aragonite, calcite, and vaterite, Busenberg and Plummer (1986) for witherite, and Busenberg et al. (1984) for strontianite (see Appendix A.2). The equilibrium concentrations of Ca^{2+} of calcite, aragonite and vaterite, Ba^{2+} of witherite, and Sr^{2+} of strontianite in equilibrium with an open carbonate system (B). See Figure 2.9 and Appendix A for a description of aqueous carbonate in equilibrium with the atmosphere.

By combining the open system aqueous carbonate model (see Figure 2.9 B) with the carbonate solubility products at 25 °C, the equilibrium concentrations of Ca^{2+} from calcite, aragonite, and vaterite, Ba^{2+} from witherite, and Sr^{2+} from strontianite can be plotted against pH (see Figure 2.9 B). It is evident in Figure 2.9 B that carbonate solubility strongly depend on pH.

Precipitation of carbonates can be conducted in a number of ways, using different starting materials, temperature, additives, and mixing conditions. By controlling these parameters specific phases, crystals, and aggregate morphologies can be obtained. Wray and Daniels (1957) showed that by changing temperature and ageing time, one can produce pure calcite, aragonite, and vaterite phases as well as the intermixed phases from mixtures of $Ca(NO_3)_2$ and Na_2CO_3 solutions. At 30 °C the dominant polymorph is vaterite at short ageing times. However, this vaterite transforms completely into the more stable calcite after 18 hours of ageing time. No aragonite was formed during these conditions. By raising the temperature, mixtures of calcite and aragonite were formed, and at 70 °C the only phase produced was aragonite. As drying the precipitated carbonate will prevent phase transitions, it is possible to obtain any ratio of the desired calcium carbonate phases by varying basically time, temperature, and pH. Formation of aragonite is also promoted by the presence of Sr^{2+}, Ba^{2+}, and Pb^{2+} at high pH. These cations are larger than the calcium ion and force the structure into the aragonite-type even at very low concentrations (Wray and Daniels, 1957). The direct inorganic precipitation described by Wray and Daniels (1957) was slightly modified by Katz et al. (1972) who added strontium to the solutions to favour aragonite precipitation. Preheated solutions of mixed $CaCl_2 \cdot 2H_2O$ and $SrCl_2 \cdot 6H_2O$, and Na_2CO_3 produced high purity less than μm sized aragonite needles. Furthermore, adsorbed ions can also influence which phase is crystallised. It has been shown that the presence of dissolved Mg^{2+} favours the precipitation of aragonite over calcite (Morse, 1983). Temperature has also a great influence on the phase precipitated. High temperatures favours precipitation of the aragonite phase. Using especially Ba^{2+}, Sr^{2+}, or Pb^{2+} carbonate seeds during the crystallisation favours the formation of aragonite (Zhou and Zheng, 1998).

Several additives, including anions like phosphates and sulfates (Mucci et al., 1989), cations like Mg^{2+} and Fe^{2+} (Reddy and Wang, 1980; Pokrovskiy and Savenko, 1995; Gutjahr et al., 1996), and various organic compounds (Kitano and Hood, 1965; Meldrum and Hyde, 2001) have shown to have a inhibiting effect on the crystallisation of calcite. The presence of additional ions can effect the precipitation and dissolution rates in two ways. They can adsorb to the crystal surface, especially at high energy sites that are more exposed to the solution, such as kinks and steps. These sites are also preferred during crystal growth and dissolution (Morse, 1983). This decrease

in crystallisation rate of calcite in the presence of additional ions is believed to be caused by such a mechanism (Gutjahr et al., 1996). Furthermore, the addition of foreign ions can also have a second effect on reaction rates as they can form complexes with the primary reactants, thereby altering activity coefficients and the saturation state of the system (Morse, 1983). Gratz and Hillner (1993) showed that phosphates reversibly attach to growth steps on the calcite crystal, and inhibits further growth as long as it is adsorbed. The effect of added magnesium ions is however much less than that of phosphates. Magnesium in particular has been studied in terms of calcium carbonate crystallisation as it is believed to be the cause of the preferential precipitation of aragnonite instead of calcite in seawater (Berner, 1975; Pokrovskiy and Savenko, 1995). Aragonite precipitation is relatively unaffected by the presence of Mg^{2+} as it is not easily adsorbed onto the surface of aragonite crystals, nor incorporated into the lattice to any great extent. In the case of calcite, Mg^{2+} is believed to be adsorbed. It can also be incorporated in the crystal lattice to form high-Mg calcite, which can be much more soluble than pure calcite (Berner, 1975). However, Pokrovskiy and Savenko (1995) showed that Mg^{2+} only inhibits precipitation at high levels of supersaturation, not at the low-level supersaturation that occurs in seawater. Rare earth elements, such as lanthanum and ytterbium, have also shown to have an effect on calcium carbonate precipitation. Akagi and Kono (1995) and Tsuno et al. (2001) have shown that lanthanum ions (La^{3+}) can inhibit the formation of calcite. Calcite solubility was effectively increased 10 times when the lanthanum to calcium molar ratio was 1/4000. It was further shown that the presence of lanthanum can inhibit the transition of vaterite to calcite; a phenomenon believed to be caused by adsorption of lanthanum on the active sites, thereby blocking the transition (Tsuno et al., 2001).

Clearly, the presence of impurities can have a strong influence on precipitation of carbonates. Reaction rates are affected but also the morphology and crystallinity of the crystal. It is believed that polycrystalline aggregates are formed when the inhibition of nucleation and growth of crystallites (caused by adsorbed additives) is strong enough so the only possible way to overcome the critical nuclei size for further growth is by aggregation of smaller crystallites (Meldrum and Hyde, 2001). In the next section examples are given on the morphological influence of particular additives.

2.2.4.3 Control of crystal morphology

The formation of carbonates with particular size and shape depend strongly on the experimental design. As carbonate precipitation can be conducted in numerous ways, of which a few parameters are; sources and concentration of carbonate and metal ion, temperatures, and with various additives, the resulting carbonate crystals can adopt

different habits. Most of the research into morphological control has focussed on $CaCO_3$ mineralisation, since it is very important for biomineralisation and also for industrial applications (Cölfen, 2003). In this section, some precipitation techniques and the use of particular additives are explored, especially focussing on the morphology of the carbonate precipitates, as this is particularely interesting relating to morphogenesis of biomorphs.

Manoli and Dalas (2000) showed that alcohols, such as ethanol, isopropanol, and diethylene glycol also can have an influence on $CaCO_3$ polymorphism and morphology. In the presence of 10% v/v of the alcohols mentioned above, aggregated vaterite crystals with unusual morphology were precipitated, and the vaterite to calcite transformation was hindered by the alcohol. The crystallisation rate was also observed to increase compared to experiments without alcohol (Manoli and Dalas, 2000).

Instead of using soluble carbonate salts as source of CO_3^{2-}, one can use urea ($CO(NH_2)_2$), which hydrolyses in neutral to basic aqueous solutions to form carbonate ions with a concomitant increase in pH according to the following reactions (Aiken et al., 1988; Wang et al., 1999);

$$CO(NH_2)_2 \rightleftharpoons NH_3 + HNCO \rightleftharpoons NH_4^+ + NCO^- \tag{2.12}$$

$$NCO^- + OH^- + H_2O \rightleftharpoons NH_3 + CO_3^{2-} \tag{2.13}$$

Since the rate of this reaction can be precisely controlled, it has been shown that the use of urea in carbonate precipitation experiments can lead to well defined uniform particles .

Wang et al. (1999), Sondi and Matijevic (2001), and Sondi and Matijevic (2003) examined the influence of decomposition of urea, with and without the urease that catalyses urea decomposition, on calcium, strontium, and barium carbonates. Wang et al. (1999) showed that very uniform aragonite needles can be precipitated by ageing a solution containing 0.25 M $CaCl_2$ and 0.75 M urea at 90 °C for 3 hours (see Figure 2.10 A). Increasing the $CaCl_2$ concentration resulted in a mixture of calcium carbonate phases with irregular shapes, whereas changing the urea concentration only had a slight decreasing effect on the size of the crystals. It was also shown that agitation can have a strong effect on the phase and morphology of the carbonate produced. At the extreme, when a magnetic stirrer was used, calcite rhombohedra precipitated instead of aragonite (see Figure 2.10 B). One interesting effect of mixing procedure was identified. If the respective solutions were preheated to 90°C followed by rapid mixing, the resulting precipitates after 3 hours were vaterite 'flowers' (see Figure 2.10 C). Using additives like Ba^{2+}, Sr^{2+}, and Mg^{2+} generally yielded smaller particles, but at higher concentrations of $BaCl_2$ (0.025 M) partially resulted in calcitic precipitates. It

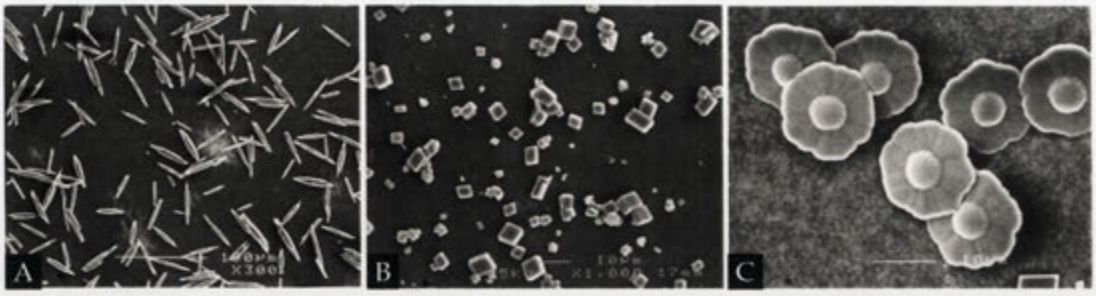

Figure 2.10: SEM images of aragonite (A), calcite (B) and vaterite 'flowers' (C) described by Wang et al. (1999). The aragonite needles were produced by aging 0.25 M $CaCl_2$ in the presence of 0.75 M urea for 3 hours at 90 °C. The calcite rhomohedra resulted when the solution was magnetically stirred during otherwise the same conditions. The vaterite flowers were produced if the solutions were preheated before they were mixed. Adapted from Wang et al. (1999).

was suggested that the aragonite structure get destabilised at high Ba^{2+} substitution in the crystal lattice. Several surfactants and polymers were also investigated, and it was shown that the ones containing sulfate ions resulted in spherical aggregates made of a mixture of vaterite and calcite (Wang et al., 1999). Using cationic dextran in the reaction mixture produces a mixture of the carbonate aggregates seen in Figure 2.10 after 4 hours at 90 °C (Hardikar and Matijević, 2001). Using urease to catalyse the decomposition of urea at room temperature has a strong influence on the carbonate phase and morphology produced (Sondi and Matijevic, 2001). No aragonite was observed. Instead, in the early stages of the reaction, an amorphous carbonate phase appeared, that transformed to first vaterite and then calcite as the reaction proceeded. This is especially true for the samples prepared with high concentrations of urease. Low concentrations of the enzyme generally increase the calcite crystallinity. Changing the concentrations of urea and $CaCl_2$ did not have a strong effect on the precipitates, however higher concentrations of urease increased precipitation rates. Again, it was shown that agitation of the system had an effect on the precipitates. A smaller amount amorphous phase and more, but smaller, nano crystalline vaterite were produced. Sondi and Matijevic (2001) also discussed the mechanisms that could be in place for 'size enlargement'. Two models were were suggested that could account for this effect: 1) adsorption of ionic or molecular species on the crystal surfaces (as discussed above), and 2) aggregation. Since the vaterite was nano crystalline, Sondi and Matijevic (2001) concluded that most important process governing the precipitate morphology is the agglomeration of nano sized precursors. This model has also been acknowledged for numerous colloidal system (Privman et al., 1999; Sondi and Matijevic, 2001).

In the case of urease catalysed reaction on the barium and strontium carbonates,

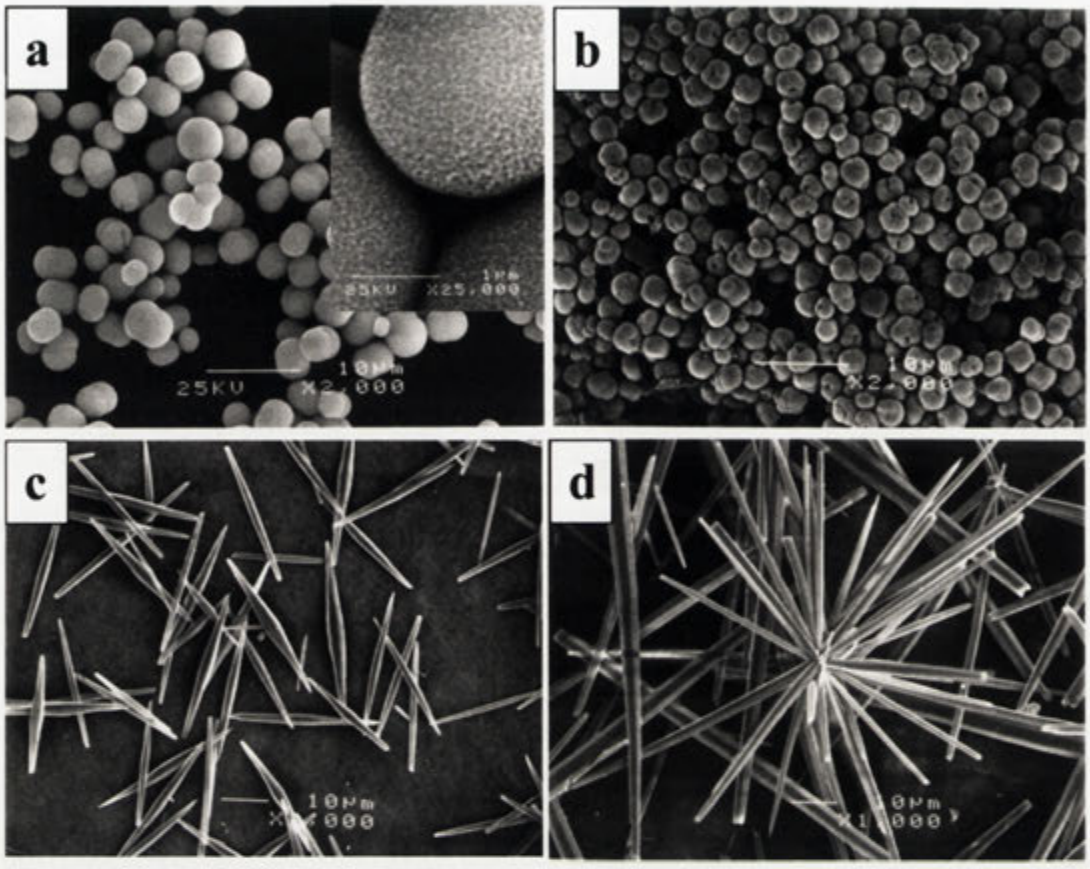

Figure 2.11: SEM images of crystal morphologies described by Sondi and Matijevic (2003); (a) spherical strontium carbonate particles where the inset shows higher magnification image of the particles, (b) spherical barium carbonate particles. Both (a) and (b) were produced by the urease catalyzed decomposition of urea after 2 minutes of ageing time. (c) strontium carbonate needles and (d) barium carbonate needles, produced by the same solutions as in (a) and (b) but without urease, and aged at 90 °C for 2 hours. Adapted from Sondi and Matijevic (2003).

spheroidal particles consisting of ~20 nm (based on evaluation of XRD pattern) sized subunits were formed at 25 °C and after only two minutes of reaction time (see Figure 2.11 a and b). At longer reaction times these spheroidal particles developed needle-like behaviour on behalf of the cores. At 90 °C without the urese (temperature catalysed decomposition of urea), needle-like precipitates formed after 2 hours (see Figure 2.11 c and d). Changing the concentration of urease did neither affect the morphology nor the growth pattern and crystallinity of the aggregates, but higher concentrations increased precipitation rates (Sondi and Matijevic, 2003).

Chen et al. (2001) used a semi-batch crystalliser to study the effect of nucleation and growth kinetics on the morphology of $BaCO_3$ crystals under constant pH. It was shown that the morphology of precipitated $BaCO_3$ crystals strongly depends on the initial

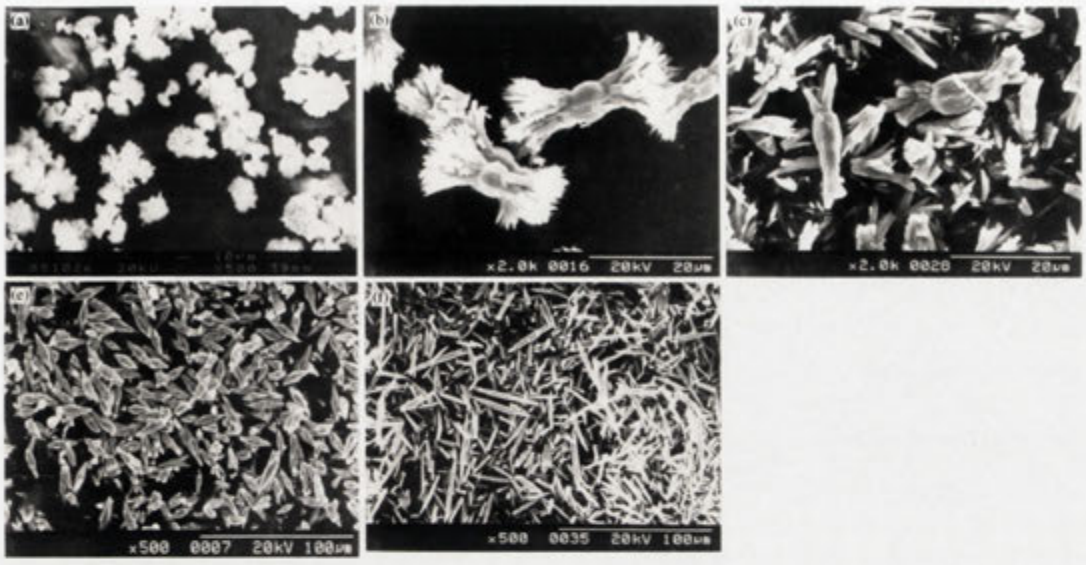

Figure 2.12: The crystal morphologies of $BaCO_3$ described by Chen et al. (2001); floc (a), candy-like (b), olive-like with end dendrite (c), olive-like (e), and needle-like (f). Adapted from Chen et al. (2001).

concentration and pH of the solution. Five main morphologies were determined, named olive-like, olive-like with end dendrite, candy-like, needle-like, and floc. At high pH (>10) and higher initial concentration the floc crystals were formed, while at lower concentration the olive-like with end dendrite crystals were produced at the same pH. The olive-like crystals were formed at lower concentrations and below pH 10. Candy-like crystals, on the other hand, precipitated at intermediate conditions. However, the morphology is not only dictaded by the pH. The floc and candy-like crystal structures are formed at higher supersaturation (Ω >9), which translates to higher nucleation rates. Intermediate supersaturation (7< Ω <9) produces candy-like crystals, and lower supersaturation results in olive-like and needle-like precipitates. Furthermore, the needle-like and the olive-like crystals, precipitated at relatively low supersaturation, were found to have a growth rate that is mostly controlled by the surface integration step, whereas the growth rate for the other crystals are mostly controlled by the diffusion step (Chen et al., 2001).

Organic additives such as synthetic and biological polymers have shown to have a strong influence on morphogenesis of carbonates (Cölfen, 2003).

For instance, Yu et al. (2004b) showed that $BaCO_3$ can obtain complex morphologies in the presence of polymers. Two low molecular weight polymers were used in their experiments; poly(sodium 4-styrenesulfonate) (PSS for short) that is negatively charged at the experimental conditions (pH 5), and poly(allylamine hydrochloride) (PAH), which is positively charged. As a carbonate source, they used crushed am-

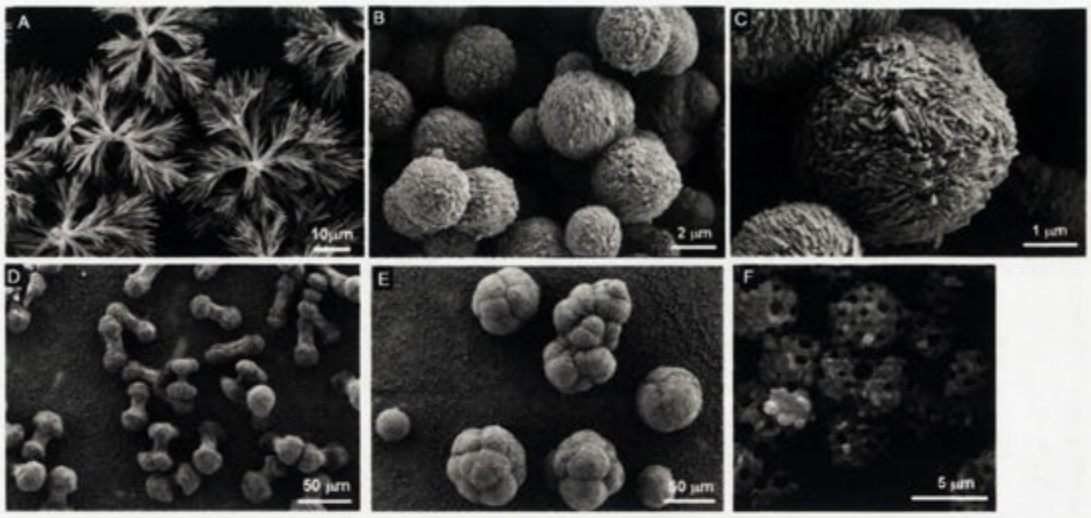

Figure 2.13: SEM images of $BaCO_3$ particles described by Yu et al. (2004b). Dendritic particles were obtained in the absence of any additives (A). Precipitation with 1g/l PSS resulted in spherical aggregates (B), consisting of nano-sized rods (C). $BaCO_3$ formed in the presence of PAH adopted an initial dumbbell-like structure (D) that with time transformed into a sphere-like aggregates (E). Introducing air-bubbles, which can act as a static template, into the $BaCl_2$ solution with added PSS resulted in a spherical aggregates with holes (F). Adapted from Yu et al. (2004b).

monium carbonate, which decomposes into NH_3 and CO_2, which absorbed into the $BaCl_2$ solution with the added polymer. In absence of any polymer, the precipitate adopted a dendritic structure (see Figure 2.13 A). However, in the presence of the negatively charged PSS, spherical aggregates consisting of ~50 nm in diameter rod-like crystals were produced (see Figure 2.13 B and C). Shaking the solution with added PSS before mineralisation began, so as to produce bubbles, resulted in aggregates with holes (see Figure 2.13 F). These aggregates were less structured than their bubble-free counterparts, a feature possibly due to attractive force exerted on the amorphous carbonate precursor by the air-bubble interface. It has previously been shown that the air/solution interface can temporarily stabilise nano sized particle aggregates in the $CaCO_3$ case with added polymers (Yu et al., 2004b).

As was discussed in previous section, Mg^{2+} can influence which $CaCO_3$ polymorph of that will precipitate. Meldrum and Hyde (2001) showed that citric and malic acid, in the presence of added Mg^{2+}, give rise to amazing structural variety of $CaCO_3$. The carbonate products were precipitated from a saturated calcium bicarbonate solution with various concentrations of the organic and magnesium additives. In the absence of any organic additive, preferential precipitation of aragonite over calcite occur with increasing concentrations of Mg^{2+}. However, in the presence of malic or citric acid in addition to Mg^{2+}, calcitic aggregates with remarkable morphology,

ranging from elongated rhombohedra to inter-grown triangles, lobes, dumbells, and inter-grown spheres with increasing Mg^{2+} concentration, were precipitated. Different morphologies precipitated on the bottom compared to the air/solution interface in the crystallisation dish. Precipitation at such an interface is common in systems where a concentration gradient exist across the solution. Both organic additives inhibit nucleation and growth of calcium carbonate by binding to specific faces of the crystal, leading to elongated crystals along the *c*-axis. Additional Mg^{2+} enhanced the effect induced by the organic additives, and a larger morphological variety was observed.

More complex polymers have also been successfully used to induce specific carbonate morphologies. Yu et al. (2003) used double hydrophilic block copolymers (DHBCs) to modify the morphology of several metal carbonates, including $BaCO_3$ and $PbCO_3$, using ammonium carbonate in the gas diffusion system as described above. DHBCs are specifically designed to affect crystal morphologies in that they consist of two hydrophilic blocks; one designed to interact with the mineral, and one that only weakly interacts with the material, but promotes aqueous solubilisation. These types of polymers have shown to exert a great effect on $CaCO_3$ crystallisation (Cölfen and Qi, 2001; Qi et al., 2002; Yu et al., 2003). In the $BaCO_3$ case, four different DHBCs were used in the precipitation experiments; 1) poly(ethylene glycol)-*block*-poly(methacrylic acid) (PEG-*b*-PMAA); 2) a monophosphonated version of 1) called PEG-*b*-PMAA-PO_3H_2 (21% phosphonation degree); 3) a phosphorylated poly(ethylene glycol)-*block*-poly(hydroxyethyl-ethylene) (PEG-*b*-PHEE-PO_4H_2); and 4) poly(ethylene glycol)-*block*-poly(ethylene imine)-poly(acetic acid) (PEG-*b*-PEIPA). These different DHBCs all interact differently with the carbonate and therefore give rise to distinct morphologies (see Figure 2.14). In the case of PEG-*b*-PMAA a change in morphology with time was observed (see Figure 2.14 A-D). After 3 hours of reaction time, highly monodispers 350 nm spherical aggregates were observed (see Figure 2.14 A), that later transformed into rods, dumbbells, and larger spheres (see Figure 2.14 B-D). The mechanism for this sphere-rod-dumbbell-sphere transition is unknown, but a similar transition has been observed in gelatin grown fluoroapatites hierarchical aggregates (Busch et al., 1999; Yu et al., 2003). In the fluoroapatite case, a transition from hexagonal rods to dumbbells to spherical aggregates have been seen to proceed by fractal growth at the ends of the rods, that with time close up to spherical aggregates. This type of growth have been proposed to be caused by the presence of an intrinsic electric fields that direct the crystal growth (Busch et al., 1999). Yu et al. (2003) proposed a mechanism for the transitions observed in the presence of DHCBs, based on the mechanism proposed by Busch and co-workers (see Figure 2.15). However, Yu et al. (2003) showed that the fractal behaviour of the $BaCO_3$ in the presence of PEG-*b*-PMAA could not be caused by long-range Coulombic interactions caused by

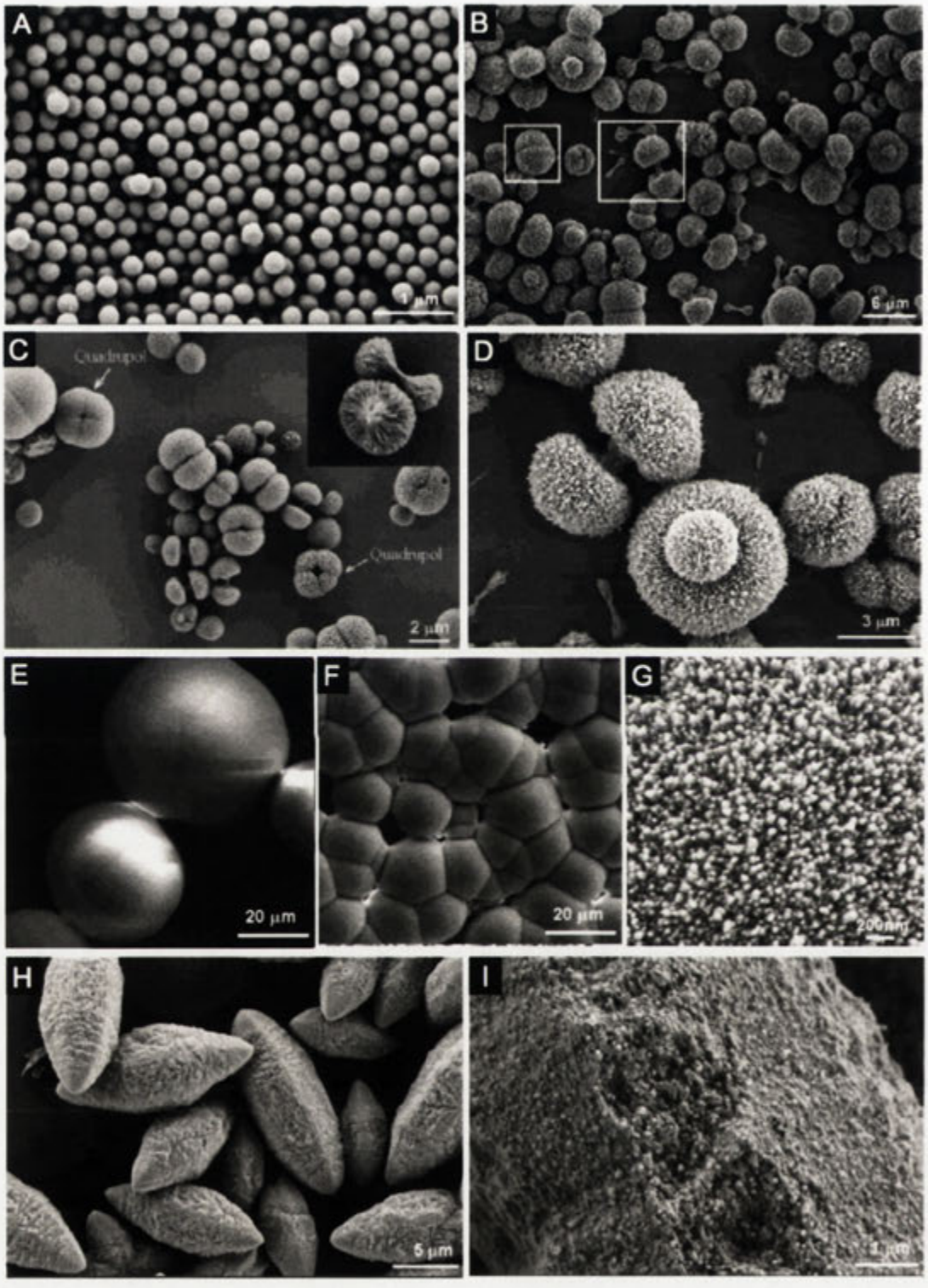

Figure 2.14: SEM images of $BaCO_3$ particles precipitate d in the presence of three different DHBCs; PEG-*b*-PMAA (A-D), PEG-*b*-PMAA-PO_3H_2 (E-G), and PEG-*b*-PHEE-PO_4H_2 (H-I). Adapted from Yu et al. (2003).

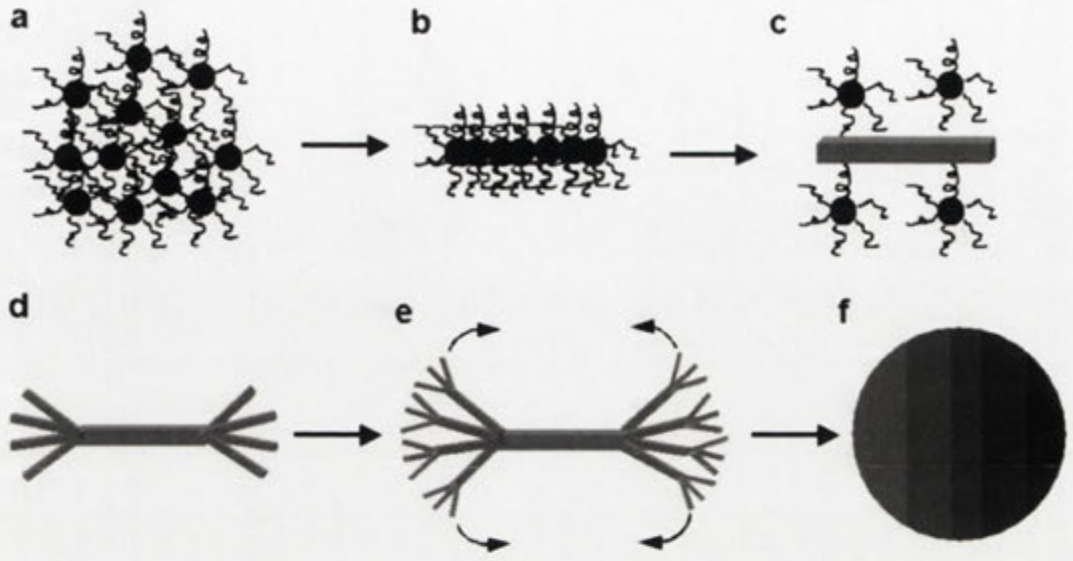

Figure 2.15: Proposed mechanism for the transitions observed for $BaCO_3$ in the presence of DHBCs. Initial spherical nano-sized aggregate (a) transforms into rod-like crystals (c), which in turn develop dendritic growths at the ends (d-e), finally resulting in a larger spherical aggregate (f). Adapted from Yu et al. (2003).

an electric field. Increasing the ionic strength of the solution by adding up to 2 M NaCl didn't have any effect on the morphology of the produced $BaCO_3$ aggregates. This is in strong contrast to the $CaCO_3$ case, where an increase in ionic strength produces regular rhombohedral calcite, i.e. the directing effect of the DHCB is lost. The fact that the morphology wasn't affected by the increased ionic strength indicates a strong interaction between the polymer and the mineral surface even though the polymer activity is decreased at higher ionic strengths, due to salting out of the DHBC. Using the partially phosphonated polymer PEG-*b*-PMAA-PO_3H_2 resulted in spherical aggregates, which consisted of 40 nm fine particles (see Figure 2.14 E-G). The phosphonate part of the DHBC apparently interacts strongly with the mineral surface that stabilises the formation of smaller particles. A completely opposite effect resulted from using PEG-*b*-PEIPA, which gave rise to coarse grained surfaces, but the overall morphology remained the same. Yu et al. (2003) therefore concluded that the surface properties can be tailored by using appropriate DHBCs. A completely different morphology was obtained when the partially phosphorylated PEG-*b*-PHEE-PO_4H_2 was used (see Figure 2.14 H-I). Only 8-30 μm sized oval aggregates, composed of ~40 nm sized crystals, were precipitated (Yu et al., 2003). These sets of experiments clearly indicate the power DHBCs exert on carbonate morphogenesis, but at present, the mechanism for this structure directing effect is not known.

Yu et al. (2002) also investigated the role of DHBCs in calcium carbonate mor-

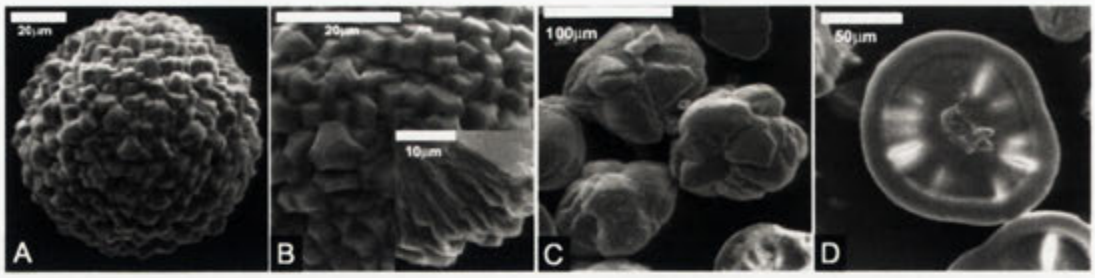

Figure 2.16: SEM images of $CaCO_3$ grown in the presence of PEG-*b*-PMAA (A-B) and PEG-*b*-PHEE-PO_4H_2 (C-D). Adapted from Yu et al. (2002).

phogenesis in a ammonium carbonate diffusion system previously discussed. Large spherulitic calcite was produced in the presence of PEG-*b*-PMAA and PEG-*b*-PEIPA (see Figure 2.16 A). In both cases the spherule surfaces are rough, however the building blocks show differing degree of crystallinity. Different crystalline faces are exposed in the two samples, which can be explained by the different functional groups on the DHBCs preferential interaction with specific faces. The morphologies produced with added PEG-*b*-PHEE-PO_4H_2 are very different from the previous discussed spherules. Instead, large irregular globules and disk-like morphologies were produced (see Figure 2.16) composed of fine particles. These disk-like morphologies are in many ways similar to some biomorphs presented in Chapter 3. Yu et al. (2002) suggested that PEG-*b*-PHEE-PO_4H_2 can interact with all crystal surfaces, which results in less rough surfaces as compared with the other DHBCs used. However, no specific mechanism for the formation of these complex structures are known to date (Yu et al., 2002).

Other interesting $BaCO_3$ morphologies can be derived by carbonate synthesis in reverse micelles. Qi et al. (1997) showed that single crystal $BaCO_3$ nanowires can be produced in nonionic reverse micelles of $C_{12}E_4$ (tetraethylene glycol monododecyl ether). The wires can grow up to 100 μm in length and have diameters between 10-30 nm. Changing the reaction conditions such as concentration of water, $C_{12}E_4$, and barium and carbonate concentrations only affected the length of the wires, the diameter remained constant. By TEM analysis it was shown that the early stages of the reaction contained tiny amorphous particles that with time aggregated and aligned to form single crystal nanowires with the *c*-axis along the length of the wire. Qi et al. (1997) suggested that preferential adsorption of the surfactant headgroups onto specific crystal planes parallel to the *c*-axis may be the cause of wire formation. Other $BaCO_3$ morphologies, such as rods and ellipsoidal crystals, can be obtained in micelles systems (see Qi et al. (1997) and references therein).

Unusual helical and 'herringbone' type filamentous carbonate structures have also been reported that are reminiscent of biomorphs. Yu et al. (2004a) produced

Figure 2.17: SEM images of $BaCO_3$ filaments grown in the presence of PEG-*b*DHPOBAEE, at an initial pH of 4. Adapted from Yu et al. (2004a).

such precipitates by slow diffusion of carbon dioxide (produced by decomposition of ammonium carbonate) into a 10 mM $BaCl_2$ solution containing 1 g/l of the DHBC polyethyleneglycol-*b*-[(2-[4-dihydroxyphosphoryl]-2-oxabutyl) acrylate ethyl ester] (PEG-*b*-DHPOBAEE) at pH 4. After two weeks, very long (millimeteres) filaments with a diameter between 200 to 500 nm are obtained. 90% of the filaments synthesised are helical in nature, and less than 10% are of the herringbone type (see Figure 2.17). Equal numbers of right- and left-handed helices are produced, and they consist of parallel aligned nanocrystals, ~30 nm in diameter and 200 nm long, along the growth direction (see Figure 2.17 C). Increasing the initial pH to 5.6 results in predominantly herringbone-like structures, while increasing the polymer concentration to 2 g/l leads to short densely packed fibres. The self-assembly of the helical and herringbone structures are believed to be the result of specific interaction of the polymer with specific crystal faces. Crystal modelling has shown that the (110) faces carry a net positive charge that can interact with the negatively charged phosphonated polymer. Specific polymer adsorption on these faces therefore hinders the aggregation at this site. The other faces, (020) and (011), are free to aggregate in an epitaxial arrangement, that is only (020)-(020) and (011)-(011) interactions occur, and the latter is the most favourable, as each nanocrystal has 4 (011) faces compared to 2 (020) faces (see Figure 2.18). Crystal-crystal aggregation then also leads to 'favourable' and 'unfavourable' (110) adsorption sites due to steric hindrance of the polymer (see Figure 2.18). A helical arrangement can then be explained by the change from (020)-(020) to (011)-(011) aggregation, with the concomitant growth in a staggered arrangement (see Figure 2.18). In the herringbone case, the structure can be explained by nanocrystal aggregation with their (110) faces in the absence of polymer. As soon as such a defect arrangement has been formed, the following nanocrystals will align in a similar way if no polymer is adsorbed (see Figure 2.18) (Yu et al., 2004a). A similar mechanism could be in place for the herringbone-like arrangement of carbonate crystals seen in some biomorphs, using negatively charged silica instead of organic polymers.

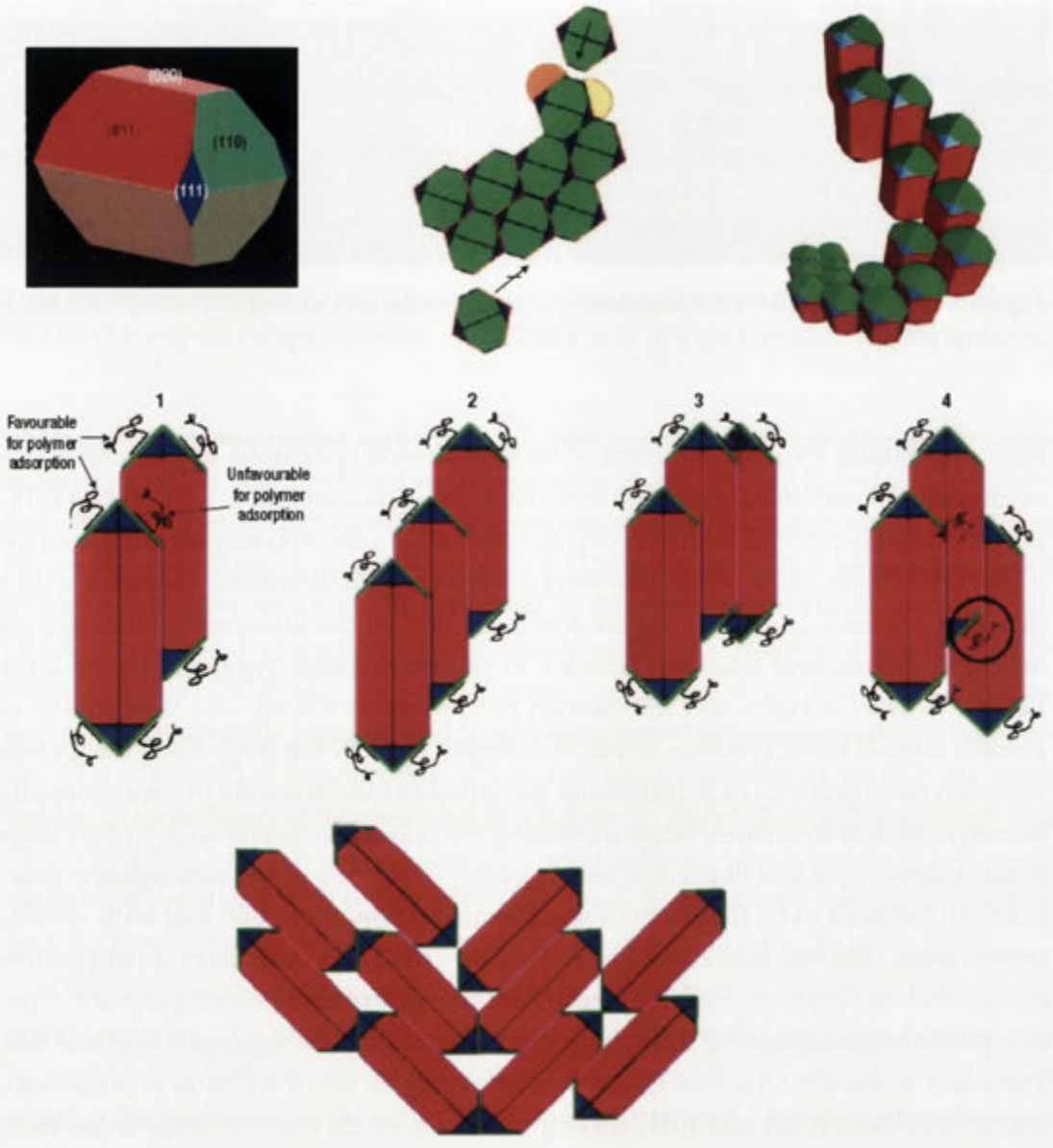

Figure 2.18: Proposed mechanism of formation for helical and herringbone morphologies obtained in the presence of PEG-*b*DHPOBAEE. Barium carbonate crystal illustrating the relevant faces (top left). The preferential adsorption of the polymer on (110) faces (green) and the crystal aggregation with their (020) and (011) faces leads to 'favourable' and 'unfavourable (110) sites sites for polymer adsorption (see middle 1). Particle aggregation in a staggered manner (see middle 2) is then preferred over other energetically less favourable arrangements (see middle 3 and 4). Aggregation occur with (020)-(020) and (011)-(011) faces, no (011)-(020) interactions occur (see top middle), and the orange spot indicates the most favourable (011) aggregation site for the incoming particle, so the helical turn is continued. Particle aggregation and the specific adsorption on favourable (110) faces then lead to a helical arrangement of nanocrystals (see top left). The herringbone structure will form when aggregation takes place on the (110) faces in the absence of the polymer (see bottom). Adapted from Yu et al. (2004a). Note that different cell parameters are used than the one described in Section 2.2.1; $a = 6.43$, $b = 5.32$, and $c = 8.90$ Å.

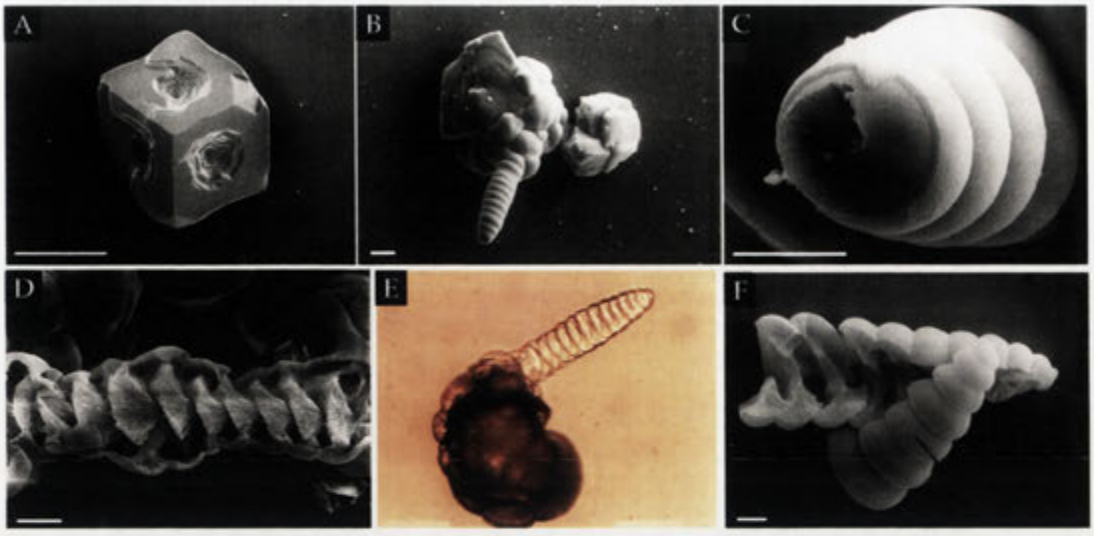

Figure 2.19: SEM images (A-D,F) and an optical image (E) of calcium carbonate precipitates in the presence of poly(aspartate). Calcite crystal displaying spiral pits (A) is produced when the concentration of poly(α,L-aspartate) is 0.5 μg/ml. At 10 μg/ml poly(α,L-aspartate) vaterite helixes are formed (B-F) as well as deformed rhomobedral, and rounded aggregates. The helical aggregates are polycrystalline in nature, and surrounded by an outer membrane (C). Gentle acidic etching of the helices shows that the outer membrane is more resistant to such treatment than the interior carbonate (D). Some of the helices are naturally hollow (E-F). Scalebar in A 100 μm, B 10 μm, C 10 μm, D 10 μm, and F 10 μm. Adapted from Gower and Tirrell (1998).

Helical carbonate crystal aggregates are not only restricted to silica-carbonate systems, but can also be produced in the presence of poly(aspartate). Gower and Tirrell (1998), and Gower and Odom (2000) showed that poly(aspartate) have a great influence on the precipitated calcium carbonate morphology and the polymorph produced. The carbonate aggregates are produced by slow diffusion of ammonium carbonate into a 12.5 or 20 mM calcium chloride solution containing various concentrations of poly(aspartate). At low concentrations of the polymer (0.5 μg/ml) distorted rhombohedral calcite crystals are produced, some of which display spiral pits (see Figure 2.19 A). At higher concentrations of poly(aspartate) (1-5 μg/ml) calcitic aggregates are produced that at further increased polymer concentrations (5-30 μg/ml) tend to form rounded aggregates. Some of these rounded aggregates have spiral growths (see Figure 2.19 B-F). Both left and right handed helixes are produced regardless of the chirality of the poly(aspartate). At this high polypeptide concentration calcium carbonate films are also produced, that are of three distinct types; single crystal mosaic films composed of calcite, a film composed of the hexhydrate form of calcium carbonate, and spherulitic polycrystalline films composed of vaterite. The latter is associated with the

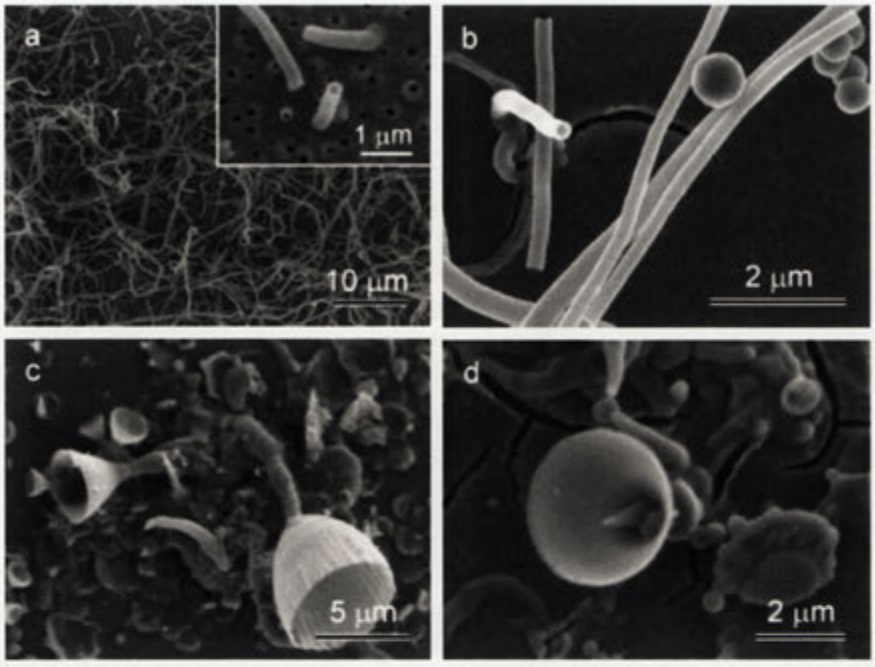

Figure 2.20: Vaterite tubes (a-b) and cups (c-d) produced by electrolytical deposition on silicon wafers. Adapted from Fan and Wang (2005).

helical vaterite growths and can be seen as a membrane around the helices, and Gower and Tirrell (1998) suggested that this film is the cause of this unusual spiral precipitate. The carbonate film and the membrane on the helices are of the same thickness, and in the case where the helices are hollow, the crystallites seem to grow inward from the external membrane, a feature indicative of the importance of the membrane for spiral growth. Changing the reaction temperature, calcium and polymer concentration, and polymer chain length alters the dimension and the occurrence of the spirals. At lower temperatures (4 °C) helices are shorter and fatter (200 μm in diameter, 250 μm in length), and fewer in number compared to synthesis at room temperature. Higher concentrations of poly(aspartate), or using shorter polymer chains, generally produces more helices and films. At optimal conditions, up to 70 % of the aggregates contain helical growths that can extend up to 700 μm in length. No polymer could be detected within any of the aggregates, however, polymer concentrations below the detection limit of X-ray microanalysis cannot be ruled out (Gower and Tirrell, 1998).

Other methods exist for producing unusual crystal morphologies, even in the absence of organic modifiers. Fan and Wang (2005) reported nanobubble templated growth for vaterite tubes and cups in an electrolytic deposition system (see Figure 2.20). In this system, the carbonate precipitates are produced on the silicon wafer cathode at which either H_2 or OH^- is produced. The produced OH^- increase the pH

and cause localised supersaturation resulting in calcium carbonate formation on the wafer. Several different morphologies can be obtained this way, however, the vaterite tubes and cups reported by Fan and Wang (2005) are limited by the concentration of the calcium concentration in solution. Vaterite tubes were produced at 25 °C in a solution with $[Ca^{2+}]$=12.7 mM and $[HCO_3^-]$= 22 mM at pH 6.9, whereas cups were produced at the slightly higher calcium concentration of 18 mM at otherwise the same conditions. In both cases, a ~ 100 μm thin vaterite film was always produced out of which the more complex morphologies grow (see Figure 2.20. The tubes are of uniform size throughout its length, have a outer diameter between 150-300 μm, an inner diameter between 80-200 μm, and they can grow up to 38 μm in length. TEM analysis revealed that the tubes are partly mono crystalline, and a single crystal entity can be maintained for up 3 μm along the tube before the direction of the crystal changes. The vaterite cups have an irregular tube growth at the base, and are normally between 1-10 μm in diameter and less than 50 nm thick at the cup edge. These unusual vaterite morphologies are believed to be a consequence of nanobubble formation on the cathode. The early precipitation of the vaterite film have a bubbly appearance, caused by the underlying H_2. As the pressure increases with reaction time, holes appear in the film. Continued growth, fuelled by the produced H_2 and OH^-, are then directed into the growing tubes. The dimension of the precipitates are probably due to a fine tuned balance between cathode reaction and crystal growth.

The interaction between silica and carbonate is most important for biomorph morphogenesis. Only a few experimental investigations into the effect of silica on carbonate morphogenesis have been reported to date, excluding the work by Juan Manuel García Ruiz described in Chapter 1 and our own work. Until now, most of the work has been conducted in silica gels.

Kotachi et al. (2003) and Kotachi et al. (2004) used silica gels to precipitate carbonate films on chitosan coated glass slides. Both barium and strontium carbonate films show radial vein-like texture (see Figure 2.21), and are composed of stacked planar hexagonal nanocrystals, where each crystal has the *c*-axis perpendicular to the substrate and is covered in silica. The crystal orientation is more distinct in the barium carbonate case compared to strontium carbonate films. Reducing the concentration of silicate by lowering the pH produces stacked hexagonal crystals with larger subunits (see Figure 2.21 C), suggesting a growth-restrticting effect of the silica on carbonate crystals. In the calcium carbonate case, the films contained a mixture of calcite, aragonite and vaterite, and the crystal arrangement is random. In the presence of poly(acrylic acid) (PAA), without silica, also produced calcium carbonate films, which suggests a similar effect of silicate anions and PAA on calcium carbonate precipitation. Kotachi et al. (2004) suggested that the carbonate films are a result of the interaction between the

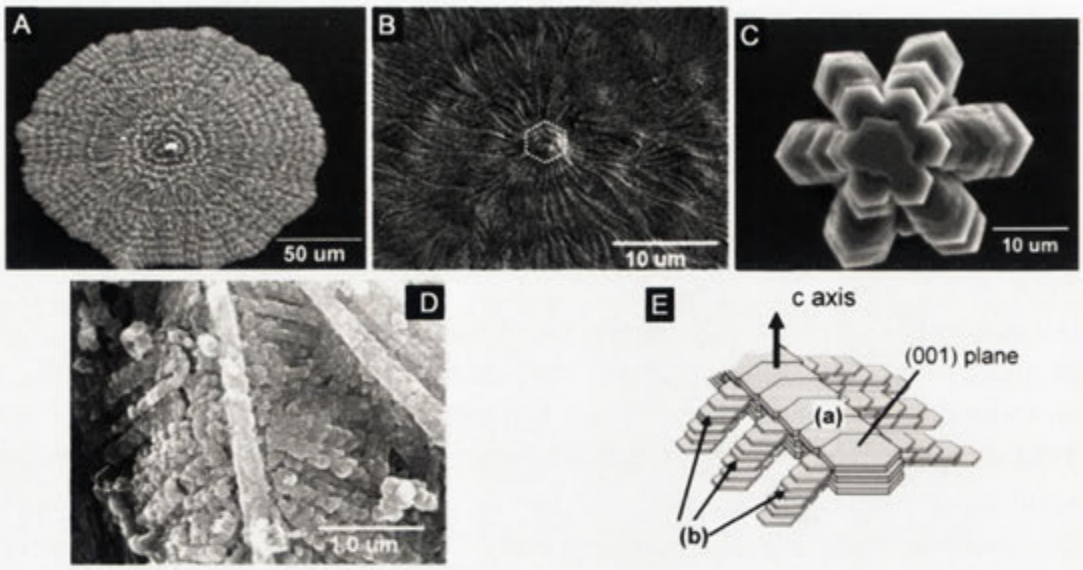

Figure 2.21: Barium carbonate film produced on chitosan surfaces at pH 10.5 in the presence of silicate anions (A-B). Strontium carbonate stacked precipitate produced at pH 9.5 (C). After sodium hydroxide treatment of the barium carbonate films, the planar crystal arrangement is clearly visible (D), and (E) shows a schematic arrangement of these hexagonal planar crystal units. Adapted from Kotachi et al. (2004).

dissolved silicate anions and the chitosan substrate, and the minutarising effect on the carbonate crystals by the polymerisation of silica on the crystal faces. The strong interaction between the polyalcoholic chitosan surface and the anionic silicate ions induces silicate polymerisation. Subsequent nucleation and growth of the carbonate subunits are templated by this polymerised silicate. It is believed that the directed growth and orientation of the barium or strontium carbonate sudunits are dictated by the silica, as the distance between the anionic oxygens (0.525 nm) in the silicate is similar to the distance between adjacent carbonate ions in the (001) plane (see Figure 2.22). This silica templating effect can then explain the preferential orientation of the carbonate nanocrystals with the *c*-axis perpendicular to the substrate. Continued silicate polymerisation on the carbonate crystals in turn induce directed nucleation and growth of subsequent stacked carbonate layers. Dendritic growth is then realised through radial growth from the corners of the carbonate hexagonal plates (Kotachi et al., 2004).

Evidently, the morphology of carbonates can be efficiently altered by both inorganic and organic additives. As knowledge of silica chemistry is crucial to the understanding of how it possibly interacts with carbonates, the next section of this chapter will discuss aspects such as various polymorphs of silica and silicates, silica polymerisation and speciation in solution. Geological occurrences of siliceous species are also discussed.

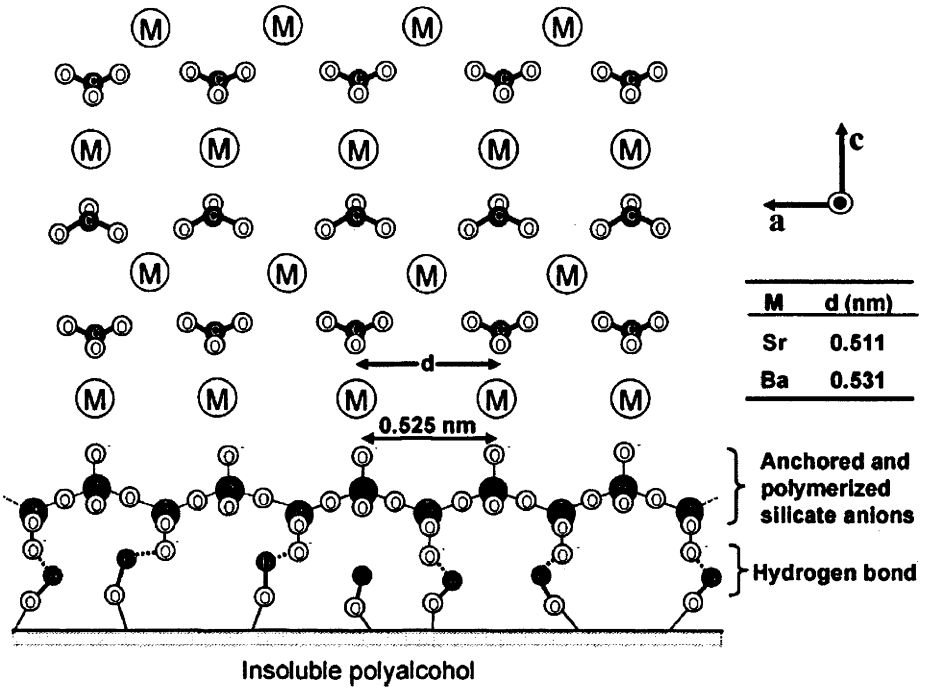

Figure 2.22: A proposed mechanism for the orientation of carbonate relative the silicate. The alcohol groups on the chitosan surface hydrogen bond with polymerised silicate anions. The distance between the ionic oxygens in the polymeric silicate (0.525 nm) closely matches that between the carbonate ions on the (001) plane in barium and strontium carbonate. Adapted from Kotachi et al. (2004).

2.3 Silicate chemistry

As the formation of biomorphs is closely related to the aqueous chemistry of silicate, a brief summary of solubility, polymerisation, and natural occurrences of various silicate phases is presented.

Silicon is the second most common element in the crust after oxygen (21.2 atom% compared to 62.6 for oxygen) (Swaddle et al., 1994). It almost always occurs as an oxide in amorphous and crystalline phases, such as quartz and silicates found in rocks and clays. As biomorphs contain amorphous silicate, this section will primarily concern this phase. However, crystalline silicates of well-characterised related composition will be discussed first, as a basis for comparison.

2.3.1 Silicate polymorphs and geological occurrence

The vast number of crystalline silicates reflects the numerous structurally different ways of combining tetrahedra consisting of a central Si^{4+} coordinated to four O^{2-} located at the apices: the basic building blocks of all silicate minerals. These tetrahedra

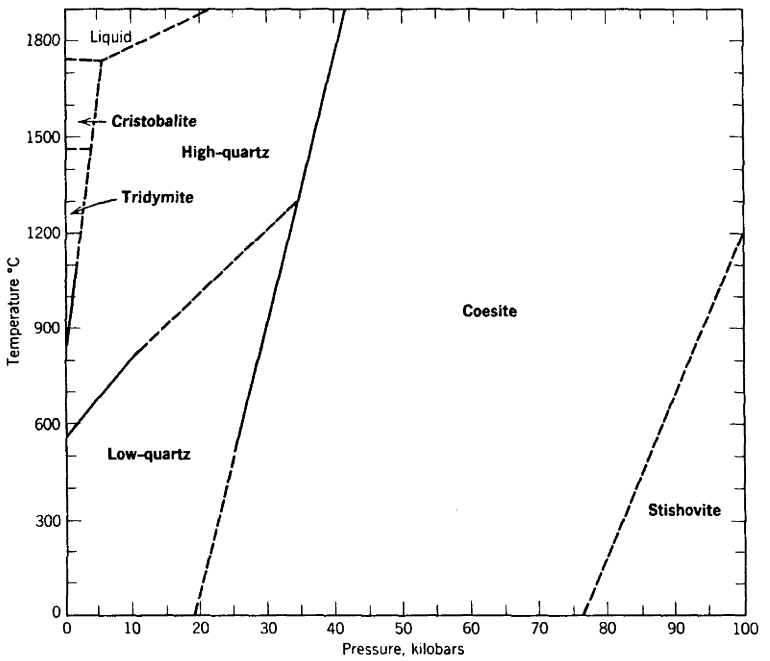

Figure 2.23: Phase diagram of the silica system. Adapted from Klein (2002)

can share zero, one, two, three, or all four oxygens giving rise to a great diversity in structural silicate configurations. Silicate minerals can be classified into six groups depending on the connectivity of these tetrahedra: 1) orthosilicates (isolated tetrahedra); 2) sorosilicates (isolated double tetrahedra); 3) cyclosilicates (ring-forming tetrahedra); 4) inosilicates (single- and double-chain silicates); 5) phyllosilicates (sheet-silicates); 6 tectosilicates (framework silicates). Furthermore, aluminium, which can coordinate to both four and six oxygens, can substitute for silicon in the tetrahedra and occupy octahedral sites within the structure. Other ions, 6-coordinated to oxygen, commonly found in silicates include Mg^{2+}, Fe^{2+}, Fe^{3+}, Mn^{2+}, and Ti^{4+}. Calcium and sodium ions are larger and/or less charged and are often coordinated to eight oxygens in silicates. The very large barium ion is not easily accommodated within the crystal structures of common rock-forming silicates, and only occurs in high-coordination sites (Klein, 2002). Ba-silicates often have distinctive crystal structures. Silicates with essential Ba include sanbornite ($BaSi_2O_5$), krauskopfite ($BaSi_2O_4(OH)_2$), and bigcreekite ($BaSi_2O_5 \cdot 4H_2O$), which are all very rare minerals.

Crystalline phases of pure silica include α- and β-quartz (low- and high-quartz respectively), various structures of tridymite, α- and β-cristobalite, coesite, stishovite, and moganite (Heaney and Post, 1992; Heaney, 1994). These are structures composed of a three-dimensional network of tetrahedra interlinked by sharing all four oxygens. Amorphous silica is mostly found in biominerals, but abiogenic silica glasses can also

be produced in association with geysers that discharge silica rich fluids (geyserite), by lightening strikes (lechatelierite) and within tektites formed through meteorite impacts (Heaney, 1994). Opal is a natural hydrated form of SiO_2, and occurs in both amorphous and microcrystalline forms. The latter may be cristobalite-like or intermediate between cristobalite and tridymite in structure. Opal may show higher order microstructure; this is the case in precious opal, which consist of a regular array of closely packed equal sized silica spheres (Graetsch, 1994).

The most common geological occurring silica mineral is α- quartz, which is stable at low temperature and pressures (see Figure 2.23). Some of this quartz may have previously existed as β-quartz, β-cristobalite or tridymite, that with time transformed to α- quartz (Heaney, 1994). Sedimentary quartz occurs as microcrystalline quartz, chalcedony (microcrystalline fibrous variety), megaquartz, and as opaline silica. Microcrystalline quartz is dominant in cherts, and occurs as fine grained (< 1 to ~ 50 μm in size) α- quartz crystals. Chalcedony and megaquartz are often found in cavities and fractures where secondary precipitation from silica rich solutions occurs. Chalcedony grows radially inward from the wall of the cavity that in its centre contain megaquartz. This characteristic is thought to reflect decreasing concentration of dissolved silica during crystallisation and/or reduced rate of crystallisation. Opaline silica is main silica phase that is precipitated today, due to its occurrence in the biogenic shells of diatoms in plankton. The origin of widespread ancient silica deposits, which were formed prior to the evolution of diatoms and other silica-secreating organisms, is not fully understood (Knauth, 1994). The state of the Archean ocean in terms of silica content will be further discussed in Chapter 5.

2.3.2 Silica dissolution and precipitation

The aqueous chemistry of silica is a complex interplay between dissolution/precipitation, adsorption/desorption, and complexation. Early studies show great discrepancies between reported solubility data, an effect that has been attributed to non-equilibrium conditions. Long equilibrium times are required for a solution in contact with the solid phase. Different silica phases show different solubilities in water, with amorphous silica being the most soluble phase (see Figure 2.24). However, solubility is also affected by particle size, temperature, pressure, pH and the presence of additional electrolytes (Iler, 1979; Dove and Rimstidt, 1994). Smaller particles show a higher degree of solubility due to the smaller positive radius of curvature. Larger particles therefore grow at the expense of the smaller ones; a process known as Ostwald ripening (Dove and Rimstidt, 1994). Concave surfaces (negative radius of curvature) on the other hand, have a low equilibrium solubility. Two adhering particles will therefore dissolve on

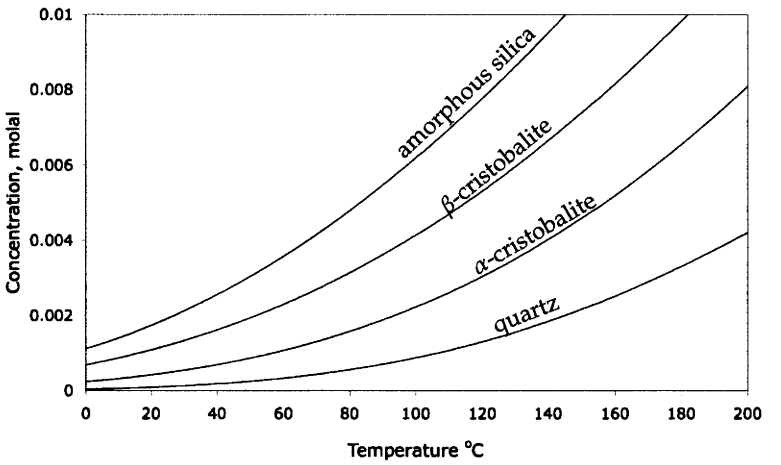

Phase	log K_1
Amorph. silica	-2.71
β-cristobalite	-2.92
α-cristobalite	-3.32
quartz	-3.96

Figure 2.24: Aqueous solubility of amorphous silica, cristobalites, and quartz at different temperatures. The table to the right indicates the equilibrium constants at 25 °C. The data is based on equations taken from Rimstidt and Barnes (1980) (see also Appendix B.)

the convex surface and deposit in the concave adhering point to reduce the negative curvature (Iler, 1979). As can be seen in Figure 2.24 increasing temperature leads to increased solubility, although silica solubility is very much affected by the pH. High pH shows increases in solubility due to the formation of anionic species in addition to the $Si(OH)_4$ which is in equilibrium with the solid phase. The solubility and speciation of the anions, can be described according to the following equilibria:

$$SiO_{2(s)} + 2H_2O \overset{K_1}{\rightleftharpoons} Si(OH)_4 \tag{2.14}$$

$$Si(OH)_4 \overset{K_2}{\rightleftharpoons} SiO(OH)_3^- + H^+ \tag{2.15}$$

$$SiO(OH)_3^{-1} \overset{K_3}{\rightleftharpoons} SiO(OH)_2^{2-} + H^+ \tag{2.16}$$

$$4Si(OH)_4 \overset{K_4}{\rightleftharpoons} Si_4O_6(OH)_6^{2-} + 2H^+ + 4H_2O \tag{2.17}$$

where K are the equilibrium constants. $Si(OH)_4$, which can be seen as a diprotic acid (pK_2=9.84 and pK_3=13.43 at I=0)' , is quite a weak acid and will substantially dissociate at around pH 9 (Dove and Rimstidt, 1994; Sjöberg, 1996). Reaction 2.14 and 2.15 represent a geologically important buffer system that ensures that the pH remains below pK_2 of silica. However, in synthetic silica processes the higher dissociation reactions are important (Dove and Rimstidt, 1994). For a solution in equilibrium with amorphous silica, the different concentrations of the various species that change with pH can be seen in Figure 2.25 A. The solubility of silica is also affected by additional species in solution. Total SiO_2 solubility is increased if reaction occurs to produce additional complexes: both organic and inorganic species can form such complexes (Iler, 1979). Furthermore, a change in water structure can increase total solubility of

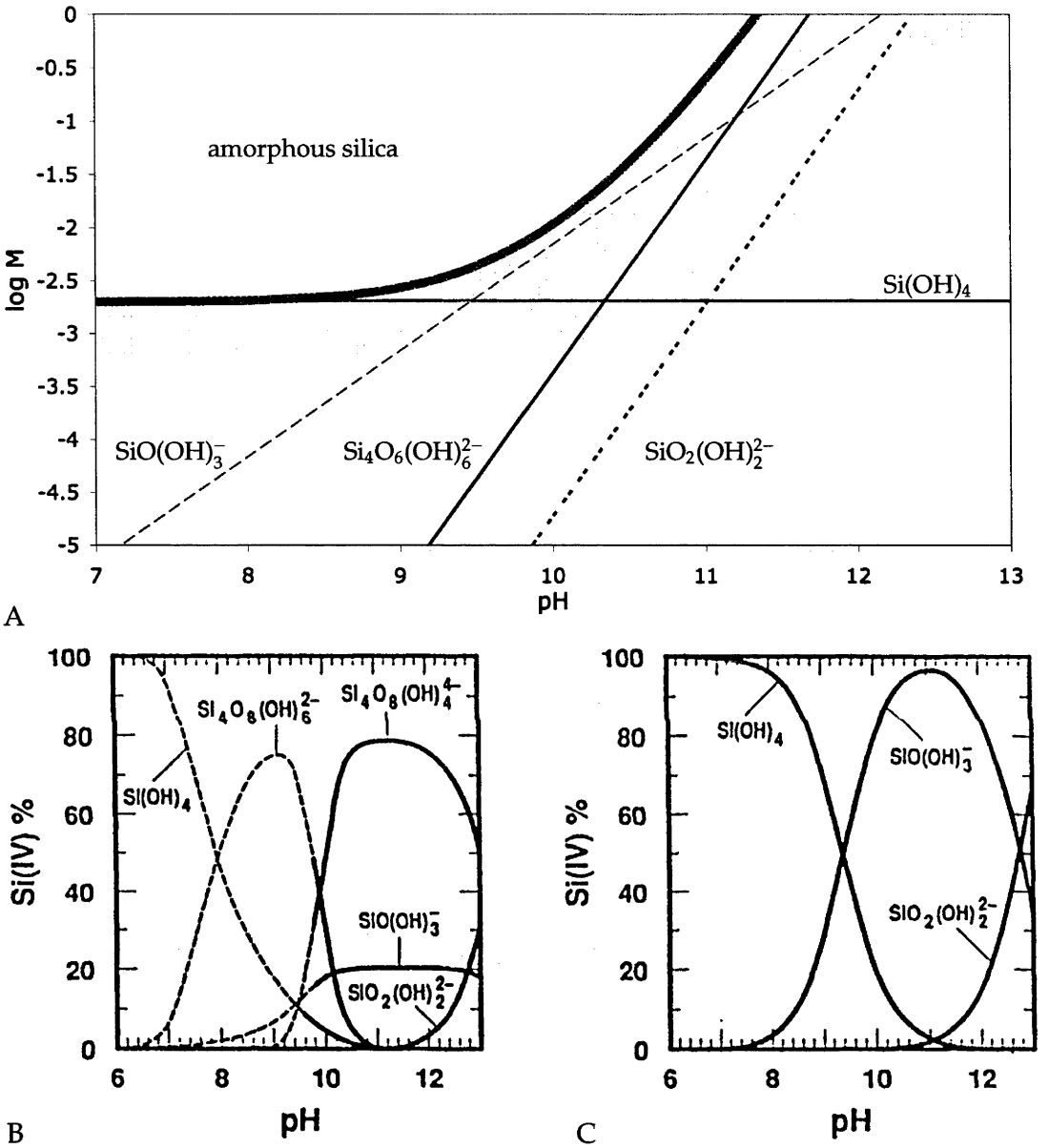

Figure 2.25: Distribution of aqueous silicate species with pH. In A, the system is in equilibrium with amorphous silica (thick black line). The equilibrium constants used are valid for 25 °C, and I= 0.5; $\log K_1$ -2.7, $\log K_2$ -9.46, $\log K_3$ -12.56, $\log K_4$ -12.57. The shaded area represents the region of where significant amounts of polynuclear species are believed to exist (Dove and Rimstidt, 1994; Stumm and Morgan, 1996). In B and C, the total Si concentration is 0.1M and 10^{-5} M respectively in a system with an ionic strength of 3. Adapted from Brinker and Scherer (1990), after Baes and Mesmer (1986).

by stabilising highly hydrated silica species. This is believed to be the mechanism causing the observed increase in solubility of quartz in the presence of NaCl (Dove and Rimstidt, 1994). Dove and Nix (1997) were the first to report the effect of Ba^{2+} on the dissolution rates of quartz, and it was found that it increased by a factor of 40 compared to deionised water at 200 °C. Other alkaline and alkaline- and alkaline earth cations also increased the dissolution rate of quartz in the following order; $Mg^{2+} < Ca^{2+} \approx Li^{+} \approx Na^{+} \approx K^{+} < Ba^{2+}$. This effect was believed to be caused by the different solvation properties.

Figure 2.25 A is a very simplistic view of the equilibrium system, as there are a myriad of polynuclear species present at increased concentration and high pH. Previous reports have suggested that only mononuclear species are present in neutral to slightly alkaline solutions in equilibrium with amorphous silica (Stumm and Morgan, 1996). Harris et al. (1980) showed through ^{29}Si NMR that 0.01 M sodium silicate solutions enriched in ^{29}Si at pH above 10 only contain monomeric species. However, several reports have since shown otherwise. Cary et al. (1982) analysed ^{29}Si-enriched silica solutions at low concentration using NMR, and showed that even at pH 7.2 a 97.1 ppm silica solution contain dimeric species. This conclusion was also supported by Raman studies on dilute (~ 3 mM) silicate solutions by Alvarez and Sparks (1985). The situation gets even more complicated at higher pH and concentration. 19 silicate species, including linear, cyclic and cage-like polymeric species with up to 10 Si have been identified (Harris et al., 1981; Svensson et al., 1986; Bass and Turner, 1997). However, at concentrations <0.01M the major silicate species present are monomeric (Felmy et al., 2001).

A silicate solution at high pH is stabilised by electrostatic repulsion of the anionic silicate species. However, if the pH is reduced, or the concentration is increased, polymerisation will occur. Below pH 2 the reaction is catalysed by H^{+} whereas above pH 2, OH^{-} can be seen as the catalyst as it is generating anionic species. The polymerisation process can be described according to the following three steps: 1) condensation of monomer to form dimer, trimer etc. 2) nucleation of colloidal particles, and 3) growth of colloidal particles. The first step, condensation of silica monomers catalysed by OH^{-}, is generally described according to the following reaction (Iler, 1979):

$$\equiv Si{-}OH + HO{-}Si\equiv \xrightarrow{OH^{-}} \equiv Si{-}O{-}Si\equiv + H_2O \qquad (2.18)$$

Continuous reaction between monomer and dimer, trimer etc eventually produces a small particle. At pH >7, further growth progresses at the expense of smaller particles (Ostwald ripening), and particles quickly form whose size increases with temperature, due to the greater silica solubility. At pH <7, on the other hand, particles rapidly

aggregate into a gelled network due to the reduced ionic charge on the particles (see Figure 2.27) (Iler, 1979; Brinker and Scherer, 1990). Polymerisation rates are influenced by temperature, pH, ionic strength, and degree of supersaturation. Around pH 7 and at high ionic strength, oligomerisation is fast (Iler, 1979; Icopini et al., 2005). Adding a salt to a silica sol at high pH reduces the charge repulsion between the particles, which induces aggregation and gelling (see Figure 2.27).

Apart from aqueous silicates, a wide range of silicon alkoxides, such as tetraethoxy- and tetramethoxysilane (TEOS and TMOS respectively), can be used to prepare silica gels and particles. Two reactions, in addition to reaction 2.18, are generally used to describe the hydrolysis and condensation of such silica precursors:

$$\equiv Si{-}OR + H_2O \rightarrow \equiv Si{-}OH + ROH \tag{2.19}$$

$$\equiv Si{-}OR + HO{-}Si\equiv \rightarrow \equiv Si{-}O{-}Si\equiv + ROH \tag{2.20}$$

Condensation reactions using TEOS therefore either produce water or ethanol, and can occur simultaneously with the hydrolosis. Since TEOS is immiscible in water, ethanol is often used to homogenise the system. However, as ethanol is produced during the hydrolysis reaction, gels can be formed without the addition of alcohol. Alkoxides are now the most common precursors for siliceous materials in sol-gel processing applications (Brinker and Scherer, 1990).

As this thesis is dealing with silica solutions at high pH and in the presence of alkaline earth metals, the possibility of silicate formation should be considered in addition to silica precipitation. If a solution of a polyvalent salt is added to a dilute silicate solution, precipitation of the corresponding silicate will occur. Several amorphous and crystalline barium silicates can precipitate by mixing sodium silicate and $BaCl_2$ solutions. Generally, it has been noted that crystallinity and composition of the silicate depends on Ba:Na:Si ratios, temperature, and reaction time (Krüger and Wieker, 1965; Iler, 1979).Yadava and Ghosh (1957) proposed the following reactions to take place in such systems:

$$MCl_2 + Na_2O(SiO_2)_x \rightleftharpoons MO(SiO_2)_x + 2NaCl \tag{2.21}$$

$$MO(SiO_2)_x + H_2O \rightleftharpoons M(OH)_2 + (SiO_2)_x \tag{2.22}$$

where M denotes Ba or Sr. A precipitated barium silicate is in equilibrium with with Ba^{2+}, $BaOH^+$, and the various silicate anions in solution (Krüger and Wieker, 1965). The solubility of the alkaline earth hydroxides increase down the Group IIa elements (see Table B.1), and the association constant for $BaOH^+$ is relatively large (K=0.5 (Li and Jean, 2002)) such that even at pH 11, $[BaOH^+] \leq 5 \cdot 10^{-4}[Ba^{2+}]$. The formation

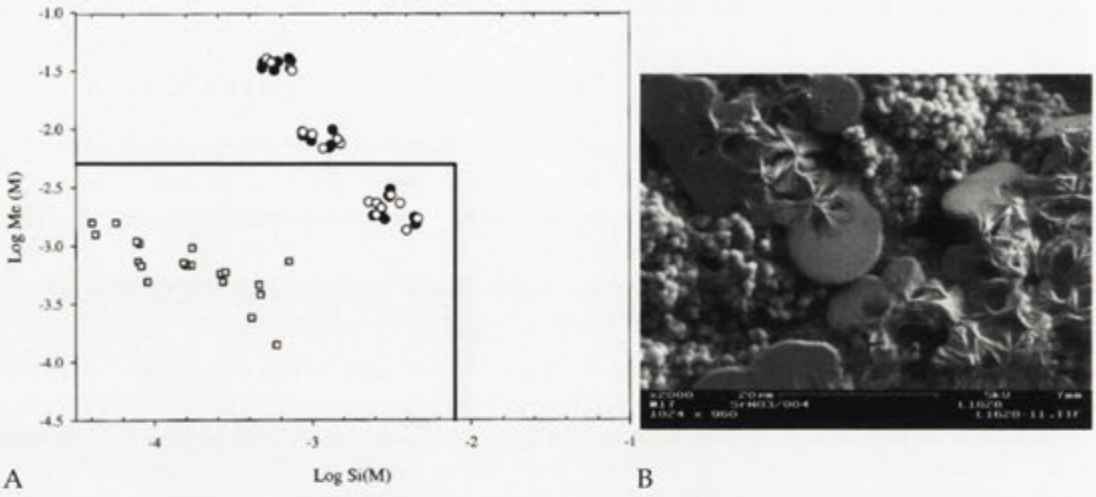

A B

Figure 2.26: In A, the Si and Sr or Ca concentrations in equilibrium with $Sr_5Si_6O_{16}(OH)_2 \cdot 5H_2O$ (circles) and Ca silicate hydrate (squares). The intersection of the thick lines represents the reaction conditions used for some of the biomorphs (at usually lower pH). In B, an SEM micrograph of the fine grained texture and the developed 'sheaf of wheat' structures observed during drying of the strontium silicate phase. Adapter from Felmy et al. (2003).

of barium or strontium hydroxides precipitate corresponding carbonates if in contact with carbon dioxide. This effect was also noticed by Liebsch and Dornberger-Schiff (1958) and Galstian et al. (1982), who showed that barium silicates dried in contact with air contain significant amounts of barium carbonate. Felmy et al. (2003) showed that amorphous strontium silicate becomes crystalline ($Sr_5Si_6O_{16}(OH)_2 \cdot 5H_2O$) upon ageing at room temperature and pH $\geq$11.5. This strontium silicate was considerably more soluble than corresponding Ca-silicate hydrate (see Figure 2.26 A). The granular precipitate was somewhat unstable during washing, which resulted in development of 'sheaf of wheat' structures. This effect was also enhanced during drying at elevated temperatures (see Figure 2.26 B). (Iler, 1979) concluded that the nature of the precipitate will vary depending on the mixing conditions as the ratio of the reactants change. A mixture of amorphous metal silicates of varying compositions are therefore expected at ordinary temperatures. However, microcrystalline silicates can form during aging if the reactants are present in stoichiometric proportions, or at elevated temperatures (Iler, 1979). Solutions giving rise to biomorphs can therefore be expected to contain some amorphous barium silicates upon mixing the reactants.

Colloidal chemistry of silica

As was described in the previous section, silica polymerisation inevitably produces particles of amorphous silica. Under the right conditions these particles can be sta-

bilised so as to produce an aqueous solution containing colloids with a particular diameter. The colloidal state encompasses particles (spherical, needle-like, or other) in the 1 nm to 1μm range; a colloidal dispersion therefore contains particles small enough not to be affected by gravity. A dispersion of stable silica colloids in water is normally referred to as a silica *sol* (Bergna, 1994). Several different methods exist to produce monodispersed silica sols, using both water-glass and tetraalkoxysilanes as starting materials (Stöber et al., 1968; Yoshida, 1994). Particle size can be tuned by using high temperature and the slow addition of oligomeric 'active' silica that can directly polymerise with the growing particles. The monodisperse silica colloids are then stabilised against aggregation by charge repulsion, or by the adsorption of an inert coating on the particles. Silica sols can be stable for decades if prepared correctly, and have proven very valuable for industrial processes as fillers, chromatography and catalysis support, and for materials engineering (Iler, 1979). In analogy with natural opals, silica colloids can be periodically arranged in three dimensions, showing great promise in the fabrication of photonic crystals (Vlasov et al., 1997).

Aggregation of the colloidal particles can occur in several ways, of which gelling is just one type of aggregation. During gelling, the sol becomes viscous as larger chains are formed that eventually interconnect and the sol becomes rigid. A gel is therefore seen as an open network of particle chains, which forms when there is appropriate surface charge that allow the particles to collide and further polymerise. The structure of the final gel therefore depends on the particle size distribution and the degree of attraction between them. As can be seen in Figure 2.27 B, sols are generally stable at pH above 8 as the particles have an increased surface charge. At pH around 6-7, decrease in surface charge results in very rapid gelling times. Between pH 2 and 6, gel times decrease, and are proportional to the $[OH^-]$. At pH 2, the observed gelling times are quite long, due to the fact that the colloidal surface exhibits no charge and are stabilised somewhat by the strong adsorption of water, however, addition of HF (normally present as impurity) decreases gelling times, as the F^- acts in very similar fashion to OH^-, and can catalyse the formation of siloxane bridges (Iler, 1979; Brinker and Scherer, 1990).

Depending on concentration, pH, and type of salt, a precipitate instead of a gel can be formed. A neutral or alkaline silica sol containing considerable amounts of salt will form a precipitate, and not a gel. In contrast to gels, the precipitate contains a higher concentration of silica particles compared to the original sol and settles out. Coagulation can occur as a result of decreased surface charge and hydration of the colloidal surface, and can be brought about by the addition of 'bridging-agents' between the particles. Cations, and especially divalent cations, induce coagulation between charged particles. Divalent cations, like Ca^{2+} and Ba^{2+}, can therefore link two parti-

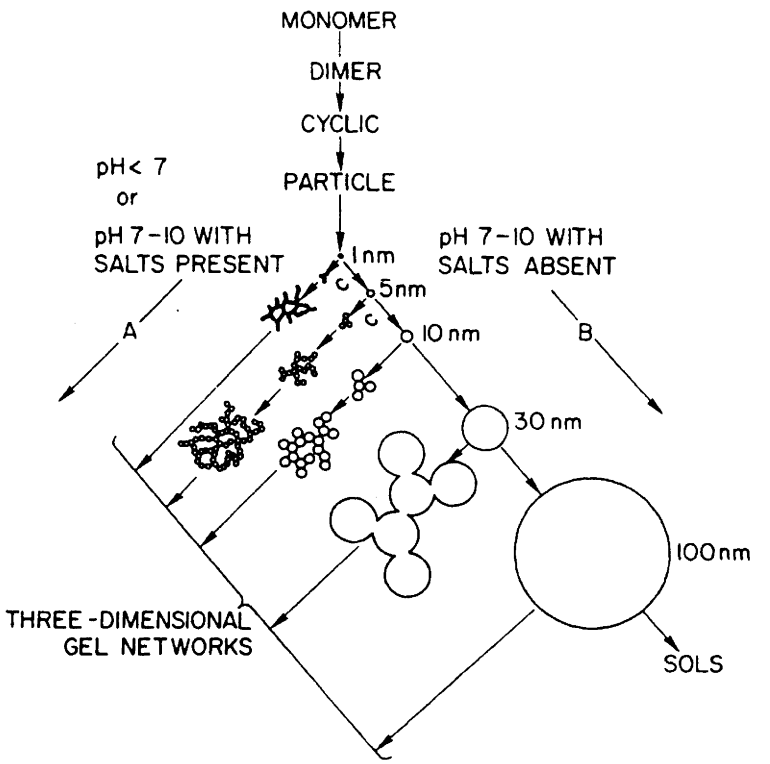

A

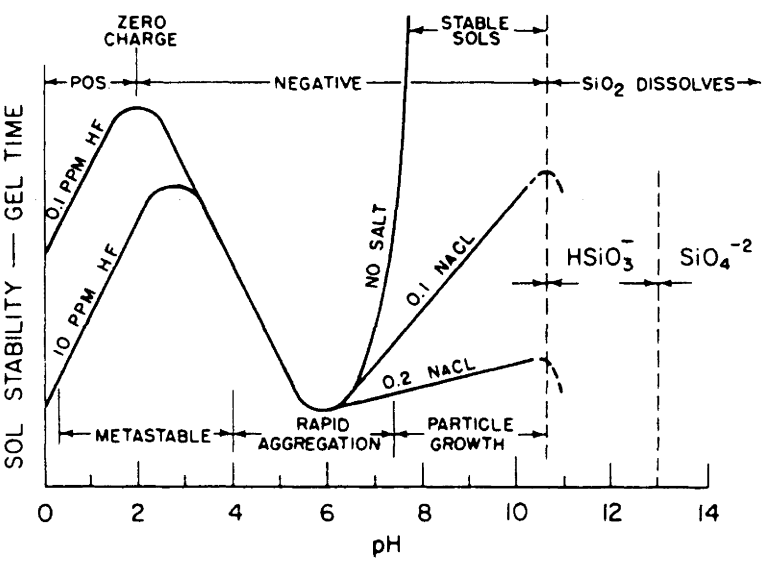

B

Figure 2.27: The classic schematic polymerisation behaviour of silica (A), and the effect of pH on sol stability and gelling time. Adapter from Iler (1979).

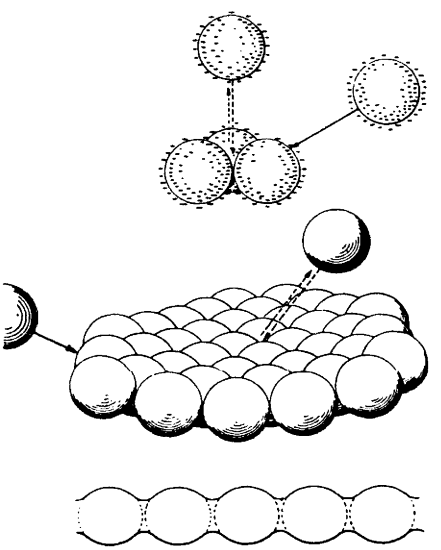

Figure 2.28: Aggregation of colloidal silica particles into sheets. When a cluster of three particles has formed, aggregation of the next particle occurs on the edge of the sheet as the repulsive force is larger on the face than on the edge. Adapter from Iler (1979).

cles together and coagulation occurs well before the colloid surface is saturated with cations. Such adsorption of alkaline earth cations involves proton exchange. The specific surface interaction depends on pH, concentration, and the degree of hydration, and the addition of such cations can induce charge formation on the surface (Tadros and Lyklema, 1969; Dove and Craven, 2005):

$$\equiv Si{-}OH + Ca^{2+} \rightarrow \equiv Si{-}O^{-} - Ca^{2+} + H^{+} \quad (2.23)$$

$$\equiv Si{-}OH + Ca(H_2O)_n^{2+} \rightarrow \equiv Si{-}O^{-} - Ca(H_2O)_n^{2+} + H^{+} \quad (2.24)$$

$$\equiv Si{-}OH + Ca^{2+} + H_2O \rightarrow \equiv Si{-}O^{-} - Ca(OH)^{+} + H^{+} \quad (2.25)$$

of which the latter reaction becomes significant only at higher pH. As the alkaline earth ions are divalent, complex formation with two neighbouring silanol groups is also possible. However, it has been shown that the number of protons exchanged per cation is close to 1 for these ions. This indicates that every complexation with a silanol sheds only one proton (Persello, 2000). It has been shown that alkaline earth ions specifically adsorb and form complexes with the silica surface with the following trend of increasing adsorption $Sr^{2+} < Ba^{2+} < Ca^{2+} < Mg^{2+}$ at pH$\gtrsim$6.5 and at both low and high metal concentration (Iler, 1979; Persello, 2000; Karlsson et al., 2001; Dove and Craven, 2005).

Except for the Sr and Ba ordering, this trend is opposite to the Hofmeister series, which rank ions on the basis of their 'salting in' and 'salting out' effect on proteins. In the Hofmeister series the alkaline earth cations show increasing destabilising effect with an increase in molecular weight, and decrease in solvent structuring ability (Cacace et al., 1997). The hydration of these ions decreases with increasing molecular weight, and their hydroxides become more and more soluble. Dove and Craven (2005) suggested that the cation specific dependence on the increasing negative surface charge observed at pH$\gtrsim$7 may be due to solvation entropy differences between the ions. However, the opposite trend has been observed by Tadros and Lyklema (1969). Adsorption and complexation of cations with silica is clearly a very complex phenomenon.

Large polyvalent cations, such as La^{3+}, have been shown to adsorb practically irreversibly to silica surfaces due to the high polarisability and/or hydration, and will cause coagulation at very low concentrations. If the pH is sufficiently high that the solubility product of the corresponding hydroxide is exceeded, coagulation will occur in the presence of the hydroxide.

Flocculation agents, such as large cationic surfactants, effectively link colloidal particles through their hydrophobic tails, which form micelles inbetween the colloids. Low concentrations of cetyltrimethylammonium chloride (CTAC) have shown to give rise to sheet-like aggregates of silica particles at high pH. A mechanism for such

aggregation can be seen in Figure 2.28. It is believed that the surfactants are only adsorbed at the point of contact, so particle adhesion on the surface of the sheet is prevented by the repulsive ionic charge on the colloids themselves. At the edge of the sheet, however, such repulsive forces are apparently overcome by the presence of surfactants (Iler, 1979). A similar effect has been noted in solutions containing cellulose, which induce the precipitation of sheet-like silica composed of ~4 nm sized silica particles (Perry and Lu, 1992).

The silica surface and stability of sols

The properties of the silica surface depend strongly on the way it is prepared and the aqueous conditions. At its surface, silica consists of silanol groups (-Si-OH) and siloxane bridges (-Si-O-Si-). The number of silanol groups, and their spatial relationship, as well as the number of siloxane bridges affect strongly the characteristics of the silica surface. Silicas prepared in aqueous environments are characterised by predominantly hydroxylated surfaces (El Shafei, 2000). The hydrophilic silica surface, populated by silanol groups become 'hydrophobic' upon thermal treatment under vacuum, as neighbouring silanol groups condense to form siloxane bridges. The degree of condensation is dependent on the temperature, morphology, and crystallinity of the sample, and it has been shown to be a completely reversible process (Feng et al., 1996) (c.f Bolis et al. (1991)). Water is strongly adsorbed to the silanol groups through hydrogen bonding in aqueous environments. As was mentioned earlier, depending on the pH, silanol groups can become ionic; at pH below the point of zero charge (PZC ~ pH 2) protonation of the silanol groups occur and the surface can act as an anionic exchanger. Conversely, at pH above PZC, deprotonation results in negatively charged -Si-O^- groups able to adsorb cations (Iler, 1979; El Shafei, 2000).

Colloidal stability is generally described by the DLVO theory (named after its creators; Derjaguin, Landau, Verwey, and Overbeek), which treats the net force between particles as the sum of the attractive van der Waals forces[1] and the repulsive electrostatic forces, created by the adsorbed ions on the colloid surface. The electrostatic energy of repulsion (V_R) depends on the adsorbed ions and the surface ions of the colloidal particle, which together constitute the double layer (see Figure 2.29). Counterions in solution adsorb to the surface and effectively screen the surface charge. The surface potential ϕ drops linearly through the Stern layer, where counterions and water are tightly bound to the surface. In the diffusive double layer ions move freely and

[1]A collective term for permanent dipole/permanent dipole (Keesom interactions), permanent dipole/induced dipole (Debye interactions), and induced dipole/induced dipole (London dispersion forces). van der Waals forces are almost always attractive, and relatively long-range (Hiemenz and Rajagopalan, 1997).

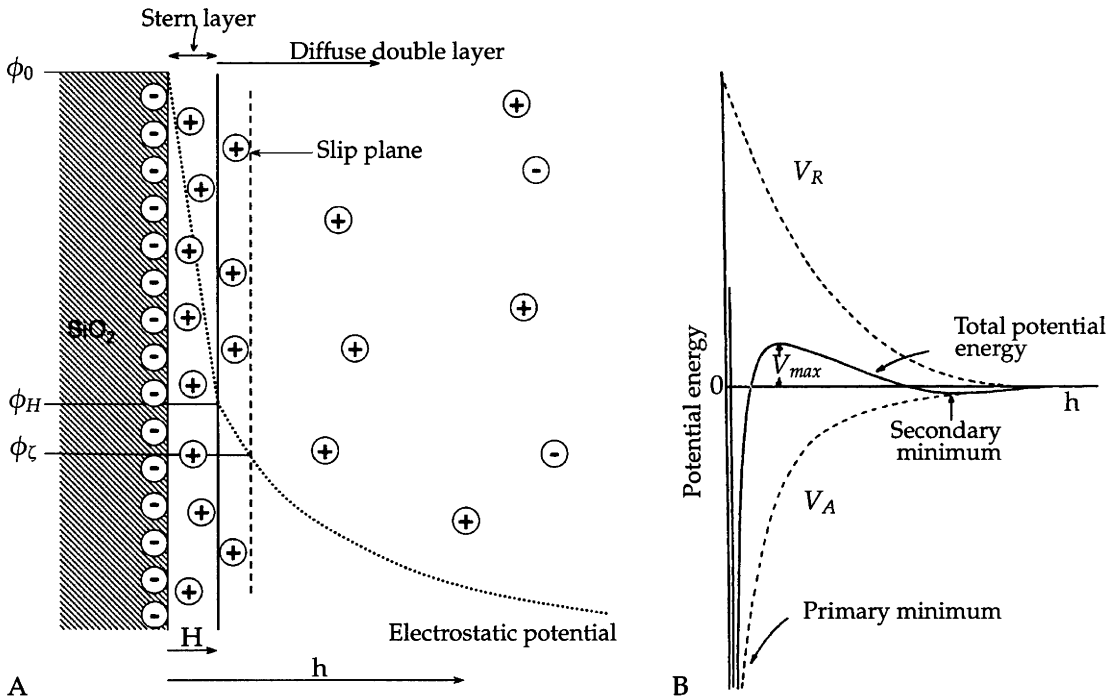

Figure 2.29: Schematic representation of the electrostatic double layer (A), where ϕ is the potential at the surface (ϕ_0), at the Stern layer (ϕ_H), and at the slip plane (ϕ_ζ, the zeta potential), h is the distance from the surface. The total potential experienced between two approaching particles, predicted by the DLVO theory (B), where V_R is the repulsive electrostatic potential and V_A is the attractive van der Waals potential. Adapted after Brinker and Scherer (1990).

the potential decreases as the distance from the surface increases:

$$V_R \propto e^{-\kappa(h-H)} \quad , \quad \frac{1}{\kappa} = \sqrt{\frac{\varepsilon\varepsilon_0 kT}{\sum c_i(z_i e)^2}} \approx \frac{3.04 * 10^{-1}}{\sqrt{C}}$$

where $1/\kappa$ is the Debye-Hückel screening length, ε is the dielectric constant of water, ε_0 is the permittivity in vacuum, k is Boltzmanns constant, c_i and z_i are the the concentration (molecules per cubic metre) and valence of counterion i, and e is the charge of an electron. For 1:1 electrolytes such as NaCl in aqueous media at 25 °C, $1/\kappa$ is 0.96 nm and 9.6 nm at 0.1 M and 1 mM concentration C respectively (Evans and Wennerström, 1999). The total potential experienced by two approaching particles depends on the magnitude of V_R and V_A. At low counterion concentration, $1/\kappa$ is large, resulting in a large screening length. The repulsive potential extends far into the solvent under such conditions, and the sol is stable. Increasing the concentration of counterions results in tightly bound counterions at the surface, and the electrostatic potential drops more rapidly. In such a scenario the attractive potential is dominating, and the particles can coagulate. The primary minimum at very short distances of separation is produced

by the van der Waals forces which can cause coagulation if the repulsive barrier (V_{max}) can be overcome. The secondary minimum is generally not deep enough to result in coagulation (Brinker and Scherer, 1990). Due to the surface charge of the colloidal particles, they will move in an electric field (electrophoresis), and carries the adsorbed counterions towards the electrode with opposite charge. The slip plane defines the boundary where the outer solution is free flowing, and is not affected by the electric field. The potential at the slip plane, the zeta potential ($\phi\zeta < \phi_0$), determines the rate of movement, and can be measured. DLVO theory predicts that a silica sol should not be stable at around pH 2, the isoelectric point and PZC, however, as can be seen in Figure 2.27 B, this is not the case. It is believed that the stability seen at this low pH is due to strong adsorption of water (Brinker and Scherer, 1990).

Due to the unique surface properties, adsorption on amorphous silica is now widely used for many industrial purposes, such as support material in chromatography and for catalysts. Preferential partitioning of adsorbates and the silica surface can be manipulated through control of the chemical nature of the solvent, the type of adsorbate, and the nature of the silica surface. The intermolecular forces governing the adsorption involves hydrogen bonding, electrostatic, and hydrophobic interactions. Silanol groups on the surface can, through hydrogen bonding and electrostatic interactions, adsorb a great variety of neutral polar organic molecules, ranging from small alcohols, aromatics, to larger polymers, surfactants, and proteins (Iler, 1979; Nawrocki, 1997; Parida et al., 2006). Aromatic hydrocarbons, such as benzene, have been shown to adsorb to silica through the interactions of delocalised π-electrons with silanols. Phenol and formaldehyde, which are adsorbed and polymerised on biomorphs in Chapter 6, can therefore interact with silica by hydrogen bonding and π-electrons. Cationic surfactants, such as CTAB, have been shown to go through several stages of aggregation on silica surfaces relating to the concentration and the critical micelle concentration (CMC) of the surfactant in question (Atkin et al., 2003).

As CTAB will be used as an additive in a series of biomorph synthesis experiments, a brief discussion regarding CTAB adsorption on silica surfaces is in order. The CMC of CTAB in pure water is 0.9 mM, a value that decreases with increasing ionic strength (for instance CMC is 0.125 mM at 10 mM KBr (Atkin et al., 2000)). In Figure 2.30 a depiction of the behaviour of CTAB adsorption with increasing concentrations can be seen. At low concentrations, scheme A in Figure 2.30 ([CTAB]$\ll$CMC), CTAB is electrostatically adsorbed on the anionic silica surface, which further promotes ionisation around the adsorption site as neighbouring hydroxyl groups become more acidic. Increasing the surfactant concentration, scheme B in Figure 2.30 ([CTAB]<CMC), results in increased adsorption at the induced charged sites, where neighbouring CTAB molecules interact through hydrophobic forces. The adsoption is therefore driven by

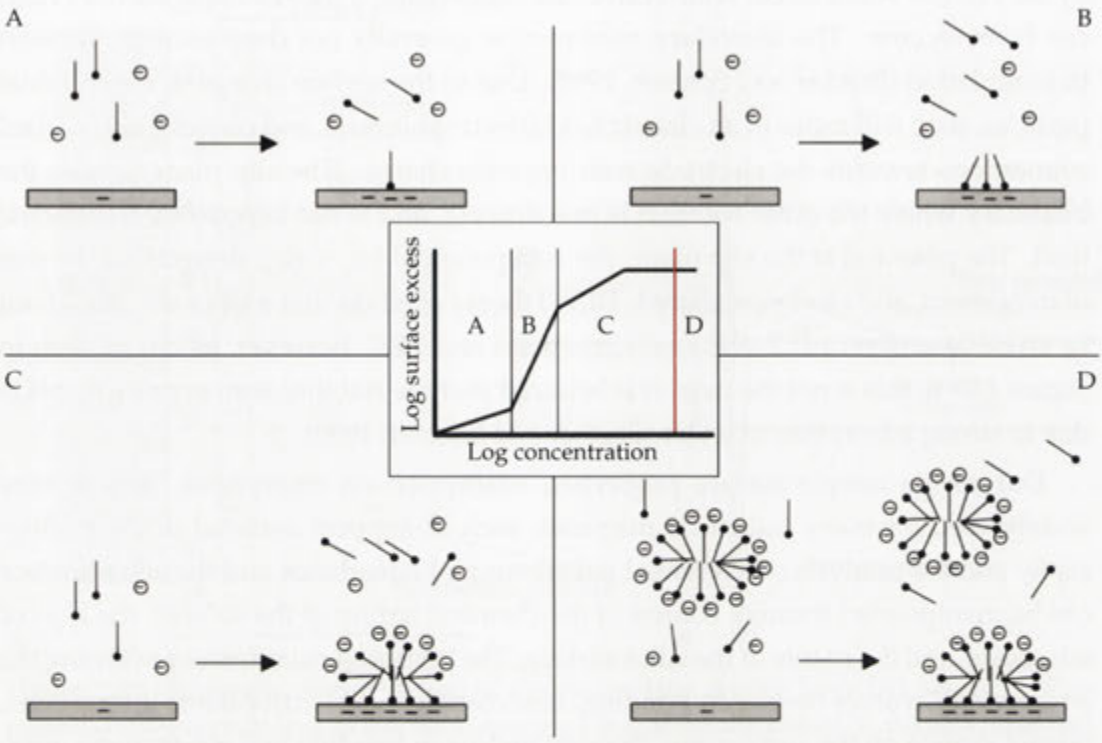

Figure 2.30: Schematic illistration of the influence of surfactant concentration on CTAB adsorption on silica surfaces. Red line marks CMC. See text for details. Adapted after Atkin et al. (2003).

both electrostatic and hydrophobic interactions. The silica charge increases as more and more surfactants are adsorbed. At the maximum concentration in scheme B, the overall surface charge is balanced between the ionised silanol groups and the adsorbed surfactants; the surface charge is neutralised and the surface is made hydrophobic due to the hydrocarbon chains. Even higher surfactant concentrations, scheme C in Figure 2.30 ([CTAB]≤CMC), result in micellar aggregation on the surface, which renders the surface hydrophilic as the surfactant headgroups face outward into the solution. The aggregation is driven by hydrophobic interactions between the hydrocarbon chains. The overall charge is now positive due to the surface excess of CTAB. At concentrations slightly below CMC, the surface is saturated with surfactant micelles, and increasing the concentration further will not result in increased adsorption. At concentrations above CMC, scheme D in Figure 2.30 ([CTAB]≥CMC), micelles may adsorb directly on the surface (Atkin et al., 2003). The maximum equilibrium surface adsorption of CTAB on silica is ~1.6 mg m^{-2} (Atkin et al., 2000). When a large surface area for adsorption is present, the result may be a significant depletion in the concentration of CTAB in solution. This will typically be more significant at low concentrations.

Figure 2.31: Chemical gardens displaying colourful 'plant'-like structures. The various colours are due to the different metal salts used; for example Ni^{2+} green, Fe^{3+} reddish brown, Co^{2+} and Cu^{2+} blue, Ca^{2+} white. Adapted from `http://www.technion.ac.il/ASRI/stars.html`.

Surface adsorption of CTAB will be relevant in Chapter 3 when the origin of biomorph morphology will be discussed.

2.3.3 Self-assembly of siliceous materials

In this section a brief overview of the variety of self-assembled siliceous structures acquired from aqueous solutions is given. Porous structures of both crystalline silicates (zeolites), and amorphous silica will be discussed, as well as the generation of chemical gardens. These examples will give an insight into the various self-assembly processes that involves siliceous species.

Chemical gardens

Silica, silicate, or chemical gardens are spectacular inorganic tree like structures formed when placing a crystal of a soluble metal salt in a diluted silica solution (see Figure 2.31). Most children with a chemistry set are familiar with these formations, as they can easily be prepared and grow colourful 'landscapes' within minutes. The colour produced depend on the metal salt used; calcium salts result in white silicate gardens, cobalt salts in dark blue ones, and nickel salts in green etc (see Figure 2.31).

Even though this reaction system has been known for well over two hundred years, very few investigations concerning the composition and formation mechanism have been conducted, and the topic is still not completely understood (Coatman et al., 1980; Cartwright et al., 2002). It was realised early on that the remarkable growths are a result of an osmotic pressure across a semipermeable membrane that forms when the metal salt comes in contact with the silica solution. The influx of water across this membrane dissolves the crystal and increases the pressure within the 'vesicle' until it is high enough to rupture the gelatineous membrane. Continuous outflow of the salt solution reacts with the silicate solution at the tip of the membrane, forming tubular

structures as the reaction proceeds (see Figure 2.32). Influx of hydroxide ions are responsible for the precipitation of silica on the outside of the tubes, and metal oxides on the inside. A compositional change with the tube length is therefore expected. Furthermore, such changes can occur even after the growth has stopped, and with time, the structures harden as deposition continues (Cartwright et al., 2002). The widths of the tubes are normally reduced as the reaction proceeds. It is believed that the reduced flow rate of the salt solution, and the increased length of the tube itself cause the reduction in tube diameter with time (Cartwright et al., 2002).

It seems that precipitation of some chemical gardens are accompanied by a small gas bubble at the tip of the tube (Collins et al., 1998; Thouvenel-Romans et al., 2005), in which case a bubble-guided mechanism for the growing tubes can be proposed, a mechanism common in many natural occurring systems (Stone and Goldstein, 2004). The structures formed are dependent on the silicate concentration as well as the type of salt used. If the water glass solution is too concentrated, the membrane will be strong enough to withstand very high pressures and will only rupture with difficulty (Coatman et al., 1980). At low silicate concentrations, the membrane is very flexible, resulting in globular structures. Using different metals give rise to different morphologies, as the silica-metal interaction as well as salt solubility varies between salts (Coatman et al., 1980). The optimum silica concentration for creating chemical gardens with $CoCl \cdot 6H_2O$ lies between 1.56 and 0.625 M (Cartwright et al., 2002). A wide range of metal salts can be used to form silicate gardens, except the alkali metals as the silicate forms are quite soluble (Clunies Ross, 1910; Coatman et al., 1980; Cartwright et al., 2002). Furthermore, similar structures can be formed using aluminates, borates, phosphates, chromates, and even carbonates as anions instead of silicate. One can also produce similar structures by injecting a solution of the metal salt into the silicate solution (Thouvenel-Romans and Steinbock, 2003; Thouvenel-Romans et al., 2004).

Cartwright et al. (2002) followed the formation of a chemical garden with interferometry and showed that the morphogenesis is a combined effect of the chemical reactions taking place, and osmosis-driven forced convection and buoyancy-driven free convection. As all tubes always grow upwards, regardless of the placement of the crystal, buoyancy must be important to the morphogenesis of chemical gardens. Microgravity experiments have shown that the reaction is much slower and other morphologies also come into play when free convection is removed from the system (Jones and Walter, 1998).

Most of the chemical garden structures are amorphous precipitates, but it was recently shown that tubes formed in the aluminosilicate system have hierarchical domains composed of nanorods of amorphous silica (Collins et al., 1998). The same silicate garden has also shown to be catalytically active (Collins et al., 1999). Other

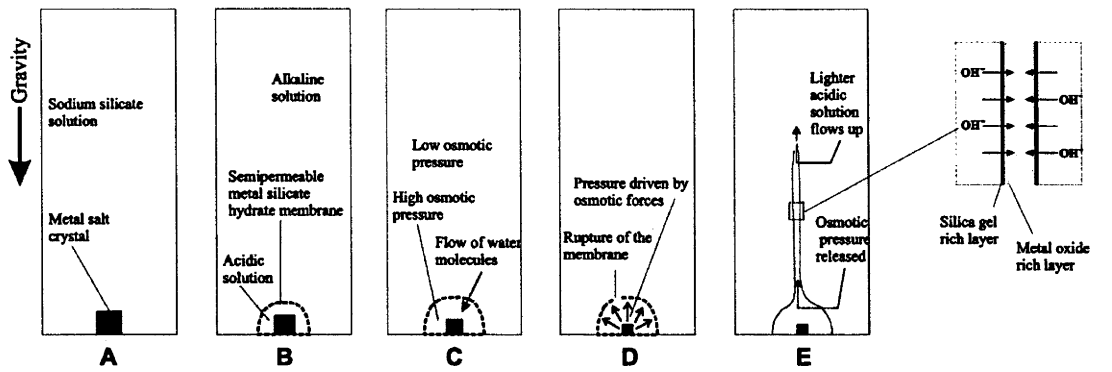

Figure 2.32: Schematic representation of the growth of a chemical garden. The initial conditions before the growth has started can be seen in A. In the first reaction step, the semipermeable membrane is formed between the acidic solution that surrounds the dissolving crystal and the alkaline silicate solution (B). As water flows through the membrane into the 'vesicle' it expands (C), till its limits has been reached and it ruptures at weak points (D). Tubular growths are formed as the acidic metal salt solution is injected into the alkaline silicate solution (E). The membrane acts as an osmotic pump and continuous outflow fuels the precipitation of metalsilicate at the tip of the forming tube. Influx of hydroxide ions across the tube wall cause silica and metal oxide to precipitate on the outside and inside of the tube wall. Adapted from Cartwright et al. (2002).

interesting chemical garden phenomena include spiral tube growth in the presence of a magnetic field. The chirality of the tubes can be controlled by the direction of the magnetic field, as well as the positioning of the metal salt crystal, i.e. near the container wall or not (Duan et al., 2005). Large twisted ribbon like structures (~ 1.5 mm in width) have also been observed when a 0.5 M cupric sulphate solution is injected into a 2.5 M silicate solution. These helical structures are thus formed at high silicate concentrations where there is a large density difference between the silicate solution and the metal salt solution, which causes the tubes to collapse (Thouvenel-Romans et al., 2005). All collapsed tubes show similar behaviour, and a possible explanation for the twisted structures must therefore relate to tube composition and mechanical characteristics, that causes the tubes to collapse.

Apart from being spectacular structures, chemical gardens have also been shown to have industrial applications. For instance, the hydration of Portland cement can be seen as a reverse silicate garden, in which silicate grains are immersed in a metal salt solution. The formation of a calcium-silicate-hydrate gel subsequently interlocks grains with its tubular growths. A thorough understanding of chemical gardens will therefore aid the development of cements with specific properties. Furthermore, as chemical gardens are grown from solutions containing sodium silicate and soluble metal salts, their relevance to biomorph formation is noteworthy.

Micro- and mesoporous structures

Porous materials in the micro- and meso-range, have by definition pore diameters ($d0$ in the <2 nm, and 2< d < 50 nm size respectively. Macroporous materials have pores with a diameter larger than 50 nm (Soler-Illa et al., 2002). Zeolites (from greek, *zein*, to boil, and *lithos*, stone) are characterised by a crystalline aluminosilicate framework with a large internal regular pore system (see Figure 2.33 A and B). These channels are occupied by water and various weakly bond cations, which make up the charge deficit due to having aluminium in the crystalline network (see Figure 2.33). These materials, first described by A. F. Cronstedt in 1756, are the most important class of microporous solids, as they are widely used for industrial applications, such as catalysis, adsorption, and detergents[2]. The reason for the extensive use of zeolites is the intrinsic surface properties of the channel system, which allow selective adsorption, reactions, and exchange of molecular species. Due to specific pore size distributions, only compounds with restricted molecular dimensions can adsorb into the zeolite structure (Davis and Lobo, 1992; Soler-Illa et al., 2002). Naturally occurring zeolites are more restricted in the size and shape of the pore systems than their synthetic counterparts. Using different synthesis procedures can be used to tailor the properties of zeolites, including generation of pores larger than in natural zeolites (Davis and Lobo, 1992). Traditionally, zeolites have been synthesised using gels at high pH and temperatures that contain silica, aluminium, and a variety of cations. However, many zeolites require organic compounds to obtain specific topologies. The main factors influencing the crystallisation of zeolites are: 1) SiO_2/Al_2O_3 ratio; 2) pH; 3) the type of cations present (inorganic, organic); 4) the type and amount of solvent; 5) temperature and duration of reaction; 6) the type of stirring, if present; and 7) order of mixing (Soler-Illa et al., 2002). The SiO_2/Al_2O_3 determines the composition of the framework, which in turn affects the physical properties of the zeolite (thermal stability, hydrophobicity, cation exchange properties etc.). The type of cation is especially important for the structure of the porous network. These ions effectively determines the topology of the crystalline zeolite, as they direct the channel morphology of particular structures. However, a full understanding of this templating effect is lacking.

Two main formation mechanisms have been proposed to explain the crystallisation of zeolites (Soler-Illa et al., 2002; On and Kaliaguine, 2004). The first one describes the process as a heterogeneous solid-solid transformation of the gel, where nucleation proceeds as a result of reorganisation of the solid network. In the second one, on the other hand, crystallisation is believed to take place in the solution, where the gel acts as a reservoir of reactants. Both of these mechanisms have been shown to apply during

[2]The world annual consumption in 1998 exceeded 1000 000 tons (Soler-Illa et al., 2002).

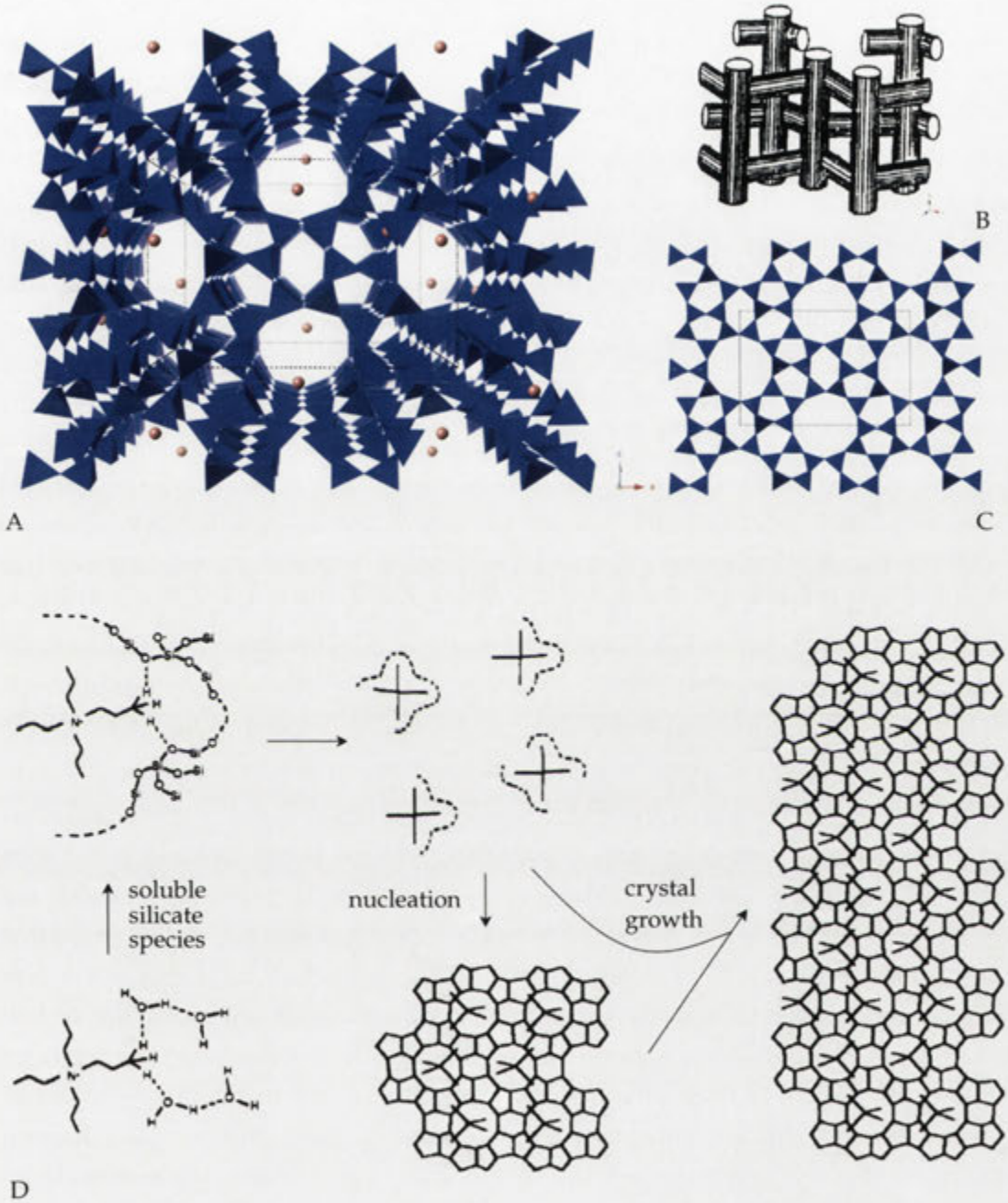

Figure 2.33: The crystal structure of silicalite-1 (ZSM-5, MFI topology) viewed along the *b*-axis (A, C) displaying the intricate channel-system (B) that characterise zeolites in general. In D, a proposed mechanism for the formation of silicalite-1, using TPA as a structure directing agent, can be seen. Crystal structures seen in A and C was made with CrystalMaker, using crystallographic data from the CrystalMaker Library. Channel system in B is adapted from Soler-Illa et al. (2002), and mechanism in D is adapted from Burkett and Davis (1994).

synthesis of various zeolites (On and Kaliaguine, 2004). The synthesis of silicalite-1, which has a simple channel system and a framework with Si/Al ratio > 500, has received a lot of attention as a 'model zeolite' for studying formation mechanisms. This structure can be synthesised using many different organic species, however, the use of tetrapropylammonium cations (TPA^+) results in a pure phase (Soler-Illa et al., 2002). Burkett and Davis (1994) proposed the model schematically represented in Figure 2.33 D. It is believed that the structure directing effect by TPA^+ is a result of van der Waals interactions between the silicate species and the organic template, which cooperatively self-assemble during nucleation and crystal growth. The silicate is moulded around the TPA^+ molecule, as one molecules is present at each tunnel intersection (see Figure 2.33 B). This model is in support of the solution mediated crystallisation mechanism, and has been confirmed by others (see Soler-Illa et al. (2002) and references therein). Irrespective of which mechanism is in place, the generation of the porous structure is a result of the close interaction of the cationic organic or inorganic species with that of silicate. Because of the tuneable characteristics of zeolites these materials have shown widespread use within a number of applications, as discussed above. However, the limitations of the pore sizes, which restricts the uses to small molecules, pushed efforts into making porous materials in the mesoporous range. This was accomplished in the early 90's by researchers from Mobil Oil (Kresge et al., 1992; Beck et al., 1992) (although, earlier reports of similar synthesis conditions have been found in the literature (Di Renzo et al., 1997)).

In contrast to zeolites, mesoporous materials are predominantly amorphous, however, they posses long range order stemming from the highly ordered pores with narrow size distribution. By analogy to some zeolites, mesoporous materials are synthesised using organic molecular templates, however, these templates are large micellar aggregates, and not molecular as in the case of zeolites. Synthesis procedures involve an aqueous solution of surfactants and inorganic or organic source of low molecular weight silica, at alkaline, neutral, or acidic pH, and moderate temperatures (Palmqvist, 2003). The resulting material is composed of a regular arrangement of surfactants, embedded in amorphous silica. Removal of the organic template through calcination at high temperatures results in a porous non-crystalline siliceous material (see Figure 2.34). The surfactants are usually cationic, such as CTAB, or non-ionic, such as triblock copolymers of polyoxyethylene-polyoxypropylene-polyoxyethylene ($EO_x - PO_y - EO_x$, Pluronics), though anionic surfactants have also been used. A characteristic of amphiphilic molecules is their ability to self-assemble, above a critical concentration, into structurally different aggregates (see Figure 2.35), so as to keep the nonpolar part separate from aqueous solvent (Evans and Wennerström, 1999). These aggregates can further arrange into phases possessing long range order, so called liq-

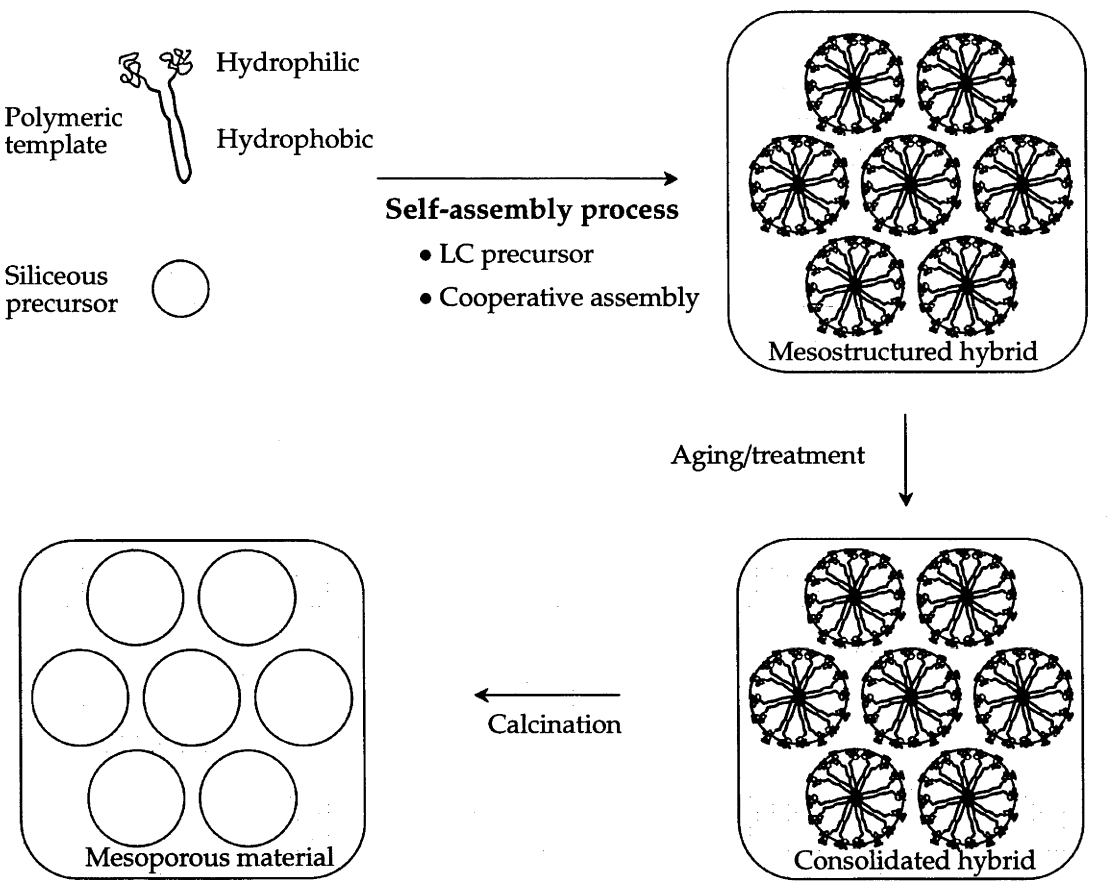

Figure 2.34: Schematic representation of the self-assembly process of mesoporous silicas. Adapted after Soler-Illa et al. (2002) and Soler-Illa et al. (2003).

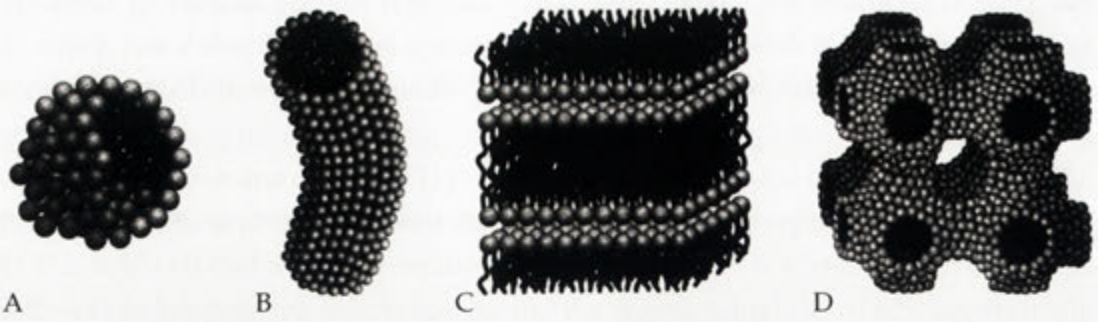

Figure 2.35: Four examples of amphiphilic micellar structures; A) spherical micelle; B) cylindrical micelle; C) planar bilayer; and D) bicontinuous structure. Adapted from Evans and Wennerström (1999).

uid crystals. The binary phase diagram for such amphiphiles in water are dependent on concentration and temperature (Raimondi and Seddon, 1999). During synthesis of mesoporous silica, the close interaction between the silicate species and the polar organic moiety of the amphiphiles, together with the finetuning of silica polymerisation kinetics, are responsible for the formation of a specific mesoporous structure.

Several different mechanisms have been proposed to explain the formation of mesoporous silicas, and these differ in two principal ways regarding the role of the surfactant. In the liquid crystal (LC) templating route, mesoporous silicas are formed by silica polymerisation around a pre-existing organic LC phase, which do not go through any phase changes throughout the synthesis. The mesoporous structure is thus directly templated by the surfactant aggregates, and the type of structure formed can be predetermined by the binary phase diagram of the surfactant/water system. It has been shown that some mesoporous silicas form by this mechanism (Attard et al., 1995; Wong and Knowles, 2004). This synthesis route requires a relatively high concentration of the organic template, and could therefore not explain the self-assembly process in dilute systems, where no such complex organic phase exist. Instead, a model based on the cooperative interaction between the polymerising silica and the surfactants was put forward. In such dilute systems, it is believed that the coupled interaction between the template and the silicate are at the source of the formation of specific mesoporous structures. Depending on the nature of the surfactant (charge, hydrophobicity etc.) and the charge and polymerisation state of the silica, several interactions (also active in the LC templating route) can be identified, some of which are (S surfactant, I silica; X halogen, M metal): 1) S^+I^-, MCM-41(two-dimensional hexagonal structure) precipitated at high pH with CTAB as surfactant; 2) $S^+X^-I^+$, SBA-3 precipitated at low pH with CTAB, X^- is Cl^-/Br^-; and 3) $(S^0H^+)(X^-I^+)$ as in the case of synthesis of SBA-15 (two-dimensional hexagonal structure) using Pluronic P123 at

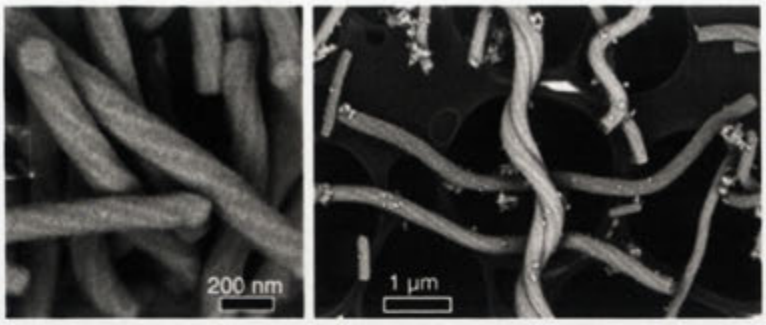

Figure 2.36: SEM images of chiral twisted 2D hexagonal mesoporous silica. Adapted from Ohsuna et al. (2005).

acidic pH (Huo et al., 1994; Wong and Knowles, 2004). These electrostatic and van der Waals forces are at the core of the self-assembly process. It is believed that such interactions, coupled with the continuous polymerisation of silica leads to the formation of polymer-silica nuclei. With time these aggregates grow, fed by surfactants in solution (at the expense of micelles), and organisation into specific phases depend on the cooperative interaction between the inorganic and organic reactants. Further condensation of silica species can lead to phase changes in response to a net change in charge density at the interface (Soler-Illa et al., 2002; Edler, 2005). Although the mechanisms causing the formation of mesoporous silicas are highly complex, and not completely understood, it is clear that in all of the mechanisms proposed, a balanced interaction between silica and amphiphile is essential to the formation of ordered mesoporous materials with small pore size distribution. The phase and geometrical dimensions of the pores and the walls can be controlled somewhat through manipulating the reaction conditions. For instance, in the Pluronics case, it has been shown that the length of the EO blocks have a large effect on both the structure, and the wall thickness, whereas the PO block affects the size of the pores. It is further believed that the hydrophilic EO blocks extend into the polymerising silica, causing micropores to form within the amorphous walls. By choosing the right conditions (EO length, PO-lenght, temperature etc) it is therefore possible to manipulate the final product having desirable properties (Kipkemboi et al., 2001; Flodström and Alfredsson, 2003).

By using chiral surfactants it is possible to synthesise highly ordered chiral 2D hexagonal mesoporous silica with a twisted morphology (Che et al., 2004). The helical arrangement of the hexagonally ordered pores is induced by the stirring rate during the first 10 minutes of the synthesis. Higher stirring rate results in particles with larger diameter and increased pitch length. Both right- and left-handed twisted morphologies are obtained with the ratio 7.5:2.5 (Jin et al., 2006). The chirality of the porous material is however not necessarily due to the use of chiral surfactants. Wang

et al. (2006) showed that helical mesoporous silica can be produced with achiral CTAB. The origin of the twisted morphology is therefore not clear. Due to the high porosity and tunable pore sizes, mesoporous materials have shown promise as potential catalysts. Furthermore, they can be functionalised through secondary treatments, thereby adding to the repertoire of possible uses (Fryxell, 2006).

One key drawback with these types of materials is their low hydrothermal stability and acidity compared to crystalline zeolites. A key objective of mesoporous research has been to find a synthetic route to mesoporous zeolites. This was accomplished only very recently by Choi et al. (2006) who used a specifically designed amphiphilic organosilane as a template. Furthermore, the mesopore size could be manipulated by varying the chain length or the temperature. These materials therefore show great promise as new catalysts, and will undoubtedly instigate a wealth of scientific research.

Siliceous materials evidently participate in a variety of self-assembly processes, from very chaotic silica gardens to highly ordered micro- and mesoporous materials. As in the case of carbonates, self-assembly processes are governed by specific interactions between the precipitating phase and the modifying agent; a method perfected by biological systems. Biomineralisation can produce the most amazing inorganic-organic functional structures, a topic discussed in the next section.

2.4 Biomineralisation

Biomineralisation involves biological processes that give rise to minerals (Lowenstam and Weiner, 1989). Over 60 different biominerals have been identified, and they often display stunning morphologies and superior properties compared to abiological/inorganic counterparts. For instance, shell nacre (mother-of-pearl) is composed of ordered arrays of aragonite plates, sandwiched between thin layers of macromolecules, a design that makes nacre ~3000 times as tough as pure aragonite (Mann, 2001). Almost all biominerals are such composites of inorganic and organic matter, and have been developed to perform various functions from skeletal support and protection to gravity and magnetic field perception (Lowenstam and Weiner, 1989). The associated biomolecules are believed to control the nucleation, growth, polymorph, and morphology of biominerals; processes that are largely unknown. Some organisms can produce different morphologies of the same mineral in different tissues (Addadi and Weiner, 1992). In many aspects, the often hierarchical behaviour of biominerals show similarity to biomorphs described in this thesis. This section will give a basic overview of some carbonate and silica biominerals, and the underlying processes that govern the amazing display of morphological variety seen in biominerals in general.

Understanding the interaction between the inorganic precipitating biomineral and

Mineral	Formula	Organism	Location	Function
Calcite	$CaCO_3$	Molluscs	Shell	Exoskeleton
		Birds	Eggshell	Protection
		Mammals	Inner ear	Gravity receptor
		Foraminifera	Shell	Exoskeleton
Aragonite	$CaCO_3$	Scleractinian corals	Cell wall	Exoskeleton
		Molluscs	Shell	Exoskeleton
		Cephalopods	Shell	Buoyancy device
Vaterite	$CaCO_3$	Gastropods	Shell	Exoskeleton
		Ascidians	Spicules	Protection
Amorphous carbonate	$CaCO_3 \cdot nH_2O$	Plants	Leaves	Calcium store
Mg-calcite	$(Mg, Ca)CO_3$	Echinoderms	Shell, spines	Strength, protection
Silica	$SiO_2 \cdot nH_2O$	Diatoms	Cell wall	Exoskeleton
		Radiolarians	Cellular	Micro-skeletons
		Limpets	Teeth	Grinding
		Plants	Leaves	Protection

Table 2.5: Examples of calcium carbonate and silica biominerals and their function in various organisms. Adapted after Mann (2001).

that of the organic biopolymer phase is at the core of biomineralisation science. The processes that result in biominerals are generally divided into two types: *biologically controlled mineralization* and *biologically induced mineralization* (Lowenstam and Weiner, 1989; Mann, 2001). These two processes differ in regards to the extent of control that is asserted by the organism during mineralisation. Precipitation scenarios in which the organisms maintain very little control over the mineralisation process, such as those occurring outside the cell, are termed biologically induced mineralisation. These are a result of biological activity and the surrounding environment, where no specialised compartmentalisation or macromolecules exist to promote a specific mineral phase or morphology. Removal of metabolic products across the cell membrane can result in mineralisation on the cell wall. These minerals often display irregular structures and inhomogeneous composition. Resulting morphologies are sometimes very similar to abiologically produced minerals.

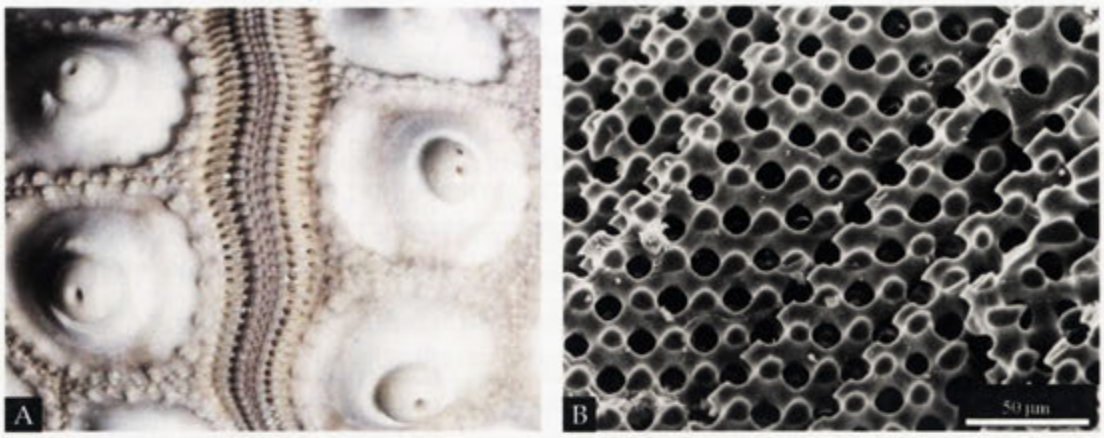

Figure 2.37: Detail of a sea urchin skeleton (test) in A, and SEM micrograph of the periodic calcitic structure. Image in A adapted from `http://www.rsphysse.anu.edu.au/admin/php/images/photos/shell.jpg`, Urldate 2006-09-18; B adapted from Yue et al. (2006).

Biologically controlled mineralisation

The great structural complexity often identified with biominerals is a result of the cellular control over the crystallisation process. This is accomplished by mineral deposition in a specialised environment, such as a membrane bound vesicle, in which the physiochemical conditions are controlled (Lowenstam and Weiner, 1989). Lipid vesicles, whose membrane structure is composed of a lipid bilayer with associated proteins, efficiently provide an aqueous microenvironment, where the flux of ions is regulated that in turn control the saturation state of the solution with respect to the mineral in question. Within this specialised compartment nucleation and growth is further controlled and directed by the organic matrix. Other ways to compartmentalise the mineralising space is to use preassembled cells, macromolecular networks, and combinations of the two (Lowenstam and Weiner, 1989; Mann, 2001). These biominerals are characterised by reproducible well-defined composition, structure, size, and morphology, which are very different from usual abiological minerals. Furthermore, these biominerals often have a morphology with hierarchical structure (an architecture composed of building blocks on many length-scales) with a preferential crystallographic orientation.

In Table 2.5 some examples are given of biominerals belonging to calcium carbonate and silica. Calcium carbonate is by far the most common biomineral, and occurs as several polymorphs including calcite, aragonite, vaterite, but also as amorphous calcium carbonate and as monhydrocalcite (Addadi et al., 2003).

Perhaps the most beautiful example of calcium carbonate biominerals is that of the

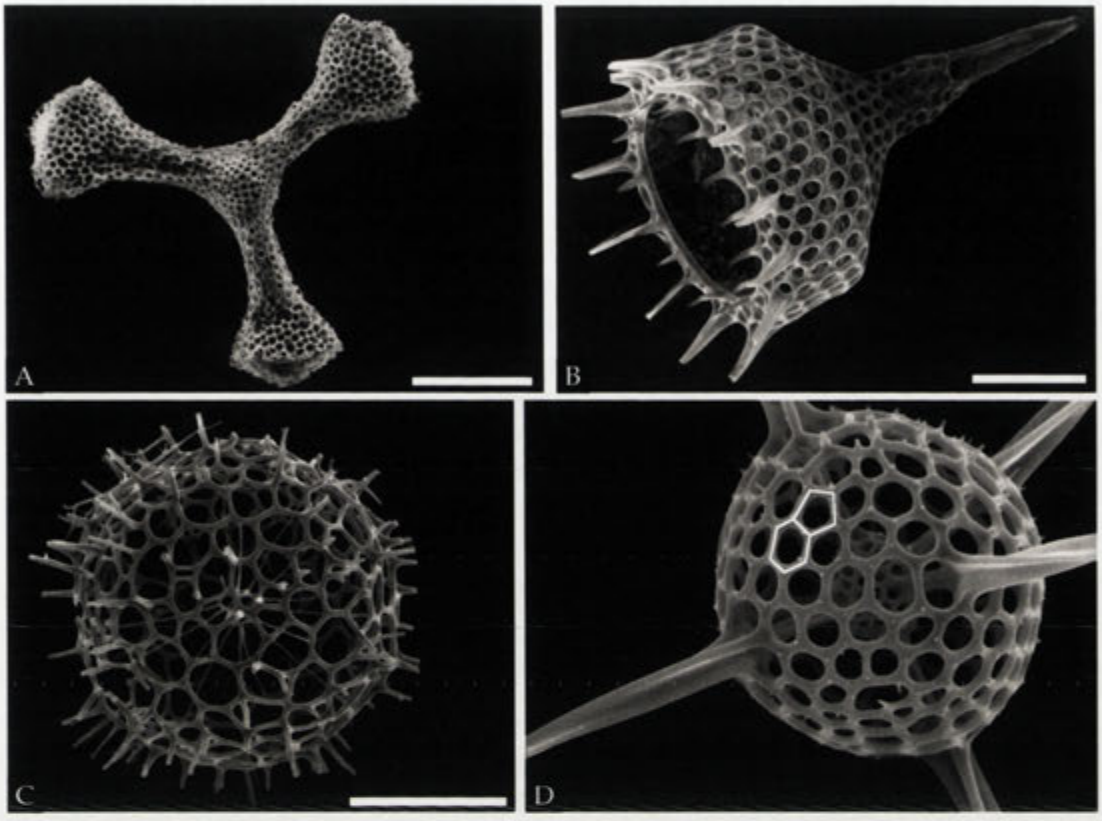

Figure 2.38: SEM micrographs showing the structural variety and complexity of silica biomineralsation in radiolarians. In D one pentagon, and one hexagon is outlined. Scale bars in A, and C; 100 μm, and in B 50 μm. Image courtesy of Dr. Roger Heady.

skeleton (test) of sea urchins (see Figure 2.37). The smoothly curved and patterned skeletal plates is made up of a single crystal of Mg-bearing calcite, which on the microscopic level form a bicontinuous porous structure (see Figure 2.37 B) (Donnay and Pawson, 1969; Addadi and Weiner, 1992; Yue et al., 2006). The size of the pores are in the micrometer range, and their arrangement are closely associated with the cellular architecture (Mann, 2001). It is believed that these remarkable structures form by the templating effect of these cells. The crystals form within large vesicles, that are formed by the fusion of cells, which in turn provide the necessary raw material and control for the crystal growth. The first precipitate is believed to be amorphous carbonate, that transform into crystalline calcite as the growth proceeds (Politi et al., 2004). The identification of an amorphous calcium carbonate phase as the precursor for the crystalline phase in many carbonate biominerals might speak for the versatility in moulding such a phase into the superstructure normally observed (Addadi et al., 2003). The macromolecules that reside within the porous structure have shown to adsorb on specific crystal planes, and are incorporated into the crystal. It is believed that this

inorganic-organic relation is responsible for the improved mechanical properties seen in these biominerals (Bermann et al., 1988; Addadi and Weiner, 1992).

Apart from the precursor amorphous carbonate discussed above, the most common non-crystalline phase in biominerals is silica. Silicon is present in all life-forms, and is in many cases an essential element, as it is required for structural support and metabolic pathways (Perry and Keeling-Tucker, 2000; Hamm et al., 2003). Diatoms and radiolarians have elaborate skeletons composed of amorphous silica, which display a remarkable degree of complexity (see Figure 2.38). These aquatic unicellular organisms have the ability to produce silica skeletons within minutes during cell division, as they can adsorb aqueous silica from solutions highly undersaturated in comparison to amorphous silica. Precipitation takes place within a specialised 'silica deposition vesicle', which, in cooperation with an arsenal of proteins and macromolecules specifically interacts and induces silica polymerisation, (Perry and Keeling-Tucker, 2000; Sumper, 2002; Noll et al., 2002). The porous structure is patterned by silica deposition around pre-assembled close packed cells (like a foam) adhering to the cell wall, producing the elaborate skeletal structures observed (Mann, 2001).

Biomineralisation processes have inspired new concepts for material science, evident by the synthesis strategies described for zeolites and mesoporous materials. Increasing knowledge of the control that is asserted during such mineralisation will lead to new composite materials with increased mechanical properties. So far the discussion on morphological evolution has been focussed on carbonate and silica examples, as this is most relevant to biomorphs. Many abiotic synthesis procedures, including biomorph syntheses, use empirical 'see-what-happens' methods that give rise to various crystal and composite morphologies. Understanding the molecular interactions and larger scale driving forces that cause morphological patterning and structural evolution is therefore crucial for developing theories of why such morphological modifications occur. Biological mineralisation comprises one end of the spectrum of morphological modification, and as has been discussed above, is caused by complex interactions, not yet fully understood. Complex structural evolution is however not restricted to biology; a theme that is running throughout this thesis. Natural phenomena are known to produce patterns and structures that self-assemble by chemical and physical forces. The next section will give an introduction to morphology and pattern formation, beyond the atomic or polyatomic scale, that occurs in nature, and the forces that govern their evolution.

2.5 Self-assembly and pattern formation

Several structure-forming agents have been mentioned in previous sections, such as micellar aggregates and foams. These systems are self-assembled structures that occur in biological as well as abiological systems, and arise in close to equilibrium conditions. Systems that give rise to ordered forms may also occur at non-equilibrium conditions. In this section both equilibrium and non-equilibrium pattern forming systems will be discussed. Such systems include chemical waves and convection cells, diffusion limited aggregation (DLA) and fractals.

Surfaces and volume packing

Bubbles, foams, and micellar aggregates partition space according to rules that minimise total free energy. In many cases, the dominant contribution to free energy is the surface tension (area). The most stable conformation is that which minimises the surface area and maximising the volume it encloses, such as a sphere. However, if such spherical aggregates touch, new configurations will emerge. In 2D, such as in the case of packing of a layer of bubbles between two surfaces, a hexagonal pattern, with 120° angles between walls, will minimise the surface area. For radiolarians, whose structures can be seen as a foam packing on a spherical surface, hexagons are mixed with pentagons, so as to fill the space (see Figure 2.38 D)[3]. In 3D, the evolving foam structure is much more complex, using bubble-cells having both hexagonal and pentagonal faces and intercepting vertices with different angles - the so called 'minimal foam' (Ball, 1999).

In aqueous solutions containing surfactants, the situation is even more complicated. Depending on surfactant type, concentration and temperature, various micellar structures (liquid crystals, or mesophases) are adopted, some of which was already introduced in Figure 2.35. The driving force for the self-assembly of various configurations is to keep the the hydrophobic tails within an environment free of water and to pack the surfactants efficiently, given their relative 'head-to-tail' volumes. For single chained amphiphiles, preferential aggregation occur at the air-water interface upon initial addition to water (as described above). Higher concentrations, above the critical micelle concentration (cmc), spherical micelles begin to form. Increasing the concentration further, results in hexagonal, lamellar bilayers and at even higher concentrations, a range of cubic bicontinuous phases form. These bicontinuous structures partition space in two interwoven frameworks - one tunnel system will never join the other. The interface between these tunnels belongs to the three-periodic *minimal*

[3]Exactly 12 pentagons are needed regardless of the size of the sphere.

surfaces, that is, the 3D interface has a mean curvature of zero; (Hyde et al., 1997). The local geometries of the surfactant aggregates are characterised by the shape and volume of the surfactants (determined by the chemical nature of the surfactant), and therefore how they pack in 3D space. Different amphiphiles show therefore different self-assembly behaviour. For example, surfactants with double hydrophobic tails conform to bilayered structures due to the increase hydrophobic tail volume (Hyde et al., 1997; Evans and Wennerström, 1999). At very high surfactant concentration reversed phases will form, in which the the hydrophilic head groups encompass the aqueous solvent, and the hydrophobic tails are sticking out. These surfactant aggregates belong to the lyotropic liquid crystalline phases that exhibit orientational order (see Collins and Hird (1997)).

So far structures that arises at, or very close to, equilibrium conditions have been discussed. However, it is well known that many patterns and structures are a result of processes occurring far from equilibrium conditions. Some of these patterns and their origins will be discussed in the next sections.

Dynamic non-equilibrium patterns

Dynamic systems far from equilibrium can grow into varied patterns (Ben-Jacob and Garik, 1991). Random processes, like that of chemical garden formation discussed in Section 2.3.3, can induce chaotic systems to form morphologies with structural order. A classic example of a non-equilibrium system is the Belousov-Zhabotinsky (BZ) reaction, in which an oscillating system (chemical clock) is established between the reactants and products, and can be sustained for quite a while. In a well-stirred vessel this can be visualised by observing the colour change that is related to the concentration of reactants and products, which will oscillate between one and the other. In 2D, without stirring, concentric rings (target patterns) develop, which travels outward from the original centres, like chemical waves. If the system is disturbed, propagating spiral waves are developed. The chemical mechanics behind these pattern formations lies in the autocatalytic behaviour of the reaction; one of the products will catalyse the formation of another. The concentration of products quickly increase, which eventually favour the backward reaction, and an oscillating reaction is created that will swing backwards and forwards till equilibrium is established. In stationary systems, the propagating waves are described as a reaction-diffusion system, in which the the advancing wave is dependent on diffusion of the reactants. Such systems have been proven to yield a great variety of patterns, such as Liesegang band formation, porous ionotropic gels, and other so-called dissipative structures (Prigogine and Lefever, 1968), which operate far from equilibrium.

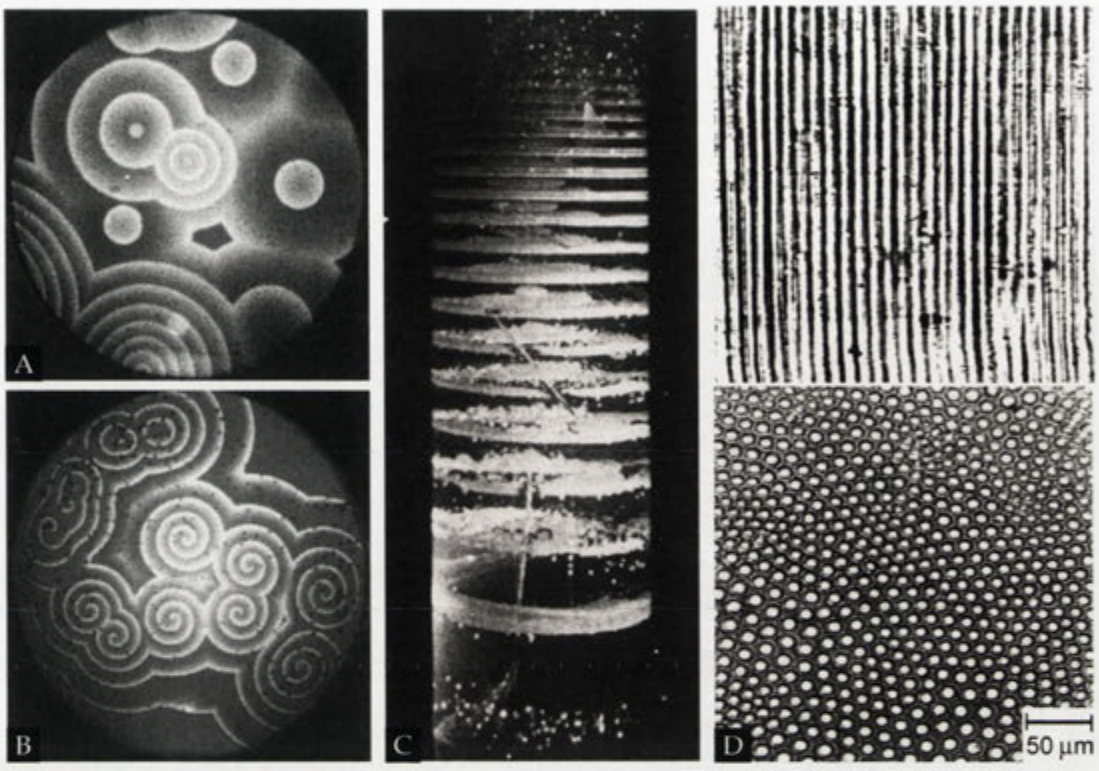

Figure 2.39: Various pattern formation in systems out of equilibrium mentioned in the text. The self-catalytic BZ-reaction can produce target patterns (A) and spiral waves (B) in . Liesegang ring formation of calcium phosphate (C). Spiral growth of $K_2Cr_2O_7$ in gelatin, scale bar 5 mm. Vertical, and horizontal cross-sections of porous alginate gel (D). Images adapted from Ball (1999) (A, B) ; Henish (1970) (C); Treml et al. (2003) (D).

Liesegang rings, in analogy with the chemical wave phenomenon, also produces concentric rings (in 2D media), but they are however chemically 'fixed'. They are the result of punctuated precipitation reactions during diffusion of one reactant through a gel that contains the other reactant. In 3D, in which a solution of say $Pb(NO_3)_2$ is allowed to diffuse into a columnar gel containing KI, precipitating bands of PbI_2 are easily observed (see Figure 2.39 C). The spatial distribution and width of these bands increase with time. Furthermore, if the system is disturbed in some way, spiral growth can occur. It is believed that these structures arise due to the rapid reduction of saturation state as the precipitation takes place, leading to the spacing observed between the bands (Henisch, 1973; Cartwright et al., 1999).

Anther reaction-diffusion system far from equilibrium is that of ionotropic gels, which under certain conditions can produce highly ordered patterns. Under controlled conditions, regular parallel pores with a diameter in the 8-300 μm range can develop as a Ca^{2+} solution is allowed to react with a sodium alginate (linear polyan-

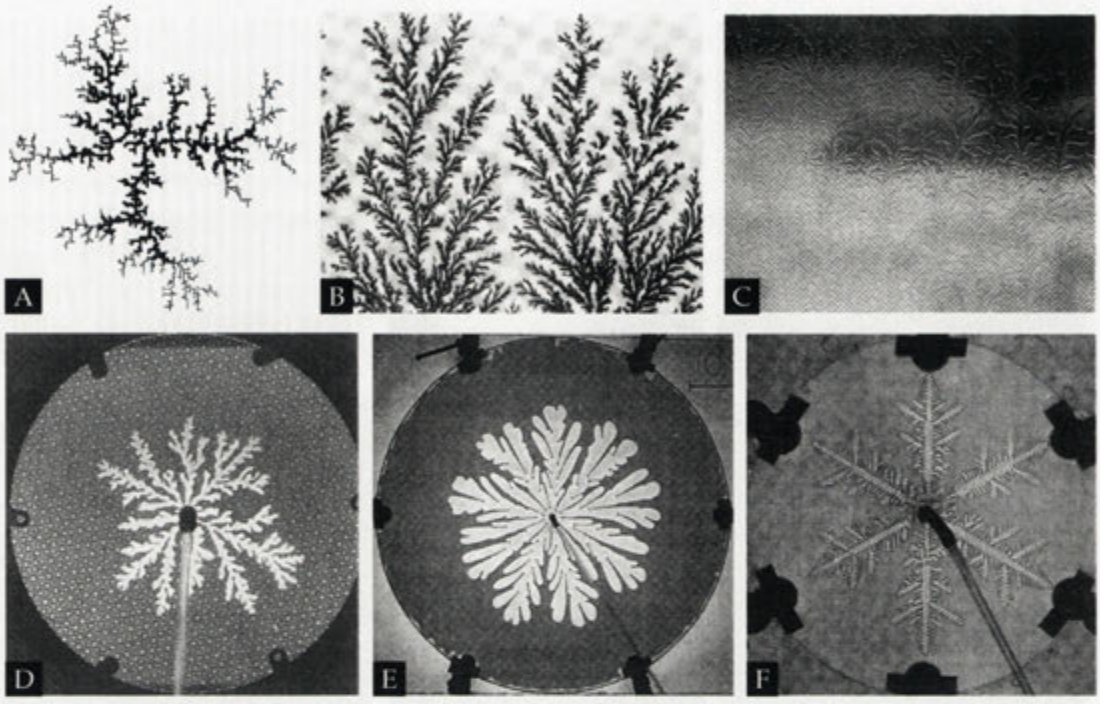

Figure 2.40: Various branched patterns formed in systems out of equilibrium mentioned in the text. DLA computer simulation with 3000 particles, of which the first 1500 are seen as the darker region (A). Manganese oxide deposit with D of 1.78 (B), and viscous fingering observed in a window (C). The Hele-Shaw cell can produce DLA-type (D), viscous fingering (E), and snowflake-like patterns depending on the experimental setup. Images adapted from Witten and Sander (1983) (A); Vicsek (1993) (B); García-Ruiz (1993) (C); Ball (1999) (D-F).

ionic carbohydrate formed from mannuronic and guluronic acid monomers) solution, producing the porous gel (see Figure 2.39 D). As a Ca^{2+} or Cu^{2+} solution is brought in contact with an alginate solution, complexation between the cation and the polysaccharide occurs, which induce gelling. These gels are referred to as ionotropic gels. It is believed that these 'fixed' dissipative structures form by the evolution of convective cells, which drive the ordering of metal-polysaccharide complexes into regions between these cells. Furthermore, the crosslinked chains are packed perpendicular to the growth direction of the pores (Thumbs and Kohler, 1996; Woelki and Kohler, 2003).

Morphogenesis of branching structures

The standard crystal habit of the calcium carbonates, as described in Section 2.2.2, is the result of slow growth under close to equilibrium conditions. As was further discussed in Section 2.2.4.3, these habits can specifically be modified by the presence of impurities. Many natural and synthetic crystallisation systems are far from equi-

librium, which induces morphological changes of the growing aggregate. Branched or dendritic aggregates are common morphologies observed in a variety of systems far from equilibrium. Such branched forms are ubiquitous in nature, ranging from snowflakes, and mineral formations to dust and the growth of cellular colonies (Ball, 1999) (see Figure 2.40). The morphology of such structures are determined by the interplay between macroscopic (diffusion) and microscopic (surface tension , crystallinity etc.) interactions.

In this section, diffusion-limited aggregation (DLA) and viscous fingering will be discussed as two models of dendritic growth. In DLA, diffusion of atoms, molecules or aggregates is the limiting factor controlling the growth, which develop open branched dendritic morphologies. The growth of such dendritic structures can effectively be modelled by Monte Carlo simulations (Brownian motion, random walk) of particles (Witten Jr and Sander, 1981). In this model, particles stick irreversibly to the growing aggregate upon first contact (no rearrangement allowed), which produces open dendritic morphologies. The outer branches grow faster (see Figure 2.40 A) as the diffusing particles are more likely to be caught before being able to diffuse into the core of the structure. Any produced branching therefore gets amplified, and shield the inner structure towards incoming particles. Mathematically, these structures can be analysed in terms of fractal growth. Fractals are self-similar structures, that is, they have the same characteristic structure on different length-scales. Dendritic structures are often self-similar over a few orders of magnitude, and can be characterised in terms of fractal geometry, in which the fractal dimension is a useful property. The fractal dimension D of physical objects can be seen as how densely it fills space, and can also be used to characterise the growing aggregate in relation to its size. For particle aggregation, the lower and higher cut-off of the length-scale is that of the aggregating particles and the aggregate size respectively. For a fixed size of an aggregate, the number of balls with radius l needed to cover the entire aggregate, is proportional to l^{-D}, and D approximates according to:

$$D = \lim_{l \to 0} \frac{\ln N(l)}{\ln(1/l)}$$

as the size of the balls becomes infinitely small. In general, D is smaller than the dimension of the space in which it is embedded (Vicsek, 1989). For simple objects, like a curve, or a disk, D coincides with the standard notation of dimension; D equals 1 for a curve, and 2 for a disk. Aggregates of particles, such as in DLA, have a non-integer dimension of D. Pure DLA simulations of aggregation in 2D gives rise to an aggregate with fractal dimension of 1.7, whereas in 3D, it equals 2.4 (Sander, 1986). The manganese oxide deposit, seen in Figure 2.40 B, has been analysed using a

similar method, giving a fractal dimension of 1.78, which is very close to that of DLA. Even though the use of fractals may be geometrically significant, the determination of D will not give any information on how the structure formed, as several different mechanisms can give rise to similar structures. Furthermore, DLA is a result of random diffusion, and does not take into account any surface kinetics or anisotropy of the solid structure, which are important in the formation of many other branched morphologies. In Figure 2.40 D-F three different branched morphologies can be seen, all of which are produced using the Hele-Shaw cell. In this experimental setup, the different morphologies are produced by injecting one fluid, or gas, of low viscosity into another fluid of high viscosity, sandwiched between two plexiglass plates of narrow spacing. By varying the viscosity of the two fluids, applied pressure, plate spacing, and controlled anisotropy of the cell (by scoring the plexiglass) different branched morphologies can be obtained, such as DLA-like fractal morphology, dense-branching morphology, and snowflake-like morphology (see Figure 2.40 D-F) (Ben-Jacob et al., 1986; Ben-Jacob, 1997). The morphological evolution in the Hele-Shaw cell can be explained by the competing effects of pressure instabilities at the growing interface and surface tension and kinetics. As the interface between the two phases grow, instabilities at the interface cause the surface to bulge. At the tip of the bulge, the pressure difference is highest, which causes the bulge to grow faster, and the interface is split into fingers. Under certain conditions (low surface tension), where this type of instability is the only driving force, viscous fingering can grow into DLA type morphologies. More often, dense-branching morphologies develop (see Figure 2.40 E). These morphologies consist of fat fingers, and have a characteristic length scale (not fractal). The development of broad fingers, and not random fractal DLA-type morphologies, is caused by the effect of surface tension, which acts so as to reduce the pressure gradient across the interface. This results in the stabilisation of the growing surface and resists the appearance of new highly branched fingers Ben-Jacob (1997); Ball (1999). These dense-branching morphologies can develop in most varied situations, ranging from electrochemical deposition, precipitation from supersaturated solutions, cooling of melts, and even in windows of certain Spanish five-star hotels (see Figure 2.40 C) (García-Ruiz et al., 1993; Ball, 1999). In the case of precipitation of crystalline materials, anisotropic effects arising from the crystal structure has to be taken into account. This can be simulated with the Hele-Shaw cell by engraving a regular lattice of grooves in one of the plexiglass plates. In the case of a hexagonal lattice, structures with dendritic arms with sixfold symmetry develop in analogy with snowflakes (see Figure 2.40 F). The grooves serve as structure directing agents, as they increase the velocity of the growing front. Varying the depth of the grooves (in effect the anisotropy) and the applied pressure give rise to very different structures again,

indicating complex interaction between surface kinetics, surface tension, and pressure instabilities. The structure that will form is the one that adopt the lowest free energy, and it has been suggested that the fastest growing structure is selected (Ben-Jacob et al., 1988; Ben-Jacob, 1997).

The case of spirals

As spiral morphologies are of particular interest in this thesis, some emphasis should be given to the little there is known about the formation of such structures. A curious example of large spiral growth of potassium dichromate ($K_2Cr_2O_7$) has been observed in gelatin by Suda and Matsushita (1995). It was noted that under certain conditions huge crystalline spirals (see Figure 2.41 A)(20-25 mm long, 2-4 mm wide, 2-6 mm pitch length) with large preferential right-handedness could be grown from gelatin containing dissolved $K_2Cr_2O_7$ at low temperatures (6-8 °C) (Suda and Matsushita, 1995; Suda et al., 1996). The slow drying of the gel under these conditions eventually results in supersaturation of $K_2Cr_2O_7$ which then precipitate. Optimal conditions resulted in spirals after 7-21 days of growth with a maximum growth of 8 mm/day. It was found that by systematically changing the concentration of gelatin while keeping the $K_2Cr_2O_7$ concentration constant, very different structures could be observed. At low concentrations, the gel is very loose, which results in thin plate-like crystals. Increasing the gelatin concentration give rise to spherulities, square pole-like crystals, spirals, and DLA dendritic crystals, with increasing concentration (Suda et al., 1996). It was proposed that the successive morphological change seen with increasing gelatin concentration reflects the progressive influence of the solid gelatin network on the $K_2Cr_2O_7$ crystal growth, from reaction-limited at low concentrations, to diffusion-limited at high concentrations. The conditions that allow spiral growth lie in the cross-over point between the two systems. However, it was suggested that spiral growth probably was reaction-limited, as the gelatin network can be seen as an impurity affecting the crystal growth - a known phenomenon in such systems. Furthermore, the spirals themselves are composed of stacked pole-like crystals with a consecutive clock-wise internal twist, speaking for such a conclusion (Suda et al., 1996). The chiral nature of the spirals was explained based on the ordering of collagen macromolecules within the gelatin. The formation of right-handed triple helices of collagen macromolecules was proposed to be the underlying cause of the preferential right-handed spirals (Suda et al., 1998). The use of non-collagenous gels did not result in spiral growth, and the addition of acidic amino acids resulted in increased number of left-handed spirals, however, the reason for this chirality change is not understood (Suda and Matsushita, 2004).

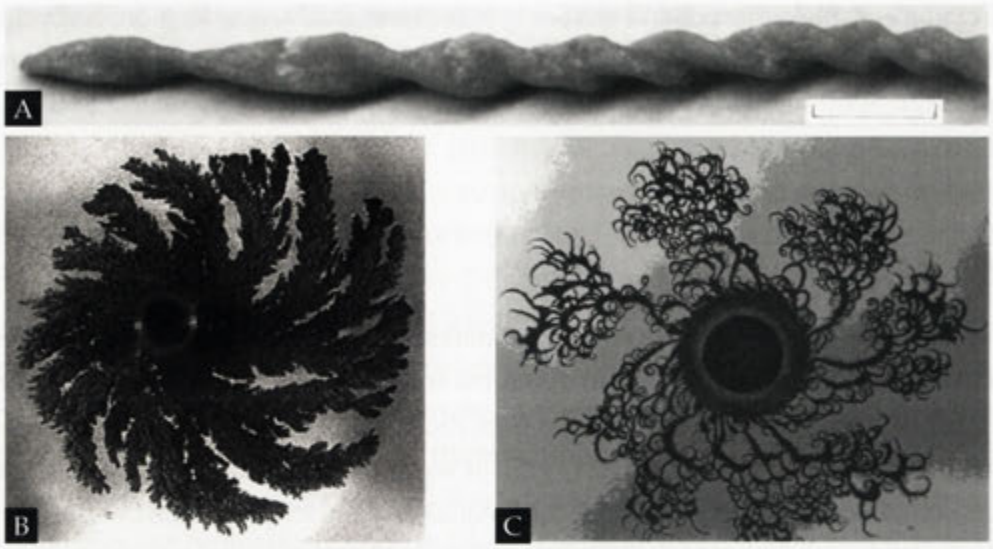

Figure 2.41: Various spiral structures formed in very different systems. 3D spiral growth of $K_2Cr_2O_7$ in gelatin, scale bar 5 mm (A). 2D spirals produced by the electrochemical deposition of copper with an applied magnetic field (0.4 T, vertically upwards) (B), and chiral colonial growth of *Bacillus subtilis* (C). Images adapted from Suda et al. (1998) (A); Ní Mhíocháin and Coey (2001) (B); Ben-Jacob (1997) (C).

Chiral growth of spirals (see Figure 2.41 B and C) has also been observed in electrochemical deposition of copper (Figure 2.41 B) and bacterial growth (Figure 2.41 C) under certain conditions. In the former case, fractal DLA-like spiral growth was observed in the presence of a magnetic field. The chirality of the spiral reversed as the magnetic field was reversed. It was suggested that the magnetic field influence the convective flow, increasing the diffusion coefficient, which affected the growth. The resulting chiral structures was interpreted to be an intermediate between dendritic and DLA morphologies (Coey et al., 1999; Ní Mhíocháin and Coey, 2001), as was also suggested for the $K_2Cr_2O_7$ spirals. DLA modelling using forces that restrict the diffusion of particles and thereby reducing the randomness of the system have shown to produce spiral growth in both 2 and 3 dimensions (Davidovitch et al., 2000; Lomas, 2006). In particular the models produced by Andy Lomas[4] both spherical and spiral aggregates can be produced by adjusting the different forces as well as limiting the area from which the particles are released and the volume of the system. The forces are used to bias the random walk of the spherical particles. For the production of a spiral morphology, three forces are used; a radial, axial, and a vortex force, which are not affected by the growing aggregate. These forces, in combination with the use of a cylindrical bounding volume, produces helical morphologies. Such models do

[4]see http://www.andylomas.com/

not account for anisotropic effects as the aggregation is solely based on irreversible sticking of spherical particles on first contact with the growing aggregate.

No simple universal explanation for the growth of spiral morphologies in natural systems can be expected.

2.6 Discussion

In this chapter, the chemistry of aqueous carbonate and silicates, as well as their morphogenesis during precipitation, have been discussed. Silica-carbonate biomorphs display remarkable growth phenomena in terms of morphologies produced. In this section, I discuss what parameters could be important for the morphogenesis observed. In particular, this will be useful as a basis for trying to deduce the origin of such structures. Some preliminary discussion of the relevance of the wealth of work on carbonate polymorphism, biominerals, pattern formation, and silica templating is in order.

Crystallinity and crystal habit

Biomorphs have so far only been produced with carbonates of the aragonite-type crystal structure. Why is this the case? As was discussed in Section 2.2.1, the $CaCO_3$ polymorphs display very different crystal structures, and therefore also crystal habit. The elongated nature of aragonite-type carbonates, compared to the rhombohedral habit of calcite, could be important for the crystal-crystal epitaxy and the packing of such carbonate crystallites. Furthermore, the presence of silica in the reacting solution during biomorph growth can effectively alter both morphology and aggregation of such crystallites. It is clear that complexation and adsorption between carbonate and silica species is expected during the precipitation of biomorphs. As was seen in the helical and herringbone-like $BaCO_3$ case (Figure 2.17 and 2.18), epitaxial aggregation of carbonate crystals, limited by the adsorption of polymers on specific crystal faces, can result in peculiar morphologies. Similarly, silica is believed to be the cause of the formation of carbonate films on chitosan surfaces (Figure 2.21 and 2.22). It has been shown that the distance between consecutive silanol groups closely match that between Ba and Sr in their respective carbonate forms. This could indicate that silicate ions can specifically adsorb onto the carbonate crystallites, thereby poisoning further growth on that crystal plane. Adsorption of silicate could also then also affect the way the crystallites are assembled in the final structure.

Aqueous carbonate and silica chemistry

During synthesis of biomorphs, carbon dioxide is adsorbed from the air that at high pH produces carbonate ions thereby lowering the pH. As pH has a great effect on both silica and carbonate solubility, it in turn has implications on the chemistry of the system and asserts influence on the morphology produced. Low pH favours silica precipitation, but increases carbonate solutbility, so a fine balance between the precipitation of the composite material must exist. In the carbonate case, the first production of CO_3^{2-} at initially high pH will convert to HCO_3^- as the pH reduces with time (see Figure 2.8). The balance between the two species could be important for the formation of biomorphs. Furthermore, temperature also affect solubility of carbonate and silica, as well as the adsorption of carbon dioxide. High temperature favours silica dissolution, but reduces aqueous carbonate adsorption and solubility. As will be evident in the next chapter, temperature have a great effect on the morphology produced, and the combined effect of carbonate and silica solubility, as well as the diffusion of these species in solution influence the self-assembly of such aggregates.

Colloidal behaviour

Evidently, the presence of additives can specifically alter the morphology of a growing carbonate aggregate. As was discussed in Section 2.3.2, close interaction between anionic silanol groups and the metal cations during the formation of biomorphs is unavoidable, and it is therefore expected that silicate complexes form as soon as the alkaline earth solution is mixed with the silica sol, long before the appearance of biomorphs. Analyses of the barium- and silica-rich sol presented in Chapter 4show that this is the case. In analogy with zeolite synthesis, such aggregates could then serve as a reservoir of reactants during the synthesis of biomorphs. A controlled release of Ba coupled with the uptake of carbon dioxide from the air could then provide a constant flow of carbonate particles to the growing aggregate. The stability of both carbonate, silicate, and silica colloids play therefore a possibly crucial role in the growth of biomorphs. As was discussed in Section 2.3.2 stability of colloids depend on the type of ions present and there interaction with the colloidal surface. As the concentration of both the alkaline earth metal and silica is important for the growth, the colloidal stability of the system will change as the concentration of the reactants change. High concentration of the alkaline earth metal has a destabilising effect on the colloidal system, and precipitation is expected. Such precipitation is visible during the formation of structures called floral spherulites, which are formed at 0.5 M $BaCl_2$. Furthermore, the presence of additional electrolytes, especially higher valence ones, have a great potential to affect the growth of biomorphs, as they will

affect the interaction between colloids by screening the surface charge. Colloidal aggregation can also be directed into producing sheets in the presence of surfactants. Such sheets are similar to the colloidal skin seen on some biomorphs. In Chapter 4 a discussion regarding the significance and origin of this sheet for the formation of spiral structures is given.

Self-assembly

The self-assembly process is in general governed by the competition between both intrinsic and extrinsic forces. Anisotropic effects of the carbonate crystallites is one possible reason for the ordering observed. In systems close to equilibrium, liquid crystal structures are produced by an ordered array of molecules under the right conditions. As was discussed in Section 2.3.3 silica condensation on such a template results in highly ordered micro- and mesoporous materials. However, it is not clear that the crystallite ordering is governing the overall morphology of the aggregate. It could also be the reverse; the aggregation mechanism could result in a morphology that dictates the packing of crystallites. Systems far from equilibrium have shown that diffusion can exhibit great influence on the morphology of evolving structures. In silicate gardens for instance, the rupturing of the silicate membrane followed by forced convective flow can give rise to ordered microstructures in a seemingly disordered macrostructure. Diffusion limited aggregation has further shown that complex morphologies can arise based on pure aggregation of particles. As will be shown in the next chapter, under certain conditions DLA-like morphologies can be produced, indicating that diffusion and aggregation is important to the formation of biomorphs. The self-assembly of helical aggregates can be seen in both carbonate and silica systems. In the carbonate case, these morphologies are observed in the presence of polypeptides, and are composed of ordered polycrystalline vaterite encased in a film also made of vaterite. A similar behaviour is seen in biomorphs, in which spiral aggregates are covered with a colloidal silica skin. The presence of the silica skin could therefore be important for the development of spiral structures. In any case, deciphering self-assembly mechanisms is a complicated task when the system is possibly governed by many complex interactions and reactions. In Chapter 4 a further discussion regarding the self-assembly of biomorphs is given in an attempt to elucidate the origin(s) of the morphologies observed.

In the next chapter, synthesis and morphological evolution of biomorphs are described. The construction of morphology diagrams across different parameters could aid the development of theories on the formation of these aggregates.

Chapter 3

Biomorph syntheses

3.1 Introduction

In this chapter the synthesis procedures and results are presented for the growth of biomorphs. As was explained in Chapter 1, these silica-carbonate aggregates can be synthesised in both silica gel and sol. Although the gel-synthesis procedure has been studied by Juan Manuel García-Ruiz and others, syntheses of biomorphs from silica sols have not been thoroughly explored. This chapter is therefore exclusively concerned with growth of biomorphs from sodium silicate solutions. Several parameters are important for the genesis of particular biomorph morphologies: principally concentration of the reacting molecular species, pH and temperature. In this chapter the morphological change that stems from variation of these parameters is given. Selected morphologies are also analysed regarding elemental composition and crystallographic properites.

The aim of this chapter is to investigate the morphological variety with different synthesis conditions, to provide essential insights and guides to the development of a theory of how these structures are formed. Biomorphs can be synthesised using various metals, i.e. Ba, Sr and Ca, all of which can form carbonate precipitates with the aragonite-type structure. The crystallographic relationship between crystallites within the biomorph structure is therefore correlated with biomorph growth and is potentially important for the morphogenesis. In Chapter 4 a discussion of possible mechanisms for the morphological evolution of biomorphs is given together with some initial analyses of the reaction media resulting in biomorphs.

3.2 Experimental procedure

A standard recipe for synthesising biomorphs from silica sols is the following: A concentrated waterglass solution is diluted 350 times (17.8 mM), which is subsequently mixed 20:1 (v/v) with 0.1 M NaOH, that is then mixed 1:1 with 0.01 M $BaCl_2$. 2 ml of this

reaction solution is then pipetted into sterile plastic tissue culture plates (Linbro, 24 flat bottom wells, 2.0 cm^2 area, 3.5 ml well capacity). From this reaction mixture spiral and worm-like biomorphs can be collected after ca. 10 h. By changing temperature, the concentration of the silica solution, $BaCl_2$, and the amount of added NaOH, various biomorphs with different morphologies are obtained. In all cases, chemicals were used as purchased. Plastic bottles were used to store the silica,$BaCl_2$, and NaOH solutions so as to avoid silica contamination. Barium chloride stock solution was prepared to desired concentration (1.0 M, or 10 mM) in distilled water (Milli-Q plus, ~18 MΩcm). Sodium silicate (ca. 27% SiO_2, 14% NaOH, density 1.390 g/cm^3) was obtained from Sigma-Aldrich.

pH was measured using a TPS smartCHEM-Lab multi-parameter laboratory analyser with automatic temperature compensation, equipped with a plastic-body pH sensor. Two-point calibration was performed using pH 9.00 and pH 12.00 buffers obtained from Riedel-deHaën. The pH of the buffers at the specific temperature were calculated for each calibration using information given on the bottles.

High temperature experiments were performed in a Memmert U200 oven with a temperature accuracy of ±0.1°C, operating at full fresh air supply and natural air convection. A standard experiment was performed at room temperature, to make sure the air supply was sufficient. Low temperature experiments were conducted in the laboratory fridge, also at full air supply.

After desired growth was achieved, pH of the solution was measured, and the aggregates were washed using aliquots of distilled water (4 x 2 ml). Routinely, the cleaned biomorphs, still in the wells, were imaged using a Leica MZ 12 stereomicroscope fitted with a Nikon Coolpix 8800 (8 megapixel) digital camera. In some cases the aggregates are attached to the bottom of the wells; a paintbrush was then used to gently loosen the biomorphs from the surface.

To retrieve separate individual biomorphs, it was found that the following method worked well. Using a disposable Pasteur pipette, the cleaned biomorphs were transferred from the tissue culture wells to a plastic petri dish in a small volume of distilled water. The excess water was then carefully removed using the same glass pipette. A small volume of ethanol was added to disperse the biomorphs on the petri dish, which was subsequently dried in an oven at 70-80 °C. Using this method aggregation of biomorphs was limited, which simplified the handling of specific individual biomorphs.

To prepare the samples for FESEM analysis, individual biomorphs were placed on double sided carbon tape mounted on an aluminium stub using a fine needle, glass fibre, or a fine brush. Alternatively, very fragile biomorphs were grown on aluminium plates, with or without double sided carbon tape, placed at the bottom of the wells.

No difference in morphology was observed between samples grown in wells using this technique compared to samples without these plates. These plates were gently dipped in distilled water to clean the samples after growth.

The samples were then coated in either Au or Au/Pd using an Emitech sputter coater, operating at 5 mA for a duration of up to 4 minutes, using a tilted rotational stage. This technique proved to be superior to stationary, non-tilted coating techniques for the structurally complex biomorphs. Biomorphs were routinely imaged using a Hitachi S4500 Field Emission SEM, operating at 3 kV. Both upper and lower secondary electron detectors were used, and images were acquired using ImageSlave slow-scan image acquisition system.

Elemental analyses of biomorphs were performed using a JEOL JSM6400 SEM equipped with Oxford ISIS EDXA system, operating at an accelerating voltage of 15 kV and beam current of 1 nA. Samples were analysed for Si, Ba, Na, and Cl, using sanidine, barite, albite, and tugtupite as standards respectively. Samples analysed using EDXA were all carbon coated.

Some structures were characterised by electron diffraction, using a Philips EM430 TEM, operating at 300 kV, and equipped with Oxford ISIS EDXA. These samples were prepared by growing them on carbon-holey copper grids, attached to carbon tape on an aluminium plate.

A Philips CM300 FEI was also used to acquire high resolution information on thin sections of particular structures. These thin sections were made by gluing the aggregates on to tape attached to a microscope slide. For the twisted structures especially, it involved aligning long structures vertically straight on the tape. The samples were then embedded in epoxy resin under vacuum so as to reduce the effect of bubbles trapped in within the structures and the resin. Thin sections were then made by polishing the sample and finally by ion-thinning methods. Harri Kokkonen and Dr John Fitzgerald at the Research School of Earth Sciences prepared the thin sections according to this technique, and Dr Fitzgerald also analysed the sample using TEM.

Some aggregates were also analysed using X-Ray Computed Tomography (X-ray CT). This instrument uses a X-Tek RTR-UF225 X-ray source and has a Roper PI-SCX100:2048 X-ray camera, and an Newport RVI20PP rotation stage. A special in-house built mounting stage was used to aid the alignment of the biomorphs that were in turn mounted on a tip of a glass-fibre. The glass-fibre was glued to a needle that in turn fitted on the mounting stage. For more information on the technique, see Sakellariou et al. (2004).

Figure 3.1: A taste of the different biomorph morphologies discussed in this chapter; worms (A), trumpets and cones (B, F, J), coral-like floral spherulites (C, N), globular (E, K), pinnacles (G), disks (H), double helices (I), sheets (F, L, M), bands (O). An aggregate displaying a mixture of different morphological traits (sheets, globules, pinnacles) can be seen in D.

3.3 Results

3.3.1 Overview

Due to the large number of different biomorph morphologies produced using different synthesis conditions, this section gives a short overview of these morphologies. The observed morphologies have been given names that reflect the shape of the aggregates. In Chapter 1, such classification was introduced by the 'worms', 'spirals', and 'sheets'. Many more morphologies will be introduced here. This will aid the reader to follow the morphological changes observed using different reaction conditions.

In Figure 3.1 a collection of images of some of the different morphologies observed in this chapter is seen. A 'worm', 'double-helix', and 'globules' can be seen in Figure 3.1 A, E, and I respectively. These morphologies will be discussed in Section 3.4.1. Coral-like morphologies, named 'floral spherulites' display a spherical morphology of interwoven sheets (Figure 3.1 C) will in turn be discussed in Section 3.4.4.

Helical barium carbonate containing biomorphs, synthesised according to the 'standard' conditions, will be discussed first. These conditions will serve as the nil experiment, and any parameter excursion will be related back to the 'standard' synthesis.

3.4 Barium carbonate biomorphs

Various morphologies are obtained depending on the concentration of barium chloride in the reaction solution. In the first instance, the aggregates observed using the 'standard' synthesis conditions will be discussed. Subsequent sections will analyse the effect of changing parameters, such as pH, concentration of both silica and $BaCl_2$, temperature, and additives on biomorph morphology.

3.4.1 Standard experiment

The preparation of biomorphs using the standard conditions is achieved by mixing a 10 mM $BaCl_2$ solution with a 17 mM water glass solution containing 18 mM NaOH (pH 11.3) resulting in a clear solution of pH around 11.0. Using these conditions results in biomorphs having globular, sheet-like and helical morphologies. Precipitation of biomorphs preferentially occurs at the bottom of the wells, however, aggregates can sometimes also be seen growing at the air/solution interface. As was mentioned in Chapter 2, this is a common phenomenon in systems where a concentration gradient is present across the solution.

Light microscopy observations

By using both transmission and reflection light microscopy, the growth of biomorphs synthesised at room temperature can be easily observed. From recorded movies of the growth of such aggregates (Figure 3.2), several characteristics can be observed regarding the development of the different types of morphologies. In all cases, the first stage in growth is the emergence of globular aggregates (see Figure 3.2 A). These globular nuclei become visible after ca. 0.5-2 hours, possibly depending on the carbon dioxide concentration in the solutions used. It is therefore always best to use freshly prepared solutions. During further growth, the globular aggregates evolve to form either sheets, helices or worms, or stop growing altogether (see arrow in Figure 3.2 B). All of these forms can be seen growing at the same time in a single experiment.

The growth of helices progress very uniformly with constant diameter; they can grow up to hundreds of micrometers in length. Some helical aggregates thicken into a worm during the later stages of growth (see red arrow in Figure 3.2 D). As can be seen in Figure 3.2 D and E, this budding of the helices can occur at different times during the growth. Further aging of such aggregates produces worm-like aggregates that eventually increase in width and develop what we call 'heads' (see red arrow in Figure 3.2 F). Worms most often develop without preexisting helices, and the growth proceeds in layer-by-layer twist, that curls around the central axis along the growth direction. Increasing diameter is sometimes seen during later stages of the growth and continued growth can result in the development of large snail-like heads. However, most aggregates remain very uniform, and stop growing without any development of large heads. It is also noted that the development of these large heads is only observed on some aggregates within a single batch, and in many cases it can be seen to develop on biomorphs that are actively growing. Several worms can grow from the same globular aggregate, creating a bundle of two or three worms at one nucleation point, however, individually grown worms are also commonly present. As is also the case of helices, worms grow independently of each other, in that one worm may continue to grow while its neighbouring worm does not. It is further observed that helical and worm-like biomorphs can extend in any direction from the globular nuclei.

Sheets are only occasionally observed, and they are only seen to grow at the bottom of the wells, with their long growth axis parallel to the surface. They appear early during the growth, and often develop heart- or leaf-like morphologies, which abruptly stop growing. In Figure 3.2 it is also evident that these morphologies grow very quickly (1.3–2 μm/min). This sudden termination of growth is also observed in both helices and worms.

As can be seen in Figure 3.2 increased precipitation of flocculated material occurs

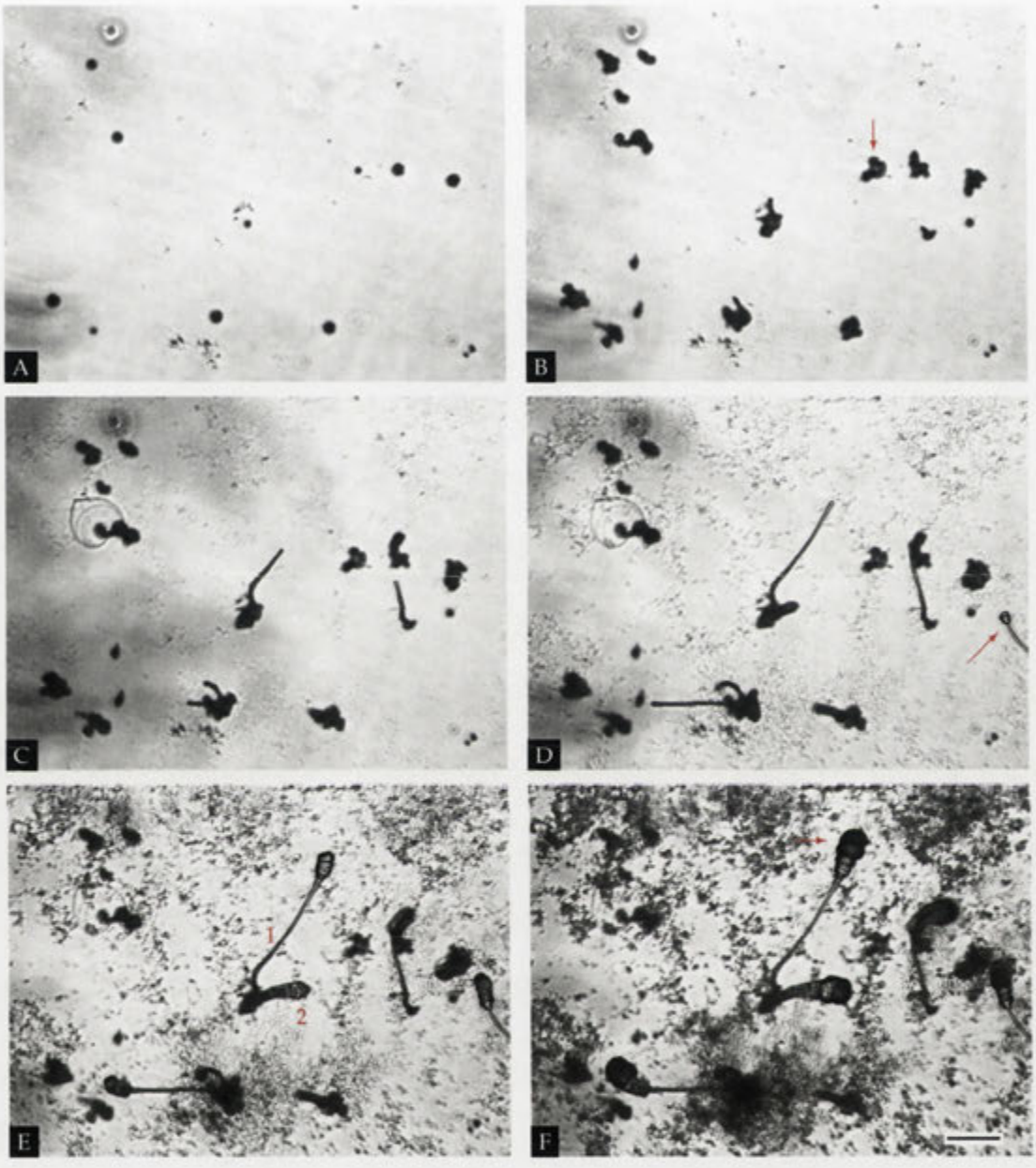

Figure 3.2: Time series of biomorph growth during standard conditions ([$BaCl_2$] 5 mM, [SiO_2] 8.5 mM, pH 11.0, room temperature), A 1 hour, B 3 hours, C 5 hours, D 7 hours, E 10 hours, and F 17 hours. Scale bar in F is 100 μm.

with time. pH measurements throughout the synthesis can be seen in Figure 3.3, where also optical images showing the growth progress (of cleaned samples) are shown. In this experiment, globular aggregates were observed after 120 minutes, at a pH of 10.6. The spirals and worms emerged at around pH 10.3 after 5.5 h of growth, and continued to grow till the experiment was terminated after 10 hours at which the pH

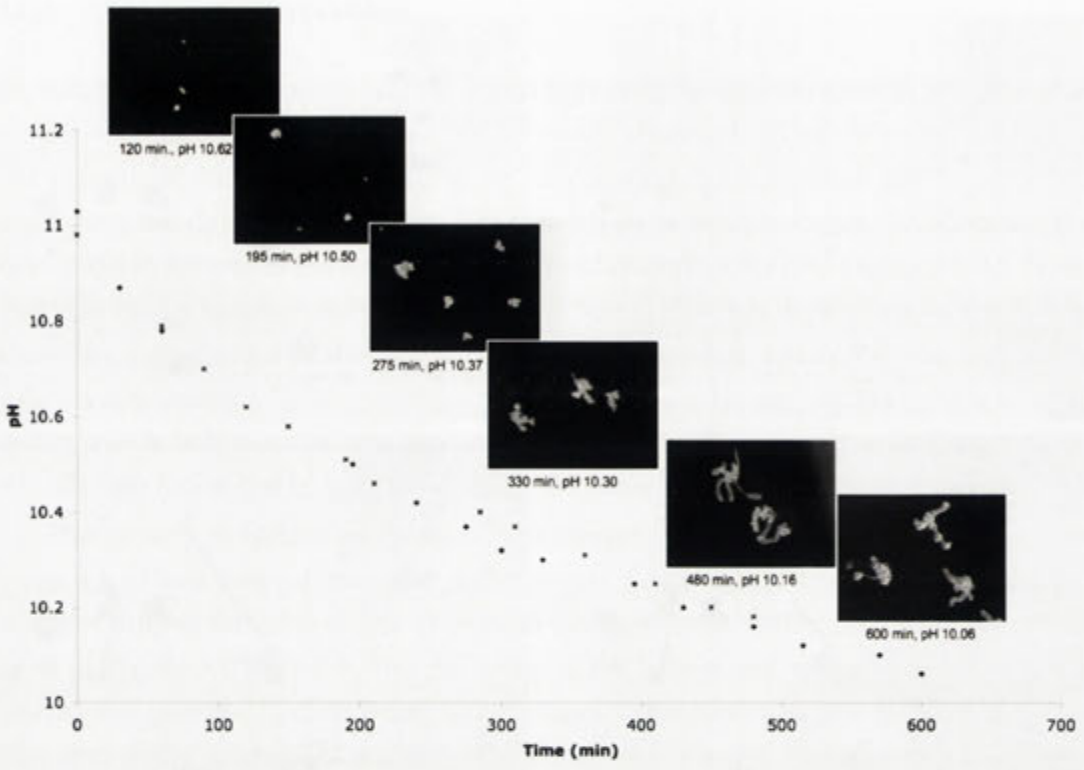

Figure 3.3: Optical images taken during the synthesis of biomorphs with an initial pH of around 11.

had dropped to around 10.0-10.1. 8-10 h of growth is sufficient to produce worms and helices that are not overgrown by large euhedral witherite crystals; Increasing growth times produces biomorphs that are overgrown with witherite. Calculated growth rates for the helices and worms are very constant within each experiment during the growth process. For instance, the double helix and the worm, labelled 1 and 2 respectively in Figure 3.2, extend with a constant rate of 0.85 and 0.36 μm/min respectively during the earlier stages of growth. Towards the later stage of growth, growth rates tapers off till the aggregates stop growing. For the double helix 1 in Figure 3.2 E, budding where spirals thickens into worms, has a growth rate comparable to that of the worm (0.35 μm/min). However, it has been noticed that different growth rates can be observed between different runs. Worms have shown to develop at a growth rate of up to 0.86 μm/min. In all cases, the growth rate was determined by measuring the length of the aggregate as it changes with time. These calculation do not account for differences in the surface area of the growing tip.

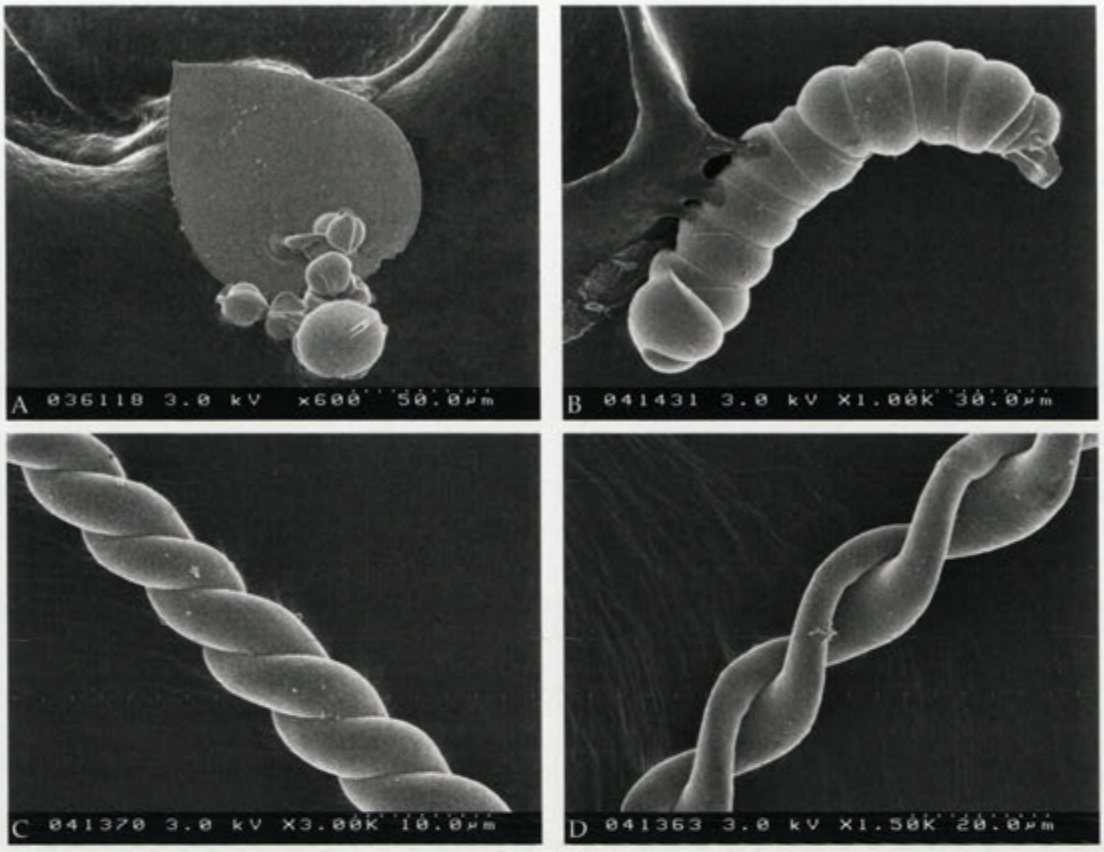

Figure 3.4: FESEM images of biomorphs generally seen using standard conditions; heart-shaped sheet (A), worm (B), double helices (C, D).

Electron microscopy observations

In the first instance, the macroscopic observations are discussed, followed by a micron scale analysis of the aggregates. FESEM images of aggregates synthesised under standard conditions confirm the presence of globular, sheet-like, helical, and worm-like morphologies (Figure3.4). The manifestation of these morphologies can vary between experiments. Worms are the most common morphology seen, followed by helical aggregates. As mentioned above, sheets are rarely present, and are not analysed further, as only a few aggregates were observed in contrast to gel biomorph syntheses. Furthermore, these sheets have a tendency to firmly stick to the bottom of the cell, making it difficult to process them for FESEM analysis.

From the optical analysis, the first precipitates observed during synthesis have globular morphology. In Figure 3.5 electron micrographs of such aggregates can be seen. As is evident in A and B, globular aggregates often develop 'tongues' that extrude from the aggregate in a disk-like manner. These tongues are believed to be the starting point of all the morphologies seen in the standard experiment. One

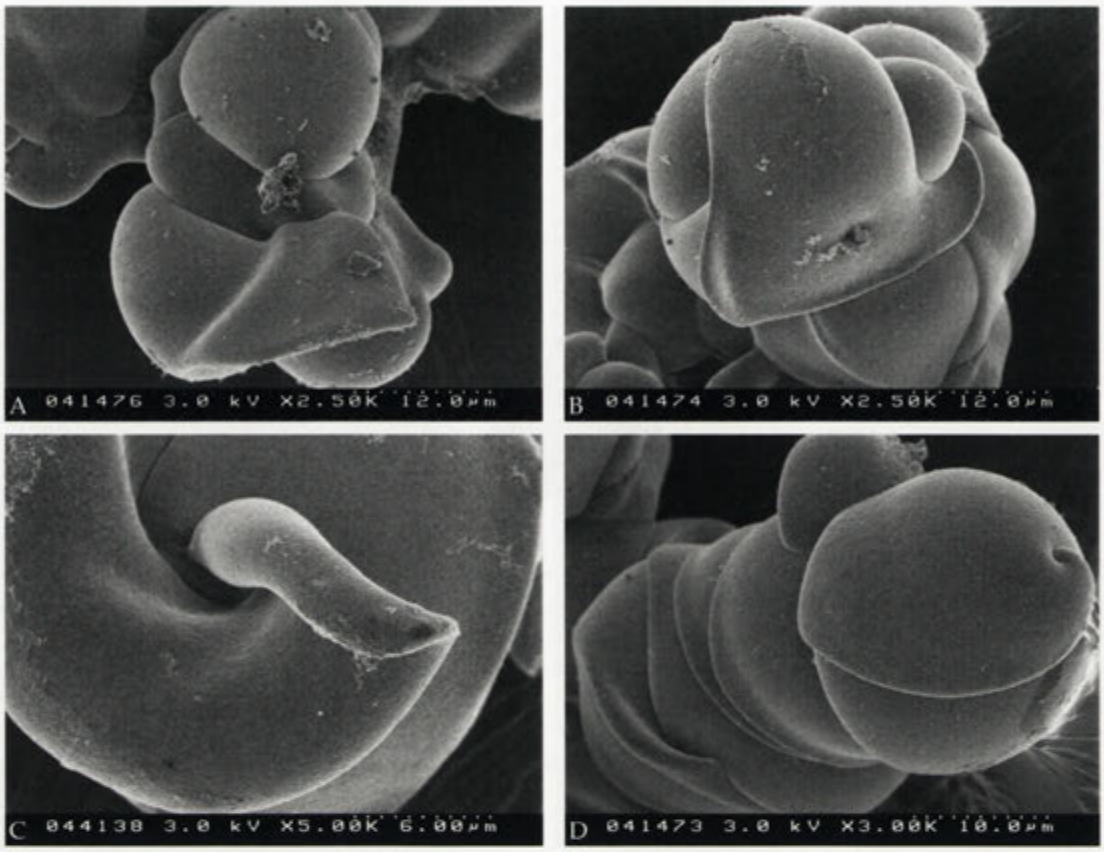

Figure 3.5: FESEM images of globular aggregates observed during synthesis of biomorphs using standard conditions (5 mM $BaCl_2$, 8.5 mM SiO_2, pH 11.0, ambient temperature and pressure). In A the extrusion of a tongue, or sheet, can be seen. The stability of this tongue will determine the morphology produced. If lip-curling at the edges occurs (C), a helical aggregate will develop. If the tongue wraps around a pre-existing globular aggregate (B, D), as worm is the outcome.

can discern the evolution of sheets, helices and worms in Figure 3.5 A, C and D respectively. The distinction between the aggregates relates to the fate of this tongue. If the growth is undisturbed a sheet will form, however, if the sheet at some point begins to wrap around itself, a helix or a worm is formed. In the case of the helices, one can often see that a large sheet curls at the edges, in opposite direction, which then upon further growth produces a twisted aggregate. In the case of the worms, the scenario is different. The tongue wraps around itself onto the preexisting globular aggregate, and growth proceeds in essentially a 2D fashion (see Figure 3.5 D).

Growth of worm-like aggregates most often proceeds without a preexisting helix, and can grow to considerable lengths (hundreds of μm). Worms are generally of consistent diameter of around 15-25 μm, but this can vary between samples, and also within a single aggregate. Variations in diameter are related to the thickness of the

Figure 3.6: FESEM images of a helix-worm transition. The red arrows indicate one strand while the black arrows indicate the other. The red dashed arrows indicate the disappearance and resurfacing of the the red strand. In C an overgrown worm is seen with a characteristic head as well as large euhedral witherite crystals.

growing tongue as well as the way it curls around itself. In many cases it can be noted that each segment, or each twist of the tongue, overlaps with the previous one. Such 'backlashing' can be extensive (see Figure 3.4 B), and up to five layers have been observed in a single cross section of a worm. Occasionally 'errors' occur during the growth of worms where a backlashing segment buckles and produces a globular aggregate on the side of the biomorph (see for example Figure 3.16 A). Continued growth results in an increase in diameter and the development of of a head, which at prolonged growth becomes covered in larger witherite crystals. It should be noted that the development of such heads are only observed on some aggregates within a single experiment.

As mentioned previously, the growth of the double helices usually proceeds with constant diameter. This is, however, not always the case. In some cases one can see a change from a perfect helical aggregate to a worm-like aggregate. The increase in diameter can occur gradually or quite drastically, and this change in shape is often observed during the later stages of growth. It is believed that the balance between the two strands that make up the double helix is perturbed, which causes one to overcome the other. This results in what appear to be a singly wound thickened spiral, as is the case of the worms. In Figure 3.6 A it is noted that one of the strands shrinks (indicated by red arrows) and seems to be lost within the aggregate, while the other (indicated by black arrows) inflates and from thereon can be followed around the outside of the aggregate till it abruptly stops growing. A new strand then appears (red arrow 2) which continues to grow, forming an inflated head. Further growth produces overgrowth of euhedral witherite crystals on this head. It is difficult to tell whether this new strand is the same as the one previously observed shrinking and disappearing within the aggregate. The transition from a perfect helix into a worm is a complex phenomenon difficult to observe with microscopy techniques on non-broken

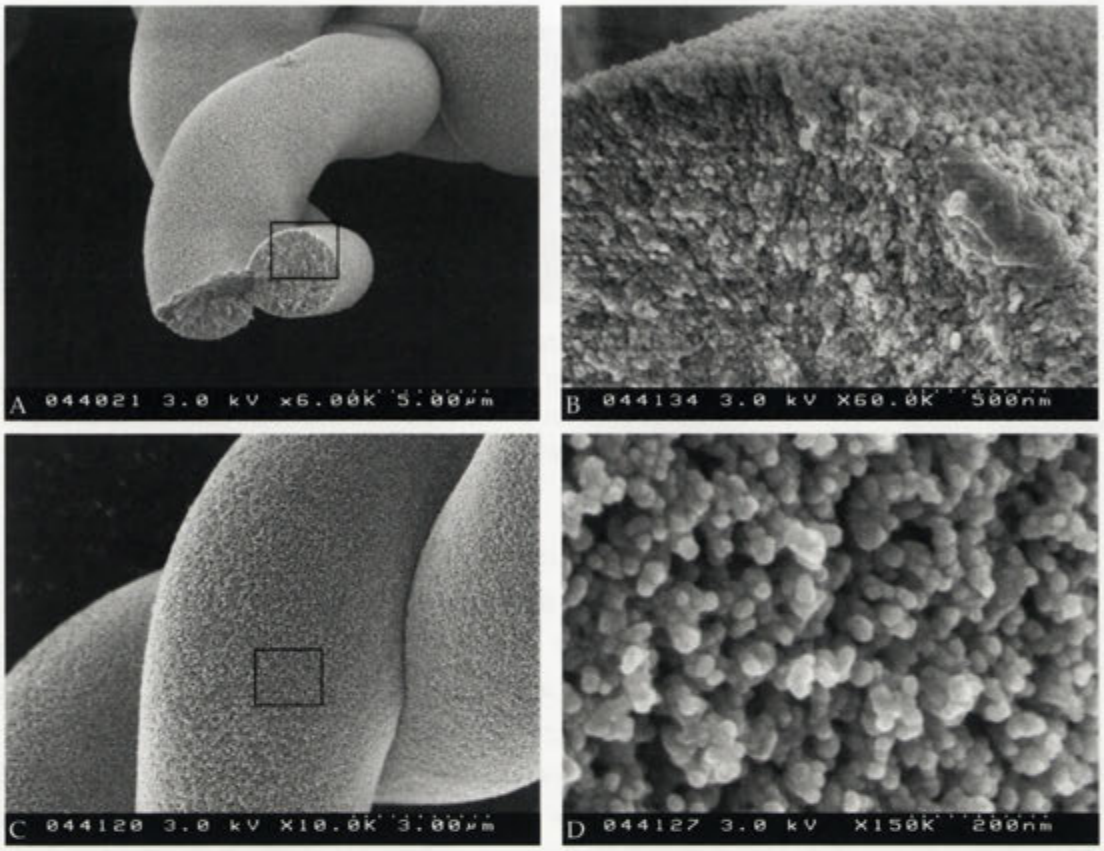

Figure 3.7: FESEM images of helical aggregates observed during the early stages of growth (4 h) using standard conditions (5 mM $BaCl_2$, 8.5 mM SiO_2, pH 11.0, ambient temperature and pressure). The areas seen in B and D are magnifications of the rectangular areas seen in A and C respectively.

aggregates. One can, however, conclude that such transitions only occur from double helix to worm, the reverse has never been accounted.

Growth of double helices can therefore be categorised into different stages; 1) growth of an initial globular aggregate, which extrudes a tongue; 2) the curling of the edges of this tongue in opposite directions; 3) the continued growth of a double helix; 4) the development of a worm-like aggregate on the pre-existing double helix; 4) possible inflation and overgrowth of traditional witherite crystals. Worms on the other hand grow from the same initial globular aggregate in which the tongue somehow is attracted to the globule and wraps around itself.

In addition to the complex 'macroscopic' morphology (μm scale) seen in these biomorphs, the atomic and meso-scale structures of these aggregates are also intriguing. For instance, in Figure 3.9 the interior makeup of a worm can be seen. It is evident from Figures 3.9 B that each twisting sheet-segment is composed of nano-sized crystallites exhibiting orientational order (García-Ruiz et al., 2002). The rod-like crystallites

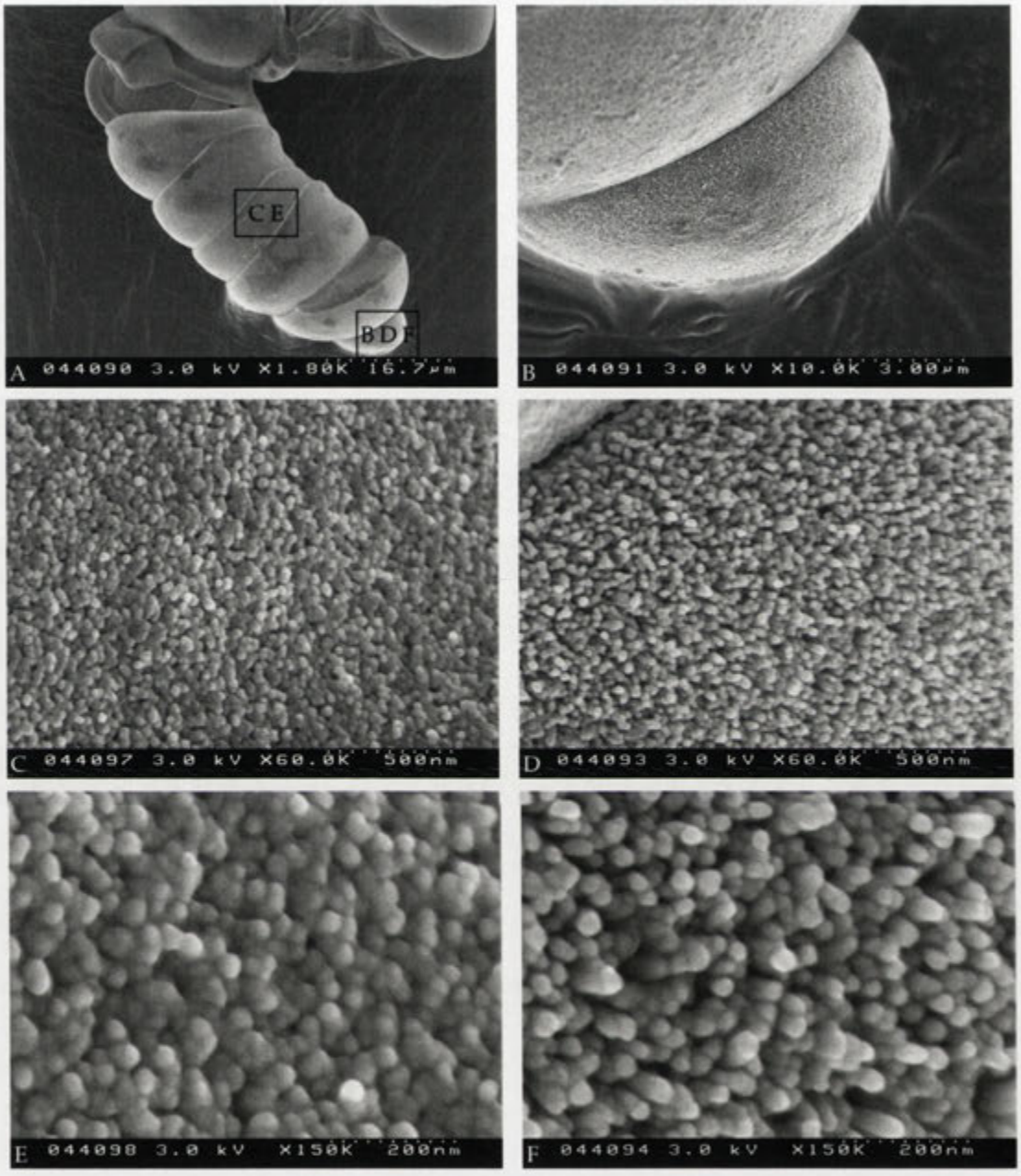

Figure 3.8: FESEM images of a worm-like aggregate observed during the early stages of growth (4 h) using standard conditions. The rectangular areas marked with letters correspond to the respective images.

are packed together with a slight twist between adjacent rods. At the surface in the growing direction of the worm, the crystallites seem to be more or less perpendicular to the surface, whereas this is not the case for the underlying surface. The crystallites then also rotate around the central axis of the worm as the sheet or tongue grows,

giving rise to all possible tilt angles relative to the central axis of growth direction of the worm. All crystallites can therefore be seen aligned in the growth direction of the tongue.

The thin backlashing layers have a different crystallite orientation relative to the underlying twisted segment (see Figure 3.9 C). At the interface between the two layers the crystallites in the backlashing layer seem to be oriented towards the beginning of the worm. A consecutive twist between the crystallites towards the outer surface gives rise to the orientational ordering seen in Figure 3.9 C.

A similar situation is present in the double helices (see Figure 3.10). In the lip-curling edge of the helix the consecutive tilt between the crystallites are slightly higher than in the worms, which also reflects the higher degree of curvature seen in these morphologies compared to worms. The orientational ordering is evident and is a possible origin of the μm-scale morphology.

In Figures 3.9 and 3.10, the crystallites are seen as slightly elongated rods having diameter on the order of 50 nm. The length of the crystallites seem to vary between samples from almost globular crystallites to long clearly rod-like in character.

The micronscale analysis of worms and double helices reveal that the makeup of such aggregates is inherently complex, and composed of nano-sized crystals (see Figure 3.9 and 3.10).

As also seen in Figures 3.9 A and C, and Figure 3.10 B, the surface of the aggregates are covered in a skin. By treating these biomorphs with a weak acid the skin can easily be seen as a hollow cast of the original morphology (see Figure 3.11 B) (García-Ruiz et al., 2002; Hyde et al., 2004). In Figure 3.11 the skin is shown to be composed of ~100nm globular particles, which form a layer around the aggregate. The thickness of the skin can vary between aggregates, but also within each biomorphs as shown in Figure 3.11 F. Furthermore, it can also be observed in Figure 3.11 that the skin possesses grooves matching the pitches of the worm.

In no case have internal sheets of silica dividing the segments been identified. This suggests that the skin is only a surface feature, and does not occur within the aggregate itself. The presence of such a skin is also observed in biomorphs synthesised using a silica gel. However, as mentioned in Chapter 1, this is not always the case. Even though it sometimes is relatively easy to recognise the presence of a thick skin, as seen in Figures 3.9 and 3.10, often much thinner skins are observed, barely recognisable on a non-broken surface (see Section 3.4.2). Furthermore, the presence of this silica skin seems to vary between aggregates, precipitated in different experiments, as occasionally no silica skin is seen left behind after acid treatment. This further suggests that the silica skin is not necessary for the development of the helical and worm-like morphologies seen in the standard experiment. It may be that the silica skin is a secondary

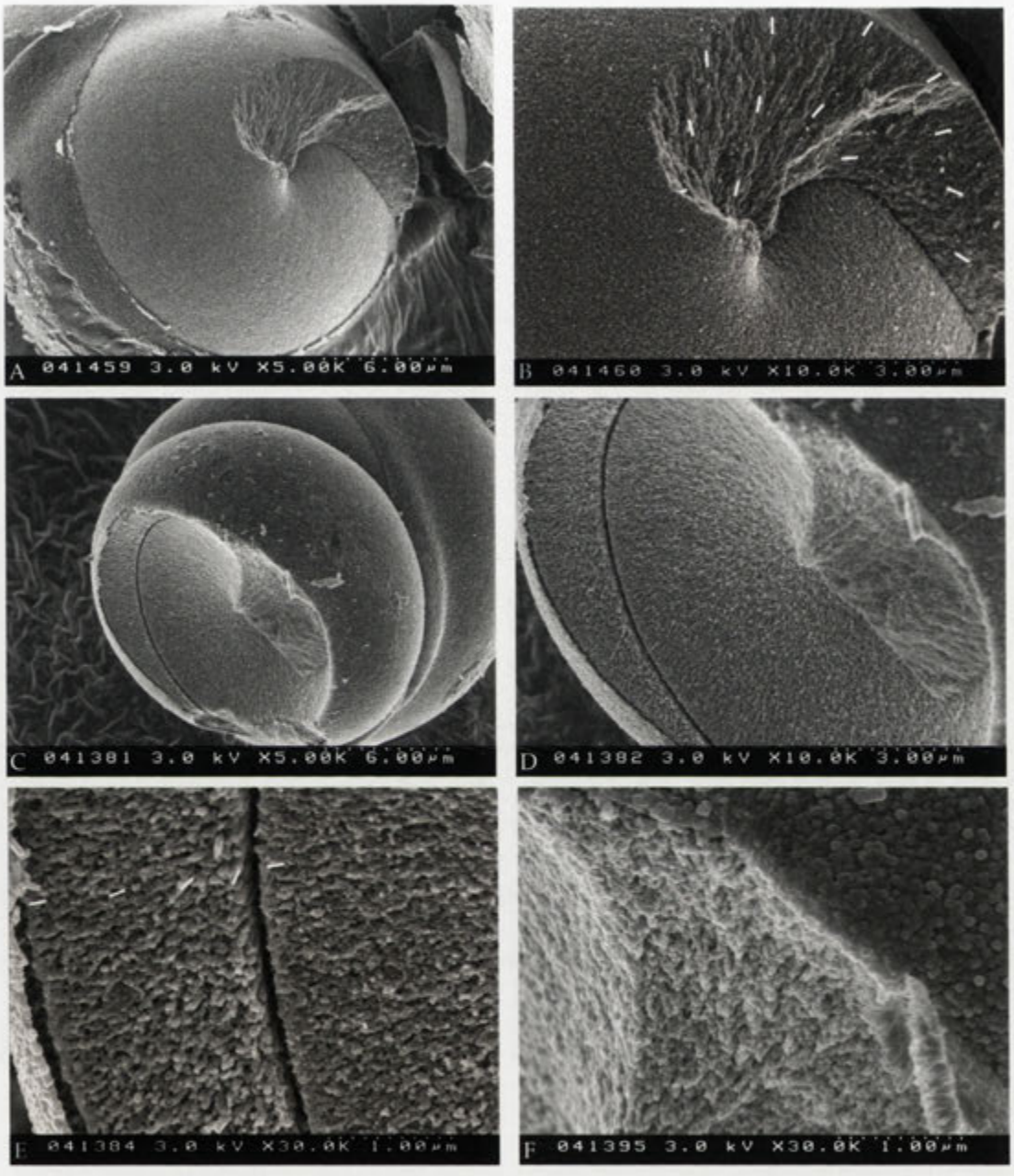

Figure 3.9: FESEM images of the interior of worms. The broken worm in A–B is viewed from the top, in opposite direction to the growth direction, and clearly shows that worms are composed of a twisting sheet. In B, the orientation of the crystallites in this sheet is indicated by the white markers. The broken surface seen in C–F is viewed along the growth direction of the worm. Here, the overlapping segment (backlashing) is easily seen as a couple of μm thin strip surrounding the inner core of worm. The crystallite orientation, indicated by white markers in E, in this backlashing segment is almost perpendicular to that seen in the immediate neighbouring crystallites in the core of the worm. Both of these aggregates (A, C) are surrounded by a visible skin.

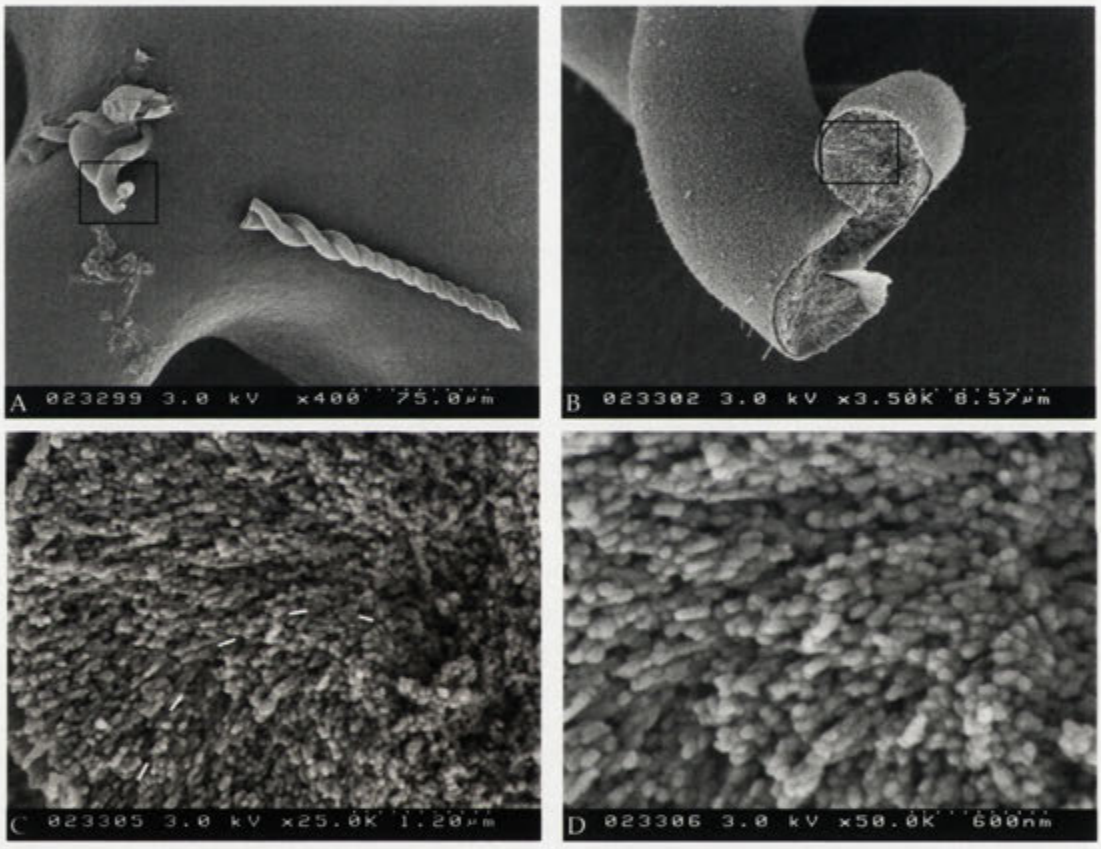

Figure 3.10: FESEM images of the interior of a broken helix indicated by the rectangles in A and B. The crystallite orientation is twisting relative to each other as indicated by white markers in C. In D the varying size and slightly elongated character of these crystallites is observed.

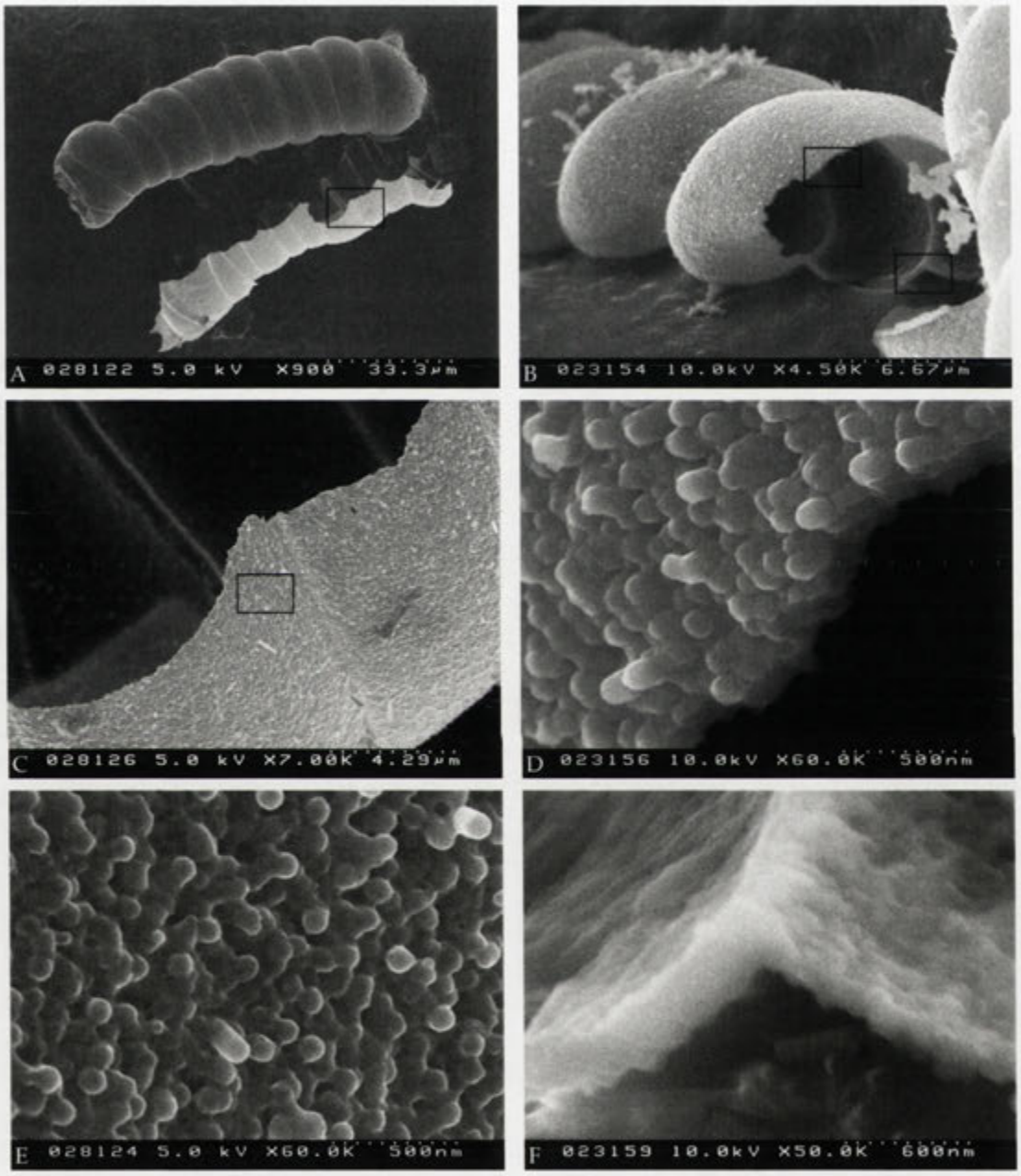

Figure 3.11: FESEM images of the silica skin of worms. Images A–C show a consecutive magnification series, indicated by the rectangles, of a detached silica skin. This sample was slightly etched with 0.1 M NaOH possibly aiding the silica skin to fall off. The surface of this skin (E) shows the globular nature of this skin. Images B–F show a silica skin left after acid dissolution of the carbonate entity. Both the external (D) and internal (F) surface of the skin is shown, indicated by the rectangles in B respectively.

feature that is formed as the pH drops below the solubility of amorphous silica. The formation of colloidal silica and/or silica precipitation on the surface of the biomorphs is therefore likely to be related to the chemical state of the solution and the number of aggregates growing per cell.

TEM observations

Transmission electron microscopy analyses requires the production of thin sections, made by Harri Kokkonen and Dr John Fitzgerald. Ann-Kristin Larsson and J. Fitzgerald performed the imaging and diffraction work reported here.

The optical images of the prepared thin section seen in Figure 3.12 A and in particular B show that the crystallites are highly oriented. Each segment displays an extinction pattern in form of a Maltese cross, which is a result of the fact that the principal vibration directions coincide with that of the polarisation directions in the darkened areas. The anisotropic witherite crystals (biaxial (-)) are oriented within the isotropic amorphous silica in such a way that no light can go through the upper polariser, causing the biomorph to go dark. This is consistent with crystallites oriented with their *c*-axis (length fast axis) outward towards the edge of the aggregate, as indicated in the FESEM images (see Figure 3.9). The interference colours therefore suggest a continuously varying orientation of the witherite crystallites, consistent with the FESEM observations described above. Each segment shows almost identical extinction patterns, indicating that the orientational ordering of the crystallites is uniform between the segments.

Electron diffraction was performed on a selected area shown in Figure 3.12 C. The electron diffraction pattern (EDP) seen in D is a powder-like EDP as concentric rings of reflections are present. However, it is also evident that some reflection rings are broken, which indicate an increased orientational order between the crystallites as compared to powder rings. The indexing of the EDP is done using the orthorhombic cell parameters given in Section 2.2.1, and as indicated by the concentric red rings, some reflections overlap. For instance, the 022 and 112, and 200 and 130 planes all have very similar d-spacings, causing apparent broadening of the overlapping reflections. As several zone axes seem to be present in this EDP, the interpretation of the crystallite orientation is not straight forward. However, the 002 reflection on the other hand is more readily identified and occurs as an isolated arc, as indicated by the red arrow in Figure 3.12 D. The length of the arc-like *c*-axis reflections defines the angular crystallite distribution, which is about 60°, showing a large spread in crystal orientations within the area analysed.

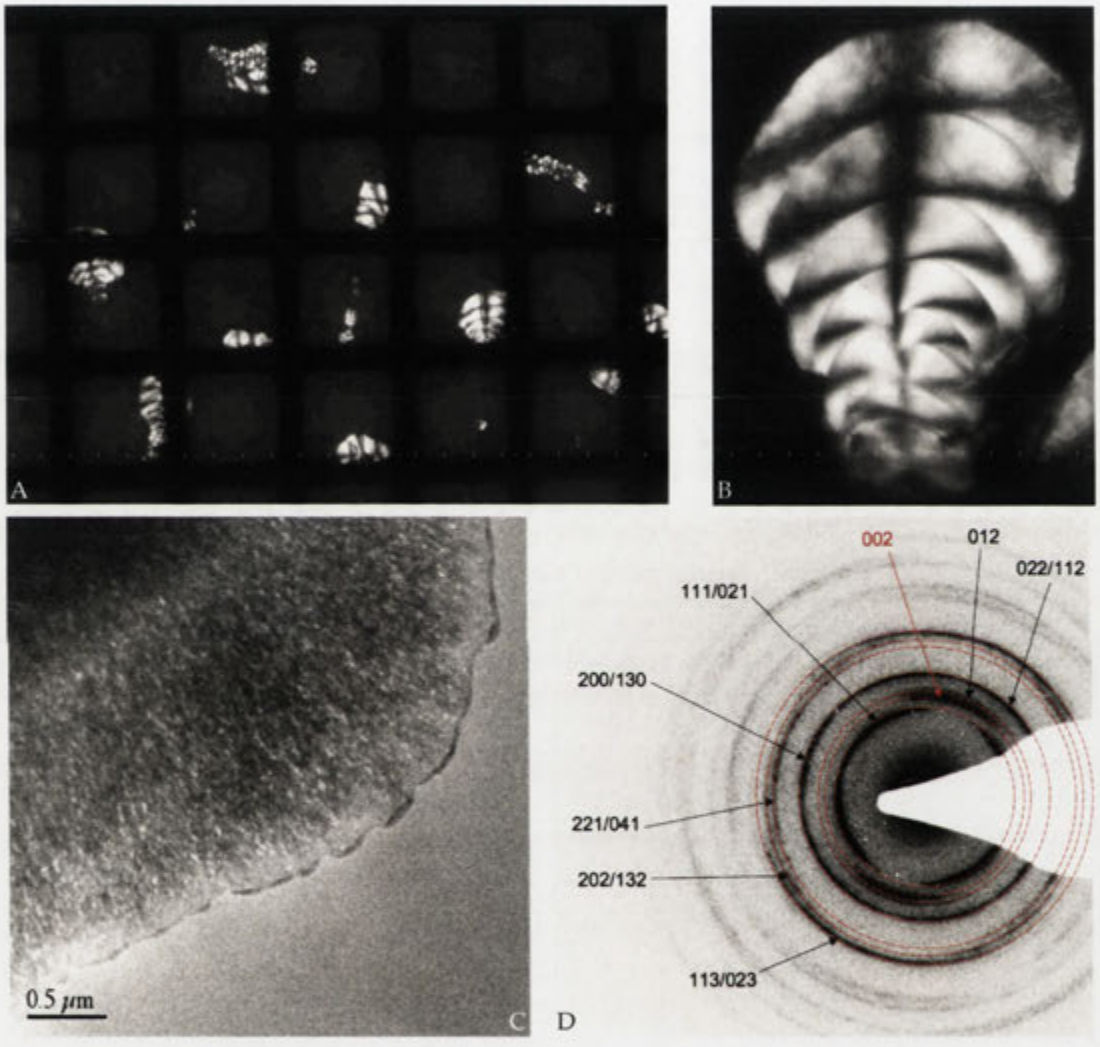

Figure 3.12: Transmission light microscopy images of thin section (A) and the worms analysed in the TEM (B). In C a low resolution TEM image of the area analysed can be seen. D shows the diffraction pattern obtained, where EDP indexing is in the orthorhombic system.

Discussion

In this section characterisation of the morphologies produced using 5 mM $BaCl_2$, 8.5 mM SiO_2, pH 11.0, ambient temperature and pressure have been discussed. Globular, sheets, helical and worm-like morphologies can be produced within 10 hours

of growth as carbon dioxide is absorbed into the silica sol. All biomorph growth observed begin with the development of a globular aggregate. The extrusion of a sheet-like tongue from the globule defines the onset of either sheet, helical or worm-like growth. Both right- and left-handed worms and helices are observed, and they can grow as individual precipitates or in clusters. Upon prolonged growth some helices are seen to expand in diameter to produce a worm-like aggregate at their ends. Such helix-worm transition is only seen in some helices even in the same sample. Both worms and helices can also develop large heads, which can be seen as the onset of overgrowth of euhedral witherite. This suggests that the silica concentration has dropped below a concentration threshold of where it efficiently interacts with precipitating witherite. The sodium silicate concentration is therefore important for the development of biomorphs at high pH.

Many of the morphologies analysed under these conditions are surrounded by a silica skin. This is evident from both FESEM analysis of as-prepared biomorphs. This skin can more easily be observed through dissolution of the carbonate entity with a weak acid, and show colloidal character; being composed of globular particles of around 100 nm in diameter. As mentioned in the previous section, it is believed that this skin is only an outer surface feature, as it has never been encountered (although not proven) to exist in between individual layers of worms or helices. As such, it may serve as a secondary precipitation of silica as pH is dropped during the course of the synthesis.

Helical and worm-like aggregates are further characterised by a local orientational order between the crystallites. The long axis of the crystallites is aligned with the *c*-axis of witherite, and is oriented towards the growth direction. As the the growing edge of the aggregate is sheet-like and twists around the growth axis of the biomorph, a consecutive twist between the crystallites is seen. This is also confirmed by TEM analysis, although the EDP in question is difficult to interpret.

During the course of this work it has also been noted that during some syntheses, preferential growth of helices over other morphologies are observed. Similarly, in some cases, only worm-like morphologies develop. Such inconsistencies where at the time believed to be caused by slight variations in initial concentration, pH or temperature. During the precipitation, barium and silica concentrations as well as pH are reduced. Given these circumstances, and the effect on morphological evolution (globular to helix to worm transitions), the effect of changing the initial conditions (pH, sodium silica concentration, $BaCl_2$, and temperature) are explored in the following sections.

3.4.2 Variation in pH

Slight variations in morphologies can sometimes be seen between experiments using the standard conditions previously discussed. These variations are believed to be caused by differences in initial pH and carbonate concentration. Furthermore, the presence of a silica skin is not always evident from FESEM observations, a fact that could also be due to variable pH. To investigate the influence of pH on the morphological evolution, as well as the presence or absence of silica skin, a series of experiments were performed on the same day using the same stock solutions. By changing the amount of added NaOH (see Section 3.2) pH can be varied while keeping the silica concentration constant at 8.5 mM (see Table in Figure 3.13). Changing the initial pH of just one pH unit was shown to have a strong effect on the morphology of the aggregates produced (see Figure 3.13). The pH change observed after 10 hours of growth is also much larger at high pH compared to low pH values.

At low pH (10.46-10.80) globular aggregates are formed that with increasing pH become more complex. Increasing pH also increases the nucleation density and a larger variety in morphologies is seen. As can be noted in Figure 3.13, worm-like biomorphs are easily visible at a pH interval of around 10.85-11.42. Double helixes, on the other hand, occur more frequently at higher pH of between 11.11-11.42. It should be noted that both worms and helices are observed at pH 11.51, but much less frequently so. At this pH, smaller aggregates with sheet-like and bud-like morphologies are more commonly observed (see Figure 3.14 $K_1 - K_3$). To investigate if morphological variation with pH is accompanied with compositional variation between the morphologies, EDX analyses were performed on as prepared aggregates[1]. In the following sections, the result of such analyses and their interpretation will be discussed in relation to pH and morphologies produced.

Globular aggregates

As observed in the optical images (Figure 3.13) and FESEM images (Figure 3.14) low pH conditions result in globular aggregates of various sizes. Even though biomorph growth using the standard experimental conditions always begin with development of such aggregates, the ones described here do not proliferate into helical or worm-like morphologies within the time period of experimentation. As can be seen in Figure 3.15, globular aggregates synthesised between pH 10.46 and 10.68 contain particles in the 50-100 nm range that are composed of almost almost pure witherite (see Table

[1]As making thin sections of biomorphs is inherently difficult, it was concluded that a more efficient way of acquiring compositional data on a large number of morphologies could be done on biomorphs as prepared, without any further preparation.

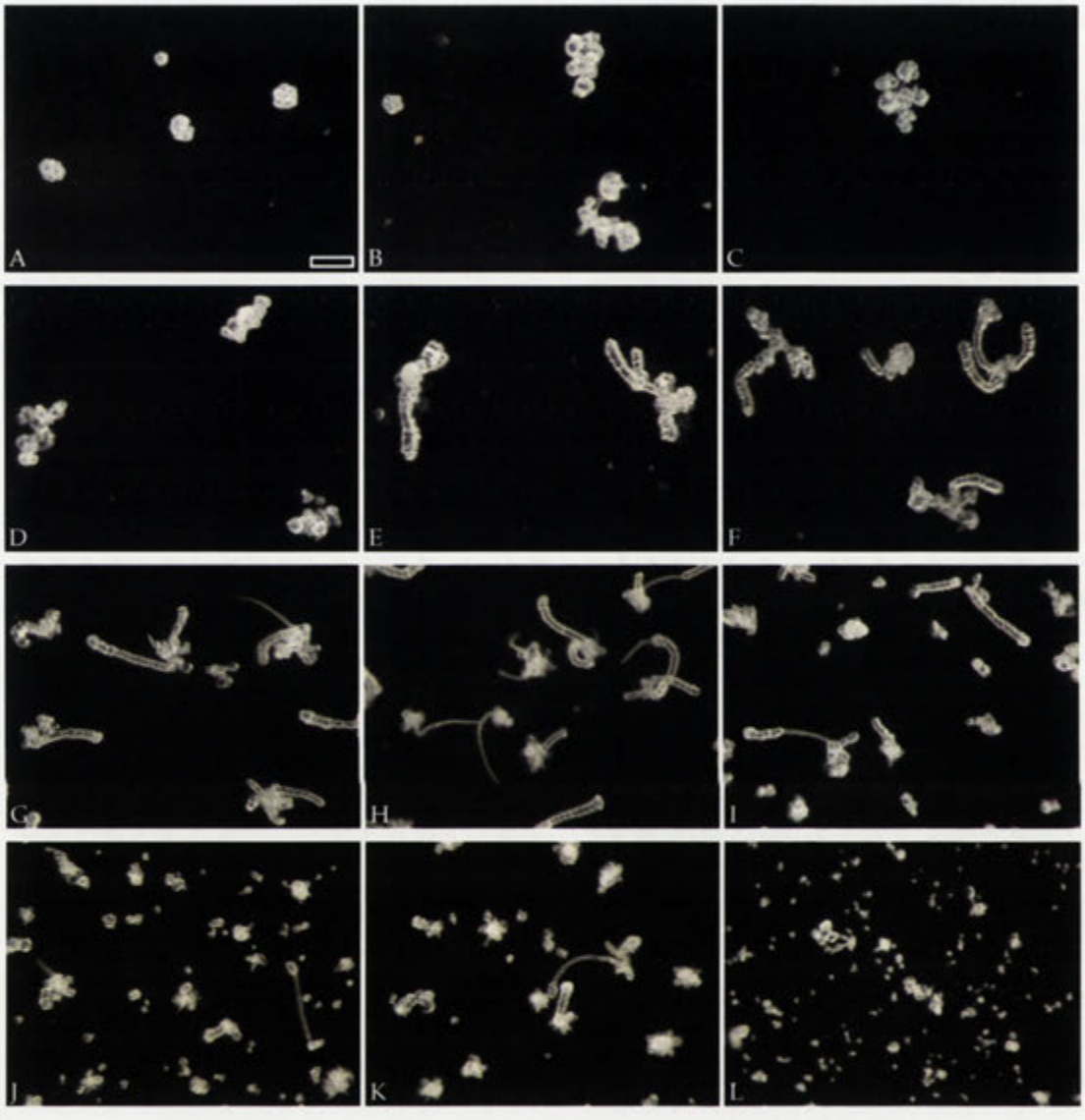

Sample	A	B	C	D	E	F	G	H	I	J	K	L
[NaOH] (mM)	7.0	7.4	7.8	8.2	8.6	9.0	9.4	9.8	10.2	10.6	11.4	11.8
pH_0	10.46	10.58	10.68	10.80	10.85	10.99	11.11	11.21	11.26	11.35	11.48	11.51
Δ_{pH}	-0.42	-0.53	-0.58	-0.68	-0.85	-0.92	-1.02	-1.10	-1.15	-1.21	-1.28	-1.29

Figure 3.13: Optical images of biomorphs produced after 10 hours at different initial pH (pH_0), displayed in the table, but at otherwise the same reaction conditions. The observed pH change after 10 hours within each experiment is seen as Δ_{pH}. Scale bar 100 μm in pH 10.46 is valid for all the images.

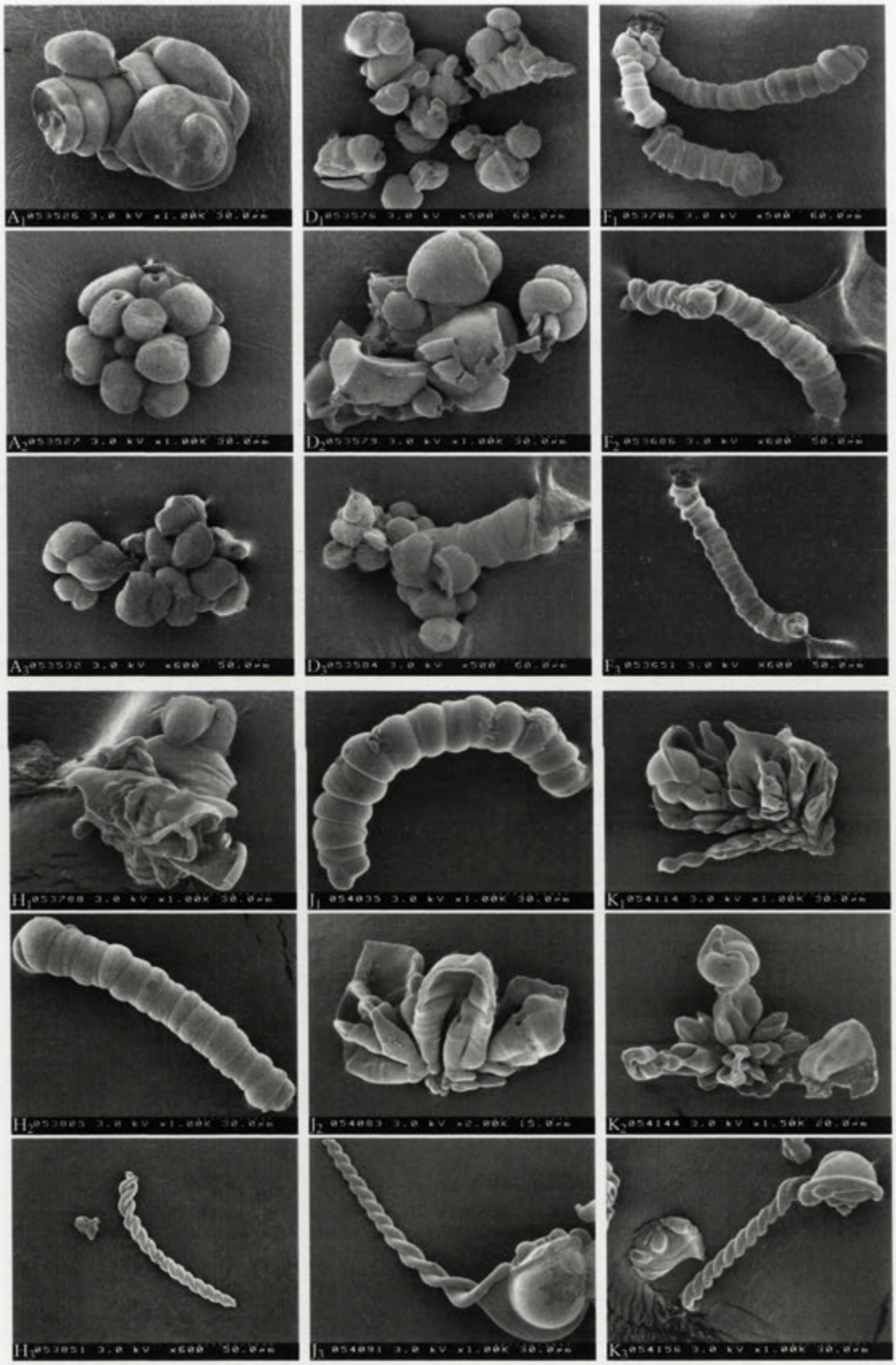

Figure 3.14: FESEM images of biomorphs produced after 10 hours at different initial pH, but at otherwise the same reaction conditions (see Figure 3.13. A pH 10.58; D pH 10.80; F pH 10.99; H pH 11.21; J pH 11.35; K pH 11.48).

Elemental composition of globular aggregates

Compound	A_1	A_2	A_3	A_4	A_5	C_1	C_2	C_3	C_4
Na_2O	0.09	1.04	0.88	0.92	0.82	1.08	1.27	1.24	1.04
SiO_2	0.58	0.75	1.37	6.85	0.08	0.86	0.88	1.07	1.75
Cl_2O_{-1}	-	0.07	-	-	-	0.12	0.11	0.13	0.10
BaO	59.34	60.81	54.04	52.19	51.04	68.97	66.85	70.18	61.92
CO_2 (calc.)	17.03	17.45	15.51	14.98	14.65	19.80	19.19	20.15	17.77
Total	77.04	80.11	71.80	74.93	65.58	90.81	88.29	92.77	82.59
Si/Ba atomic ratio	0.02	0.03	0.06	0.33	0.004	0.03	0.03	0.04	0.07

Table 3.1: EDX results (wt% oxide, Si/Ba ratio) of the surface of globular aggregates synthesised at low pH, i.e. 10.46 and 10.68. The alphabetical notation reflects the initial synthesis conditions, represented in Figure 3.13.

3.1). Most often ~1wt% silica and 50-70 wt% Ba are seen in the aggregates. In the following analyses the Si/Ba atomic ratio will be noted as the basis of comparison for morphological composition. Such a ratio is more significant compared to absolute values as the total wt% can significantly vary between analyses (see Table 3.1). The low totals seen in almost all biomorph analyses reflects the fact that the surface area of analyses are in most cases not flat, and can in many cases be seen to be porous. Furthermore, adsorbed water is also believed to be a major cause of the low totals seen. In addition to Si and Ba, Na and Cl are often seen in the EDX analyses. In all cases, it is assumed that Cl exist as NaCl, and the small amount present is most likely due to incomplete washing, and drying effects. The excess Na present can be explained as sodium silicate ($Na_{2x}SiO_{2+x}$). The Si/Ba ratio of globular aggregates is most often <0.07, however, in one case an Si/Ba ratio of 0.33 was observed. The composition of the interior of such aggregates is consistent with analyses performed on the outer surface of the aggregate, i.e. Si/Ba 0.01-0.07, indicating the absence of increased silica concentration on the surface. If these aggregates have a silica skin, an increase in Si/Ba ratio is expected from analyses performed on the surface.

Worms

As indicated by the optical images in Figure 3.13, the lowest initial pH that yields worms after 10 hours is around 10.85. Such aggregates are more frequently formed around pH 11.00-11.26, where they can grow to appreciable lengths. At the low pH range many of the worms show an increasing degree of disfigurement (see Figure 3.16), with a number of extra blobs extruding from the sides of the aggregate, and

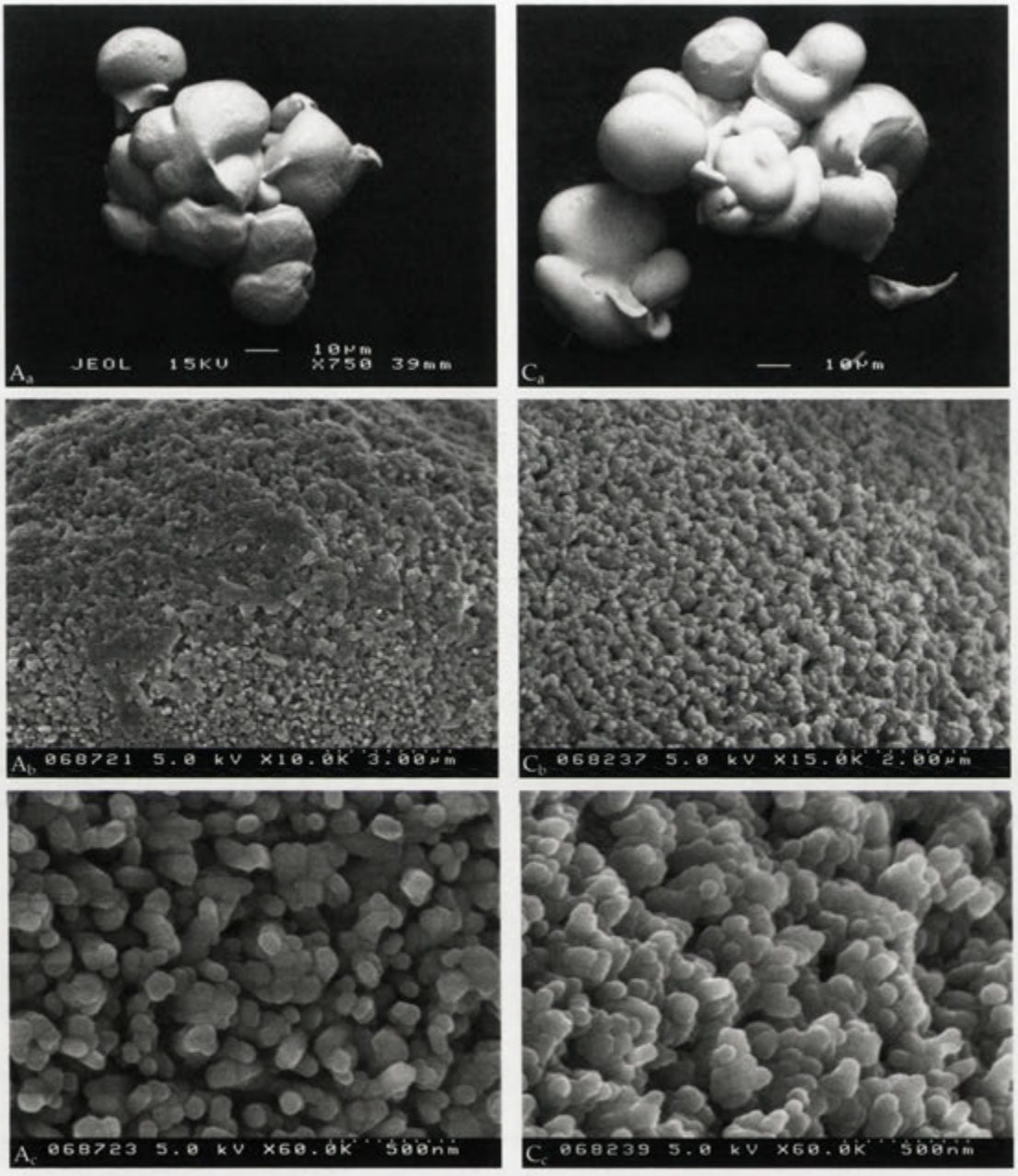

Figure 3.15: Backscattered SEM images and high resolution FESEM images of two aggregates produced at pH 10.46 (A) and pH 10.68 (C) respectively. The composition of such aggregates, deduced from EDX analysis, is listed in the table as wt% oxides.

extensive visible back-lashing. At higher pH more uniform aggregates are formed. In this section elemental analysis of worm-like aggregates are discussed relation to the initial experimental pH. Special attention will be given to the nature of a silica skin, and how this can be detected. As indicated in Table 3.2, the pH doesn't seem to have

Elemental composition of worms

Compound	E_1	F_1	F_2	H_1	I_1	I_2	J_1	L_1	L_2
Na_2O	1.27	1.04	0.94	1.38	0.73	1.19	1.04	0.87	0.93
SiO_2	2.18	7.55	1.47	3.22	1.16	1.03	3.14	0.92	8.62
Cl_2O_{-1}	-	0.12	-	-	-	-	-	-	-
BaO	66.37	55.34	64.89	60.08	65.44	77.15	70.83	65.83	66.69
CO_2 (calc.)	19.05	15.89	18.63	17.25	18.78	22.15	20.33	18.90	19.14
Total	88.86	79.94	85.93	81.74	86.11	101.5	95.35	86.43	95.39
Si/Ba atomic ratio	0.08	0.35	0.06	0.14	0.05	0.03	0.11	0.04	0.33

Table 3.2: EDX results (wt% oxide, Si/Ba ratio) of the surface of worms synthesised at various pH. The alphabetical notation reflects the initial synthesis conditions, represented in Figure 3.13. In contrast to the other samples, I_1 was acquired from the interior of a worm.

any effect on the composition of the worms. The Si/Ba ratio varies between 0.4-0.02 with seemingly no effect on morphology.

Four worms synthesised at an initial pH of 10.85 (notation E in Figure 3.13) were analysed in terms of elemental composition using EDX, one of which can be seen in Table 3.2 E_1. These samples showed Si/Ba variation between 0.27 to 0.05. In three of the worms Si/Ba ratios decreased along the growth direction of the worm, indicating a smaller composition of silica in the aggregate as it lengthens. However, in one case, a constant Si/Ba ratio of $\sim$ 0.08 could be seen across the entire length of the worm (see Figure 3.16). This variation in composition is related to the silica present within the structure as well as the existence of a silica skin. The presence of thin layer of contaminating colloidal silica was also shown to increase the Si/Ba ratio from 0.08 to 0.36, indicating the high sensitivity of the surface concentration of silica on the EDX results (see Figure 3.16). In all cases, the Si/Ba ratio is either constant or decreases along the growth direction. The reverse has never been accounted. The same behaviour is observed in all worms analysed irrespective of the pH at which they were produced.

At an initial pH of 10.99 (standard experiment) some worms exhibit constant Si/Ba whereas others show a decreasing ratio with growth direction. The highest Si/Ba ratio observed in these samples is 0.4, which decreased to 0.06 at the end of the worm. Similarly, at pH 11.21, worms have a maximum Si/Ba ratio of 0.2, which also is seen decreasing along the growth direction (see Figure C.1).

At pH 11.35 or higher, worms are often seen growing in conjunction with sheets. In Figure 3.17), one such example is shown, where the Si/Ba ratio is also decreasing towards the end of the aggregate. In this case, the surface textures differ from the

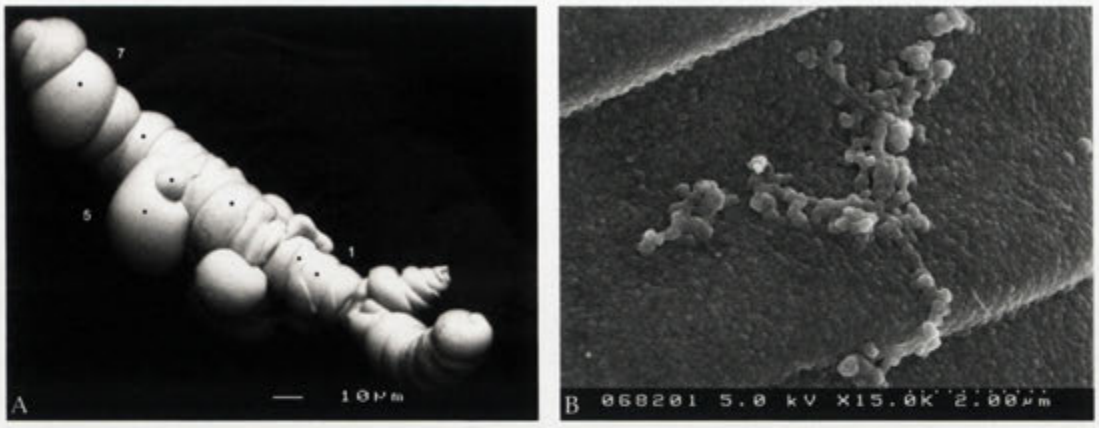

Figure 3.16: A back-scattered SEM image (A) and a FESEM image (B) of the surface of a worm, synthesised at pH 10.85 (notation E in Figure 3.13). Elemental spot analyses (1-7) show a constant Si/Ba ratio of ~ 0.08, except no 2 which has an Si/Ba ratio of 0.36. This is explained by the contamination of colloidal silica seen in B. See Table 3.3 E_1 for further elemental composition of the worm (point 3 in image A).

beginning to the end. As can be seen in Figure 3.17 D high Si/Ba ratio corresponds to areas where particles are densely packed. Very low Si/Ba ratios on the other hand are observed where particles adopt a much looser configuration. However, it is difficult to assess whether the porosity can cause the drop in the Si/Ba ratio, or if this is an actual effect of lower silica concentration. As other samples with high Si/Ba ratio can show similar surface texture, it is believed that the lower Si/Ba ratio is caused by a drop in silica concentration within the aggregate. For instance, in Figure 3.18 a worm synthesised at pH 11.51 is shown. The Si/Ba ratio of this sample is around 0.33 at both spots indicated in Figure 3.18 A. The surface texture varies from densely packed to quite loose, without any change in composition. At the highest pH analysed here, pH 11.51, the Si/Ba ratio of worms ranges between 0.35 and 0.04. In two out of three worms analysed, a constant Si/Ba ratio of 0.35 or 0.05 was observed along the growth direction of the worm. In the third case a decreasing ratio, from 0.16 to 0.04, with length was seen.

To investigate how susceptible the Si/Ba ratio is to surface topology, a series of line scans were performed across the aggregates, which in all cases were aligned towards the X-ray detector. As can be seen in Figure 3.19, such a scan reveals a constant composition across a wide distance of the worm, indicating that as long as the spot analysis is performed close to the middle axis, a reproducible result is obtained. The scan further indicated an increased concentration of Si relative to Ba at the edges of the aggregate. Performing similar line scans on silica poor aggregates revealed a similar behaviour in two out of three cases. In the third case, the wt% Si tapers off at the

Elemental composition of helices

Compound	F_1	F_2	H_1	H_2	I_1	J_1	J_2	L_1	L_2
Na_2O	0.63	0.82	1.06	1.05	0.93	0.98	1.05	1.15	0.92
SiO_2	6.85	3.59	4.19	2.87	5.80	9.97	2.72	1.26	0.68
Cl_2O_{-1}	-	0.24	0.11	0.07	-	-	-	0.08	-
BaO	59.28	60.69	63.63	63.61	66.21	63.12	67.63	69.47	68.11
CO_2 (calc.)	17.01	17.42	18.26	18.26	19.01	18.12	19.41	19.94	19.55
Total	83.77	82.77	87.26	85.85	91.94	92.19	90.81	91.90	89.26
Si/Ba atomic ratio	0.29	0.15	0.17	0.11	0.22	0.40	0.10	0.05	0.03

Table 3.3: EDX results (wt% oxide, Si/Ba ratio) of the surface of worms synthesised at various pH. The alphabetical notation reflects the initial synthesis conditions, represented in Figure 3.13. In contrast to the other samples, I_1 was acquired from the interior of a worm.

edges of the aggregate. The observed variations in line scans across the diameter of the aggregate is not easily explained. A straightforward explanation for the increased Si/Ba ratio seen at the edges of such scans is the presence of a silica skin. However, as the silica-poor aggregates also show similar behaviour, one has to consider other possibilities such as geometrical effects. The effective interaction area of the electron beam is increased at the edges of the biomorph (see Figure C.2), which results in a relative increase in the sampling of the silica skin. This is the scenario at a convex interface seen in worm-like biomorphs. It is therefore suggested that the increased Si/Ba ratios seen in line scans such as the one displayed in Figure 3.19 is due to increased silica concentrations, such as the presence of a silica skin.

As can be seen in Table 3.2 I_1, the interior of the worms also contain very little silica. In Figure 3.20 FESEM images reveal a homogenous nature of both the inside and the outside of the aggregate. Both spot analyses and line scans across the aggregate show a homogenous composition (Si/Ba ~ 0.05) within the structure (see Figure 3.20). If all worms are considered to be of essentially similar interior composition, then worms displaying Si/Ba ratios of <0.1 can be considered to be devoid of an outer silica skin. In the next section helices will be discussed which will shed more light on issues concerning the presence or absence of silica skin.

Helices

Although not visible in Figure 3.13, helices also occur in sample F, i.e. at a pH of 10.99. The helices observed at this lower end of the pH range are often formed in conjunction with worms, and a helix-worm transition is often observed (see Figure 3.21 A). At

higher pH very long and uniform helices are formed. As in the case of worms, the elemental composition of helices varies within and between samples synthesised at different initial pH. In Table 3.3 the Si/Ba atomic ratio can be seen to vary between 0.03 to 0.40 with no systematical variation with pH.

In Figure 3.21 high resolution FESEM images shows the presence of a thin silica skin, or film, on this helix, which has a Si/Ba atomic ratio of around 0.3. High Si/Ba ratios can therefore be indicative of the presence of such a skin, otherwise not clearly discernible through microscopy observations without acid treatment.

In Figure 3.22 electron micrographs of a double helix that turns into a worm can be seen. The Si/Ba ratio of around 0.15 is more or less constant throughout the aggregate, indicating that the helical-worm transition is not due to any compositional variations within the two different morphologies. This is also confirmed in aggregates with much higher Si/Ba ratio (see Figure 3.21), further indicating that such transitions occur irrespective of silica concentration. Even though no skin is visible in the Figure 3.22 C, acid treatment of this aggregate does indeed show the presence of such a skin (see Figure 3.22 D).

Even lower Si/Ba ratios were observed in helices synthesised at pH 11.51. The double helix seen in Figure 3.23 has a Si/Ba ratio of around 0.03 and, as seen in Figure 3.23 C-F, the surface texture is very different from aggregates having higher silica concentrations. The aggregate is composed of 50-100 nm globular particles that have the same appearance inside and on the surface of the aggregate. No silica skin is observed, although it may be present as a thin film, as in Figure 3.22 C. However, the very low Si/Ba ratio speaks against such a feature.

Also present in the high pH experiments are aggregates having quite different morphologies. Some of these can be observed in Figures 3.18, 3.23, and 3.24. These aggregates are generally more silica rich than the double helices and worms seen in the same sample. For instance, the sample seen in Figure 3.24 A has Si/Ba ratios between 0.34 and 0.69. The latter value was acquired from point 2 seen in Figure 3.24 B, which should be considered slightly elevated due to topological effects discussed above. Spot 1 and 3 show Si/Ba ratios of 0.34 and 0.42 respectively. As evident in Figure 3.24 D, and also indicated by the analyses, a silica-rich skin is present. In this case the skin is around 240 nm thick, which is significantly thicker than the skin observed observed on helices at lower pH (see for instance Figure 3.21 D). The backscattered electron image of this sample shows the opposite colouring (the internal barium carbonate rich area is bright, whereas the outer surface is slightly darker) compared to Figure 3.24 A–C. Such a skin is also clearly visible in Figure 3.24 G-I. This sample shows similar Si/Ba ratios as the aggregate in Figure 3.24 A. Similarly, the sheet-like aggregate seen in Figure 3.18 has a Si/Ba ratio of ~0.35, a value more or less identical to the worm

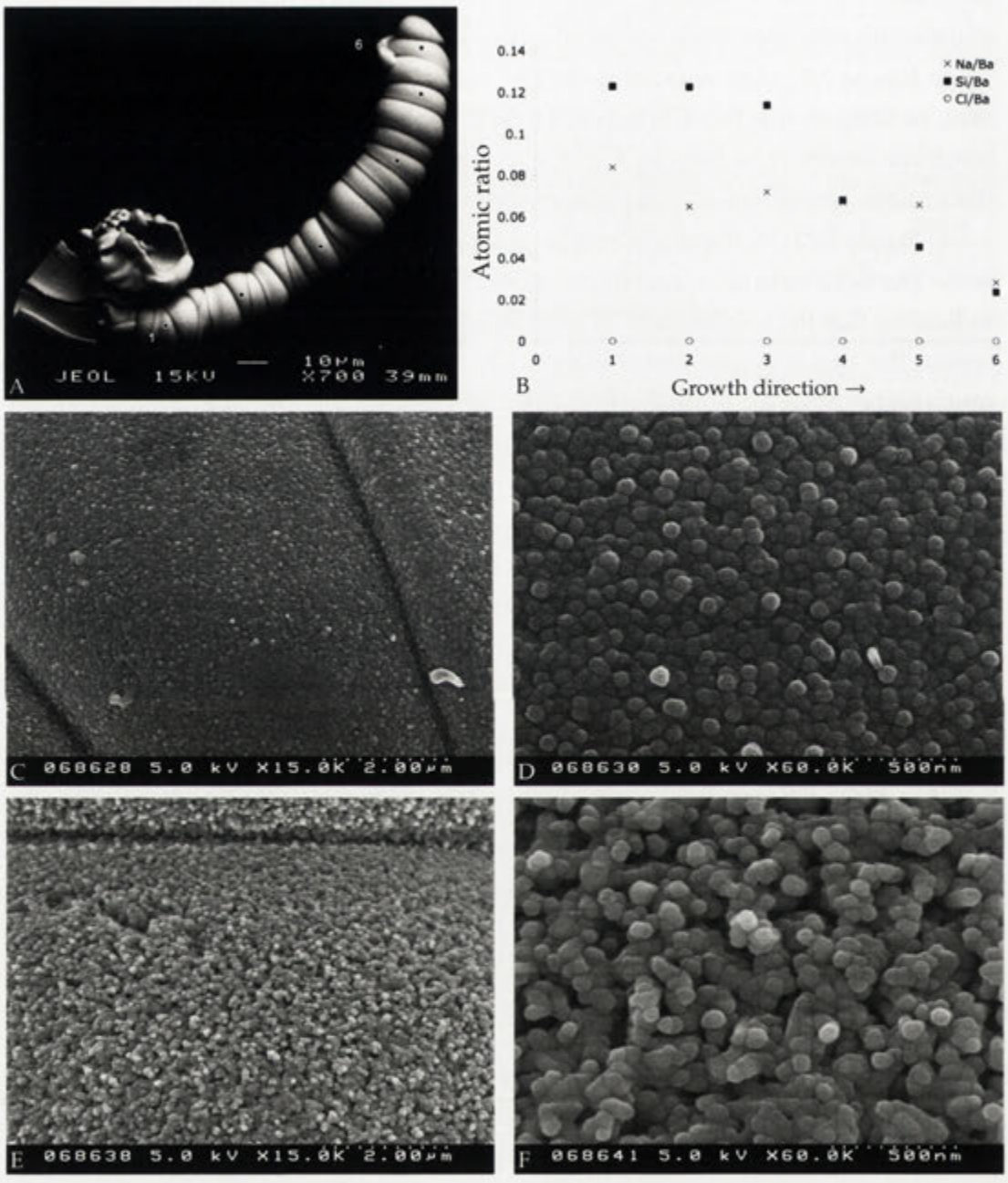

Figure 3.17: Back-scattered SEM image (A) and FESEM images (C-F) of a worm, synthesised at pH 11.35 (notation J in Figure 3.13), and a graph displaying the atomic ratios of Si, Na, and Cl compared to Ba (B). Images C and D are from spot 2, and E and F are from spot 6. See Table 3.3 J_1 for further elemental composition of the worm (point 3 in graph B).

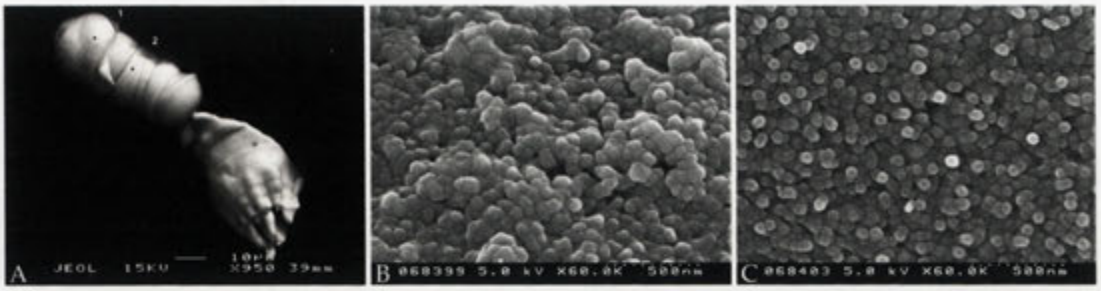

Figure 3.18: Back-scattered SEM image (A) and FESEM images (B, C) of a worm, synthesised at pH 11.51 (notation L in Figure 3.13). Image B is acquired from spot 1, and C from spot 2 respectively. See Table 3.3 L_2 for further elemental composition of the worm.

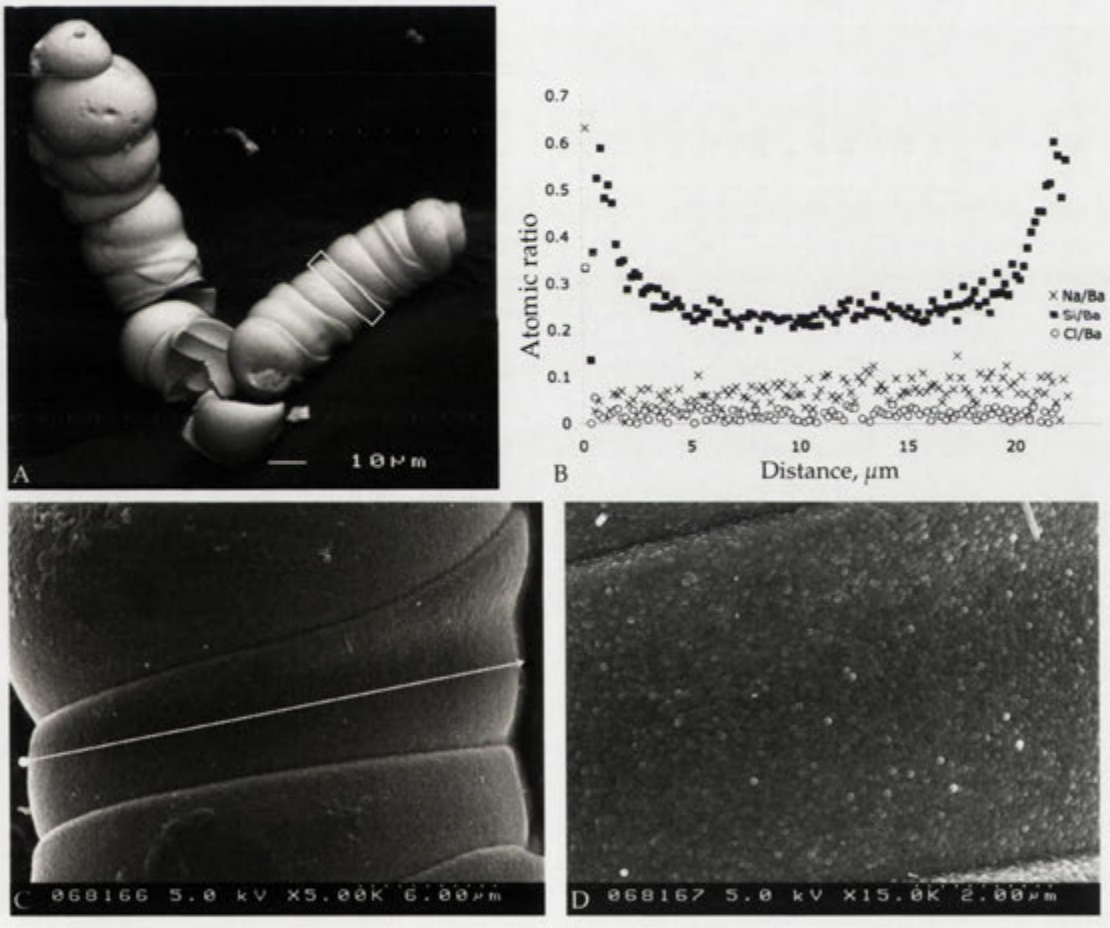

Figure 3.19: FESEM images of a worm, synthesised at pH 10.99 (notation F in Figure 3.13), and a graph displaying the atomic ratios of Si, Na, and Cl compared to Ba (B) acquired from a line scan shown as the white arrow in C, also indicated by the white box in A.

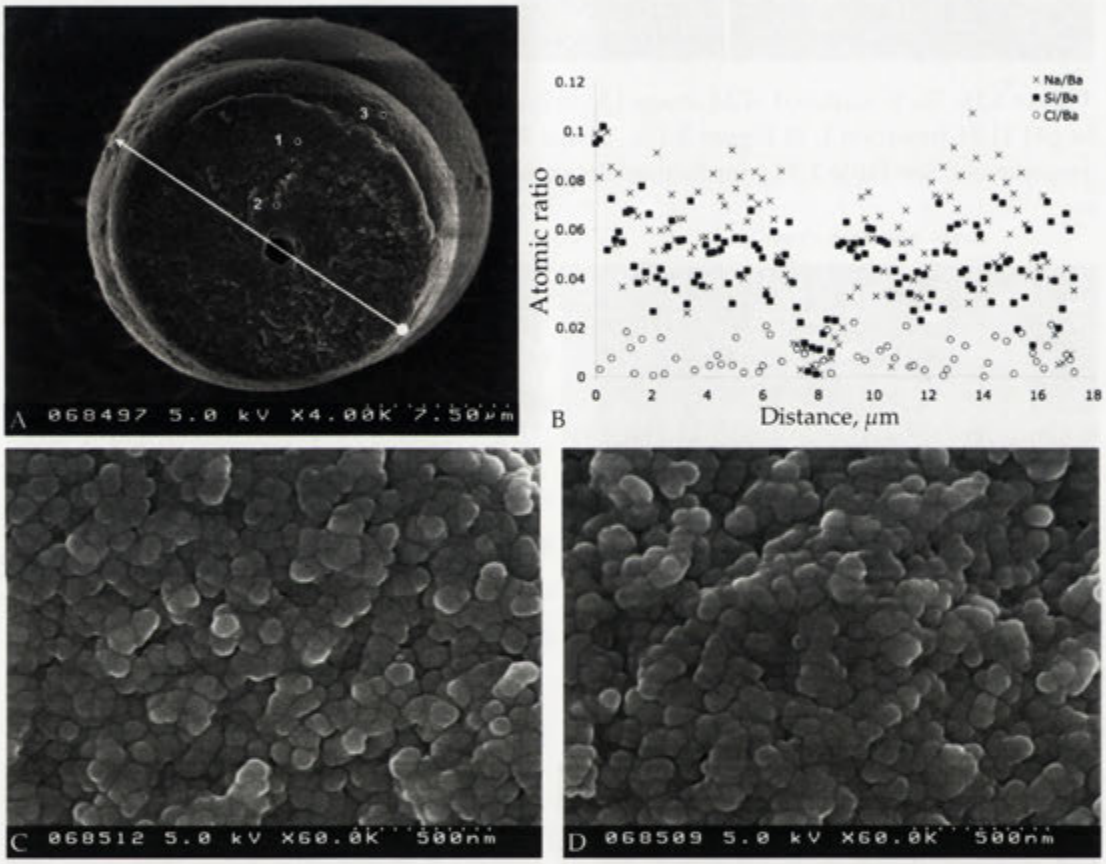

Figure 3.20: FESEM images of a cross-section of a worm, synthesised at pH 11.26 (notation I in Figure 3.13), and a graph displaying the atomic ratios of Si, Na, and Cl compared to Ba (B) acquired from a line scan shown as the white arrow in A. Spot no 2 (C) and 3 (D) are similar in texture as the surface of the worm (not pictured). See Table 3.3 I_1 for further elemental composition of the worm (point 2 in A).

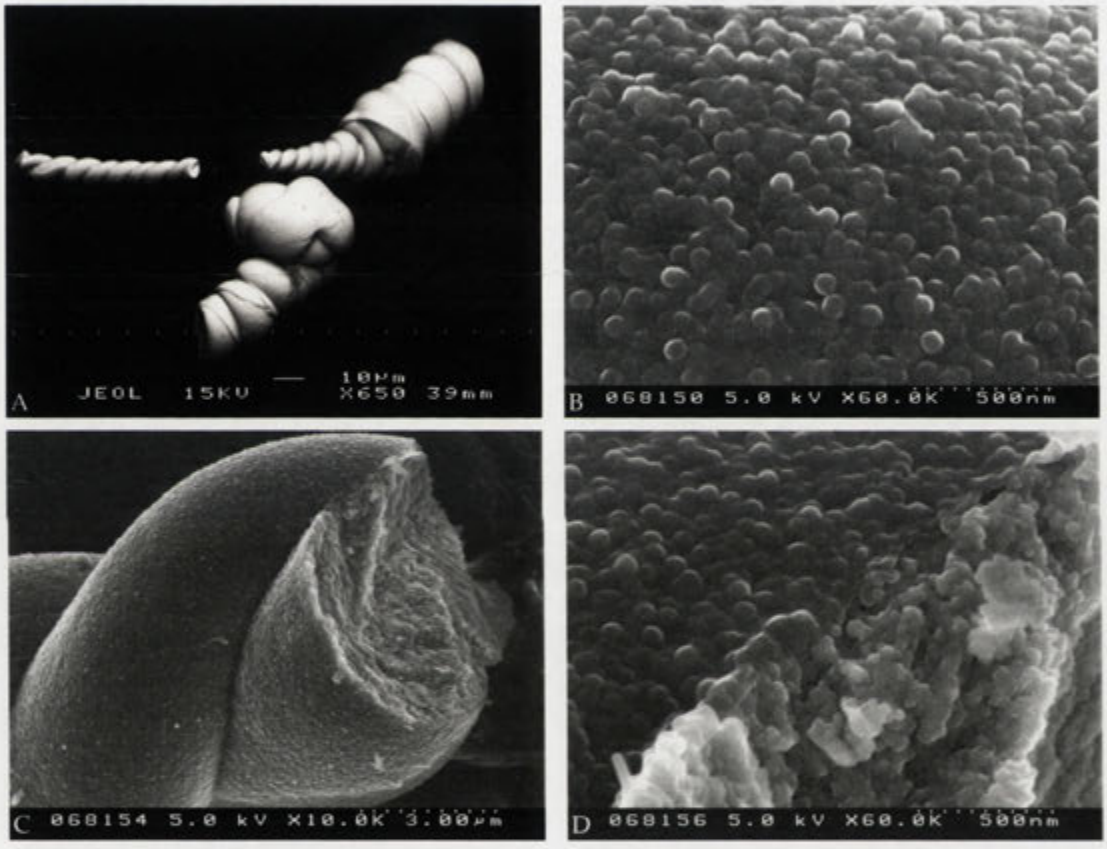

Figure 3.21: Backscattered SEM image (A) and FESEM images of a helix, synthesised at pH 10.99 (notation F in Figure 3.13). In D a thin skin can be observed without acid treatment. The Si/Ba atomic ratio of this sample is ~ 0.3, see Table 3.3 F_1 for elemental composition of the helix.

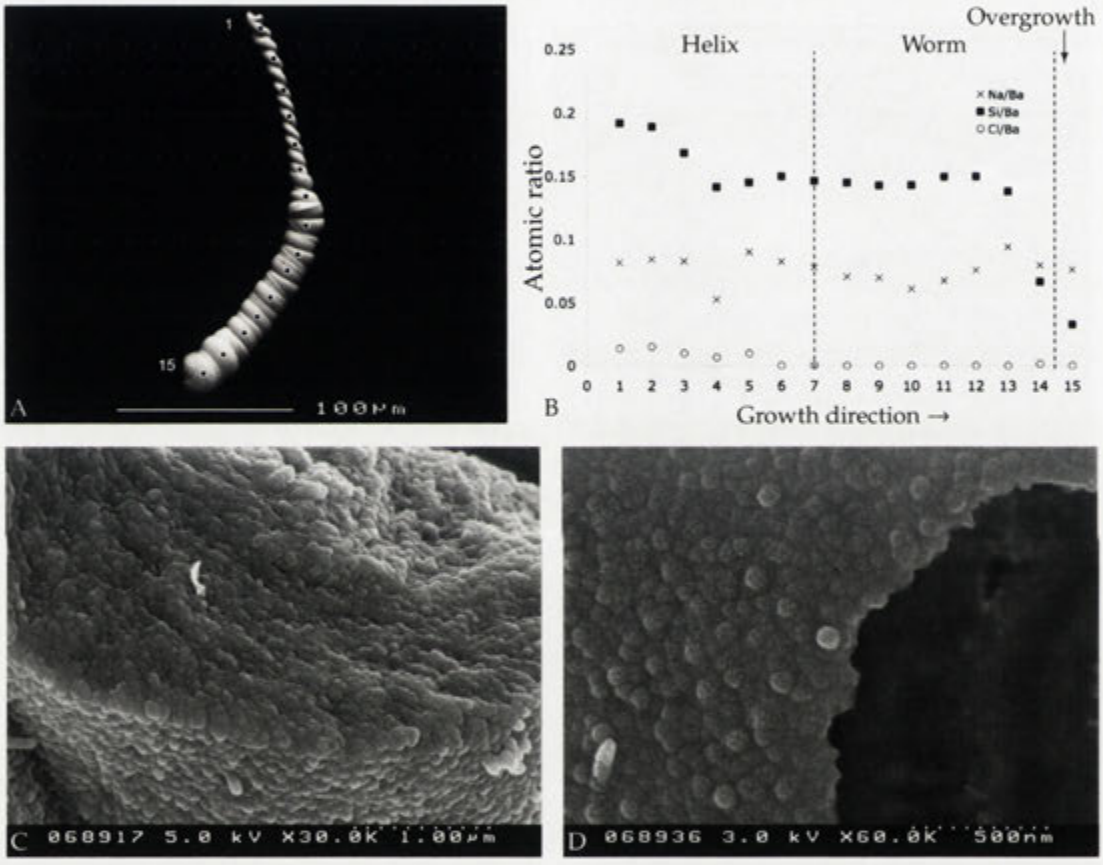

Figure 3.22: Atomic ratios (B) of Na, Si and Cl relative to Ba along the growth direction of a helix that turns into a worm (A), synthesised at pH 11.21 (notation H in Figure 3.13). In C the beginning of the helix can be seen, and in D a thin skin can be observed after acid treatment.

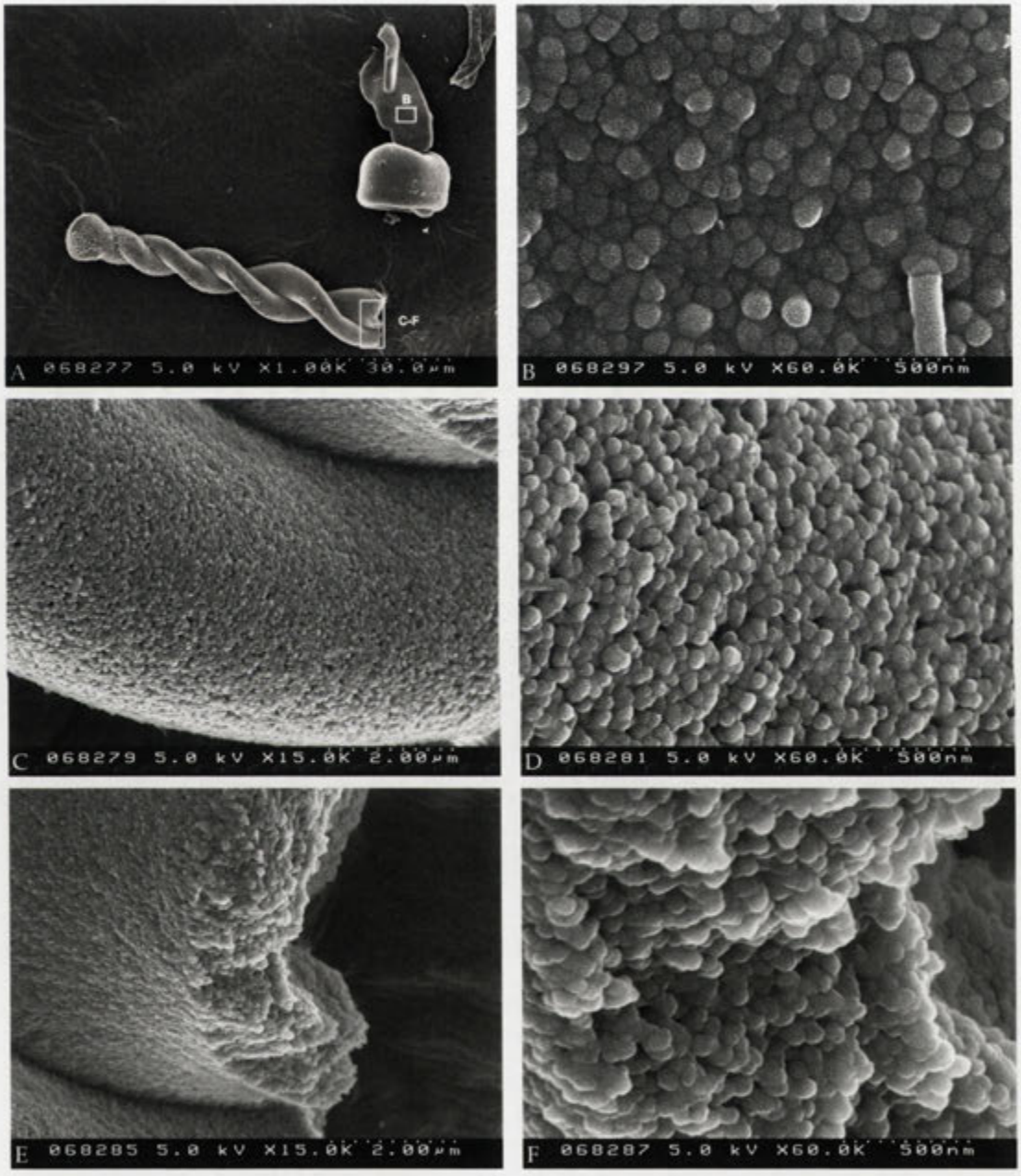

Figure 3.23: FESEM images of a helix, synthesised at pH 11.51 (notation L in Figure 3.13). The Si/Ba atomic ratio of this sample is ~ 0.03, see Table 3.3 L_2 for elemental composition of the helix.

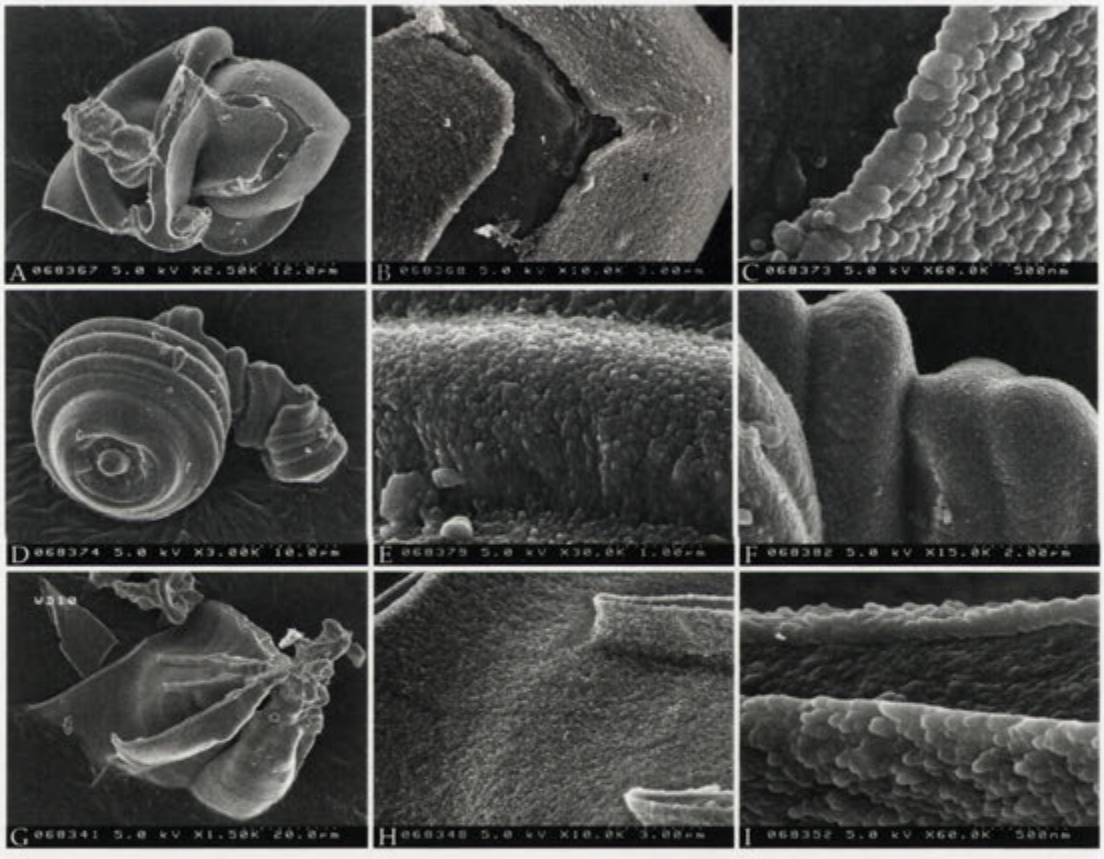

Figure 3.24: FESEM images of a aggregates synthesised at pH 11.51 (notation L in Figure 3.13). Images B and C are magnifications of A; E and F are magnifications of D, and H and I are magnifications of G. See also Figure 3.18 and 3.23 for additional morphologies.

attached to the sheet. The sheet has also a visible skin, which accounts for the high silica concentration. Furthermore, the aggregate seen in Figure 3.23 A (indicated by B) has a Si/Ba ratio of 0.50 and a surface texture (Figure 3.23 B) very different from the helix seen in the same image. These additional morphologies seen at high pH can therefore be characterised as containing high concentrations of silica compared to some of the worms and helices observed under the same conditions.

Discussion

In this section aggregates grown by varying the initial reaction pH have been discussed both in terms of morphology and composition. It is clear that the globular aggregates, produced at low pH, contain very little silica relative to barium carbonate. At higher pH more silica is incorporated into the structure, but not in any systematic way. Using higher initial pH also gives rise to more varied morphologies and increases the number of nucleation points in the system.

The increased number of aggregates at higher pH further points towards a higher supersaturation state at the start of precipitation. As more actively growing aggregates are produced in solutions at high pH, one can expect that such morphologies are smaller than the ones observed at lower pH, which is indeed the case. The solution chemistry throughout growth must therefore depend on the pH and number of nuclei.

Si/Ba ratios of both worms and double helices span a wide range of values, from 0.03 up to 0.50 (see Figure 3.25). This wide range indicates at first instance that Si/Ba ratios are not critical for the morphological evolution, assuming silica is not redissolved after growth. However, such ratios only make sense if all the crystallites are of the same size, a fact that is also doubtful considering the particles observed are almost globular in some aggregates compared to rod-like in others (compare Figure 3.20 and Figure 3.23 to Figure 3.9 and Figure 3.10 respectively). Realising that the presence of a contaminating silica on the surface of aggregates with low Si/Ba ratio results in a more than four-fold increase of such values, it is assumed that if a silica skin is indeed present it should show elevated Si concentrations. Furthermore, the interior of worms contain very little silica (Si/Ba ratio of 0.05-0.06), suggesting that aggregates which do have a silica skin will have an increased Si/Ba ratio. This is observed in some cases, but the Si/Ba values vary tremendously between aggregates even produced from the same batch. Such varying compositions should reflect the presence or absence of a silica skin. As all twisted and sheet-like aggregates previously synthesised using the standard conditions have a silica skin, it has been suggested that the silica skin is important for the growth of such biomorphs (see Chapter 1). The very low Si/Ba ratio

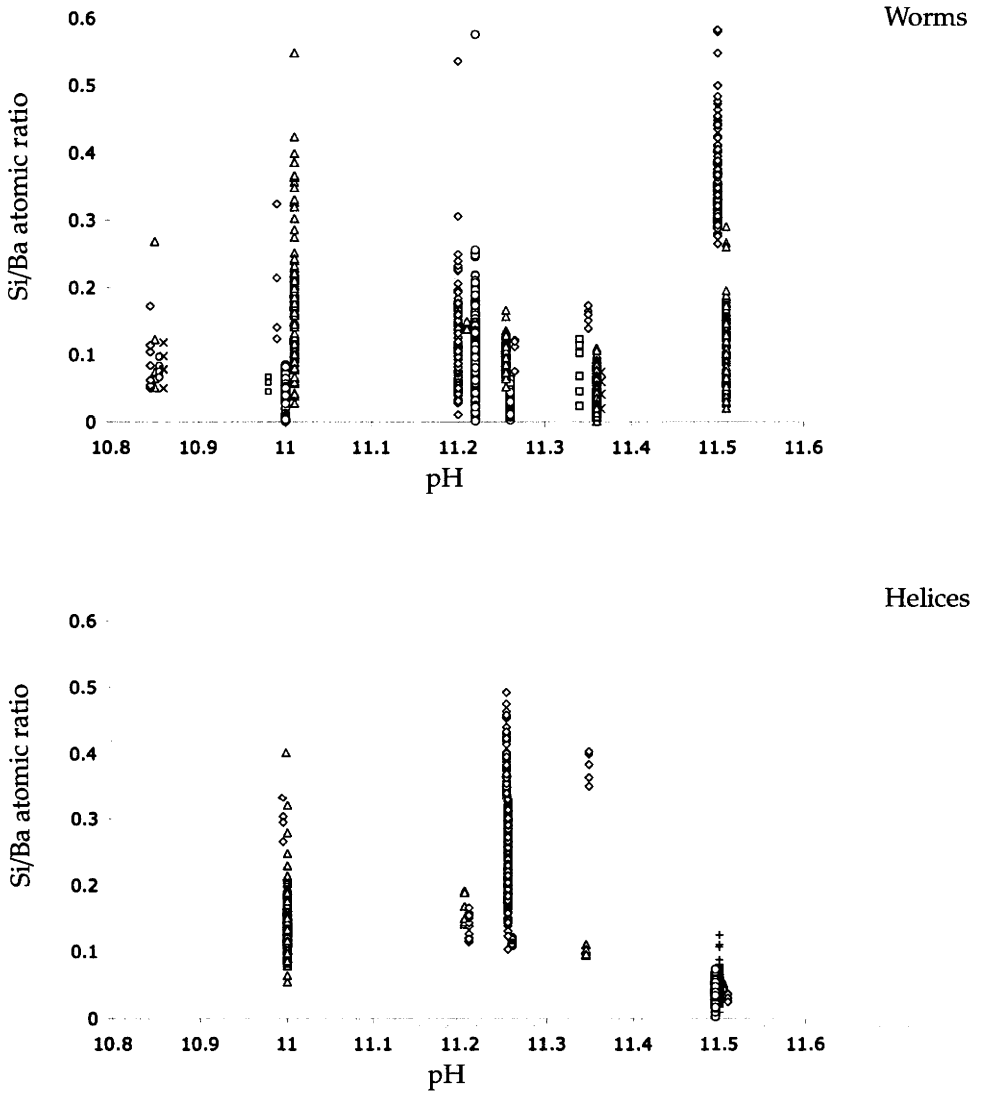

Figure 3.25: Graphical representation of the Si/Ba atomic ratios observed in worms and helices with pH.

observed in some aggregates discussed here show that such a skin may not always present. From the above discussion it is then clear that the nature and origin of the silica skin and the total silica concentration is ambiguous. Two main reasons for this ambiguity can be identified; 1) cleaning procedure 2) local environments during growth, both of which will be discussed.

The biomorph harvesting procedure from the reacting solution can be argued to have caused the varied Si/Ba ratios observed. As the aggregates are washed with

distilled water some dissolution of the aggregates can occur in respect to both the silica and the barium carbonate present. This could also account for the porous nature of some aggregates. Cleaning of the aggregates was done with minimum amount of water and as quickly as possible. However, it is possible that the aggregates observed in this section reflects a silica depleted composition. Dissolution and possibly coarsening of the crystallites could account for the observations reported here. One can conversely argue that subsequent drying of aggregates could leave a thin film of precipitated silica on the surface of the aggregates if the solution was contaminated by soluble silica. I believe that both these arguments are in error for the following reasons;

1) The cleaning procedure is conducted with minimal amount of water, and has shown to give aggregates with silica skin present (see Figure 3.9 and Figure 3.10), and if dissolution would take place one would expect all aggregates to show similar compositions;

2) if the aggregates were contaminated by silica from the original solution, it is unlikely that this silica would form a homogenous skin surrounding the entire, or parts of, aggregate. In this case, one would presume that such contamination would form sporadic patches of increased silica concentration, or colloidal aggregates (as seen in Figure 3.16). One would further expect conventional barium carbonate crystals to form sporadically on the surface of the aggregates, which is not the case. The NaCl present in the EDX results is more likely due to surface adsorption of these elements during growth, and not as a result of drying effects of contaminated solutions. The final stage of the cleaning procedure is conducted in ethanol, which should reduce the occurrence of the above effects. One final aspect of the cleaning procedure should be noted. It is possible that the aggregates with low Si/Ba ratio once had a silica skin that fell off during the cleaning procedure. If this is the case, one would then expect to find these skins in the Petri dish in which the samples are stored. As this has never been the case, it is assumed that such a scenario is unlikely.

Given these observations, it is suggested that the results from the analysis are caused by the as-produced aggregates, which are not affected by the cleaning procedure to any greater extent. The varying compositions must therefore be the true reflection of variations caused during growth. As was discussed in Section 3.4.1, both double helices and worms can be seen growing at the same time in the standard experiment. This suggests that whatever the underlying cause of the two different morphologies, they are a local phenomenon, and therefore governed by local physiochemical conditions. This is further supported by the fact that the budding often seen in the helix-worm transition occurs at slightly different times in different aggregates during the same synthesis batch.

All of the aggregates analysed in this section were allowed to grow for 10 hours.

Note that in these experimental systems pH was only varied one pH unit. It is expected that at even lower pH less aggregates will form, which will adopt globular morphologies, whereas at even higher pH more nucleation points are expected and therefore smaller and a more varied mixture of morphologies should be observed.

The varying Si/Ba ratio observed in both double helices and worms could be caused by the varying adsorption of soluble silica or silica colloids on the already formed aggregate. The constant or decreasing Si/Ba ratio would speak for such a scenario. Especially in the latter case, preferential adsorption would have to occur at the base of the aggregate, and continue in the growth direction. This argument is only possible if the composition of the interior of the aggregate remains constant throughout the aggregate; a fact that has not been shown. As reaction time is increased, the concentration of soluble silica able to interact with the witherite crystallites is reduced, which could account for the decreasing Si/Ba ratio seen in some biomorphs. The ambiguities regarding the presence of a silica skin further suggests that this skin is a secondary phenomenon, not related to the growth mechanism of twisted aggregates.

3.4.3 Variation in sodium silicate concentration

By changing the initial Ba/Si ratio, one would expect the production of additional distinct morphologies. Decreasing the sodium silicate concentration should decrease the effective ability of silica to modify the morphology. Increasing the sodium silicate concentration, on the other hand, can have two effects on biomorph growth. First, the interference of silica should increase as a result of higher concentrations. Second, higher concentration should also lead to more precipitated amorphous barium silicate during the initial stages of the synthesis. Such precipitation would effectively reduce both barium and silica activities in the system. The Ba/Si ratio in the initial reaction mixture is therefore believed to be important for the morphogenesis of biomorphs. In this section results from experiments conducted with varying sodium silicate concentrations are presented.

Varying the sodium silicate concentration, while keeping all other parameters constant, evidently has an effect on the morphology produced. In Figure 3.26 a series of optical images can be seen where the silicate concentration varies from around 4 to 10 mM while keeping pH around 11 and [$BaCl_2$] at 5 mM. In this figure it is evident that higher silica concentrations give rise to fewer and larger particles compared to lower concentrations. It should be noted that the pH varies especially between Figure 3.26 A and F compared to the others which are closer to pH 11. Low sodium silicate concentration also results in a more rapid change in pH with time, as seen in the table in Figure 3.26. At sodium silicate concentrations higher than that of the standard (8.5 mM,

seen in Figure 3.26 B) results in biomorphs with increasingly globular morphologies as the concentration is increased. At 9.9 mM, large aggregates are formed that contain clusters of globular and short helical and worm-like morphologies. Using even higher sodium silicate concentrations (14.9 mM) results in increasingly worm-like growth over that of double helices, and mainly globular morphologies are produced. At a sodium silicate concentration of 0.03M (29.7 mM) very little growth can be seen within 10 hours. Increasing concentrations of sodium silicate also results in increasing degrees of flocculation upon mixing with the $BaCl_2$ solution, which also results in a drop in pH.

Using lower concentrations of sodium silicate as compared to the standard experiment results in increasingly varied morphologies. The size of the aggregates are reduced, and a slight increase in the relative number of helices compared to worms is seen at 5.9 mM SiO_2. Using even lower concentrations results in a complete disappearance of the helical and worm-like morphologies, and growth of small aggregates with varied morphology is seen. Further lowering the sodium silicate concentration (0.9 mM SiO_2) dumbbells of various sizes, depending on pH , can be seen.

FESEM images of some of the aggregates observed can be seen in Figure 3.27, which shows that at low sodium silicate concentrations produces aggregates having sheet- and pinnacle-like morphologies. They grow in small clusters and can extend up to around 50 μm in length. Sheet-like aggregates often show great variance in curvature especially as their size increases (compare Figure 3.27 A and C). Pinnacles are, on the other hand, very straight but with fluctuating diameter. In some cases these morphologies are also seen to merge at their tips (see Figure 3.27 A and B). The fluctuations in diameter and the evident banding seen in some of these morphologies could be due to Liesegang patterns as described in Section 2.5. Increasing sodium silicate concentration successively gives rise to increasing presence of helical, worm-like, and globular morphologies, as is present in the standard experiment.

The result of varying both sodium silicate concentration and pH at 5 mM $BaCl_2$ can be seen in Figure 3.28. In this Figure it is evident that high pH and low silica concentrations give rise to the most nucleation points with the effect of very small sized aggregates. Conversely, low pH and high sodium silicate concentration result in fewer aggregates with predominantly globular morphology. Helical and worm-like morphologies are restricted to both pH and silica concentration. These morphologies are most prominent close to standard conditions of 8.5 mM SiO_2 and pH around 11. Helical aggregates can still be observed at 5.9 mM SiO_2, but much less so, and often occur with a wide range of other types of morphologies as preciously discussed. These conditions can be seen as a lower boundary for the formation of helical aggregates. Increasing pH and sodium silicate concentration increases the presence of these typed

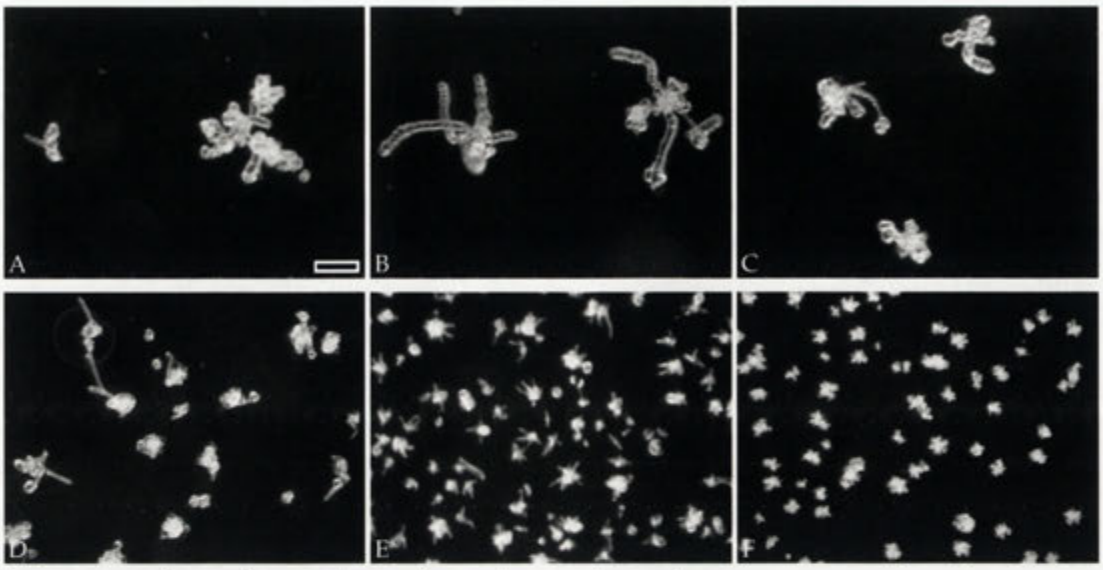

Sample	A	B	C	D	E	F
$[SiO_2]$ (mM)	9.9	8.5	7.4	5.9	5.0	4.2
pH_0	10.88	10.99	10.94	10.99	11.07	11.14
Δ_{pH}	-0.93	-0.92	-0.92	-1.15	-1.22	-1.32

Figure 3.26: Optical images of biomorphs produced after 10 hours (A 11 hours, and F 6 hours are the exceptions) at different sodium silicate concentrations, displayed in the table, around pH 11. Scale bar 100 μm in A is valid for all the images.

of aggregates.

FESEM images of biomorphs produced at low sodium silicate concentration and high pH are seen in Figure 3.29. These images show the presence of pinnacle-like biomorphs, as are also present at lower pH. Cones and sheets are also present but to a much lesser degree compared to pinnacles. Pinnacles generally have a varying diameter in the 3-6 μm range, and the base of the pinnacle can sometimes be seen as a sheet that tapers off into a pinnacle. The growing edge is often very flat (see Figure 3.29 D, F-I), although this varies between the aggregates (compare with Figure 3.29 A and E). These morphologies clearly show evidence of banding, which can be seen to correlate between aggregates (see Figure 3.29 G-I). Furthermore, this banding seems to become more prominent during the later stages of growth. The growth of these types of morphologies is seen to begin with the formation of a dumbbell (see Figure 3.30). In Figure 3.30 A and C, the morphological continuum from a dumbbell to a pinnacle containing aggregates is seen. The dumbbells present in this sample have different morphologies, from very compact structures as seen in E, to more branched and open structures as seen in B and C. Some of these dumbbells are not directly related to any pinnacle growth and may be the result of much later precipitation. The more branched

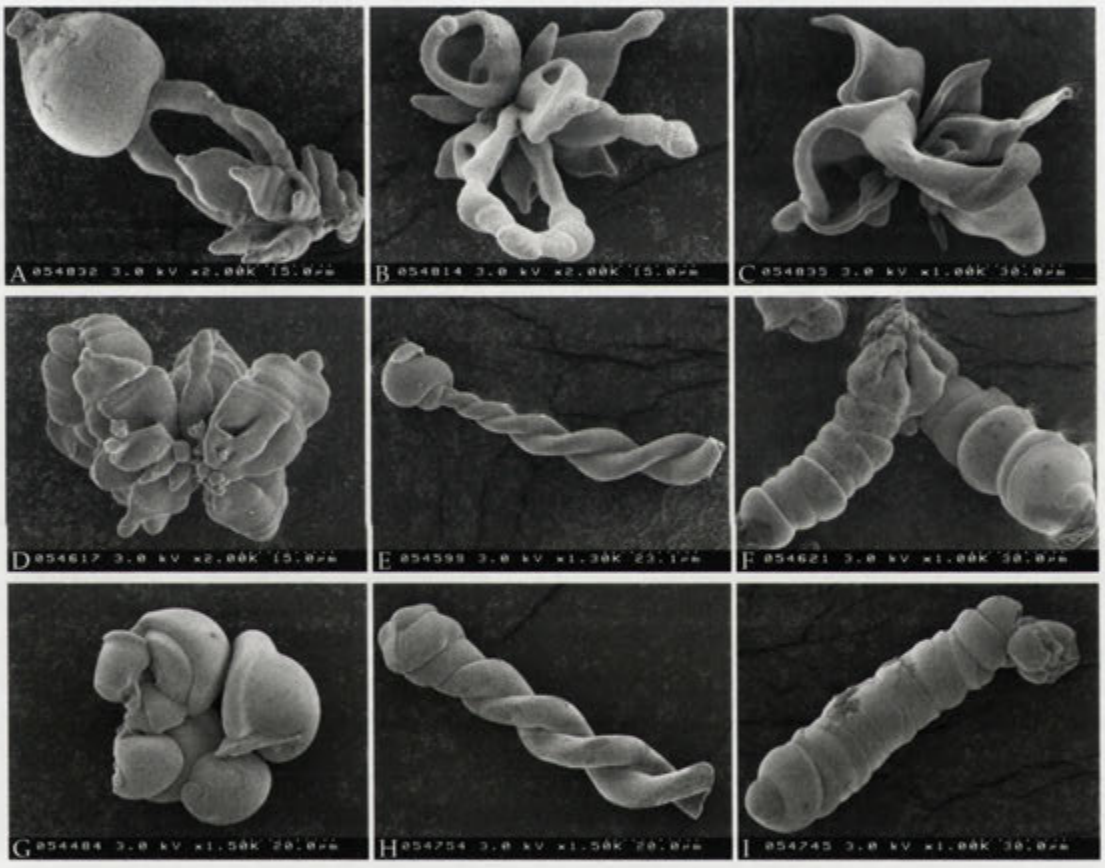

Figure 3.27: FESEM images of a aggregates synthesised at pH ~ 11 with different sodium silicate concentrations; A-C 5mM, D-F 5.9 mM, and G-I 7.4 mM.

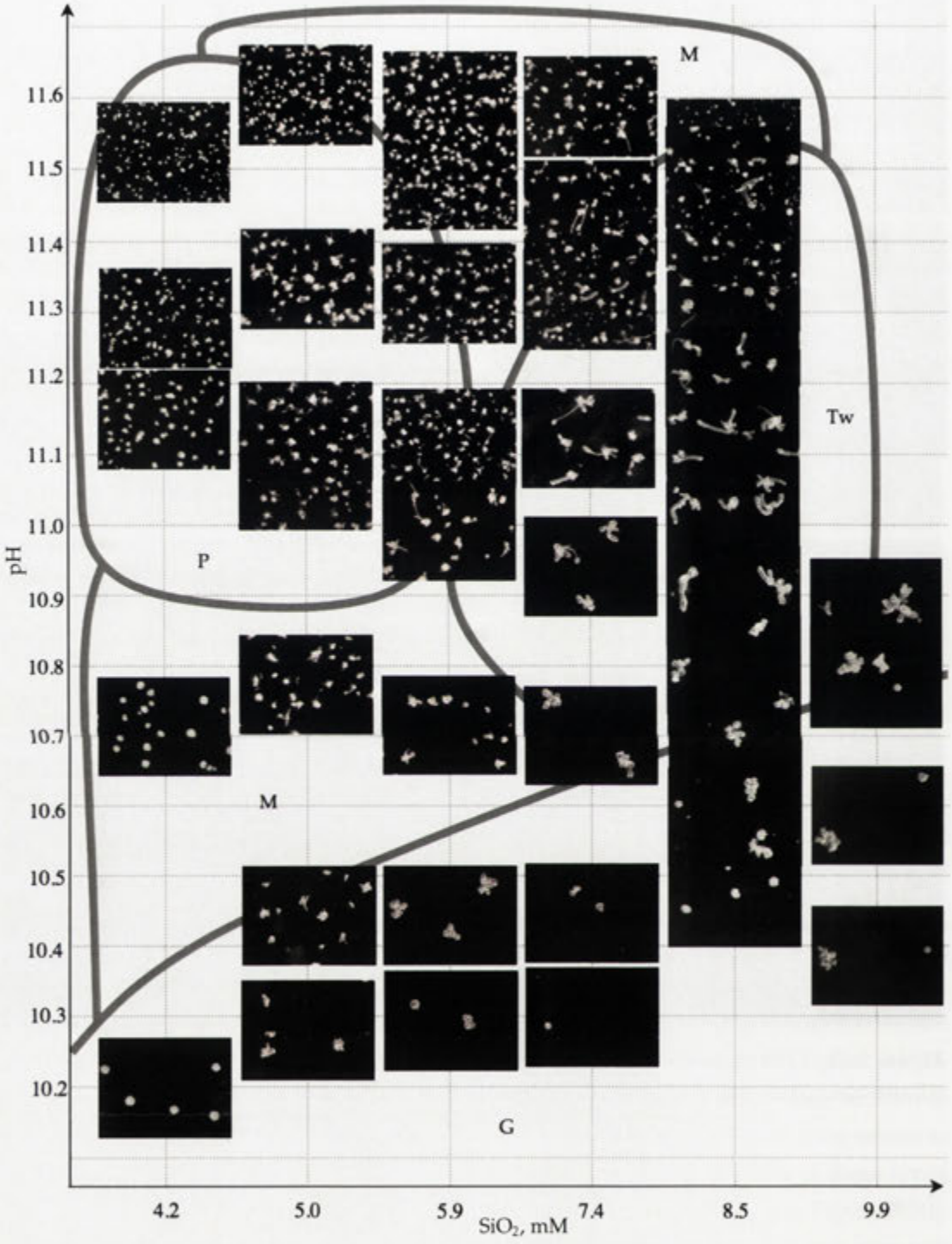

Figure 3.28: Optical images of aggregates synthesised at various pH and sodium silicate concentrations at otherwise the same conditions (5 mM $BaCl_2$, room temperature). Note that the SiO_2 axis is not linearly scaled. The marked areas represent rough indications of different morphologies; mixed (M), pinnacles (P), twisted aggregates (Tw), and globular (G).

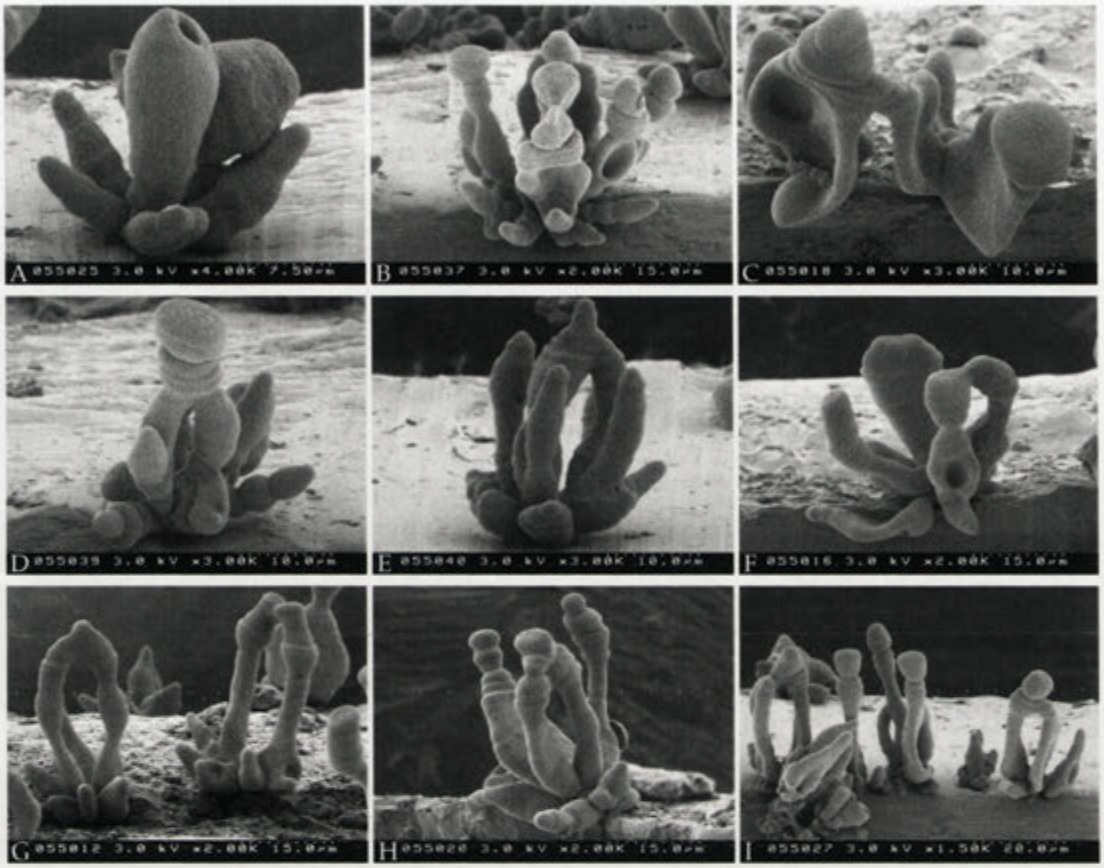

Figure 3.29: FESEM images of a aggregates synthesised at pH ~ 11.3 with a sodium silicate concentration of 5.0 mM at room temperature. A mixture of morphologies are observed, from cone-like (A) and sheets (C), to is pinnacle-like structures (D–I). These morphologies often show evidence of banding as is seen in G and I.

variety, seen in Figure 3.30 A and C clearly is, and is seen to be composed of bundles of crystallites (see Figure 3.30 D). These bundles of crystallites are around 0.45 μm long and 0.30 μm wide and stack together so as to form the central bar of the dumbbell. The bundles decrease in size and become less prominent as branching of the dumbbell proceeds. At the point where pinnacle-type growth begins, the bundles can not be recognised anymore, and a continuous arrangement of elongated crystallites or fibers can be seen. As in the case of most morphologies that will be discussed in this chapter, these crystallites are elongated in the growth direction (see Figure 3.30 G-I), and have a diameter around 40-60 nm and a length of ~ 300 nm. Smaller particles (20x60 nm) are also seen cemented to the larger crystallites, and account for the globular texture of the larger crystallites.

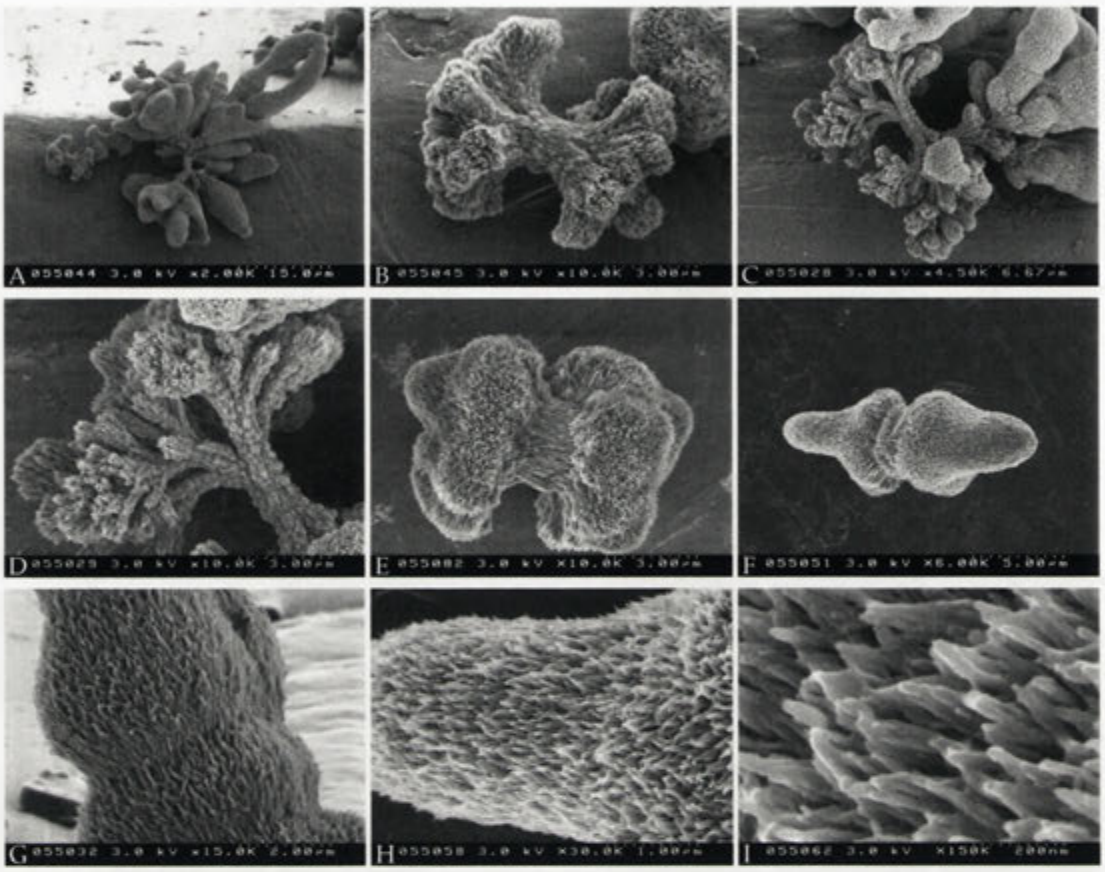

Figure 3.30: FESEM images of different types of dumbbells (A–F) and surface features of pinnacles (G–I) observed at high pH and low concentration of sodium silicate (see Figure 3.29). The dumbbells are believed to be the earliest stages of growth, as they can be seen at the base of the pinnacles (A and C). The surface of the pinnacles are composed of hair-like particles that are elongated in the growth direction.

Discussion

This section has presented the morphological change observed with varying the initial sodium silicate concentration. The increasing nucleation points and reduction in biomorph size is evident when the effective silica concentration is reduced. The pH change observed under such conditions during growth is more rapidly reduced as compared with higher sodium silicate concentrations. The relative activity of barium ions should increase as the Ba/Si ratio is increased at lower silicate concentrations. The amount of barium silicate precipitation is also reduced, although measurements relating to such precipitates have not been conducted under these conditions. One can still speculate regarding the possible causes of the morphological changes seen with changing the initial sodium silicate concentration. The increasing number of aggregates seen growing at any one time is increasing at reduced sodium silicate

concentration. This is related to the supersaturation state of the solution, and therefore to the barium and carbonate activities. Increased supersaturation will give rise to more nucleation points, and it is therefore suggested that the effective barium ion concentration is increased as compared to higher sodium silicate concentrations at the same initial pH. Similarly, at high pH, while keeping the sodium slilicate concentration constant, also results in an increased number of biomorphs.

3.4.4 Variation in $BaCl_2$ concentration

In this section experimental results stemming from varying the initial concentration of $BaCl_2$ are presented. Such variation is also shown to have a strong effect on the morphogenesis of biomorphs. In the first instance, a morphological overview of the observed effects is given. The remainder of this section will mostly be concerned with structures that are precipitated when increasing the $BaCl_2$ by a factor of 100 compared to the standard experiment.

From light microscopy analysis, the morphological change seen with a slight change in barium concentration is shown in Figure 3.31. At pH ~11, increasing the $BaCl_2$ concentration from 2.5 to 7.5 mM results in increasingly branched morphologies. These branched morphologies, obtained at 7.5 mM $BaCl_2$, contain clusters of both helical aggregates and worms that are generally shorter than the ones synthesised at 5.0 mM (standard conditions). At pH of 10.4, globular morphologies are produced that do not express any helical growth. As is the case for 5 mM $BaCl_2$ experiments, increasing pH at both 2.5 and 7.5 mM $BaCl_2$ results in an increase in the number of actively growing particles and a reduction in size. Higher pH is also coupled with a larger decrease in pH within the 10 hours of growth. This effect is also greater at higher $BaCl_2$ concentrations.

At low sodium silicate concentrations the morphologies observed are quite different (Figure 3.32). In this Figure, it is evident that the number of nucleation point increase with an increase in barium chloride concentration as well as pH. In all cases globular morphologies are produced at low pH. At 50 mM $BaCl_2$, cones and sheets are produced at pH ~11.2.

Further increasing the $BaCl_2$ concentration results in more branched and sheet-like morphologies. At a $BaCl_2$ concentration 100 times greater than the standard conditions drastic changes of morphology occurred. At 0.5 M $BaCl_2$, large spherulitic aggregates formed. When mixing equal volumes of a 1.0 M $BaCl_2$ solution with a 17 mM silicate solution at pH of 11.6, the pH is substantially reduced and the solution becomes opaque within minutes. This white flocculate is believed to be composed of amorphous barium silicate 'cements', and the growth of biomorphs under these

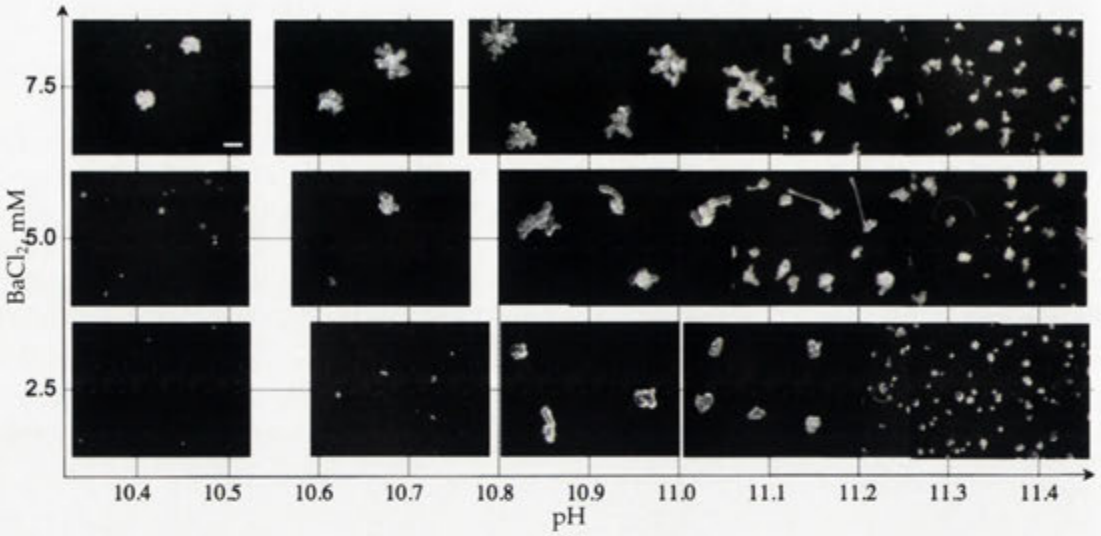

$[BaCl_2]$, mM	Sample	A	B	C	D	E	F
7.5	pH_0	10.41	10.65	10.89	11.09	11.21	11.35
	ΔpH_{10h}	-0.68	-0.85	-1.01	-1.22	-1.25	-1.4
5.0	pH_0	10.43	10.68	10.91	11.13	11.19	11.35
	ΔpH_{10h}	-0.54	-0.79	-0.94	-1.14	-1.18	-1.33
2.5	pH_0	10.43	10.69	10.93	11.12	11.18	11.34
	ΔpH_{10h}	-0.45	-0.69	-0.88	-1.04	-1.15	-1.22

Figure 3.31: Optical images of aggregates seen after 10 hours of growth at different $BaCl_2$ and pH at 8.5 mM SiO_2. Scale bar is 100 μm and valid for all images. The table indicates initial pH and the pH change observed after 10 hours of growth for each sample.

conditions occured within this precipitate. These aggregates, which are termed *floral spherulites* (Hyde et al., 2004), can be described as interconnecting sheets, radiating from a central core within the aggregate.

From light microscopy analyses, the first growth of these types of structures can be seen within a couple of hours (see Figure 3.33). These early precipitates display spherical raspberry-like morphology that grow radially outwards to form floral spherulites with time. Nucleation of such aggregates can occur throughout the experiment, and often several different stages of growth can be observed at any one time. As can be seen in Figure 3.33, prolonged growth gives rise to large (>100 μ in diameter) aggregates after ca. 10 hours. Further growth results in coarsening of the edges. These aggregates grow suspended in the amorphous precipitate (different focus in Figure 3.33), and the growth is also affected by the presence of other aggregates. As indicated by the red arrows in Figure 3.33 D, the growth of two adjacent aggregates is hindered at their point of closest contact, whereas the rest of the aggregate continues to grow.

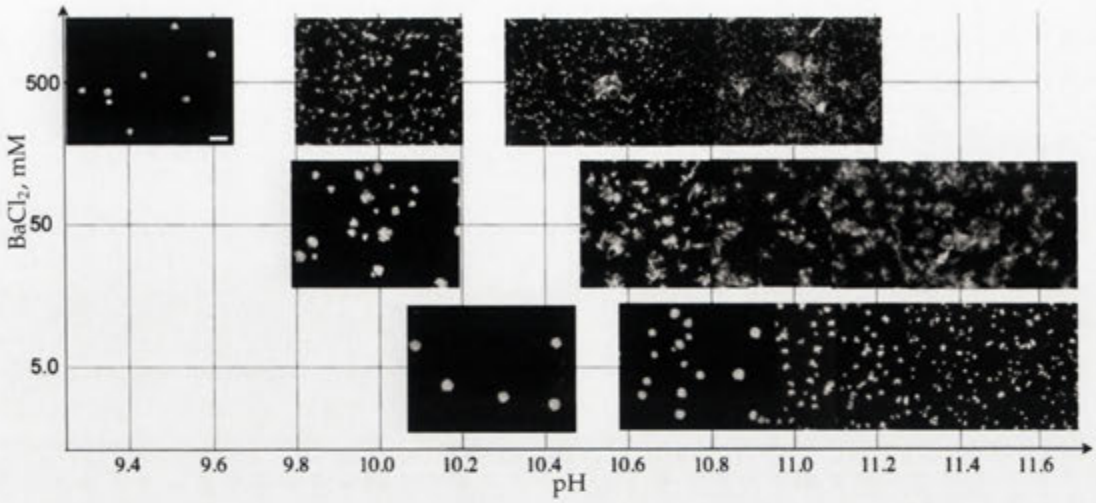

$[BaCl_2]$, mM	Sample	A	B	C	D	E
500	pH_0	9.40	10.00	10.50	10.72	10.98
	$\Delta pH_{9.5h}$	-0.69	-1.06	-1.46	-1.62	-1.77
50	pH_0	9.99	10.56	10.99	11.19	11.42
	ΔpH_{8h}	-0.81	-1.22	-1.53	-1.64	-1.63
5.0	pH_0	10.20	10.71	11.14	11.29	11.53
	ΔpH_{7h}	-0.65	-1.03	-1.32	-1.40	-1.31

Figure 3.32: Optical images of aggregates seen after 7–9.5 hours of growth at different $BaCl_2$ and pH at 4.2 mM SiO_2. Scale bar is 100 μm and valid for all images. The table indicates initial pH and the pH change observed for each sample.

As is the case of all biomorph growth described in this dissertation, the pH was lowered during progressive growth. In Figure 3.34 the decrease in pH is coupled to the growth of these aggregates. Since the ionic strength of the reacting solutions is above 0.1 M, pH measurements are necessarily approximate and complicated by the precipitation of the amorphous flocculate. The pH data here should therefore be taken only as an indication of the trend. The growth curves displayed in Figure 3.34 shows a constant growth rate of about 25-30 μm per hour during the early stages of growth. After ca. 10 hours the growth rate has significantly slowed, a result which can be coupled to the onset of overgrowth by large barium carbonate crystals.

As can be seen in Figure 3.35 A-D, the early globular raspberry-like precipitates develop with time pits on their surfaces. As these pits grow, sheets eventually emerge, and continue to grow outward from the edges of the pits. The resulting aggregate has a coral-like morphology consisting of interconnected sheets. These sheets are typically fused to give 120° intersections (see Figure 3.35 F). The sheet thickness therefore varies somewhat with time, however, aggregates grown for 4-5 hours generally have sheets

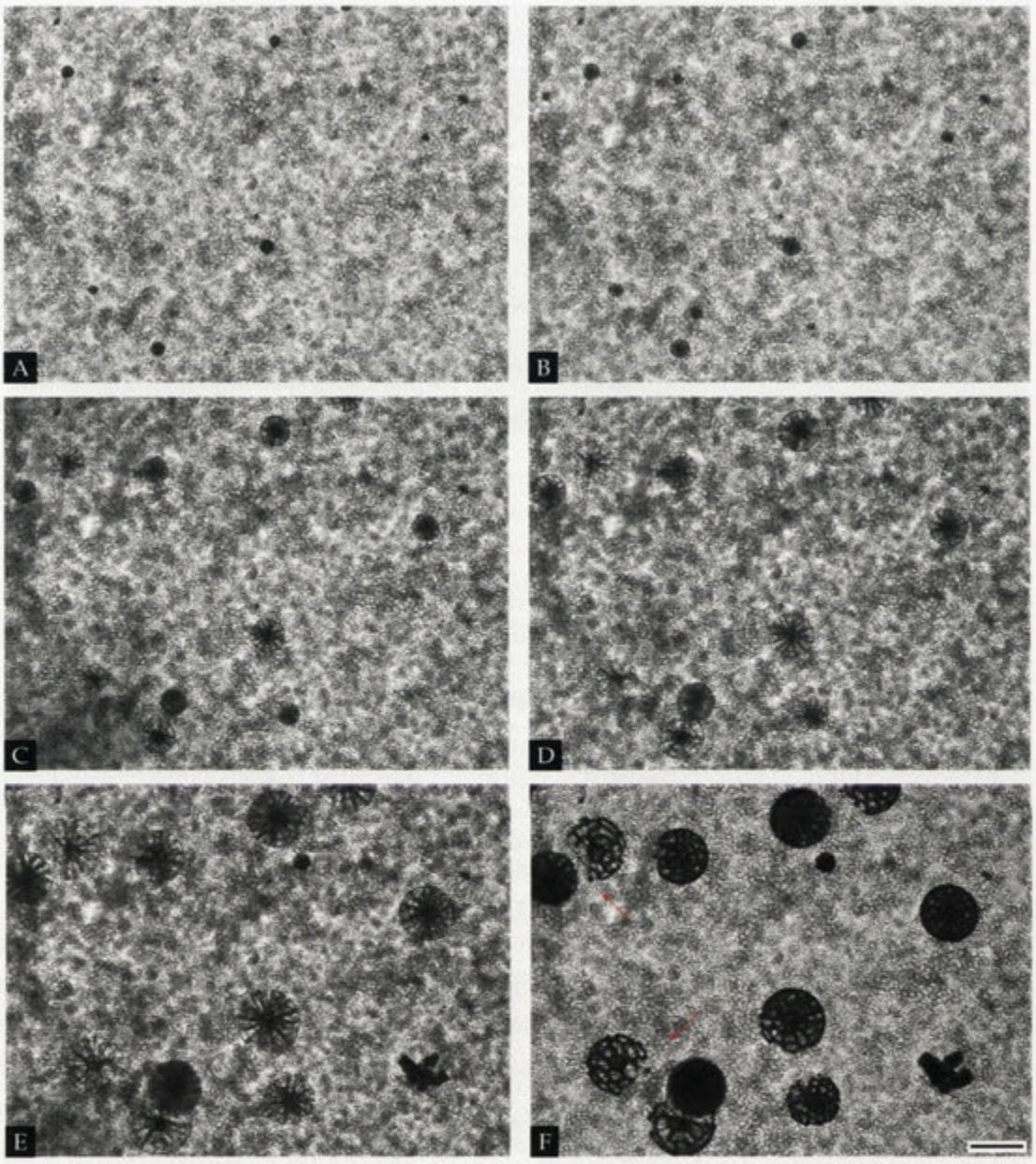

Figure 3.33: Time series of floral spherulites grown under the following initial conditions: 0.5 M $BaCl_2$, 7.4 mM SiO_2, pH 10.40, room temperature, A 3.75 hour, B 4 hours, C 5 hours, D 6 hours, E 10 hours, and F 18 hours. Scale bar in F is 100 μm.

1-2 μm thick. Furthermore, the microstructure of floral spherulites also varies with time.

In Figure 3.36 FESEM images of cross sections and surfaces of sheets can be seen. Particles, which are globular and slightly elongated in the growth direction are shown in cross section in Figure 3.36 E; they have diameters around 50 nm. In many cases the

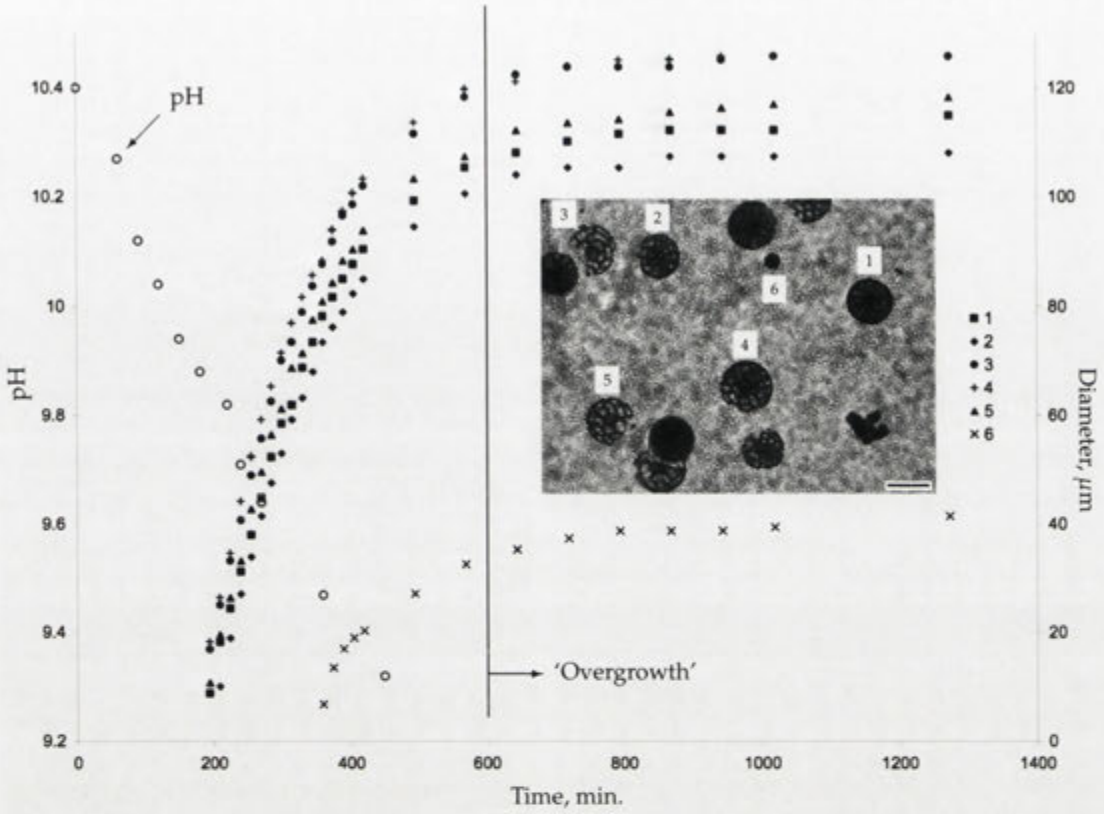

Figure 3.34: Time series of floral spherulites growth by measurement of the aggregate diameter (1-6, inset), coupled with the pH measurements with time (min), under the following initial conditions: 0.5 M $BaCl_2$, 7.4 mM SiO_2, pH 10.40, room temperature. Scale bar in inset image is 100 μm.

texture of the outside surface is very similar to the cross sections and no discernible silica skin is observed. However, the surface texture changes with time, and the particles become more and more elongated (see Figure 3.36 F). At prolonged growth times, the aggregates begin to overgrow with large barium carbonate crystals (see Figure 3.37). Expansion of the sheet edges is often seen in aggregates (see Figure 3.36 A) of the onset of overgrowth. This overgrowth preferentially occurs at the sheet intersections (Figure 3.37 A), and can show beautiful rose-like aggregations of intergrown crystals (Figure 3.37 C). Continuous growth results in complete coverage of the aggregate by these crystals (Figure 3.37 B), which form a network across the surface of the aggregate (Figure 3.37 D and E). The surface of such overgrown floral spherulites has a fibrous texture elongated in the growth direction.

X-ray computed tomography of these aggregates reveals the complexity of these types of structures on the micron scale. In Figure 3.38 A and B two cross-sections of the tomogram (3D data set that represents the volume) are shown. In these images it is evident that the central core and the connection points between the sheets have

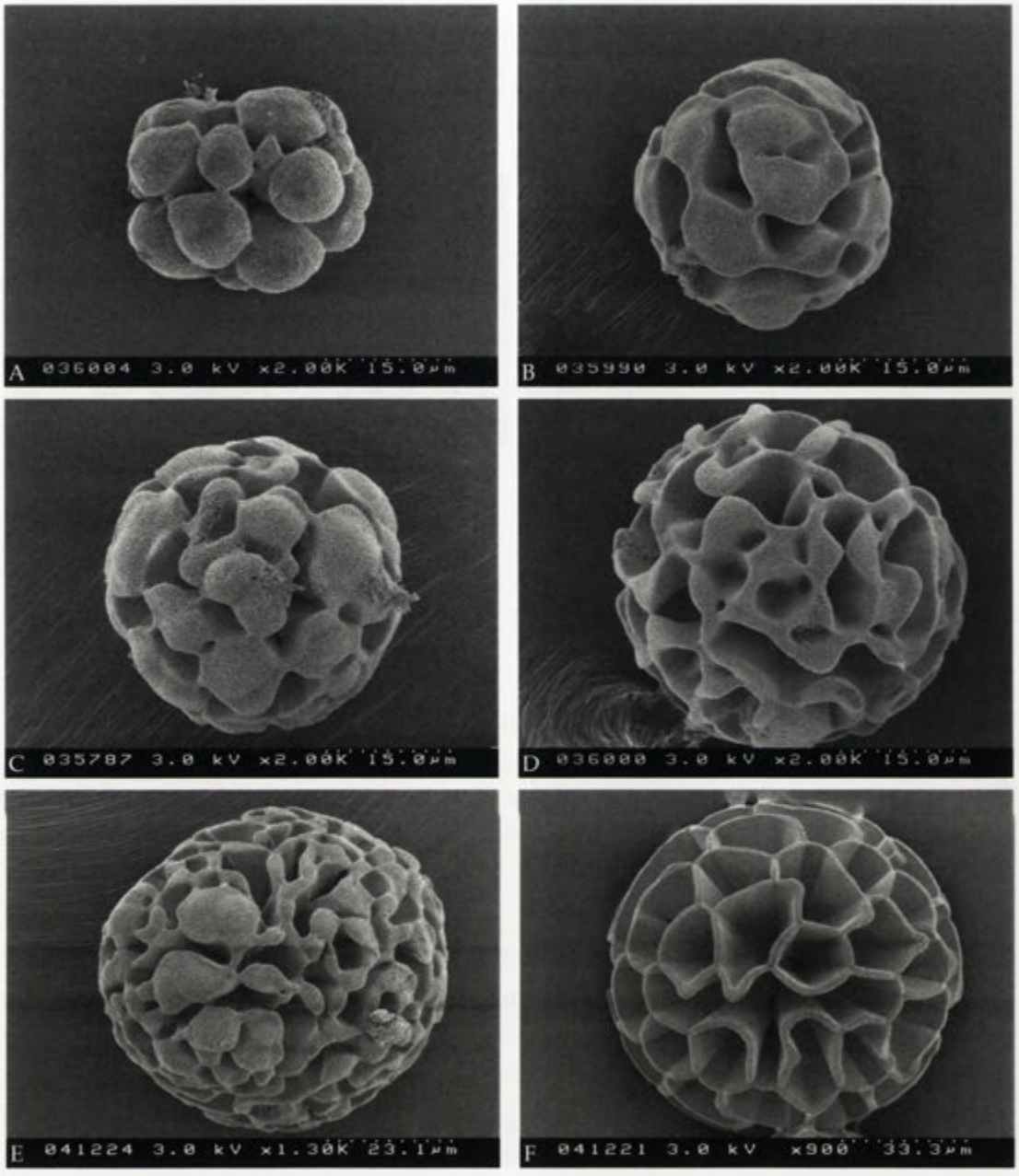

Figure 3.35: FESEM images of successive growth series of floral spherulites.

higher X-ray contrast than the sheets themselves (red coloured regions means lower contrast compared to blue coloured regions). This implies higher density, possibly due to higher Ba:Si ratio within the aggregate compared to the surface. However, other causes can result in the X-ray contrast differences seen in Figure 3.38 A and B. Beam hardening is stronger on thicker and denser materials. Beam hardening is a result of low energy X-rays being preferentially absorbed compared to high energy

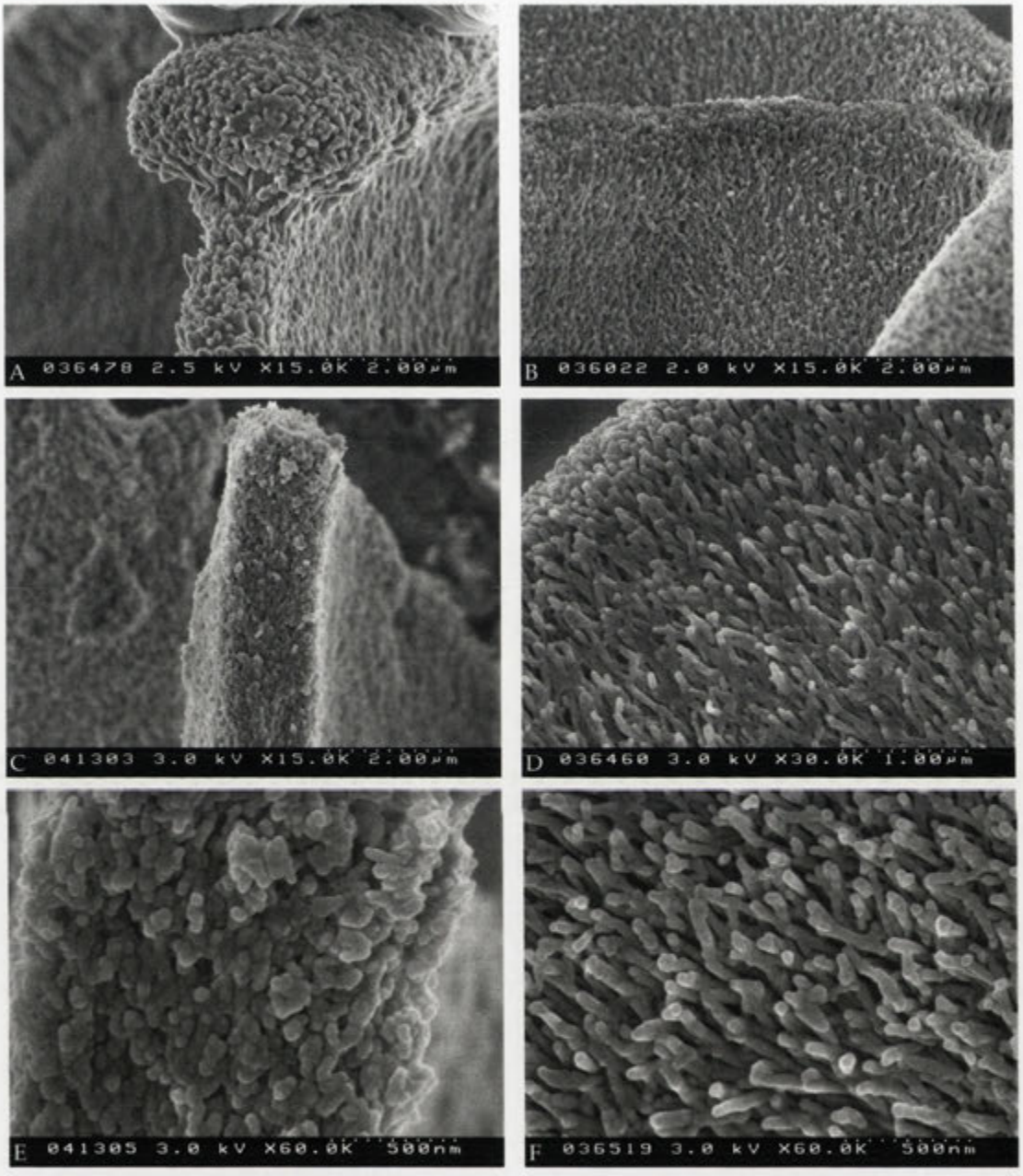

Figure 3.36: FESEM images of the walls and associated texture of floral spherulites.

X-rays. However, as the floral spherulites are very small (~ 100 μm in diameter) and have open structures, beam hardening is not expected to be the cause of the density variations seen. A more probable cause is the resolution of the machine, which is limited to 2 μm. The tomogram was collected at ~0.7 μm resolution, which results in a 6 voxel blur. This blurring could cause the contrast variations observed, suggesting that compositional differences are difficult to obtain with this machine on aggregates

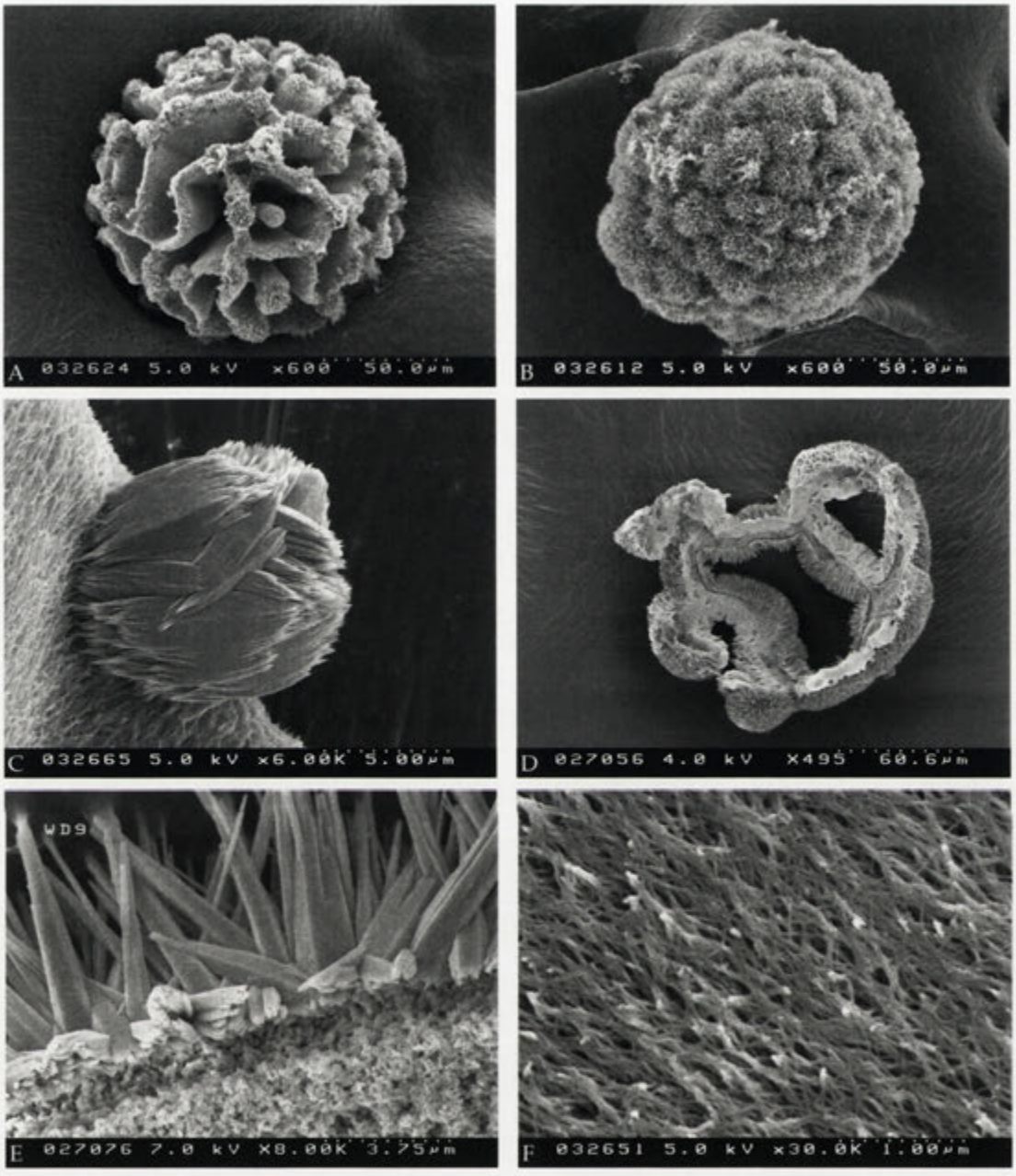

Figure 3.37: FESEM images of overgrown floral spherulites, where carbonate crystals have been growing on the edges of the aggregates (A). If allowed to grow further the entire aggregate is covered in this crystal beard (B and C).

with such fine detail.

As stated earlier, the surface character changes with time, which affect the result of acid treatment of floral spherulites. Early precipitates dissolve completely in 0.1 M HCl, whereas aged samples retain the overall morphology upon such treatment. This indicates an increase in silica deposition within the aggregate with time.

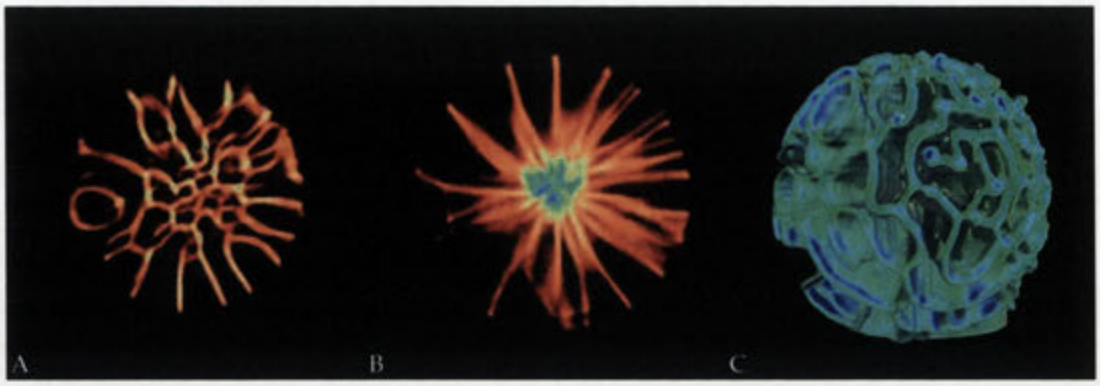

Figure 3.38: X-ray CT images (A and B) and the 3D rendered surface (C) of a floral spherulite.

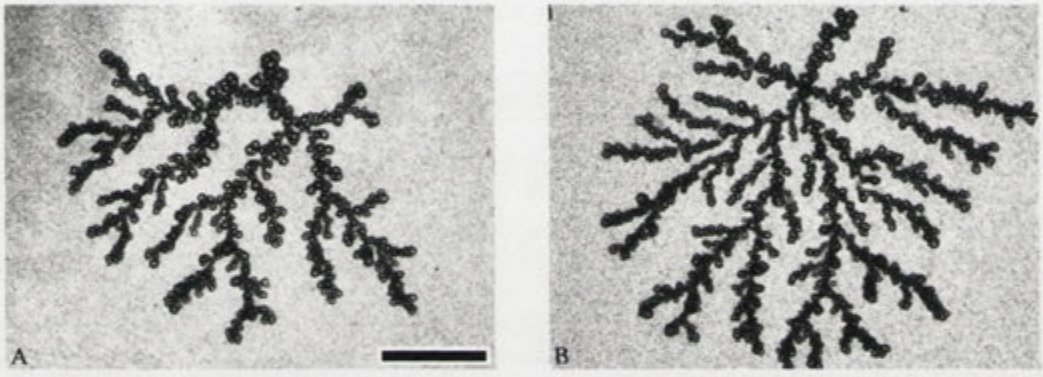

Figure 3.39: Optical images of dendritic structures produced after 18 hours from filtered solutions. Scale bar 200 μm in A is valid for both images.

The colloidal precipitate that forms upon mixing the sodium silicate and barium chloride solutions are important for the development of these morphologies. A series of experiments were conducted in which this precipitate was more or less removed from the synthesis mixture. The morphologies observed in these experiments are very different from those of floral spherulites. Instead, 2D dendritic structures are formed at the bottom of the wells (see Figure 3.39). These structures look very similar to DLA-type structures discussed in Section 2.5. A further observation is that the growth of floral spherulites is not restricted to sodium silicate concentrations in the 8.5 mM region, as worm-like and helical morphologies generally are. These types of structures can be seen in systems with widely ranging silicate concentrations from 4.2 mM to at least 30 mM, however, at very low concentrations very few floral spherulites are produced compared to higher concentrations. The development of floral spherulites is therefore much more independent of sodium silicate concentrations than other morphologies investigated so far.

TEM observations

Thin sections of floral spherulites were prepared by Harri Kokkonen and John Fitzgerald as described in Section 3.2. John Fitzgerald also performed the TEM analysis described in this section.

In Figure 3.40 A-B, TEM images of parts of the thin section of floral spherulites are shown. From these images it is evident that these structures are made up of crystallites that are ~40 nm in diameter and ~200 nm long, also seen in the FESEM images. They are seen to align parallel to the mid-plane of the extending sheets, a feature also confirmed by optical microscopy under crossed polarisers (Figure 3.40 C). In contrast to what is visible in the FESEM, TEM images further revealed the porous nature of these crystallites. These crystallites show evidence of nano pores of variable sizes, as is evident from the paler areas seen in Figure 3.40 B. Selected area electron diffraction further confirms that the *c*-axis is parallel to the long axis of the crystallites, and that the crystallites are preferentially oriented in the growth direction of the sheet. In Figure 3.40 D and E, one such EDP is viewed with and without indexing. Similar to the case of the worms, EDPs of sheets of a floral spherulite show broken powder rings, indicative of some orientational ordering. Most noteworthy is the 002 reflection, which forms a dotted arc with an angular spread of around ±30°. This is in agreement with Figure 3.40 A, in which particles at the surface are seen to diverge from the mid plane of the sheet. Furthermore, the 020 reflection is present as a weak arc, which is significantly stronger than in the EDP of the worm in Figure 3.12. This is compatible to the suggestion given by Terada et al. (2003), described in Section 1.2, that the *b*-axis is preferentially aligned in the plane of the sheet. EDX analysis in the TEM shows no compositional differences between the inner core and the outer regions of the floral spherulite.

Discussion

Changing the initial barium chloride concentration has shown to have a strong effect on biomorph morphology. The number of nucleation points do not seem to vary with a change in $BaCl_2$ concentration; at least not within 2.5–7.5 mM concentration span at the same pH. Increasing pH has a stronger effect on the number of nucleation points than that of $BaCl_2$. Increasing the barium concentration results in increases initial precipitation of amorphous barium silicate. At 0.5 M $BaCl_2$, this precipitate forms the framework from which floral spherulites grow. Furthermore, the presence of such precipitate is important for the development of these structures. This suggests that the silicate present provides the necessary chemical feedback with respect to both barium and silica to the growing biomorph. As was mentioned in Section 1.2, Terada et al.

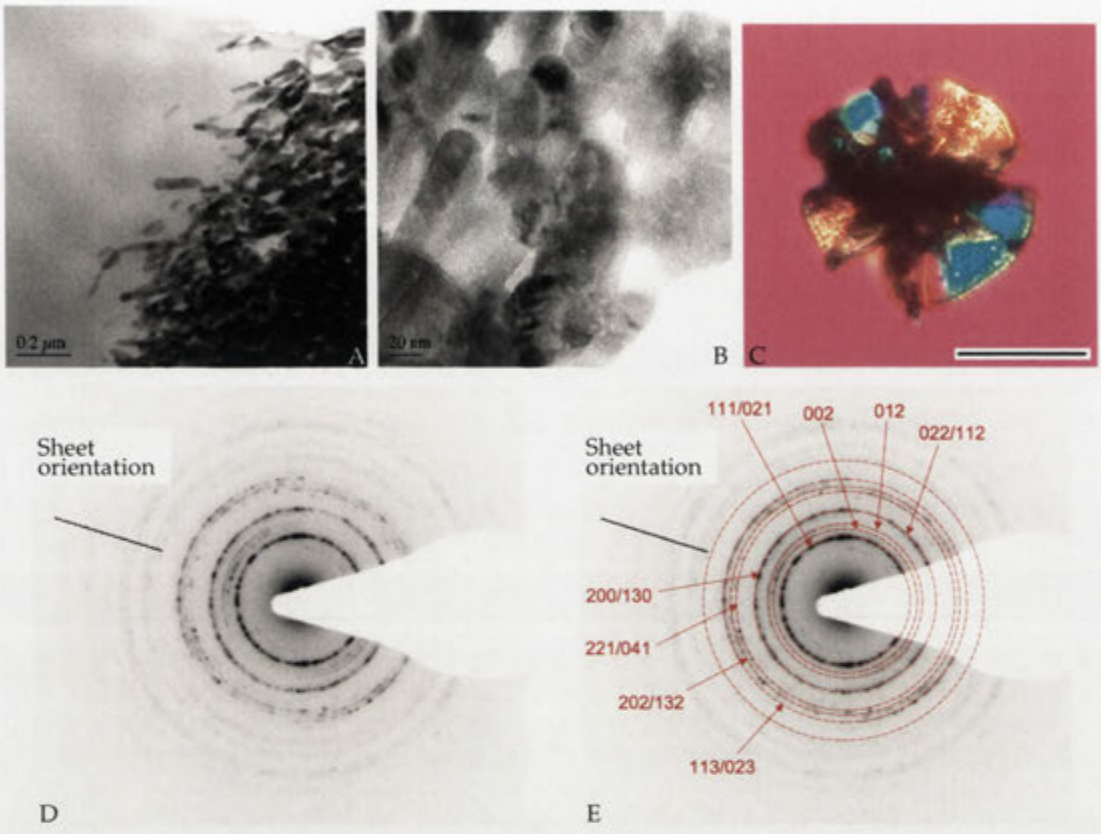

Figure 3.40: TEM images of details of floral spherulites (A-D), and an EDP with (E) and without (D) indexation. The black line in the EDPs indicate the mid plane direction of the sheet. An optical image viewed under crossed polars (scale bar 60 μm) is seen in C.

(2003) have reported the same kind of structures, made of $SrCO_3$, grown in silica gel. A similar growth behaviour was observed in their case, although, spirals also developed at the end of the sheets for aggregates grown in silica gels. This is not the case here, or for the $SrCO_3$ floral spherulites grown in solution at 0.5 M $Ba/SrCl_2$(see Section 3.4.8, possibly due to the limiting reservoir of reactants. However, further experimental analyses of biomorphs produced between 5 mM and 0.5 M salt concentrations are necessary to pinpoint under which conditions helical morphologies are observed.

3.4.5 Effects of temperature

Changing the reaction temperature of the experiments has a dramatic effect on morphology, which becomes more complex at increasing temperatures (see Figure 3.41). Temperatures ranging from 4 to 70 °C will be discussed here. For the synthesis it should be noted that no morphological difference could be seen when the barium and the silica solution were preheated before mixing.

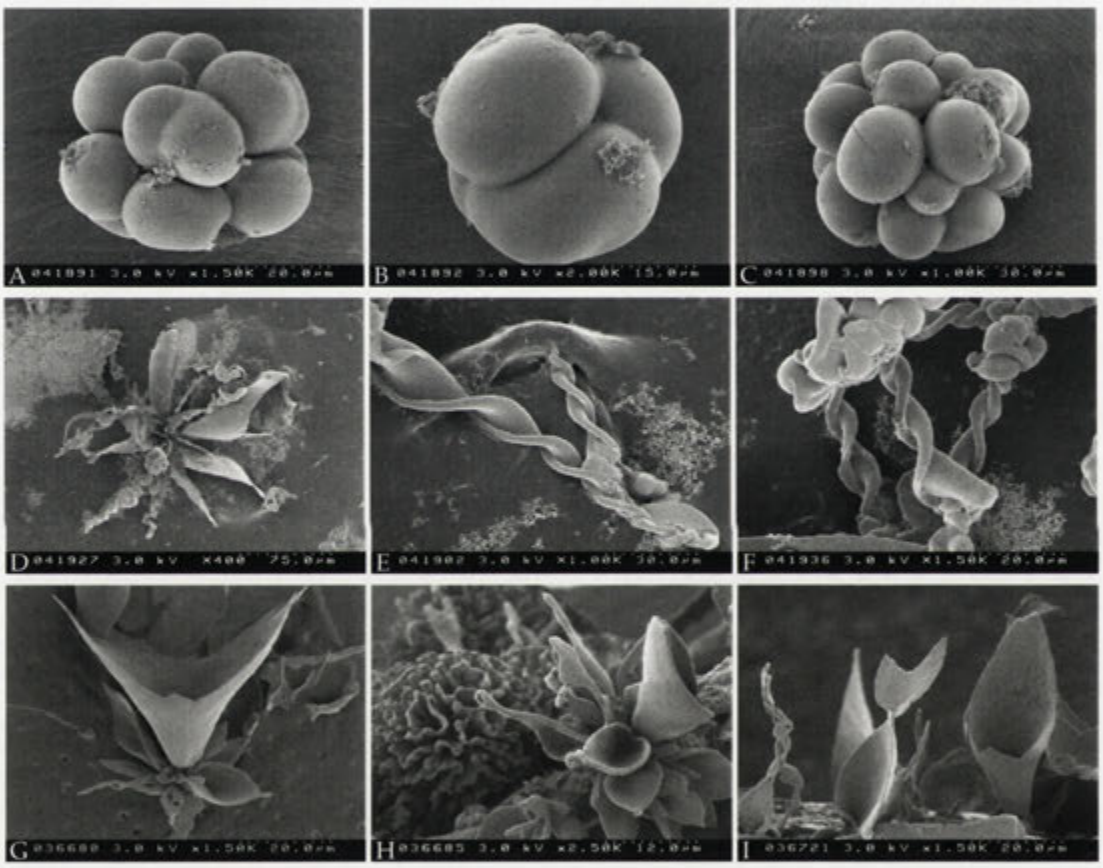

Figure 3.41: FESEM images of a aggregates synthesised at at different temperatures using standard conditions. A-C 4° C, D-F 45° C, G-I 70° C.

At low temperatures globular raspberry-looking aggregates typically develop over the course of hours to days depending on the temperature. For instance using standard concentrations and pH experiments performed over night during winter (a badly insulated laboratory at temperatures around 10° C) often resulted in globular aggregates with a small amount of worm-like aggregates. No helical morphologies were ever observed under such conditions. The morphological evolution under low temperatures was also confirmed by biomorph synthesis in the laboratory fridge, set at a temperature of 4° C. Globular morphologies are clearly preferred at low temperatures.

Room temperature experiments at 20-25° C produce a mixture of worms, helices and globular morphologies, and only very rarely are sheets observed as discussed in previous sections.

At 45° C cones and helical morphologies are observed (see Figure 3.41 D-E). No worms are seen at this temperature. The helical morphologies are generally more sheet-like in nature and not as tightly wound as their room temperature counterparts.

At even higher temperatures of 70-80 ° C, a complex mixture of morphologies develop. These biomorphs, which are very thin and fragile, are quite difficult to clean without damaging the structures. As such, these biomorphs were synthesised on a substrate placed in each well (see Section 3.2). TEM grids can easily be prepared in this way and analysed using TEM without any further preparation. Most of the results presented here are of 70° C experiments.

70 °C

Where reaction mixtures prepared at room temperature give rise to worms and spirals, at higher temperatures these form a very complex mixture of morphologies. At 70 °C very fragile structures, including sheets, cones, bands, tentacles, and coral-like structures form within three hours. Treatment of these biomorphs with a weak acid dissolves the sample entirely, indicating a very low silica composition of the aggregates. The characteristics of each of these types of morphologies have been explored using optical, FESEM and TEM analysis.

In Figure 3.42 a series of optical images of biomorphs synthesised at 70 °C can be seen. The growth of this complex mixture of aggregates begins with the formation of small nuclei. Within 1 hour visible sheets and cones form (Figure 3.42 A). Continued growth results in the formation of large thin sheets and cones, as well as long thin extrusions, like tentacles, which can be seen in Figure 3.42 B-C. Viewed under reflective light, the cones and sheets show beautiful interference colours (see Figure 3.42 D). The pH is reduced during the course of growth from the initial 11.0 to 10.0 after 3 hours.

In Figure 3.43 FESEM images of various types of cones or trumpets can be seen.

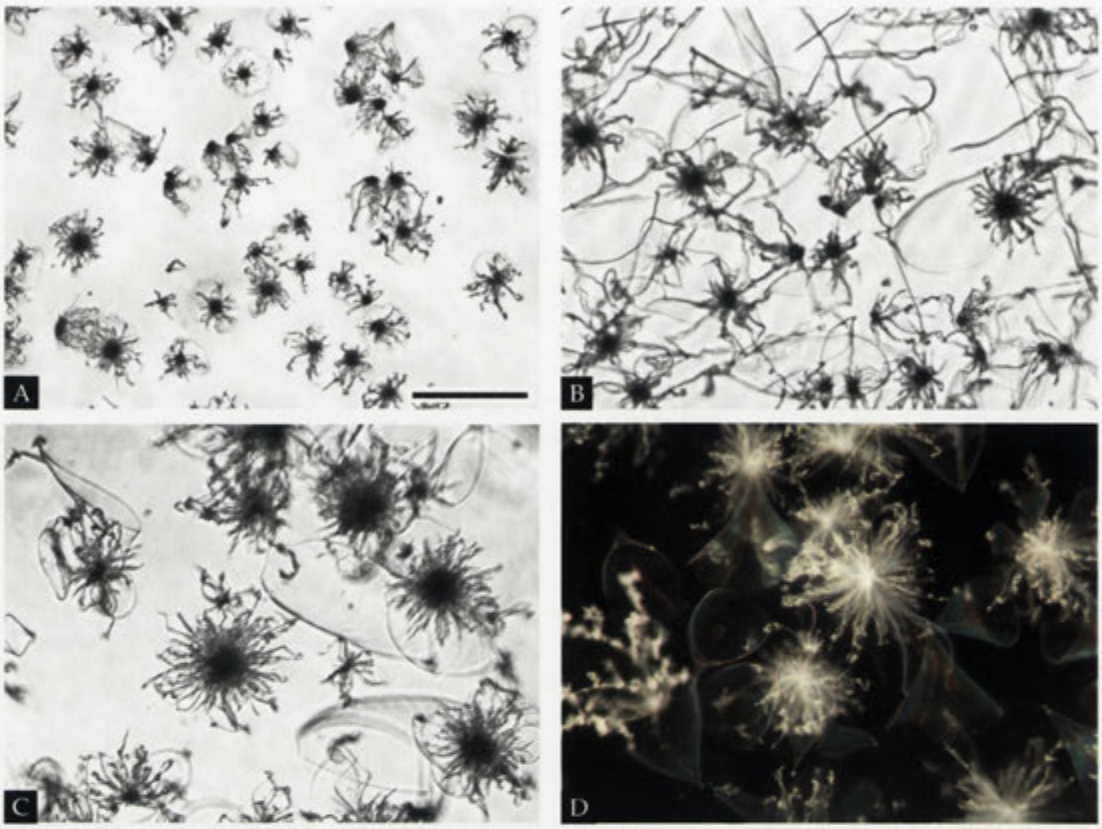

Figure 3.42: Optical images of biomorphs synthesised using standard conditions ([$BaCl_2$] 5 mM, [SiO_2] 8.5 mM, pH 11.0) but at 70 °C instead of room temperature, A 1 hour, B 3 hours, C 3 hours, D 2 hours. Scale bar in A is 100 μm for A-C, observed in transmission light microscope, and D is viewed using reflection light microscope.

Both symmetric (Figure 3.43 A and B) and non-symmetric (Figure 3.43 C-E) cones are present which can show a great variety in diameter and height. Open structures, like curled sheets (waffle cones) (Figure 3.43 G and H) as well as flat sheets are also present, some of which grow along the plate surface. These can grow as individual structures, but are more than often associated with a group of cones and sheets emerging from a central core.

At the micron scale, both sheets and cones have very similar texture; they are generally very thin, between 300-500 nm, and composed of elongated crystallites, preferentially ordered with their long axis along the growth direction (see Figure 3.44). The crystallites are around 30 nm in diameter and often arranged in a herring bone pattern. This configuration is therefore very different and much less ordered than the ones observed in sheets grown at room temperature (see Chapter 1).

As is evident in Figure 3.45, many sheets grow 'tentacles' from the very tip of the structure. These structures have the same crystallite size and orientation as their parent

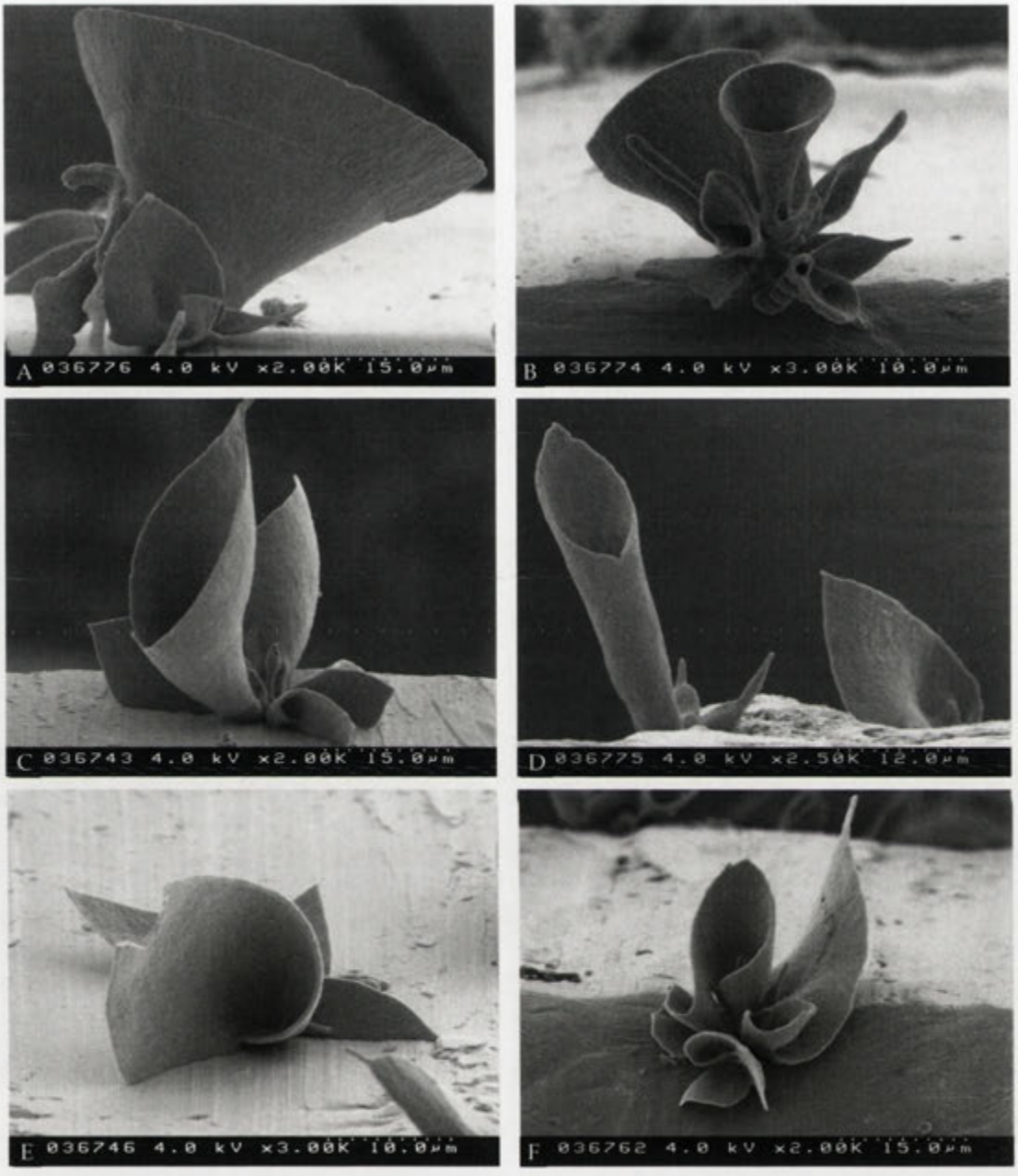

Figure 3.43: FESEM images of cones and sheets synthesised at 70 °C for 2 hours. Both symmetric (A, B) and non-symmetric (C, D) cones are observed, as well as sheets of highly variable curvature (D–F).

sheets, and can intertwine with other tentacles originating from different aggregates (Figure 3.45 C and D). Sometimes the tip can split, so as to form new cone-like structures (Figure 3.45 E, F, and H). Tentacles are also seen growing from the edges of another type of aggregate also present in the same sample; 'corals' (see Figure 3.46). Corals have a similar morphology to the floral spherulites previously discussed (see Figure

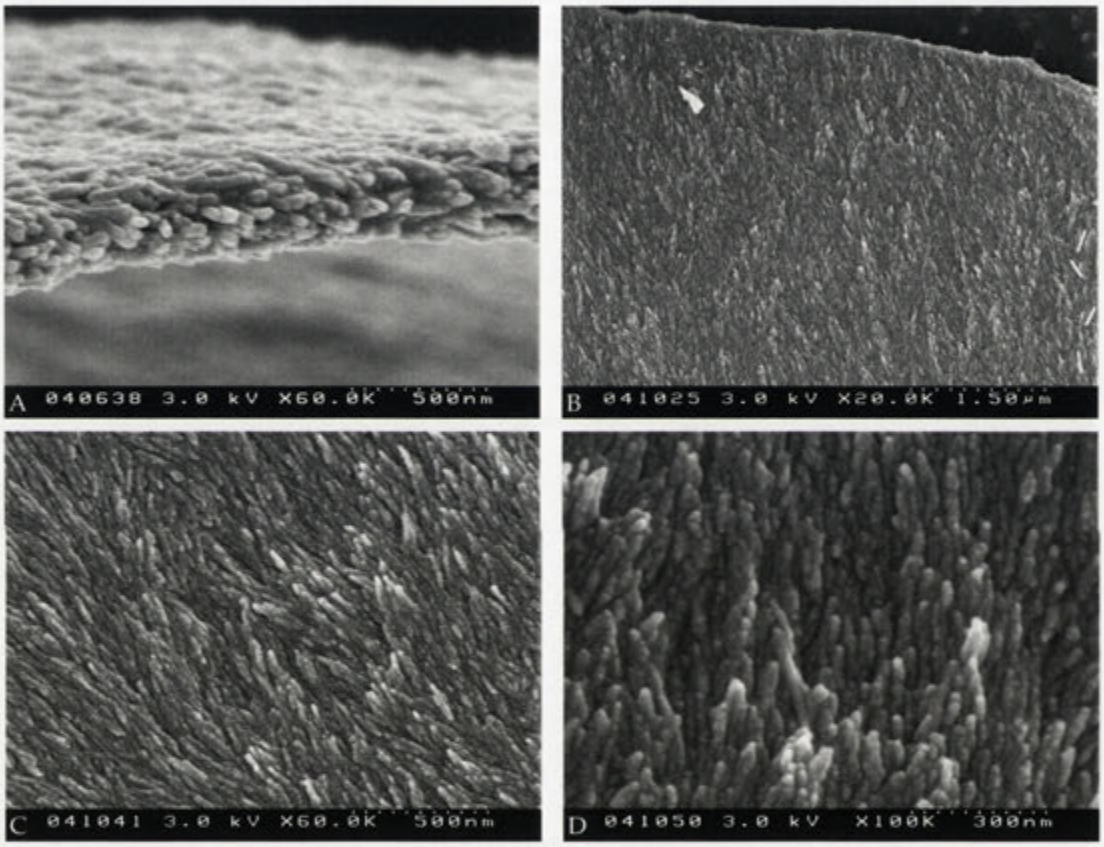

Figure 3.44: FESEM images of the surface of sheets, synthesised at 70 °C for 3 hours (B-D) using otherwise standard conditions, revealing the thin nature and complex crystallite ordering of these structures.

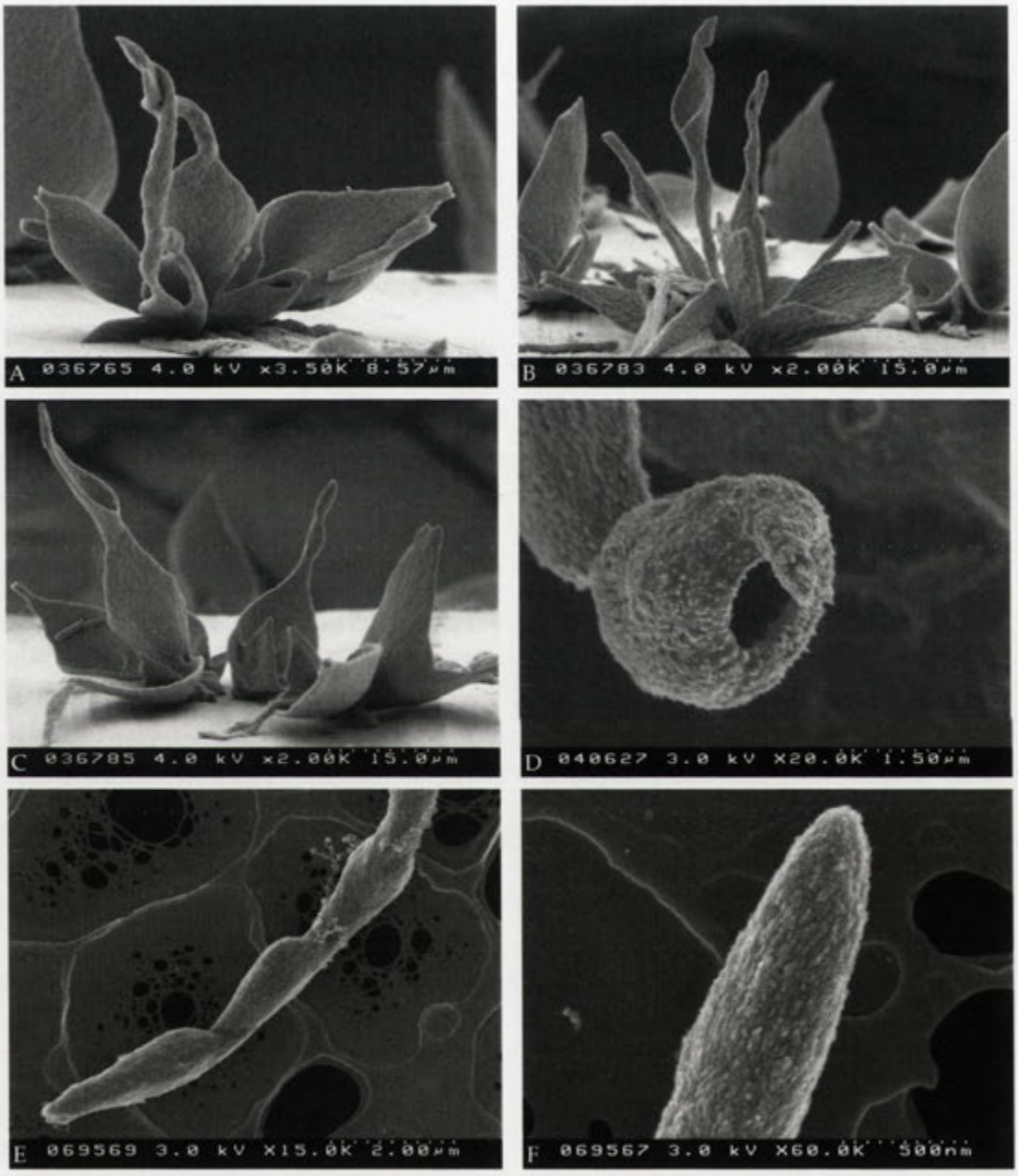

Figure 3.45: FESEM images of sheets and associated tentacles synthesised at 70 °C. Tentacles are seen growing off the tips of sheets and cones (A–C), and occasionally they can entangle in each other (A). They can be straight and smooth, or show evidence of periodic growth burst that produces a tentacle of variable diameter (E). Tentacles, as well as sheets, are composed of nano-sized crystallites that are elongated in the growth direction (D, F).

3.33). In many cases, these aggregates can be seen dividing into two halves, like an advanced stage of dumbbell growth (see Figure 3.46 B). In between these two halves, a connecting bar consisting of bundles of neatly stacked parallel crystals can be seen.

Apart from the tentacles, another type of filamentous structure also occurs. We call these 'bands' (see Figure 3.47). Bands and tentacles can be identified in Figure 3.42 B as fibrous structures. They typically appear during the later stages of growth. They are always associated with sheet-like structures that are of a very different kind to the ones encountered so far, and referred to as 'plates'. In contrast to the morphologies discussed earlier, bands and their associated plates have elongated crystallites ordered with the long axis roughly perpendicular to the growth direction (see Figure 3.47 E and F). These plates do not exhibit significant curvature as compared to the other type of sheets found in the same sample, and are also substantially thicker (~1 μm as compared to hundreds of nm). Bands develop from the tip of the plates, retaining the original orientation of the crystallites. They can grow to several hundreds of μm in length, and 25 μm in width. However bands having a width of around 1–2 μm occur most frequently (see Figure 3.47 A and B). The wider the band, the greater sinuosity of the width can be seen. Thinner bands are, on the other hand, very uniform in width, and in this case the crystallites are highly ordered parallel to each other. A slight difference in angle between the crystallites can be seen from side to side in the wider bands (See Figure 3.48 B-D). The crystal size can vary between bands from quite chunky large crystals, ca. 200 nm (see Figure 3.48 A), to small ca. 20-30 nm in diameter (see Figure 3.48 E and F). The crystal size of ca. 20-30 nm is more or less identical to the ones identified in the other aggregates observed under these conditions.

TEM observations

As witherite crystals are normally elongated along the *c*-axis, it was assumed that the long axis of the crystallites observed in the FESEM images coincides with the crystallographic *c*-axis of witherite. To confirm this we performed electron diffraction experiments on many of these biomorphs.

In Figure 3.49 B-D electron diffraction patterns (EDPs) from a ~1 μm^2 area of the band seen in A are shown. The EDP in Figure 3.49 B is viewed down the $<010>_o$ (subscript o indicate orthorhombic indexing) zone axis EDP of witherite, although the *h0l*, *h* odd reflections are very weak (for example see Figure 3.49 B 102_o reflections). A small spread in crystallite orientation can be discerned as the reflections are arc-like. Upon tilting the band 30° (not 90°) around the witherite c^*-axis, the zone axis $[110]_o$ should appear. However, the EDP in Figure 3.49 C is not compatible with this as weak extra reflections appear. Instead, this EDP corresponds to that of an <100> zone axis,

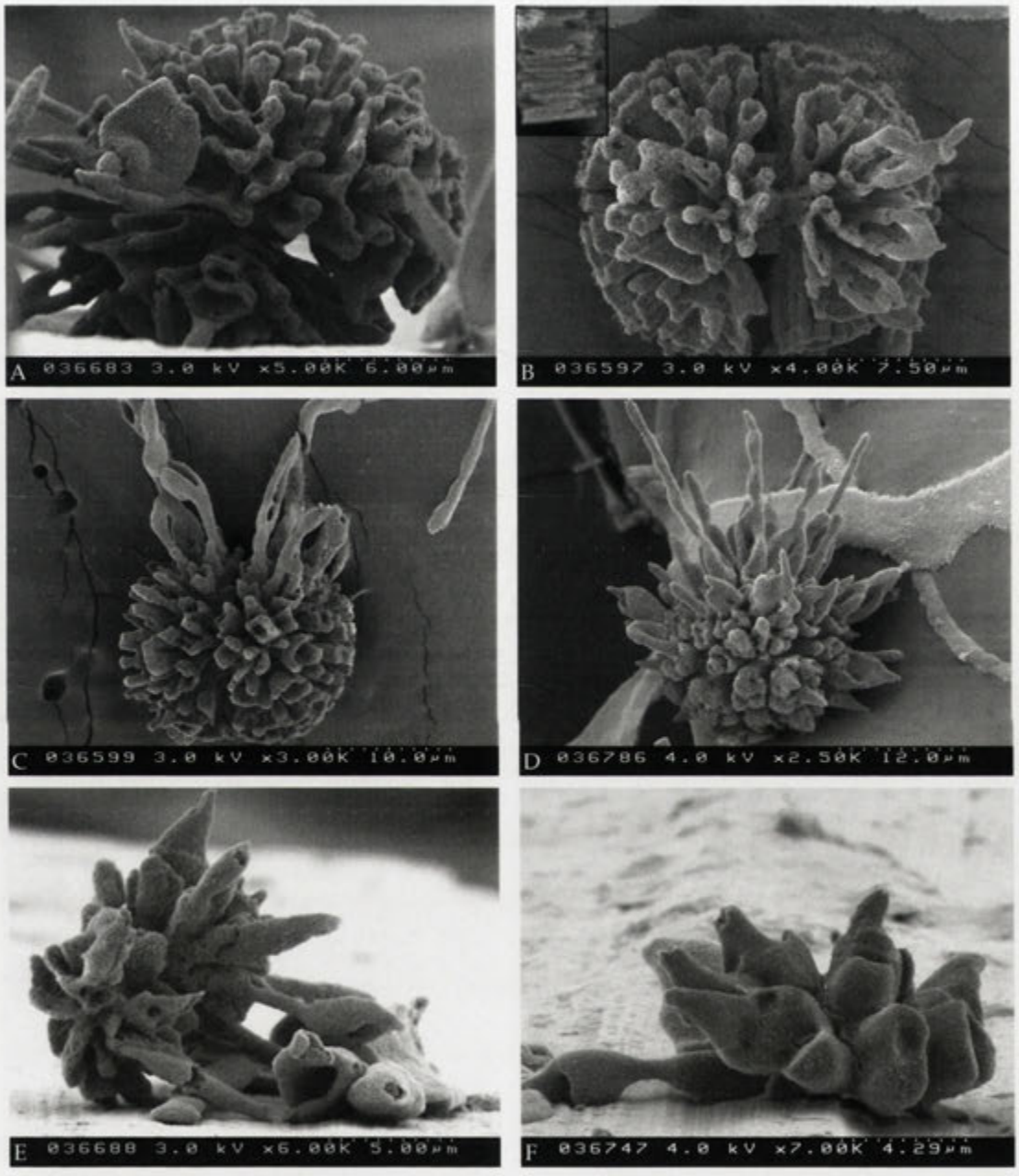

Figure 3.46: FESEM images of corals synthesised at 70 °C. Some of these morphologies (A–C) are similar to floral spherulites, discussed in Section 3.4.4. Many of these corals are seen being composed of two halves (A, B), in which the mid section has perfectly aligned crystallites (see inset in B). Tentacles are also observed growing from the edge of these coral-like structures (C, D). Smaller bud-like morphologies (E, F) are also present in this sample.

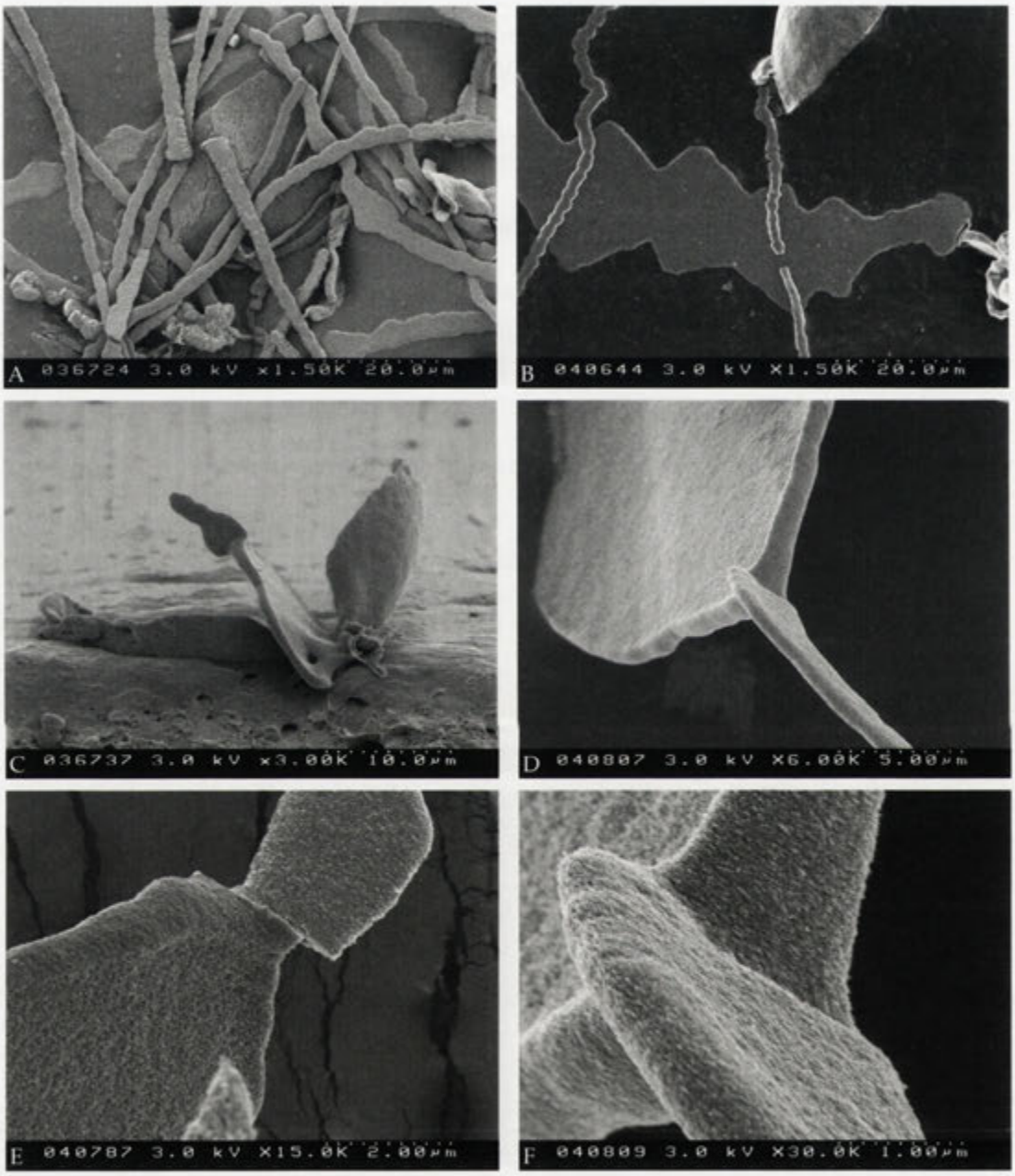

Figure 3.47: FESEM images of bands and associated plates synthesised at 70 °C under otherwise standard conditions. Bands can have a wide range of diameters and sinuosity (A, B) and are seen growing off the tips of plates (C, D); a different type of sheet compared to the ones discussed so far. In both bands and plates, the crystallites are oriented perpendicular to the growth direction (E, F).

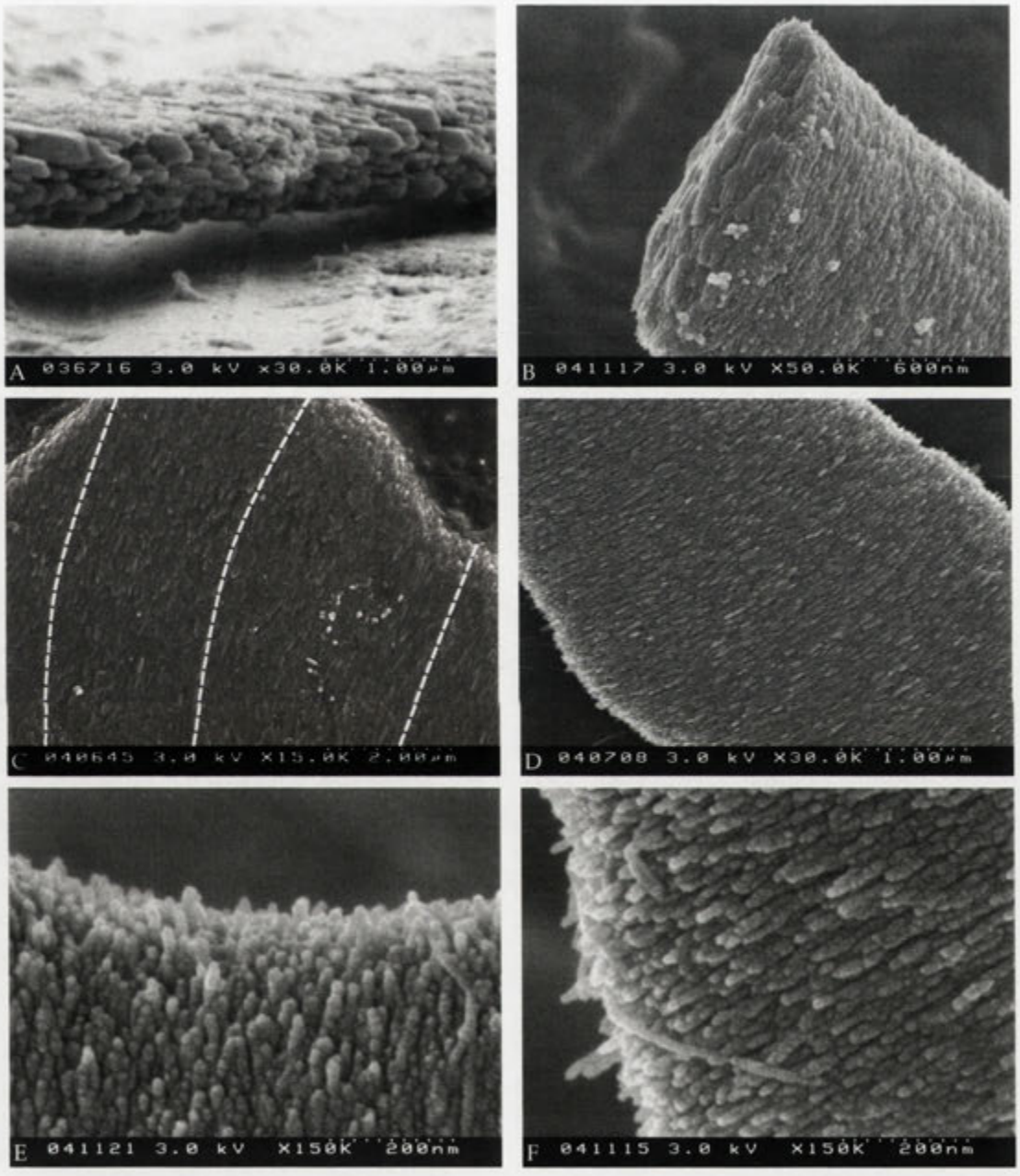

Figure 3.48: FESEM images of bands synthesised at 70 °C. Although variable crystallite size can be seen in between samples (A, B, E, F), they are in all cases oriented perpendicular to the growth direction. Depending on the sinuosity of the band, some shift in orientation can be seen between the edges of a band as indicated by the dashed white lines in C.

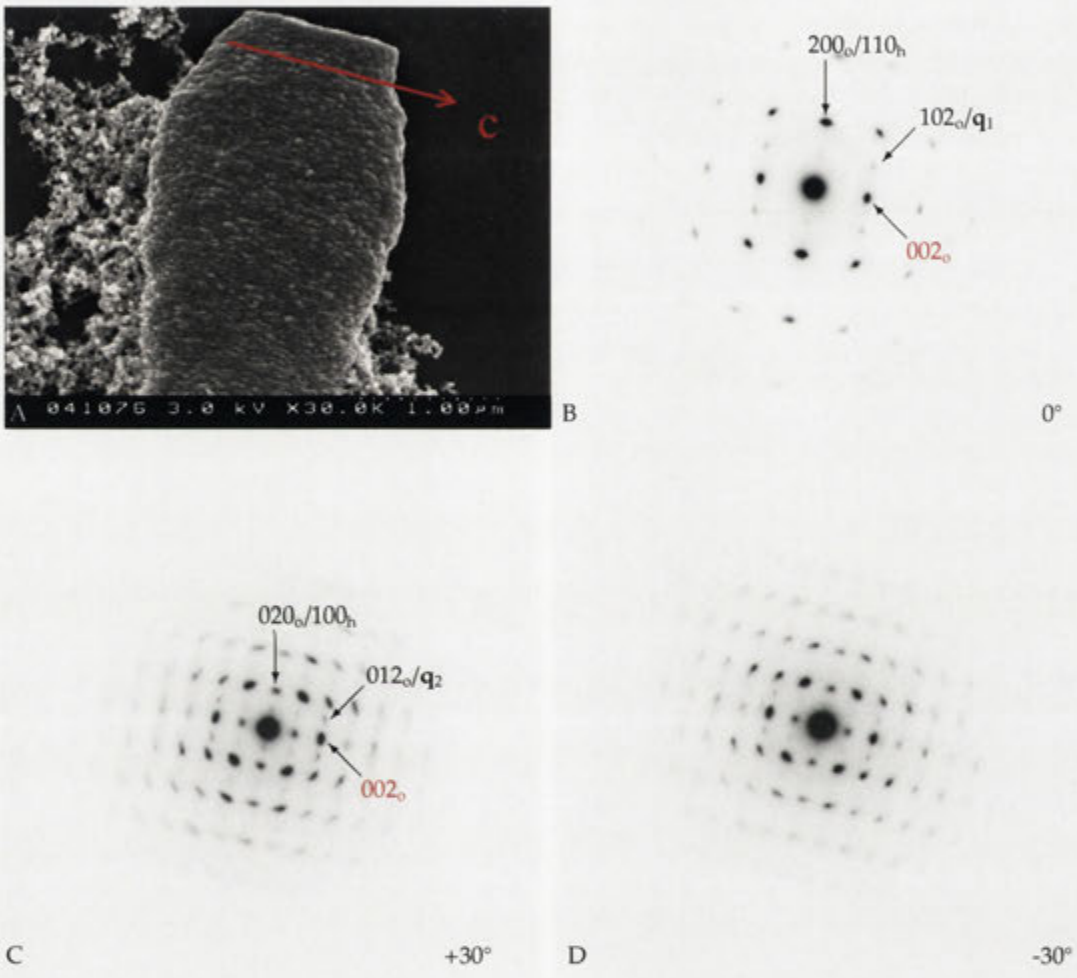

Figure 3.49: The two types of diffraction patterns observed while tilting the band seen in A around the *c*-axis. Reflections are indicated using the orthorhombic (o) and the hexagonal (h) lattice systems. (The reflections with $\mathbf{q}=1/2[100]^*_h$ are not visible in the zero order Laue zone.) The modulation wave vector **q** can be used to describe the twinning behaviour of witherite in the hexagonal lattice system.

but with the 0*kl*, *k* odd reflections very weak. Identical patterns are obtained if instead the band is tilted -30° around the c^*-axis (see Figure 3.49 D). To interpret this behaviour, which is not compatible with a single crystal EDP of witherite, it is necessary to note the twinning behaviour of witherite (see Section 2.2.2).

In witherite, as was described in Section 2.2.1, the barium atoms approximate an hexagonal closed packed array. The space group symmetry of such an array is ideally $P6_3/mmc$, and the Bragg reflections would form an hexagonal lattice such as the large black discs in Figure 3.50 A-D. The carbonate groups lie flat parallel to (001) in all octahedral interstices of the hcp array (see Figure 2.2), but are displaced so as to take one of two different heights (and also adopt two different orientations). The ordering pattern of the carbonate groups into these positions destroys the overall hexagonal symmetry. The resulting space group then becomes *Pmcn*, which is the space group of witherite. In reciprocal space, this gives rise to additional reflections compared to the underlying hexagonal (indicated by h) sublattice. These extra reflections can be described with a modulation wave vector $\mathbf{q}=1/2[100]^*_h$, which means that all the Bragg reflections of witherite can be characterised by $\mathbf{H} = \mathbf{G} + 1/2[100]^*_h$, where **G** is the set of Bragg reflections from the hexagonal subcell. In the hexagonal reciprocal sublattice there are three equivalent $<100>^*_h$ directions, but the orthorhombic witherite structure gives rise to reciprocal lattice points half way to only *one* set of 100_h reflections (i.e. if $\mathbf{q} = 1/2[\bar{1}10]^*_h$, then not $1/2[010]^*_h$ nor $1/2[100]^*_h$) (see Figure 3.50). Note also that **q** can be expressed differently; $\mathbf{q} = 1/2[110]^*_h$ represent the same lattice points as $\mathbf{q} = 1/2[\bar{1}10]^*_h$. For example, assuming that the EDP seen in Figure 3.49 B is viewed along zone axis $[\bar{1}10]_h$, along the arrow in Figure 3.50 A (with $1/2[110]^*_h$ reflections present although weak), then upon tilting the band 30°, the zone axis $[010]_h$ is reached (see Figure 3.50 B). However, according to Figure 3.50 A, no extra reflections should be present at $1/2[100]^*_h$, but in the experimental EDP, they clearly are. A 90° tilt (viewed along zone axis $[110]_h$) should be necessary to see those reflections. The explanation for this is that all three possible twin orientations with the hexagonal sublattice are present and contribute to each experimental EDP. This is visualised in Figure 3.50 B-D. In B and C the other two possible twin orientations are shown, while in D the reflections of all twins are present. Successive tilting of 30° of the situation seen in Figure 3.50 D gives rise to the reflections seen in the EDPs in Figure 3.49. Experimental EDPs of bands are therefore only compatible with a model in which all three twins are present in roughly equal amounts within the selected area apperture. It is difficult to assess from the EDPs whether these twins are all present within each crystallite, or if each crystallite contains only one, or two of the possible twins. Furthermore, the EDPs seen here most likely derived from crystallites present at the very edge of the band, as the beam barely penetrates the thicker central part of the band.

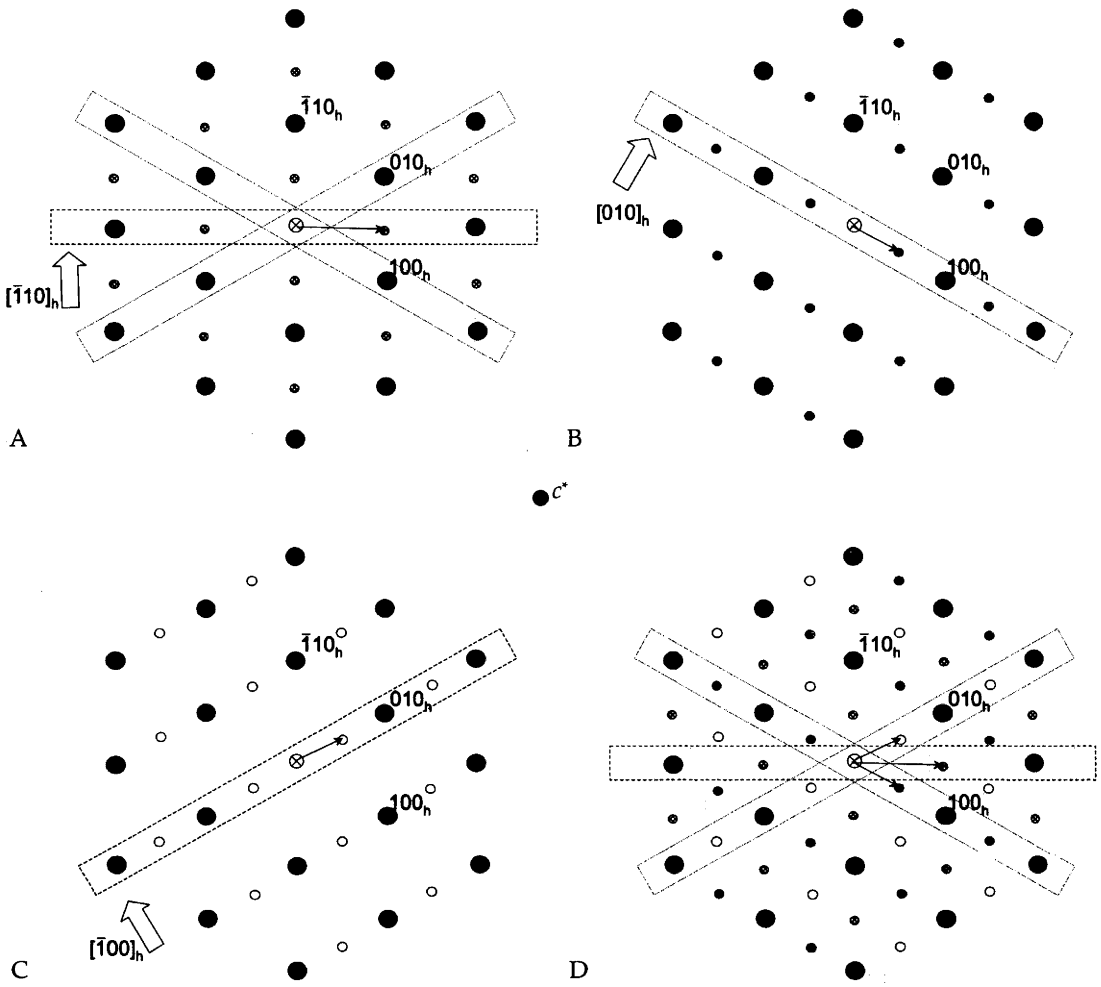

Figure 3.50: The reciprocal hexagonal lattice viewed along c^*-axis. The EDPs that arises from each twin, viewed perpendicular to the c*-axis (fat arrow), can be described using modulation wave vectors (q). All the twins are present in D, and their respective reflections are 1/3 of the intensity as seen in A-C.

In the sheets, FESEM observations have shown the presence of elongated crystallites in the growth direction of the sheet, however, the crystallite orientational order is more complex than in the bands (compare Figure 3.44 and 3.48). To investigate the crystallite orientation within the sheets, EDPs were recorded from selected areas of such aggregates. In Figure 3.51 such EDPs are shown. At first instance they have the appearance of being partially ordered powder EDPs. The arc-like 020 reflections are strong in all EDPs, except in C, indicating that the *c*-axis are in the sheet-plane and directed towards the periphery. In C, however, the *c*-axis is not exactly in the plane of the sheet. Furthermore, the EDPs seen in Figure 3.51 are not symmetrical around the *c*-axis; they do not exhibit an mm symmetry. This could be compatible with a bimodal

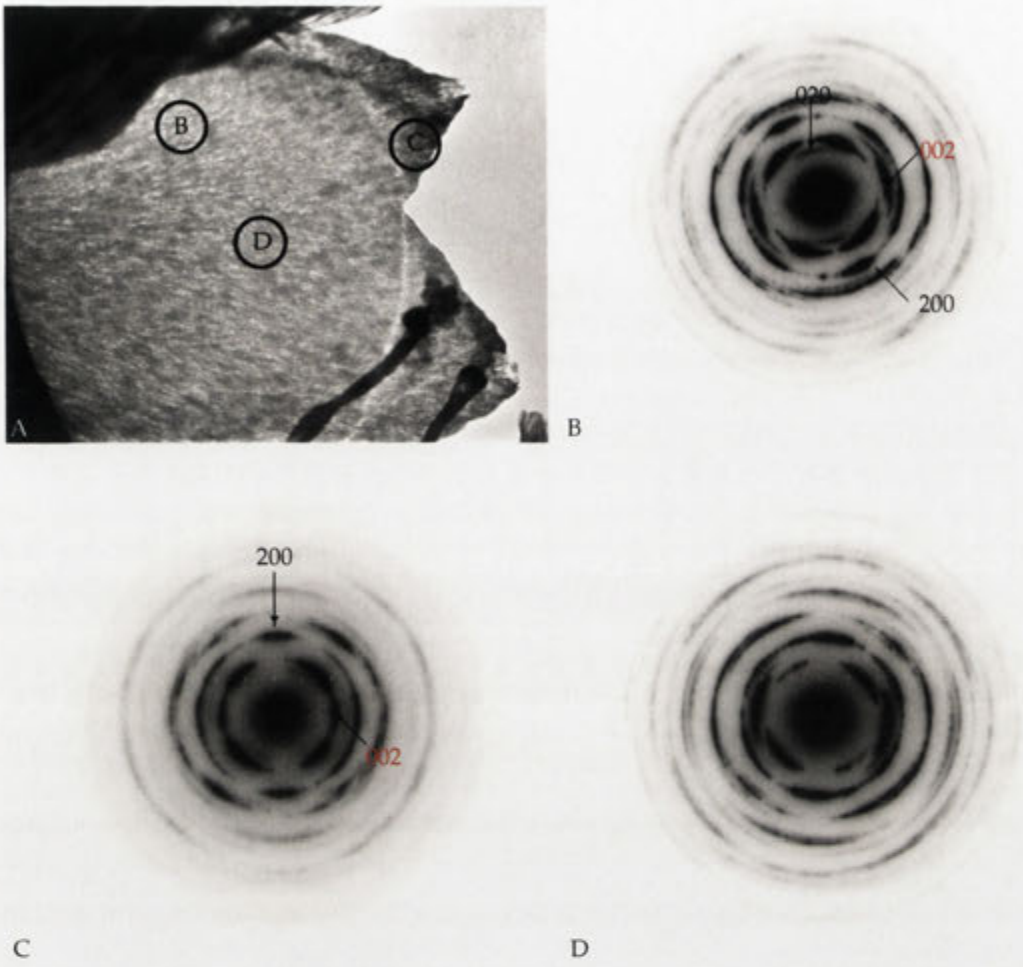

Figure 3.51: EDPs (B–D) of different areas of a sheet indicated by rings and letters in A. Most noticeable in these EDPs is the orientation of the 002 reflection, which is arc-like and always in the direction towards the edge of the sheet.

orientational crystallite distribution, indicating a more complex orientational order.

Discussion

In this section, biomorphs precipitated at various temperatures using the standard synthesis conditions have been discussed. It is evident that at higher temperature a very complex mixture of morphologies are observed. As summarised in Figure 3.52, the morphological evolution from low to high temperature can be seen as a gradual change from globular → globular, worms → globular, worms, helices, (sheets) → helices, sheets → complex mixture of sheets, corals, bands. This morphological sequence involves a reduction in the dimensionality of the aggregate with increasing temperature. 3D globular aggregates preferentially form at lower temperatures, whereas high

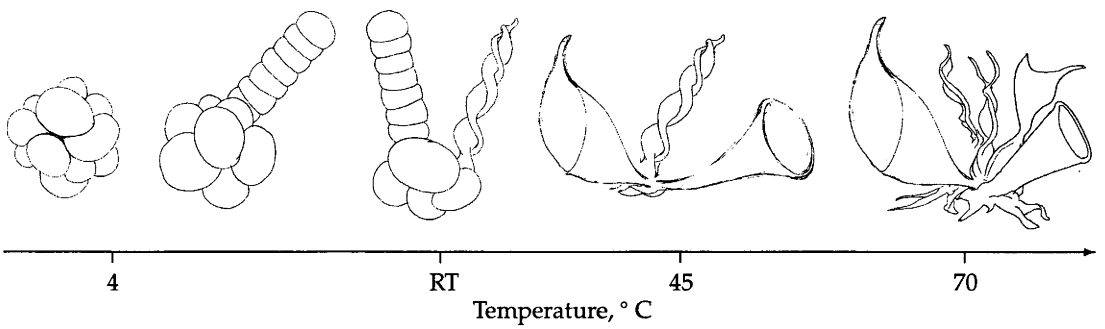

Figure 3.52: Schematic drawing of the different morphologies observed at different temperatures using standard condition.

temperatures produces 2D sheets and cones, as well as quasi-1D bands. Worms and helices have a dimension somewhere in between; they grow as a 2D sheet that twist around itself to produce an aggregate with a lower dimension than 3.

It is also clear that the time required for biomorph growth decreases with temperature. This is most likely caused by the decreased solubility of barium carbonate at higher temperatures (see Section 2.2.4.2). Carbon dioxide is less soluble at higher temperatures, but the high pH acts as a sink for carbon dioxide and quickly converts it to aqueous carbonate. Carbonate supersaturation is therefore reached very quickly at high temperatures, leading to many more actively growing aggregates compared to lower temperatures.

The morphological sequence can therefore be related to deposition rates. At low temperatures, 3D globular aggregates form in response to slow deposition rates which act to grow spherical morphologies from initial dumbbell-like aggregates (see Section 2.2.4.3, Figure 2.15). It is believed that these dumbbells are present as the growth seed of all the different morphologies observed. All aggregates produced at 70 ° C can be seen in relation to dumbbells. It is therefore suggested that the relative growth of specific areas of the dumbbells can explain some of the morphological differentiation observed. For instance if preferential growth occurs along a rim on the growing dumbbell, which overtakes the growth of the inner parts of the aggregate, a sheet or a cone could be produced. The crystal direction in these sheets are more or less aligned in the growth direction, as indicated by both FESEM and TEM analyses.

TEM observations of the high temperature aggregates show that the crystalline order in these morphologies varies between the aggregates. The bands show the presence of all three twins that are well ordered around the *c*-axis. Other morphologies, like the sheets for instance, show a higher degree of disorder between the crystallites.

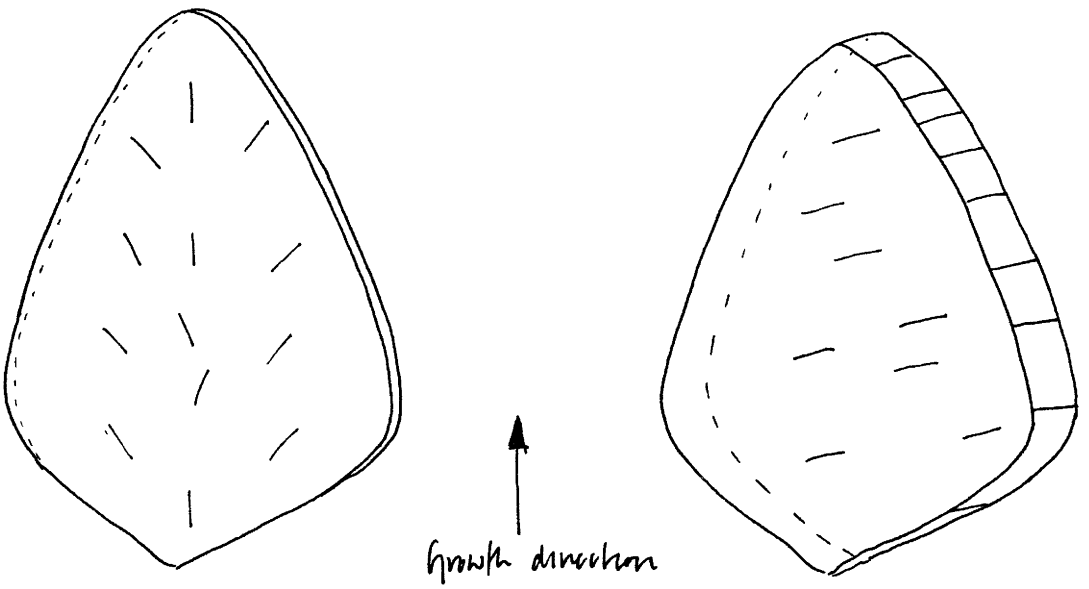

Figure 3.53: Schematic drawing of the two different types of sheets observed at 70 °C. Filaments can grow outwards from the tip of these sheets, which will adopt the crystal orientation of the sheet in question. In sheets where the crystals are aligned along the growth direction, tentacles having the same crystal orientation can emerge. In sheets where the crystals are perpendicular to the growth direction, bands retaining this orientation can grow outward.

3.4.5.1 High temperature and low silica concentration

Experiments performed using low sodium silicate concentration and high temperature further revealed a different morphology, *palm trees*, produced using 4.2 mM SiO_2 and 5 mM $BaCl_2$ at 80° C. In Figure 3.54 a selection of optical images can be seen of these morphologies, formed at different initial pH. As is the case in other biomorph growths, nucleation sites increase with increasing pH, producing smaller aggregates. At pH 10.2, more than 200 μm long aggregates are produced, and the length decreases as the pH is increased. However, in all cases the aggregate structure is retained irrespective of pH. The morphology produced under these conditions are reminiscent of palm trees in that they contain a stem from which 'leaves' extend (see Figure 3.55). The leaves further display a six-fold rotational symmetry around this stem, as visible in Figure 3.55 A. Such symmetrical morphologies are indicative of twinning, as discussed in Section 2.2.2.

Under crossed polars, the orientational ordering of the crystallites is easily visible (see Figure 3.55 B-D). The entire aggregate seen in Figure 3.55 B has a uniform blue colour throughout the aggregate, except in the central stem which shows slightly more yellowish colour. A piece of a stem viewed under crossed polars can be seen in Figure

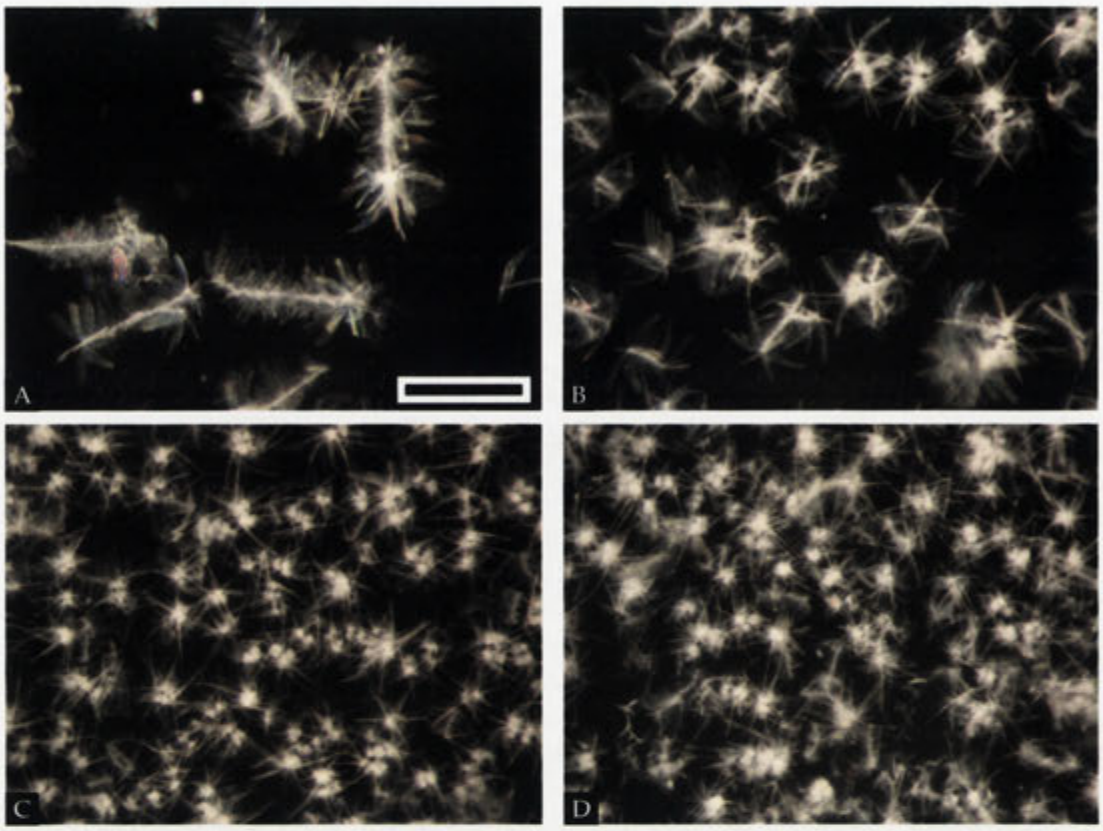

Figure 3.54: Optical images, taken using reflection light microscope, of biomorphs synthesised at 80°C (3 hours of growth) using [$BaCl_2$] 5 mM, and low [SiO_2] 4.2 mM, and varying initial pH; A pH 10.20, B pH 10.71, C pH 11.14, D pH 11.29. Scale bar in A is 200 μm and valid for all images, .

3.55 C, which shows red colouring on the fringes of leaves attached to the stem, which in turn has an almost grey-ish colour. Leaves are most often seen having a uniform colour throughout the structure, however, very large leaves can display a continuous variation in coloration. As interference colours are dependent on the thickness and the direction of the plane polarised light compared to the crystallographic orientation (different refractive indices along the three axis), it is at first hand not easy to interpret these images. Even though witherite is biaxial, n_β (refractive index along the *b*-axis, 1.676) and n_γ (refractive index along the *a*-axis, 1.677) only differ by 0.001. It may therefore not be possible to observe the birefringence in such thin materials as the palm tree unless viewed normal to [001]. Furthermore, as all witherite twins share the same *c*-axis, it is not possible to observe any twinning under such conditions (Brown et al., 1962). The leaf seen in Figure 3.55 D has an interference colour indicative of a single crystal. The witherite present has the same crystallographic orientation all through the leaf. The same is observed for the fringes seen in C. It seems that the

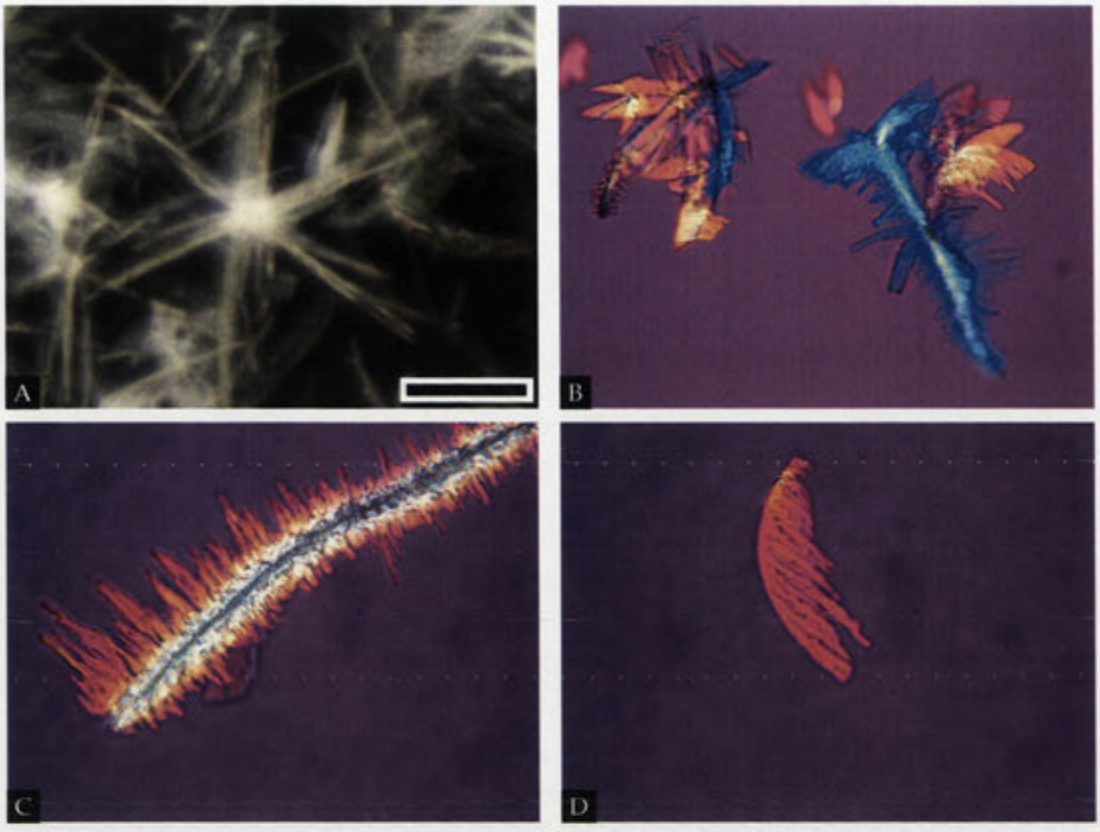

Figure 3.55: Optical images of 'palm trees' using both reflection (A) and transmission microscopy under crossed polars (B-D). Scale bar in A is 50 μm.

entire palm tree has the same witherite crystallographic orientation throughout the morphology even though the structure contains branching leaves. This suggests that all leaves present including the stem is in fact one crystal.

FESEM analysis further revealed the unusual morphology of palm trees. In Figure 3.56 B it can be seen that the leaves show a six-fold rotation axis around the stem as also indicated in the optical images. The leaves are seen extending from the central stem as plates, whose thickness seem to vary. Layers of leaves can be seen growing outward in the same direction on top of each other. In Figure 3.56 A it can also be observed that they can split into several growing tips along the growth direction. The thicker part of the leaves, seen close to the stem, is around 3 μm in diameter, whereas the thickness is reduced to around 200 nm further away from the stem. The leaves also show very flat surfaces, that in some cases are pitted with ~50 nm holes (see Figure 3.56 C-E). At the edges of such leaves, small elongated fringes that are perpendicular to the growth direction extend from the short surface of the leaves (see Figure 3.56 E). These fringes are around 10 nm in diameter and, in contrast to previous structures

discussed, these fringes do not seem to from individual particles that are cemented with silica. Although it is difficult to tell from FESEM analysis, it seems that these fringes are all connected, and not separated by amorphous silica; i. e. no individual particles can be seen. Further pointing towards a crystallographic reasoning behind these types of structures are the apparent 'fish-tail'-like morphology of some of the cross section of the leaves very close to the stem. The angle between the two tails ranges between 120-130°, which is similar to the normal {110}twinning angle seen in witherite.

TEM observations

To further investigate the crystallographic properties of this type of morphology TEM analyses were performed on as-prepared samples. The palm leaves are so thin that no preparation was needed for electron diffraction, and the samples were directly grown on the TEM grids. From the optical and FESEM images it is not obvious how this biomorph is structurally ordered, as no elongated crystallites can be seen. As witherite crystals are normally elongated along the *c*-axis, it was assumed that the long axis of the palm leaf morphology, as observed in the FESEM and optical images, coincides with the crystallographic *c*-axis of witherite. To confirm this electron diffraction was performed on these samples.

Figure 3.57 C to F show EDPs taken from the palm leaf seen in A, specifically on the selected areas indicated by red circles in B. The EDP seen in Figure 3.57 C is compatible with a $< 3\bar{1}0 >_o$ zone axis EDP of witherite. At first sight it seems to be a normal single crystal EDP. However, a closer look reveal the 'apparent' weak satellite reflections at $\mathbf{q} = 1/4[130]^*_o$, indicated by a blue circle in Figure 3.57 C. To interpret this behaviour it is, again, necessary to consider the twinning behaviour of witherite. Tilting +30° around the *c*-axis from the EDP seen in Figure 3.57 C, the EDP in D is observed. This EDP is compatible with a $<100>_o$ zone axis EDP of witherite. The 0kl, k odd reflections are more intense compared to the ones observed for the bands (see Figure 3.49), but not as intense as in a single crystal of witherite. An identical EDP is observed when tilting -30 ° around the *c*-axis from the EDP seen in Figure 3.57 C.

All these observations are compatible with the presence of two out of the three possible twins. Analogous to the reasoning presented for the bands in Section 3.4.5, consider the reciprocal lattice seen in Figure 3.58 A. Assuming the EDP seen in Figure 3.57 C is viewed along zone axis $[3\bar{1}0]_o$, along the arrow in Figure 3.58 A, it is evident that no reflections at $\mathbf{q}=1/2[110]^*_h$ are observed. Upon tilting the palm leaf +30° around the *c*-axis, the zone axis $[100]_o$ (= $[010]_h$) is reached (see Figures 3.57 B and 3.58 A). The modulation wave vector $\mathbf{q}=1/2[100]^*_h$ is now present and correspond to 010_o. However,

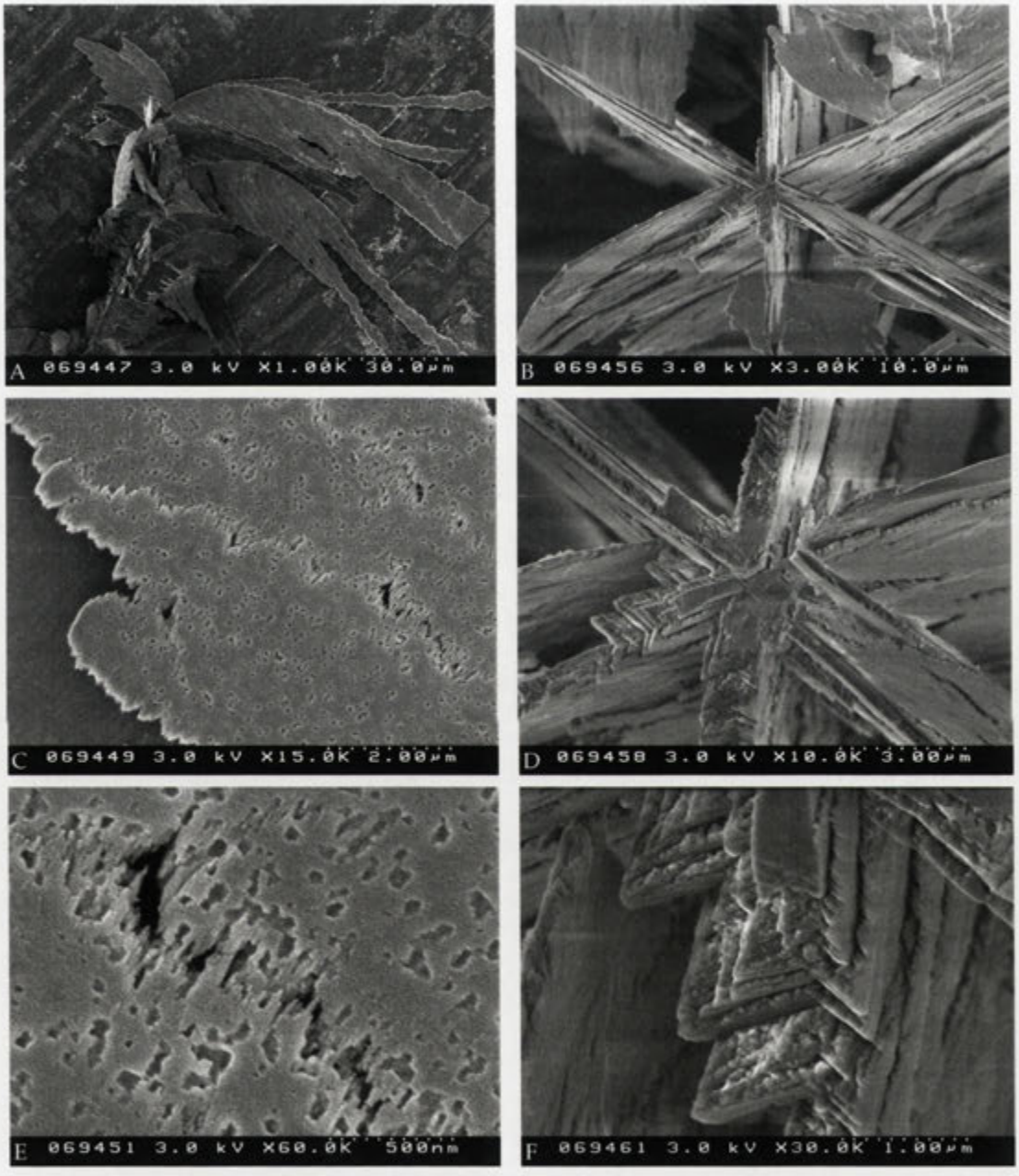

Figure 3.56: FESEM images of palm trees synthesised at 80 °C. These morphologies are characterised by a thin leaves growing off a central stem (A, B).). Leaves are composed of fingers and show a pitted surface (C, E). In many cases such morphologies adopt a six-fold rotational symmetry around this stem (B). At the base of the leaves, close to the stem, fish-tail-like patterns are seen, indicative of twinning (D, F).

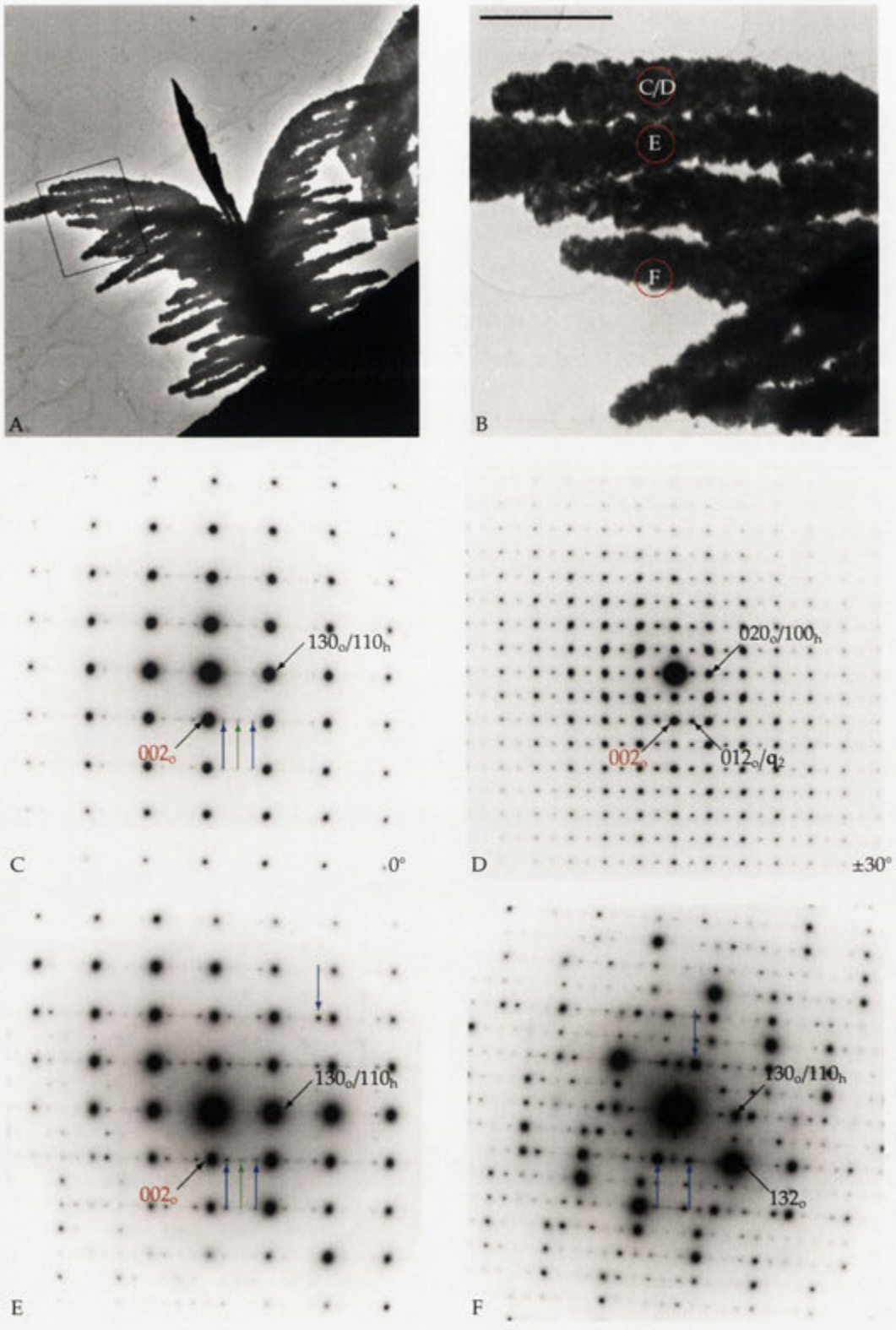

Figure 3.57: Diffraction patterns of selected areas of a palm leaf structure (A), indicated by red rings in B. Scale bar in B is 2 μm. Reflections are indicated using the orthorhombic (o) and the hexagonal (h) lattice systems. The coloured arrows in C, E, and F indicates $1/4[110]^*_h$ reflections (see text and Figure 3.58 for details). The EDP shown in D is observed when tilting ±30° away from C along the *c*-axis. The EDPs seen in E and F correspond to areas seen in B.

upon tilting -30°, the EDP is identical to the EDP in Figure 3.57 B, which is clearly not compatible with a single crystal of witherite (as there is no modulation wave vector $\mathbf{q}=1/2[010]^*_h$ in Figure 3.58 A). Instead, this is compatible with the scenario depicted in Figure 3.58 B, where 010_o now coincides with $\mathbf{q}=1/2[010]^*_h$. Both these orientations of the witherite reciprocal lattice are drawn in Figure 3.58 C and it is clear that this model accounts for all observations: when the zone axis is normal to the palm leaf, the EDP is compatible with a $< 1\bar{1}0 >_h$ zone axis of the underlying hexagonal substructure. If the palm leaf is tilted ±30° around the *c*-axis (corresponding to the stem direction), the EDPs must be described with a modulation wave vector in addition to the underlying hexagonal sublattice: $\mathbf{q}=1/2[100]^*_h$ in the case of +30° and $\mathbf{q}=1/2[010]^*_h$ in the case of -30° (Figure 3.58 C). It is hence shown that only two of the three possible twins are present in each leaf. A closer look at the EDP in Figure 3.57 A reveals weak additional reflections at $\mathbf{q}=1/4[110]^*_h$ indicated by the coloured arrows. Such a modulation vector is not compatible with the reciprocal lattice of witherite. The zone axis $[3\bar{1}0]_o$ is a minor axis in witherite and it is evident from tilting experiments that these reflections are from higher order Laue zones (HOLZ). The reflections indicated by blue arrows are enhanced in Figure 3.57 E and F, which represent different fingers of the same palm leaf. A slight off axis viewing direction will give rise to stronger $\mathbf{q}=1/4[110]^*_h$ reflections indicated by the blue arrow in Figure 3.58 D. Although a small orientational difference can be seen between Figure 3.57 C, D, and E (a 9° tilt between zone axis $[3\bar{1}0]_o$ in C and zone axis $[\bar{1}\bar{7},7,2]_o$ in F), it is evident that the *c*-axis is oriented perpendicular to the extending fingers. This also confirms that the elongated stem is aligned with the *c*-axis, and the palm leaves retain this configuration upon growth. All weak reflections visible in Figure 3.57 C can therefore be explained as originating in the modulation wave vector $\mathbf{q} = 1/2 < 100 >^*_h$ of HOLZ. The effect is increased by the fact that the structure is very thin so that the reflections are rod-like along the viewing direction. This means that the HOLZ reflections cut the Ewald sphere closer to the origin of the EDP. The weak reflections indicated by a green arrow in Figure 3.57 C can also be due to trace levels of the third twin. Part of these reflections could be due to dynamic scattering, but the elongated reflections indicate a slight hint of the third twin, which is most likely present as stacking faults in small domains.

Discussion

In this section morphologies arising from low sodium silicate concentration and high temperature conditions have been discussed. Although the resulting palm tree-like morphology is clearly different from normal witherite morphology, this type of morphology is probably on the boundary of what can be seen as biomorphs. No individual

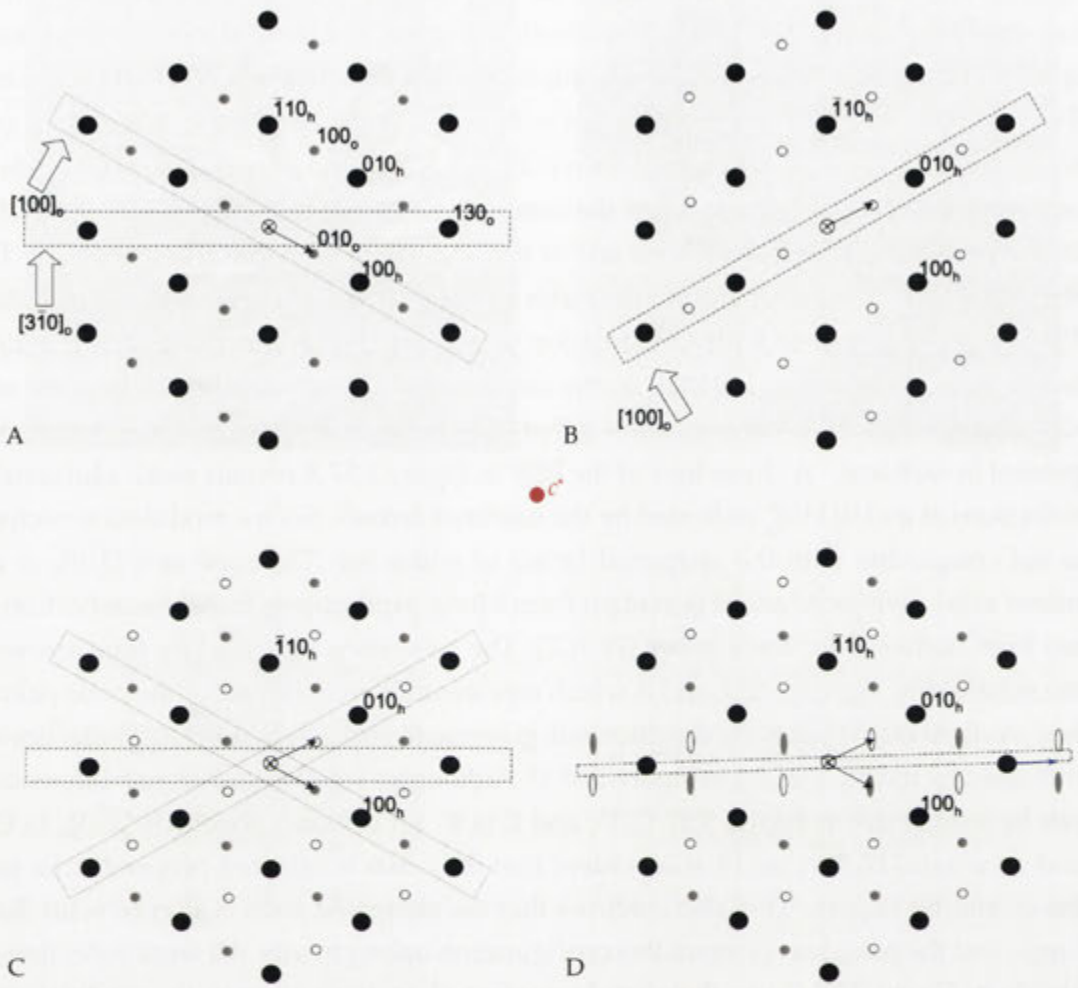

Figure 3.58: Schematic representation of the reciprocal lattice of twinned witherite viewed along the c^*-axis. Rectangles show the reflections present in Figure 3.57, viewed along the different directions indicated by the fat arrows. In D the elongated reflections give rise to the apparent modulation wave vector $\mathbf{q}=1/4[110]_h^*$ indicated by the blue arrow.

crystallites are easily discerned, and the crystallographic order is consistent with a twinned crystal of witherite. The orientation of the *c*-axis, which is the long axis of the interior stem, is preserved throughout the palm tree.

The crystallographic order seen in the palm leaf discussed above should also apply to all other palm leaves around the central stem. As the palm trees contain a six-fold rotation axis around the stem from which the palm leaves extend (see Figures 3.55 A and 3.56), and each leaf contains two out of three witherite twins, there is only one simple way of describing the morphological and crystallographic order seen in these structure. This is visualised in the model seen in Figure 3.59, which shows that the entire palm tree is composed of six twins with three different directions indicated by

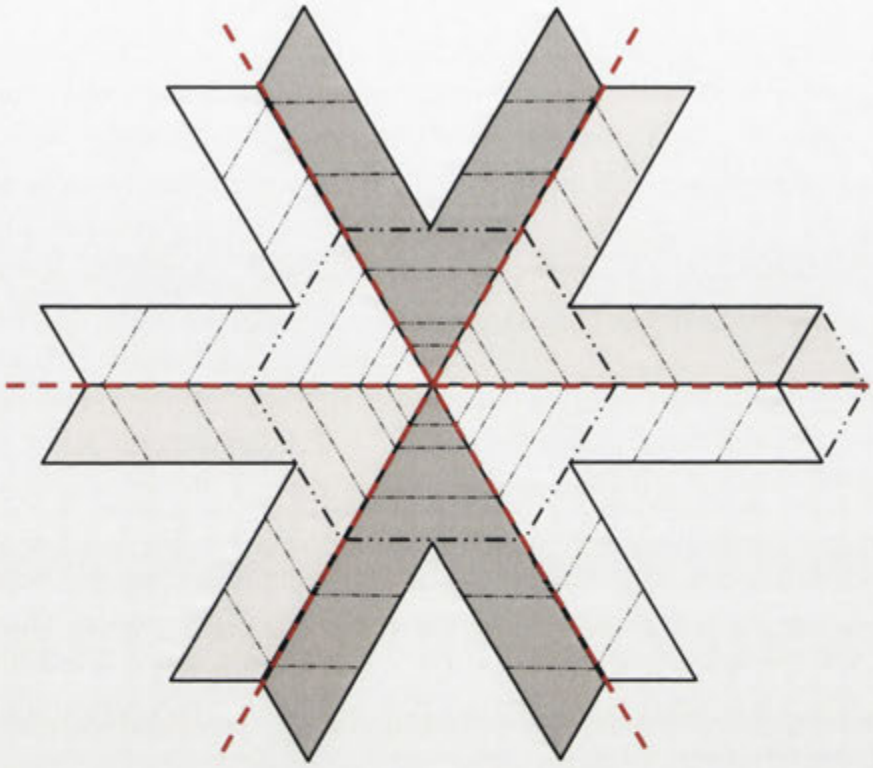

Figure 3.59: Schematic representation of a model of the palm trees. Red dashed lines represent the {110} twin planes, black dashed lines represent the {010} planes, and solid black lines represent the {110} faces. The thick black dashed line in the interior represents the stem from which the leaves can be seen growing. The different shades of grey represent the different twins.

the different shades of grey. The interior stem is visible as a thick black dashed line, which shows the {010} faces forming a hexagonal outline. In this model, each twin is v-shaped and bounded by {110} twin planes. The {110} planes also form the faces of the entire palm tree, forming fish-tailes at the leaf forming edge. This is consistent with the FESEM images seen in Figure 3.56 D and F. However, it is also possible that the {010} planes are formed at some of the growing edges of the leaves (see Figure 3.59). Regardless of which edge is forming the outer boundary of the leaves, the model is consistent with a star-shaped morphology exhibiting a six-fold rotation axis around the central stem; all of which is in line with TEM and FESEM observations presented in this section. The growth of palm trees can be seen as beginning with a normal witherite growth of pseudo-hexagonal columns. Preferential growth along the twin planes (along the [110] direction), gives rise to extended leaves from central stem. The same morphology arises more or less irrespective of pH, although the

dimensions of the aggregates decrease at higher pH. As discussed in previous sections, high pH ensures high solubility of both carbon dioxide and silica. However, at high temperature carbon dioxide and $BaCO_3$ solubility are reduced, so dissolution of carbon dioxide quickly results in high barium carbonate supersaturation which forms more nucleation points as compared to lower pH. The low concentration of sodium silicate used in these experiments is probably present as precipitated amorphous barium silicate in the initial stages of the synthesis. However, the high temperature used in these experiments further increases the solubility of such species. The initial growth of the pseudo-hexagonal stem, which is similar to standard witherite morphology, results in a further reduction of the pH and barium concentration, which reduces silica solubility. The growth of the leaves can therefore be seen as an effect of the presence of silicate, as is the case of all biomorph growth. Anionic silicate species can effectively adsorb onto the growing crystal thereby altering the morphology produced. In the palm tree case, one can speculate regarding such an interaction. As the large surface of the palm leaves display {110} faces, which show a pitted surface, it is believed that silica effectively adsorbs onto these faces and poisons further growth. This scenario then favours the presence of {010} faces at the growing edge, as previously discussed. Apparently, growth along the twin planes are favoured in this system, causing the branched leaf-like morphology to arise.

It is evident that even very low concentrations of silica can have an effect on the morphology produced at high temperatures. The leaves are in some ways reminiscent of the bands seen in similar experiments at higher silica concentrations. Both these morphologies have the *c*-axis perpendicular to the growth direction. All three twins are present in the bands, whereas only two are seen in each leaf. In the bands, particles of barium carbonate are present, a feature not seen in the leaves, and the silica is seen to poison all faces, causing a miniaturising effect on the crystals. In the leaves, silica is seen poisoning mainly {110} planes. Although it is difficult to draw any parallels between the two morphologies, it appears that low sodium silicate concentration and high temperatures favour witherite growth perpendicular to the *c*-axis.

As was described in Section 2.2.4.3, Kotachi et al. (2003) and (Kotachi et al., 2004) reported the formation of barium carbonate films on chitosan surfaces in the presence of silca. Those structures formed planar hexagonal subunits, which are believed to have been formed by the preferential interaction of silica on the {001} faces (see Figure 2.22). A similar reasoning can be applied in the palm tree case. The {110} faces, seen in the palm trees, have alternating layers of barium and carbonate ions. Adsorption of anionic silicate ions can effectively screen the surface charge of the barium layers thereby limiting further growth.

3.4.6 Variation in type of additive and concentration

As was discussed in Section 3.4.1, the synthesis of biomorphs under standard conditions results in globular, worm-like, helical and, occasionally, sheet-like morphologies. If the growth of these biomorphs is a colloidal phenomenon, it should be affected by the presence of additives, as colloidal interactions between carbonate and silica can be tuned by the presence of extraneous electrolytes. Recall that the colloidal stability of carbonate and silica colloids is also affected by increased ionic strength (see Section 2.3.2). Adsorption of ions at the surface reduces the screening length, which can cause flocculation at sufficiently high concentrations. Furthermore, carbonate precipitation and growth in the presence of additives can effectively alter the morphology produced. Both carbonate growth and the colloidal stability of the biomorph growing system should therefore be affected by foreign species.

In this section the effect of adding NaCl, CTAB, $LaCl_3$ and $Yb(NO_3)_3$ to the standard synthesis of biomorphs is presented. The syntheses were conducted by Matthias Kellermeier in 2005 (Kellermeier, 2005).

NaCl

In these experiments the NaCl concentration was varied between 0.5 mM - 1.0 M at pH 10.80. Upon mixing the NaCl-containing $BaCl_2$ solutions with the sodium silicate solution, the resulting reaction mixtures became slightly opaque at a total NaCl concentration $\geq$0.5 M, whereas at $\leq$0.05 M NaCl the solutions remained transparent. The resulting biomorphs were collected after 10 hours of growth.

At low NaCl concentrations (0.5 and 1.0 mM) no significant morphological difference can be seen compared to morphologies observed in the standard reference sample. Both worm-like and helical morphologies are obtained, as well as globular aggregates. The morphological variety seen in the reference sample is slightly different compared to what was reported in Section 3.4.2, in which no helical aggregates were observed at such low pH. We note that the morphological comparison reported here is with a standard experiment conducted at the same time from the same stock solution as the experiments conducted in the presence of NaCl. It is, however, important to note that slight morphological differences can occur between samples supposedly conducted using the same conditions (pH, sodium silica concentration, and $BaCl_2$ concentration).

Stronger morphological change is observed at a NaCl concentration of 0.05 M. The main morphology observed in this sample is globular aggregates that on occasion have short worm-like extrusions (see Figure 3.60). One helical aggregate showing unusual internal morphology was observed in this sample. In Figure 3.60 D-E the broken helical aggregate can be seen to be composed of overlapping twisting sheets.

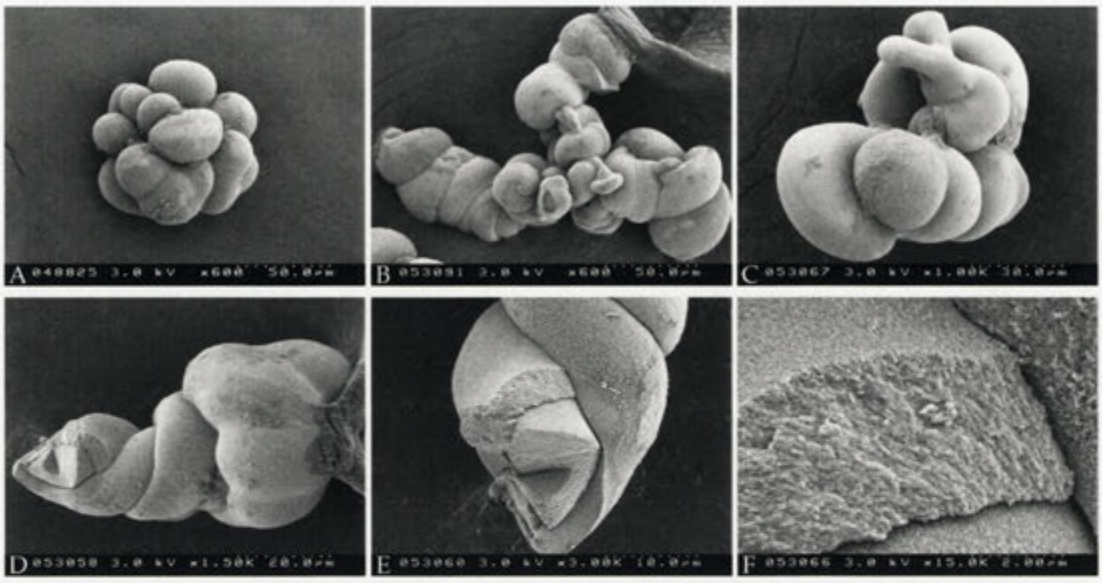

Figure 3.60: FESEM images of a aggregates synthesised at pH 10.8 with a NaCl concentration of 0.05 M after 10 hours of growth at otherwise standard conditions.

Furthermore, this aggregate does not seem to have any obvious silica skin.

The prevailing globular morphology seen at 0.05 M NaCl vanishes completely at NaCl concentrations >0.5 M. In fact, no biomorphic growth is observed at all; at least not within the 10 hours of growth allowed in these experiments. High concentrations of NaCl can evidently prevent biomorph precipitation all together. To further investigate the effect of electrolytes, we have used polyvalent electrolytes. At such high pH values, used for the biomorph synthesis, the only polyvalent additives are rare-earth salts. Their effective charge in these solutions is likely 2–3+.

Trivalent lanthanides

Both lanthanum and ytterbium occur ideally as electropositive trivalent ions; La^{3+} is similar in size to Ca^{2+} while Yb^{3+} is smaller (Shannon and Prewitt, 1969). In these sets of experiments, lanthanide concentration was varied from 0.1-1.0 mM. Upon mixing the lanthanide-containing $BaCl_2$ solutions with the sodium silicate solution, the pH is decreased with increasing lanthanide concentration. This is a likely result of the formation of lanthanide-hydroxo complexes. The lanthanide-containing silica sol was then adjusted to the pH of the reference, in this case 10.8, by the drop-wise addition of 1 M NaOH. The resulting reaction mixtures showed evidence of flocculation due to further formation of hydroxides. As a result of this flocculation, biomorphs produced under these conditions were formed within this gel-like precipitate. The reference experiment, without added lanthanide, showed normal biomorph growth at the bot-

Elemental composition of disks

Compound	La_1	Yb_1	Yb_2
Na_2O	0.92	0.67	0.96
SiO_2	4.56	4.94	1.86
Cl_2O_{-1}	-	-	0.01
BaO	61.77	60.56	63.57
Ln_2O_3	0.99	-0.22	0.14
CO_2 (calc.)	17.73	17.38	18.25
Total	85.95	83.39	84.95
Si/Ba atomic ratio	0.19	0.21	0.07

Table 3.4: EDX results (wt% oxide, Si/Ba ratio) of the surface of disks synthesised in the presence of lanthanides (Ln), either ytterbium (Yb) or lanthanum (La).

tom of the wells from transparent solutions. After 9 hours of growth, remarkable morphological differences with increasing lanthanide concentration is observed (see Figures 3.61 and 3.62).

In the lanthanum case, low concentrations (<0.325 mM) results in mainly helical aggregates with small contributions of worm-like aggregates (see Figure 3.61 A-C). These aggregates form clusters with globular centres. The double helices grow to around 90 μm in length and often show an increase in diameter towards the end. Higher lanthanum concentrations (0.55 mM) result in increasingly helical aggregates that emerge from sheet-like cores (see Figure 3.61 D and F). In Figure 3.61 D a beautiful example of how the growth of a spiral is preceded by the curling of the sheet in opposite directions can be seen. These double helices are generally slightly shorter than the ones observed at lower concentrations, and some also show evidence of imperfect growth and Liesegang ring-type patterns (see Figure 3.61 E). At even higher lanthanum concentration (> 0.775 mM) the observed morphology is dramatically changed; circular sheets or disks are almost exclusively produced. As can be seen in Figure 3.61 G-H, these disks can adopt various Gaussian curvatures, from being almost flat to large cone-like aggregates. The disks are also seen to form complex 3D aggregates of intergrown sheets. The disks have a diameter of around 60 μm and a thickness of 1.5-3.5 μm. In several cases the edge of the disk is seen to scroll over. Most disks also show Liesegang ring-type patterns as concentric rings on the surface (see Figure 3.61 I). From FESEM analyses it is also evident that the carbonate particles are elongated in the growth direction of the disk, i.e. along the radius.

Elemental EDX analysis of these disks has a Si/Ba ratio of 0.2, which in one case was

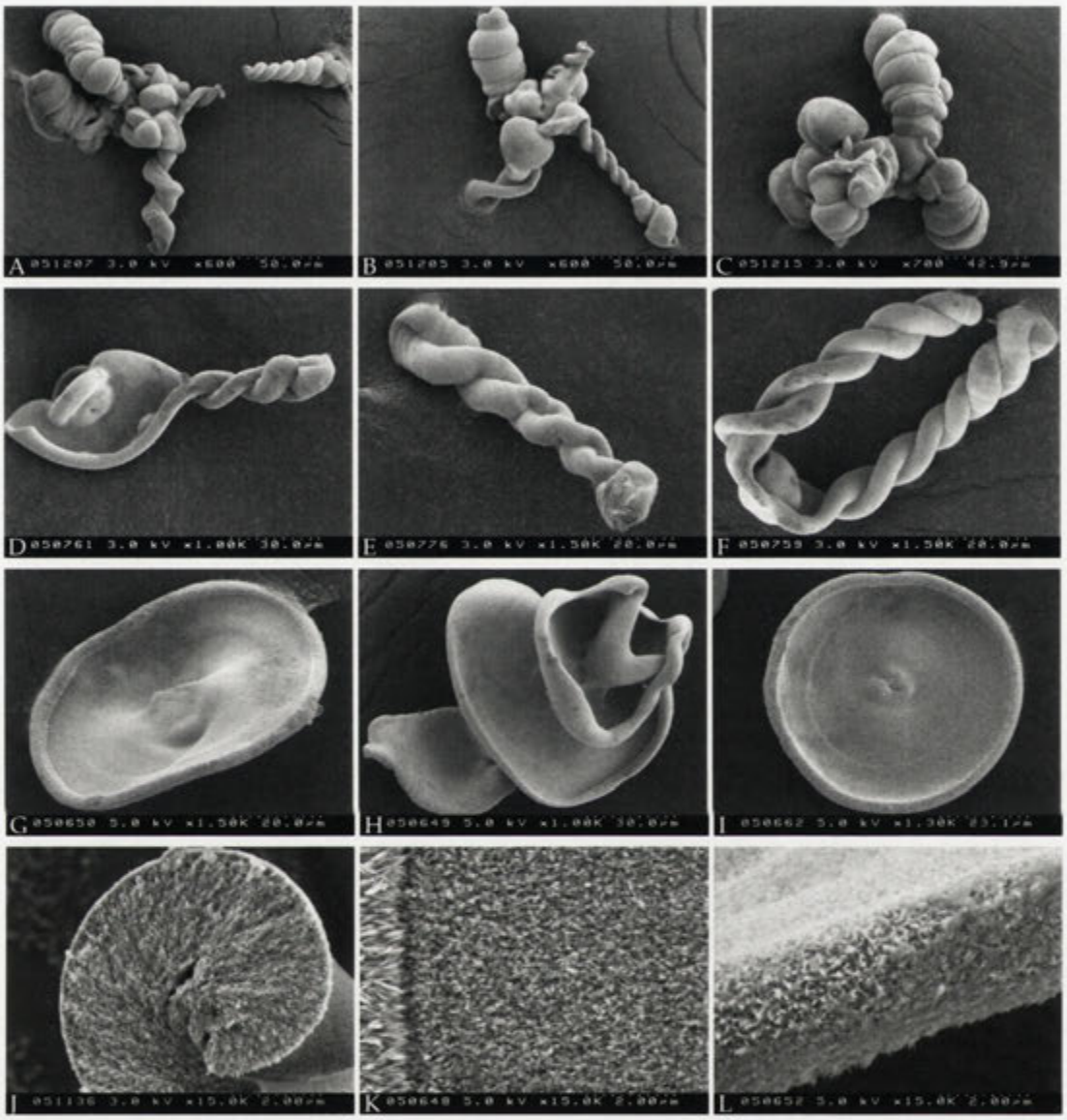

Figure 3.61: FESEM images of a aggregates synthesised at pH ~ 10.8 with different $LaCl_3$ concentrations; A-C 0.1mM, D-F 0.55 mM, and G-I 1.0 mM, at otherwise standard conditions. In J, part of a cross-section of a helical aggregates is shown. In K and L, parts of the disk surface can be seen.

seen to decrease at the edge of the disk to 0.07 (see Table 3.4). None of the aggregates analysed showed lanthanide concentrations above the ~0.2% detection limit. The reported values in Table 3.4 are all below detection limit, and in one case a negative value was obtained. Lanthanide concentrations within the aggregates are expected to be low, as very low concentrations were added to the synthesis, and the analysis in Table 3.4 confirms that this is the case if ytterbium or lanthanum are present.

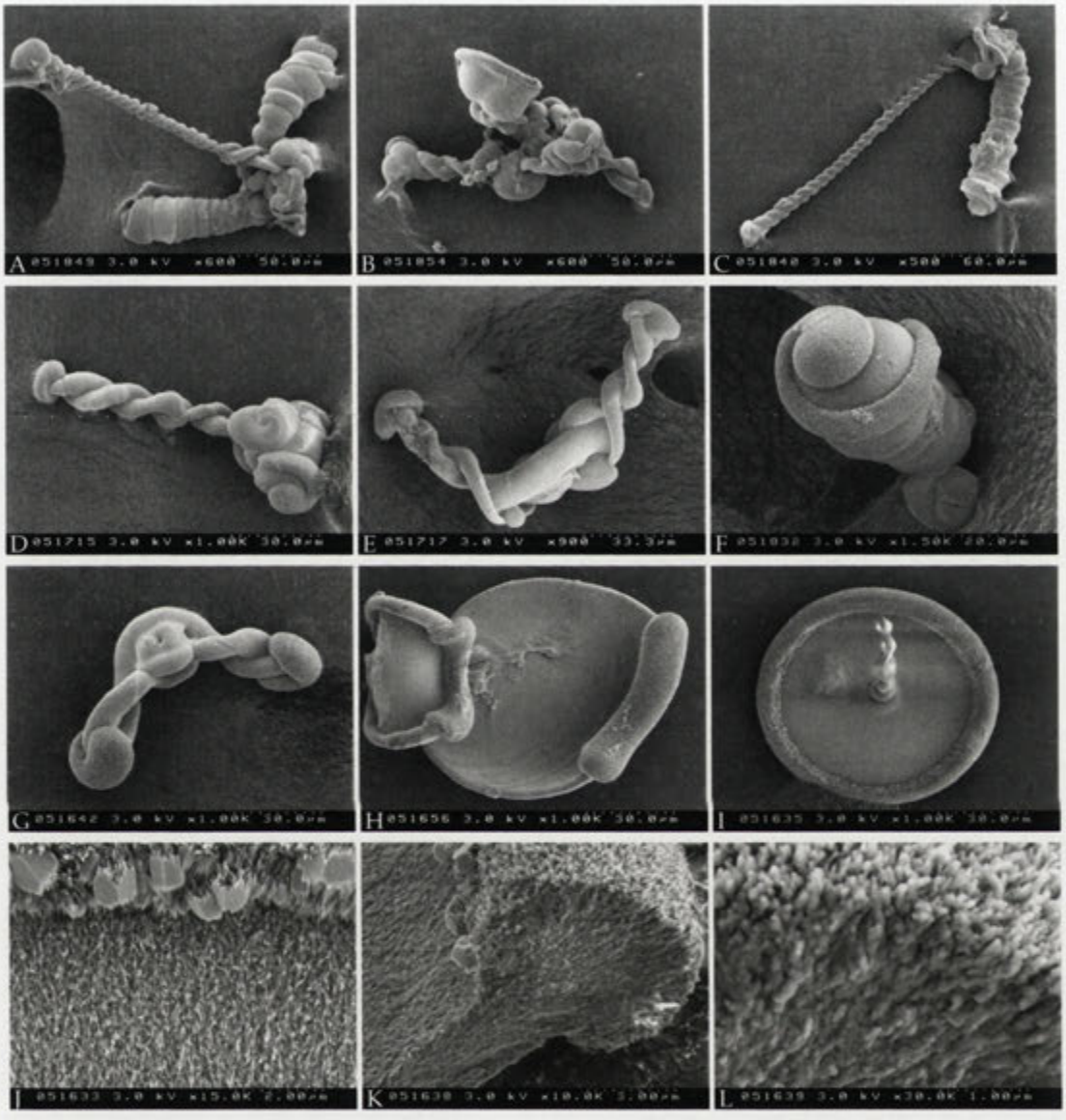

Figure 3.62: FESEM images of a aggregates synthesised at pH ~ 10.8 with different $Yb(NO_3)_3$ concentrations; A-C 0.1mM, D-F 0.55 mM, and G-L 1.0 mM, at otherwise standard conditions. In J-L details of the surface and interior of disks can be seen.

Very similar morphological evolution is seen in the ytterbium case. At low concentrations (≤0.55 mM) helical and worm-like aggregates are the dominant morphologies observed. Helical aggregates grow up to 200 μm in length, which is significantly longer than in the lanthanum case. Increasing concentration of $Yb(NO_3)_3$ yields shorter helices and worms, often seen emerging as single entities instead of clusters, as is the case at lower concentration (see Figure 3.62 A-C and D-F)). At even higher concentrations

(≥0.775 mM) disk-like aggregates are formed that have morphology comparable to the disks seen in the lanthanum case. Some of the disks produced at 1.0 mM $Yb(NO_3)_3$ have extrusions growing outward from the centre of the disk (see Figure3.62 I), while others do not show any evidence of such growth. Disks are seen to grow up to more than 100 μm in diameters, but are generally in the 60-70 μm range. As is the case with lanthanum as an additive, ytterbium also produces curved disks or sheets, which in some cases show evidence of lip-curling (see Figure 3.62 H). At 1.0 mM $Yb(NO_3)_3$ some evidence of helical growth is also seen in addition to the disks. In Figure 3.62 G it is shown that these helical aggregates are very short and not well developed. After 9 hours of growth, some of the disks show overgrowth of blocky crystals at the rim of the disk (see Figure 3.62 J). These crystals are presumably regular witherite crystals. Some of the faces of these crystals are very smooth (possibly {110}, or {010}) compared to the ragged face perpendicular to the smooth faces (possibly {021} or {012}). The interior of the disks are composed of crystallites elongated in the growth direction (see Figure 3.62 K and L).

CTAB

We have noted above that biomorph growth typically occurs at the bottom, or at the well walls, as well as on the air-solution interface. Further exploration of this propensity has been conducted by adding simple cationic surfactants that provide an electrolytic effect and a surfactant effect by likely aggregation in solution. We use CTAB, a well-explored single-chain surfactant.

As was discussed in Section 2.3.2, CTAB has an affinity for silica surfaces. The addition of CTAB to the standard synthesis reaction mixture is therefore expected to induce morphological changes, as biomorph formation is believed to be caused by a balance of interactions between carbonate and/or silica colloids. In these experiments the CTAB concentration was varied between 0.01-1.10 mM at pH 10.92. Upon mixing the CTAB-containing $BaCl_2$ solutions with the sodium silicate solution, the resulting reaction mixtures were, in all cases, free of any visible precipitate. As with most biomorph syntheses, precipitation at the air-solution interface also took place. The degree of surface precipitation decreased as the CTAB concentration increased. The morphological variety seen after 9 hours of growth in the presence of various CTAB concentrations can be seen in Figure 3.63.

At low CTAB concentrations (<0.50 mM) the morphological change is minor compared to the standard reference experiment conducted without the addition of CTAB (see Figure 3.63 A-C). It can be noted that the amount of helical aggregates are reduced and mostly overtaken by worm-like growth at 0.01 mM CTAB concentration. Increas-

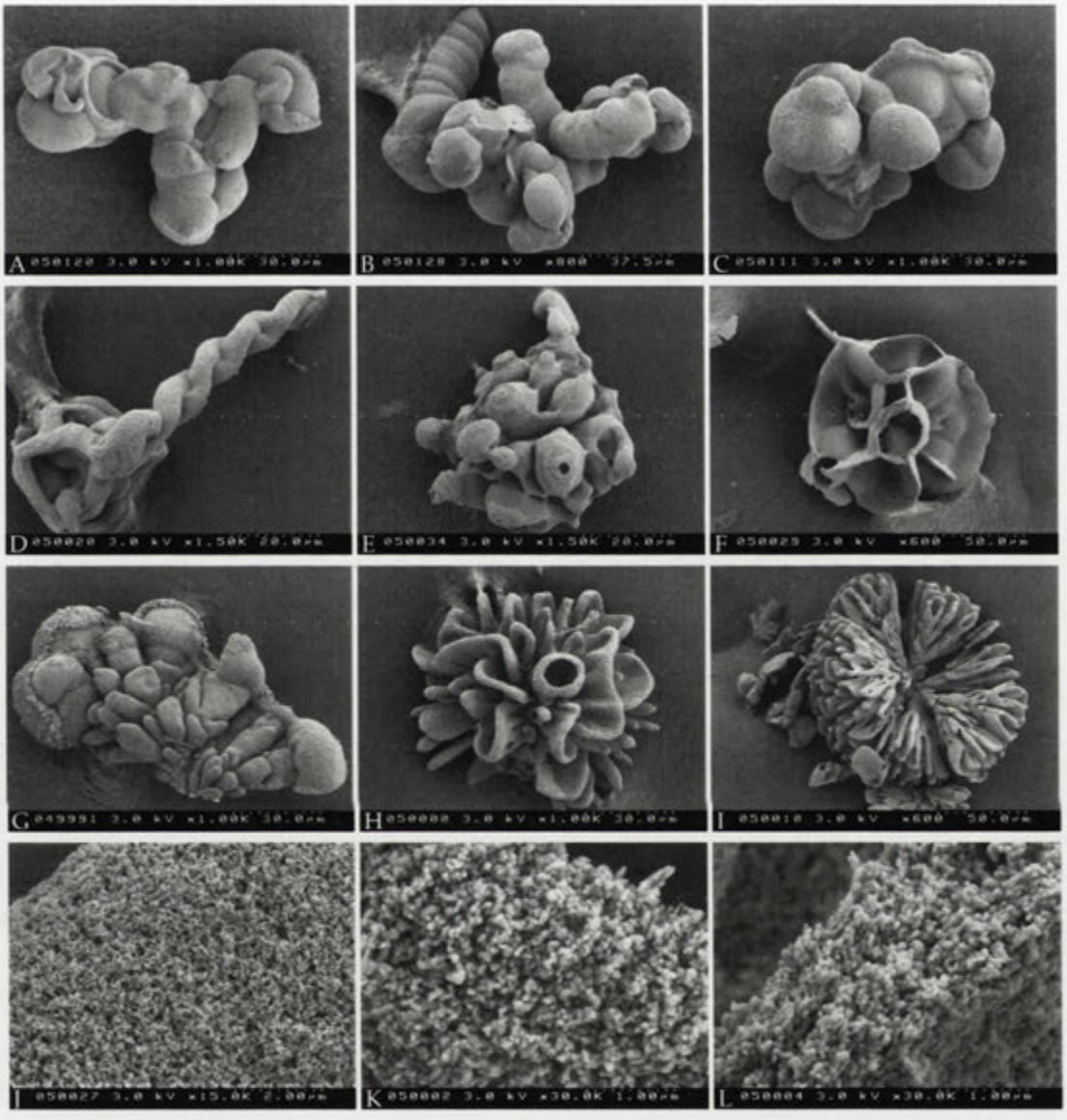

Figure 3.63: FESEM images of a aggregates synthesised at pH 10.9 with different CTAB concentrations; A-C 0.1mM, D-F, J 0.5 mM, and G-I, and K-L 1.0 mM, at otherwise standard conditions.

ing the concentration further (0.10 mM) results in shorter and less regular worms, extruding from undefinable globular aggregates. No double helices are observed in this sample.

Above a CTAB concentration of 0.5 mM more significant morphological changes are observed. Worms are diminished altogether, and growth of mainly globular, sheet-like aggregates, and occasionally helical aggregates are seen. The few helices observed

are short and irregular in nature (see Figure 3.63 D). The more common morphologies seen in this sample are aggregates that display a tendency to grow sheets. There seems to be a continuous variation from globular to floral spherulite-type aggregates at 0.5 mM CTAB concentration. At even higher concentrations (1.0 mM) this tendency is more pronounced.

It is clear from Figure 3.63 G-H that CTAB concentrations of 1.0 mM induce a large morphological change in the biomorphs produced. Aggregates produced during these conditions display a wide range of morphologies, from raspberry-like to aggregates having a morphology very similar to floral spherulites (compare Figure 3.35), or corals synthesised at high temperatures (compare Figure 3.46 A and B) (see Figure 3.63 H and I). Globular aggregates are composed of increasingly smaller globular entities towards the interior of the aggregates (see Figure 3.63 G), resulting in a 'tree' of globules with branching morphology.

FESEM analyses of aggregates produced in the presence of CTAB also reveal the rough porous surface texture and easily visible particles that are the building blocks of these aggregates (see Figure 3.63 J-L). No silica skin is recognisable on any of the aggregates analysed. This is further confirmed by the dissolution of the carbonate entity by a 0.01 M acetic acid, which results in complete dissolution of the entire aggregates. No silica skin is observed after such treatment. However, as has been previously discussed, it seems that excessive cleaning of biomorphic aggregates can etch the structure. The porous nature of these aggregates indicates that some of the silica could have been dissolved during the cleanup procedure.

As is evident in Figure 3.63 the presence of CTAB can efficiently alter the developing morphology at concentrations above ~ 0.5 mM.

Discussion

As is evident in Figures 3.63, 3.61, and 3.62, additives clearly exert a morphological change in aggregates synthesised using otherwise standard conditions. The specific type of additive further induces specific morphologies, which in the lanthanide case are unique. Perfectly concentric disks, such as those seen in Figure 3.61 G and I, have not been encountered in any of the biomorph systems studied so far. The specific effects induced by additives are not straightforward, and some discussion on how this effect is manifested in the biomorphs synthesised is in order. In this section a brief discussion is given regarding the possible cause of morphological change seen by each additive.

The effect of adding salt to the biomorph synthesis mixture increases the ionic strength of the solution, which affects both carbonate and silicate chemistry. As dis-

cussed in Section 2.2.4.2, higher ionic strength reduces the activities of all solutes and therefore affects carbonate precipitation thermodynamics, kinetics and morphology. Additives can adsorb on the crystal surfaces at high energy sites which reduces crystallisation rates and also affects the way the crystal grows. The colloidal stability of carbonate and silica colloids is also affected by increased ionic strength (see Section 2.3.2). Adsorption of ions at the surface reduces the screening length, which can cause flocculation at sufficiently high concentrations.

The details of interactions present in the biomorph producing system are difficult to assess as it is a very complex, undefined, mixture of carbonate and silicate species in solutions whose composition changes with time. However, as the biomorphs produced contain both silica and crystalline barium carbonate, one can generalise the interactions to these two components. First, the additive can interact with silicate species, which effectively reduces the silicate concentration available for biomorph precipitation. Furthermore, such interactions can also occur with barium and carbonate species, which also reduces the activity of these ions. Second, additives can adsorb on the witherite crystal surface, effectively changing the interactions between the crystals and the silicate species. Third, the presence of the additives can affect the growth of the aggregate in that it adsorbs on specific surfaces of the biomorph, thereby directing the morphology of the aggregate. Poisoning of growth in certain directions is then expected. All of these interactions should be considered in relating the morphological change seen in the presence of the additives studies here.

Cationic interaction with especially anionic silicate species will, at sufficient concentrations, induce polymerisation and silicate flocculation. For instance, the addition of high concentrations of NaCl or lanthanides results in clouding of the silicate sol. This clouding can be caused by either hydroxide or silicate precipitation.

In the NaCl case sodium silicate precipitation is more likely as the corresponding hydroxide is soluble. In such a scenario competing interactions of Na and Ba with available slilicate species most likely produce an undefinable silicate mixture. At high NaCl concentrations the Na-silicate interaction is likely to overcome that of the barium even though barium is divalent. The development of globular aggregates at 0.05 M NaCl concentrations is consistent with low silica concentrations and low pH (see Figure 3.28). This could indicate that the effective silica concentration is significantly reduced at such high concentrations. Even higher concentrations resulted in complete inhibition of biomorph growth, which further points towards a drastic drop in soluble silicate species. Adsorbed Na on colloidal witherite or silica will reduce the electrostatic repulsive force, which can aid the interaction between these colloids.

In the lanthanide case on the other hand, both hydroxide and silicate complexation can occur. As mentioned in Section 2.3.2 La^{3+} have been shown to have a very high

affinity for silica and can cause flocculation at low concentrations. Furthermore, lanthanides can also form complexes with both carbonate and hydroxide species at high pH (Lee and Byrne, 1992), which further makes it difficult to assess the specific causes for the morphogenesis seen in these samples. As was also mentioned in Section 2.2.4.1, lanthanum can at very low concentrations (μmol) inhibit calcium carbonate precipitation, which is believed to be caused by surface adsorption of the trivalent lanthanum ions. In the system studied here, $Ln(CO_3)_2^-$, $Ln(CO_3)^+$, and the hydroxy complexes $Ln(OH)_{1-3}^{0-2+}$ are expected to be present in various amounts. The activity of the lanthanide counterion will therefore be reduced. Free Ln^{3+} is highly unlikely at the high pH present in the silicate sols used for biomorph precipitation. Regardless of which lanthanide state is prevailing (silicate-, hydroxide-, or carbonate complex), the morphological change seen asserted by lanthanum and ytterbium is very similar. The morphological effect observed increases with lanthanide concentration, suggesting that these ions or complexes increasingly interfere in the process giving rise to the biomorph morphology. Increasing lanthanide concentration first induces helical aggregates over worm-like biomorphs, which at even higher concentrations almost exclusively result in disk-shaped aggregates, whose composition is similar to standard worm-like and helical aggregates reported in Section 3.4.2. However, the disks observed here do not seem to be encased in a silica skin. This may suggests that the lanthanide present affects the self-assembly process by electrostatic interactions with witherite crystallites or silica species or colloids, which somehow effectively stabilises the growth of sheets or disks. These disks are morphologically very similar to the calcitic disk-like aggregates described in Section 2.2.4.3 (see Figure 2.16). The systems producing the disk-like morphologies are very different; the calcitic disks were produced in the presence of double hydrophilic block copolymers (DHBCs), whereas in our case a complex silicate mixture involving unidentified lanthanide complexes are causing the growth of aragonite-type disks. It is therefore very difficult to draw any parallels between the two systems other than to conclude that similar morphologies are formed. No definitive reason for the formation of these disks can be given at this time.

In the CTAB case, hydrophobic interactions need to be considered in addition to pure electrostatic interactions. As described in Section 2.3.2 adsoption of CTAB on silica is substantial well below CMC. Though we have not measured the CMC for CTAB in biomorphic solutions, it is reduced at high ionic strength, and likely to be below 0.9 mM (CMC for CTAB in pure water) and possibly below 0.125 mM (CMC for CTAB in 10 mM KBr). It is possible to interpret the morphological evolution seen in biomorphs in respect to CTAB concentration as an effect of surface charge and adsorption (see Section 2.3.2).

Compared to standard experiments without CTAB, low concentrations of CTAB (0.10 mM) largely result in globular aggregates with small contributions of worm-like aggregates (see Figure 3.63) A-C). Increasing the CTAB concentrations results in increasingly sheet-like growth, which at 1.0 mM develops into floral-spherulite-type aggregates. These structures are similar to the ones produced at 0.5 M $BaCl_2$ (see Figure 3.35) or at high temperature (see Figure 3.46). This sequence observed with increasing CTAB concentration evidently results in an increase in the total surface area of the biomorphs. For instance, the globular aggregate seen in Figure 3.63 C has significantly less surface area compared to the aggregate seen in Figure 3.63 H. As previously discussed, CTAB has a great affinity for silica surfaces. The degree of adsorption of CTAB depends on the concentration available in solution relative to the CMC. In our systems, the actual concentration in solution will be influenced by the surface area available for adsorption. A simple calculation reveals that a considerable proportion of the available CTAB is present as adsorbed species effectively lowering the CTAB concentration in solution. In all cases, CTAB adsorption will change the charge and hydrophobicity of the silica surface. At low CTAB concentrations, the surface is hydrophobic and charge neutral (see Figure 2.30 scheme B). The hydrophobic nature of such a surface will favour morphologies that minimise surface area. Such a scenario could explain the globular morphologies observed at low CTAB concentration. These globular aggregates have less surface area compared to the extended double helices and worms that otherwise occur under standard conditions, in the absence of CTAB. Electrostatic adsorption of CTAB generates a hydrophobic neutral surface, which drastically reduces the surface potential. Both the surface of biomorphs and other anionic aggregates such as silica colloids would be affected by adsorbing CTAB. Increasing concentration of CTAB results in surface charge reversal, leaving the surface cationic and hydrophilic. This increasingly cationic hydrophilic surface will result in fractal surfaces as growth is prevented in valleys by electrostatic repulsion. Surfaces with positive Gaussian curvature will therefore preferentially grow. Such a scenario could account for the change in morphology to higher surface area to volume seen at higher CTAB concentrations. At concentrations close to CMC, the surface is covered with admicelles and the cationic charge is at a maximum, which can explain the highly dendritic and open structures seen at 1.0 mM.

So far, the discussion has only been related to the actual structure directing effect as a response to surface charge. In the biomorph system, the initial conditions upon mixing the CTAB enriched $BaCl_2$ solution with the sodium silicate solution could also be affected by varying the CTAB concentration. No large scale flocculation was observed in any of the solutions, irrespective of CTAB concentration, possibly indicating that the initial conditions are superficially constant in all experiments. CTAB effectively

competes with divalent barium ions for anionic silicate species and colloids present. Due to the very high initial concentration of $BaCl_2$ compared to CTAB in all the experiments, as well as the divalent charge on the barium ions, it is believed that barium-silicate interactions will out-compete the CTAB-silicate during the first stages of synthesis. As the carbonate concentration is increased, barium carbonate will eventually form, leaving CTAB to interact with both carbonate and silicate. Due to the fast exchange of the small amount of adsorbed CTAB and the large positive Gaussian curvature of nano-sized carbonate or silica particles, the interactions between such particles will not be greatly affected by the presence of CTAB. The total surface area free to interact with CTAB increases with time, as the number of aggregates (biomorphs, colloidal silica and carbonate) increases with time. The progressive morphological development seen when increasing the CTAB concentration, indicates that whatever the state of the adsorbed CTAB, it is clear that milli molar concentrations have a great effect on biomorph morphology. This lends us to believe that the nature of the biomorphs surface, i.e. charge and hydrophobicity, may be important for the development of specific morphologies.

The experiments presented in this section further confirm the importance of electrostatic interactions between Ba^{2+}, CO_3^{2-}, and anionic silicate species, and the aggregate for the biomorph morphogenesis.

3.4.7 Variation in silicate source

This chapter has so far been concerned with biomorphs produced using sodium silicate solutions. Under certain unknown conditions, the morphology developed using standard conditions are not always exactly the same. Several possible explanations for this occasional non-reproducible character can be identified, of which one is the source of silica. Concentrated sodium silicate solutions contain ~ 27% SiO_2 and ~14 % NaOH, and its chemistry is complex as it is composed of an undefinable mixture of silicate species. The age of water glass solutions is expected to change with time, as adsorption of carbon dioxide from the air will affect the pH and therefore its chemistry. As has been shown in this chapter, pH and silica concentration is crucially important for morphogenesis of biomorphs, and as such, investigations into other silica sources, whose chemistry is more well-defined, is equally important. As already mentioned in Chapter 1, using silica gels is one way to produce biomorphs. However, it is very difficult to follow the chemistry of individual biomorph morphologies with time as growth of a wide range of morphologies are seen in a single experiment. Solution based experiments is therefore an advantage, as has been shown in this chapter. The most natural choice of silica source is tetraalkoxysilanes ($Si(OR)_4$). These are available

pure, easily dissolve in water-miscible organic solvents such as ethanol, but hydrolyse readily in water to produce silicates and only alcohols as byproducts, which are easily removed. These materials are commonly used in the synthesis of mesoporous silicates (see Section 2.3.3).

Series of experiments have recently been conducted by Matthias Kellermeier and Alina Voinescu that show that biomorph synthesis using TEOS indeed produces the same morphologies as described in this dissertation. These experiments were conducted in the presence of ethanol, so as to increase the solubility of TEOS, which was fully hydrolysed before mixing with $BaCl_2$ solutions. Ethanol (EtOH) is also produced during the hydrolysation of TEOS. In that sense, the addition of EtOH may be unnecessary for the sake of TEOS hydrolysis. As was described in Section 2.2.4.3, alcohol can affect carbonate precipitation. This is also the case in biomorph synthesis. The presence of alcohol during the precipitation does significantly affect the specific morphologies produced (Voinescu et al., 2006a). High EtOH concentrations (≥5 vol%) result in mainly large globular aggregates in the 100-150 μ range. Also evident at high EtOH concentrations is the increase in nucleation points that give rise to biomorphic growth.

3.4.8 Variation in metal carbonate

So far, biomorphs synthesised with barium as the carbonate cation has been discussed. Considering the different solubilities of the aragonite-type carbonates and their different interaction with soluble silicates, one would expect a difference in the morphologies produced between the different alkaline earth carbonates. In this section, preliminary results are presented concerning the use of strontium and calcium as carbonate cations during biomorph synthesis.

At high concentration of $SrCl_2$, the morphologies produced are very similar to the $BaCO_3$ biomorphs. Floral spherulites with their interconnected sheets are produced at 0.5 M $SrCl_2$ concentration. The growth of these morphologies was described in Section 3.4.4, and the Sr case shows a similar growth pattern, as can be seen in Figure 3.64. The growth rate, calculated by the diameter of the aggregate, is linear during the early stages of growth, and decreases with time. For example, floral spherulite 1 in Figure 3.64 has an initial growth rate of 0.37 μm/min, compared to 0.24 μm/min for aggregate 5. However, the growth rates are steadily reduced with increasing time for all aggregates, and are at any one time similar in all the aggregates irrespective of when the aggregate started growing.

At lower concentrations of $SrCl_2$, different growth patterns evolve compared to the $BaCl_2$ case. Studies made by Alina Voinescu have shown that floral spherulite-

type morphologies develop that, with time, develop helical aggregates at the tips of the sheets.This behaviour is very similar to the gel-grown strontianite biomorphs as reported by (Terada et al., 2003) (see Chapter 1). Those were, however, grown at 1.0 M $SrCl_2$. Strontium carbonate is less soluble than barium carbonate, which could then be related to the morphological effect observed. More experimental investigations are needed to show such correlation.

As calcium carbonate, specifically in the aragonite form, is a major biomineralisation material that is known to produce the most intricate morphologies (see Section 2.4), the prospect of forming biomorphic materials with calcium carbonate is of considerable interest. Using $CaCl_2$ in the alkaline sodium silicate solutions at variable pH at room temperature gives rise to calcite crystals, easily identifiable by their rhombohedral nature. However, on very rare occasions, morphologies reminiscent of floral spherulites have been spotted. The reproducibility of these morphologies is very low, and therefore no detailed analysis of these structures was performed. Recently, Alina Voinescu and Matthias Kellermeier (Voinescu et al., 2006b) have reproducibly produced both floral spherulite-type morphologies and dumbbells in experiments at high temperature (80 °C) using TEOS as silica source. These morphologies consist of densely packed aragonite crystallites encased in a silica, similar to biomorph morphologies in general. Higher temperature favours the formation of aragonite over calcite, which seems to be a requirement for the synthesis of silica-carbonate morphologies. This suggests that the synthesis of biomorphs is related to the crystal structure of the carbonate in question.

It is therefore shown that biomorphs can be produced with aragonite-type carbonates, although the specific morphology produced will be determined by the specific chemical and physical interactions between the species in solution. Some plausible mechanisms of formation of biomorphis materials will be discussed in the next chapter.

3.5 Discussion

This chapter has explored the morphological changes observed upon changing pH, concentration of the reacting species, and temperature. The great variety of morphologies observed reflects the complex nature of biomorph formation. To summarise the effects observed, the following points can be made:

- *pH* effects both carbonate and silica solubility, and the morphological changes observed with varying initial pH should be related to such changes. High pH results in an increased number of growing aggregates, and smaller and more varied morphologies that are somewhat enriched in silica as compared to low

pH conditions. The number of nucleation points is related to the supersaturation state of the biomorph nuclei, which may be controlled by the carbon dioxide absorption and conversion to aqueous carbonate species. This reduces the pH with time, which affects the concentration and speciation of silica in solution. The lower the pH, the greater the relative presence of polynuclear silica species with less anionic character. As such, the silica-enriched morphologies produced at high pH can reflect the increased anionic nature and of available silica able to interact with precipitating barium carbonate. The morphological change observed with increasing pH can be described as an increase in aggregate dimensionality; low pH produces globular aggregates of 3D structure. At higher pH, increasingly sheet-like and more branching structures are produced.

- *Sodium silicate concentration* has also been shown to affect the morphologies produced. A decrease in concentration results in more nucleation points, and smaller aggregates. As in the case of pH, the morphological evolution with a deacrease in sodium silicate concentration can be described as an increase in the dimension of the aggregates. Pinnacles, which are produced at low concentrations are The pH change observed is also greater, possibly reflecting the decreased buffering capacity of silica at low concentrations. Less visible barium-silicate precipitation is evident at lower sodium silicate concentrations, and the silicate species available in solution will therefore depend on the effective interaction with Ba^{2+}.

- *Barium chloride concentration* affects the number of actively growing aggregates. Higher concentrations result in an increase in nucleation density, which show increasing floral spherulite-like character. More initial precipitation of presumably amorphous barium silicates is also evident at higher concentrations. This phase may serve as a resource of reactants to sustain the growth biomorphic aggregates. The growth behaviour of floral spherulites is related to that of dumbbells, which are the earliest forms observed. Preferential growth along rims of such aggregates leads to the development of interconnected sheets, consisting of nanocrystalline carbonate particles aligned parallel to the growth direction.

- *Temperature;* increasing temperature produces increasingly sheet-like and branching aggregates and growth proceeds much faster than at lower temperatures. The morphological evolution observed with increasing temperature can be described as an increase in the aggregate dimensionality as follows; globular (low T) 3D; helical- and worm-like aggregates (RT) >2D; sheets ~2D, bands ~1D and corals <3D (70 ° C. Helical aggregates are not present at 70° C within the 3 h time-frame analysed. These morphologies are most prominent at 45° C. High temperature

experiments conducted with low sodium silicate concentration result in the development of palm trees. These morphologies are characterised by the growth of extended leaves from a central stem. These leaves exhibit a 6-fold rotational symmetry around this stem. In contrast to the other morphologies described in this chapter, palm trees are not polycrystalline. They consist single crystal, in which each leaf contain two twin orientations. The large faces of the leaves correspond to {110}faces, which are believed to be inhibited to further growth by the preferential adsorption of silicate species.

- *Additives* can effectively alter the growth of specific morphologies. This is especially the case for CTAB, and lanthanum and ytterbium salts. At present, it is not clear how the additives affects the morphology, but it may be related to surface adsorption and surface charge effects, or to interaction with available silicate species.

- *Metal carbonate;* the type of alkaline earth carbonate precipitated also has an effect on the morphology produced, depending on the reaction conditions. High concentrations of Sr result in floral spherulites, as is the case for barium carbonate biomorphs. At lower concentrations, a different growth patterns is observed; floral spherulites are initially produced that grow helical protrusions from the edge of the sheets. This suggests that the solubility of the alkaline earth carbonate is important for the growth of specific morphologies. In the Ca case, the aragonite polymorph of $CaCO_3$ gives rise to biomorphic aggregates. This signifies that crystal structure is important for biomorph growth.

In the next chapter, investigations into the nature of particles observed in the solution with time is given, as well as discussions regarding possible biomorph formation mechanisms.

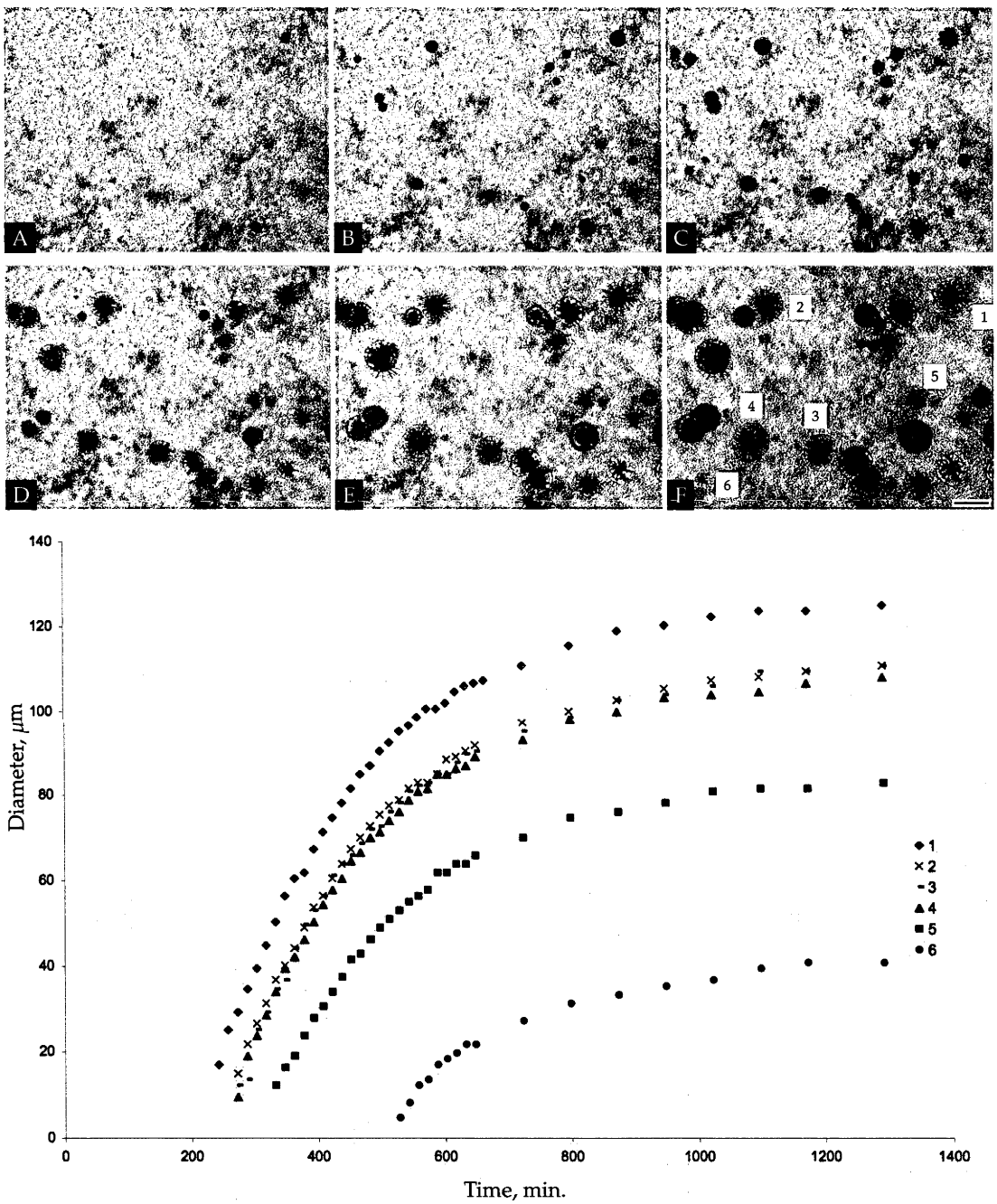

Figure 3.64: Time series of floral spherulites growth (A-F), and a graph displaying measurements of aggregate diameter (1-6) with time as defined in F under the following initial conditions: 0.5 M $SrCl_2$, 7.4 mM SiO_2, pH 10.2, room temperature. Scale bar in F image is 100 μm.

Chapter 4

Nucleation and growth of biomorphs

4.1 Introduction

The morphologies of silica-carbonate biomorphs are extremely varied, as seen in the previous chapter. Although these morphologies are different in shape and size, they are all composed of crystalline barium carbonate and amorphous silicate. It is likely that full analysis of the reaction medium will give clues to the nature and concentrations of the reacting species, which in turn can aid the development of a reaction mechanism for these biomorphic structures. In this chapter, results concerning the solutions, from which the various biomorphs grow, are analysed with the help of Transmission Electron Microscopy (TEM), Dynamic Light Scattering (DLS), Attenuated Total Reflectance Infrared Spectroscopy (ATR IR) and ^{29}Si Nuclear Magnetic resonance (NMR). The objective was to deduce the distribution of chemical species and particles in the solutions, and their change during biomorph synthesis. I conclude this chapter with a discussion on possible formation mechanisms based around chemical and morphological arguments.

4.2 Materials and Methods

All silicate solutions were prepared by diluting concentrated sodium silicate solution (Aldrich, reagent grade) with distilled water (MilliporeQ) and 0.1M NaOH. Subsequent mixing with $BaCl_2$ solutions of various concentrations yield the reacting solutions for biomorph synthesis as described in the previous chapter (see Chapter 3). The particles forming in the sol during mixing of the silicate and the alkaline earth metal solution were analysed regarding size and shape with both dynamic light scattering (DLS) and TEM. The DLS experiments were conducted on a Malvern Autosizer 4700 by David Dunstan at the Department of Chemical and Biomolecular Engineering, the

University of Melbourne.

The speciation of silicate and carbonate was analysed using ^{29}Si NMR and IR spectroscopy. IR spectra were obtained using a Mettler Toledo ReactIR 4000 spectrometer using a diamond composite attenuated total reflection probe was used to asses the chemical composition of the solutions. 256 scans at a resolution of 4 cm^{-1} were collected for each sample. All spectra were obtained by subtracting a pure water spectrum from the sample spectrum.

For TEM analyses, copper grids were made hydrophilic, thus facilitating easy spreading of aqueous solutions, by treatment in a Emitech Glow Discharge Unit operating at 15 mA for 2 minutes. A drop of solution was then placed on the grid and with the use of a filter paper the superfluous solution was absorbed from the grid, leaving a thin film of solution on the grid which was left to dry. No staining was needed to view the particles in the TEM. Two different transmission electron microscopes were used. A Hitachi H7100FA TEM operating at 75 kV was used to image the particles extracted from solution. A SIS Megaview III Widefield CCD camera (1300 x 1024 pixel, 12 bit) was used to collect the images. Some samples were also characterised by electron diffraction and elemental analyses, using a Philips EM430 TEM, operating at 300 kV, and equipped with Oxford ISIS EDXA.

4.3 Particle analyses

From the previous chapter, it is clear that pH, temperature and concentration have a strong effect on the morphology produced. High initial pH induces an increase in the density of biomorph nucleation sites, which results in smaller biomorphs. There is an associated increased drop in pH during growth, Δ_{pH}. The morphology produced is also increasingly sheet- and pinnacle-like, which can be seen as an effective decrease in the degree of dimensionality of the morphology with an increase in pH. At low pH, on the other hand, globular morphologies are produced. Using a low initial pH also produces less actively growing biomorphs, and a smaller Δ_{pH} is evident. The reaction temperature also has an effect on the morphologies produced. Proceeding from low to high temperature, one can see the following sequence of morphology development: globular to a mixture of globular, helical, and worm-like morphologies to helical and sheet-like morphologies to a complex mixture of sheets, bands and coral-type morphologies at high temperature (see Figure 3.52).

Another factor affecting the morphology is the concentration of sodium silicate. Low concentrations give rise to increasingly pinnacle-like morphologies that evolve from a large number of nucleation sites. Δ_{pH} observed after growth is larger at low sodium silicate concentrations. Increasing the sodium silicate concentration results in

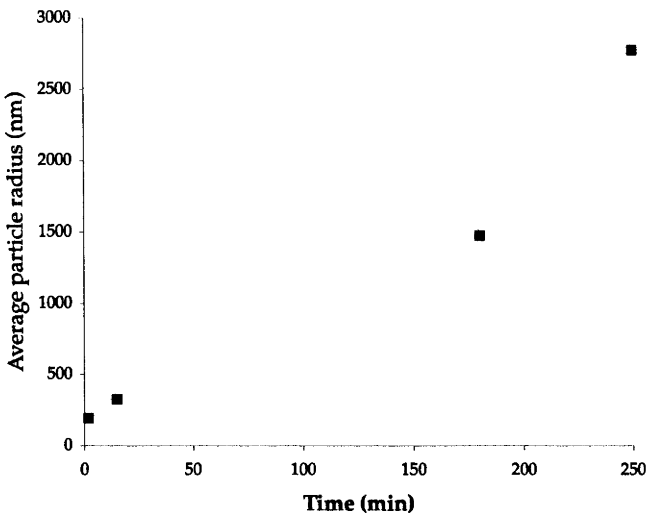

Figure 4.1: Particle size observed (DLS) with time in solutions used for the standard synthesis of biomorphs. Analysis conducted using the Malvern Autosizer 4700 at a scattering angle of 90 °.

increasingly globular morphologies with a decrease in the Δ_{pH}. At high concentrations of sodium silicate, early precipitation of a flocculate is evident during the first minutes after mixing the solutions. This effect is also evident at higher $BaCl_2$ concentrations. Even at standard conditions, flocculation occurs as soon as the sodium silicate solution is mixed with that of the $BaCl_2$. This is invisible to the naked eye, but is evident from light scattering and TEM analysis of the sols.

Dynamic light scattering investigations show the presence and growth of particles in the reaction mixtures with time. In Figure 4.1 it is evident that particles of a couple of hundreds of nanometres in radius form as soon as the $BaCl_2$ is in contact with the silicate solution. These particles continue to grow to considerable sizes of several micro metres over time. Higher $BaCl_2$ concentrations result in a quicker growth of large particles compared to the standard conditions. At lower concentrations of $BaCl_2$, a longer time is needed to reach a given particle size.

From TEM analysis of the solutions with time, it is evident that particles are formed instantaneously after mixing. In Figure 4.2, TEM images reveal that the particles observed 5 minutes after mixing, as observed with DLS, are a conglomerate of smaller globular particles that form a dendritic network, similar to that of diffusion limited aggregation of particles (see Section 2.5). These globular particles generally have a diameter in the 30-40 nm range, and are believed to be primary particles of the flocculated material. Some of these particles show a darker core region and the presence of smaller ~10 nm surface features (see Figure 4.2 C and E). After 2 hours,

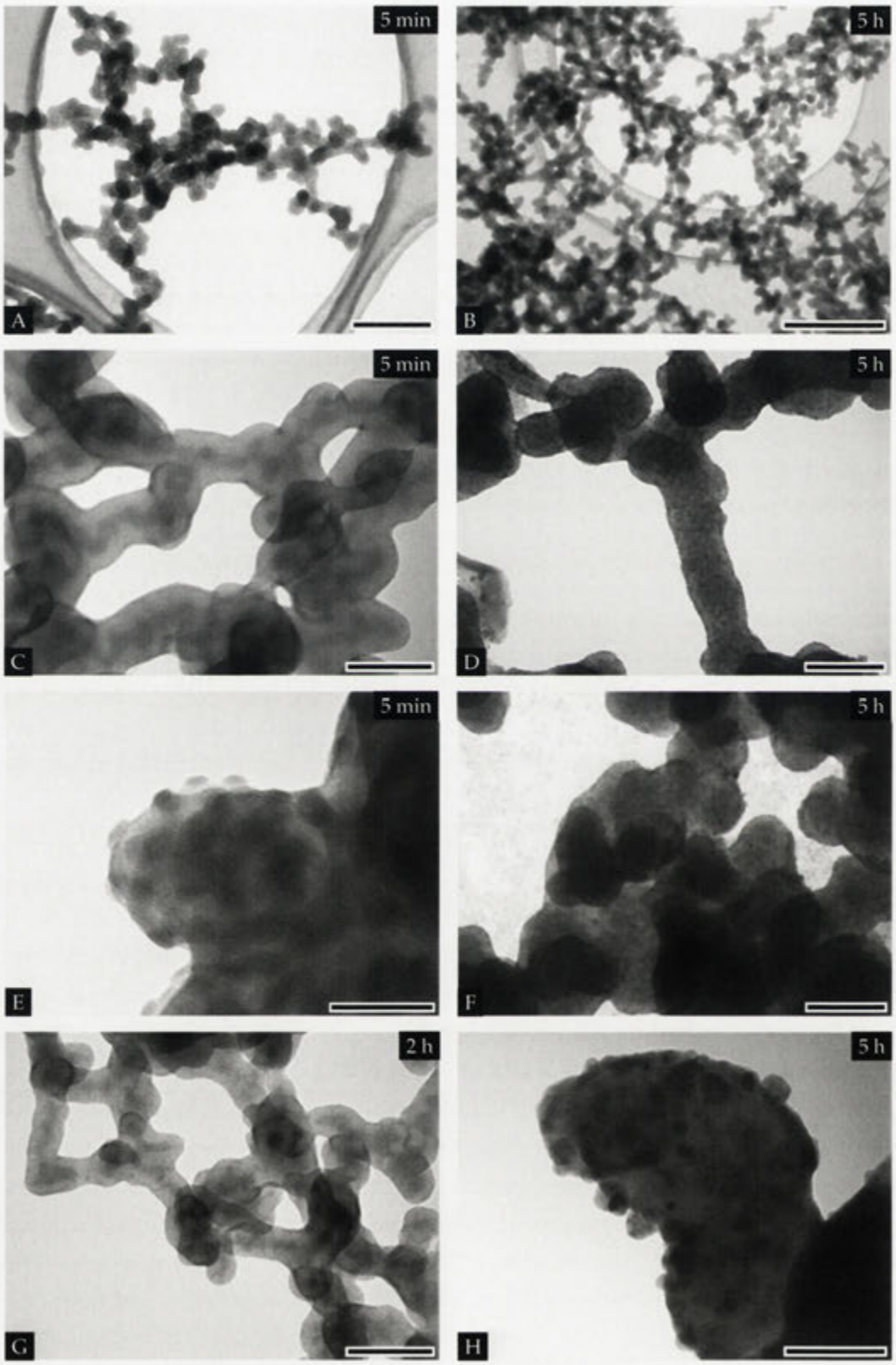

Figure 4.2: TEM images of particles extracted from the solution between 5 minutes and 5 hours after mixing, as indicated in the images. Scale bars; A 200 nm; B 300 nm; C 50 nm; D 100 nm; E 30 nm; F 100 nm; G–H 50 nm.

more particulate material is deposited on the grid compared to the 5 minute sample. Similar to the particles observed after 5 minutes, darker core regions are also observed in particles in the 2 hour sample (Figure 4.2 G). With increasing time, the particles observed show increasingly wider size distributions. After 5 hours of growth, a bimodal distribution of particle sizes is observed. Smaller and also brighter particles in the 15-30 nm range are seen (see Figure 4.2 B) as well as larger and darker particles with a diameter in the 70-100 nm range (see Figure 4.2 D and F) are seen. Many of these particles also contain smaller (5-15 nm) globular particles on the surface (Figure 4.2 H). However, as can be seen in Figure 4.2 F, the carbon film also shows evidence of similar features, suggesting that they may not be an integral part the primary particles. 6 hours after the synthesis experiment begun, three different particles sizes are noted (see Figure 4.3 A); large (100–150 nm), medium (50–70nm), and small (35–50nm). These different particles are compared in Figure 4.3 B–D. All these particles contain darker core regions, as also noted for other particles extracted at different times. The larger particles show a 'striped' pattern (see Figure 4.3 B), whereas the medium and smaller sizes particles have a single dark core. This single dark core is further seen to be continuous across particle intersections and branches between adhering particles (see Figure 4.3 C and D). In cases where a junction adopts a bottle-neck configuration, no dark core is seen. It is further noted that the size of the core in relation to the particle size is constant (~0.3-0.4).

In a different sample, synthesised under the same conditions and extracted after 6 hours, no such dark core regions could be observed. Instead, most particles show the presence of the nm sized particles on the surfaces (see Figure 4.3 E and F), as also observed in other samples (see Figure 4.2 H). Both features could be related to contamination or drying effects. The presence of nm-sized particles attached to the aggregates and the carbon film can either be interpreted as evidence of smaller particles in the sol that are deposited during sample preparation, or an effect related to drying of an aqueous film covering the particles. The presence of such films is suggested in Figure 4.3 E where it is seen connecting between two particles. A scenario for the formation of particles containing dark cores and striped patterns is that the particles have formed by the initial precipitation of a barium-rich phase (dark) that is later covered by a silicate phase that is depleted in barium relative to the darker inner core. The large striped particles, seen in Figure 4.3 B, can therefore be interpreted as having formed by episodical precipitation of barium-rich and barium-poor silicate. Each dark 'stripe' then represents a shell of a silicate phase rich in barium. As the cores generally have constant diameter in relation to that of the host particle, another explanation for this feature could possibly be related to partial drying of Ba-rich aqueous particles. During evaporation, the drying front will propagate towards the

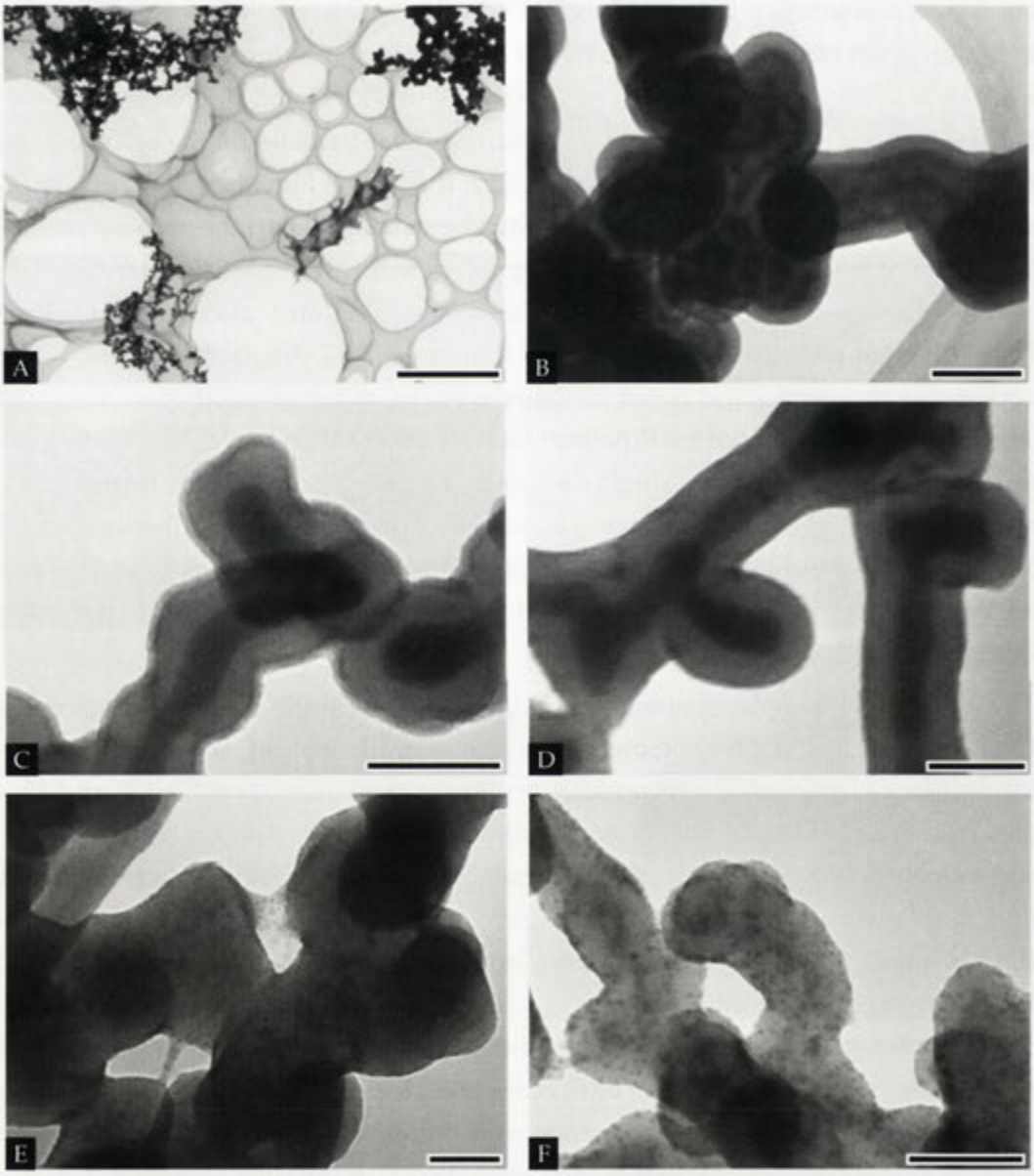

Figure 4.3: TEM images of particles extracted from the solution 6 hours after mixing, showing three different particle sizes as seen in A. Scale bars; A 2 μm; B 100 nm; C–F 50 nm.

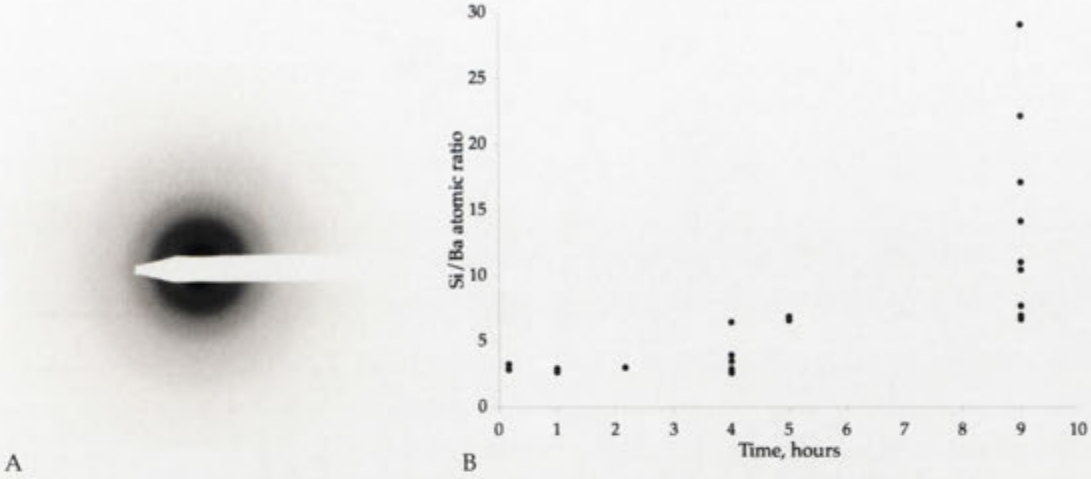

Figure 4.4: EDP of particles extracted after 2 hours (A), and the observed Si/Ba ratio of particles analysed at different time during the synthesis using standard conditions (B).

centre of the particle increasing the concentration of barium as the particles dry. The dark core could therefore be a barium-rich deposit within the particles as an effect of drying. However, such a scenario does not explain the striped pattern seen in the larger particles (see Figure 4.3 B).

Some samples were further analysed in terms of composition and crystallinity by A-. K. Larsson using the Philips EM430 TEM. All particles analysed so far (5 min – 9 hours) are amorphous as indicated by the EDP seen in Figure 4.4 A. This EDP is compatible with EDPs of amorphous silica, as observed by others, see for instance Holtzhüter et al. (2003). EDX analyses further reveal that the particles are composed of an ill-defined barium silicate ($Ba_xSi_yH_zO_{(x+2y+\frac{z}{2})}$) in which the Si/Ba ratio is seen to vary between 2.7 to 29 with time (see Figure 4.4 B). It is evident that particles observed during the early stages of synthesis contain considerably more barium compared to some of the ones observed after 9 hours (see Figure 4.4 B). One explanation for this behavior is that as biomorphs continue to grow, the solution pH is reduced and continuously depleted in Ba^{2+}, leading to barium-depleted particles. Furthermore, Figure 4.4 can also be taken as an indication that the initial Ba-rich particles serve as a source of barium during biomorph growth; the depletion seen is then a secondary effect. However, as described in Section 3.4.1, it is evident that particle precipitation increases with time, which suggests that the particle compositions seen after 9 hours are a result of ongoing precipitation. Barium-depleted particles would then represent precipitation at a later stage compared to barium-enriched particles.

On rare occasions, other particles, in addition to the barium silicate ones, were also

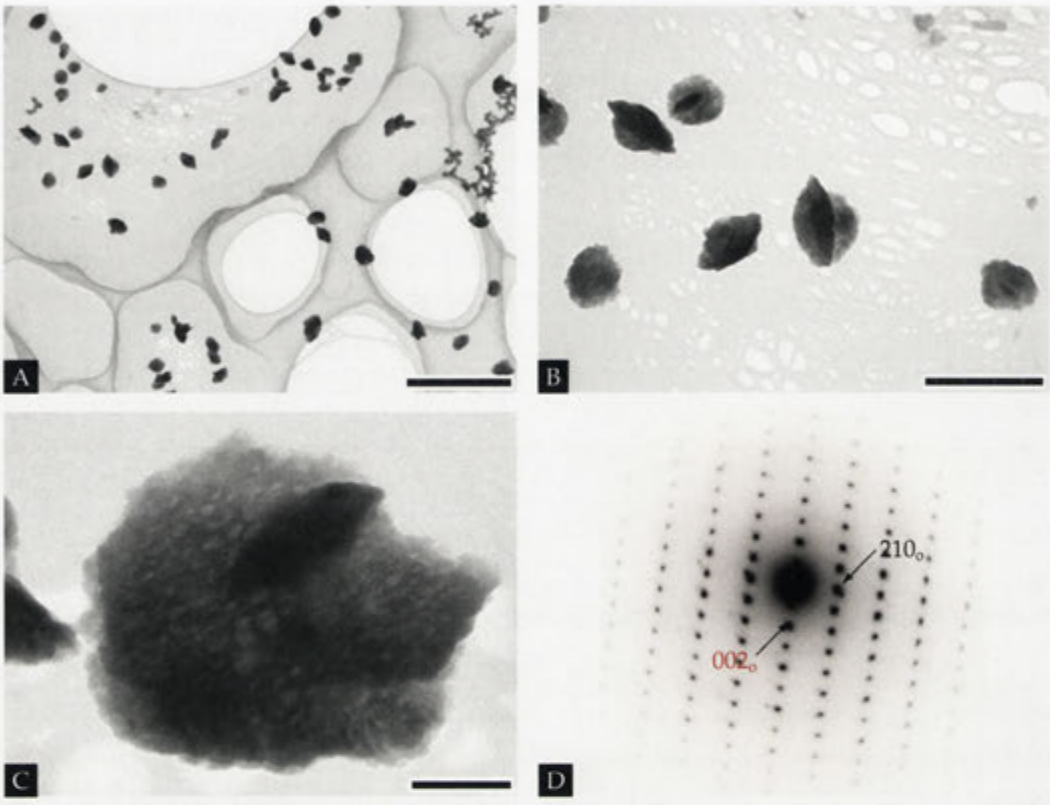

Figure 4.5: TEM images of particles (A–C) and corresponding EDP (D), which is compatible with barite. This is also supported by EDX analyses. Scalebar in A 1μm, B 300 nm, C 50 nm.

observed on the TEM grids (Figure 4.5). These particles are a couple of hundreds of nm in diameter and have, in many cases, a porous spindle-like morphology. From EDX analysis and TEM diffraction (see Figure 4.5 D), it is evident that these particles are composed of barite. Significant amounts of silica (Si/Ba ratio between 0.15–0.22) are also present in the EDX analysis, which can correspond to the nano-porosity seen in Figure 4.5 C. The EDP seen in Figure 4.5 is consistent with a <120> zone axis, as is indicated by the indexing. As these particles are rare, they are not believed to play an important role in the biomorph morphogenesis. They are likely to be a consequence of sulfate contamination from the laboratory, and as such will not be discussed further.

No crystalline barium carbonate particles were ever observed in either of these samples. This could be taken as evidence that carbonate precipitation is restricted to the growing biomorph. However, they may have been present in the solutions and were not deposited on the TEM grids. Recently, TEM analyses of similar samples, by M. Kellermeier, have indeed shown that carbonate crystallisation occurs on these particles. This suggests that these particles serve as nucleation sites of carbonate crystallites. The lack of particles associated with carbonate, as observed in Figures

4.2 and 4.3, may suggest that some proportion of particles only play a background role during biomorph growth. Further TEM investigations are needed to elucidate the interplay between carbonate crystallites and soluble silicates in solution.

Given the observations discussed in this chapter as well as Chapter 3, one can construct different models for the formation of the various morphologies produced. The following discussions are speculative at present, and more work on the nature of the medium giving rise to biomorphs is needed before a more conclusive mechanism of formation can be given.

4.4 Models of biomorph formation

In this section models are presented of how biomorphs may obtain specific morphologies under specific conditions. First, nucleation of biomorphs will be discussed, followed by models of biomorph growth.

4.4.1 Nucleation

The number of nuclei giving rise to biomorphs increases with an increase in pH, temperature, and barium chloride concentration, and with a decrease in sodium silicate concentration. From Figures 3.28 and 3.32 one can construct graphs that display the nucleation behaviour of biomorphs (Figure 4.6). In graph A, one can observe that to maintain the same nucleation density while increasing the barium concentration a 100 times requires a pH decrease of one unit. As such, a schematic equation for nucleus formation can be written as

$$\textit{'precursor'} + Ba^{2+} \rightarrow \textit{nucleus} + 2H^{+} \tag{4.1}$$

since a 10-fold increase in H^+ is equivalent to a 10^2=100-fold increase in barium concentration, assuming $[H^+]^2/[Ba^{2+}]$ is constant for constant nucleation density. In the sodium silicate case, a decrease in concentration at constant pH give rise to greater density of nuclei. It can be noted in Figure 4.6 B that an increase in sodium silicate from 4.2 to 8.5 mM requires an increase in pH from 10.2 to ~11.1 to maintain constant nucleation density. As a first approximation, one can then similarly write the reaction as

$$\textit{'precursor'} \rightarrow \textit{nucleus} + 3Si^{4+} + H^{+} \tag{4.2}$$

as roughly a 2^3=8-fold increase in H^+ is equivalent to a 2-fold decrease in sodium silicate concentration. Equations 4.1 and 4.2 can be combined:

$$\textit{'precursor'} + Ba^{2+} \rightarrow \textit{nucleus} + 6Si^{4+} + 2H^+ \quad (4.3)$$

The *'precursor'* in these equations most likely contains various carbonate and silicate species, which form crystalline barium carbonate upon nucleation. The *nucleus* can therefore be seen as the first precipitation of barium carbonate with the concomitant release of part of the silicate species and a reduction in pH. The silicate species are then free to interact with the growing carbonate crystallite, which hinders the growth of macroscopic witherite crystals.

As discussed in the previous section, particles form as soon as the alkaline-earth metal solution is mixed with that of the sodium silicate. Since these particles are composed of both barium and silicate, they can serve as both starting points for carbonate precipitation, and as a resource of silicate and barium during biomorph growth. Nucleation of barium carbonate is most likely heterogeneous, given the presence of such nanoparticles in suspension. That such association between carbonate crystallites and silicate particles exists has been shown by M. Kellermeier. At any given pH, number of nuclei giving rise to biomorphs increases with a decrease in sodium silicate concentration. This suggests that the formation of barium silicate particles prevents nucleation. Less particulate matter is evident at lower concentrations of sodium silicate. In other words, the relative concentration of Ba^{2+} increases under such conditions, which renders barium carbonate supersaturation to be reached relatively quickly. High supersaturation results in increasing number of stable primary nuclei that can develop into biomorphs. Secondary nucleation is evident at high barium chloride concentrations, as is shown for the synthesis of floral spherulites. Here, secondary aggregates are nucleated during growth of already developed biomorphs. This does not generally occur during the standard synthesis of helical and worm-like morphologies.

In many cases (floral spherulites, pinnacles, high temperature experiments), the morphologies produced can be seen growing from a dumbbell-like aggregate. It is therefore suggested that before the onset of the morphological differentiation, the core, or nucleus, of biomorphs consist of such dumbbells. A discussion on what determines this differentiation of different morphologies under certain conditions is given in the next section.

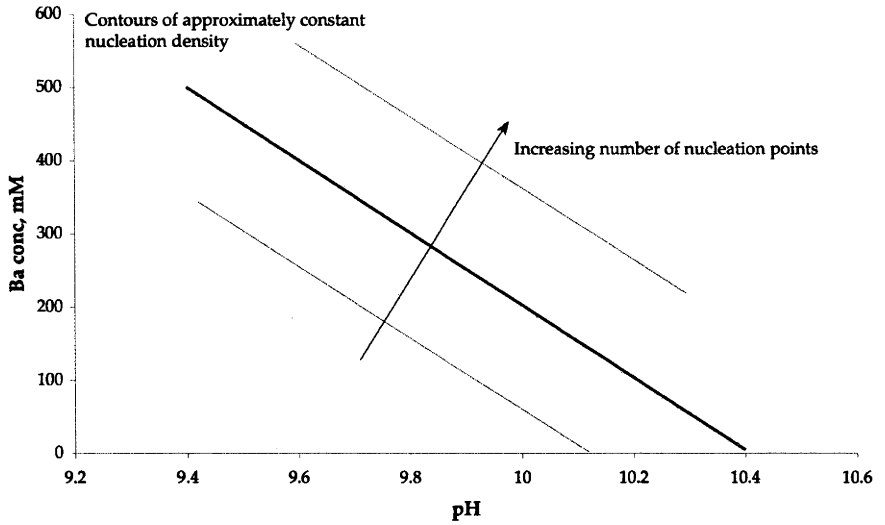

A

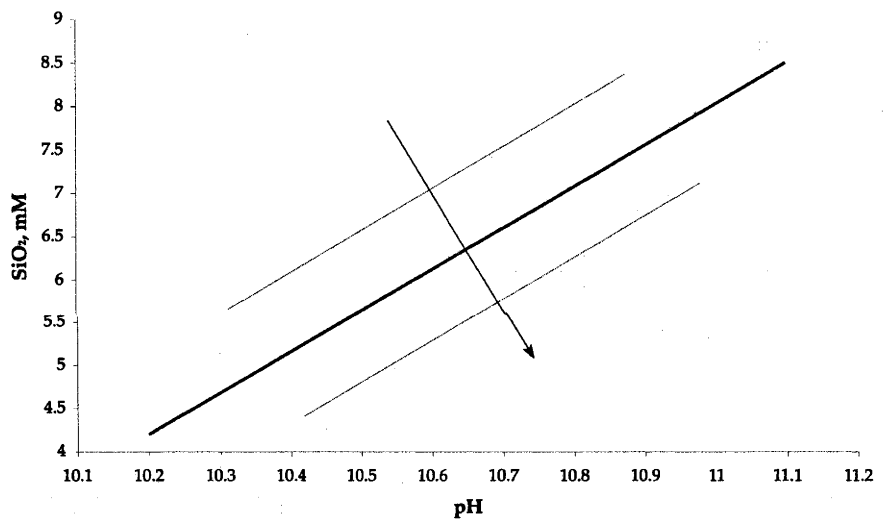

B

Figure 4.6: Schematic representation of the change in nucleation density with a change in concentration of $BaCl_2$ (A) and SiO_2 (B) with pH. The construction of these graphs is based on Figures 3.28 and 3.32, where rough correlations between the number of growing biomorphs and reaction conditions can be made. The graph in A is valid for 4.2 mM SiO_2, whereas B is valid for 5 mM $BaCl_2$.

4.4.2 Biomorph growth

Growth of biomorphs with a particular morphology from the initial nuclei strongly depend on reaction conditions, as seen in Chapter 3. In this section a discussion on how the growth may proceed and why such morphological variety is observed.

Judging from the overall morphology, it is noted that relatively slow growth produces globular aggregates compared to fast growth, which tends to produce more varied morphologies. Temperature and pH, for instance, have such an effect on the

gross morphology. Reduced temperature or pH produces raspberry-like aggregates, whereas increasingly helical and sheet-like morphologies are seen at elevated temperatures or increased pH. These morphologies may be a consequence of both kinetic and thermodynamic factors. Kinetic controls may include absorption of carbon dioxide and diffusion of reactants to the growing biomorphic aggregate. Thermodynamic controls include solubility of carbonate and silicate. In the initial stages of synthesis, biomorph precipitation is inhibited by the lack of carbonate species in solution. A sufficient uptake of carbon dioxide is necessary for precipitation to begin. As such, the precipitation is diffusion-limited with respect to carbonate. The rate of diffusion in relation to that of the reaction then becomes important for the biomorph growth.

Diffusion vs. reaction limited growth

As discussed in Section 2.5, diffusion-limited growth processes are known to give rise to varied morphologies, characterised by their branched nature. It is therefore possible that that diffusion-limited kinetics are important for biomorph morphogenesis. If one considers branching, or decreased morphological dimension, as a signature for diffusion-limited growth, non-branched morphologies having high dimensionality are then suggestive of a system in which diffusion does not have a significant effect on the morphology produced.

For instance, the slowly growing globular aggregates, produced at low temperature or pH, have a high dimensionality compared to the sheet-like and helical aggregates produced at higher temperature or increased pH. This change from 3D to 2D and aggregates with even lower dimensions (tentacles and bands) is compatible with the notation of diffusion-limited growth. Increasingly branched biomorphs are produced for instance with increasing temperature.

To be able to differentiate between diffusion- and reaction limited growth, a simple model has been employed based on the following assumptions: 1) The number of potential nucleation sites is proportional to the surface area advancing throughout growth; 2) Growth is further assumed to proceed layer by layer; 3) For reaction-limited growth, the flux of reactants is sufficiently large so to continuously replenish the boundary layer, which has a constant and high concentration of reactants (see Figure 4.7); 4) The rate of the reaction is therefore seen to be the rate determining step for the growth; 5) For diffusion-limited growth, on the other hand, the boundary layer is at risk of depletion of reactants due to sufficiently slow diffusion through the bulk solution. The concentration gradient across the boundary layer is reduced with time (see Figure 4.7). A graphical representation of the differences between diffusion- and reaction-limited growth, as defined for this model, can be seen in Figure 4.7.

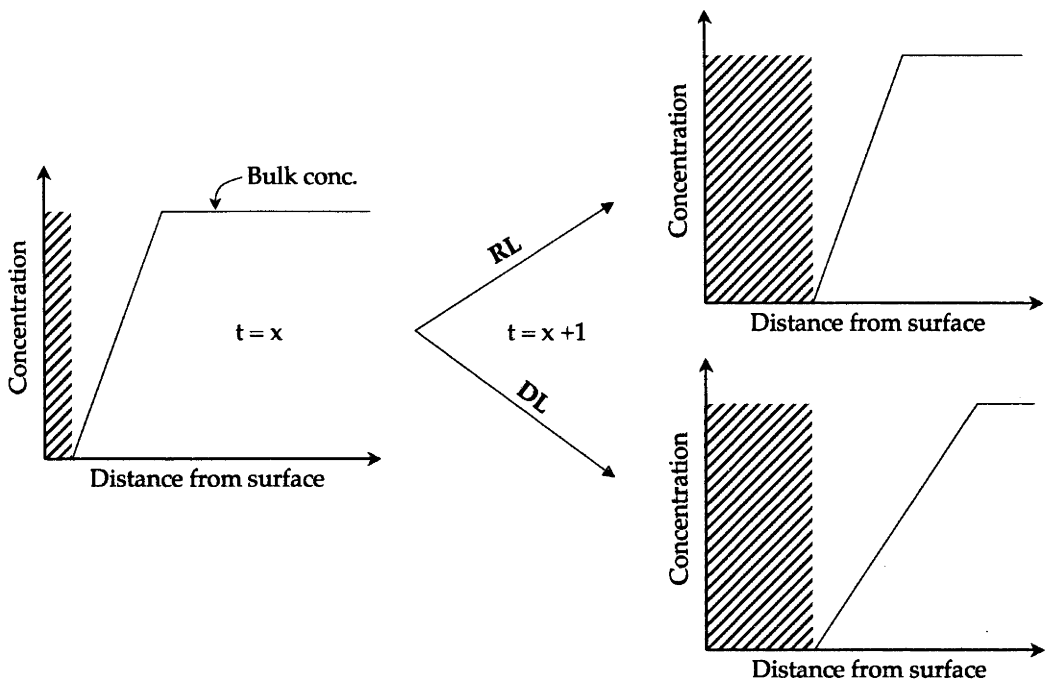

Figure 4.7: Schematic representation of the difference between reaction-limited (RL) and diffusion-limited (DL) growth as defined for the model explaining the growth behaviour of biomorphs. In RL, the concentration gradient across the boundary layer remains constant as the biomorph grow (indicated by the shaded area). In DL, this concentration gradient is reduced with time, as indicated by the decreasing slope.

Using these assumptions, the rate of growth in relation to the area of the advancing surface may provide clues as to which step is rate-limiting. For diffusion-limited growth, the volume change observed with time (dV/dt) should be constant irrespective of the surface area (A) exposed to the solution under constant flux of solutes. In extreme cases, dV/dt will decrease due to starvation, but may then jump upwards, if the biomorph sprouts a new projection into undepleted solution. Hence, dV≤ constant. For reaction limited growth, on the other hand, dV/dt should increase with an increase in area. The interpretation of the growth behaviour will then depend on the shape of the growing surface. Consider a 2D radially growing sheet characterised by radius r and thickness b at time t. Assuming the thickness does not change with time, the precipitation flux is then $dV/dt = 2\pi r \cdot dr/dt \cdot b$. If the growth of such a sheet is characterised by diffusion-limited growth ($dV/dt = k \not< A$), then the observed change of r with time is proportional to 1/r ($dr/dt \propto 1/r$). For a sheet that is preferentially growing at a tip (cardioidal growth), $dV/dt = (2 - x)\pi r^{1-x} \cdot dr/dt \cdot l$, where x represents the reduction in dimension of the sheet as growth does not occur perfectly radially. In such cases diffusion-limited growth is characterised by $dr/dt \propto 1/r^{1-x}$. Both sheets and flo-

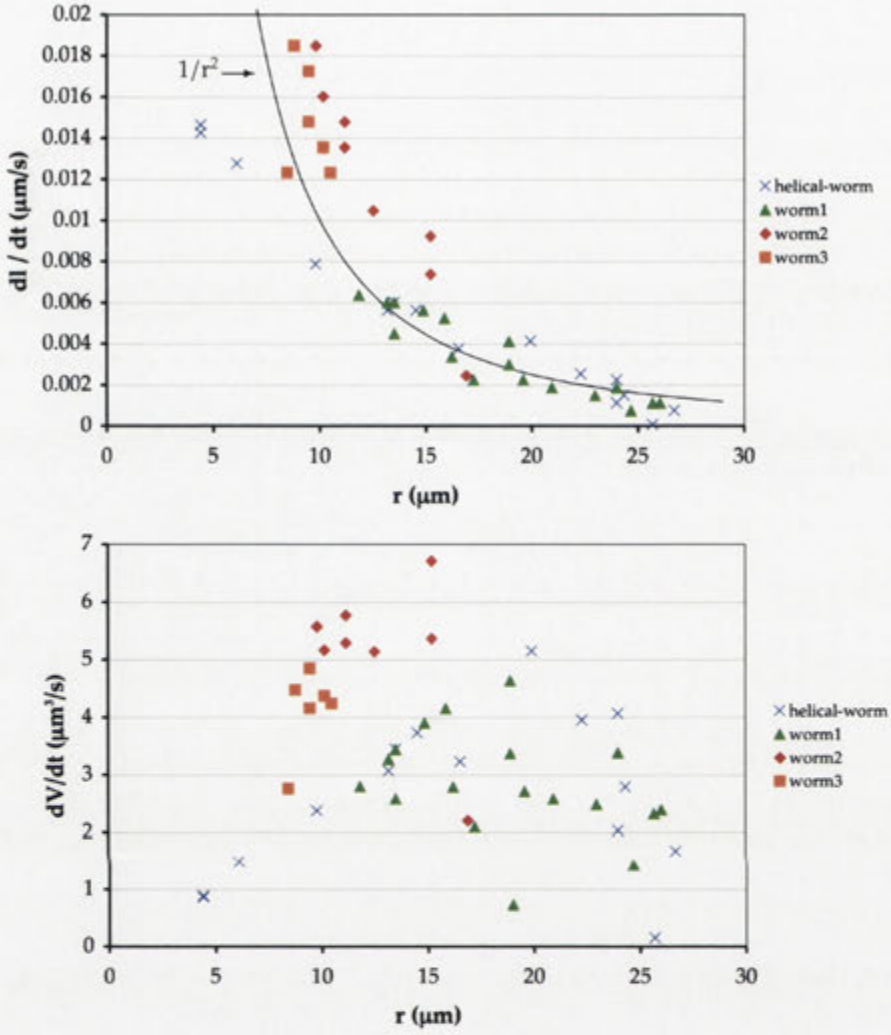

Figure 4.8: Growth rates, expressed as dl/dt (A)and dV/dt (B), for worms and one helical aggregate exhibiting a transition into a worm-like aggregate during the later stage of growth (at r ~6 μm). The data was acquired from two sets of experiments, indicated by warm and cold coloured data points. The black line in A represents $1/r^2$, which is consistent with the trend observed for dl/dt for the worm-like growth.

ral spherulites should, under diffusion limiting conditions, follow such trends. Floral spherulites can be considered a special case of such growth, as sheet-like elements, with constant thickness, are extruded radially from the central core of the aggregate.

For helical and worm-like aggregates, similar arguments can be made. If one approximates the shape of such aggregates as being similar to a cylinder, characterised by radius r and length l, then $dV/dt = \pi r^2 \cdot dl/dt$ if r remains constant throughout growth. It follows that $dl/dt \propto 1/r^2$ under diffusion-limited conditions.

In order to test whether worm-like aggregates and floral spherulites obey such

models, a more quantitative analysis of the growth rates of such biomorphs is called for.

In the case of worms and helical aggregates, interpretation of the growth behaviour is more complex. In Figure 4.8, dl/dt and dV/dt are plotted against the radius of the aggregates. Two different experiments are shown in each graph; warm colours represent one set, and cold colours represent the other set of experiments. One of the samples, marked with blue crosses, represent an aggregate that initially grows as a helical aggregate that at approximately r = 6 μm develops into a worm. In Figure 4.8 A, dl/dt is seen to decrease with an increase in r, proportional to $1/r^2$. The helical aggregate grows with a constant diameter and dl/dt till it transforms into a worm. This later stage worm then follows the same growth behaviour as other worms that developed without a pre-existing helical aggregate. In Figure 4.8 B, the dV/dt is seen to be generally constant, although scattered, over the four worms analysed. The helical aggregate grows with a constant dV/dt till it develops a worm, where dV/dt is seen to slightly increase with respect to r, until it drops off at the final stages of growth. The growth behaviour of worms are therefore consistent with diffusion-limited growth, given the behaviour of dl/dt and dV/dt with respect to r. The helical aggregate grows with very constant diameter, and as an effect the dV/dt as well as dl/dt are both constant. Note the reduced dV/dt in comparison to worms in general, indicating a possibly higher degree of diffusion-limited growth or a reduced flux of reactants.

In the floral spherulite case, both strontium and barium carbonate containing biomorphs were analysed (see also Figures 3.34 and 3.64). In Figure 4.9 the behaviour of dr/dt with respect to r can be seen for the two samples. In the barium case (Figure 4.9 A), variations are seen between the different aggregates, from dr/dt depending almost linearly with r (see for example aggregate number 2, indicated by green diamonds) to an initial independence of dr/dt with r at low values of r that declines linearly at larger values of r (see for example sample number 3, indicated by red circles). In the strontium case, on the other hand dr/dt is in many cases seen to vary proportionally to $0.051/r$ (see for example sample numbers 2 and 5, indicated by green diamonds and orange triangles respectively in Figure 4.9 B). This is most noticeable at small values of r, where a large change in dr/dt is evident. Given these observations, it seems that the growth of floral spherulites can be characterised by an initial reaction limited growth phase, followed by growth that is diffusion-limited. That diffusion of reactants is important to sustain the growth is evident by the fact that two neighbouring aggregates may poison further growth at the surfaces that are in close proximity (~80 μm separation) to each other (see Figure 3.33 F).

Given these observations, the growth of floral spherulites and worm-like aggregates, is consistent with diffusion-limited growth, in so far one can differentiate be-

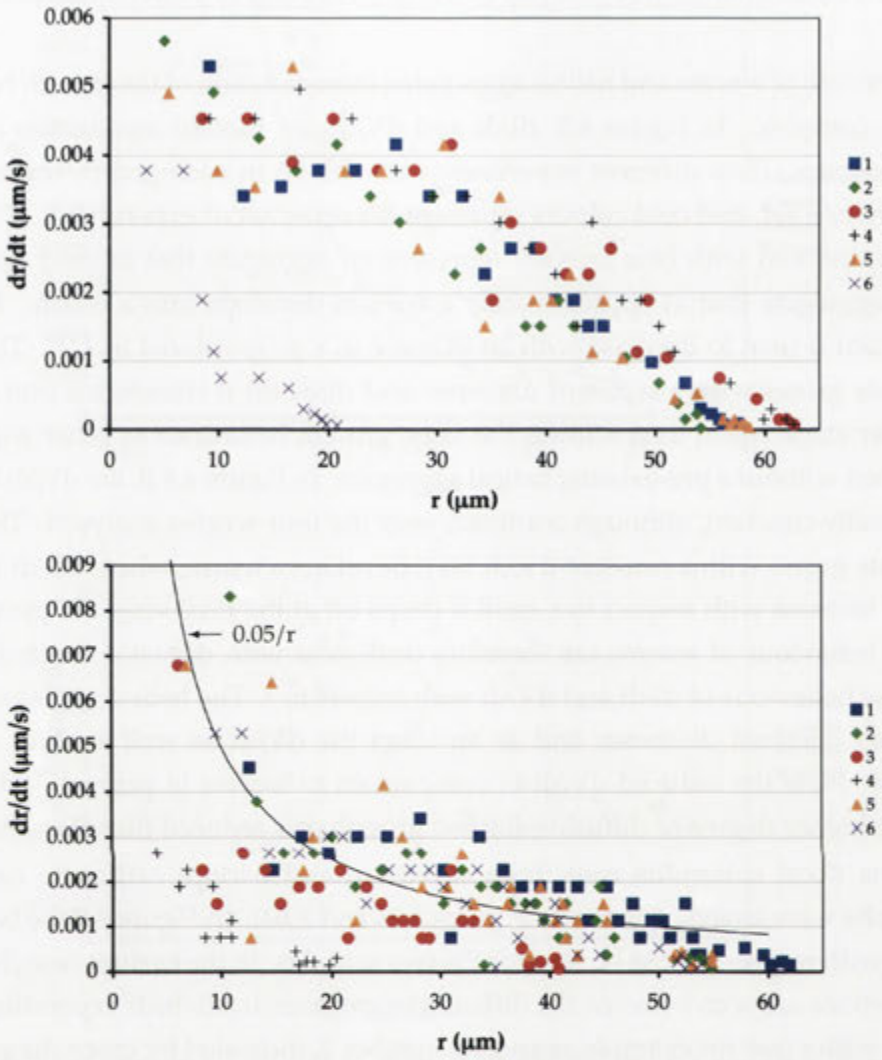

Figure 4.9: The observed change in dr/dt with the size of the floral spherullites of Ba- (A) and Sr- (B) carbonate-type.

tween diffusion and reaction limited growth by estimating dV/dt. One can further speculate on how diffusion-limited growth can influence biomorph morphology, using this model as a starting point. Other morphologies, such as sheets, cones and coral-like aggregates synthesised at high temperature, can also tentatively be explained as being caused by diffusion-limited growth. In the next section, discussions are presented concerning the morphogenesis of specific morphologies with respect to the degree of diffusion limitation on the proliferation of the inital dumbbell-like aggregate.

4.5 Discussion

The development of specific morphologies from an initial dumbbell-like aggregate can be seen as growth that depends on the rate of diffusion of the reactants and precipitation of carbonate and silicate at the dumbell surface; i.e. reaction and/or diffusion-limited growth. A discussion regarding how these modes of growth can affect the biomorph morphology is presented in the following section, using the temperature series (see Section 3.4.5) as a model example.

Effects of temperature

The morphological evolution seen with increasing temperature (see Figure 3.52) seems to point towards an increasing degree of diffusion controlled growth at higher temperatures, as such aggregates display open and branched characteristics. Conversely, raspberry-like globular aggregates, observed at low temperatures, have a higher dimensionality compared to aggregates synthesised at higher temperatures. The very non-branched nature of these morphologies may indicate that the growth of these aggregates are much less limited by the diffusion of reactants than their high temperature counterparts. Furthermore, these low temperature morphologies grow considerably slower compared to sheets, cones, and bands synthesised at high temperature. Considering the 3D morphology and the apparent slow growth rate of raspberry-like aggregates observed at low temperature, the growth rate seems to a lesser degree be dependent on diffusion. Conversely, at high temperature, the solubility of barium carbonate is significantly reduced, leading to a higher degree of diffusion limitation for the growth compared to biomorphs grown under room temperature conditions or at 4 ° C.

Since diffusion-limitation may be more rate limiting at higher temperature, the morphological evolution seen with time, from an initial dumbbell-like nuclei to cones and sheets etc., can tentatively be explained as an effect of preferential growth in the direction towards the strongest diffusive flux.

The proliferation of specific morphologies from an initial dumbbell-like aggregate can be seen as growth that depends on the rate of diffusion of the reactants and precipitation of carbonate and silicate at the dumbell surface; i.e. reaction and/or diffusion-limited growth. For the development of raspberry-like aggregates, the bulging surface is then seen as an effect of some preferential growth along one direction, caused by a surface perturbation during early stages of growth, which is to some extent amplified with continued growth (see Figure 4.10). Low temperature also results in slower diffusion of reactants, however, in this model the rate of the reaction is affected to a greater extent than that of the diffusively.

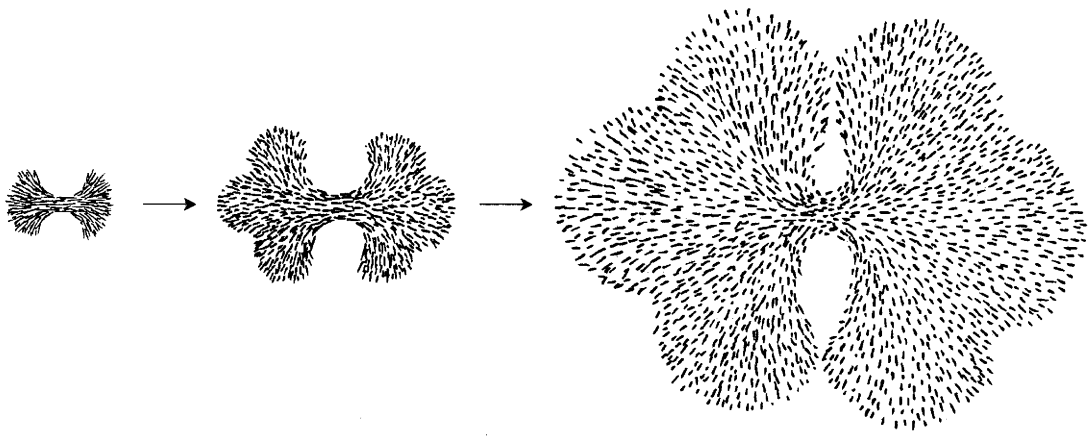

Figure 4.10: Schematic drawing of the development of raspberry-like aggregates from an initial dumbbell-like seed. The lines represent the direction of the witherite crystallographic *c*-axis, which is parallel to the growth direction.

At 70 ° C, the situation is different; although diffusivity of reactants is higher at higher temperature, diffusion is still rate limiting. The driving force for crystallisation has increased, due to a higher degree of supersaturation compared to low temperatures. This results in early proliferation of the dumbbell morphology, as reactant-starved areas are inhibited for further growth. An instability of such a surface will cause a small bulge to develop, which then will grow faster than any other surface due to the greater accessibility to the influx of reactants. Cones, for instance are then interpreted as being formed by preferential growth along a circular rim on the initial dumbbell surface, which continues to propagate at the expense of starved areas (Figure 4.11). Preferential growth on one end of the circular edge of the growing cone results in the development of a non-symmetrical cone. The growth of coral-like aggregates can be seen as preferential growth along many planes and points along the dumbbell surface. The plates and associated bands, which are composed of crystallites oriented with their *c*-axis perpendicular to the growth direction, can be related to the dumbbell structure as depicted in Figure 4.11. However, these morphologies are possibly a result of a different formation mechanism compared to other biomorphs, as the crystallite orientation is different. Further indications that diffusion of reactants vs. precipitation is important for biomorph growth is the presence of banding, or Liesegang ring-type patterning, on some morphologies. Biomorphs that exhibit such banding include high temperature morphologies (e.g. sheets), floral spherulites (high barium concentration), high pH morphologies, and pinnacles (low sodium silicate concentration and high pH) (see for example Figure 3.24 D and G, and Figure 3.29

Figure 4.11: Schematic representation of the development of morphologies observed at high temperature, e.g. cones, plates, bands, coral-like aggregates with associated tentacles. The lines represent the direction of the witherite crystallographic *c*-axis, which is in all cases elongated in the growth direction except for the plates and associated bands.

H). Biomorphs synthesised under standard conditions do not exhibit any Liesegang ring-type patterning. What characterises the growth of these banded morphologies is early and dense nucleation, which suggests that supersaturation is reached quickly, as well as quick growth of aggregates. As was described in Section 2.5, Liesegang ring formation is related to the punctuated precipitation, in which the saturation state is rapidly reduced. A fluctuating saturation state at the biomorph interface, caused by reactant depletion after a pulsated precipitation can therefore be the reason of the presence of banding. In the high temperature case, this may be an effect of the reduced solubility of barium carbonate. At high pH, one can conversely make the connection to increased production of soluble carbonate ($CO_2 + OH^- \rightarrow HCO_3^-$). The precipitation of strontium carbonate biomorphs also provides clues to the mechanism of biomorph formation. The development of floral-spherulites at low concentrations of strontium, suggests that the driving force for the development of such morphologies is similar to the barium carbonate case at much higher barium concentrations. Strontium carbonate is less soluble than barium carbonate, which then favours the notation that increased diffusion limitation tends to form more sheet-like aggregates.

It is interesting to recall that biomorphs can be produced in both solution- and gel-based systems, which exhibit very different mass transport characteristics. Biomorph growth in gels, in contrast to growth in solutions, has suppressed convection and the transport of solutes to the growing aggregate is limited to diffusion through the gelled silica network. The fact that identical morphologies occur in both systems, and especially the notion that helical filaments have been observed growing through

the gel boundary into the adjacent solution, have previously been taken as evidence that diffusion is *not* the main factor for the morphogenesis (Hyde et al., 2004). However, it has been noted that solution based synthesis according to the 'standard' recipe tends to produce increasingly globular aggregates if the system is shaken so as to destroy pre-existing concentration gradients, thus simulating convection. Maintaining concentration gradients may therefore be important to the development of specific morphologies, and at room temperature experiments, the convection cells are operating on a significantly larger scale compared to biomorphs, and as such do not affect the morphogenesis. An alternative explanation for the filament grown through the gel boundary may then be that the relative *diffusion* of reactants is similar in the two different phases. If this is the case, the gel pore size is evidently large enough to sustain similar diffusion characteristics of reactants.

Other factors, apart from the kinetics of mass transport vs. reaction, that can have an effect on morphology of biomorphic aggregates are crystallinity and the interaction between the carbonate and silicate phases. These topics will be explored in the following section.

Silica-carbonate interactions and the role of crystal structure

The growth of biomorphs with particular morphologies is sensitive to reaction kinetics; diffusion of reactants to the growing aggregate's surface. Since there has been no chemical investigations of how the composition of the reaction mixture changes with time, it is not known which species are the growth limiting factor. The diffusion rates are expected to vary between the reactants, depending on the size of the reactive precursors and concentration gradient through the solution. As biomorph growth requires absorption of carbon dioxide from the air, it is reasonable to believe that diffusion of carbonate species is rate limiting at least during the early stages growth. Conversely, the reaction system has a limited supply of barium and silicate, so supply of these species may become more critical towards the later stages of growth. Furthermore, the reaction conditions change with time (pH, concentration and polymerisation state of the reacting species), which will affect the relative diffusion of barium, carbonate and silicate species to the growing biomorph interface.

As all biomorphs are nanocrystalline, one of the main roles of silicate is evidently to reduce crystal size. Without silicate present, macroscopic $BaCO_3$ form. The relative adsorption of silicate species to barium carbonate should be dependent on the polymerisation state and charge of the silicate species, as well as the charge density and conformation of the specific crystal faces. Different witherite crystal faces may show different degrees of silicate adsorption. At present, there is still little experimental

evidence of what carbonate faces are exposed and the nature of silicate species that are preferentially adsorbed. One type of biomorph does, however, give some information on preferential adsorption; the palm trees. These morphologies, which are grown under low sodium silicate concentrations and high temperature conditions, are composed of twinned crystals of witherite having large {110} faces (see Section 3.4.5.1). As such, it can be argued that low molecular weight silicate species are preferentially adsorbed to the {110} faces. Increasing sodium silicate concentration, or reduced temperature, produces biomorphs that are much more strongly affected by the presence of silicate.

Judging from the strong orientational order evident between carbonate crystallites, adsorbed silicate does not negate crystallite to crystallite interactions. The small degree of twist observed between neighbouring crystallites in most biomorph growth demonstrates that perfect epitaxial ordering is not present. In the bands, however, strong epitaxial ordering can be seen, but in a different orientation. This suggests that the amount of adsorbed silica within biomorphs may be important for crystallite orientation, although experiments thus far suggest that this is not the case. The twist between crystallites is particularly prominent in dumbbell growth where so-called 'branching' or 'tip-splitting' causes the crystallites to diverge relative to each other. This effect has been proposed to be related to intrinsic electric fields (Busch et al., 1999). The crystallite divergence seen in biomorphs may be related to such effects. This is consistent with previously developed models on biomorph formation, as discussed in Chapter 1. Imai et al. (2002) and Terada et al. (2003) envision the structure-directing effect as a result of silicate adsorption onto specific crystal faces. Branching along the witherite b-axis then causes the twist seen in sheets. An instability at the growing tip causes the sheet to curl, which, upon further growth results in a helical protrusion.

From the discussion above, it is evident that morphology may be a function of kinetics, which in turn is a function of environmental variables such as pH, temperature, and concentration of barium and sodium silicate. Therefore, the shape of biomorphs is, in principle, an indicator of conditions of growth, as suggested by García-Ruiz (2000). However, since morphology depends on combinations of environmental variables, estimation of any single parameter would require additional evidence.

In the next chapter, I discuss the Archean environment, in relation to atmosphere and ocean composition, in which biomorph formation may have occurred. Understanding the geological composition of this environment is vital in establishing and seeking to better the criteria for the detection of the earliest forms of life on Earth.

Chapter 5

The Archean Earth and the record of early life

5.1 Introduction

As described in a previous chapter (see Chapter 3), our silica-carbonate aggregates show a very wide degree of morphological varieties, some of which strongly resemble living organisms. As first pointed out by García-Ruiz (see Chapter 1), biomorphs can show both morphological overlap with some of the most ancient fossilised microorganisms dating from the Archean. As is discussed in Chapter 6, . The objective of this chapter is to describe the geochemistry of the Archean eon (2.5- ~3.8 Ga) of the early Earth, as this interval reveals the earliest geological evidence of life. This will in subsequent chapters be compared to conditions resulting in biomorph formation. If the natural paleoenvironment is similar to the laboratory synthesis conditions, i.e. high pH with high concentrations of silica and barium or strontium (calcium?), biomorphs could have been naturally produced. Therefore, structures that have been interpreted as microfossils based on their morphology and chemistry, could therefore just be 'fossilised' biomorphs. The efficacy of 'microfossils' as indicators of early life would then be thrown into doubt.

This chapter presents an overview of the early Earth; the chemistry of its atmosphere and oceans and some key geological areas, as well as a description of the earliest traces of life.

The Archean atmosphere and ocean are believed to have been very different from today, although the details are still highly debated. Particularly important in the context of this study are the concentrations of Ba, Si and CO_2, and the pH of the ocean (or localised areas) since these are directly relevant to the conditions of biomorph formation. The criteria for ancient life detection are presented in some detail (see Section 5.3), which will be tested in the following chapter on silica-carbonate biomorphs. The validity of these criteria are of great importance to both terrestrial paleontologists, who

search for evidence of life on earth, as well as to astrobiologists, who are interested in finding life elsewhere in our solar system and universe. To explore the possibility of extraterrestrial life (as well as early terrestrial life), it is important to understand the nature of early life likely to leave behind a suite of biogenicity indicators that can show that, indeed, life was present.

5.2 Early Earth

The Earth's geological time scale spans more than 4 Ga (Giga anni $=10^9$ years), and is divided hierarchically into eons, eras, periods, epochs, and ages, with decreasing durations (see Figure 5.1). It is generally believed that Earth-Moon system formed 4.6 Ga years ago during a massive impact of a Mars-like object. The Hadean ('Hell-like') early Earth (~4.6-4.0 Ga) is traditionally considered to be characterized as a violent and hot period, plagued with frequent meteor impacts, during which the formation of the first crust as cooling of the surface continued, though this has been recently questioned (Wilde et al., 2001; Watson and Harrison, 2005). The known geological exposures from the first billion years comprise in total ~10 000 km^2 (roughly 15% of the area of Tasmania) (Nutman et al., 2001). The early Archean geological record is scarce compared to subsequent eras, and is dispersed all over the world. In fact, rocks of Archean age are present on all continents (Bowring and Housh, 1995; Nutman et al., 2001). The Itsaq Gneiss Complex in Greenland, the Uivak Gneisses in Labrador, and the Narryer Gneiss Complex in Western Australia comprise the largest areas dating $\geq$ 3.55 Ga (Nutman et al., 2001). These rocks are usually severely altered by geological processes like plate tectonics, weathering and metamorphism (high temperature and pressure deformation and recrystallisation) leaving little trace of the original composition and structure (Altermann and Kazmierczak, 2003). Although no crustal rocks older than about 4.03 Ga have been documented (Bowring and Williams, 1999), several occurrences of zircons dating >4.1 Ga (the oldest of which is 4.4 Ga) suggests that a continental crust as well as liquid water was present at that time (Wilde et al., 2001; Cavosie et al., 2005).

The Archean geological record comprises three main terrane types; (1) granite-greenstone terranes; (2) craton cover and craton margin sequences; and (3) high grade gneiss terranes (Lowe and Gary Ernst, 1992). Archean greenstones were principally formed during three events of which the earliest induced the Isua supracrustal sequence in West Greenland. Two of the oldest best preserved cratons in the world are the Kaapval Craton of South Africa and the Pilbara Craton of Western Australia. These ancient cratons date back >2.7 Ga and are believed to have been parts of the same early continent, named 'Vaalbara' (Zegers et al., 1998). The Pilbara Craton is

discussed in this and following chapters as this area hosts the oldest evidence of life on earth in the form of putative stromatolites and microfossils, both of which will be discussed in detail below. Specific geologies of one key location in the Pilbara will be detailed in Section 6.4 where geochemical analysis of one rock from this area will also be presented. A field trip to the area in June-July 2005 enabled me to have a first hand view of these ancient rocks and stromatolites, and the discussions that followed were very informative regarding the ancient atmosphere and ocean, as well as the earliest signs of life.

5.2.1 The Archean atmosphere and ocean

This discusses theories of the composition of the early atmosphere and ocean. Again, details of the chemical makeup of especially the Archean ocean will prove useful when hypothesising about natural biomorph synthesis. Elevated concentrations of barium (or strontium) and silica, as well as a source of carbonate are needed to produce biomorphic aggregates discussed in this dissertation. Clues to the chemistry of the early atmosphere and ocean are hidden in the Archean geological record, and this section provides an introduction to the main tools and theories that are used to decipher what the Earth may have been like during its first billion years.

The prebiotic atmosphere and ocean were very different from today. The contemporary atmosphere is largely composed of nitrogen (78%), oxygen (21%) and argon (1%) with numerous trace gases (Seinfeld and Pandis, 1998). The chemical composition of the atmosphere is a dynamic system where gases are produced and removed by numerous mechanisms in a cyclic fasion. For instance, gases are released by volcanic eruptions, or produced by chemical reactions in the atmosphere, and biological activity, and removed by chemical and physical reactions in the atmosphere, biological activity, and deposition and adsorption of the earth and ocean. The first accumulation of oxygen in the early atmosphere at around 2.3-2.4 Ga was a consequence of the imbalance between the oxygen producing and consuming processes (e.g. oxygenic photosynthesis and carbon/pyrite burial vs. oxidation of reduced species/gases and weathering) (see (Canfield, 2005) and references therein). Since biological processes have a large impact on atmospheric composition, a prebiotic and early biotic atmosphere would have differed enormously from the one today (Seinfeld and Pandis, 1998). This becomes evident when considering the 'Faint Young Sun' (FYS) paradox and the geological, bio-geological and paleontological data. Solar theory indicates that the sun was much less luminous in the past, and has increased its luminosity ever since during its evolution. If the early earth had the same atmosphere and albedo as today, the ancient oceans would have frozen over, since the average surface temperature

Figure 5.1: The geological time scale. Note that the various divisions are not done to scale. Adapted from `www.stratigraphy.org`.

would have been below the freezing point of water. Yet the presence of sedimentary rocks, pillow lavas and stromatolites suggests that liquid water was abundant in the Archean (Sagan and Mullen, 1972). This problem is referred to as the FYS paradox. Several theories have evolved to accommodate this necessary temperature increase, of which the one concerning the presence of greenhouse gases is most likely (Sagan and Mullen, 1972; Newman and Rood, 1977; Kasting, 2005). Greenhouse gases such as water vapor, CO_2, NH_3, CH_4 and O_3 absorb and reemitt IR radiation emitted from the surface of the Earth, thereby heating up the atmosphere. As early as the 19^{th} century the Swedish scientists S. Arrhenius and A. Högbom realised the warming effect of water and carbon dioxide in the atmosphere, and proposed that decreased concentrations of these gases could have caused glaciations (Arrhenius, 1896).

5.2.1.1 Atmosphere

Knowledge of the ancient atmospheric composition (CO_2, O_2) is important to argue that biomorphs could have been naturally produced in the Archean. As biomorphs contain carbonate, the atmospheric carbon dioxide concentrations is of particular interest. Atmospheric oxygen levels are further important to the stability of certain minerals and hydrocarbons produced at that time. Deciphering ancient atmospheric conditions is a very complex task, involving a thorough understanding of the geological record and its processes that can give indications of what such an atmophere would have been like. Today there are two major theories regarding the early atmosphere; the more popular 'Cloud-Walker-Holland-Kasting' (C-W-H-K) and the Dimroth-Ohmoto (D-O) model. They differ radically in the timing of atmospheric oxygen evolution and the suggested greenhouse gases to accommodate the FYS problem (see Figure 5.2).

The C-W-H-K model proposes that the early atmosphere was reducing (CH_4- and CO_2 rich) (Lowe and Tice, 2004; Kasting, 2005) and that free O_2 only became available after a major rise in atmospheric O_2 at around 2.3 billion years ago (named 'The Great Oxidation Event') (Kasting and Walker, 1981). This rise is believed to have been a consequence of a gradual increase in the oxidation state of hydrothermal inputs and volcanic gases, which allowed free O_2, produced by photosynthesising bacteria, to accumulate in the atmosphere (Kump et al., 2001; Holland, 2002). The Archean ocean is therefore believed to have been anoxic, with the occasional localized oxygen oasis (Kasting, 1993), and essentially sulfate-free (Canfield, 1998; Canfield et al., 2000; Habicht et al., 2002).
The D-O model on the other hand states that the O_2 concentration in the atmosphere arose very quickly after the formation of the continents and oceans, possibly as early

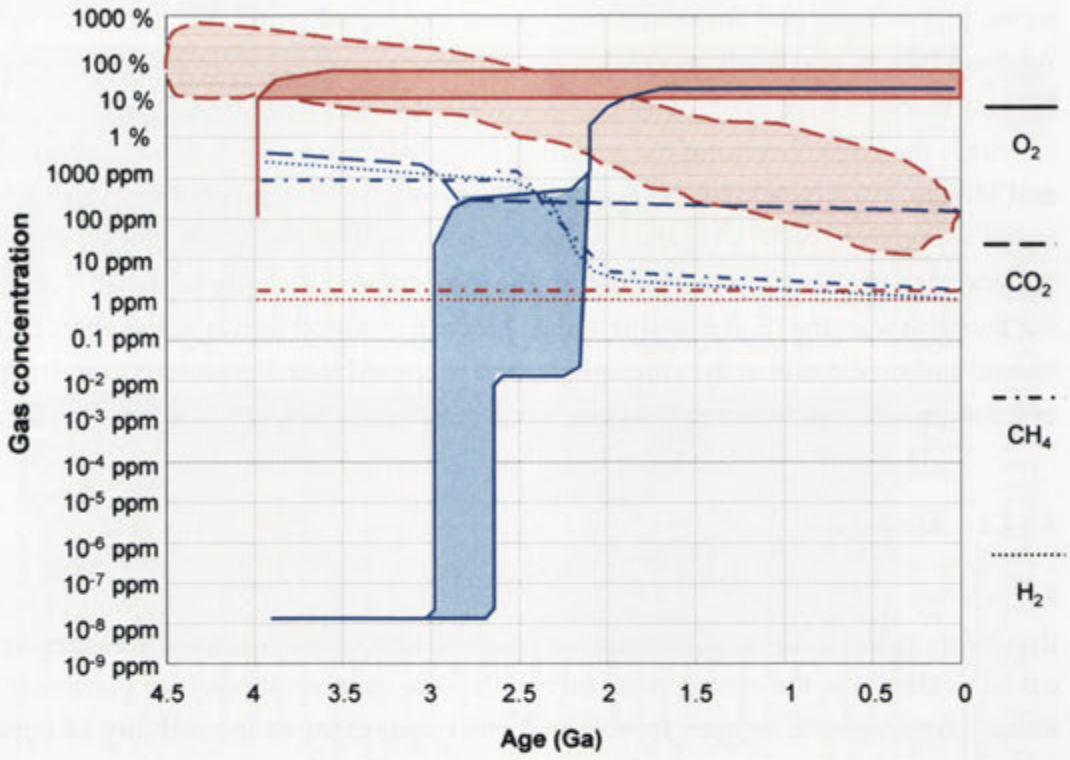

Figure 5.2: Comparison of the atmospheric composition (ppm and %) according to the C-W-H-K model (blue) and the D-O model (red) with time. The shaded areas are possible concentration limits of the gas in question. Adapted from (Ohmoto, 2004).

as 4.0 billion years ago. This major rise in O_2 is postulated as an effect of the early emergence of oxygenic photosynthetic organisms. The O_2 concentration is believed to have been high ever since (Lasaga and Ohmoto, 2002; Ohmoto, 2004), between 0.6 and 2 PAL (present atmospheric level), which would have caused the oceans to become completely oxic except for a the occasional anoxic basins, (Lasaga and Ohmoto, 2002; Ohmoto, 2003, 2004). Furthermore, this model postulates high concentrations of CO_2 as the only available greenhouse gas to accommodate the FYS paradox (Ohmoto, 2004).

These models, although very different, arise from contrasting interpretations of the same geological and biogeochemical data (Ohmoto, 2004). The evidence for an anoxic environment before ~2.3 Ga is largely drawn from the occurrence of banded iron formations (BIFs) (Cloud Jr, 1968; Cloud, 1973a) and iron-depleted paleosols (Rye and Holland, 1998), detrital redox-sensitive minerals such as uraninite (UO_2), pyrite (FeS_2) and siderite ($FeCO_3$) in alluvial sediments (Rasmussen and Buick, 1999), and mass-independent fractionation of sulfur isotopes (Farquhar et al., 2001b). The evi-

dence of an oxic environment after ~2.3 Ga is deduced from the presence of oxidized paleosols, e.g. redbeds, and extensive deposits of gypsum ($CaSO_4 \cdot 2H_2O$) and anhydrite ($CaSO_4$) (Cloud Jr, 1968).

Banded iron formations

Massive deposits of banded iron formations are common in rocks older than about 2000 Ma, but rare in younger ones (Cloud Jr, 1968; Cloud, 1973a; James, 1983). These unique sediments consist of altering iron-poor and iron-rich silica layers. The iron-rich layers are largely composed of iron oxides, such as magnetite (Fe_3O_4) and hematite (Fe_2O_3), but other iron-rich minerals like the iron carbonates siderite ($FeCO_3$) and ankerite ($Ca(Fe, Mg, Mn)(CO_3)_2$), and iron silicates such as greenalite ($(Fe^{2+}, Mg)_3Si_4O_{10}(OH)_4$), minnesotaite ($(Fe^{2+}, Fe^{3+})_{2-3}Si_2O_5(OH)_2$) and stilpnomelane ($K(Fe^{2+}, Mg, Fe^{3+})_8(Si, Al)_{12}$-$(O, OH)_{27} \cdot nH_2O$) can also be constituents of these bands. The iron-poor layers, on the other hand, are composed of finely crystalline quartz, normally referred to as chert (James and Trendall, 1982; Holland, 1984). The depositional setting of BIFs have been widely debated (Holland, 1973, 1984; Trendall and Blockley, 2004) and a current model proposes an oceanic origin of the ferrous iron, which is then transported in upwellings to localized oxygenated surface waters where it is precipitated. The alternation of Fe-rich and Fe-poor layers can then be explained as seasonal variations in hydrothermal activity and deep ocean upwellings. This scenario requires an anoxic deep ocean to account for the large-scale transportation of iron (Holland, 1973, 1984). Ferrous iron (Fe^{2+}) is soluble in water, while the ferric counterpart (Fe^{3+}) is much less so. The oxidation of ferrous iron could have been accomplished by abiotic (oxidation by ultraviolet solar radiation) and biotic processes (photosynthesising bacteria or direct oxidation by iron-utilizing bacteria) (Trendall and Blockley, 2004). The disappearance of BIFs after ~1.8 Ga was originally thought to have been caused by the increased concentration of oxygen. However, a competing model suggests that it was the increased concentration of sulfur that caused the removal of iron as sulfides from the oceans that prevented the formation of BIFs (Canfield, 1998).

Ohmoto, on the other hand, believes that BIFs are evidence *for*, and not against, an oxygen-rich early atmosphere (Ohmoto, 2004). Ohmoto came to the conclusion that BIFs were formed by mixing of Fe^{2+}-rich hydrothermal fluids with oxygenated water producing abundant ferric oxides and hydroxides; a process believed to have been the cause of the modern analogue of BIFs, like the Red Sea iron-rich deposit. This suggests that the atmosphere has been oxygenated since ~3.8 Ga (Ohmoto, 2002, 2004).

Others do not see a connection between the Red Sea iron deposits and the Precam-

brian BIFs, and claim they are 'utterly unlike' each other (James, 1969; Trendall and Blockley, 2004). Trendall and Blockley (2004) have suggested that it is difficult to draw conclusions about the atmospheric composition from the presence or absence of BIFs, since BIFs need anoxic oceanic deep water and that in itself does not necessarily put constraints on the atmospheric concentration of oxygen.

Paleosols

Chemical profiles of ancient soils, which formed in contact with the atmosphere, also known as paleosols (Rye and Holland, 1998), have been used extensively, and with much controversy (see (Palmer et al., 1989a; Holland and Feakes, 1989; Retallack, 1989; Palmer et al., 1989b), (Ohmoto, 1996; Holland et al., 1997; Ohmoto, 1997) and (Palmer et al., 1989a; Holland and Feakes, 1989; Retallack, 1989; Palmer et al., 1989b)), to indicate the atmospheric oxygen concentration (Gay and Grandstaff, 1980; Holland, 1984; Prasad and Roscoe, 1996; Ohmoto, 1996; Rye and Holland, 1998; Yang et al., 2002). The geochemical indicator most often used to infer oxic or anoxic atmospheric conditions is the loss or retention of Fe during weathering relative to immobile chemical species such as Al, Ti and Zr. In low-oxygen environments Fe is mobilized from the parent rock during weathering (as soluble Fe^{2+}), whereas in high-oxygen environments Fe is oxidized and therefore retained (as insoluble Fe^{3+} containing minerals) (Ohmoto, 2004). It is generally believed that most paleosols older than ~2.2 Ga show evidence of Fe loss, and younger paleosols show evidence of Fe retention, indicating that the oxygen concentration on pre-2.2 Ga Earth was low (Maynard, 1992; Holland et al., 1997). The fate of the released iron (under anoxic conditions) depends in part on the P_{CO_2}. Either it is lost to groundwater or it is precipitated in the lower parts of the profile as either siderite ($FeCO_3$) if p_{CO_2} is high, or as an iron bearing silicate if p_{CO_2} is low (Rye et al., 1995). Rye et al. (1995) used the fact that pre-2.2 Ga paleosols do not contain any siderite but abundant iron silicates to calculate an upper limit on available CO_2 to $10^{-1.4}$ atm (Rye et al., 1995). They also noticed that this CO_2 concentration was too low to compensate for FYS and suggested that sufficient concentrations of methane could have coexisted with CO_2 to allow for an efficient greenhouse effect (Rye et al., 1995). The ~2.76 Ga Mount Roe paleosol in Western Australia also contains organic carbon with negative isotopic values (see Section 5.3.1.1 for description of carbon fractionation) perhaps indicative of methanotrophs (bacteria that utilises methane as their only source for carbon and energy) as well as fragments of what is believed to be microbial mats. The presence of methanotrophs implies that the atmosphere was rich in methane ($\geq 20\mu$atm $\approx$2.03 Pa), which could account for the FYS problem (Rye and

Holland, 2000b).

Of particular interest to dating the rise of atmospheric oxygen are the paleosols that are overlain by redbeds, such as the 2.44-2.2 Ga Hokkalampi paleosol in Finland, the 2.38-2.215 Ga Ville Marie paleosol in Canada and the 2.245-2.203 Ga Hekpoort paleosol in South Africa, since these sediments record a clear change in oxygen concentration in the atmosphere (Rye and Holland, 1998). In particular, the Hekpoort paleosol has undergone extensive research since it is one of the youngest paleosols showing Fe depletion (Rye and Holland, 2000a; Yang and Holland, 2003; Driese, 2004). Ohmoto on the other hand believes that 'Essentially all paleosols, regardless of age, retain some characteristics of soils formed under an *oxic* atmosphere, such as increased Fe^{3+}/Ti from their parental rock' and suggests that the *minimum* oxygen concentration was around 0.003 atm (>1.5% PAL) (Ohmoto, 1996). (Recent investigation of the 2.45 Ga Pronto paleosol in Canada by Ohmoto and coworkers refined the atmospheric oxygen concentration to between $7.44 \cdot 10^{-5}$ atm ($3.5 \cdot 10^{-4}$ PAL) and $2.23 \cdot 10^{-3}$ atm (1.1% PAL) (Nedachi et al., 2005).) Hydrothermal alteration and/or the effect of organic acids produced by microorganisms was proposed to explain the Fe-loss in an atmosphere rich in oxygen. This type of alteration promoted the reduction of Fe^{3+} to Fe^{2+}, which was subsequently removed. Holland and Rye found this explanation unlikely and concluded that the best and simplest interpretation of the available data is that the early Archean atmospheric oxygen concentration was low ($P_{O_2} \leq 0.002$ atm) and that it quickly rose between 2.25 and 2.05 Ga (Holland et al., 1997). However, Driese (2004) concluded that both models, ie. very low P_{O_2} conditions as suggested by Holland and coworkers or the presence of organic matter in a oxidized environment as suggested by Ohmoto, could account for the geological evidence found in the Hekpoort paleosol. Utsunomiya et al. (2003) analysed the ~2.45 Ga weathering profile located near Cooper Lake, Canada, previously described as a 'definite' paleosol by Rye and Holland (1998), and found several characteristics indicative of anoxic weathering. This paleosol showed a decrease in Fe^{2+}/Ti, $\sum Fe/Ti$ and Fe^{2+}/Zr, $\sum Fe/Zr$ as well as constant ratios of Fe^{3+}/Ti and Fe^{3+}/Zr towards the top of the profile. The decrease in Fe^{2+} and $\sum Fe$, and the constant concentration of Fe^{3+} throughout the paleosol is consistent with weathering under anoxic conditions (Utsunomiya et al., 2003), even according to the criteria described by Ohmoto (1996). Furthermore, no evidence of hydrothermal alteration was found, and since no extensive biomass could account for the chemical profile in the paleosol, Utsunomiya et al. (2003) came to the conclusion that this profile was formed during anoxic weathering. Still, it has been suggested that iron-loss from paleosols are not conclusive evidence of anoxic weathering. Through experimental investigation of the relative mobility of Fe, Al, P and Cu during simulated weathering of basalt under both oxic and anoxic conditions, and with and without organic ligands

(citrate), Neaman et al. found that the loss of Fe and P was significant regardless of p_{O_2} in the presence of organic ligands (Neaman et al., 2005). Furthermore, Cu showed minor mobility during anoxic conditions, and major mobility during oxic conditions which was enhanced by the organic ligands. Comparing these experimental results to the relative mobilities of Fe, Al, P and Cu in both Mount Roe and Hekpoort paleosols, it was shown that these paleosols are consistent with both weathering under an anoxic and oxic atmosphere respectively (Neaman et al., 2005).

Detrital minerals

Detrital pyrite (FeS_2) and uraninite (UO_2) are very rare in sediments younger than 2000 Ma due to their instability under oxidizing conditions (Holland, 1984; Rasmussen and Buick, 1999). Their presence in Archean sedimentary units therefore restricts the amount of available free oxygen, and through calculations of dissolution kinetics of uraninite it has been estimated that the oxygen levels might have been between 10^{-2} – 10^{-6} PAL (Grandstaff, 1980). Detrital uraninite and pyrite grains have been found in the ~2.8 Ga Witwatersrand Supergroup (Smith and Minter, 1980), the ~2.3 Ga Elliot Lake, Canada and in 3250-2750 Ma siliclastic sediments (sediment composed of siliceous fragments or clasts) from the Pilbara Craton in Western Australia (Rasmussen and Buick, 1999). Since detrital uraninite has been found in the modern Indus River (Simpson and Bowles, 1977), it has been argued that the presence of such minerals in ancient sediments does not necessarily constrain the concentration of atmospheric oxygen at that time (Clemmey and Badham, 1982; Robinson and Spooner, 1984). However, Maynard et al. (1991) argued that Indus River is a bad analog to the Witwatersrand deposition since the former lacks signs of chemical weathering compared to the latter. This implies that the atmospheric oxygen concentration must have been low to allow the survival of detrital uraninite and pyrite in the highly weathered Witwatersrand sediments (Maynard et al., 1991). Although a hydrothermal origin has been suggested for the uraninite and pyrite found in the Witwatersrand basin in South Africa (Phillips et al., 1987; Barnicoat et al., 1997), rounded pyrite grains show Re-Os ages that predate the deposition of the conglomerates, thereby reinforcing the detrital origin for the Witwatersrand samples (Kirk et al., 2002). The ones found in the siliclastic sediments in the Pilbara Craton show no evidence of hydrothermal alteration and are considered to be detrital minerals (Rasmussen and Buick, 1999). It is therefore believed that these detrital redox-sensitive minerals are indicative of a low-oxygen atmosphere (Frimmel, 2002; Canfield, 2005).

Mass independent fractionation of sulfur isotopes

Perhaps the most compelling evidence for an almost completely anoxic atmosphere comes from mass-independent fractionation (MIF) of sulfur isotopes. The first chemically produced mass-independent fractionation of isotopes was reported in 1983 by Thiemens and Heidenreich and has since then shown to have wide applications especially in chemistry and evolution of the atmosphere (Thiemens and Heidenreich, 1983; Thiemens et al., 2001).

In contrast to mass-dependent fractionation of isotopes, as occurs in biological, thermodynamic and kinetic fractionation processes, mass-independent fractionation, which has been observed in a number of gas phase reactions, is not governed by the mass difference between isotopes (Farquhar et al., 2000a, 2001b). The origin of MIF remains uncertain (Thiemens, 1999), but it is believed to be related to rotational-vibrational excited transition states of the molecules as well as to the density and symmetry of these states (Bhattacharya et al., 2000; Gao and Marcus, 2001).

Mass-independent sulfur fractionation has been observed in sulfide and sulfate minerals in martian meteorites (Greenwood et al., 2000; Farquhar et al., 2000b) and Precambrian rocks older than 2.09 Ga. Younger rocks show isotope signatures consistent with mass-dependent fractionation (Farquhar et al., 2000a). Farquhar et al. (2001b) showed that Archean sedimentary sulfur isotope anomalies are similar to wavelength-dependent sulfur isotope data obtained from sulfur dioxide photolysis experiments. The lack of a protective ozone layer in the oxygen-poor Archean atmosphere would allow deep penetration of 190-220 nm wavelengths into the atmosphere allowing photolysis of SO_2 resulting in mass-dependent sulfur fractionation. This theory thus puts constraints on the oxygen concentration and presence of a UV shield, such as ozone as well as an organic haze, in the early atmosphere (Farquhar et al., 2001b).
Ohmoto et al. (2001) questioned these results and suggested that the mass-independent fractionation observed by Farquhar et al. could have arisen from the analytical technique used. This criticism was in turn contested by Farquhar et al. (2001a), who reanalysed the samples with different techniques and concluded that the original interpretation of the isotope data was still valid. Subsequent independent analyses conducted by Mojzsis et al. (2003) verified the previous mass-independent sulfur fractionation results by Farquhar et al.. It is believed that this isotopic signature is transferred from the atmosphere as sulfur containing aerosols and/or dry particle and gas deposition, and incorporated into sulfur-containing sediments (Pavlov and Kasting, 2002). According to theoretical models, this mass-independent isotope signature could only have been observed in an atmosphere containing $<10^{-5}$ PAL of oxygen (Pavlov and Kasting, 2002). The lack of oxygen in the atmosphere would have a sup-

pressing effect on the oxidative weathering of sulfides, thereby limiting the amount of sulfate in the oceans (Canfield et al., 2000; Habicht et al., 2002). The concentration of sulfate in the early Archean ocean is therefore thought to have been <200 μM, compared with today's concentration of 28 mM, as evident from strong variations in sulfur isotopic compositions in pyrite.

Ohmoto remains unconvinced by the MIF of sulfur isotopes as a sign of low-oxygen concentration in the atmosphere, since there are differences between naturally and synthetically produced MIF of sulfur isotopes as well as the presence of MIF in younger geological samples (Ohmoto, 2003).

Although the CWHK- and DO-models are very different they both agree on at least one thing; the atmosphere contained CO_2. As with the case of concentration of atmospheric oxygen, the amount of CO_2 in the atmosphere is still speculative. As discussed earlier, Rye et al. (1995) used the absence of siderite in paleosols to put an upper limit on the CO_2 in the atmosphere. Interestingly, siderite is present in ancient deposits, and several researchers have used this to put a *lower* limit on concentrations of carbon dioxide. Hessler et al. (2004) estimated that the CO_2 levels in the atmosphere must have been greater than $p_{CO_2} > 2.51 \cdot 10^{-3}$ bar from the occurrence of Fe^{2+}-rich carbonates and the absence of Fe^{2+}-rich silicates in pebble rinds found in 3.2 Ga fluvial deposits. Ohmoto et al. (2004) concluded from the presence of abundant massive siderite-rich deposits in pre-1.8 Ga sequences that the CO_2 atmospheric concentration must have been at least 100 times the present day value (which is similar to early values estimated by Kasting (1987)). They also explained the absence of siderite in some paleosols by unfavorable pH and O_2 conditions resulting in precipitation of ferric minerals instead of siderite. This high level of CO_2 would be sufficient to keep surface temperatures above freezing point, so no additional greenhouse gas is needed. Kasting and others have argued that methane might have been abundant in the early anoxic atmosphere to account for low CO_2-levels (Pavlov et al., 2000; Kasting et al., 2001; Pavlov et al., 2001b, 2003; Kasting, 2005). Both abiotic and biotic sources of CH_4 could have accumulated in the early atmosphere, thereby increasing the greenhouse effect. Methane could have been degassed from hydrothermal vents in mid-ocean ridges, been photochemically produced in an anoxic ocean (Bange and Uher, 2005), and once life had evolved methanogenic bacteria could have produced a substantial amount of CH_4 (see (Pavlov et al., 2000) and references therein). A high level of atmospheric methane is only possible in a reduced atmosphere, since CH_4 and O_2 react photochemically to produce H_2O and CO_2 (Pavlov et al., 2000, 2003; Ohmoto, 2004). Pavlov et al. (2001a,b) proposed a level of <100 ppm CH_4 and $\geq$0.2 bar CO_2 prior to the origin of life, after which the methane concentrations quickly grew, while the CO_2 level was reduced. Photochemical models predict that when the

ratio $CH_4/CO_2 \geq 1$, polymerisation of methane could have caused an organic haze of hydrocarbons to be produced in the atmosphere (Pavlov et al., 2001a,b). Small changes in this ratio would have great effects on the climate of the early Earth. A thick high altitude organic haze would absorb and re-emit sunlight into space thereby cooling the atmosphere, a process known as 'anti-greenhouse effect'[1], which is believed to occur today on Saturn's moon Titan (Pavlov et al., 2001a; Kasting, 2005). For that reason, the haze must have been thin enough to sustain methanogenic bacteria. Pavlov et al. argued that extremely low-^{13}C kerogens (see Section 5.3.1.1 for explanation of carbon isotopes) in Late Archean (2.5-3.0 Ga) sediments could be explained by the presence of such a haze. Since atmospheric polymerisation of CH_4 could produce isotopically light organic particles and if the initial CH_4 already had a $\delta^{13}C$ of ~40‰, this would translate into organic particles with extremely low $\delta^{13}C$ (-50‰-65‰), matching the values of Archean kerogens. These isotopically light kerogens can therefore be taken as evidence for methanogenesis. They further suggested that the decline in atmospheric CH_4 levels, as a cause of decrease in CH_4 production from methanogenic bacteria due to the increased population of sulfate-reducing bacteria (which would compete for H_2 or convert CH_4 to CO_2), could have triggered a possible global glaciation at ~2.3 Ga, as evident from geological evidence (Pavlov et al., 2001b).

The hypothesised presence of high levels of CH_4 in the early atmosphere has received some criticism. Ohmoto and Watanabe (2004) argued that there is no biogeochemical evidence to support the existence of methanogens prior to the emergence of cyanobacteria. That is to say that there is no proof of a widespread methanogenic community able to produce the amount of CH_4 needed to sustain a high level of atmospheric CH_4 before the appearance of cyanobacteria. Also, an early organic haze is not compatible with the MIF of sulfur (Canfield, 2005), as discussed above.

5.2.1.2 The Archean ocean

This section presents a brief overview of the current knowledge of pH, and Ba, Si and CO_2 concentrations in the Archean ocean. Keep in mind that our biomorphs can only be produced at relatively high pH and in the presence of significant amounts of barium (or strontium), silica, and CO_2.

pH

As an immediate consequence of the different Archean atmosphere, the composition of the ancient ocean was also different from today. For example, the presence of CO_2

[1]The 'greenhouse effect' is caused by re-radiation of outgoing thermal infrared radiation by gases in the atmosphere - thereby warming the Earth's atmosphere and surface

in the atmosphere has a direct impact on the pH of the ocean (and vice versa (Walker, 1985)) through the following equilibrium reactions (See also Section 2.2.4 where the carbonate system is discussed):

$$CO_2(aq) + H_2O \rightleftharpoons H_2CO_3 \rightleftharpoons HCO_3^- + H^+ \rightleftharpoons CO_3^{2-} + 2H^+ \quad (5.1)$$

There is no firm indication of the pH-state of the ancient ocean as there has been arguments for both an acidic ocean (Russell and Hall, 1997), one whose pH is close to modern conditions (pH 8.1) (Grotzinger and Kasting, 1993) as well as an alkaline 'soda' ocean (Kempe and Degens, 1985; Kempe and Kazmierczak, 2002).

An acidic ocean has been inferred from the proposed higher partial pressure of CO_2 in the Precambrian atmosphere (Walker, 1985; MacLeod et al., 1994; Ohmoto et al., 2004). High levels of CO_2 in the atmosphere would lower the pH of the ocean and rainwater through the equilibrium reactions stated above (see Equation 2.2). Ohmoto et al. (2004) suggested that the pH of the ocean was between 5.5 and 7.5, with rainwater having a pH of <4.4 based on their high levels of carbon dioxide in the atmosphere. With an increased CO_2 partial pressure on the early Earth, the ocean is predicted to contain larger amounts of calcium, bicarbonate and hydrogen ions, and lower concentrations of carbonate and sulfate ions (Walker, 1983). At a level of $\sim 10^{-1}$ atm of carbon dioxide in the atmosphere, Ba^{2+} could have been present at concentration between $10^{-5.2}$ to $10^{-6.7}$ M. Ba was therefore present at higher concentrations in the early oceans than today. Maisonneuve (1982) also proposed that the ocean was acidic, but this acidity would lead to chemical weathering that would release Ca^{2+}, Mg^{2+}, Na^+, Fe^{2+} as well as other cations increasing the pH of the ocean to between 8-9. This could lead to a fluctuating pH state of the ocean (Maisonneuve, 1982).

It has also been suggested that the early ocean was alkaline, like the modern soda lakes (Kempe and Degens, 1985; Kempe and Kaźmierczak, 1994; Kazmierczak et al., 2004). There are a number of lakes today that have a pH of >9.5, such as Lake Mono in USA (pH 9.6), Lake Magadi in east Africa (pH 10.5) and Caohi Laguna in South America (pH 10.6) (see (Kempe and Degens, 1985) and references therein). Almost all contemporary soda lakes are related to volcanic rocks, where weathering of silicate rocks produces solutions dominated by sodium and carbonate (Kempe and Kazmierczak, 2002; Kempe and Kaźmierczak, 1994). These alkaline systems are formed during evaporation of waters with a small excess of carbonates compared to Ca^{2+} and Mg^{2+}, and excess of Na^+ and K^+ compared to Cl^- and SO_4^{2-}. As evaporation continues, Ca- and Mg-salts will precipitate first owing to their lower solubility, which will cause the pH to increase as concentration increases (Garrels and Mackenzie, 1967; Kempe and Kazmierczak, 2002). Kempe and Degens proposed that the chemistry of

such alkaline lakes resemble that of the Precambrian ocean (with the exception of lower silica concentrations today, due to the presence of diatoms in modern environments), which would explain the coexistence of chert, siderite and Fe-silicates in BIFs and the widespread chert- and dolomite formations, which could only have formed in a high pH alkaline environments (Kempe and Degens, 1985). Furthermore, they suggested that the presence of contemporary microbialites in the highly alkaline Lake Van in Turkey showed that such biologically mediated structures are compatible with a soda ocean chemistry (see Section 5.3.4 for description of stromatolites). Since these types of structures are present in the Precambrian geological record, it could be taken as evidence of such an ocean (Kempe and Kaźmierczak, 1994). Kempe and Kaźmierczak (1994) proposed that the early ocean was highly alkaline (>100meq/l) with a high pH (pH ~10) and a low concentration of Ca^{2+} ($[HCO_3^-]>>2[Ca^{2+}]$) for the first billion years of the Earth's history. Sumner and Grotzinger (2000) criticized the theory of a soda ocean based on the abundant precipitation of calcium carbonate in the Archean. They argued that according to this theory, not enough Ca^{2+} was present to account for these enormous marine sedimentary units. Kempe and Kaźmierczak (1994), on the other hand, reasoned that deep sea carbonate deposits could form in association with hydrothermal vents that increased the Ca concentration. The evolution of life would also have been favored in such an environment as it allowed the survival of phosphates, proteins and other dissolved organic molecules (Kempe and Kazmierczak, 2002). A soda ocean is therefore in contradiction to high $p(CO_2)$ levels that induce a more acidic ocean with high concentrations of Mg, Ca and Cl (Kempe and Kaźmierczak, 1994). For a soda ocean to have been a reality in the Precambrian, an additional greenhouse gas, like methane, would have been necessary to keep the oceans above freezing point (Franck et al., 2002; Kempe and Kaźmierczak, 1994).

Modern oceanic pH values for the Archean ocean have been proposed by several researchers (Holland, 1984; Grotzinger and Kasting, 1993). Holland proposed that the early ocean was dominated by Na^+, Mg^{2+}, K^+, Ca^{2+} and Cl^-, more or less as it is today. pH would have been close to neutrality as rapid weathering reactions would balance the volcanic acid influx (Holland, 1984). Grotzinger and Kasting predict pH values between 5.7 to 8.6 for the early ocean even at high (p_{CO_2}). However, they realize that simple models may not correctly predict the oceanic pH since much more information is needed to do so with accuracy. Furthermore, this ocean would have been saturated with respect to calcite and would contain very small amounts of sulfates. The absence of gypsum evaporites, and the abundancy of carbonate sediments speaks for such a conclusion. Sulfur isotopes of sedimentary sulfides also suggests that the ocean changed from being iron-rich in the Archean to sulphidic in the early Proterozoic (Cameron, 1982; Canfield, 1998; Canfield et al., 2000). Canfield proposed that as

the atmospheric oxygen concentration increased, terrestrial sulfide weathering would be promoted leading to increased sulfate levels in the ocean. Enhanced levels of sulfate would in turn induce higher rates of sulfate reduction by sulfate-reducing bacteria giving rise to highly fractionated sulfides. Sulfur isotopic studies suggests that the Archean oceanic sulfate concentration was <200 μM which increased to $\geq$1 mM between 2.2 to 2.3 Ga (Canfield et al., 2000; Habicht et al., 2002). At around 1.8 Ga the sulfide levels were high enough to precipitate all of the available Fe as pyrite, diminishing the oceanic iron content that resulted in a cessation of BIFs (Canfield, 1998; Poulton et al., 2004). This model also suggests that the deep ocean remained anoxic till the Neoproterozoic era (1.0 to ~0.54 Ga) (Canfield, 1998, 2004).

Barium and strontium

As mentioned previously, the early ocean could have been enriched in Ba compared to today. The average contemporary seawater concentration of Ba^{2+} is around 20 μg/l (~0.15 μM) (Hood and Pytkowicz, 1974). The Ba^{2+} concentration varies both with depth and the ocean in question, but it is generally believed that the modern seawater is close to saturation with respect to barite ($BaSO_4$) (Monnin et al., 1999). As with the case of barium, the Archean ocean is also believed to have been enriched in strontium (Veizer, 1982). Present day average seawater concentration of Sr is around 8000 μg/l (~91 μM) (Chester, 1990). High oceanic levels of both Ba^{2+} and Sr^{2+} could have been a consequence of large scale pumping of seawater through the oceanic crust as a response to increased hydrothermal activity throughout the Archean (Veizer, 1982, 1983). It is believed this water-crust interaction was the most important factor influencing the composition of the early ocean. Veizer (1982, 1983) and Veizer et al. (1989b,a) have analysed a number of Archean carbonates in terms of chemical and isotopic composition (particularly Sr isotopes), which indicate that they do have a hydrothermal origin. Such carbonates show an increase in concentration of both Ba and Sr, and it has been shown that these Archean carbonates are enriched by a factor of ~10 in Ba and by a factor of ~3-6 in Sr compared to Phanerozoic counterparts (Veizer et al., 1989b). High levels of Ba^{2+} and Sr^{2+} in these carbonates would then translate to high oceanic concentration as well. Maisonneuve (1982) also suggested that the Precambrian ocean could have maintained a high level of Ba^{2+}, due the lack of sulfates. Ba-solubility was only limited by Ba carbonate solubility (Maisonneuve, 1982) (pK_{sp} 8.56, see Section 2.2.4.1, and Appendix A.2). If the 'Canfield'-model of the early ocean (low sulfate and anoxia) is correct (see Canfield (1998) and Canfield (2004)), this would allow an increased seawater concentration of Ba^{2+} and Sr^{2+}.

Silica

The early ocean is also believed to have been rich in dissolved silica as evidenced by the large amounts of Archean siliceous rocks (Siever, 1957). The modern oceans are depleted in silica due to the presence of diatoms, radiolaria and silica sponges sequestering most of the aqueous silica species(Siever, 1957; Cloud, 1973a; Knauth, 1994; Knauth and Lowe, 2003), giving an average oceanic silica concentration of ~ 70 μM (Tréguer et al., 1995). Silica precipitation today is mostly in the form of biogenic opal (see Section 2.3.1 for description of opals and other naturally occurring silicas) (Knauth, 1994). The pre-biological silica cycle, a process not fully understood, must therefore have been solely governed by abiotic inorganic precipitation and dissolution reactions (Siever, 1957). The influx of dissolved silica to the ocean today is dominated by tectonism, weathering and hydrothermal input; processes that would have been active in the abiotic world (Siever, 1992). Increased hydrothermal activity and volcanism in the Precambrian would have supplied increased levels of silica to the oceans as compared with today. The increased level of silica in hydrothermal solutions is derived from alteration and dissolution of silicate minerals (Siever, 1957). Contemporary hydrothermal waters (>300 °C) can contain up to 19 mM dissolved silica, whereas the cold waters around mid-ocean ridges are around a few micromolar. This low concentration is caused by dilution as well as precipitation of amorphous silica around the vents (Tréguer et al., 1995).

Sugitani (1992) suggested that the 'Pilbara Ocean' was rich in both silica and iron that originated from hydrothermal activity. Geochemical analysis of several Archean cherts in the Pilbara region showed evidence of extensive precipitation of iron oxides and carbonate. It is believed that chert layers, without sedimentary structures like ripple marks etc., were precipitated as an amorphous silica gel (Sugitani, 1992). Silica efflux from the ocean would, in the absence of biologically mediated precipitation, be controlled by reactions, interactions and precipitation with clay minerals, zeolites and other silica phases, as well as with organic matter (Siever, 1992). It has been suggested that silica complexation and interaction with organic materials could have been important reactions in the Proterozoic ocean (Siever, 1992). Numerous laboratory experiments have shown enhanced dissolution rates of quartz in organic-rich aqueous solutions, an effect attributed to complexation between silica and organic species (Bennett and Siegel, 1987; Bennett et al., 1988; Bennett, 1991). That such an interaction can occur is also known from the fossilisation of certain microbes where the cell-wall may act as nucleation sites for precipitation of silica (Knoll, 1985; Westall, 1999). As was discussed in Section 2.3, silica chemistry is very complex, and not completely understood. Silica complexation with numerous ions/molecules in any natural system

is expected.

Maliva et al. (2005) comparatively analysed a number of Proterozoic and Phanerozoic cherts to evaluate the origin of the silica and the way it was deposited. They identified four main chert types in the Precambrian rocks older than 1.8 G.; 1) late carbonate replacement, 2) silicified evaporites, 3) early diagenic[2] peritidal (often associated with fossilized microbes), and 4) early diagenic subtidal cherts[3]. The latter is only present in cherts older than 1.8 Ga, indicating a high concentration of silica in the ocean at that time, able to precipitate directly out of the open seawater. Concentrations would likely have been at or above the equilibrium concentrations for amorphous silica and opal-CT. Younger Proterozoic rocks, on the other hand, contain some early diagenic peritidal cherts, whereas they are absent in Phanerozoic ones. These cherts of various age therefore record a change in silica concentration with time, with progressively less dissolved silica present in the younger oceans (Maliva et al., 2005). High concentration of silica is also compatible with an alkaline soda ocean as predicted by Kempe and Kaźmierczak (1994).

Knauth and Lowe (2003) suggested that the lack of biological silica precipitation in the Precambrian ocean, together with silica efflux from submarine activity and weathering could cause the oceans to contain >300 ppm silica. Furthermore, they also proposed, based on oxygen isotope geochemistry of 3.5 Ga cherts in the Swaziland Supergroup, that the Archean climate was very hot, with an averaged surface temperature between ~55-85 °C (Knauth and Lowe, 2003).

Although current climatic and oceanic models for the early Earth remain speculative, at some time during the Hadean and Archean periods, life managed to establish itself on this planet. Clearly the early atmosphere and ocean provided the necessary settings for the emergence and maintenance of life, maybe as early as 3.8 Ga years ago.

In relation to biomorph synthesis one can conclude that silica concentrations are believed to have been high, possibly higher than 300 ppm, and very similar to those in some of our experiments (see Chapter 3). Barium and strontium concentrations are also believed to have been higher than today, although no definitive concentrations of these species can be given. Furthermore, pH could have been high (globally or locally) as suggested by Kempe and co-authors.

The next section will discuss the evidence for early microbial life and how it is identified.

[2]Diagenesis refers to the sum of all changes (physical, chemical, and biological) that can occur in a sediments after deposition. Weathering and metamorphism is not included (Lapidus, 1990)

[3]Peritidal rocks are deposited in an area associated with a tidal flat. Subtidal refers to deposition below the low-tide level

5.3 The record of early Life

This section describes the findings of the earliest putative signs of life on Earth centered around some famous examples, how they were identified and the debates that followed. The search for the earliest of life continues to stimulate intense debate regarding significant indicators of biogenicity. Textbooks commonly reveal that life was flourishing and widespread 3.5 billion years ago (Cowen, 1995; Madigan et al., 1996; Schopf, 1999a) (c.f.(Armstrong and Brasier, 2005)). However, these claims are now being questioned as the awareness of abiotic explanations of apparent life-like fossil records is increasing. As a result the search for definitive evidence of early life is becoming more and more demanding. The key source of evidence lies within the geological record, but most Archean rocks are severely metamorphosed and the capacity to find unaltered evidence of life is rather limited. As these rocks have experienced high temperatures and pressures one needs to be very careful in making claims about the existence of life within them.

The potential evidence of early life, fossilised in the geological record throughout billions of years, can be grouped into three different categories: chemical evidence (isotopic signatures and biomarker detection), morphological evidence (microfossils) and biological mediated sedimentation (structures like stromatolites). Here I provide a discussion of such evidence of life anchored around a few examples that emphasize the problem of distinguishing the real biological evidence from abiotic and fake counterparts such as biomorphs. I pose the question; Is it possible to distinguish between true microfossils and biomorphs according to the criteria used to assure a biogenic structure?

5.3.1 Chemical signatures of early life

In this section a brief overview of the biological signatures drawn from atomic and molecular evidence of carbon is given. Other elements and compounds, e.g. sulphur and nitrogen isotopes, are also of importance to this field but are not discussed any further. Carbonaceous material, derived from transformations of mostly biological debris but also from possible abiotic carbonization reactions, is common in metasedimentary rocks. The life-time of the chemical character of biomarkers in the geological record and therefore the ease of identification, is constrained by degradation kinetics of such molecules. Proteins and DNA, which are undoubted indicators of biology at work, have very low preservation potential as these molecules are degraded very easily. Proteins and their component amino acids are degraded and lost in the geological record within $10^5 - 10^6$ years. DNA, which is even more fragile than proteins, is not preserved for more than 10^4 years (Bada et al., 1999). Other biomacromolecules, like lignins and

tannins, are more resistant to degradation and are therefore selectively enriched in sedimentary organic matter (De Leeuw and Largeau, 1993). If compressed or heated under reducing conditions, which occurs during burial, the ultimate fate of all these organic compounds is to convert into graphite-like materials, losing non-carbon atoms and distinctive functional groups as they do so. The exact nature of the degraded hydrocarbons is strongly dependent on the time-temperature history experienced by the sample. Different carbonaceous material can display different degradation kinetics, which can result in graphitic matter coexisting with both amorphous carbon as well as relatively unaltered waxy hydrocarbons (Large et al., 1994). In this section carbon isotopes, biomarkers and kerogen will be discussed as they are commonly used to indicate the presence of early life.

5.3.1.1 Carbon isotopic signature

Isotopic signatures of carbon are extensively used as biosignatures of life. Biological carbon is enriched in the light isotope ^{12}C with respect to the inorganic counterpart such as sedimentary carbonate. This carbon fractionation arises from the preferential uptake of ^{12}C over ^{13}C during assimilation of CO_2 in autotrophic (in particular photosynthetic) microorganisms. Discrimination of ^{13}C is a result of physiochemical effects during enzymatic reactions in the first carbon-fixing step (Schidlowski, 2001). The depletion of ^{13}C is normally expressed as $\delta^{13}C$, in terms of the parts per thousand difference in the ratio $^{13}C/^{12}C$ of the sample (sa) compared to a standard (st) known as Pee Dee belemnite (PDB):

$$\delta^{13}C = \left[\frac{(^{13}C/^{12}C)_{sa}}{(^{13}C/^{12}C)_{st}} - 1\right] \times 1000 \qquad (5.2)$$

$\delta^{13}C$ values of down to -80‰ have been reported for specific metabolites, but on average the total contemporary biomass displays a $\delta^{13}C$ depletion of about -26±7‰. This is significantly lighter than atmospheric CO_2, which has a $\delta^{13}C$ of about -8‰(Francey et al., 1999), while carbonate carbon clusters around 0‰(Marais, 2001). This isotopic signature is retained in the organic material after cell death. Most of the biological matter ends up as CO_2 during degradation. On average, 99.8 % of biological matter is recycled back to CO_2. However, a small fraction of biopolymers and other degradation resistant biomolecules may be preserved in sediments and undergo geochemical alteration eventually resulting in isotopically light kerogen; an insoluble mostly aromatic highly condensed endproduct of biogenic organic matter (Durand, 1980a; Schidlowski, 2001). In the geological record, isotopic carbon signatures apparently compatible with a biological origin date back ~ 3.8 billion years, raising the possibility of photosynthetic

microorganisms at a time when the Earth was still suffering a heavy bombardment of asteroids (Mojzsis and Harrison, 2000; Schoenberg et al., 2002; Ueno et al., 2002, 2004).

5.3.1.2 The case of Isua and Akilia

A celebrated and currently much disputed example of isotopic evidence for early life comes from ^{13}C-depleted graphite found in metasedimentary rocks in the Isua Supracrustal Belt and on Akilia Island in West Greenland (Mojzsis et al., 1996; Rosing, 1999; Moorbath, 2005). These rocks constitute some of the oldest known well exposed rocks on Earth and date back to ~3.85 billion years (Black et al., 1971; Moorbath et al., 1973; Nutman et al., 1996) and have been exposed to high-grade metamorphism (amphibolite facies; moderate to high temperature 500-700 °C and low pressure), altering the original composition and texture of the rock. These most ancient rocks have been the subject of intense debate whether or not they contain the oldest proof of terrestrial life. There have even been reports of microfossil-like objects resembling yeast (Pflug and Jaeschke-Boyer, 1979), but these claims were later refuted due to the severe metamorphism of the rock, during which no morphological traces of fossils could have been preserved (Appel et al., 2003). Several research groups have described findings of ^{12}C enriched carbonaceous matter in the rocks of West Greenland (Oehler and Smith, 1977; Perry Jr. and Ahmad, 1977; Mojzsis et al., 1996; Rosing, 1999; Ueno et al., 2002; van Zuilen et al., 2003). Mojzsis et al. (1996) argued that carbonaceous inclusions in minute grains of apatite (calcium phosphate, $Ca_5(PO_4)_3(F, Cl, OH)$) found in a rock interpreted to have originated as a sedimentary banded iron formation (BIF) on Akilia Island could only have been formed by biological processes and life must therefore have emerged prior to 3.8 billion years before present (Mojzsis et al., 1996). Since then, these findings have been the subject of great controversy, focussing primarily on whether these rocks hosting apatite grains in fact are sedimentary. Fedo and Whitehouse (2002) argued that the rocks were derived from metasomatic events (volcanic intrusions) that subsequently experienced repeated events of metasomatism and metamorphism thereby altering the composition, resulting in a rock superficially similar to a BIF. This demonstrated that these rocks could not have been hosting life at the time of formation. It was later suggested that those rocks analysed by Fedo and Whitehouse were different from the ones in which the apatite grains containing graphite were found (Nutman et al., 2004). Newly analysed rocks from the very same BIF in Akilia Island show iron and sulphur isotopic composition indicative of a sedimentary origin (Mojzsis et al., 2003; Dauphas et al., 2004). But controversy still remains. Lepland et al. (2005) reanalysed the original rock sample in which Mojzsis et al. (1996) reported graphite inclusions in supposedly biogenic apatite, as well as 16

other samples from the area. Several apatite crystals were found but none contained any graphite. This casts a great shadow of doubt on the original study, and has raised questions of the location of the original graphite-containing sample (Dalton, 2004; Moorbath, 2005).

An important twist to the story of isotopically light graphite is that this feature is not necessarily exclusive to biological matter (see also Section 5.3.1.5). van Zuilen et al. (2002) showed that carbonate-rich rocks in Isua contain ^{13}C-depleted graphite associated with iron-bearing carbonates and magnetite which could be explained by inorganic abiotic processes. It has been shown experimentally that siderite (iron carbonate) thermally decomposes to form graphite, non-graphitic carbonaceous matter and magnetite at temperatures above 300 °C (Perry Jr. and Ahmad, 1977; van Zuilen et al., 2002; McCollom, 2003). An abiotic origin of graphite could therefore be inferred based on the minerals present as well as the thermal history of the rocks. Equilibrium isotope fractionation during siderite decomposition could explain the isotopic signature ($\delta^{13}C$ between -12 to -10 ‰) of the graphite decomposition product (van Zuilen et al., 2002, 2003). Even lighter ($\delta^{13}C \sim$ -28‰) carbon phase found in sedimentary rocks with low graphite content were explained as being recent contamination introduced by percolating ground water (van Zuilen et al., 2002). van Zuilen et al. (2003) concluded that all $\delta^{13}C$ signatures observed in metacarbonate rocks (secondary carbonate veins) within Isua Supracrustal Belt can be explained by disproportionation of iron carbonates during high-grade metamorphism (see section 5.3.1.5).

Yet another explanation for the isotopically light carbon was given by Schoenberg et al. (2002) who suggested that a meteoritic origin should be considered, since debris from carbonaceous chondrites carrying insoluble carbon particles with ^{13}C of around -18‰could have been deposited within the sediments (Schoenberg et al., 2002).

The early Archean rocks of West Greenland have been interpreted as the oldest known sedimentary formations on Earth and its geological interpretation is therefore crucial to the investigation of early life. Since these rocks have been altered through geochemical processes, the debate has centered on carbon isotopic signatures. A crucial aspect, often overlooked, is the fact that carbon isotopic fractionation is not exclusive of biological systems. *Any* physical process involving atomic transport, from chemical reactions to diffusion, will induce molecular fractionation. Plausible geochemical processes, including siderite decomposition, serpentinization and Fischer-Tropsch processes (Holm and Charlou, 2001), can result in carbonaceous materials with substantial ^{13}C depletion (Horita and Berndt, 1999; Kelley and Früh-Green, 1999; McCollom and Seewald, 2006). For instance, Lancet and Anders (1970) showed that Fischer-Tropsch-type reactions can give rise to hydrocarbons with $\delta^{13}C$ of well below -35‰(minimum of close to -100 was observed for CH_4 early during the reaction, and

heavier 'waxy' carbon showed a $\delta^{13}C$ of ~-60‰), very similar to biologically produced carbonaceous matter, as well as organic material found in meteorites. McCollom and Seewald (2006) further confirmed the $\delta^{13}C$ depletion in hydrocarbons (mainly alkanes) produced by Fischer-Tropsch-type reactions under highly reducing hydrothermal conditions, similar to those occurring in geological systems. The thermodynamics of the system, including temperature and pressure, will then determine the degree of fractionation. More detailed analysis of these parameters will establish whether the carbon isotopic signatures of these ancient rocks really evidence biological remnants.

5.3.1.3 Biomarkers

Molecular 'fossils', or biomarkers, are chemically degraded biomolecules - typically derived from lipids and biopolymers - that are characteristic constituents of organisms. Such molecules are found in sedimentary rocks, where they have survived billions of years retaining structural and isotopic compositions reminiscent of molecular species found in extant micro-organisms. Originating from the cellular membrane, these fossilised lipids can provide information on prehistoric biodiversity and environmental conditions. Since many microbes require specific habitats, discovery of corresponding biomarkers affords valuable inferences about the paleoenvironment in which the microbe once lived (Brocks and Summons, 2004). During fossilisation biolipids degrade and lose functional groups, leaving a hydrocarbon skeleton as a relic of the original molecule. Many biomarkers are diagnostic for certain groups of organisms. For example, it has been shown that the hydrocarbon botryococcane is exclusively produced by the alga *Botryococcus braunii* (Brocks and Summons, 2004). Such diagnostic biochemicals within the geological record can then be used to prove the presence of specific taxa at the time of sedimentation.

Brocks et al. (1999); Summons et al. (1999) showed that sedimentary bitumen from the 2700 million-year-old Fortescue Group of Pilbara Craton and ~ 2500 million-year-old Mt. McRae Shale of Hamersley basin, both in Western Australia contains significant amounts of 2-methylhopanes. These hydrocarbons are the derivatives of 2-methylbacteriohopanepolyols, diagnostic for photosynthetic cyanobacteria (see Figure 5.3) (Summons et al., 1999). This places oxygen producing bacteria well before the generally agreed time when the terrestrial atmosphere developed considerable amounts of free oxygen. Brocks et al. (1999) also showed that steranes, characteristic of eukaryotes, are present in ~2700 million year-old shales of Roy Hill, Jeerinah Formation Western Australia. However, the possibility of contamination cannot be underestimated when examining biomarkers from extremely mature or metamorphosed rocks, and all current evidence should be interpreted with caution (Brocks et al., 2003).

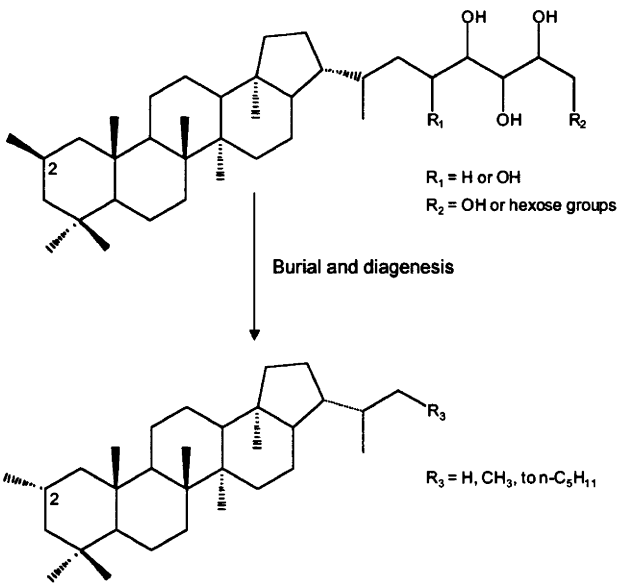

Figure 5.3: The chemical structure of 2-β-methylbacteriohopaneols (top) synthesised by cyanobacteria and the corresponding derivative 2α-methylhopanes (bottom) found in the sedimentary record. Adapted from (Summons et al., 1999), see also (Brocks and Summons, 2004) for more information on biomarker structures and degradation pathways.

These biomarkers provide compelling evidence that eukaryotes were present in the late Archean (Brocks et al., 1999), prior to the oldest known microfossil evidence that are certainly eukaryotic at ~1.5-1.4 Ga from the Roper Group, Australia (Javaux et al., 2001, 2003, 2004). More ancient findings of allegedly eukaryotic microfossils have been reported in the 1.87 Ga Negaunee iron formation, Michigan (Han and Runnegar, 1992; Schneider et al., 2002), but the interpretation of these fossils has been questioned, due to the lack of structural features indicative of eukaryotes (Samuelsson and Butterfield, 2001).

5.3.1.4 Kerogen

In contrast to the recent discovery of biomarkers in the geological record, recognition of highly degraded biomolecules, termed kerogen, has long been associated with detection of ancient life. The term kerogen was originally coined by A. Crum-Brown to describe waxy distillation products from the Lothian oil shales (from Greek Keros = wax). The use of the term is closely linked to the research of oil shales and its origin and has had various meanings and definitions throughout history (Durand, 1980b). Kerogen is a generic name for a class of compounds, as is proteins or metals, and is defined as the phase of sedimentary organic matter that is insoluble in organic solvents and capable of generating petroleum (Vandenbroucke, 2003). Kerogen is intermediate

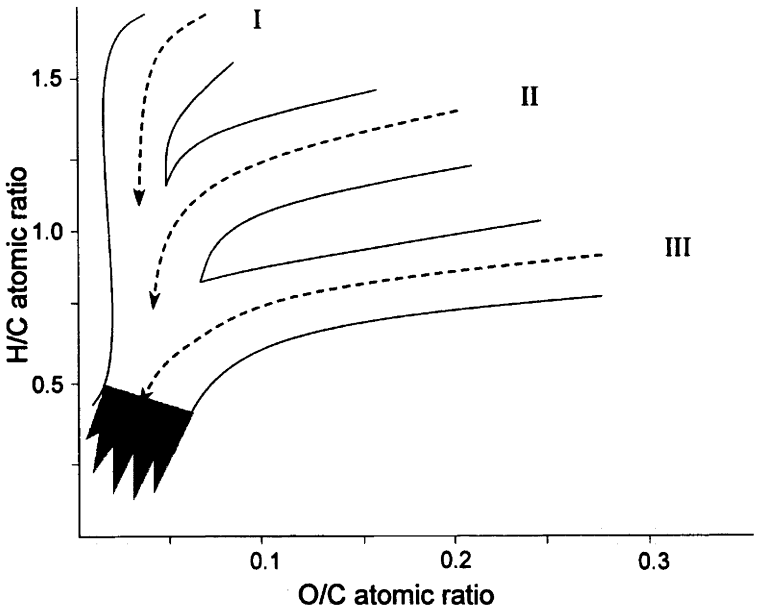

Figure 5.4: Typical Van Krevelen diagram, showing evolutionary pathways (dashed arrows) of the three different types of kerogen. The highlighted area represents the zone where severe structural rearrangement of the carbon skeleton occur. Adapted from Durand and Monin (1980)

in chemical character between carbonaceous cellular material and graphite. Depending on the degree of metamorphism it ranges in colour from brown (immature) to black (metamorphosed), as functional groups are lost and condensation continues to form an increasingly aromatic phase that may eventually approach the chemical characteristics of graphite (Hayes et al., 1983). The composition of kerogen depends on the initial source of organic matter (algal, higher plants etc.) and maturity. Immature kerogens are therefore a complex network of degradation resistant biopolymers interconnected with polycyclic, aromatic and linear compounds. Elemental analysis of kerogens have identified three types of kerogen, named I, II and III, distinguished by their H/C and O/C ratios (and their origin), see Figure 5.4, (although other classifications exists they will not be discussed here, see (Hunt, 1979) and references therein). Type I is particularly hydrogen-rich and believed to be derived from microbial debris, II with an intermediate composition of H and O is often associated with a marine environment with a strong planktonic source of carbonaceous matter, whereas type III is distinguished by a high oxygen content and mainly derived from higher plants (Hayes et al., 1983; Vandenbroucke, 2003).

The three types and their evolutionary pathways during diagenesis, catagenesis and metagenesis, terms that are explained further below, are distinguished by their chemical composition. Plots of elemental H/C vs. O/C, called van Krevelen diagrams,

have been used extensively as a tool for determining the degree of maturation as well as to get an idea of the molecular structure of various kerogens (Baskin, 1997). As can be seen in Figure 5.4 immature type I kerogens contain low amounts of oxygen and initial high H/C ratio, reflecting a very strong aliphatic contribution to the composition. Type II, which is associated with sulfur, contains more aromatic and aliphatic cycles than type I. Type III, on the other hand, has contributions from both highly aromatic structures as well as aliphatic moieties (Vandenbroucke, 2003). As kerogen matures, large amounts of oxygen is lost mainly as CO_2 and H_2O during the first transformation of the organic matter, as is evident for the evolutionary pathways for kerogen type II and III in Figure 5.4. These first reactions, called diagenesis, involve both biological, physical and chemical alterations at low temperature (Hunt, 1979). As burial depth increases, so does the temperature (ca 2-5°C per 100 metres), which further alters the kerogen, a process called catagenesis. During catagenesis, cracking of the kerogen produces low molecular weight hydrocarbons that may eventually be expelled as petroleum (Hunt, 1979). In the van Krevelen diagram it is evident that type I kerogens have the most petroleum generating potential as this type has the highest H/C ratio (although other factors such as the thermal history of the sediment and organic migration potential within the rocks are important to oil field formation). During catagenesis, lighter and lighter hydrocarbons are expelled leading eventually to gaseous products, leaving an insoluble condensed highly aromatic type of kerogen. Below an atomic H/C ratio of about 0.6 all kerogen types merge in the van Krevelen diagram. The shaded area in Figure 5.4 represents the last stage of kerogen maturation, metagenesis. Vandenbroucke (2003) suggested that during metagenesis, no further condensation of aromatic units occur. Instead, rearrangement of the aromatic carbon skeleton produces a more stack-like ordered structure of aromatic units consisting of almost pure carbon. Even though all kerogen types appear to be chemically similar at this stage, the size of these aromatic units is, apparently, specific of kerogen type (Vandenbroucke, 2003).

It has been suggested that petroleum generation may date back as early as the Archean, as abundant deposits of organic matter is deposited within the sediments. Thermal indicators point to a 200-300 °C temperature history of the rocks, and with extensive deposits of pyrobitumen, expulsion of oil and gas must have been widespread in the Archean (Rasmussen, 2005). In addition to elemental analysis, kerogen has traditionally also been analysed in terms of crystallinity using x-ray analysis and transmission electron microscopy (TEM), molecular composition using infrared spectroscopy and with optical techniques to allow colour recognition, and also for carbon isotopes (as discussed in Section 5.3.1.1) (Hayes et al., 1983). Rock-Eval analysis of kerogens has become a standard method to evaluate the quality of organic matter in

rocks for the petroleum industry. This technique, which had been used for over 20 years, is based on pyrolysis of bulk rocks that yields information on the quantity of gas+oil, hydrocarbons produced from thermal cracking of insoluble kerogen, as well as the Total Organic Carbon (TOC) and mineralitic carbon content of the rock. The temperature, at which the maximum yield of thermally produced hydrocarbon from kerogen, is referred to as T_{max} and is used as a measure of the maturity of the kerogen, the higher T_{max} reflects a more mature kerogen (Lafargue et al., 1998; Behar et al., 2001). (For more information on geochemical organic matter and other techniques used to characterise kerogen, see (Engel and Macko, 1993).)

Most of these techniques require relatively large rock samples for bulk analysis of the organic matter present. Bulk analyses of kerogen in sedimentary rocks are not especially useful for establishing the chemical composition of minerals and their interaction with kerogen. Such analyses are normally performed with Raman spectroscopy, which allows *in situ* characterisation of the sample. This is a popular technique for characterising all sorts of carbonaceous material, synthetic as well as natural, as it is especially sensitive to structural and chemical differences in carbon.

Raman spectroscopy of carbonaceous materials

A separate section on Raman analysis of carbonaceous materials is included here, as this technique is often used to characterise the carbon entity of microfossils, and is also used in the following chapter (Chapter 6) to analyse adsorbed and cured hydrocarbons on biomorphs.

Raman spectra of carbonaceous material are normally divided into two regions; the first order region between 1000-1800 cm^{-1} and the second order region between 2200-3400 cm^{-1} (Beyssac et al., 2003). The first order region is the one that will be discussed here, since this region is the one of most interest in terms of comparison to Raman spectra of kerogen to those of other carbonaceous materials. The second order region contains peaks that can be assigned to overtones and/or combinations of the first-order bands, and their significance is not yet understood (Vidano and Fischbach, 1978; Nemanich and Solin, 1979; Vidano et al., 1981; Beyssac et al., 2002).

As has been discussed previously, kerogen maturity is related to the physiochemical environment. It has been shown that the degree of metamorphism (temperature and pressure effects) has a large effect on the degree of carbon ordering in carbonaceous matter, detected with the aid of Raman spectroscopy (Beny-Bassez and Rouzaud, 1985; Pasteris and Wopenka, 1991; Wopenka and Pasteris, 1993; Yui et al., 1996; Jehlička et al., 2003). Heat treatments of natural and synthetic carbonaceous materials show an evolution towards graphite with increasing temperature (Beny-Bassez and Rouzaud,

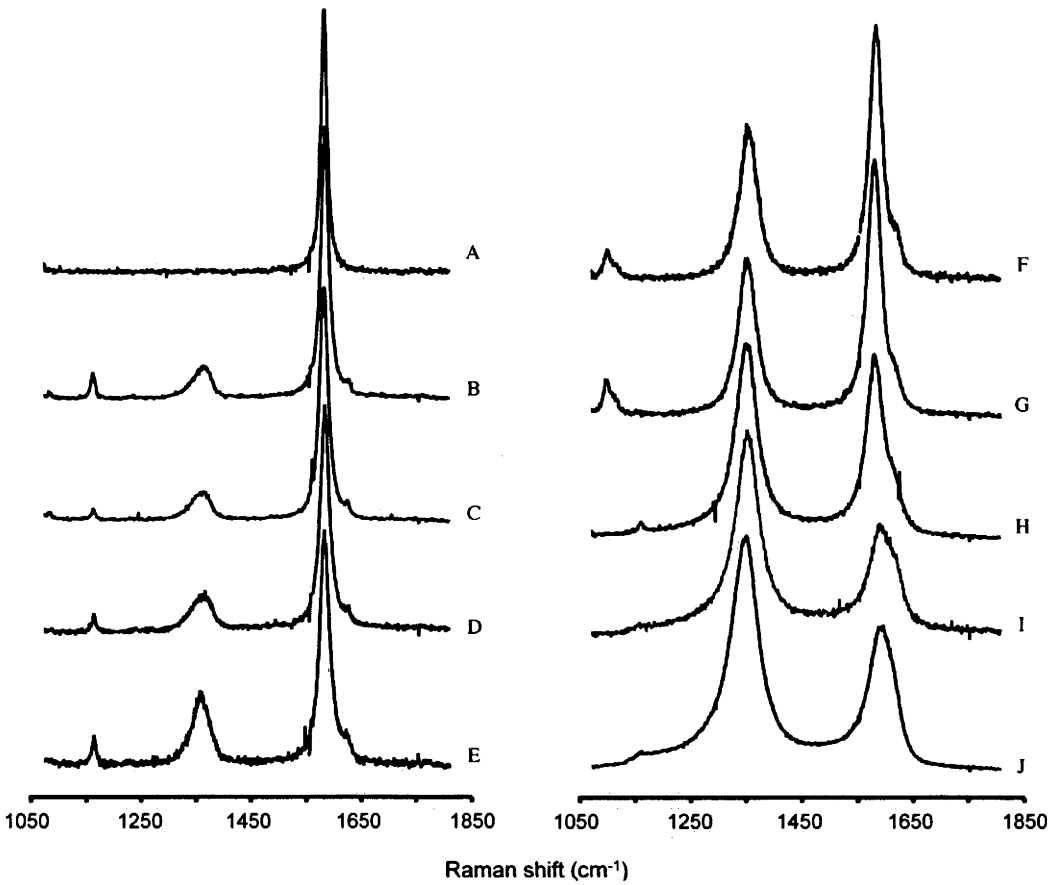

Figure 5.5: First-order Raman spectra of carbonaceous material from rocks with different metamorphic grade, which decreases from (A-J), showing the evolution of a more ordered carbonaceous material with increasing metamorphic grade (see text for details). The experienced average peak temperature and pressure for the various samples are: (A) 725 °C and 32 kbar, (B) 550 °C and 6 kbar, (C) 530 °C and 9 kbar, (D) 500 °C and 20 kbar, (E) 500 °C and 3 kbar, (F) 480 °C and 9 kbar, (G) 440 °C and 8 kbar, (H) 390 °C and 19 kbar, (I) 330 °C and 13 kbar, (J) 330 °C and 6 kbar. The bands at 1050-1100 are due to the mineral matrix. Adapted from Beyssac et al. (2002), see also references within for more information on the individual samples.

1985). Raman spectra of various kerogen samples can be seen in Figure 5.5. These samples differs in metamorphic grade, with (A) having experienced the highest, and (J) the lowest temperature and pressure. In all, but one sample (A), two peaks related to carbonaceous materials are observed in the Raman spectra; one at ~1350 cm^{-1} and another at ~1600 cm^{-1}. These peaks are normally referred to in the literature as D (disordered) and G (graphitic) band respectively and both are common in disordered carbonaceous materials.

Numerous papers have appeared in scientific journals regarding Raman spectroscopy of crystalline and disordered carbonaceous materials since the 1970's in at-

tempts to deduce the information stored in the spectra. Tuinstra and Koenig (1970) reported in their pioneering Raman investigation of graphite that only one Raman line at 1575 cm^{-1} is observed in a single crystal of graphite: the G band. The G band position for crystalline graphite was later refined to 1582 cm^{-1} (Dresselhaus and Dresselhaus, 1982). All other carbonaceous or graphitic materials show an additional band at 1355 cm^{-1}: the D band (Tuinstra and Koenig, 1970). They also observed that the relative intensities between these two bands varies according to the type of graphitic sample, a feature also recognised in Figure 5.5. The intensity of the D band increases with an increase in the degree of disorder in the sample, and with a decrease in crystal size of the sample (Tuinstra and Koenig, 1970). The G band is present in all graphitic/carbonaceous samples and occur as a result of in-plane bond-stretching of pairs of sp^2 carbon atoms (Vidano and Fischbach, 1978; Ferrari and Robertson, 2000). This band always occur between 1500-1630 cm^{-1} and is not restricted to aromatic carbon rings, as it is present in spectra of both aromatic and olefinic molecules (Ferrari and Robertson, 2000). In disordered carbons, this peak is broader than in crystalline graphite and is shifted to higher wave numbers (Tuinstra and Koenig, 1970; Nakamizo et al., 1974). This shift in the G band position has been attributed to the appearance of an additional peak at ~1620 cm^{-1}, the so called D′ peak (Vidano and Fischbach, 1978). With increasing processing temperature, the D′ peak decreases in intensity while the G peak narrows and increases in intensity, thereby lowering the position of this composite peak to lower wave numbers (Vidano and Fischbach, 1978). In very disordered carbons (or very small crystal size) the D′ and G peaks merge into a single broader peak (Escribano et al., 2001), see Figure 5.5 J. The D′ peak is dependent on structural disorder, as is the D peak, and their intensities increase with an increase in structural disorder (Vidano et al., 1981). The D peak at 1355 cm^{-1} is also believed to be associated with in-plane vibrations due to structural imperfection and, although its presence is not completely understood, has been tentatively related to crystal size (Tuinstra and Koenig, 1970; Vidano and Fischbach, 1978; Marshall et al., 2005). Bands at 1150 and ~1500 cm^{-1} can also be observed for very disordered sp^2 carbonaceous materials. The ~1500 cm^{-1} band in particular can be seen as a broad band between the G and the D bands in Figure 5.5 spectrum J. The origin of the 1150 cm^{-1} band is not known. The ~1500 cm^{-1} band has been attributed to both out-of-plane defects such as tetrahedral carbons (Beny-Bassez and Rouzaud, 1985), as well as an amorphous form of sp^2 carbon (Marshall et al., 2005). Variables such as sp^2/sp^3, carbon ring sizes, and domain size and shape are important in deciphering the true meaning of Raman spectra. Clearly it is a very complicated issue, and is likely to be dubious given the extreme structural variability in amorphous carbons.

Beyssac et al. (2002) showed that the ratio R2=D/(G + D + D′) (calculated using

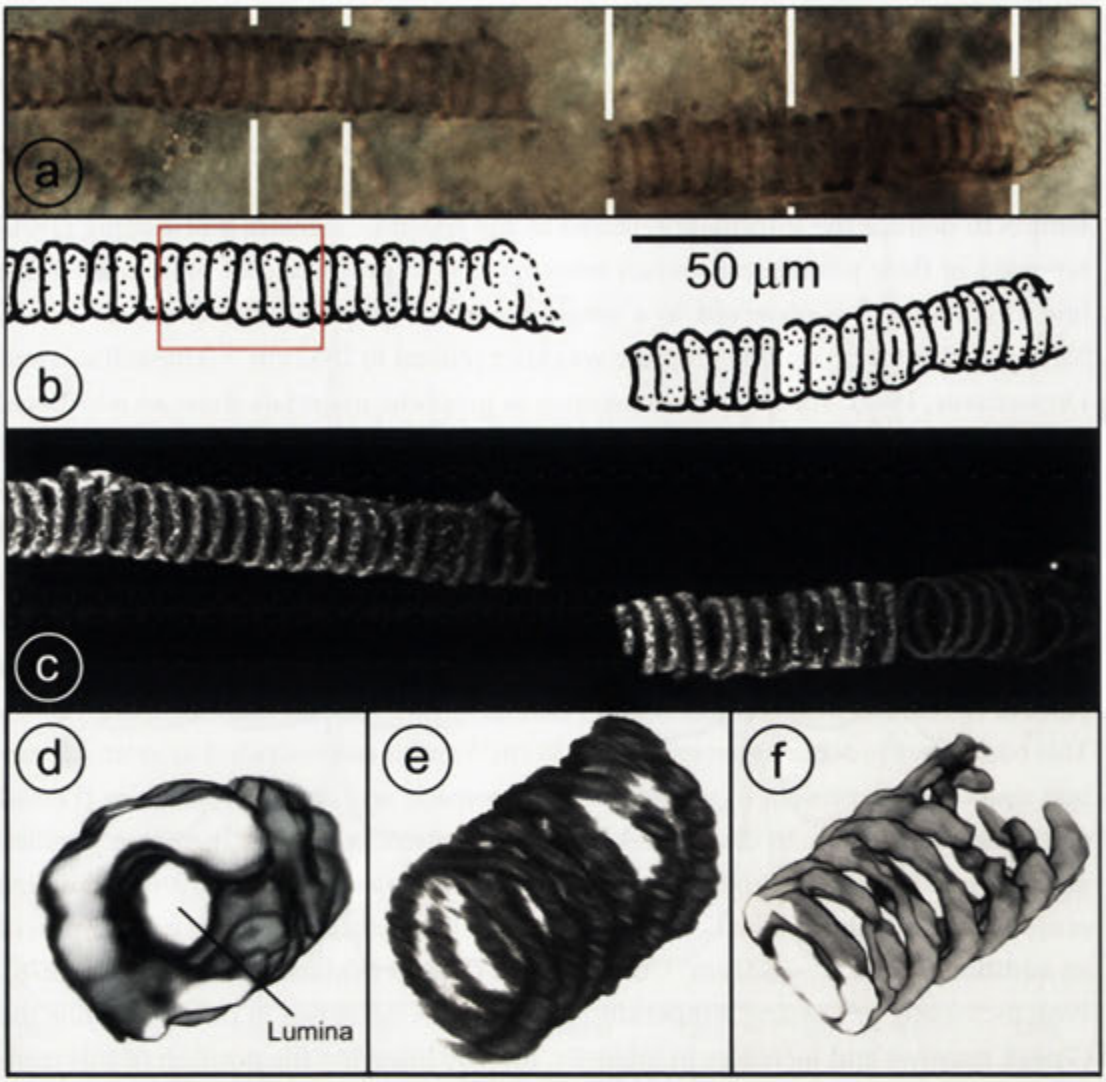

Figure 5.6: Fossilised unnamed cyanobacterium from a conical cherty stromatolite in the 650-Ma-old Chichkan Formation in Kazakhstan. (a) Photomontage of optical images, (b) interpretive drawing, (c,e) 3D confocal laser scanning microscopy images of the selected area, marked in red in (b), and (d,f) 3D Raman images, acquired from the G band, also from the same highlighted area in (b). Adapted from Schopf and Kudryavtsev (2005) and Schopf et al. (2006).

peak areas) showed a linear correlation to the metamorphic temperature in the range 330-650 °C according to the equation $T\,(°C) = -445 \cdot R2 + 641$. This is manifested in the degree of organisation of the kerogen, which increases with increasing temperature and pressure experienced by the rocks. Due to the known degradation pathways for sedimentary organic mater, it can be used as a geothermometer of the conditions during metamorphism (Beyssac et al., 2002).

Raman spectroscopy has recently become a popular technique to study carbonaceous material associated with structures believed to be fossilised microbes (see Section 5.3.2.1 on microfossil identification and Section 5.3.3.2 on the debate of microfossils from the Apex chert). Traditionally, fossilised microbes have been identified as 'carbonaceous' largely based on colour and texture of the fossil (Schopf and Kudryavtsev,

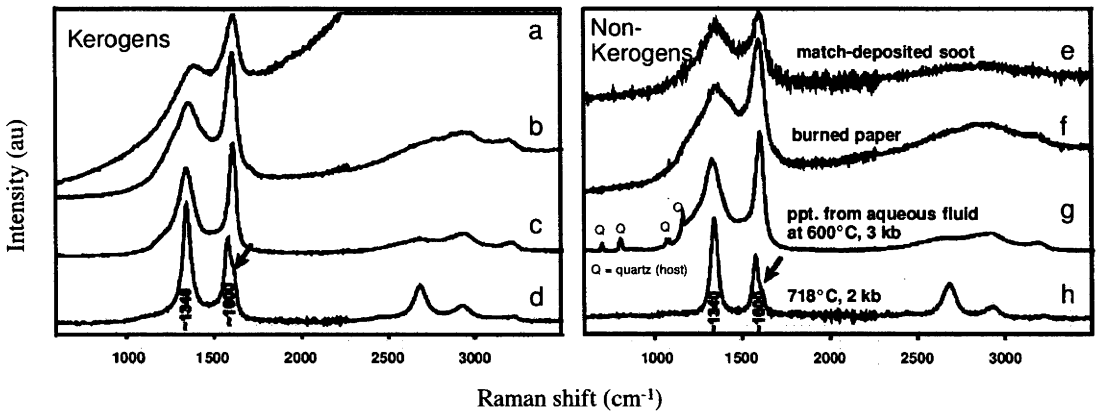

Figure 5.7: Comparative Raman spectra of kerogenous (a-d) and non-kerogenous (e-h) matter, showing the similarities between the samples. (a-d) are kerogen samples from various localities with different geological age; (a, b) are kerogens from the 1.4 Ga Roper Group that has experienced little metamorphism, (c) 2.8 Ga sample from the Fortesque Group metamorphosed to pumpellyite-epidote/actinolite grade, (d) 3.5 Ga kerogen from the Swaziland Sequence with greenschist facies metamorphism. (e-h) are abiological carbonaceous matter derived through various processes; (e) is a match-deposited soot, (f) a burned tea-bag wrapper, (g) precipitate synthesised from acetic acid at 600 °C and 3kb, (h) precipitate synthesised from methane at 718 °C and 2 kb. Adapted from Pasteris and Wopenka (2003), see also references within for more information on the individual samples.

2005). Nowadays, kerogen incorporated in organic-walled microfossils is commonly analysed by means of Raman spectroscopy (Kudryavtsev et al., 2001; Schopf et al., 2002b; Schopf and Kudryavtsev, 2005), and more recently also with Fourier transform infrared spectroscopy (FTIR) (Marshall et al., 2005), and confocal laser scanning microscopy (CLSM) (Schopf et al., 2006), which allow detailed analysis of minute samples. Both Raman spectroscopy and CLSM has been proven particularly useful since it is a non-destructive technique which can be used *in situ* on specimens within petrographic thin sections. Kudryavtsev et al. (2001); Schopf et al. (2002b); Schopf and Kudryavtsev (2005) have successfully used Raman techniology, both in spot mode as well as 2- and 3 dimensional mapping mode, to characterise numerous microfossils from various localities of different ages (see Figure 5.6 and also Section 5.3.3.2 and Figure 5.9). 2- and 3 dimensional Raman spectroscopy maps out an area or volume where a predetermined Raman band exists. In particular, the 3D Raman spectroscopy has the advantage that the 3D morphology of the sample is obtained (see Figure 5.6 d and f) (Schopf and Kudryavtsev, 2005). Similarly, 3D CLSM maps out a volume of a fluorescing sample (see Figure 5.6 c and e), but at significantly higher resolution and in a shorter time compared to the 3D Raman technique. However, CLSM is not suitable for more mature graphitised carbonaceous matter, as these samples do not fluoresce (Schopf et al., 2006). Both of these 3D imaging techniques can yield crucial information

about the full morphology and preservation of the sample that is not so easily identifiable using conventional optical microscopy (Schopf et al., 2006). Schopf et al. (2002b) indicated that Raman spectroscopy as a technique could positively identify kerogen in microfossils, thereby apparently demonstrating a biological origin. However, as is evident from the previous discussion on Raman spectroscopy analysis of carbonaceous materials and from Figure 5.7, it is impossible to distinguish biologically produced carbonaceous material from abiotic matter using Raman spectroscopy. Raman spectroscopy is a useful technique for acquiring information on structural order as well as the type of bonding in disordered carbonaceous matter, but that does not speak for or against a biological origin of the carbonaceous matter. Pasteris and Wopenka (2002, 2003) pointed out that almost all Raman spectra of ancient kerogens show features of disordered carbonaceous materials, features not exclusive to biologically produced carbonaceous materials. In fact, several non-biological disordered carbonaceous samples can produce Raman spectra identical to that of known kerogens (see Figure 5.7). However, FTIR analysis of microfossils have proven to be a promising technique to use when elucidating the chemical makeup of individual carbonaceous samples. Marshall et al. (2005) showed that FTIR analysis will give substantially more chemical information on the composition of microfossils than Raman analysis. Both FTIR and Raman spectroscopy analyse vibrational modes, but with different selection rules. FTIR will provide information such as the presence of functional groups, the aliphatic chain length and degree of branching etc., whereas Raman will provide answers on structural ordering and thermal maturity (Marshall et al., 2005). The use of FTIR in analysis of younger samples have proven very successful (Javaux and Marshal, 2006). Time will tell how informative this technique will be on very mature Archean samples.

5.3.1.5 Abiotic formation of hydrocarbons

At this point, it is appropriate to discuss abiotic routes to generate hydrocarbons, as some of these reactions have been sporadically mentioned throughout previous sections. Such reactions are also relevant to discussions in the next chapter, which will describe one synthetic route to 'kerogenous' biomorphs (see Chapter 6).

It has been widely assumed that organic matter on Earth is biologically produced, but, in fact, this is not so for all cases. Here, I discuss some important abiotic routes to hydrocarbon generation. For example, it is known that a wide range of abiotic hydrocarbons can be found in fluids and deposits in and around hydrothermal vents (Simoneit, 1993; Kelley and Frü-Green, 1999; Holm and Charlou, 2001; Simoneit et al., 2004) and in fluid inclusions and as films in basalts and xenoliths (Tingle and Hochella Jr, 1993). Furthermore, abiogenic reactions are also believed to be responsible for

organic matter present in meteorites and interplanetary dust particles (Allamandola et al., 1987; Lee and Wdowiak, 1993; Sugisaki and Mimura, 1994; Cooper et al., 2001), as well as for the methane found in the Martian atmosphere (Oze and Sharma, 2005). Lindsay et al. (2005) proposed that some, if not all, carbonaceous material, found in black chert dikes in the Strelley Pool Chert, could be of abiological origin. This conclusion was based on detailed mapping and geochemical analysis showing the hydrothermal origin of the silica dikes, suggesting the carbonaceous matter formed by Fischer-Tropsch-type reactions at elevated temperatures and pressures deep down below the paleo-surface (Lindsay et al., 2005). Prebiotic organic chemistry must have been in place before the origin of life, whether or not it took place on Earth. Clearly, organic matter can be produced without the influence of biology, which in itself raises concerns about using organic matter as an indicator of life, as previously discussed. Abiotic hydrocarbons can be produced in a variety of ways, for instance from the Fischer-Tropsch reaction, thermal decomposition of iron carbonate (McCollom, 2003), and from the abiotic photosynthetic reactions involving colloidal ferric hydroxide (Moore and Webster, 1913), all of which are related to the catalytic effect of iron, an element abundant in the Archean ocean and sediments (although, the Fischer-Tropsch synthesis works with other metals as well).

The Fischer-Tropsch-type (FTT) syntheses are probably the most well known of these methods, and have been studied for over 80 years, in part because they show commercial promise in producing clean petroleum products (Rofer-DePoorter, 1981). Commercial FTT reactions are conducted in vapor phase, where a mixture of CO or CO_2 and H_2 is catalytically converted to hydrocarbons according to the following generalised reaction:

$$CO + (1 + \frac{1}{2}n)H_2 \longrightarrow CH_n + H_2O \tag{5.3}$$

where n is the average H/C ratio that normally is between 2.1 and 2.5 (Ngantsoue-Hoc et al., 2002). Typical catalysts include metals like iron, nickel, cobalt and ruthenium that are often bound to a support like silica. FTT syntheses are optimised to produce mainly linear saturated hydrocarbons (both even and odd numbered), including oxygenated compounds. The distribution of carbonaceous material depends on the reaction conditions, such as temperature, pressure, CO/H_2 ratio, and the choice of catalyst (Röper, 1983; Anderson, 1984). Experimental investigations have shown that magnetite, a common mineral, can catalyse the conversion of CO_2 and H_2 to methanol (Voglesonger et al., 2001), methane, ethane, propane as well as solid carbonaceous products (Berndt et al., 1996), indicating the high potential of, and possibly unavoidable, abiotic synthesis in hydrothermal systems. As was mentioned earlier, this type of organic synthesis can give rise to hydrocarbons with $\delta^{13}C$ very similar to biologically

produced carbonaceous matter, as well as organic material found in meteorites (Lancet and Anders, 1970).

It has been suggested that aqueous media offer a plausible geochemical scenario for FTT reactions. McCollom et al. (1999) showed that this is indeed possible. In experiments that tried to mimic geological conditions in hydrothermal vents, McCollom et al. (1999) used formic and oxalic acids as sources for H_2, CO_2 and CO. After heating a stainless steel vessel with aqueous solution of either formic or oxalic acid, and with added montmorillonite ($(Na,Ca)_{0.3}(Al,Mg)_2Si_4O_{10}(OH)_2 \cdot nH_2O$) as a potential catalyst, to 175 °C for 2-3 days, produced homologous series of straight chain hydrocarbons, including alkanoic acids and alkyl formate esters (McCollom et al., 1999). Furthermore, Holm and Charlou (2001) demonstrated that the Rainbow hydrothermal field on the Mid-Atlantic Ridge produces linear saturated hydrocarbons with a chain length of up to 29 carbon atoms. This abiotic hydrocarbon production is thought to proceed via FTT reactions, fuelled by molecular hydrogen created by oxidation of olivine. Olivine is a solid solution of forsterite (Mg_2SiO_4) and the Fe(II) containing mineral fayalite (Fe_2SiO_4), and is a common constituent of mafic and ultramafic rocks, such as are found at or just below the ocean floor. In contact with water Fe(II) in olivine can be oxidised to magnetite with a concomitant reduction of H_2O to form H_2. This oxidation reaction is normally referred to as 'serpentinisation' as it generates serpentine ($Mg_3Si_2O_5(OH)_4$) (Holm and Charlou, 2001):

$$5Mg_2SiO_4 + Fe_2SiO_4 + 9H_2O \longrightarrow 3Mg_3Si_2O_5(OH)_4 + Mg(OH)_2 + 2Fe(OH)_2 \quad (5.4)$$

$$3Fe(OH)_2 \longrightarrow Fe_3O_4 + H_2 + 2H_2O \quad (5.5)$$

The magnetite produced during serpentinisation can catalyse the production of hydrocarbons, according to FTT reactions. The hydrogen liberated by the serpentinisation process can then, in the presence of CO_2 in hydrothermal fluids, combine to form hydrocarbons (Berndt et al., 1996). In addition, experimental simulation of hydrothermal serpentinisation reactions, using Ni-Fe alloy as catalyst and dissolved CO_2 as a source of carbon, produced methane having $\delta^{13}C$ of between -20 - -50 ‰ at 200-300 °C and at 50 MPa (Horita and Berndt, 1999).

McCollom and Simoneit (1999) also showed that a wide range of complex organic compounds can be produced by thermal decomposition of iron oxalate dihydrate ($FeC_2O_4 \cdot 2H_2O$):

$$FeC_2O_4 \cdot 2H_2O \longrightarrow aFeCO_3 + bFe_3O_4 + cCO_2 \pm dCO \pm eH_2 \pm fH_2O \pm gCH_4 \quad (5.6)$$

where gaseous CO_2 and CO can further undergo FTT reactions to produce complex

organics. Both volatile and non-volatile organic products are created from this decomposition reaction. Gaseous hydrocarbons include alkanes and alkenes and their isomers. Non-volatile products, on the other hand, include alkylated cyclic compounds, such as alkylphenols. It has been speculated that since the non-volatile, condensed aromatic products are quite different from those normally produced during FTT syntheses, the origin of the organics might involve addition of C_2 units from the oxalate rather than from the CO or CO_2, as in FTT reactions. On the other hand, similar products can possibly form under a 'H_2-starved' FTT synthesis.

Despite such possibilities, it has been concluded that this reaction scheme may not be useful as a geological model as iron oxalate is a rare mineral (McCollom and Simoneit, 1999). Interestingly, it has long been suggested that siderite, a product formed during iron oxalate decomposition, can decompose to form graphite (Perry Jr. and Ahmad, 1977). Experimental investigations by McCollom (2003) showed for the first time that this was possible. A great variety of hydrocarbons were produced when siderite was thermally decomposed in the presence of water at 300 °C, a reaction represented as:

$$3FeCO_3 + aH_2O \longrightarrow Fe_3O_4 + bCO_2 + cCO + dH_2 + \begin{matrix}\text{organic}\\ \text{compounds}\end{matrix} \tag{5.7}$$

In contrast to conventional FTT synthesis, siderite decomposition produces mainly alkylated *aromatic* compounds. Unfortunately, only the volatile and soluble organic fraction of the product has been analysed so far, so one can only speculate about the presence of higher molecular weight compounds produced (McCollom, 2003). Two possible reaction mechanisms have been proposed. The first mechanism is a consequence of FTT synthesis of the gases produced during the decomposition, perhaps under H_2-starved conditions. (However, it is known that the iron catalyst can be poisoned by condensed aromatic hydrocarbons, produced during the synthesis (Loaiza-Gil et al., 1999).) The second mechanism involves carbon polymerisation on the mineral surface as the decomposition occurs.

McCollom (2003) pointed out that this reaction could be the cause of hydrocarbons found in the Martian meteorite ALH84001, as these are very similar to the ones produced during siderite decomposition (see also Section 5.4.1). Furthermore, the very same reaction could also account for ancient sedimentary organic matter on Earth (Ueno et al., 2002; van Zuilen et al., 2003; McCollom, 2003). Some concern has been raised regarding the survival of hydrocarbons produced in hydrothermal systems, as the high temperatures could decompose the material. However, simulations of seafloor hydrothermal conditions by Williams et al. (2005) have shown that smectite-type clays can induce and protect the formation of organic compounds (up to C_{20}).

Evidently, abiotic organic material production is unavoidable under the right conditions. Both aliphatic and aromatic compounds, once abiotically produced, can then combine so as to form a wealth of other organic molecules. A very simple system that will be discussed in the next chapter (see Chapter 6) is the phenol and formaldehyde polymerisation, a reaction known to give rise to 'bakelite'.

5.3.2 Morphological evidence of early life

The most compelling evidence of ancient life comes from structures believed to be fossilised microbes. Cellularly preserved microorganisms in Archean rocks are scarce owing to the often severe metamorphism of ancient rocks that have obliterated any fossils once present (Schopf, 2004). Nonetheless, several microfossil occurrences, including the ~3.3 Ga Fig Tree and ~3.4 Ga Onverwacht Groups of South Africa (not discussed here) (Knoll and Barghoorn, 1977; Walsh and Lowe, 1985; Walsh, 1992), have been reported from ancient, comparably well preserved sediments of which the oldest date back almost 3.5 billion years (Schopf and Walter, 1983; Awramik et al., 1983; Ueno et al., 2001). Microorganisms can fossilize in various ways that retain either the full three-dimensional structure or a two-dimensional compressed object. Several characteristics of microbes can be preserved including size, shape, texture of the outer wall, organization and colonial distribution (Westall, 1999). Following extensive scientific debates regarding biogenicity of supposed fossilized microbes (Cloud, 1973b; Schopf, 1975), it is now agreed that several criteria are required to characterise an Archaean microfossil (Schopf and Walter, 1983; Buick, 1990; Westall, 1999; Schopf, 2004). These set of rules are supposed to verify the biogenicity and rule out any form of contamination and artefacts, though their sufficiency is currently open to some debate, as discussed below.

5.3.2.1 Microfossil recognition in Archean rocks

To prove that a structure is an authentic Archean microfossil it has to be demonstrated that the sample is indigenous and syngenetic with a sedimentary or meta-sedimentary rock of proven Archean age and of evident biological origin. Establishing the biogenicity of the fossil has been a most difficult task (Schopf, 2004). Several lines of evidence such as morphological characteristics of known microorganisms, the presence of carbonaceous outer envelope composed of degraded biomolecules (kerogen), and carbon isotope signatures have been used to confirm a biological origin (Ueno et al., 2001). Pseudofossils such as simple spherical objects can sometimes be difficult to distinguish from their microfossil counterpart. Filamentous objects are, on the other hand, according to Schopf impossible to fabricate through inorganic processes

and are therefore relatively easy to recognise as remnants of living matter (Schopf, 2004). However, as have been seen in Chapter 3, filamentous structures are not impossible to fabricate. True biogenic filamentous microfossils should be expected to be cylindrical, have a well-defined size, show evidence of septation, have a uniform diameter throughout their length, have distinctive end cells and occur among others with similar morphologies. They should also display varying degrees of sinuosity correlated to filament width and length, and show examples of specimens in various states of preservation (Schopf, 2004). Depending on the way the microorganism is fossilised, the structure could also be hollow (Westall, 1999).
All known Archean deposits containing fossils are metamorphosed so that the carbonaceous matter of the fossils could not chemically be established to be of biological origin (Schopf, 2004). Inorganic production of organic material that has been matured would show the same chemical signatures. The carbonaceous matter can display isotopic signatures indicative of a biological origin as previously described. Recently, ion microprobe spectrometry has been used to characterise the isotopic makeup of individual microfossils (House et al., 2000; Ueno et al., 2001), Even though these criteria seem rigorous, abiotic analogues that meet some or all of the criteria described can evidently confuse the situation. As will be shown in subsequent sections, morphology and chemistry alone cannot be used as biosignatures.

5.3.3 Pilbara microfossils

Western Australia, in the Pilbara, contains some of the best preserved Archean rocks in the world. It was in this area that the oldest putative microscopic traces of life were discovered. Several locations within the Pilbara Craton have been shown to contain 'microfossils'. The North Pole (typical Australian humour since its one of the hotter places on Earth!) and the Apex Chert are two of the most well known fossiliferous formations. Both of these areas have been subject to intense debate regarding the biogenicity of their microfossils.

5.3.3.1 The North Pole

The North Pole area is very famous for its ancient microfossils, the oldest ever found on Earth. Awramik et al. (1983) reported ~3.5 billion-year-old filamentous bacterial fossils from two localities (designated A and B) of laminated carbonaceous cherts, characterised as stromatolites (see 5.3.4 for a description of stromatolites) (Awramik et al., 1983). These microscopic structures were determined to be biological remnants because of their carbonaceous composition and their complex filamentous morphology that resemble modern known microorganisms. These results were later challenged

by Buick (1984) who suggested that the sedimentary laminae of locality B were of secondary origin and that the filaments were therefore possibly abiotic contaminants in secondary chert of much younger age (Buick, 1984). Awramik et al. (1988) reanalysed the fossil-bearing rock from locality A and stood by their original conclusion that the fossils are biogenic and syngenetic with the deposition of the chert and they are therefore around 3.5 billion years old (Awramik et al., 1988). Buick argued that as the exact site of locality A is not known, the field relationships with surrounding rocks cannot be made, which means that the results cannot be replicated, and therefore it is impossible to draw any conclusions about the filaments geological setting (Buick, 1988). The filaments in locality B were originally interpreted as possible microfossils, and are indeed very similar to the ones found by Buick. The sediment, on the other hand, in which those structures were found is quite dissimilar to the one described by Buick, thereby questioning his conclusion (Awramik et al., 1988). Buick, on the other hand, still maintained that his previous conclusion about the secondary and non-stromatolitic nature of the fossiliferous rock is correct (Buick, 1988). This dispute illustrates just how important a detailed and exact analysis of the geological context is for the microfossil interpretation. In 2001 Ueno et al reported findings of filamentous microstructures from two new localities in the chert-barite unit of the North Pole. About a hundred structures were found in silica veins. The black filaments are carbonaceous in nature, as determined from Raman spectroscopy, and are ~1μm wide and >10 μm long, and have spiral, thread-like or branched morphologies, comparable to modern filamentous bacteria and known microfossils. The carbonaceous matter of the filaments show a carbon isotopic composition consistent with a biological origin (-42‰< δ^{13}C< -32‰), since no known inorganic process could be the cause of such a result (Ueno et al., 2001). Ueno et al. (2001) suggested that the filaments were probable microfossils; it is believed that these structures together with the structures found by Awramik et al. (1983) are the oldest morphological evidence of life on Earth (Schopf, 2004).

5.3.3.2 The Apex Chert

With the discovery of additional 8 taxa of filamentous microfossils (to the previously 3 known) in the 3465 Ma Apex Chert in the Pilbara, Schopf (1993) demonstrated the diversity and extent of cyanobacterium-like life at this early stage in life history. These fossils were critically assessed as biogenic based on five principal criteria; 1) the microfossils occur in a well characterised rock, in this case a bedded chert from the Apex basalt, 2) which has been dated to ~3465 Ma, 3) the fossils were shown to be indigenous to the rock as they occur in petrographic thin sections, 4) syngenetic with

Figure 5.8: Photographs of the Apex Chert locality where J. W. Schopf discovered the microfossils. The left photo taken from the Chinaman Creek looking uphill towards the microfossil locality indicated by red circle. The right photo is taken above the microfossil locality looking downhill and across Chinaman Creek.

the deposition of the rock since the matrix, in which they are entombed, is a primary sediment, and 5) of 'assured biological origin' as their cellular complexity and organisation is similar to both modern and other younger prokaryotic fossil assemblages (Schopf, 1993). Furthermore, these carbonaceous microfossils are randomly oriented in the surrounding matrix and range in width from 0.5 to 19.5 μm. However, it was noted that the absence of microfossils in surrounding matrix and other casts could be indicative that the fossil assemblage was indeed older than the sediment as they could have been preserved in older rocks that then was eroded and redeposited in the current location. The biogenicity of the Apex Chert fossils and interpretation of their geological setting were to become (and still are case for) a major dispute between researchers in the area.

In March 2002 Nature published two articles back-to-back concerning the authenticity of these ancient fossils of life on Earth. Schopf et al. (2002b) used laser-Raman spectroscopy to analyze the carbonaceous residues incorporated in the microfossil structures. Various filamentous fossils from Precambrian cherts were analyzed (~2100-Ma Gunflint Formation of Ontario, Canada, ~3375-Ma Kromberg Formation of South Africa and ~3465-Ma Apex chert of western Australia), and they all gave Raman

spectra indicative of carbonaceous (kerogenous) materials. The Raman spectra are dominated by two peaks at ~1350 cm^{-1}, the 'D' band, and ~1600 cm^{-1}, the 'G' band (see Section 5.3.1.4 on Raman spectroscopy of kerogens). These Raman spectra together with the morphological characteristics of the structures analysed led (Schopf et al., 2002b) to the conclusion that the structures were indeed biogenic (see a selection of the material analyzed in Figure 5.9). As the Apex chert fossils resembled cyanobacteria, this conclusion suggests that oxygen producing bacteria were present 3.5 billion years ago, well before the atmospheric oxygen levels arose (see Section 5.2.1 on discussion of the early atmosphere).

Brasier et al. (2002, 2005) on the other hand, completely dismissed the claims that the fossils from the Apex chert were of true biological origin. Based on morphological and Raman studies of old and new filaments and thorough geological mapping of the area were the fossils were found, Brasier et al. (2002) came to the conclusion that the filaments probably were a consequence of thermal transformation of volcanic CO into carbonaceous material and not at all remnants of once living microbes as Schopf et al. claimed. According to Brasier et al. (2002, 2005), the rock, in which the Apex fossils were found, is of hydrothermal origin and not sedimentary bedded chert as previously described Schopf (1993). This puts into question the very nature of the 'microfossils'. If they are indeed biogenic, they would have to have been hyperthermophilic to survive in the hydrothermal environment (possibly > 70 °C) (Brasier et al., 2005). Furthermore, Brasier et al. (2005) identified 6 classes of 'microfossil' like objects with respect to their shape; 'arcs', 'dendroids', 'spherules', 'sinuous forms' (microfossil morphology previously described by Schopf (1992, 1993), 'rhomboids' and 'sub-rhomboids', of which arcs are most common and sinuous forms represent about 6% of the analysed samples.

This controversy spurred a storm of papers in the scientific community (Dalton, 2002; Gee, 2002; Kerr, 2002; Pasteris and Wopenka, 2002; Schopf et al., 2002a; García-Ruiz et al., 2002, 2003). Schopf still claims that the Apex fossils are of firmly established biological origin (Schopf, 2004).

5.3.4 Stromatolites

In addition to microscopic evidence, microorganisms can leave macroscopic imprints in the geological record. Biosedimentary evidence of life is visible in both ancient rocks as well as in modern, living analogues. There are several different types of biologically mediated sediments, distinguished with respect to their various fabrics, of which stromatolites are the most well known (Riding, 2000). The term stromatolite has been widely debated regarding the actual meaning, and various definitions therefore

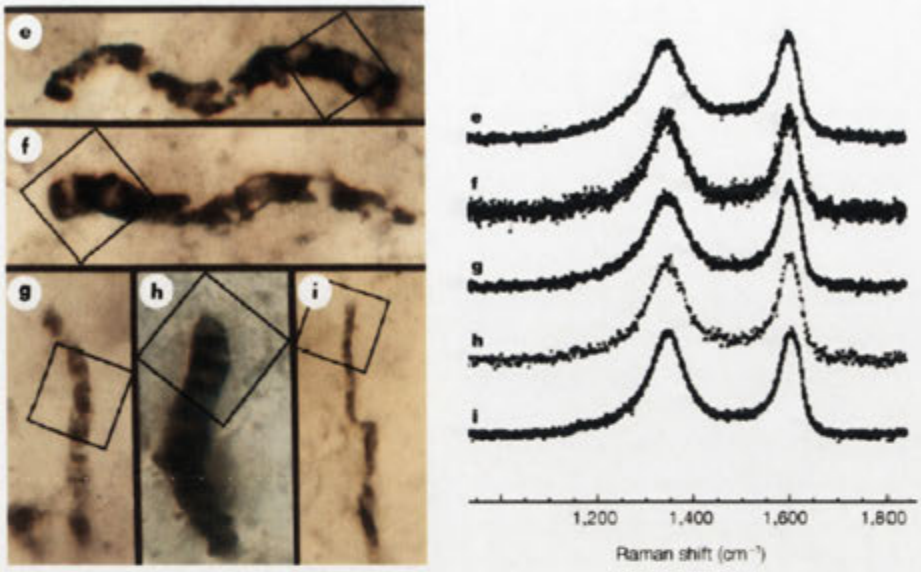

Figure 5.9: Optical micrographs of carbonaceous cellular filamentous prokaryotes from the Apex chert and the corresponding Raman point spectra. Adapted from (Schopf et al., 2002b).

occur in the literature (Grotzinger and Knoll, 1999; Riding, 1999). Malcolm R. Walter's definition from 1976 is the probably most widely used (Altermann, 2004) and is stated as (Walter, 1976):

> 'Stromatolites are organosedimentary structures produced by sediment trapping, binding and/or precipitation as a result of the growth and metabolic activity of micro-organisms, principally cyanophytes.'

These accretionary structures have been reported from all continents (Hofmann, 1973) and they can take a wide variety of forms, ranging from planar, columnar and dome-shaped structures to complex branching systems. The oldest known 'stromatolite' is around 3.5 billion years old and was found in the North Pole area of the Pilbara, Western Australia (Walter et al., 1980). This dome-shaped stromatolite is composed of thin laminae of dolomitic chert and has a structure comparable to younger stromatolitic examples. No microfossils are preserved in this stromatolite.

Although microorganisms are crucial to the formation of modern stromatolites, their remnants are rarely present in ancient examples. Probably less than 1% of all stromatolites ever described contain fossil evidence (Grotzinger and Knoll, 1999). According to Schopf et al. (1971) the rapid recrystallization and the subsequent destruction of any preserved filaments are most likely the cause of the absence of preserved microfossils in stromatolites. This lack of fossils makes it difficult to determine a biological origin of the structures and even if fossilized microbes were to be found in a stromatolite, it is not assured that those particular microbes were the cause of

Figure 5.10: Photographs of a piece of conical stromatolite I found at new stromatolite locality close to the Strelley Pool Chert. The left photo shows the top, while the right shows the bottom of the cones where individual layers can be seen.

the formation of the stromatolite in question (Grotzinger and Knoll, 1999). Furthermore, abiotic analogues mimicking the morphology and chemistry of stromatolites are present in the geological record, complicating the biogenicity assessment even more (Grotzinger and Rothman, 1996). It has therefore been suggested that the stromatolites from Western Australia should be treated with caution as evidence for early life (Buick et al., 1981). To ensure that stromatolitic structures are biogenic in nature it is crucial to find evidence of the biological-sediment interaction that is the underlying cause of their formation. The stromatolites therefore need to be well preserved where the microstructures and fabrics can offer evidence of biologically mediated sedimentation. This is rarely the case for Archean stromatolites, which have undergone diagenic and metamorphic alteration in which the original fabrics or textures have been lost (Cady et al., 2003). Buick et al. (1981) described 8 criteria to facilitate the recognition of true biogenic stromatolites: 1) The structures must be found in sedimentary or metasedimentary rocks; 2) the structures have to be synsedimentary in origin; 3) they should have a majority of convex-upward structures; 4) the laminations should thicken over the crests; 5) if they are laminated, these laminations should be wavy, wrinkled and/or have several orders of curvature; 6) microfossils should be present within the structure; 7) changes in composition in microfossil assemblages should be associated with morphological changes in the stromatolite; 8) the fossils must be organized in a way indicating that the living microbes accreted the structure by trapping,

binding or precipitation of sediment (Buick et al., 1981). Application of these criteria to Archean stromatolites more than 3,200 million years old fails to qualify any of the structures as biological (Lowe, 1994). Rather, Lowe (1994) suggested that inorganic abiological processes produced these stromatolite-like structures. Controversy still remains (Buick et al., 1995; Lowe, 1995) and while most would agree that the North Pole structures are possibly or probably biogenic, conclusive evidence is still lacking.

More recently, Allwood et al. (2006) reported seven different stromatolite facies, occurring over several kilometres in the 3430 Ma Strelley Pool Chert in the Pilbara. The presence of such a diversity of morphologically different laminations over a very large area shows that these kinds of sediments were very 'normal' in this outcrop (Awramik, 2006). Allwood et al. (2006) further argued that the complexity of the laminates pointed towards a biological origin, as no abiological precipitation mechanism can account for all the stromatolitic facies described. It was concluded that the simplest explanation is that a wide microbial ecosystem existed, producing the stromatolites within the shallow marine carbonate platform. Allwood et al. (2006) concluded that:

> 'Perhaps in this instance, abiogenesis is the 'extraordinary claim' that requires extraordinary proof, whereas biogenesis offers an ordinary, plausible explanation for the nature of the SPC [Strelley Pool Chert] stromatolitic carbonate platform.'

Indeed, these laminated structures are remarkable! Even more remarkable would be the microbial ecosystem interpreted to cause these formations. As such, proposing that biogenesis is an ordinary explanation should be treated with caution. Although stromatolites have been identified throughout the geological record and are significant to the reconstruction of the history of life, little is known about the microbes and processes that generate them. The most famous extant stromatolites are found in Shark Bay, not far from the oldest stromatolites found on Earth in the Pilbara Craton, Western Australia. A recent study on these modern stromatolites has shown that they are inhabited by a vast range of prokaryotes with diverse metabolic activities (Burns et al., 2004). Future research will provide a better understanding of these ecosystems and their influence on stromatolite generation.

5.4 Life on Mars?

Science is now revisiting a particularly exciting question that has captured the imagination far longer than Precambrian life: Did life originated somewhere else in the universe and later travelled to Earth by means of meteorites? The implications of finding life, extinct or alive, elsewhere in our universe will have profound implications for

Figure 5.11: The Martian meteorite ALH84001 (left) with a 1 cm cube to scale. Zoned carbonate 'blebs' (middle) around 200 μm in diameter, the orange centre is calcium and iron rich carbonate, the black rim contain minute iron sulfate and oxides, and the white outer rim is almost pure magnesium carbonate. Electron microscope image of a replica of what is belived (or used to be believed) to be Martian microfossils. Courtesy of NASA; `www-curator.jsc.nasa.gov/curator/antmet/marsmets/alh84001/sample.htm`.

our perception of ourselves.

5.4.1 The Martian meteorite ALH84001

Since the controversial discovery of putative microfossils and biomarkers in the Martian meteorite ALH84001 in 1996 (see Figure 5.11) (McKay et al., 1996) there has been a wealth of scientific discussion for and against the conclusion whether or not life ever existed (or still exists) on Mars. McKay et al. reported several lines of evidence to support their claim of extraterrestrial life, which also would be the oldest known life: the presence of indigenous microfossil-like objects resembling terrestrial fossilised microorganisms, polycyclic aromatic hydrocarbons (PAH) with restricted mass distribution, coexisting single domain magnetite (Fe_3O_4) and iron sulfides associated with carbonate globuls. Although, taken individually, each of these observable facts can be explained by abiotic processes, seen from a collective point of view McKay et al. (1996) argued that the best explanation is life. Since their paper in 1996, all of the above evidence has been substantially challenged as sufficient proof of life.

The famous fossilised 'worms (see Figure 5.11) were identified purely on the basis of morphology and have been questioned on the basis of their minute size and as being artefacts of sample preparation (Bradley et al., 1997). Being only tens of nanometres in diameter these structures are smaller than the theoretical smallest viable cell and it was realised that these structures were unlikely to once have been living microbes (Morowitz, 1996; Kerr, 1998). Nevertheless, nan(n)obacteria apparently found in carbonate sediments (Folk, 1993) as well as in human and cow blood (Kajander and Çiftçioglu, 1998) have a cell diameter of less than 200 nm and appear to be self-replicating in culture. These nanoforms remain deeply controversial (Cisar et al., 2000) and a biological origin of the martian nanofossils remains highly doubtful.

The strongest and last standing evidence of life was the presence of unusual crystals of magnetite. These crystals, present in the rims of carbonate globules (see Figure 5.11), were identified as biomineralization products on the basis of chemical and morphological grounds. It is well known that magnetotactic bacteria can produce intracellular pure single crystal magnetite with specific morphology and it has been stated that some magnetite present on ALH84001are very similar to terrestrial biogenic magnetite (McKay et al., 1996). Thomas-Keprta et al. (2000, 2001) described six properties of terrestrial biogenic magnetite (single domain size with restricted width to length ratios, chemical purity, no crystallographic defects, unusual crystal morphology, elongation along the [111] axis and arrangement of crystals in chains) that was applied to the elongated magnetite crystals on ALH84001. It was shown that these crystals fulfilled five out of the six criteria proposed and were indistinguishable from magnetite intracellularly produced by magnetotactc bacteria strain MV-1 (Thomas-Keprta et al., 2000, 2001). They argued that the presence of this specific Martian magnetite could only be explained by biological processes, similar to the one occurring in MV-1, since no known inorganic process can produce the same result (Thomas-Keprta et al., 2002). Recently however, it was discovered that not only are the Martian magnetite crystals morphologically different from the MV-1 magnetosome magnetite crystals but they can also be abiotically reproduced by hydrothermal decomposition of Fe-rich carbonate (siderite, $FeCO_3$) (Golden et al., 2004). No terrestrial biogenic analog for the martian magnetites is known so a biological origin for the crystals cannot be inferred. Interestingly, siderite decomposition can also explain the presence of PAHs on ALH84001 (McCollom, 2003). As was mentioned in Section 5.3.1.5, McCollom (2003) showed that a wide range of organic compounds, especially alkylated aromatic hydrocarbons, can be produced during thermal decomposition of siderite in the presence of water. The PAHs present in the ALH84001 meteorite were identified as being indigenous to the rock and to have a restricted mass distribution, but this does not infer a biological origin. In fact PAHs are found in a wide range of extraterrestrial materials such as interplanetary dust particles and carbonaceous chondrites (see also previous discussion on abiotic hydrocarbon formation in Section 5.3.1.5).

The case of ALH84001 will serve as an excellent example of how difficult it is, or can be, to distinguish between biology at work and nature itself. The close connection between the two makes it very hard to detect and define biogenicity that is required when determining the presence or absence of life on both extraterrestrial objects as well as here on Earth.

5.5 Discussion

This chapter has described the chemistry of early atmospheres and oceans, as well as criteria used to describe microfossils as true remnants of living organisms. It is evident that early life detection is filled with problems regarding the validity of standard criteria as indicators of life. Inorganic abiotic reactions and structures confuse the distinction between the living and non-living realms. As is evident from previous chapters, biomorphs display a remarkable variety of life-like morphologies. In putting forward a case for biomorphs as possible pseudo microfossils, it is especially important to compare Archean aqueous conditions with those that produce silica-carbonate biomorphs.

The synthesis conditions for filamentous worm-like biomorphs require high pH, the presence of barium (or strontium) at a concentration of 5 mM, and a silica concentration ~8.5 mM (see Chapter 3). The absorption of carbon dioxide from the air then induces biomorph precipitation. The contemporary atmospheric level of carbon dioxide is around 0.035%, a figure that in the Archean was likely to have have been higher (see Section 5.2.1). While competing theories of ancient atmospheric composition hinder definitive comparisons of biomorphic growth conditions, it is clear that significant amounts of CO_2 were present. Given the extensive carbonate precipitation during the Archean, it is not implausible to consider the existence of an environment that would result in biomorph precipitation. CO_2, however, is not the only crucial factor for the formation of biomorphs. Barium (or strontium) as well as silica concentrations and pH are equally important. As described in Section 5.2.1.2 the barium concentration in the Archean ocean is believed to have been higher than today and the presence of extensive barite precipitation indicates that significant amounts of barium were indeed around. The ancient oceans are also believed to have been enriched in silica. One report estimates the silica concentration to have been >300 ppm and speaks of an 'opal' ocean. It is also difficult to pin-point the pH of the early ocean, but support for a highly alkaline ocean indicates that this was a possibility. And even if this theory is false, there is nothing to suggest that these environments did not occurred locally, for example in an alkaline lake as found today. Given all this, could biomorphs have been naturally produced in the Archean as suggested in the introduction to this chapter? Current knowledge of the Archean ocean and atmospheric chemistry suggests that it is indeed plausible. The conditions required for biomorph precipitation evidently could have been present in the Archean. At locations where these conditions were fulfilled, extensive biomorph precipitation is certain. However, such areas with positively identified, naturally precipitated biomorphs are to date not known. Relevant areas where one may find biomorphs include any sediments that have formed from

high pH, silica, and high concentrations of Ba, Sr, and possibly Ca. Sediments from volcanic lakes, such as Magadi lake, and other hydrothermal vents around the world would be very interesting to analyse for such structures.

The next chapter will elaborate on biomorphs as abiological equivalents of fossilised microorganisms. A morphological and chemical comparison between various biomorphs and microorganisms is presented to show the similarity between the two. Mineralogical analysis of a rock from the North Pole, indicates, at least locally, high Ba concentrations (low sulfate) (see Section 6.4.1). The possiblity of naturally produced biomorphs, and their chemical and morphological similarity to ancient microorgansism, raises doubts about the biogenicity indicators, described in Section 5.3.2.

Chapter 6

Biomorphs as 'Shake and Bake' microfossils

6.1 Introduction

As the title indicates, this chapter continues the discussion on the similarities between biomorphs and the fossil traces of the earliest of life. Since biomorphs have a morphology and chemistry very similar to microfossils, biomorphs can potentially be misinterpreted as being fossil remnants of microorganisms. Therefore, biomorphs can be considered to be a special case of pseudofossils, and may convincingly mimic biological forms. In this chapter a case for biomorphs as potentially misidentified microfossils is made, and biomorphs will be morphologically and chemically compared to Archean microfossils. A morphological comparison with both living and fossilised microorganisms will be given in the first part to more clearly show such correlation. As described in the previous chapter (see Chapter 5), morphology is only one of the key criteria for detecting microfossils. Another trait of true biogenic microfossils is a carbonaceous residue with a carbon isotopic composition comparable with life. In this chapter, I describe how to produce a biomorph with a carbonaceous outer skin, while retaining the original morphology.

To argue that biomorphs could be misinterpreted as fossil remnants of Archean microbes, it is necessary to show that the Archean environment inevitably could encourage biomorph growth. As indicated in Chapter 5, the chemistry of the ancient atmosphere and ocean may have been similar to the synthetic conditions used to precipitate biomorphs: high pH, high barium and silica concentration and a source of carbon dioxide (see Chapter 3). To show the possibility of geochemically formed Archean *carbonaceous* biomorphs, a mineralogical analysis of a rock from the ~ 3.5 Ga Dresser formation is also presented. The aim of this study is therefore twofold; 1) to show that biomorph synthesis is geochemically plausible, and 2) that abiotically generated hydrocarbons could have been produced. Combining steps 1) and 2) would yield

a carbonaceous biomorph; i.e. a structure morphologically and chemically comparable to microfossils that is of *a*biotic origin.

This chapter presents experimental work that demonstrates that not only could biomorphs have been naturally produced in Archean times, but they would also be indistinguishable from true microfossils since they fulfill all currently accepted criteria for establishing biogenicity of a microfossil. Such criteria are therefore not reliable, and this is an area that requires further scientific investigation and clarification.

6.2 Biomorphs vs. microfossils

This section provides a morphological comparison between biomorphs and microorganisms. The morphological variety seen in silica-carbonate biomorphs is broad, including forms that are very reminiscent of the biological world. It is important to notice that all biomorphs are 'of biological form' (as the name suggests, see Chapter 1), however, all cannot be directly correlated to any living organism (or fossil for that matter). The morphological variety seen among microorganisms is diverse, ranging from square- to star-shaped. However, spherical (coccus), rods, and spirals are the most common morphologies observed within the microbial life forms (Burdon, 1964; Walsby, 1980; Prescott et al., 1996). Filamentous microorganisms, including cyanobacteria, have a 'string-of-pearls'-type morphology. This morphology arises from the stacking of individual cells, through binary fission along one line, enclosed within an outer organic envelope, which gives a segmented overall appearance (Madigan et al., 1996; Armstrong and Brasier, 2005).

In addition to shape, size is an important attribute for the recognition of ancient life (recall the martian 'microbe' described in Section 5.4.1). As with the case of morphology, a large variety in size is also observed in microbes. The largest prokaryote known today is *Thiomargarita namibiensis*, a bacterium which can grow up to 750 μm in diameter as a single cell (Schulz et al., 1999). The smallest known living organism is a recently discovered archaeon called *Nanoarchaeum equitans*, which is only 0.40 μm in diameter (Huber et al., 2002). Other microbes that are classified as 'small' include the spirochetes, which have helical morphology that can have a diameter of around 0.1-0.15 μm. However, they are at least 5-6 μm in length (Staley, 1999). Although still controversial, even the smallest nanobacteria has a diameter of around 100 nm (Kajander et al., 2003). It is generally believed that the lower limit for a free living organism, containing DNA, is a diameter between 0.20 and 0.25 μm (Nealson, 1999). Even within species, large varieties in size are seen that in some cases can be attributed to nutritional conditions which control growth; nutritionally starved cells are smaller than their well fed counterpart (Staley, 1999). Furthermore, depending on the stage of

development during cell division (cell cycle), significant size variations can be seen. For instance the length of *E. coli* increases by a factor of 2 before the cell divides (Prescott et al., 1996), and the size of certain coccoid cyanobacteria can develop cells that are 2-3 times the size of normal cells upon delayed division (Palińska and Krumbein, 1998). Size variations therefore depend on growth conditions and the type of microbe present. Biomorphs, on the other hand, have narrow size distributions within a single experiment, but with mean size varying depending on the specific reactions conditions (see Chapter 3.

To demonstrate the morphological similarity between biomorphs and the living realm, a set of images is presented in Figure 6.1. These images include biomorphs, living organisms, and purported microfossils. Silica-carbonate biomorphs having spiral (Figure 6.1 A2), globular (Figure 6.1 B2 and G2), worm-like (Figure 6.1 D2 and H2), trumpet-shaped (Figure 6.1 C2), band-like (Figure 6.1 F2 and I2), and a mixture of the latter two (Figure 6.1 E2) morphologies all have a living counterpart. All of these living vs. non-living pairs have very similar overall shape, but some differ in their relative size. Large size discrepancies (> factor of 2) are seen in C, D, E and I. For instance, the trumpet-shaped biomorph, seen in Figure 6.1 C2, has a similar shape to the protist *Stentor roeseli* (a unicellular eukaryote), but a vastly different size. This will serve as an example of the biomorph shape as 'of biological form', mentioned in Chapter 1.

The silica-carbonate biomorph seen in Figure 6.1 E2 is a representative example of structures synthesised at high temperatures that contain a mixture of cones, sheets and filaments. However, the biomorph has a diameter of 75-140 μm compared to ~ 30 μm for the microfossil counterpart (Figure 6.1 E1). These biomorphs are morphologically similar to microfossils, known as *Eoastrion* Barghoorn, found in the ~2.0 Ga Gunflint Chert, Ontario (Knoll and Barghoorn, 1976). Those fossils have been interpreted as a 'budding bacteria' that consist of carbonaceous filaments irregularly emerging from a central body. As no known living or well-characterised fossil counterpart could be found at the time, the new genus *Eoastrion* was created to accommodate these fossils (Barghoorn and Tyler, 1965). Later, these fossils have been described as remnants of the manganese oxidiser *Metallogenium* (Crerar et al., 1980). However, these proposed organisms remain highly controversial as to whether they are living microbes at all, or biominerals, or neither (Maki et al., 1987). Other high-temperature biomorphs, such as the 'tentacles' and 'bands' seen in Figure 6.1 F2 (see also Section 3.4.5, and Figure 3.45), have very simple morphology, and are comparable to the ~3.5 Ga North Pole microfossils, reported by Ueno et al. (2001) (see also Section 5.3.3.1). These carbonaceous filamentous microfossils are between 10 and 100 μm long with a diameter of around 1μm, emerging from a base. The band-like biomorphic counterpart can

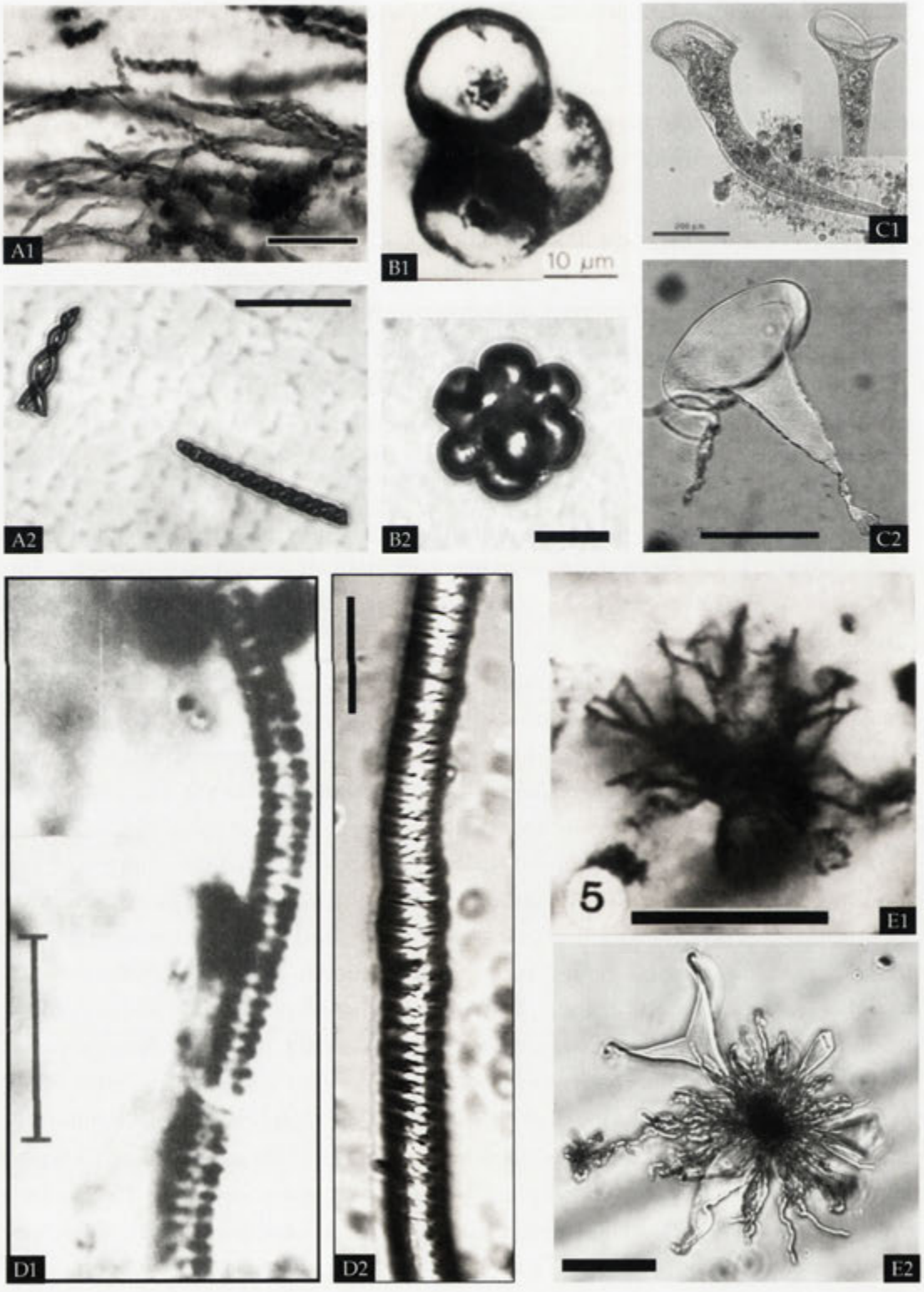
A1
B1
10 µm
C1
A2
B2
C2
D1
D2
5
E1
E2

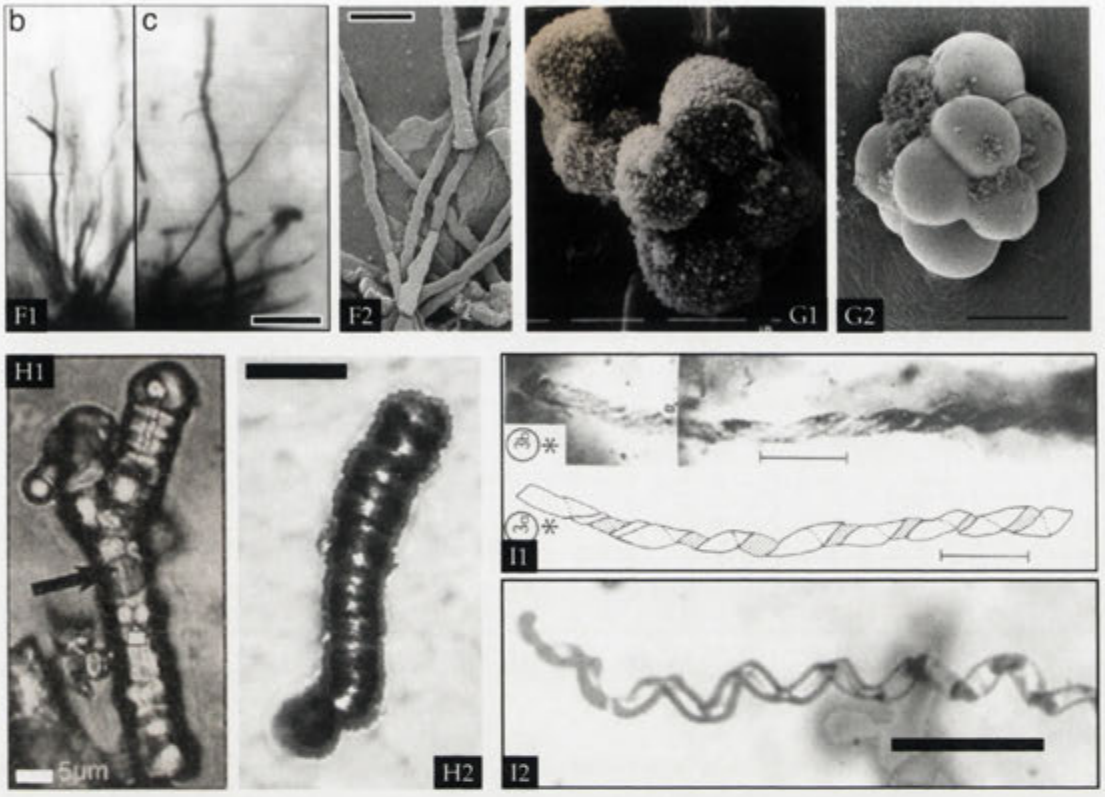

Figure 6.1: Comparison between biomorphs and microbes, which clearly shows the morphological convergence between living and non-living form. Images labelled with 1 are examples of microbial morphologies, whereas images labelled with 2 are silica-carbonate biomorphs grown under various conditions. (A1) twisted filamentous microfossils similar to modern *Gallionella ferruginea*, 50 μm scale bar (adapted from Hofmann and Farmer (2000)); (A2) optical micrograph of biomorphs with twisted morphology, 40 μm scale bar; (B1) prokaryotic coccoid microfossil *Melasmatosphaera media* from the ~2 Ga McLeary Formation, Canada (adapted from Hofmann and Schopf (1983)); (B2) optical micrograph of a globular biomorph, 20 μm scale bar; (C1) optical micrographs of *Stentor roeseli*, a large fresh water protist, 200 μm scale bar (adapted from `http://protist.i.hosei.ac.jp/PDB/Images/Ciliophora/Stentor/roeseli/index.html`); (C2) optical micrograph of a trumpet-shaped biomorph, 50 μm scale bar (adapted from García-Ruiz et al. (2002)); (D1) optical micrograph of a late Precambrian microfossil (*Calyptothrix annulata*) from Bitter Springs, Australia, 10 μm scale bar (adapted from Schopf (1968)); (D2) optical micrograph of a filamentous biomorph, 10 μm scale bar (adapted from García-Ruiz et al. (2002)); (E1) optical micrograph of ~ 2.0 Ga microfossil *Eoastrion* from Duck Creek, Australia, 20 μm scale bar (adapted from Knoll and Barghoorn (1976)); (E2) optical micrograph of biomorph, 40 μm scale bar; (F1) optical micrographs of carbonaceous filamentous microfossils from the ~3.5 Ga North Pole area, Western Australia, 10 μm scale bar (adapted from Ueno et al. (2001)); (F2) electron micrograph of silica-carbonate bands, 10 μm scale bar; (G1) ,10 μm scale bar (adapted from Zang and Walter (1992)); (G2) electron micrograph of globular biomorph, 30 μm scale bar; (H1) iron oxide containing microfossil from an inactive chimney at the East Pacific Rise, 5 μm scale bar (adapted from Foriel et al. (2004)); (H2) optical micrograph of worm-like biomorph, 20 μm scale bar; (I1) optical micrograph (upper) and reconstruction (lower) of the late Precambrian microfossil *Heliconema australiensis* from Bitter Springs, Australia, 10 μm scale bar (adapted from Schopf (1968)); (I2) optical micrograph of twisted biomorph, 200 μm scale bar (adapted from García-Ruiz et al. (2002))

exhibit larger size variations with widths ranging from <1μm up to 20 μm, however widths are more generally in the 1-2 μm range (see also Figure 3.47). Similar structures reported by Awramik et al. (1983) are interpreted as dubiomicrofossils, as some exhibit suspiciously rectilinear morphologies (Schopf and Walter, 1983). However, other filamentous structures from the same area have been interpreted as bona fide microfossils (see Schopf and Walter (1983), Photo 9-4). Silica-carbonate biomorphs of this type, also including the tentacles synthesised under the same conditions, are therefore comparable to both dubio- and biogenic microfossils that have thread-like non-segmented morphologies. Furthermore, the bands can also, in some sense, mimic compressed tubular sheaths and filaments, as these bands are flat.

The spiral fossils, seen in Figure 6.1 A1, have a diameter of <5 μm, slightly smaller than the twisted biomorphs seen in Figure 6.1 A2 (~5 μm, measured across the wider part of the twist). Hofmann and Farmer (2000) disregarded the possibility that the twisted filaments could be biomorphs, based on size range limitations, parallel orientation, and the lack of size variations with different geochemical settings. Similar arguments could possibly be made for all the other morphological comparisons seen in Figure 6.1, a point which will be discussed later in this section.

The globular biomorphs, seen in Figure 6.1 B2 and G2, have 'spherical cells' in the size range 13-26 μm, whereas the microbial counterpart, seen in Figure 6.1 B1 and G1, have individual cells with diameters in the 13-20 μm range. So equally large size variations can be seen in both samples. Coccoid unicellular microfossils make up a significant portion of the Archean and Early Proterozoic fossil record. The spherical cell size are most often < 25 μm, however larger specimens diameters of more than 40 μm are known, but of unasserted biological origin (Hofmann and Schopf, 1983). As was noted in Section 5.3.2.1, some caution is required when ascribing spherical forms to living organisms, since such morphologies can be mimicked by inorganic precipitates under a range of physical processes. According to Schopf (1999b), unicellular aggregates are to be treated with suspicion, whereas colonies of spherical morphologies can be viewed as of 'unquestionably biologic form'. This is not always true, as Figure 6.1 B2 and G2 shows.

Furthermore, even more complex morphologies, such as segmented filaments, consisting of chains of cells, are also mimicked by silica-carbonate biomorphs (see Figure 6.1 D2 and H2). As some of the most ancient microfossils belong to this morphotype and have been at the centre stage of the debate regarding biogenicity (see Section 5.3.3.2), the rest of this chapter will deal with these structures. Recall that filamentous 'segmented' inorganic objects are, according to Schopf (2004), *impossible* to fabricate. Segmentation therefore lies at the core of this discussion. Unbranched segmented microfossils are known from several Archean localities, such as the ~ 2.8 Ga

Fortescue Group and the ~3.5 Warrawoona Group, including the Apex chert discussed in Section 5.3.3.2 (Schopf and Walter, 1983). These microfossils were regarded as biological, based on the criteria discussed in Section 5.3.2.1, of which segmentation is one of the prominent criteria. Anchored in morphological arguments, some of these structures were interpreted as being remnants of cyanobacteria (see Section 5.3.3.2). The microfossil seen in Figure 6.1 H1, fossilised in amorphous silica, has a diameter around 8-9 μm, and is ~38 μm long. This is smaller than the corresponding biomorph seen in Figure 6.1 H2, which is ~15 μm in diameter and around 70 μm long. Similarly, the filamentous microfossil seen in Figure 6.1 D1, diagnosed as *Calyptothrix annulata*, which has an average diameter around 2 μm and can extend up to 70 μm in length. The corresponding biomorph (see Figure 6.1 D2) has a diameter around 5-6 μm.

It is important to note that biomorphs can have different dimensions within each type of morphology (see Chapter 3). As biomorphs are a physiochemical phenomenon, their morphology and size strongly depend on the prevailing physiochemical setting. For instance, biomorphs precipitated in silica gels, where the diffusion of reactants is kept more constant compared to the sols, produces generally longer and more uniform aggregates. Both size and shape should therefore be controllable through the synthesis conditions. However, it is also important to note that even during very fixed conditions, size variations exist. Recognising the morphological convergence between microbial life and biomorphs is one thing, but is not satisfactory to claim biomorphs as possible pseudofossils in the hunt for early life. Other attributes, such as the carbonaceous nature, are crucial for determining a biological origin of microfossils, segmented or not. In the next section experimental investigation into how to make biomorphs gain this attribute is explored.

6.3 Kerogenous Biomorphs

To compare silica-carbonate aggregates morphologically and chemically to microfossils, they have to be encapsulated in kerogen. As biomorphs are not carbonaceous by nature according to the synthesis procedure used in Chapter 3, this property needs to be conferred on biomorphs by additional processes. Abiotic reactions leading to organic products, such as Fischer-Tropsch type reactions and siderite thermal decomposition, are suggested to have been a source of organic matter on the early Earth. Kerogenous matter found in ALH84001 as well as in some structures resembling microfossils, originally interpreted as being of biological origin, has been convincingly argued to have been formed by such abiological reactions (see Section 5.3.1.5).

The siliceous nature of biomorphs can facilitate the adsorption of aqueous organic molecules. As was described in Chapter 2.3, silica is well-known for its capacity to

adsorb organic molecules, a capacity related to several factors regarding the solid silica surface, the type of organic molecules, and type of solvent, factors that collectively govern the degree of adsorption. Hydrogen bonding between silanol groups and/or Coloumbic interactions between ionised silanol groups on the silica surface are effectively involved in the adsorption of non-ionic and ionic compounds respectively. This is especially true for freshly precipitated silica surfaces that still retain silanol groups and are free from other adsorbed species. As has been shown, adsorption of polyaromatic hydrocarbons on biomorphs is feasible (García-Ruiz et al., 2002). Many starting materials, abiotic or biotic organic molecules, could have been used in this study, but it was decided that small prebiotic compounds, like phenol and formaldehyde were to be used. The rationale for this was that such molecules, when polymerised and matured, could then identify a completely abiotic route to kerogenous biomorphs. Furthermore, phenol and formaldehyde are appropriate precursors for kerogen-like material due to their well known polymerisation to phenol-formaldehyde resins, and it has also been shown that heat curing of such polymerised material form disordered carbon having a Raman spectra similar to fossils (Ko et al., 2000). As was discussed in Section 5.3.1.5 both abiotic and biotic disordered carbonaceous materials show the same Raman features.

Phenol formaldehyde polymerisation

It has been known since 1872 that phenols and aldehydes can interact to give resinous materials. Phenol and formaldehyde resins are in fact the oldest synthetic polymer systems, called *Bakelite*, first introduced by Baekeland in 1907 (Megson, 1958). Although these types of resins have been commercially available for almost 100 years, the chemical and physical properties of the materials are still not completely understood.

Depending on reaction conditions, two types of resins can be produced, called resols and novolacs. Resols are normally synthesised under base-catalysed conditions with a phenol to formaldehyde ratio of less than 1. Novolac on the other hand are synthesised with an excess of phenol under acid catalysed conditions. The main difference between the two materials is that in addition to the normal methylene bridges that occur in the case of novolacs, additional dimethylene-ether bridges between phenol groups as well as remaining methylol groups on phenolic rings can be seen in resols (see Figure 6.2) (Rego et al., 2004). However, the final products are chemically complex, and its structure strongly depend on the phenol to formaldehyde ratio, pH, and temperature and duration of the polymerisation. Under suitable conditions, a three dimensional network is formed. The polymerisation of phenol

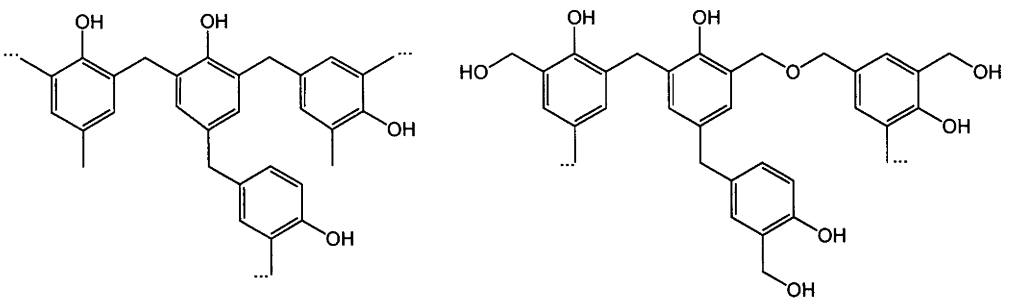

Figure 6.2: Comparison of the chemical structure of novolac (left) and resol (right). Adapted after Rego et al. (2004).

and formaldehyde involves a step-growth condensation reaction that begins with the formation of metylophenols in *ortho* and/or *para* position (see Figure 6.3 A). These metylolphenols continue to react with both other metylolphenols and phenols (see Figure 6.3 B) to produce a chemically ill-defined polymer. As can be seen in Figure 6.3 B, dimetylene-ether bridges produced during the reaction between two metylol groups can decompose with the liberation of formaldehyde. This reaction pathway is more likely to occur at high formaldehyde to phenol ratio and at temperatures above 160 ° C (Bar and Aizenshtat, 1991).

6.3.1 Formation of 'kerogenous' biomorphs

In this section the samples and preparation techniques as well as the instrumental techniques are described. The objective was to produce a biomorph with a carbonaceous shell, similar to carbonaceous filamentous fossils previously described. The experimental model was based on the technique used by Ko et al. (2000) to produce graphitised material from Bakelite-type resins.

Adsorption and thermal condensation of organic materials on already-grown worm-like biomorphs (see Chapter 3), one can form kerogenous biomorphs. These adsorption experiments were conducted in aqueous solutions at near neutral conditions, with an excess of formaldehyde. For the adsorption experiments a stainless steel bomb was used, lined with a teflon cup, where biomorphs were placed in 10.0 ml aqueous solution containing 0.01 M phenol and 0.02 M formaldehyde. The vessel was sealed and heated at 125°C for a minimum of 15 hours. The biomorphs were then collected and rinsed with Milli-Q plus distilled water and placed on a microscopic slide for additional treatment at elevated temperature to further condense the

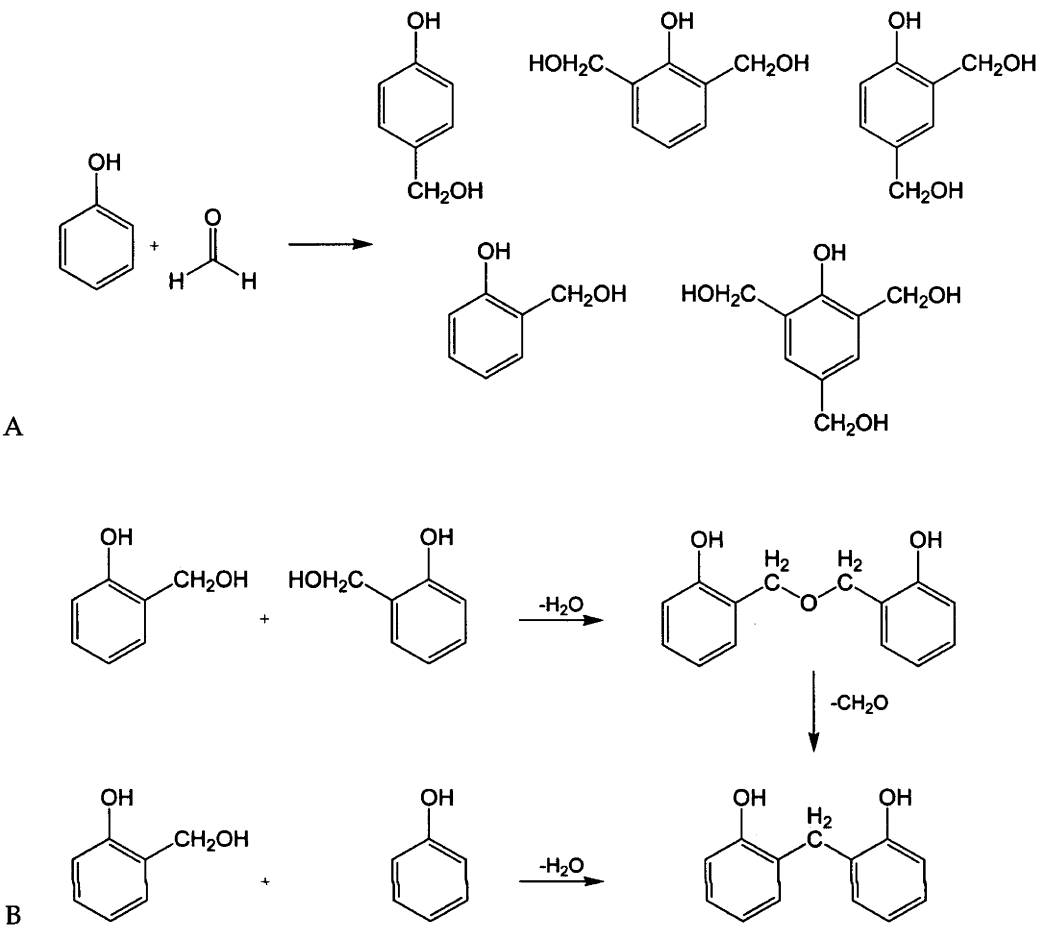

Figure 6.3: In the first step of the polymerisation of phenol and formaldehyde, addition of formaldehyde to phenol in orto and/or para position produce a variety of metylolphenols (A). These metylolphenoles react with phenol and other metylolphenols to produce the final resin (B). Adapted after Bar and Aizenshtat (1991).

carbonaceous material. The biomorphs were first aged at 160°C in air[1] before being transferred to a Lindberg Tube furnace, model 54433 equipped with an 818 temperature controller, where the material was heated in a nitrogen flow of 1650 ml/min. The samples were treated in 500°C for 5 hours or 18 hours with a heating rate of 1°C/min from 200-500°C. The specimens were then analyzed using a Renishaw Raman imaging microscope, model 2000, equipped with a Helium/Neon (632.8 nm) and low power near infrared (780 nm) lasers and a low noise (thermoelectrically cooled to -70°C) CCD. The spatial resolution of the spectra (collected with a 100x objective lens) is approximately 1 μm, with a depth of field of 2 μm. The spectra were normally collected with a 60 second scanning time with 5 full scans at 50 times magnification and with

[1]The treatment in air at 160 °C is not essential to the formation of kerogenous biomorphs, and probably reduced the presence of small volatile species on the brown biomorph.

Figure 6.4: The color change of biomorphs seen during the condensation and curing of phenol formaldehyde. Left: as prepared biomorph. Middle: Biomorph after hydrothermal treatment with aqueous phenol and formaldehyde solution. Right: Structure after curing at 500 °C. Scale bar 50 μm applies to all three images.

reduced laser power. Dr. Vincent Otieno-Alego, now at the Australian Federal Police, supervised the use of the Raman instrument at the University of Canberra.

Results

The first treatment, in which phenol and formaldehyde adsorb and condense onto the surface of the biomorphs, resulted in brown colored aggregates. When opening the stainless steel bomb, a thin translucent brown film was seen covering the surface of the solution, and brown coloured biomorphs were found at the bottom of the teflon cup. The stepwise color change following the adsorption and polymerisation of can be seen in Figure 6.4. These brown structures retained their color and morphology after treatment in a weak acid. The chemical makeup of the brown coating was confirmed with IR to be a bakelite-type material. The use of excess formaldehyde, near neutral pH, and moderate temperature (125°C) during the reaction, most likely produced a polymer with some dimetylene-ether bridges, and with many terminal alcohol groups.

The additional treatment, in which the biomorphs were subjected to high temperatures (200-500 °C), further condensed the already adsorbed hydrocarbons. This treatment resulted in biomorphs that still retained their overall morphology but now sporting a black exterior. Some biomorphs only displayed partial black coverage, others had a complete black exterior. (Partial coverage is possibly due to the high N_2 flow in the furnace, which facilitate the removal of small unpolymerised hydrocarbons.)

The black outer surface was analyzed with Raman spectroscopy. Some of the spectra collected can be seen in Figure 6.5. Similar treatments have been conducted on phenol-formaldehyde resins that resulted in a material exhibiting similar Raman

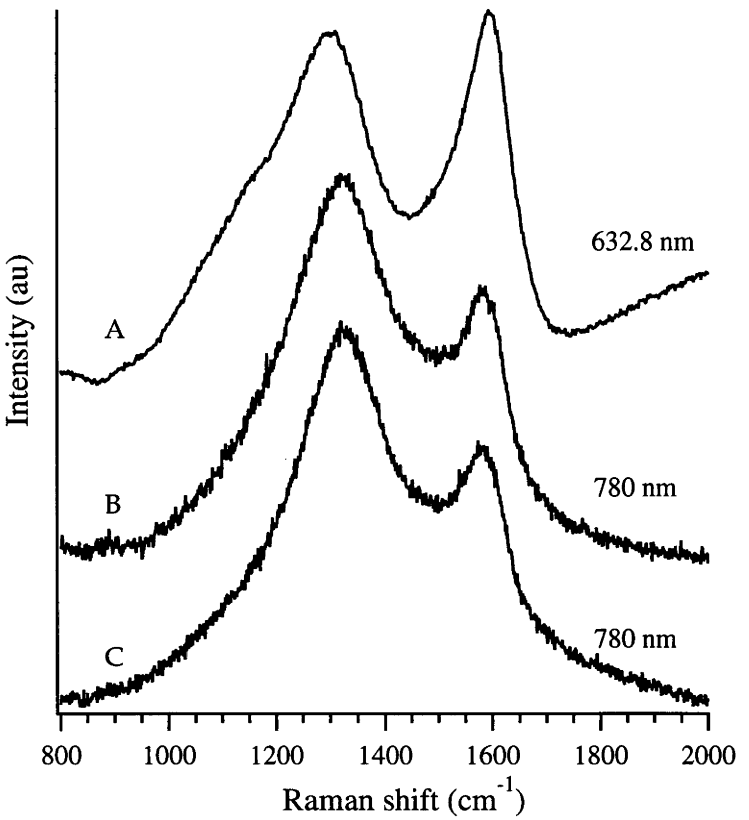

Figure 6.5: A collection of Raman spectra of carbonaceous matter on biomorphs after curing at 500 °C with various dwelling times and excitation wavelengths. A, B: Dwelling time of 18 hours. C: Dwelling time of 5 hours.

spectra (Ko et al., 2000). As was discussed in Section 5.3.1.4, Raman spectra of carbonaceous materials are characterised by the presence of D and G bands at ~1350 and ~1600 cm^{-1} respectively.

As can be seen in Figure 6.5, the D and G peaks are broad and overlapping. Raman spectrum C is one example of 7 spectra collected of samples made under the same conditions. In all cases the D and G peaks are centered at 1340 cm^{-1} and 1590 cm^{-1} respectively. They all show similar features with varying D/G intensity ratios. The average value of the intensity ratio between the D and G peak lies at 1.51, with the highest value of 1.69 and the lowest value at 1.35, indicating that the material is highly disordered. Similar features can be seen in spectrum B, in which the only difference is the increased dwelling time of 18 hours compared to 5 hours for spectrum C. This material is similarly disordered as indicated by the intensity ratio between the D and G peak, which has a value of 1.52. The sample in spectrum A was prepared with the same reaction and curing conditions as sample B, but the spectra was collected using

a different excitation wavelength. This spectrum displays several features that are different from the other two. First it is evident that the D peak has shifted to 1290 cm^{-1}, which is 50 cm^{-1} lower than the other spectra collected at 780 nm. It is well known that the position of the D peak varies with excitation wavelength, while the G and D' peaks do not (Vidano et al., 1981). The position of D peak increases and I(D)/I(G) decreases with increasing laser energy (Matthews et al., 1999; Wang et al., 1990). So it could be expected that if the same sample had been analyzed with longer wavelength (say 780 nm), the D peak would shift to even lower values. Variations in the D peak positions has been observed for different carbons with varying degree of disorder (Matthews et al., 1999). The fact that the D peaks are broad in all spectra can be explained by the varying sizes, shapes and distribution of small sp^2 domains all of which have individual frequencies. The larger the domain, the lower the frequency of the peak. The position of the D peak is then determined by the distribution, size and shape of sp^2 domains and the laser energy (Castiglioni et al., 2001). This indicates that sample a is possibly characterized by larger sp^2 domains than the samples in spectra b and c. Secondly, an additional shoulder on the low-frequency side of the D peak can be seen. This shoulder has been noted in both spectra of fossils (at ~1250 cm^{-1}) (Kudryavtsev et al., 2001) as well as for carbonized phenol-formaldehyde resins (at ~1165 cm^{-1}) (Ko et al., 2000). Ko et al. (2000) described this shoulder as an effect of unknown disordered structures caused by the cross-linking of the polymeric entities during curing of the phenol-formaldehyde resins. The intensity of this shoulder decreases with increasing curing temperature (Ko et al., 2000). This effect was also noted by Kudryavtsev et al. (2001) who assigned the shoulder to the presence of quinoid polymeric aromatic-rich organic matter that could be viewed as an intermediate between original biological constituents and the degradation products of the microbial organic matter.

The biomorphs displayed in Figure 6.4 combined with the Raman analysis in Figure 6.5 clearly shows that it is experimentally feasible to produce kerogenous structures having morphological and chemical features similar to ancient microfossils. This calls into question the validity of the biogenicity criteria used to determine a biological origin of ancient 'microfossil' structures, a topic that will be further discussed in Section 6.5. Even though that biomorphs evidently mimics microfossil-like structures, the question boils down to the likelihood of these kind of abiotic reactions occurring in the sedimentary settings containing fossilised microbes. The next section reports mineralogical analysis of a rock from the Dresser formation, that will clarify the nature of these problems.

6.4 Mineralogical analysis

The purpose of the mineralogical analysis was to obtain information on the composition and possible chemical history of these rocks, in order to see whether Archean Pilbara locations could have supported biomorph growth as well as abiotic hydrocarbon generation. Also, this was an opportunity to check if there were any structures resembling biomorphs in this sample. The Archean geochemical environment is believed to have been enriched in Ba, Si and CO_2 (see Section 5.2.1.2), all crucial elements to biomorph synthesis. The pH of these aqueous environments is not known in detail. However, the oceanic environment is believed by some to have been high in pH, as was discussed in Section 5.2.1.2. As has been described in Section 5.3.1.5, several abiotic reactions, using iron-rich compounds as catalyst, can give rise to hydrocarbons. Iron was abundant in the Archean in both the ocean and the sediments as carbonate and oxides (see Section 5.2.1.1). Abiotic origin of Archean carbonaceous matter in the Pilbara region is certainly geochemically feasible, as large hydrothermal systems were active within the Archean era that offer ideal physiochemical settings for these type of reactions (Horita and Berndt, 1999; Lindsay et al., 2005).

6.4.1 The Dresser Formation

In this section a brief overview of the Dresser Formation from which the sample was collected is given. The northern Pilbara Craton is divided into three main parts of which the East Pilbara Granite-Greenstone Terrane includes the Warrawoona Group that contains the oldest evidence of life, as discussed in Chapter 5 (see also Figure D.1 for a stratigraphic relationship within the Pilbara Supergroup). The ~3490 Ma Dresser formation is the stratigraphically lowest and therefore the oldest chert unit in the Warrawoona Group that contains both stromatolitic and microfossil evidence of ancient life, and is located in the North Pole Dome (see Figure 6.6). The geological interpretation of this area, in itself crucial for interpretations of ancient life, has varied over the decades, and only the most recent one, drawn up following mapping of the area in unprecedented detail, will be given here. (For a comprehensive review on the topic see Van Kranendonk (2006) and references therein.)

The Dresser Formation contain up to five bedded chert±carbonate±barite units that are interbedded with pillowed volcanic rocks. The lowest unit contains considerable amount of barite, which gave it the name 'the chert-barite unit' (Buick and Dunlop, 1990; Nijman et al., 1999). This unit is mainly composed of white, black, and grey cherts, bedded carbonate, sandstone, barite, and stromatolitic facies, as well as volcanoclastic rocks (Van Kranendonk, 2006). The sample from the Dresser Formation (sample 177887, see Van Kranendonk et al. (2003)) is a layered carbonate-chert rock, referred as

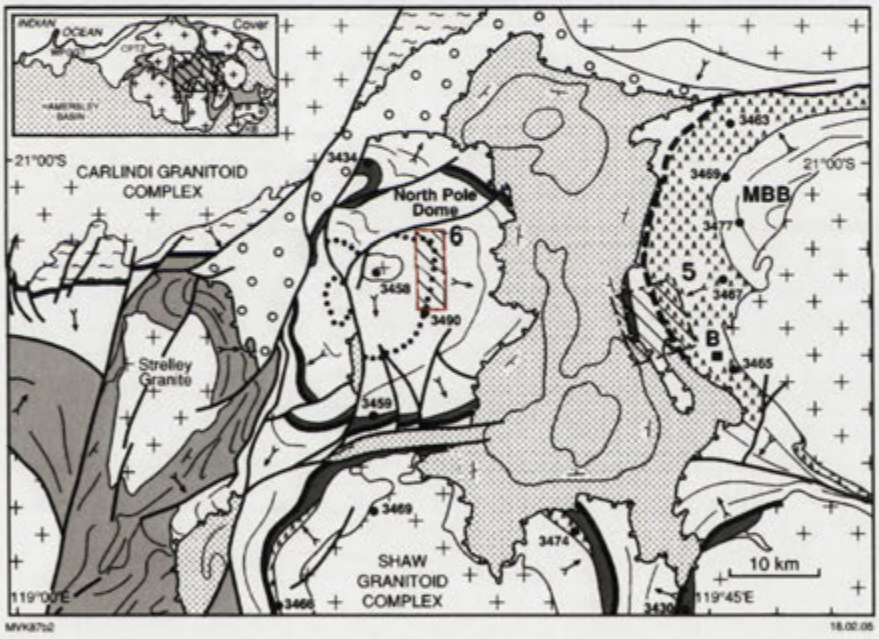

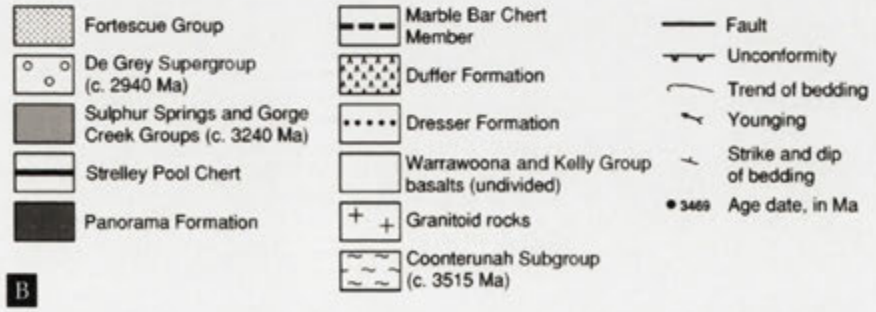

Figure 6.6: (A) Photograph showing the red and spinifex infested landscape of the North Pole area (photo courtesy of Stephen Hyde, 2005). (B) A simplified geological map of a section of the East Pilbara Granite-Greenstone terrane. Red rectangle indicates the geographical area seen in Figure 6.7. Adapted from Van Kranendonk (2006).

Figure 6.7: Schematic geological map of the Dresser Formation of the indicates the geographical area seen in Figure 6.6. Adapted from Van Kranendonk (2006).

the 'zebra' rock due to its characteristic stripes (see Figure 6.9) (Van Kranendonk et al., 2003). The rock was collected from a 1-2 m thick unit by Dr. Martin Van Kranendonk and a small piece (ca. 20x10x1 cm) was kindly given to us to analyze. This unit is overlain by a corrugated finely laminated sediment that show several small (1-2 cm in heigh, 3-12 cm in width) domal structures. This corrugated sediment is red-brown to black in colour and identical in appearance to other units interpreted to be fossil microbial mats. The zebra rock overlies 10-20 m of grey and white chert with barite layers, which is transected by several barite veins. These veins overlie hydrothermally altered pillow basalt which in turn have been crosscut by several chert-barite veins (Van Kranendonk et al., 2003). The chert-carbonate rock displays cyclic sedimentation with altering chert and carbonate layers (see Figure 6.9). The carbonate layer gradually grades into the overlying chert. The contact between the chert and overlying carbonate is on the other hand very sharp. The colour of the carbonate phase, which has been described as ankerite (Van Kranendonk et al., 2003; García-Ruiz et al., 2003), ranges from yellow to brown-black whereas the colour of the chert ranges from white to grey and green. In one of the carbonate layers one can clearly see, with the naked eye, larger crystal outlines that have been interpreted as original rosettes of gypsum crystals (Van Kranendonk et al., 2003; Van Kranendonk, 2006).

It is believed that the zebra rock was deposited directly from the warm Archean seawater (30-50 °C) with high anoxic atmospheric concentration of CO_2 (Van Kranendonk et al., 2003; Van Kranendonk, 2006). However, as has been discussed in Section 5.2.1.1, the composition of the Archean atmosphere is still uncertain. Furthermore, the cyclic nature of the sediment has been interpreted to be due to either preferential silicification of more porous carbonate, or to periodic changes in pH, causing the cyclic precipitation of preferential carbonate over silica (Van Kranendonk, 2006). Following carbonate deposition a period of hydrothermal activity in a caldera-like setting enriched the shallow basin in barite, pyrite and silica, as discussed below (see Figure 6.8). A characteristic of the North Pole area is the presence of a large scale hydrothermal system, evident by the extensive black silica-barite veins cross-cutting the Dresser formation (see Figure 6.6 and 6.7). As these veins were contemporary with the sedimentary rocks, it is believed that these veins were feeding the shallow water with Fe, Ba, Si, and H_2S and/or SO_2 during episodes of hydrothermal activity. The magmatic chamber, driving the hydrothermal system, expelled gaseous H_2S or SO_2, in both the atmosphere and in the subsurface caldera. This resulted in acid leaching of the host rock (basalt), causing enrichment of Ba, Fe and Si in the hydrothemal fluids. Cooling of this fluid produced extensive barite precipitation, both in veins and in sediments.

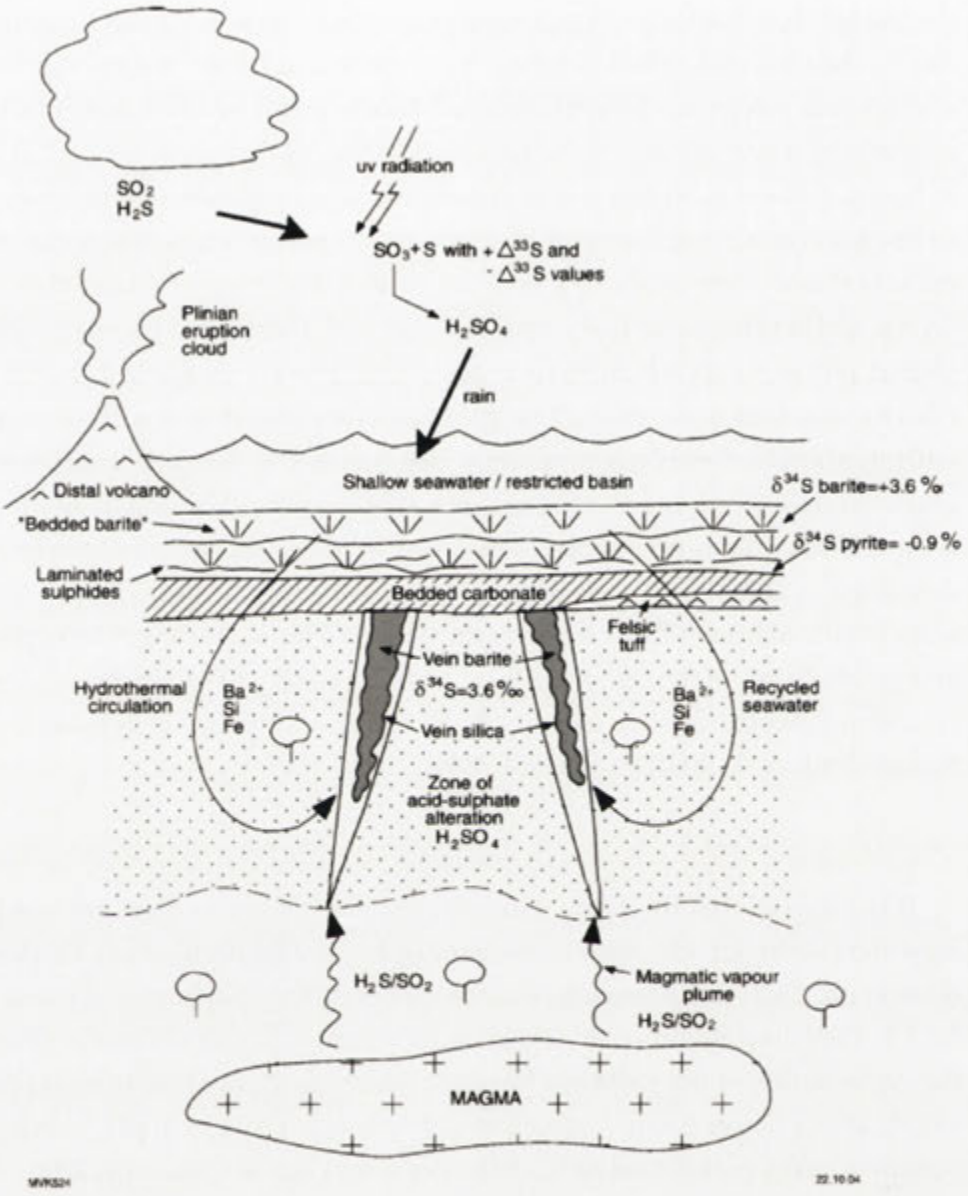

Figure 6.8: Schematic illustration of the hydrothermal Dresser system. Adapted from Van Kranendonk (2006)

6.4.2 Methods

The rock sample was given to us by Martin J. Van Kranendonk from the Geological Survey of Western Australia. Specific samples of the rock were analysed using a SIEMENS D501 Bragg-Brentano diffractometer equipped with a graphite monochromator and scintillation detector, using CuK_α radiation. The acquisition of the spectra was performed by Dr Ulrike Troitzsch from the Department of Earth and Marine Science, ANU. The samples were mounted on low-background holders of oriented

single-crystal quartz. The scan range was 2 to 100° 2θ, at a step width of 0.02°, and a scan speed of 0.5° per minute. The results were interpreted using the SIEMENS software package Diffracplus Eva 10 (2003). The XRD data were further analysed by Dr. A. -K. Larsson using JANA2000 (Petricek et al., 2000).

Major elements Na, Mg, Al, Si, P, S, K, Ca, Ti, Mn, Fe, F and Cl were assessed by X-ray fluorescence spectroscopy (XRF) on a Phillips (PANalytical) PW2400 X-ray fluorescence spectrometer. Lithium borate discs were prepared by fusion of 0.27g of dried sample powder and 1.72g of 12-22 eutectic lithium metaborate-lithium tetraborate. The major elements were calibrated against 28 international standard rock powders. The preparation of the discs was done together with Dr Troitzsch, who also acquired the XRF data.

Thin sections were also prepared and analysed with optical microscopes using both reflective- (Leica MZ 12 stereomicroscope) and transmissive light (Olympus BH-2). Images were recorded with a Nikon Coolpix 8800 (8 megapixel). The thin sections were then carbon coated for elemental analysis using a JEOL JSM6400 Scannning Electron Microscope (SEM) equipped with an Oxford Instruments light elements EDS detector and Link ISIS SEMquant software, operating at an accelerating voltage of 15 kV and beam current of 1 nA.

All of the discs prepared for XRF and one thin section was further analysed for minor elements using laser ablation inductively coupled mass spectroscopy (ICP-MS). The ICP-MS instrument, located at the Research School of Earth Sciences, ANU, used a Resonetics LPX 120 ArF^+ laser (193 nm) to ablate the sample (70 μm spot size), which was then analysed by an Agilent HP7500 ICP-MS system. Dr. Andrew Christy, at the Department of Earth and Marine Sciences, ANU, acquired the ICP-MS data and helped with the interpretation of this data.

6.4.3 Results

The position of the thin sections as well as the powder samples on the original rock can be seen in Figure 6.9, where thin sections are labelled with numbers and the powder samples with letters.

6.4.3.1 Optical microscopy

In the thin sections, individual rhombohedral crystals of carbonate, which in the most carbonate rich areas are densely packed, can clearly be seen. The carbonate rhombs, which are in the ~50–400 μm size range, have a patchy yellow to brown colour and are often lined with shiny black material (see Figure 6.9. The chert, on the other hand, is grey, and composed of very fine grained quartz with a grain size <10 μm

Figure 6.9: The 'zebra' rock from Dresser Formation, North Pole, Western Australia, showing the cyclic sedimentation of white-grey to green layers of chert, with brown bands of carbonates and oxides. The sampling regions of the disks, made for XRF and LA-ICP-MS analyses, is marked with white circles, denoted A-D. Similarly, the positions of the thin sections (1-7) as well as the XRD sampling region (E-I) can be seen, labelled with numbers and letters respectively. Optical reflection microscopy images (J-M) of the thin sections show the yellow to brown colour of the carbonate rhombs, as well as the black rims of Mn oxides. Scale bar in J is 1 mm for J, 500 μm for K, and 310 μm for L and M.

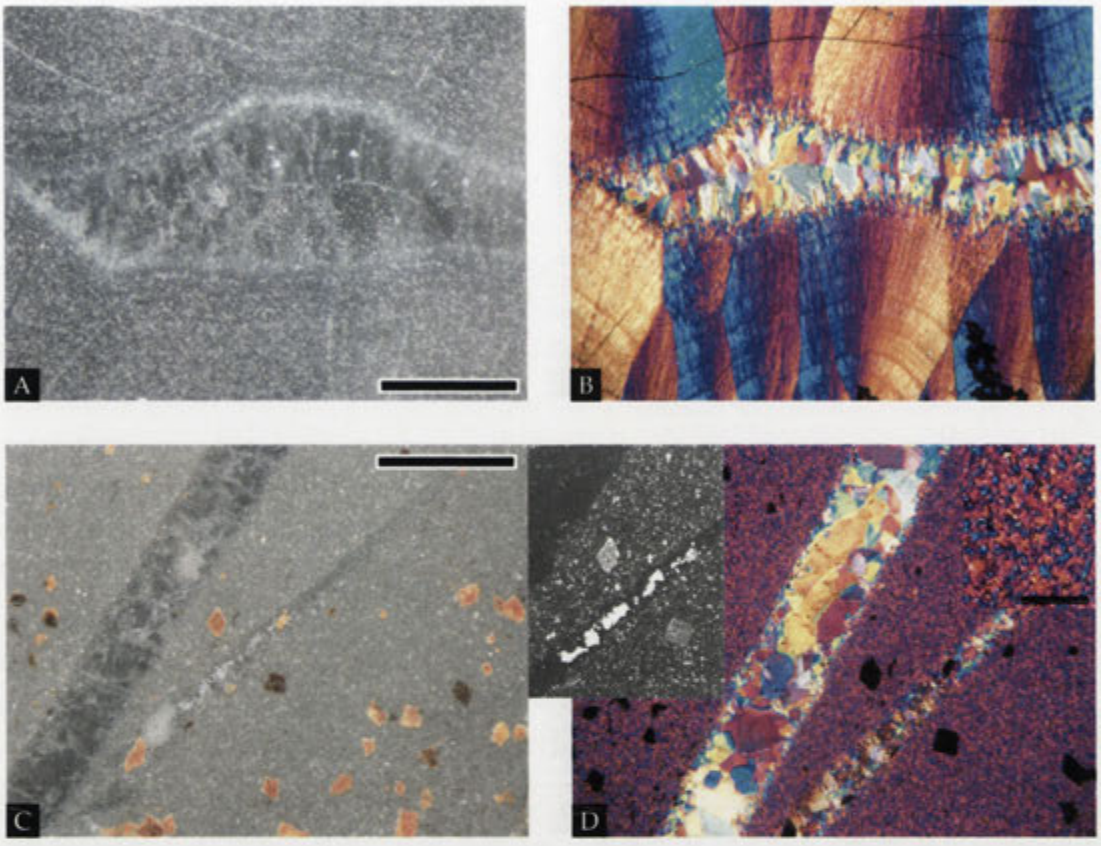

Figure 6.10: Optical images using reflection (A, C) and transmission light microscopes (viewed under crossed polars) (B, D) the respective area (B, D). Scalebars in A 500 μm, in C 1mm. Insets shows the BSE-image of a part of C as viewed in SEM (light material in the vein is barite, confirmed with EDX analysis), and the fine grained nature of the quartz (scale bar 50 μm).

(see Figure 6.10 C and D inset), and as such, classified as granular microcrystalline quartz (Knauth, 1994). The rock is also characterised by having several cross cutting veins, both parallel to and transecting the bedded planes. The quartz occurring in the veins has larger, more well-defined crystals, a type classified as 'megaquartz' (Knauth, 1994). Megaquartz also occur at the very top of the Dresser rock (thin section 1) where it can be seen in close association with fibrous silica (see Figure 6.10 A and B). The fans of fibrous silica, in turn, show evidence of zonation, possibly due to compositional differences. This kind of texture, fibrous silica (possibly chalcedony) that gradually is transformed to megaquartz towards the centre, is commonly associated with infilled cavities (Graetsch, 1994; Knauth, 1994). No structures reminiscent of microfossils or biomorphs were found in the thin sections.

6.4.3.2 XRD

Phase identification by X-ray diffraction of powdered whole rock samples from carbonate-rich parts of the rock (see Figure 6.9) all reveal the presence of quartz, calcite, goethite and dolomite. The individual diffraction data look more or less identical (see Figure 6.11 for sample I), showing the very uniform composition of the rock between the carbonate layers. Crystallographic unit cell parameter refinements of the dolomite and calcite, performed by Dr. Larsson, is consistent with the composition acquired from EDX analyses (see Section 6.4.3.5).The calculated cell parameters giving rise to the position of the diffraction peaks can be seen in the table in Figure 6.11. Similarly, cell parameters reported by Falini et al. (1998) for calcite and magnesian calcites are close to the ones observed by this sample (see also Table 2.1 for comparison of cell parameters). A small inclusion of 3 mol% Mg was necessary to reduce the cell dimensions, and the presence of variable amounts of Mg also broadens the peaks relative to pure calcite (Falini et al., 1998). The small difference between the refinement and the experimental data for the largest calcite peak indicates a close match. The dolomite cell parameter refinement is consistent with the stoichiometric formula $Ca_{1.14}Mg_{0.86}(CO_3)_2$ (see also Table 2.3 for comparison of cell parameters). The cell parameters for goethite match well with those of synthetic goethite reported by Hazemann et al. (1991).

The chert-rich sample (Figure 6.11 H) shows in addition to quartz, calcite, and dolomite, the presence of muscovite at low concentrations (Figure 6.12). As the peak heights of the sample do not match that of the standard used ($K_{0.932}Al_2(Al_{0.932}Si_{3.068}O_{10})$-$((OH)_{1.744}F_{0.256})$), some compositional differences are expected. The observed sample intensities of {110} and especially {-202} are too strong relative to the {002} intensity. The very low intensity of the peaks, which are also broad, made any refinement of cell parameters difficult. EDX analyses (see Section 6.4.3.5) indicate that the muscovite observed is rich in barium, which could cause the height variations seen.

6.4.3.3 XRF

Major elements were analysed on carbonate-rich (A, C) and chert-rich (B, C) samples respectively. The results presented in Table 6.1 indicate that the chert-rich samples are very homogeneous in composition. Small differences in CaO, MgO and Fe_2O_3 are assigned to the relative amount of carbonate present in the different samples. Similarly, the carbonate sample are also homogenous in terms of major elements present in the samples. The low totals seen in B and D is a result of the thermal decomposition of the carbonates during sample preparation, which yield lower wt%. It is also evident in Table 6.1 that the concentrations of CaO, MgO, MnO, and Fe_2O_3 are larger in the carbonate-rich samples, indicating a close association between these elements and

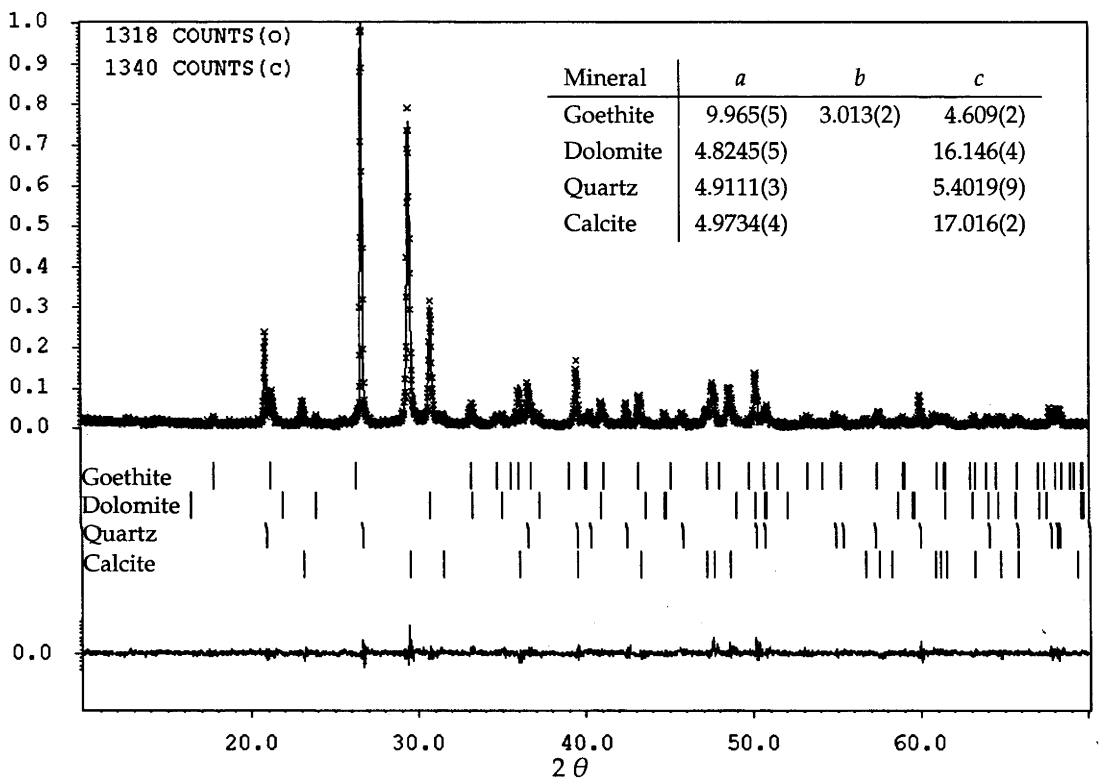

Figure 6.11: XRD data of sample I in Figure 6.9 showing the presence of calcite, quartz, dolomite, and goethite, whose corresponding peak position can be seen as |. The difference between the refinement and the experimental data can be seen in the bottom half of the image, and the table shows the cell parameters of the refined data.

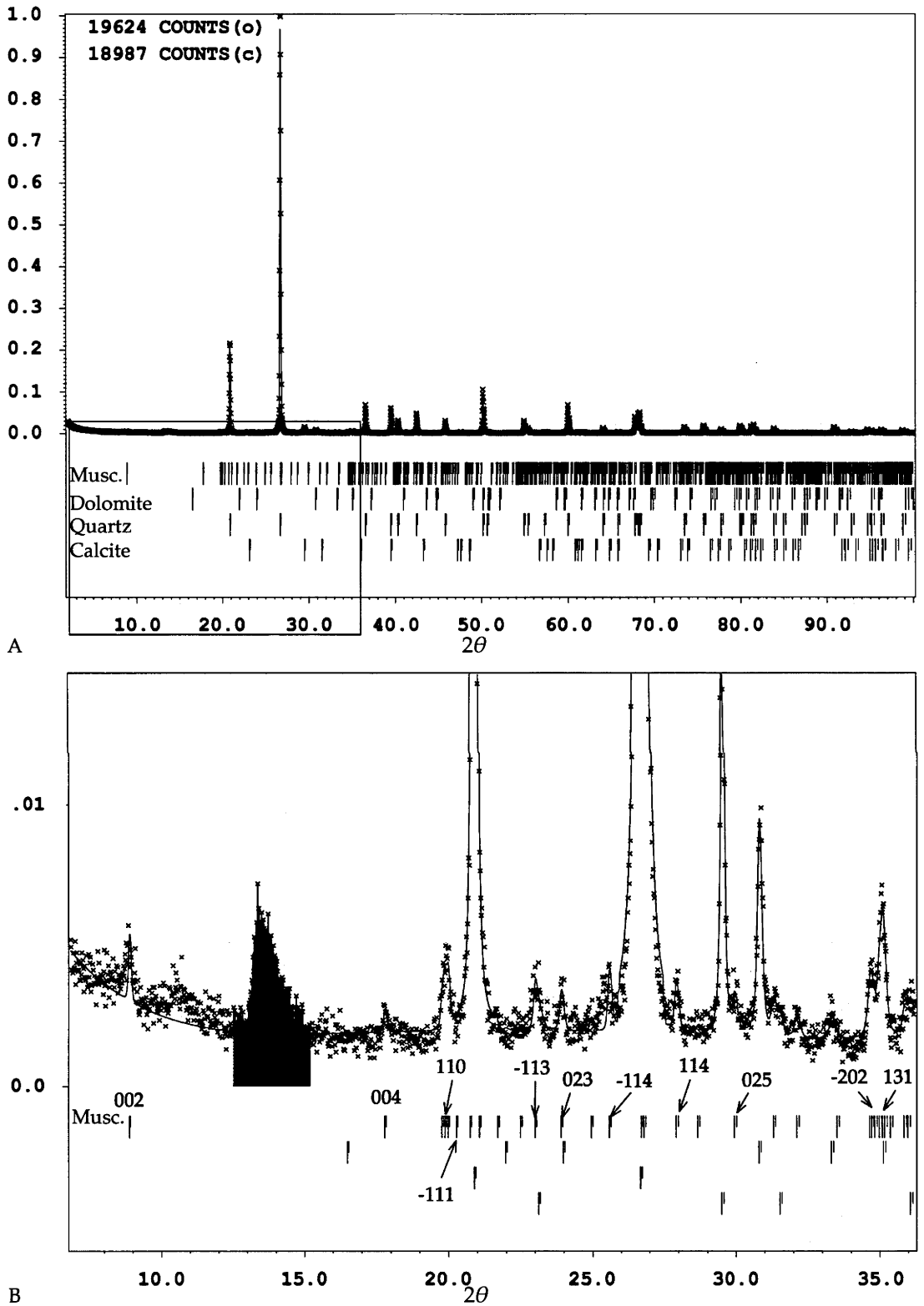

Figure 6.12: XRD data of sample H in Figure 6.9 showing the presence of muscovite, dolomite, quartz and calcite, whose corresponding peak position can be seen as | (A). The rectangular area in A is enlarged in B, where the small additional peaks are identified as belonging to muscovite. The peak height is not, however, consistent with the muscovite standard used; $K_{0.932}Al_2(Al_{0.932}Si_{3.068}O_{10})((OH)_{1.744}F_{0.256})$. The peak marked with grey, is a peak generated by a small amount of white radiation with wavelength $CuK_\alpha/2$ that is not filtered out by the monochromator.

Major elemental composition

Sample area	Chert-rich		Carbonate-rich	
Compound	A	C	B	D
SiO_2	88.95(0.20)	84.06(0.19)	37.78(0.09)	33.58(0.08)
Al_2O_3	1.91(0.01)	2.03(0.01)	1.57(0.01)	1.68(0.01)
CaO	1.97(0.01)	3.41(0.01)	24.73(0.06)	24.58(0.06)
MgO	0.09(0.01)	0.41(0.01)	1.32(0.01)	3.37(0.01)
MnO	0.18(0.01)	0.19(0.01)	1.37(0.01)	1.49(0.01)
Na_2O	0.06(0.01)	0.06(0.01)	0.08(0.01)	0.06(0.01)
K_2O	0.41(0.01)	0.45(0.01)	0.33(0.01)	0.36(0.01)
TiO_2	0.06(0.01)	0.07(0.01)	0.05(0.01)	0.06(0.01)
P_2O_5	0.01(0.01)	0.02(0.01)	0.01(0.01)	0.01(0.01)
SO_3	0.06(0.01)	0.50(0.01)	0.00(0.01)	0.00(0.01)
Fe_2O_3	0.96(0.01)	1.08(0.01)	6.99(0.02)	7.53(0.02)
F	0(124)	0(127)	1810(131)	1713(132)
Cl	6(3)	0(3)	17(2)	0(2)
Total	94.64	92.27	74.42	72.88

Table 6.1: XRF results (wt% oxide, ppm for F and Cl) of sample regions indicated in Figure 6.9.

the carbonate present. As is apparent from the XRD data, carbonate phases include calcite and dolomite, so it can be inferred that some of the CaO and MgO seen in the carbonate-rich samples belong to these phases. Similarly, goethite is present in the carbonate-rich XRD spectra, suggesting that some of the Fe_2O_3 observed in the XRF analyses is due to goethite. It is further noticed the very low concentration of Na_2O, SO_3, TiO_2 and Cl in all samples, and the relatively high concentration (ppm levels) of F in the carbonate-rich samples. The F seen in the carbonate-rich samples could be due to traces of fluorite (CaF_2). However, throughout the rock analyses presented in this chapter, fluorite was never detected.

6.4.3.4 ICP-MS

The disks prepared for XRF analyses were also used to analyse the presence of minor elements by inductively coupled plasma mass spectroscopy (ICP-MS). Significant concentrations of Ba (4900–13300 ppm), as well as Cr (670–860 ppm) and Zn (160–860 ppm) is evident from these analyses (see Table D.1). A linescan was also performed across the bedding of parts of thin section 7 (Figure 6.13. In Figure 6.13 the optical image of the linescan and graphs displaying the intensity of some of the elements

analysed as a function of distance across the linescan are shown. The interpretation of the results from the line scan (see Figure 6.13 and 6.14) is done in conjunction with the results from EDX analyses, presented in the next section (see Section 6.4.3.5).

From Figure 6.13, it is evident that concentration correlation exists between Ba and Mn, and also between Fe and Ca. Furthermore, Al and Si show similar profiles, which are not correlated to that of Ca. In Figure 6.14 additional graphs showing such elemental correlation can be seen. In Figure 6.14 A, it is further shown that Si is not related to Ca, which is expected as quartz and calcite are the minerals containing these elements, and these minerals tend to concentrate in different beds. Since the spot size of the laser (70 μm) is, in many cases, larger than the size of the minerals present, several minerals are analysed simultaneously. However, the clustering of the data points seen in Figure 6.14 demonstrates close correlation between some elements. For instance, in Figure 6.14 C and D, Fe is seen to be correlated to both Ca and Mn. From EDX analyses (see Section 6.4.3.5), iron-containing minerals include goethite, hollandite, and some solid solution in calcite. High Fe content coupled with low Ca concentrations is compatible with the presence of goethite or hollandite. Similarly, high Fe content coupled with low Mn content is suggestive of goethite as indicated in Figure 6.14 D, whereas high Mn counts are indicative of hollandite is shown. As is shown in Figures 6.13 and 6.14 E and F, Al is found in minerals containing Ba, Cr, and Si. From XRD and EDX analyses this has been shown to be muscovite (see Table 6.2). Ba and Cr not directly correlated to Al are in turn compatible with the presence of hollandite and chromite respectively. To test such correlation, Ba is graphically plotted against both Mn and Cr in Figure 6.14 G and H. It is evident from G that correlation exist between Mn and Ba at high count rates, which suggests the presence of hollandite. Low Mn and Ba counts could be indicative of muscovite, whereas high Ba counts and low Mn counts suggests the presence of barite. Similarly, Cr is present as chromite and Ba-rich and Cr-rich muscovite as evident from EDX analyses, and the Cr vs. Ba graph in Figure 6.14 G can be interpreted in relation to those minerals. High Ba counts coupled with low Cr counts, on the other hand, suggest the presence of barite or hollandite.

EDX analyses of the minerals present confirms these observations, as is shown below in section 6.4.3.5.

6.4.3.5 EDX analysis

Elemental spot analysis of thin sections labelled 1, 2, 3, 4, 5, and 7 (see Figure 6.9) showed no great variation in composition between the individual carbonate and chert layers, as also indicated by the XRD results. However, the SEM-EDX analysis pro-

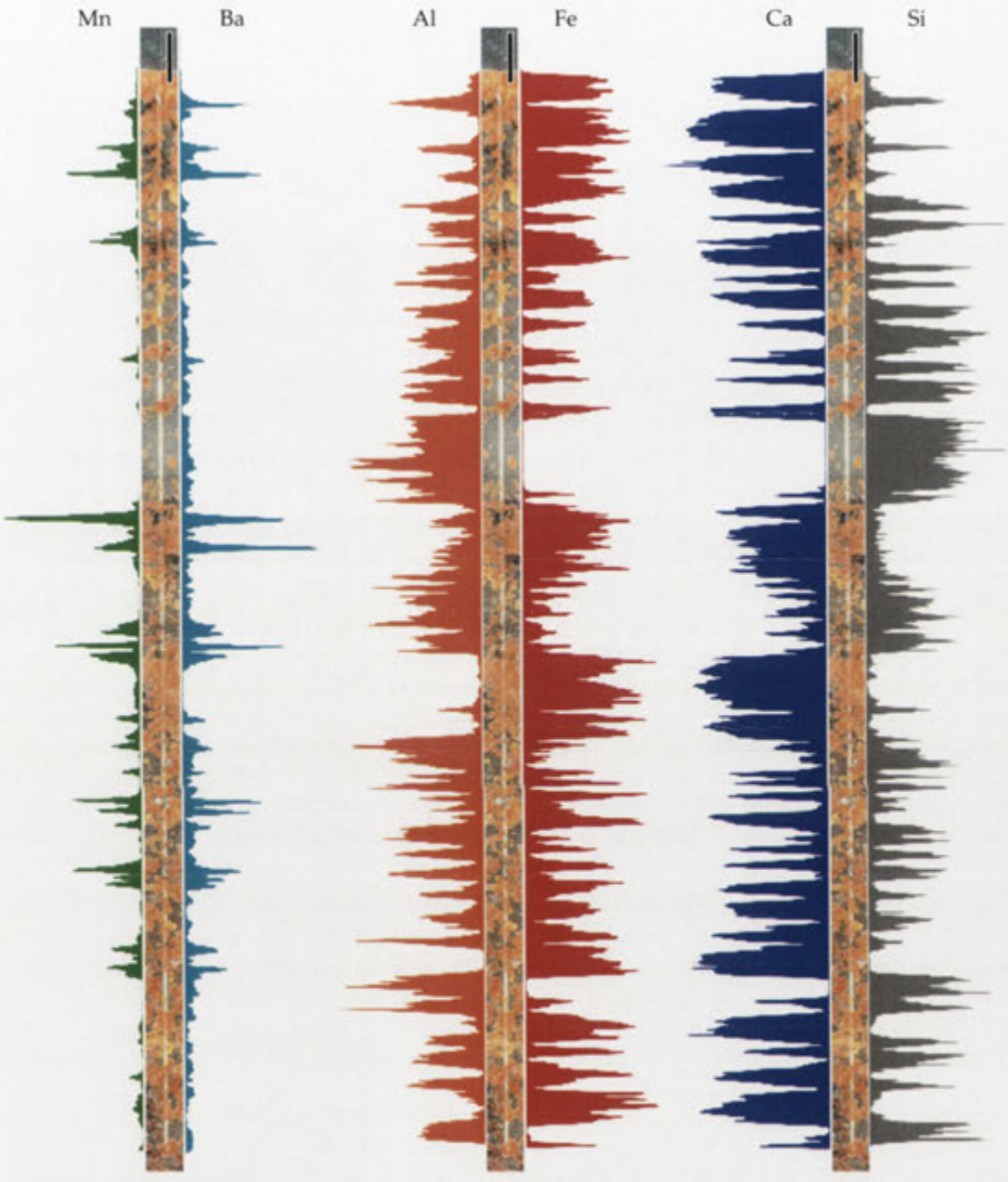

Figure 6.13: Optical images of the linescan coupled with the distribution of Mn, Ba, Al, Fe, Ca, and Si. It is evident from these images that correlation exists between Mn and Ba, as well as between Fe and Ca. Scalebar is 1 mm.

duced further information on the composition and the spatial distribution of the minerals. The composition of the individual thin sections were very homogenous, further indicating the cyclic sedimentation of carbonate and chert with more or less identical mineralogy. The silica matrix of the rock is microcrystalline quartz that is

Chert and silicate composition

Oxide	1	2	3	4	5	6	7
Na_2O	0.14	-	0.77	1.07	0.78	-	0.26
MgO	-	-	0.61	0.56	-	0.71	1.26
Al_2O_3	0.44	-	34.45	34.92	33.79	35.09	32.76
SiO_2	100.71	0.62	43.06	44.02	42.27	42.25	42.81
K_2O	-	-	6.67	6.63	6.71	7.91	8.32
CaO	-	0.22	0.25	0.27	-	0.57	0.31
TiO_2	-	100.23	-	-	-	-	0.53
Cr_2O_3	0.39	-	0.67	0.79	1.58	0.54	0.92
FeO	-	-	0.77	0.68	0.60	0.94	1.26
SrO	-	0.22	-	-	-	-	-
BaO	-	-	6.35	6.05	7.27	7.73	6.01
Total	101.68	101.29	93.61	94.99	92.99	95.75	94.18
	Number of ions on the basis of:						
Element	2 O				22 O_{eq}		
Na	0.003	-	0.209	0.284	0.216	-	0.070
Mg	-	-	0.128	0.116	-	0.148	0.264
Al (T)	0.005	-	1.971	1.948	1.982	2.107	1.987
Al	-	-	3.713	3.709	3.687	3.662	3.438
Si	0.993	0.008	6.029	6.052	6.018	5.893	6.013
K	-	-	1.192	1.162	1.219	1.408	1.492
Ca	-	0.003	0.038	0.039	-	0.086	0.046
Ti	-	0.989	-	-	-	-	0.056
Cr	0.003	-	0.074	0.086	0.178	0.060	0.102
Fe	-	-	0.090	0.078	0.072	0.110	0.148
Sr	-	0.002	-	-	-	-	-
Ba	-	-	0.349	0.326	0.405	0.422	0.330
Total	1.004	1.002	13.792	13.800	13.776	13.896	13.948
$\sum$ T	-	-	8.000	8.000	8.000	8.000	8.000
$\sum$ A	-	-	1.787	1.811	1.839	1.917	1.939
$\sum$ M	-	-	4.006	3.989	3.937	3.980	4.009

Table 6.2: EDX results (wt% oxide) of chert (1), TiO_2 (2) and silicates (3-7) occurring in the Dresser rock. The calculations of number of ions per formula for samples 3-7 are based on mica-type minerals (e.g. muscovite $K_2Al_4[Si_6Al_2O_{20}](OH,F)_4$, $A_2M_4T_8O_{20}(OH,F)_4$) where T represent tetrahedral Al and Si, and A represent large (Ba, Ca, Na, K) interlayer cations, and M medium sized (Mg, Ti, Cr, Fe) octahedral cations, and ions in the formula are calculated based on 22 O equivalents (44 negative charges).

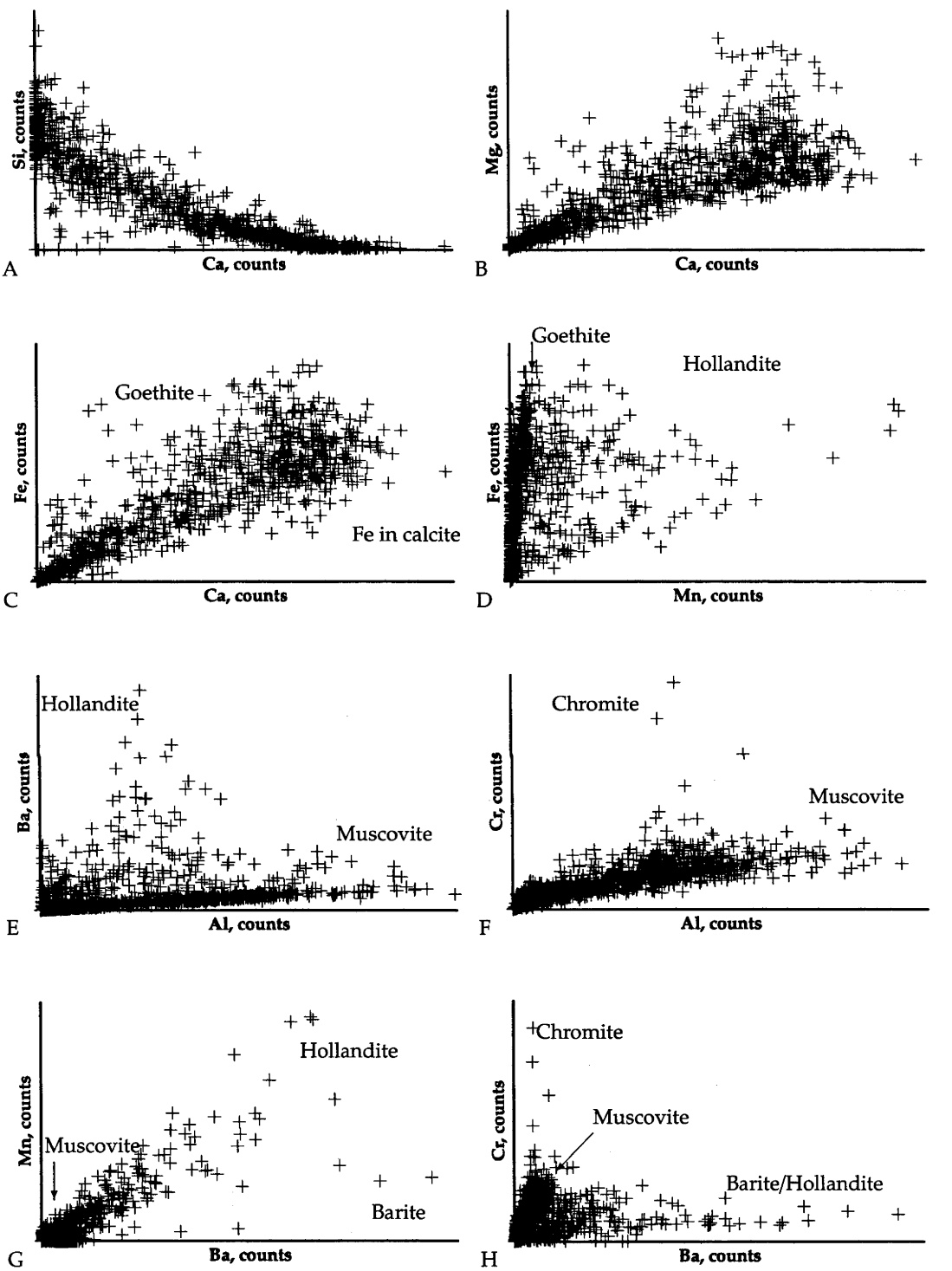

Figure 6.14: Graphical representations of correlation between elements present in the ICP-MS line scan of thin section 7 of the Dresser rock. Inverse correlation is seen between Si (in quartz) and Ca (in calcite) (A). Positive correlation exist between Ca and Mg in carbonate (B), Fe and Ca (in carbonate and goethite) (C), Fe and Mn (in goethite and hollandite) (D), Ba and Al (in hollandite and muscovite) (E), Cr and Al (in chromite and muscovite) (F), Mn and Ba (in hollandite and muscovite) (G), and between Cr and Ba (in chromite, muscovite, and hollandite) (G).

fairly very pure. However, small contributions of Hg, Cr, Ba, and Al are sometimes also seen (see Table 6.2). Occasionally, small specks of TiO_2 are also observed in the chert. Silicates are widely distributed in the chert (see Figure 6.16, Al and K), and they all contain about 5-8 wt% BaO. According to the XRD results, discussed above, muscovite is present and is known to sometimes contain Ba. It is therefore suggested that the mica phase present is a barium-rich form of muscovite. Muscovite ($K_2Al_4[Si_6Al_2O_{20}](OH,F)_4$, or $A_2M_4[T_8O_{20}](OH,F)_4$) belongs to the mica group (sheet silicates), where each layer is composed of two sheets of $(Si,Al)O_4$ tetrahedra (T) linked by octahedral cations (M). These layers are in turn sandwiched between layers of larger cations (A) (see Figure D.2) (Brigatti and Guggenheim, 2002). The analyses of these silicates, of which a selection can be seen in Table 6.2 3-7, have compositional range of Na_2O (~0-1.3 wt%), MgO (0.6-1.3 wt%), CaO (0-0.57 wt%), FeO (0.6-1.3 wt%), and in one instance 1.0 wt% SrO was observed. The highest Cr_2O_3 concentration was 1.58 wt%, as seen in Table 6.2, sample 5. The calculated ions per formula is consistent with a barian muscovite; $(K,Ba,Na,Ca)_2(Al,Mg,Fe,Cr,Ti)_4[Si_6Al_2O_{20}](OH)_4$ (see Table 6.2). The T site is filled with Al and Si (Si:Al ratio approximately 3:1), and the remaining Al, as well as Mg, Ti, Cr, and Fe were assigned to the octahedrally coordinated M site, of which all are close to 4.000. Ba, Ca, Na, and K were in turn assigned to the A site, which is not completely occupied. For example, the formula for sample 6 is $(K_{1.41}Ba_{0.42}Ca_{0.09})_{\sum 1.92}(Al_{3.66}Mg_{0.15}Fe_{0.11}Cr_{0.06})_{\sum 3.98}[Si_{5.89}Al_{2.11}O_{22}]$. To explain the composition of the barian muscovites, several possible substitutions needs to be considered. Compared to pure muscovite, the barian counterpart contains Mg, Fe, Cr, Ca, Na, and sometimes Ti and Sr in addition to Ba. To accommodate these elements, substitutions (or exchange vectors, where $[X]_1$ represents the elements that are substituted for by the [Y] elements) such as :

$$[Ba][^{IV}Al][K]_{-1}[Si]_{-1} \tag{6.1}$$

$$[Fe,Mg][Si][^{VI}Al]_{-1}[^{IV}Al]_{-1} \tag{6.2}$$

$$[Cr][^{VI}Al]_{-1} \tag{6.3}$$

could explain the composition of the barian muscovites (Dymek et al., 1983; Hetherington et al., 2003). Furthermore, the vacancies calculated for the A site could be due to $[H_3O^+][K]_{-1}$, or the presence of water (Guidotti and Sassi, 1998). This type of muscovite is very rare, known from only a few locations worldwide (e.g. Berisal Complex, Switzerland (Hetherington et al., 2003), Franklin Marble, New Jersey (Trtacy, 1991), and West Greenland (Dymek et al., 1983)). Interestingly, these analyses are very similar to (Ba, Cr)-rich muscovites found in Isua and Malene Archean supracrustal rocks in West Greenland (Dymek et al., 1983). However, a larger variety in composition is seen in the West Greenland samples (up to ~8 wt% BaO, ~17 wt% Cr_2O_3), as com-

Carbonate composition

Oxide	1	2	3	4	5	6	7	8	9
MgO	-	1.28	17.91	1.11	1.77	3.48	0.66	15.12	17.92
CaO	52.86	52.51	32.82	52.77	50.88	47.40	52.93	34.41	32.58
MnO	-	-	-	-	-	-	0.37	0.21	-
FeO	-	-	-	1.53	0.67	2.38	0.37	1.25	-
ZnO	-	-	-	-	-	-	-	-	1.06
CO_2 (calc.)	41.48	42.60	45.31	43.56	42.28	42.46	42.72	44.41	45.71
Total	94.34	96.39	96.04	98.97	95.60	95.72	97.05	95.40	97.27
Element	Number of ions on the basis of 6 O								
Mg	-	0.065	0.863	0.056	0.092	0.179	0.034	0.744	0.856
Ca	2.000	1.935	1.137	1.901	1.889	1.752	1.945	1.216	1.119
Mn	-	-	-	-	-	-	0.011	0.006	-
Fe	-	-	-	0.043	0.019	0.069	0.011	0.034	-
Zn	-	-	-	-	-	-	-	-	0.025
Total	2.000	2.000	2.000	2.000	2.000	2.000	2.001	2.000	2.000

Table 6.3: EDX results (wt% oxide), and calculated number of ions in the formula $(Mg, Ca, Mn, Fe, Zn)_2(CO_3)_2$ of some carbonates occurring in the Dresser rock.

pared to the one discussed here. The barian muscovites occur as <100 μm size flaky and soft aggregates throughout the chert, and are often seen coating the carbonate rhombs. On the surface of the rhombs they can sometimes be closely inter-grown with hollandite-type minerals (see Figure 6.17 x).

The carbonate entity of the rock is mainly composed of Ca, with varied contributions of Mg, Mn and Fe. In all cases, carbonates are closely associated with Mn and especially Fe oxides. As can be seen in Figure 6.16, Ca is the main cationic component of the carbonate rhombs, whereas Mg is irregularly distributed in the rock. As was demonstrated by the XRD results (see Section 6.4.3.5), calcite is the main polymorph of $CaCO_3$, so it is deduced that the Ca observed in the spot analysis (see Table 6.3) and elemental maps (see Figure 6.16, 6.18, 6.19, and 6.20) of rhombs belongs to calcite. Furthermore, the rhombohedral habit of the carbonate is consistent with calcite (see Section 2.2.2). As can be seen in Table 6.3, calcite is often close to the end-member composition, but it often includes Mg, Mn and Fe, and occasionally Zn. Very Mg-rich patches (dolomite) occur as a replacement texture with sharp boundaries: these are always close to the rim of carbonate rhombs (see Figure 6.16 and 6.19). Composition of the dolomite ranges from $Mg_{1.11}Ca_{0.885}Fe_{0.005}(CO_3)_2$ to pure calcite, with clustering around $Mg_{0.87}Ca_{1.13}(CO_3)_2$, and $Mg_{<0.20}Ca_{>1.80}(CO_3)_2$ (see Figure 6.15). Fe

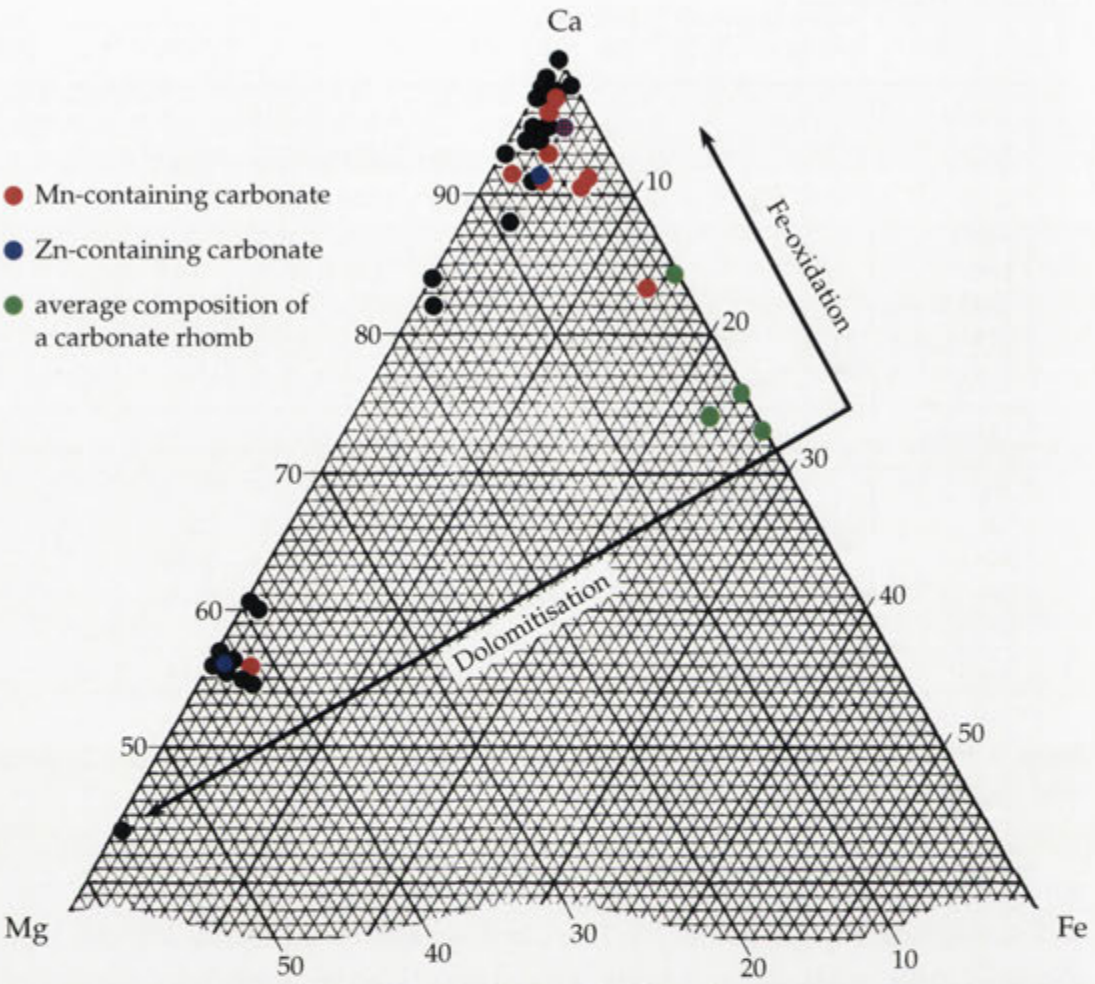

Figure 6.15: A section of the $MgCO_3$-$CaCO_3$-$FeCO_3$ phase diagram representing the composition of the carbonates in the Dresser rock (black circles). Some carbonates also contain Mn (red circles), and Zn (blue circle). The average composition of carbonate rhombs are indicated by green circles, and the area limited by the black arrows defines possible composition of the original carbonate, before oxidation and dolomitisation.

is often seen in the carbonate analysis (see Table 6.3, and Figure 6.15), some of which can not be ruled out as contamination from neighbouring goethite. The most Fe-rich sample had a composition of $Mg_{0.05}Ca_{1.67}Mn_{0.03}Fe_{0.25}(CO_3)_2$. However, most often carbonates had less than 5% Fe (see Figure 6.15). Traces of Mn also occurred frequently in the carbonates, often at levels <1%. Isolated occurrences of Zn in the carbonate phase had Zn levels <3%. These carbonates have a compositional range of $Mg_{0.06-0.86}Ca_{1.22-1.89}Mn_{0-0.01}Fe_{0-0.06}Zn_{0.02-0.03}(CO_3)_2$.

All carbonate rhombs contain oxides of Fe and occasionally also Mn. Elemental maps of selected areas (see Figure 6.16, 6.18, 6.19, and 6.20) shows a wide distribution of Fe within carbonate rhombs, never as single entities within the surrounding

Oxide composition

Mineral	Hollandite					Goethite			Chromite
Oxide	1	2	3	4	5	6	7	8	9
Na_2O	-	0.42	-	-	-	-	-	-	-
MgO	0.41	0.85	0.63	0.51	0.68	0.46	1.08	1.16	18.02
Al_2O_3	-	-	-	-	-	-	0.23	0.30	23.98
K_2O	-	-	-	0.13	0.16	-	-	-	-
Cr_2O_3	-	-	-	-	-	-	-	0.22	47.97
MnO_2	58.34	59.21	61.50	62.60	61.40	-	-	-	-
Mn_2O_3	10.32	7.72	9.81	6.11	6.55	0.36	2.13	-	-
Fe_2O_3	3.16	3.47	2.66	4.45	1.94	84.71	75.07	74.31	0.23
FeO	-	-	-	-	-	-	-	-	5.87
ZnO	-	-	-	0.82	1.24	-	-	1.41	-
SrO	-	-	0.20	-	-	-	-	-	-
BaO	14.63	13.02	14.18	13.49	12.91	-	-	-	-
Total	86.86	84.69	88.98	88.11	84.88	85.53	78.51	77.40	96.08
	Number of ions on the basis of:								
Element	16 O					$6\ O_{eq}$			32 O
Na	-	0.128	-	-	-	-	-	-	-
Mg	0.097	0.199	0.142	0.116	0.160	0.043	0.108	0.117	6.478
Al	-	-	-	-	-	-	0.018	0.024	23.978
K	-	-	-	0.026	0.031	-	-	-	-
Cr	-	-	-	-	-	-	-	0.012	47.968
Mn^{IV}	6.304	6.460	6.427	6.576	6.680	-	-	-	-
Mn^{III})	1.228	0.928	1.129	0.706	0.785	0.017	0.109	-	-
Fe^{III}	0.372	0.413	0.303	0.509	0.230	3.954	3.801	3.839	0.041
Fe^{II}	-	-	-	-	-	-	-	-	1.524
Zn	-	-	-	0.092	0.145	-	-	0.070	-
Sr	-	-	0.018	-	-	-	-	-	-
Ba	0.896	0.805	0.840	0.803	0.796	-	-	-	-
Total	8.896	8.933	8.858	8.829	8.828	4.014	4.036	4.063	24.000

Table 6.4: EDX results (wt% oxide) of hollandite-type Mn-oxides (1-5), goethite (6-8), and Mg-Al-chromite (9), accompanied by the calculated number of ions in the respective formula; $(Na, K, Sr, Ba)_{<1}(Mg, Mn^{IV}, Mn^{III}, Fe, Zn)_8O_{16}$, FeO(OH), and $Mg(Al, Cr)_2O_4$.

chert. The iron occurs mainly as fairly pure iron oxides, but also in solid solution in manganese oxides. The exact determination of the type of iron oxide using EDX on porous and not perfectly polished surfaces is impossible without additional crystallographic information. Possible minerals include hematite (Fe_2O_3), magnetite (Fe_3O_4), and polymorphs of FeO(OH) (goethite and lepidocrocite). As the XRD results show

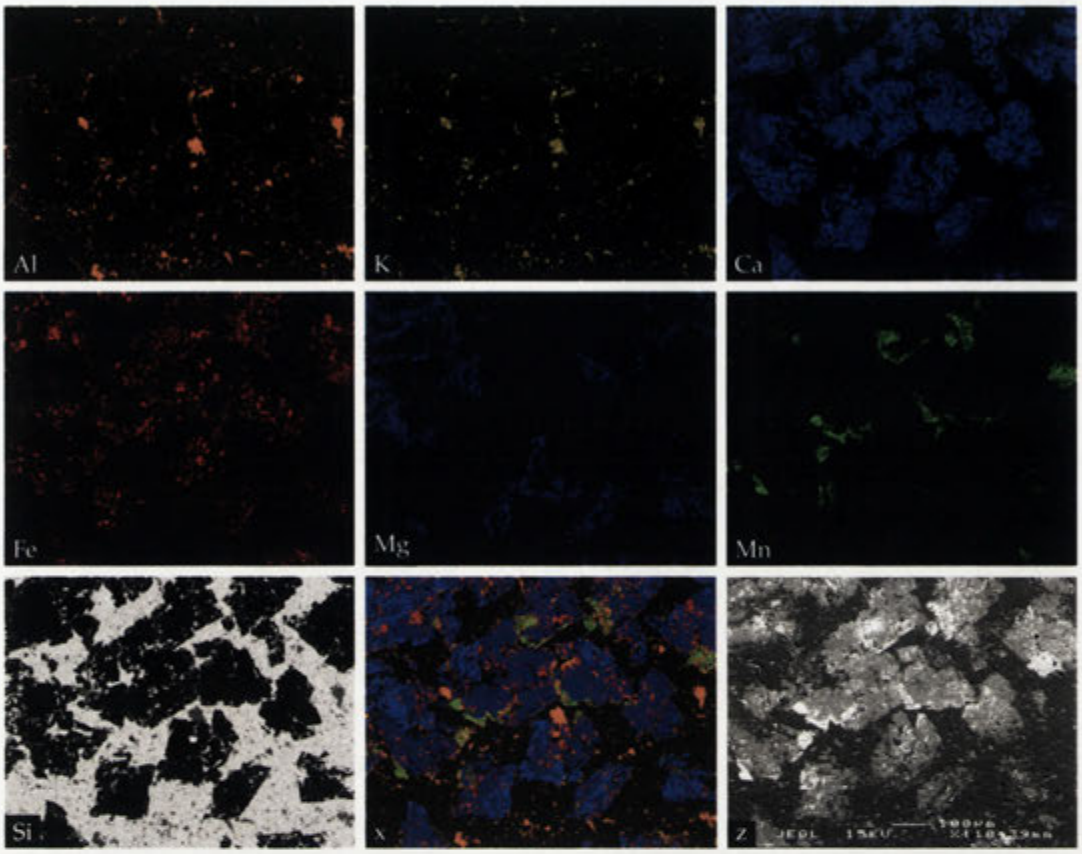

Figure 6.16: Elemental map from Dresser5 showing the distribution of Al, K, Ca, Fe, Mg, Mn, and Si, of the area shown in z (BSE image). Note the patchy distribution of Mg, which is seen occurring at the rim of the carbonate rhombs. A compilation of Al, Ca, Fe, Mg and Mn elemental maps can be seen in x, showing the spatial distribution of minerals containing these elements. (Map of Ba not shown).

the presence of goethite (see Section 6.4.3.2), it is presumed that most of the iron oxides within the rock can be attributed to FeO(OH) (see Table 6.4, sample 6-8). The predominantly yellow-brown colour of the carbonate rhombs further points towards goethite and/or lepidocrocite as the main iron oxide species (hematite is dark red to black, magnetite is black).

Mn oxides occur frequently in association with the carbonate (see Figure 6.16, 6.18, 6.19, and 6.20). In contrast to the iron oxides, the Mn oxides have commonly developed close to the surfaces of the carbonate rhombs, sometimes in association with the barian muscovites (see Figures 6.16 and 6.17). Furthermore, these oxides contain Ba (see Figure 6.20). Potential Ba-containing Mn oxides include hollandite (ideally $BaMn_8O_{16}$), and romanechite (ideally $BaMn_5O_{10} \cdot H_2O$). Like many other manganese oxides, the basic building blocks for both hollandite and romanechite are MnO_6 octahedra, that form chains separated by tunnels. These tunnels contain various amounts of water

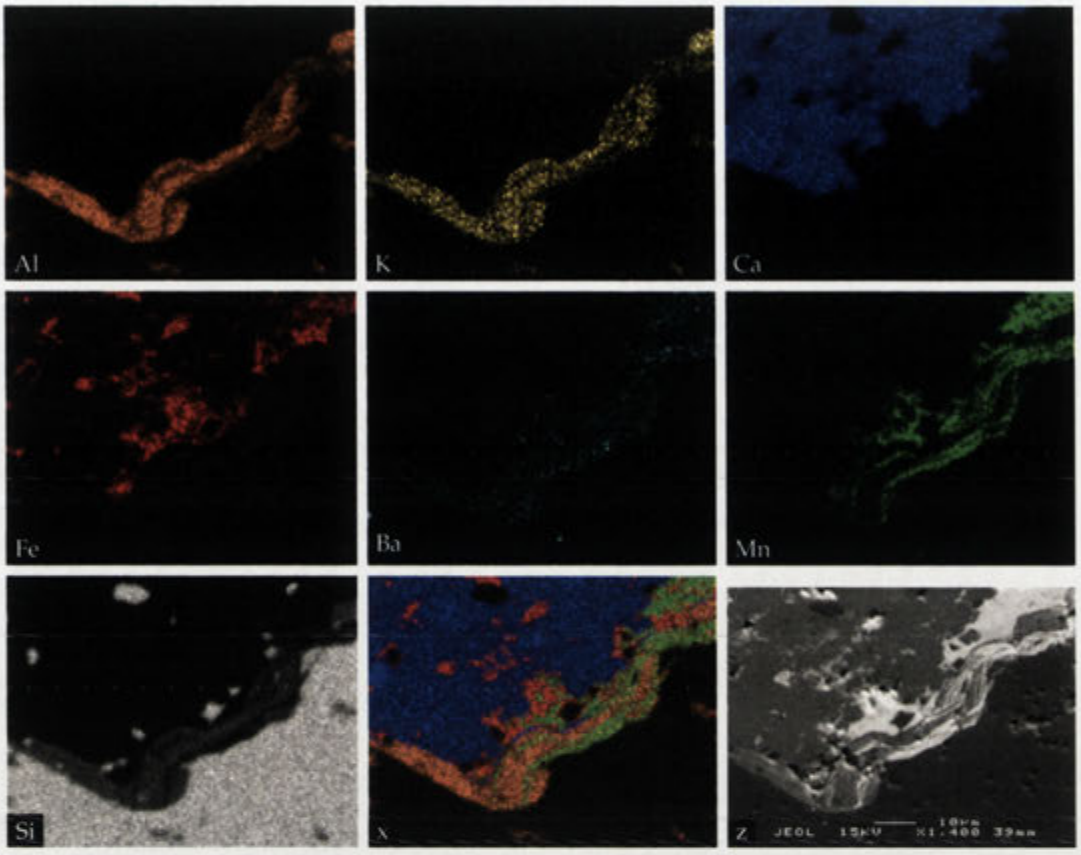

Figure 6.17: Elemental map from Dresser7 showing the distribution of Al, Ba, Ca, Fe, K, Mn, and Si, of the area shown in z (BSE image). A compilation of the elemental maps of Ca, Mg, Al, Fe and Mn, showing the close association between barian muscovites and hollandite, can be seen in x. Brighter blue areas in x represent Mg-rich areas. (Elemental map of Mg is not shown).

and large cations such as Ba, K, Na, Pb, Sr and Ca (A-site cations), whose charges are balanced by substitution of some of the Mn^{IV} for Mn^{III}, Fe^{III}, Al^{III} and other low valence cations (M-site cations) (Post, 1999) in a stoichiometry of the form AM_8O_{16} (hollandite) or $AM_5O_{10} \cdot H_2O$ (romanechite). Both romanechite and hollandite are black in colour, and both could therefore account for the black coloration seen in the optical microscope (see Section 6.4.3.1). However, as the A/M ratio in the analyses are closer to 0.125, as in hollandite, than to 0.2, as in romanechite, it is inferred that the manganese oxides in the Dresser rock are hollandite-type oxides. The analyses of samples 1-5 presented in Table 6.4 were calculated based on 8 M-site ions in total, giving an estimate of the Mn^{IV} to Mn^{III} ratio. In almost all the analyses, small contributions of Si, Ca, and occasionally Al and K, were discarded as being contaminants from the chert, carbonate, and silicates. However, it should be noted that these elements may also be part of the mineral. Furthermore, water and contributions from OH were not included in the

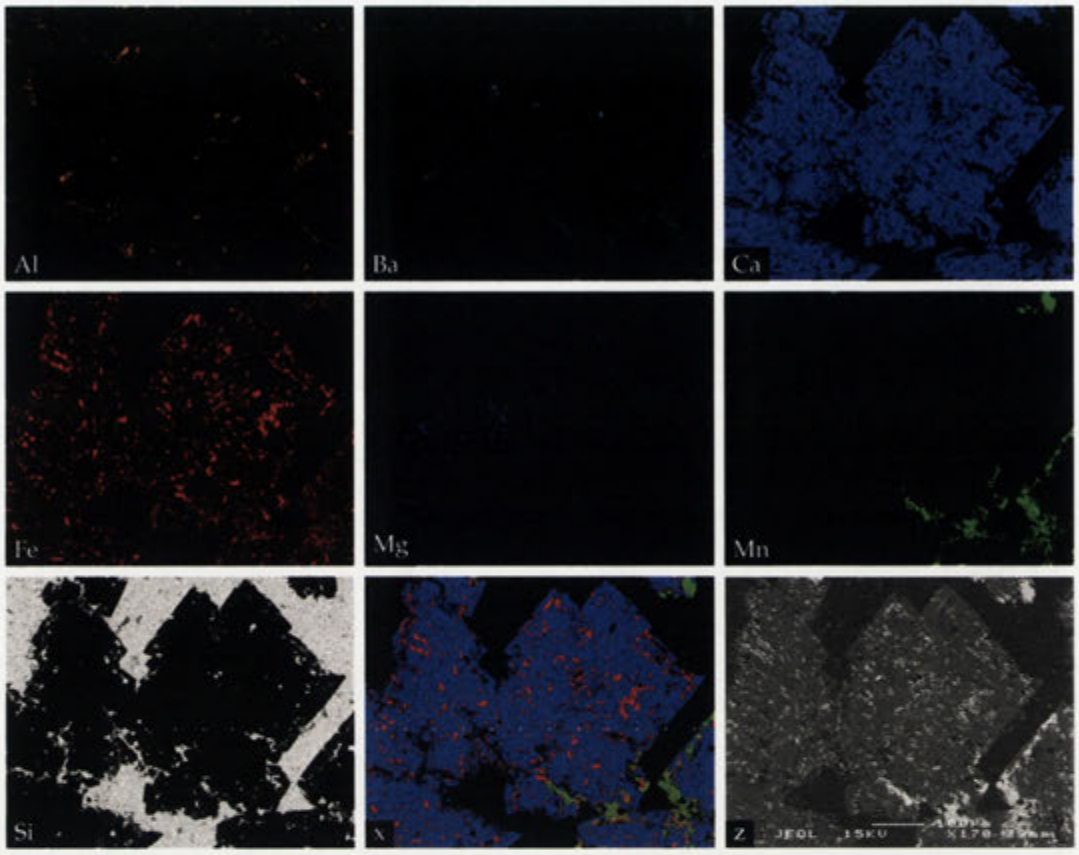

Figure 6.18: Elemental map from Dresser2 showing the distribution of Al, Ba, Ca, Fe, Mg, Mn, and Si, of the area shown in z (BSE image). A compilation of the elemental maps of Ca, Mg, Fe and Mn, showing the widespread presence of goethite within the rhomb, and hollandite on the surface of the rhomb, can be seen in x. (Map of S not shown).

analyses. That, together with the discarded elements and the porous nature of the thin section, can account for the low totals seen in Table 6.4. The hollandite-type minerals observed in the Dresser rock contain K, Na, and Sr in addition to Ba in the tunnels. Fe and small amounts of Mg are often seen as constituents of the Mn framework (assumed to be part of the structure on the basis of ionic size). Zn is also on occasion found to substitute for Mn^{IV}. The hollandites have an approximate compositional range of $(Na_{0-0.13}K_{0-0.03}Sr_{0-0.02}Ba_{0.8-0.9})[Mg_{0.1-0.2}Mn^{IV}_{6.3-6.7}Mn^{III}_{0.7-1.2}Fe_{0.2-0.4}Zn_{0-0.1}]O_{16}$. In addition to being present in the Mn oxides and silicates, Ba is also found as a constituent of barite. However, this occurrence is infrequent within the carbonate layers. More commonly barite is found in cross-cutting veins that are free of both carbonates and silicates (see Figure 6.10 inset). Other minor minerals also found are chromian spinels/chromites $((Mg, Fe(II))(Al, Cr, Fe(III))_2O_4)$ (see Table 6.4, and Figure 6.20), gersdorffite $(Ni_{1.01}As_{0.97}Co_{0.05}Fe_{0.01}S)$, and apatite $(Ca_5(PO_4)_3(OH, F, Cl))$. An unusual Bi-

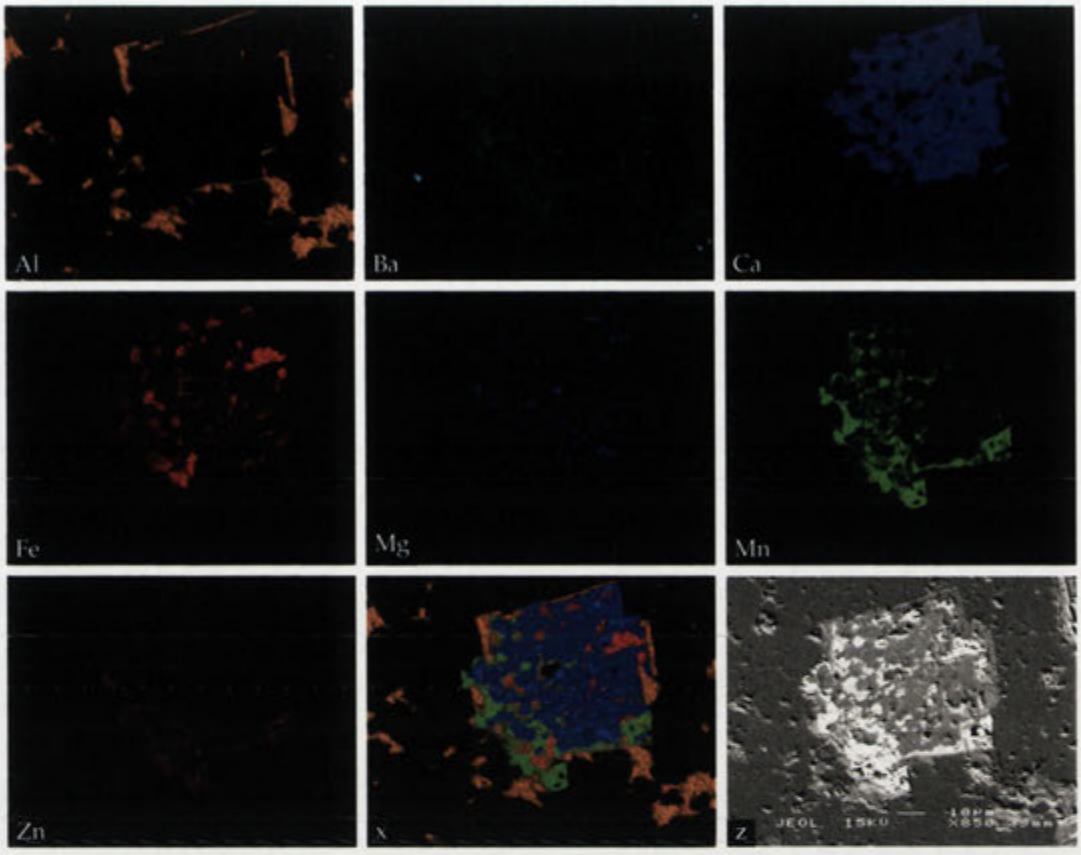

Figure 6.19: Elemental map from Dresser1 showing the distribution of Al, Ba, Ca, Fe, Mg, Mn, and Zn, of the area shown in z (BSE image). A compilation of the elemental maps of Ca, Mg, Al, Fe and Mn, showing the presence of goethite (red), barian muscovite (orange) and hollandite (green) on the surface of and within the rhomb, can be seen in x. Bright blue areas in x are indicative of dolomite. Bright spot in Ba is TiO_2. (Map of K and Si not shown).

containing form of Fe-oxide, possibly plumboferrite ($Pb_2Fe^{3+}_{11-x}Mn^{2+}_xO_{19-x}$), was also observed in one sample.

To assess 'original' carbonate composition during rock formation, quantitative analyses were performed on a large area of a carbonate rhomb. If all the oxides originally were present as carbonate, the original Fe and Mn content would have been much higher (see Figure 6.15). As Ba is not readily incorporated into the calcite structure, this element was not included in the calculation. The reconstructured average carbonate composition (including oxides), had, in one instance, a formula of $Mg_{0.05}Ca_{1.47}Mn_{0.01}Fe_{0.47}(CO_3)_2$. A similar analysis of a carbonate rhomb hosting Zn containing oxides (see Figure 6.19) showed an average carbonate composition of $Mg_{0.07}Ca_{1.07}Mn_{0.37}Fe_{0.40}Zn_{0.09}(CO_3)_2$. However, both Mg, Mn, and Zn are not uniformly distributed within the carbonate and the rock, and as such, the possibility of originating from external sources should be considered. Without these elements in-

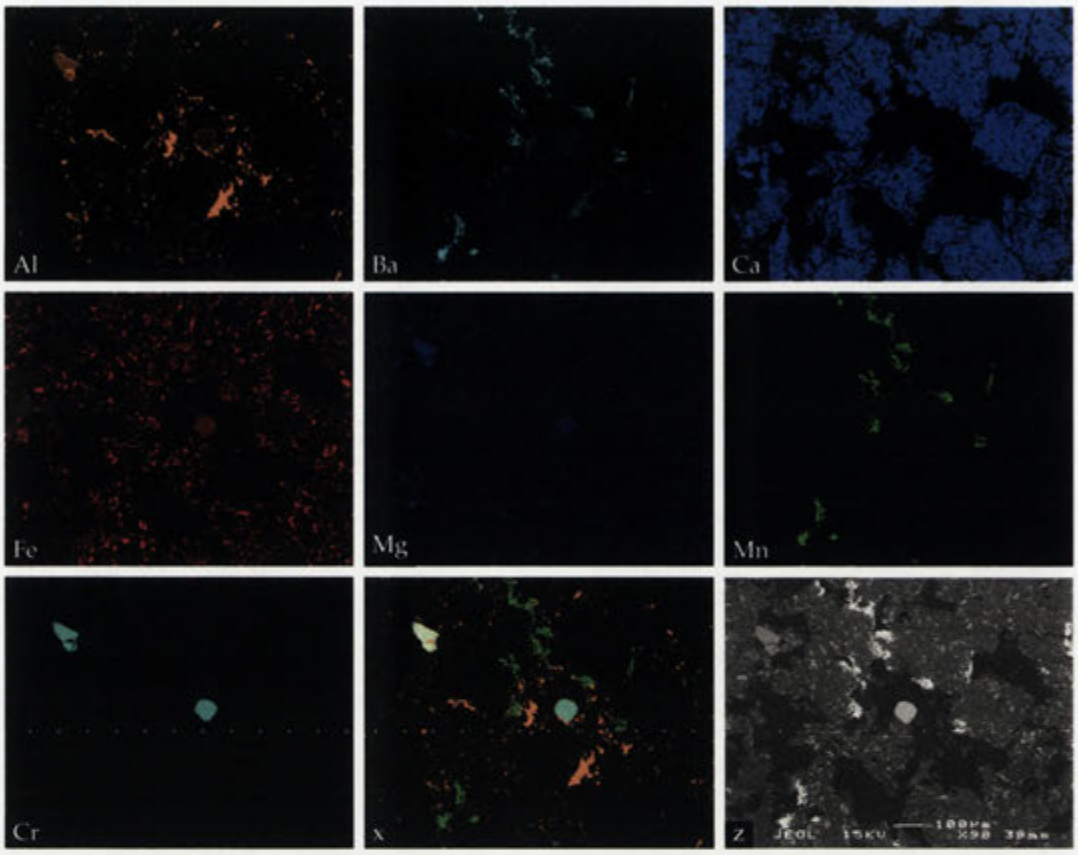

Figure 6.20: Elemental map from Dresser3 showing the distribution of Al, Ba, Ca, Fe, Mg, Mn, and Cr, of the area shown in z (BSE image). The Ba map is rescaled as to see the correlation with that of the Al map. A compilation of Al, Mn and Cr elemental maps, showing the widespread distribution of barian minerals (green for hollandite, orange for barian muscovite), and the presence of chromite, can be seen in x. (Map of K and Si not shown).

cluded in the analyses, a compositional range of $Ca_{1.46-1.67}Fe_{0.33-0.54}(CO_3)_2$ is obtained. The triangular area, limited by the black arrows, in Figure 6.15 defines the plausible compositions of the original carbonate. Fe oxidation would reduce the iron content in the carbonates, while dolomitisation would increase the Mg content, as depicted by the black arrows in Figure 6.15. Different geochemical scenarios that could account for the mineral species present, are further discussed in the following section.

6.4.3.6 Possible sediment history

Judging from the known geological interpretation of the North Pole and the mineral species present, one can hypothesise on the geological history of this rock. The cyclic sedimentation of the Dresser rock seem to be caused by seasonal variations in seawater composition, as described in Section 6.4.1. As has been discussed in Chapter 2,

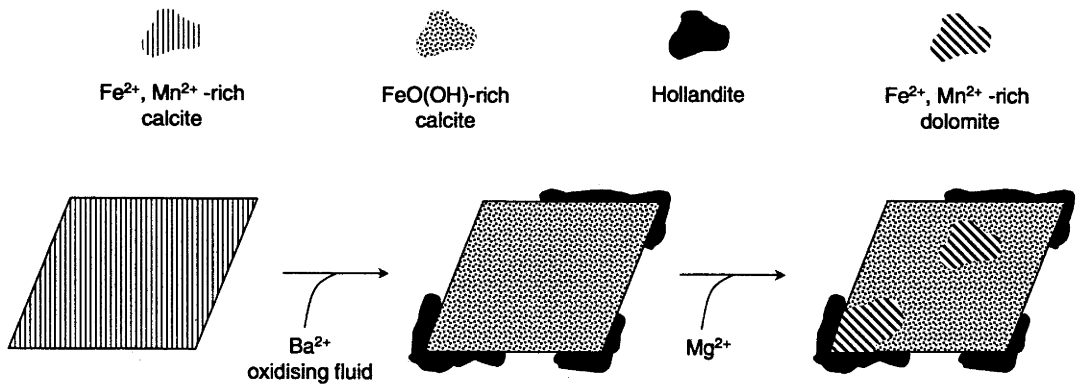

Figure 6.21: Schematic representation of a possible geological scenario for the presence of oxidised carbonates within the Dresser rock.

carbonate and silica chemistry is governed by a range of variables such as saturation state, pH, temperature and salinity. If the cyclic precipitation model of the layered rock is true, the calcite saturation went through episodes of possibly quite high supersaturation to levels where precipitation slowed and was overtaken by silica precipitation. One can envision a scenario where a concentrated silica sol possibly formed a sludge or gel on the bottom on the shallow ocean floor. A change in pH, carbonate alkalinity or temperature induced precipitation of the carbonate, which initially was very high, producing a very sharp boundary between the silica and carbonate phase. Gradual decrease in carbonate saturation state reduced the degree of carbonate precipitation, which was coupled with a continuum of silica deposition. Influx of Ca, Mg, and Fe, would then in turn start a new cycle of carbonate precipitation, which could have been facilitated by evaporation of the shallow water. As the characteristic layers have of the carbonate and chert phases of varying dimensions, each layer had individual precipitation time scales and/or saturation gradients. As the mineralogy is more or less identical, the geochemical conditions were almost constant throughout each cycle.

In Figure 6.21 a geochemical scenario for the evolution of oxide containing carbonates is depicted. In this scenario, the original carbonate has precipitated as a Fe^{2+},Mn^{2+}-rich calcite that during subsequent oxidation produced hollandite-type oxides on the surface of the carbonate rhombs, and precipitated iron oxides inside the rhombs, i.e. goethite. The remnant carbonate consisted of relatively pure calcite. A later dolomitisation process accounts for the patchy occurrence of dolomite within the rhombs.

The composition of the dolomites are outside the experimentally derived limits for dolomite and calcite solid solution (see Figure 2.7). However, similar carbonate compositions have been reported for subgreenschist metamorphic conditions (~250 ° in the

literature (see Anovitz and Essene (1987)). The composition and the patchy occurrence of dolomite in the Dresser rock suggests a hydrothermal replacement scenario.

The barian muscovites are likely to have formed by the same influx of Ba^{2+}-rich hydrothermal fluids causing the precipitation of hollandite. A similar scenario has been proposed for the barian-chromian muscovites found in Isua and Malene supracrustal rocks in West Greenland (Dymek et al., 1983). However, a metamorphic origin was also considered for the Greenland samples. The breakdown of barite at high metamorphic temperatures could supply the Ba, and chromite could have been a source for Cr. A scenario where both barite and chromite were present in chert, which produced the Ba-rich micas during metamorphism is consistent with some of their data (Dymek et al., 1983). Given the known hydrothermal circulation that occurred at the North Pole, hydrothermal remobilisation of the Ba and Cr is most likely.

6.5 Discussion

This chapter has shown that biomorphs have morphological and chemical similarities with some of the most ancient microfossils found on Earth. In this section I discuss these topics as well as the likelihood of natural biomorph formation in the Pilbara region based on geochemical arguments.

Morphology

As discussed in Section 6.2, biomorphs can display morphologies adopted by living organisms. This morphological convergence is crucially important to identifying true bona fide microfossils, as criteria for such recognition largely is based on morphology. Complex morphologies, such as segmented and sinous structures, are often believed to be exclusive to the biological world, whereas spherical coccoidal structures are known to be easily mimicked by abiotic counterparts. For this reason, the following discussion will focus on worm-like segmented morphologies, however, the general arguments can also be applied to other morphologies.

What is needed to demonstrate segmentation? Worm-like biomorphs are not strictly segmented; a very important potential difference. However, they have the appearance of being segmented (Figure 6.22). Fossils are often interpreted as having segmented morphology, based largely on 2D optical images. However, this interpretation is equivocal. Grooves on the surface of biomorphs, caused by the twisted morphology, can be suggestive of such an attribute, even when this is not the case. Three-dimensional imaging techniques, such as Raman and CLSM, of supposed segmented structures do not show this attribute either (see Figure 5.6). If anything, Figure

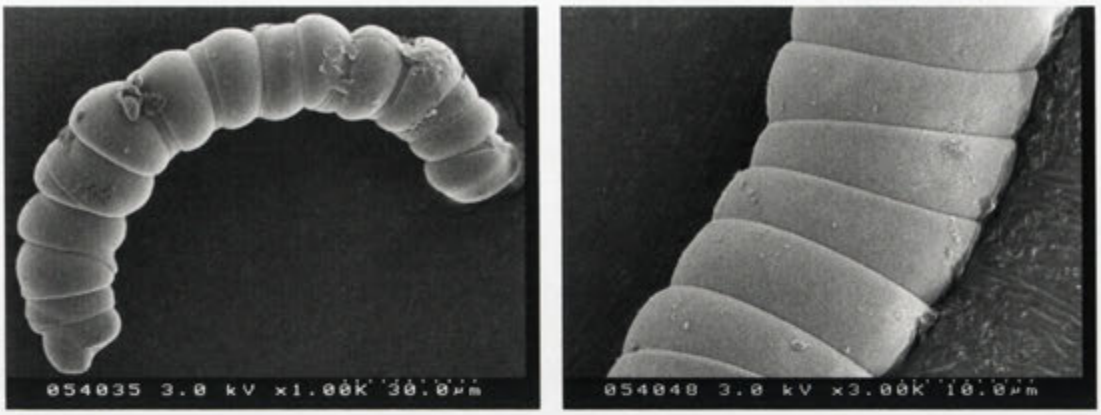

Figure 6.22: SEM images of pseudo-segmented biomorphs.

5.6 clearly demonstrates the *lack* of such segmentation, a point also noticed by Schopf et al. (2006). It was argued that the absence of walls, or evidence of partially preserved walls, that separates the individual cells is expected as these walls are much thinner and have a chemically different composition than the external walls. As such, these internal cell walls are much more likely to be detrimentally affected by degradation (Schopf et al., 2006). For the segmented nature of the microorganism to be retained during fossilisation depend on the fossilisation process as well as the thermal and geochemical history of the rock. It was further noticed that poorly preserved internal cell walls or the absence of such is a common feature of segmented microfossils (Schopf et al., 2006). It is then reasonable to pose the following questions; If segmentation and 'cellular elaboration' are crucial criteria for determining biogenicity, and the absence of internal cell walls is expected in most segmented microfossils of Archean age, then how are they identified as segmented, and therefore as biogenic? Is the supposed evidence of segmentation, as seen in Figures 6.1 D1, 5.6 and 5.9, enough to demonstrate a biogenicity claim?

According to Schopf (1999b);

> '..the evidence sought should be *positive* - evidence that affirms the biologic origin of the features detected. Evidence that is *neutral* (consistent either with biology or nonbiology) is by its nature inadequate to establish the existence of past life, and interpretations based on *negative* reasoning - inference by default, such as a claim that because a feature is not obviously mineralic it "must" be biogenic - are likely to prove erroneous.'

Similarly, Brasier et al. (2005) argues that;

> 'Ancient filamentous structures should not be accepted as of biological

> origin until all possibilities of their non-biological origin have been exhausted.'

Then, using both Schopf and Brasier's reasoning, the answers to the above questions are 'no'. It is therefore not sufficient to use indications of segmentation as demonstration of biogenicity. This becomes evident if one consider biomorphs as possible fossiliferous imitations. Worm-like biomorphs are not strictly segmented; a very important potential difference. However, their helical whorls give them the appearance of being segmented (Figure 6.22). These 'segmented' biomorphs therefore could be taken as pseudofossils of a range of microfossils with similar morphologies, including the North Pole, Apex chert, and the Bitter Springs specimens. This raises questions regarding biogenicity claims of purportedly septate filamentous microfossils. Evidently, all reportedly segmented microfossils, from both Archean and Early Precambrian, should be subjected to 3D analysis using confocal laser scanning microscopy or similar to show this feature. If they prove to lack evidence of segmentation, then, using the arguments stated above, biomorphs need to be invalidated as pseudofossils, and not the reverse, to be able to *suggest* biogenicity.

Thus, the 'standard' critieria for fossil recognition require amendment. How many fulfilled *indicative* criteria are needed to *indicate* biogenicity satisfactorily? At best, such fossil specimens will only point to a biological origin, and can as has been described in this section be mimicked by abtiotic processes. While the established criteria appear to have served well in the past, biomorphs cause problems, and further refinements are needed. The use of 3D analysis of chemical makeup and morphology allows us to re-examine the building blocks of what can be understood as a fossil, and what is not. Such techniques will become standard tools within the palaeontology community, allowing us to better idenitfy segmentation.

However, as biomorphs growth is a physiochemical phenomenon and their occurrence is restricted to a specific chemical environment, it may be possible to exclude them as microfossil artefacts. Morphological preservation at all levels is a key to distinguish biomorphs from microfossils. Instead of publishing images of only the perfectly preserved microfossil specimens, it would be very informative to look at the broken, torn, and disfigured examples. Biomorphs are somewhat brittle in nature, they will easily break off or crack. Soft matter, such as living organisms, can during fossilisation tear and therefore possibly give evidence of their flexible nature if such a feature is preserved. It should, however, be noted that the silica skin that encompass worm-like biomorphs, can show similar behaviour, but perhaps not to the same extent as a ductile cell wall. Furthermore, the criterion 'cellular elaboration' is very much case-to-case specific, as it depends critically on the kind of microbe and state of preservation, and therefore the morphological variety seen in biomorphs could be very different. Again,

a case-to-case comparison is therefore needed.

Chemistry

Biomorphs are not only morphologically similar to Pilbara microfossils, but also chemically. As shown in Chapter 1 and 3, some biomorphs retain the overall morphology by acid dissolution of the carbonate entity, leaving a hollow silica skin. ± in Table 6.5 regarding the criterion on hollow microfossils can therefore be fulfilled through such a treatment. A natural scenario for producing hollow biomorphs can be envisioned by acidic water percolating through the sediment. Hollow relics of carbonate rhombs present in Archean sediments show that such dissolution can occur in the relevant geological setting (Van Kranendonk, 2006). Importantly, such decarbonation reactions can take place after the sediment solidifies, transforming biomorphs trapped in the sediment into hollow silica casts. Alternatively, if the barium carbonate was dissolved before the sediment solidified, then the hollow silica biomorph skin could be filled with other precipitating minerals comparable to permineralised microorganisms. A wide range of mineralogical compositions could therefore be expected.

The adsorption experiments with phenol/formaldehyde mixtures (Section 6.3) clearly shows the ability of biomorphic aggregates to adsorb hydrophobic carbonaceous species. Moreover the curing of such aggregates at elevated temperatures results in black carbonaceous biomorphs retaining the original morphology. The source for the organics could be abiotic or biotic, as long as they were readily available during the Archean. If life were widespread (Schopf, 2004), biologically produced hydrocarbons could have been available. Such an assumption is however unnecessary. Abiotic hydrocarbons, produced by either siderite decomposition, serpentinization or Fischer-Tropsch processes, could also have been present in significant amounts (see Section 5.3.1.2). Given the recent abiotic interpretation of the widespread carbonaceous black cherts in the Pilbara (Lindsay et al., 2005), an environment rich in organic matter is readily conceivable. Furthermore, such abiotic organics have shown to have isotopic signatures overlapping with biotic carbons. As such, abiotic routes of the formation of biomorphs with carbonaceous shell, which could have $\delta^{13}C$ of ~ -50 to -20‰, is therefore demonstrated to be plausible for the Archean.

Geochemical scenarios

Although no known geological occurrence of biomorphs have been reported in the literature to date, the geochemical conditions for biomorph synthesis are reasonable for the Archaean, suggesting that these complex carbonaceous structures could have been produced naturally on the primitive Earth (García-Ruiz, 1998, 2000; García-Ruiz

et al., 2003). For instance, in the North Pole area, Western Australia, carbonate, silica, and barium are present in the fossiliferous chert-barite unit described in Section 6.4 giving the chemical requirements for biomorph synthesis, provided that pH and temperature were appropriate. As was described in Section 6.4.1, the North Pole area was sulfate-poor, at least periodically and locally, which would allow an increase in Ba concentration in the aqueous environment and the formation of Ba minerals other than barite. This is apparent from the mineralogical analysis presented in Section 6.4.3, as Ba is present in both muscovite and hollandite. Furthermore, the geochemical scenarios discussed regarding the sedimentation indicates a cyclic, possibly self-catalytic precipitation regime. Alternating silica and carbonate precipitation could have formed due changes in calcite saturation state with respect to silica. A possible environment could have been a shallow hydrothermal lake, with periodic updwellings, or influx, of alkaline waters. Sulfate-poor environments would restrict Ba saturation to that of carbonate as discussed in Section 5.2.1.2.

Once the structures have formed, creation of the carbonaceous shell can also be explained (García-Ruiz et al., 2003), as was experimentally demonstrated in Section 6.3. The hydrocarbons needed are small and chemically simple, and would have been readily available on the primitive Earth, irrespective of the presence of life. This is demonstrated by the recent discovery that similar organic materials can be produced by decomposing iron-carbonate at elevated temperatures (less than 350°C) in the presence of water (McCollom, 2003). This type of reaction has been suggested as a mechanism for forming isotopically light hydrocarbons (van Zuilen et al., 2002). Iron-rich carbonates are present in the North Pole area, and given the known hydrothermal origin of some of the 'microfossil'-bearing rocks, it is possible that such hydrocarbons could have been abiotically produced. Subsequent adsorption and condensation to form ^{12}C-enriched kerogen-like materials over time is equally plausible (García-Ruiz et al., 2003). The synthetic high temperature curing of the biomorphs is consistent with natural geologocal processes. Considering that the kinetics of kerogen maturation is a first order process with activation energies varying between 150 and 200 kJ/mol (Wood, 1988; Hunt et al., 1991), and assumes equal kinetics for the synthetic and natural maturation process, the Arrhenius equation ($k = Ae^{-E_a/RT}$) then implies that an average temperature of around 70 to 130°C would be sufficient to produce kerogen on a 3-billion year time scale. This range is consistent with recent geological investigations that deduce a maximum temperature of around 250 to 350°C. Hence, the synthetic production of kerogenous biomorphs is compatible with available geological data as well as kinetic calculations. Abiotic carbonaceous biomorphs, once formed, would readily be incorporated into rocks, not just those filling hydrothermal veins but also sediments downstream of the points where those veins emerged at the paleosurface as

hot springs. As such, they would also fulfil the criteria for establishing the antiquity of a microfossil, since they would be proven to be indigenous and syngenetic with the sediment and not of any later type of contamination.

How likely is this scenario from a geochemical point of view? It is true that the synthesis of carbonaceous biomorphs require quite specific conditions, but conditions that are not implausible. Although the growth of a specific morphology, such as microfossil-like 'segmented' biomorphs, requires specific conditions, the cyclic layering of the Dresser rock, interpreted as being caused by pH variations, could allow regular passage through such conditions.

At this time, no biomorphs have been identified in this rock.

Conclusion

These mineralogical studies confirm that the geochemistry of 'fossil'-bearing Archean rocks is consistent with the chemical requirements to form biomorphs. Hence, biomorphs should be considered as a possibility when attempting to identify primitive microfossils. As discussed in this chapter, the morphologies of biomorphs are very similar to those of some of the most ancient presumed microfossils. The criteria used to establish age and biogenicity are summarised in Table 6.5. As can be seen in this table, biomorphs can fulfil all these criteria. The criteria relating to the antiquity of microfossils are not fulfilled by biomorphs produced in the laboratory, but would be if they had been produced in nature. During sedimentation, biomorphs would be entombed in a similar fashion as microorganisms and would therefore be 'fossilised' within the sediment. Biomorphs would also fulfil the criteria for biogenicity marked with '$\star$'. Since naturally produced biomorphs would be embedded in the sedimentary rock, they would be found in petrographic thin-sections. Furthermore, they would also be larger than the smallest living organism, occur with others of similar morphology, and show 'cellular elaboration', such as segmentation.

As it has been noted that some microfossils are hollow (see Section 5.3.2.1), this criterion is also stated in Table 6.5. Hollow biomorphs can be produced by secondary treatments, and is thereby labelled $\pm$ in Table 6.5. The last criterion itemised in Table 6.5, regarding kerogen, is also labelled with a $\pm$, indicating that it can be fulfilled through secondary reactions. As discussed in Section 5.3.1.5, several abiotic hydrocarbon producing reactions are believed to have been operating in the Archean (and still are today). It is not difficult to envision a scenario in which biomorphs could be made kerogenous through adsorption and condensation of prebiotic organic molecules. Biomorphs can therefore also fulfil this criterion. The comment:

> 'Nine and a half out of 10 paleontologists would say that's a microfossil.'

Proven status	Criteria	Biomorphs
Antiquity	Rocks of proven Archean age	⋆
	Embedded in the rock matrix	⋆
	Syngenetic with deposition	⋆
Biogenicity	Show morphological resemblance to modern organisms; cellular elaboration	√
	Occur in a sedimentary rock	⋆
	Be larger than the smallest extant living organism	√
	Display well defined size distribution	√
	Occur with others of similar morphology	√
	Show cellular elaboration	√
	Be hollow	±
	The structure should be composed of kerogen	±

Table 6.5: The criteria used to establish antiquity and biogenicity of microfossils compared to biomorphs. ⋆ indicates that this criterion is not fulfilled by biomorphs produced in the lab. However, naturally produced biomorphs in sediments would fulfill these criteria. √ signifies that biomorphs, naturally or artificially produced, fulfil the criterion. The ± indicates that these criteria can be fulfilled through secondary reactions (see text).

stated by Prof. John Grotzinger (Kerr, 2003) regarding the carbonaceous biomorph seen in Figure 6.4 emphasises the severe ambiguities they can cause in identification of early life.

Chapter 7

Conclusions and Future Work

As witnessed in this dissertation, silica-carbonate biomorphs display amazing morphologies. These biomorphs are very different from classic crystallographic morphologies as they exhibit intricately curved and helical morphologies; characteristics that are are normally considered exclusive to the biological world. The hierarchical nature and the co-existence of amorphous and ordered nanocrystals in these composite materials are also features commonly observed in biominerals. As such, biomorph synthesis is an appropriate model for studying biomimetic self-assembly.

Their very life-like morphology has further been shown to pose implications for the identification of ancient microfossil evidence of early life. The search for ancient life has relied on a growing series of criteria and biosignatures, from the nuclear isotopic and molecular levels, to matching morphological characteristics. These criteria are employed to assess the biological origin of structures believed to be microfossils. As shown in this thesis, ancient Archaean signatures can be simulated by abiotic biomorphic materials. The adsorption and condensation of simple organics on worm-like biomorphs produces Raman signatures very similar to that of ancient microfossils. As such, biomorphs can resemble, to a remarkable degree, both chemically and morphologically, some of the allegedly oldest fossilised microorganisms on Earth. Furthermore, this dissertation shows that the early Archean environment may have been congenial for biomorph formation in nature. A mineralogical analysis of one Archean chert-carbonate rock showed barium and silica to be present in considerable concentrations. Although no biomorphic structures were detected in this rock, the presence of carbonate, silica and barium indicated that the chemical requirements for biomorph formation are fulfilled. Hence, these abiotic structures should therefore be considered when identifying ancient microfossil-like structures. Conversely, the identification of biomorphs may equally be confused by their similarities to microfossils. Propensities and probabilities, not certainties, are the best one can hope for in distinguishing the biotic from the abiotic. As biomorph morphology is a result of the environmental conditions during growth, the geological setting can provide clues to aid such dis-

tinction. The discovery of a biomorphic form in a geological setting, consistent with biomorph formation, may then be more convincingly judged to be an example of a complex abiotic structure, rather than an example of early life. Maps of biomorph morphology with respect to known reaction conditions are therefore important tools when establishing the origin of complex microstructures entombed in ancient rocks. A characteristic of biomorphs is their hierarchical structure at different length scales. This is a crucial feature of biomaterials in vivo, and biomorphs offer a useful model for complex multi-scale materials, of much interest to modern materials science. On the nano-scale, they consist of elongated silica coated carbonate crystallites exhibiting orientational order. Although this ordering varies between morphologies, in most cases the witherite *c*-axis is aligned parallel to the growth direction of the aggregate. The exception are the bands, synthesised at high temperature, in which the crystallites are almost perfectly oriented with the *c*-axis perpendicular to the growth direction. Furthermore, TEM analyses have further shown the presence of three twin orientations for the a- and b-axes around the c-axis. Other morphologies observed at high temperature show less ordered behaviour.

In the worm-like aggregates a progressive twist is seen between crystallites. Twisted morphologies are in some cases surrounded by a nm-thick silica skin, which is retained as a hollow cast after dissolution of the carbonate entity. The composition of worm-like and double helices span a wide range of Si/Ba ratios, from 0.03 up to 0.40. Such ratios may either decrease or stay constant along the growth direction of a given worm. Again, no correlation between morphology and composition is obvious.

By changing the intitial synthesis conditions (pH, concentration of the reacting molecular species, and temperature) different morphologies are observed in biomorphs. This suggests that the formation of these complex morphologies is coupled to both crystallographic and reaction-diffusion relationships. In the absence of silicate, biomorphs do not grow, but instead produces classical larger euhedral crystallites. Silica effectively poisons the growth of witherite, which results in nano-sized crystals encapsulated in silica. Epitaxial relationships between the carbonate crystallites results in partial orientational ordering among the crystals. Hypotheses regarding a formation mechanism were proposed in Chapter 4. It was suggested that the relation between the diffusion of reactants and their supersaturation at the boundary may be important for the development of specific morphologies.

From experimental observations, it is noted that slowly growing aggregates tend to produce globular morphologies, whereas increasingly sheet- and tentacle-like morphologies are observed under fast growing conditions. As such, it was speculated in Chapter 4 that growth rates may influence the morphology produced. The growth of worm-like biomorphs was shown to be characterised by $1/r^2$ dependence on dl/dt, cou-

pled to a roughly constant dV/dt. The growth of floral spherullites, are characterised by either a constant or decreasing dr/dt with respect the radius of the aggregate. These results were further interpreted, based on a model described in section 4.4.2, as potential evidence for diffusion-limited growth. However, the growth of floral spherulites also seem to have a growth rate that is dependent on reaction limited growth during the early stages of development. However, many more analyses of growth rates with respect to morphology are needed to be able to elucidate the importance of such effects on the development of specific morphologies. A severely depleted boundary layer may be responsible for branching and proliferation of the initial dumbbell-like aggregate, akin to branching in usual DLA models.

At present, however, it is not possible to deduce a uniform complete mechanism of formation for the all the different morphologies observed in relation to reaction conditions. Further experimental evidence is needed to show what influence the diffusion has on morphological evolution.

In this dissertation, several synthesis parameters, such as temperature, pH, concentration of reacting species and the presence of additives, have been explored in relation to biomorph morphogenesis. All of these parameters are evidently important to what specific morphologies are produced, and can be summarised as follows:

pH has been shown to control nucleation density, and determines the morphological variety. At low pH globular morphologies are produced, whereas at high pH, produces more varied morphologies with increasingly sheet-like shape. No definite trend in composition with respect to pH and morphology has been seen, suggesting that morphology is not an effect of compositional variation (see Section 3.4.2).

As shown in Section 3.4.3, the *sodium silicate concentration* also affects the morphologies produced. A decrease in concentration results in an increase in nucleation density and smaller aggregates with increasingly varied morphologies. For instance, sheet- and pinnacle-like morphologies, and the absence of helical aggregates, are evident under low sodium silicate concentrations.

Barium chloride concentration also controls the nucleation density and the morphology produced (see Section 3.4.4). Higher concentrations result in an increase in the number of growing aggregates, which develop, at 500 mM barium chloride concentration, floral spherulite-like aggregates. More initial precipitation of presumably amorphous barium silicates is also evident at higher concentrations. This precipitate has further been shown to be important to the development of floral spherulites, which suggests that this phase may serve as point of nucleation and source of reactants during growth. Reducing the barium concentration results in increasingly globular morphologies at constant pH.

In section 3.4.5 *temperature* was shown to assert a strong morphological effect

on the biomorphs produced. Increasing temperature results in faster growth rates that produces increasingly sheet-like and branching aggregates compared to lower temperatures. The morphological evolution observed with increasing temperature is as follows; globular (low T); helical- and worm-like aggregates (RT); sheets, bands and corals (70 ° C). Helical aggregates are not present at 70° C within the 3 h time-frame analysed. These morphologies are most prominent at 45° C and RT experiments.

Presence of *additives*, such as CTAB, lanthanum, and ytterbium salts, have also been shown to effectively alter the growth of specific morphologies at mM concentrations. In the case of the lanthanides, increasing concentration results in increasingly helical morphologies, and at the highest concentration used, 1.0 mM, concentric sheets are the dominant morphology. Using CTAB as an additive produces aggregates with morphologies similar to that of floral spherulites and corals, which are only synthesised at high barium concentrations and high temperature respectively without additives. Addition of sodium chloride to the reaction mixture induces very different morphological changes compared to CTAB and the lanthanides. Globular aggregates with occasional worm-like growth are seen at 50 mM NaCl concentration. At concentrations above 500 mM, biomorph growth is completely inhibited.

Suggestions for future work, which can fill the gaps in our knowledge of the relationships between morphology and growth conditions, are presented in the following section.

7.0.1 Future work

Many questions remain unanswered regarding both the composition, crystallographic ordering, and their relation to biomorph genesis. This dissertation has provided a small insight into the world of biomorphs and ends with a call for future research that can enhance our understanding not only of how to identify ancient life, but of the relationship between nature's abiotic building blocks - silica and alkaline earth carbonates. It is beyond the scope of this work to systematically and comprehensively investigate and deduce how specific *combinations* of environmental variables assist in the creation of different morphologies. Additional steps into the world of biomorphs must necessarily move on from mapping out their broader scientific terrain, as conducted here.

Any future biomorph experiments should be conducted using a source of silicate other than concentrated sodium silicate solutions. For instance, investigations into biomorph growth using TEOS have commenced and appear promising in examining other silicates that replicate biomorph morphologies similar to those studied in this dissertation. The key advantage of using TEOS is that it provides a constant compo-

sitional foundation from which experiments for biomorph growth can be replicated by a number of researchers. TEOS therefore enhances the capacity to dramatically expand analyses of compositional structures far beyond the few structures studied within these pages. Many more morphologies need to be evaluated to see if composition variation is a key determinant of morphology. A number of experiments come to mind that may shed light on how the combination of environmental variables direct biomorphs' characteristics. Of immediate interest are experimental designs that shed light on the solution composition with respect to both different reaction conditions and how the the concentration of reactants changes with time. Such investigations can be undertaken using ICP-MS, which will have to be conducted under strongly acidic conditions so as to reduce the possibility of adsorption to the tubes. From such experiments one cannot measure the carbonate concentration, but such testing would provide information on the silicate and barium concentrations. One can also envisage experiments in which the solutions have been centrifuged for a specific time, so as to remove the amorphous silica particles. ICP-MS measurements with and without such treatments should give indications of the concentrations of the elemental constituents in solution.

Further studies should be conducted in experiments that have different initial conditions, such as those outlined in this thesis, but also with respect to silica and alkaline earth metal concentrations in solution. Of particular interest are biomorph precipitation of calcium and strontium carbonate, as they have different solubilities with respect to barium carbonate. Morphological and compositional characterisations of such experiments would promise to tell us more about how different morphologies evolve with respect to carbonate solubility and their interaction with silicate.

Beyond suggestions for further experiments, it should also be recognised that techniques rather than those concentrated upon in this dissertation may be exploited to good effect. Further light scattering and cryo-TEM analyses of the solutions, coupled with elemental analysis should be able to detect the early carbonate crystallites, to determine if they precipitate in solution and not at the biomorph interface, as well as their interaction with silicate. To investigate the specific interaction of silicate with witherite faces, one could, for instance, set up an AFM experiment, in which one could observe and image silicate adsorption on different faces. Continued EM work on both thin sectioned and as-prepared biomorphs will give more information about crystal size differences, composition and morphological variations within and between aggregates. Especially interesting is the possibility of producing calcium carbonate biomorphs, as such structures are more directly related to biomineralisation and natural processes within silica and calcium rich environments.

Appendix A

Aqueous carbonate system

This appendix provides further information on carbonate systems used in Section 2.2.4.1. For a more comprehensive explanation see Zeebe and Wolf-Gladrow (2001), Millero (2001), and Stumm and Morgan (1996).

Activity coefficient

The activity coefficient can be approximated using the extended Debye-Hückel limiting law for I < 0.1 M (see Equation A.1 and the Davies equation for I < 0.5 (see Equation A.2):

$$\log \gamma_f = -Az^2 \left(\frac{\sqrt{I}}{1 + Ba\sqrt{I}} \right) \tag{A.1}$$

$$\log \gamma_f = -Az^2 \left(\frac{\sqrt{I}}{1 + \sqrt{I}} - 0.2I \right) \tag{A.2}$$

where $A = 1.82 \cdot 10^6 (\epsilon T)^{-\frac{3}{2}}$, ϵ is the dielectric constant for water and is ~79, $B = 50.3 \cdot (\epsilon T)^{-\frac{1}{2}} \sim 0.33$ in water at 25 ° C, a is an adjustable parameter related to the size of the ion, and T is in Kelvin (Zeebe and Wolf-Gladrow, 2001; Stumm and Morgan, 1996). At higher ionic strengths, these equations are not valid. There are models for calculating activity coefficients under these conditions, but they will not be reviewed here (see (Pitzer, 1973; Millero and Pierrot, 1998)).

Henry's Law

Henry's constant dependency on temperature and salinity can be expressed as (Zeebe and Wolf-Gladrow, 2001):

$$\ln K_0 = \frac{9345.17}{T} - 60.2409 + 23.3585 \cdot \ln\left(\frac{T}{100}\right) \tag{A.3}$$

$$+S\left[0.023517 - 0.00023656 \cdot T + 0.0047036 \cdot \left(\frac{T}{100}\right)^2\right]$$

Alkalinity and total dissolved inorganic carbon

Other important quantities for carbonate systems are the total alkalinity (TA), the carbonate alkalinity (CA), the total dissolved inorganic carbon (C_T), and ionic strength (I) which are defined as:

$$TA = [HCO_3^-] + 2[CO_3^{2-}] + [B(OH)_4^-] + [OH^-] - [H^+] + \text{other} \quad (A.4)$$

$$CA = [HCO_3^-] + 2[CO_3^{2-}] \quad (A.5)$$

$$C_T = [CO_2] + [HCO_3^-] + [CO_3^{2-}] \quad (A.6)$$

$$I = \frac{1}{2}\sum c_i \cdot z_i^2 \quad (A.7)$$

The total alkalinity also includes other components able to accept protons, such as $SiO(OH)_3^-$, HPO_4^{2-}, PO_4^{3-} as well as organics. In Equation A.7, for the ionic strength of a solution, c_i is the concentration and z_i is the charge of the ith ion. Normal surface waters that are in equilibrium with the atmospheric CO_2 (p_{CO_2}=365 μ atm) has a salinity (S) of 35, T = 25°C, pH of 8.1 and C_T = 2.1 mmol/kg. For this natural system, with pK_1^*=5.86 and pK_2^*=8.92, the concentrations of the individual carbonate species are $[CO_2]$= 10.4 μmol/kg, $[HCO_3^-]$=1818 μmol/kg, and $[CO_3^{2-}]$=272 μmol/kg, or the relation between the species is $[CO_2]$: $[HCO_3^-]$: $[CO_3^{2-}]$ is approximately 1:174.8:26.2. That is to say that most of the dissolved carbonate is in the form of bicarbonate ions and only very small amounts of dissolved carbon dioxide is present (Zeebe and Wolf-Gladrow, 2001).

A.1 Aqueous carbonate equilibrium models

There are two very useful models to show the characteristics of aqueous carbonate systems; the closed and the open systems. In the closed system, the total carbonate concentration is constant. In the open system on the other hand, carbon dioxide is exchanged between the solution and the atmosphere at constant p_{CO_2}. The distribution of the carbonate species in such systems can be seen in Figure 2.8, and this section describes the equations used to construct these graphs.

A.1.1 Closed system

The total dissolved carbonate concentration is kept constant at C_T=2.1 mM. Then it follows from Equations 2.5, 2.6, and A.6 that:

$$[CO_2] = \frac{C_t}{1 + \frac{K_1^*}{[H^+]} + \frac{K_1^* \cdot K_2^*}{[H^+]^2}} \tag{A.8}$$

$$[HCO_3^-] = \frac{C_t}{1 + \frac{[H^+]}{K_1^*} + \frac{K_2^*}{[H^+]}} \tag{A.9}$$

$$[CO_3^{2-}] = \frac{C_t}{1 + \frac{[H^+]}{K_2^*} + \frac{[H^+]^2}{K_1^* \cdot K_2^*}} \tag{A.10}$$

By plotting the logarithmic values of of the carbonate concentrations at different pH, using $K_1^* = 10^{-6.35}$ and $K_1^* = 10^{-10.33}$ as is the case for pure water, the graph in Figure 2.8 A is obtained.

A.1.2 Open system

In the open system, the aqueous solution is allowed to equilibrate with the atmospheric carbon dioxide (p_{CO_2}=365 μ atm). It follows from Henry's law and Equations 2.5 and 2.6 that:

$$\begin{aligned} \log[CO_2] &= \log K_0 + \log p_{CO_2} \\ &= -1.47 + (-3.44) \\ &= -4.91 \end{aligned} \tag{A.11}$$

$$\begin{aligned} \log[HCO_3^-] &= \log K_1^* + pH + \log[CO_2] \\ &= -6.35 + pH + (-4.91) \\ &= -11.26 + pH \end{aligned} \tag{A.12}$$

$$\begin{aligned} \log[CO_3^{2-}] &= \log K_2^* + pH + \log[HCO_3^-] \\ &= -10.33 + pH + (-11.26 + pH) \\ &= -21.59 + 2 \cdot pH \end{aligned} \tag{A.13}$$

T (°C)	Calcite	Aragonite	Witherite	Strontianite
4	8.391	8.231	8.689	9.306
25	8.480	8.336	8.562	9.271
50	8.663	8.536	8.612	9.371
70	8.868	8.752	8.748	9.541

Table A.1: Values of the thermodynamic solubility product as pK_{sp} for various carbonates at different temperatures. The data was calculated using the equations stated in Plummer and Busenberg (1982), Busenberg and Plummer (1986) and Busenberg et al. (1984). See also Figure ??.

Plotting the logarithmic values of the individual carbonate species concentration, the graph in Figure 2.8 B is obtained.

A.2 Dissolution and precipitation of carbonates

The graph displaying temperature dependance of the solubility constants were made using the following equations: Busenberg and Plummer (1986) made 150 measurements between 0 and 91°C at a total pressure of 1 atm, and they reported that the thermodynamic solubility constant can be calculated as follows:

$$\log K_c = -171.9065 - 0.077993 \cdot T + \frac{2839.319}{T} + 71.595 \cdot \log T \quad \text{(A.14)}$$

$$\log K_a = -171.9773 - 0.077993 \cdot T + \frac{2903.293}{T} + 71.595 \cdot \log T \quad \text{(A.15)}$$

$$\log K_v = -172.1295 - 0.077993 \cdot T + \frac{3074.688}{T} + 71.595 \cdot \log T \quad \text{(A.16)}$$

$$\log K_w = 607.6420 + 0.121098T - \frac{20011.25}{T} - 236.4948 \cdot \log T \quad \text{(A.17)}$$

$$\log K_s = 155.0305 - \frac{7239.594}{T} - 56.58638 \cdot \log T \quad \text{(A.18)}$$

where T is in Kelvin.

Appendix B

Aqueous silica system

The following equations were used to plot the temperature dependence of the solubility of quartz, α-cristobalite, β-cristobalite, and amorphous silica in Chapter 2:

Quartz	$\log K = 1.881 - 2.028 \cdot 10^{-3}T - 1560/T$
α-cristobalite	$\log K = -0.0321 - 988.2/T$
β-cristobalite	$\log K = -0.2560 - 793.6/T$
Amorphous silica	$\log K = 0.3380 - 7.889 \cdot 10^{-4}T - 840.1/T$

where T is in Kelvin (Rimstidt and Barnes, 1980).

Cation radii, and hydroxide solubility

Cation	r_{cryst} (Å)	r_{hyd}(Å)	Hydroxide	$\log K_{sp}$
Mg^{2+}	0.65	3.47	$Mg(OH)_2$	-11.25
Ca^{2+}	0.99	3.10	$Ca(OH)_2$	-5.30
Sr^{2+}	1.13	3.10	$Sr(OH)_2 \cdot 8(H_2O)$	-3.68
Ba^{2+}	1.35	2.90	$Ba(OH)_2 \cdot 8(H_2O)$	-3.59

Table B.1: The crystallographic and hydrated radii of the alkaline earth cations, and the solubility product of the corresponding hydroxides.

Appendix C

Biomorph synthesis

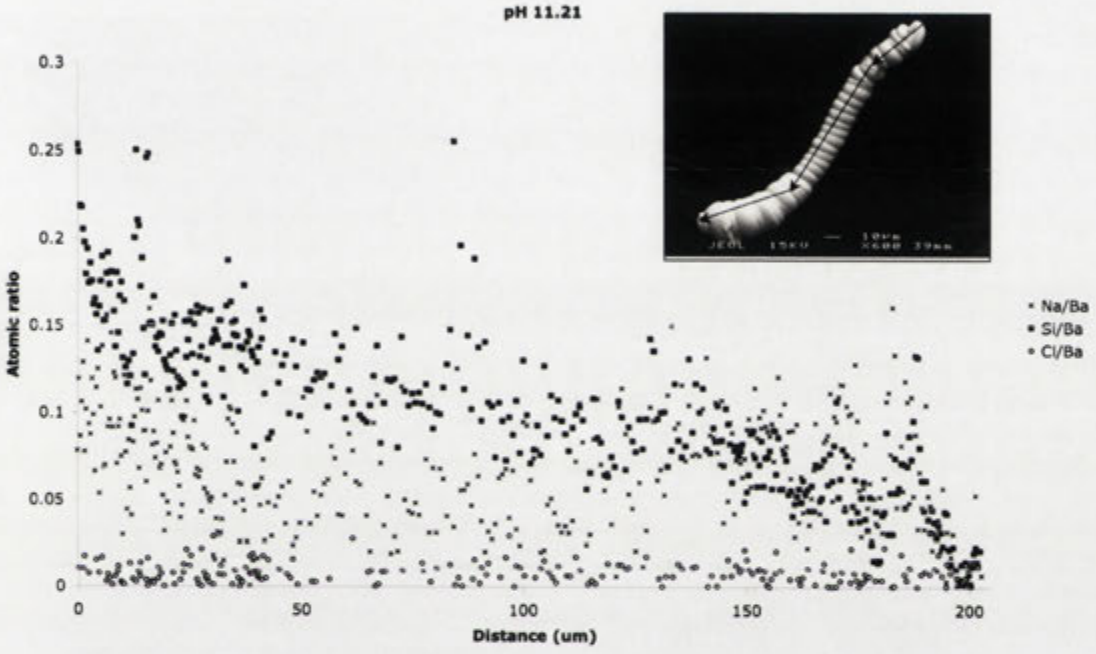

Figure C.1: Back-scattered SEM image and a graph showing the Si/Ba ratio variation with length of a worm synthesised at pH 11.21.

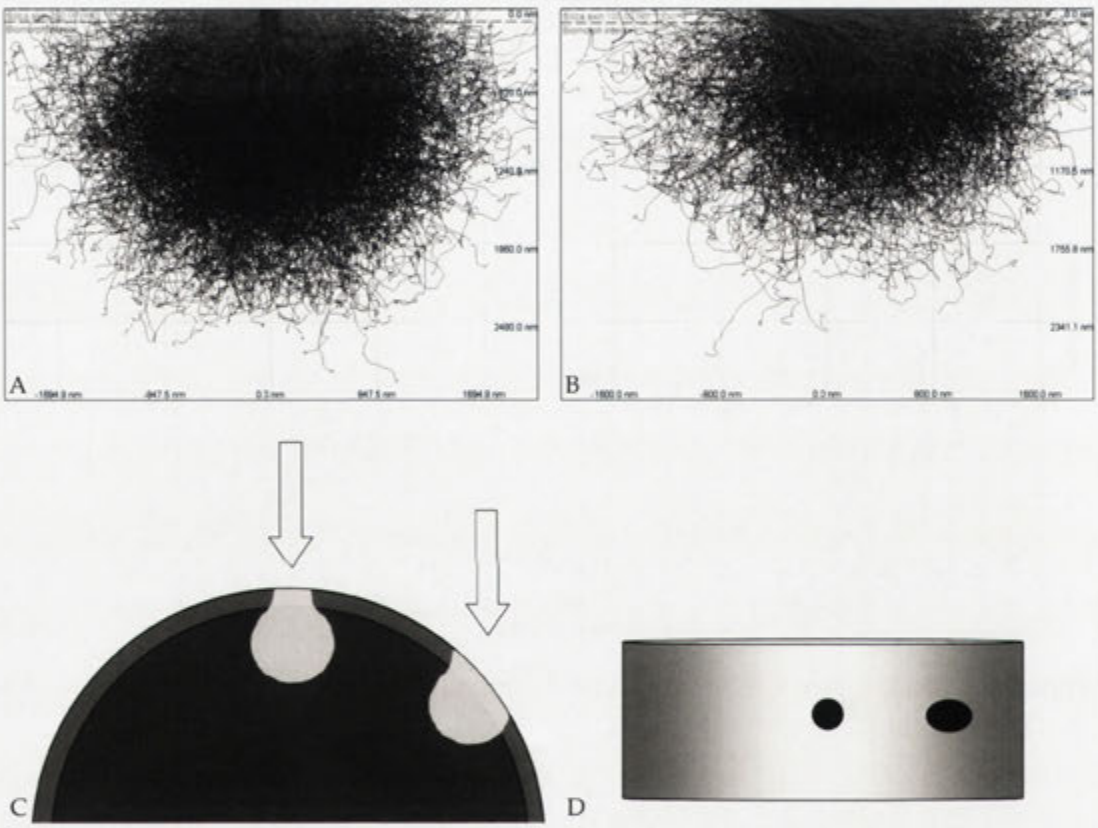

Figure C.2: CASINO simulations (A, B) of the electron beam interaction volume in a biomorph having a 100 nm silica skin (SiO_2), and an internal composition of $Ba_{100}C_{100}O_{300}Si_{15}O_{30}$. These images are simulations of 3000 trajectories at 0 (A) and 80 ° (B) angle between the electron beam and the sample. The lighter grey trajectories show the secondary electrons. Images C (cross-sectional view)and D (viewed from above) schematically show the increase in sampling of the silica skin towards the edge of the biomorph.

The Dresser Formation

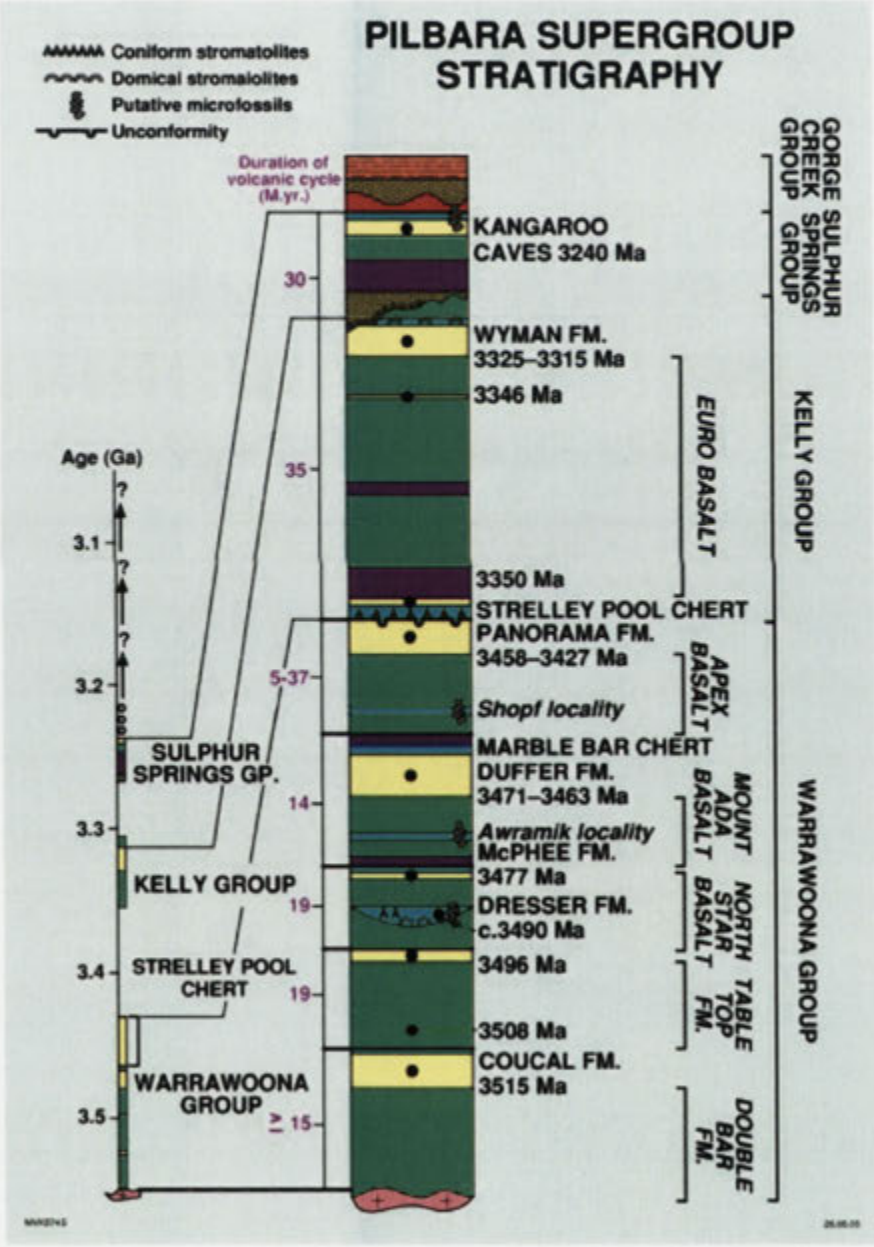

Figure D.1: Stratigraphic relationship of the Pilbara Supergroup showing microfossil and stromatolitic localities. Adapted after (Van Kranendonk, 2006).

Figure D.2: The muscovite structure, where the blue tetrahedra represents (Si, Al)O_4 tetrahedra (T) linked by orange octahedral cations (M). These layers are in turn sandwitched between large interlayer cations (A). Models were made with CrystalMaker, using crystallographic data from the CrystalMaker Library.

Minor elemental composition

Sample	Chert-rich		Carbonate-rich	
Element	A	C	B	D
Be	1.12(0.23)	0.57(0.23)	1.31(0.13)	0.90(0.11)
Sc	5.19(0.26)	7.32(0.34)	9.31(0.19)	8.56(0.16)
Ti	0.08(0)	0.10(0)	0.07(0.01)	0.08(0)
V	184.41(3.74)	182.82(3.36)	177.18(1.25)	177.31(1.23)
Cr	858.90(20.99)	842.84(21.73)	671.52(8.30)	723.77(7.91)
Ni	42.57(1.60)	37.47(1.70)	99.55(1.11)	146.69(1.52)
Cu	13.61(0.80)	20.02(0.80)	26.68(0.49)	8.62(0.24)
Zn	244.62(13.99)	158.58(7.59)	861.67(7.68)	498.34(4.45)
Ga	1.85(0.16)	2.05(0.19)	1.64(0.09)	1.83(0.08)
Ge	4.65(1.15)	8.54(1.52)	3.92(0.41)	5.98(0.29)
As	18.03(0.82)	20.89(1.01)	4.08(0.21)	12.41(0.26)
Rb	10.91(0.38)	12.45(0.53)	8.11(0.17)	9.01(0.13)
Sr	8.34(0.27)	58.20(1.18)	30.50(0.30)	77.89(0.58)
Y	2.74(0.14)	4.79(0.22)	8.32(0.14)	9.96(0.15)
Zr	5.36(0.25)	6.27(0.32)	4.53(0.13)	5.20(0.13)
Nb	0.30(0.05)	0.23(0.04)	0.31(0.02)	0.25(0.02)
Mo	2.67(0.21)	2.99(0.25)	3.77(0.17)	3.00(0.13)
Ag	0.88(0.14)	0.80(0.11)	0.84(0.05)	0.72(0.04)
Cd	1.30(0.24)	0.29(0.17)	0.20(0.06)	0.21(0.05)
Sn	0.93(0.20)	0.41(0.18)	1.72(0.10)	0.61(0.05)
Sb	0.36(0.19)	0.94(0.18)	0.92(0.06)	1.13(0.05)
Cs	0.30(0.05)	0.48(0.08)	0.23(0.02)	0.25(0.02)
Ba	5363.99(92.24)	13335.22(206.33)	5626.82(39.58)	4934.84(33.00)
La	1.38(0.09)	1.43(0.09)	2.42(0.08)	2.61(0.06)
Ce	1.19(0.07)	1.10(0.08)	2.35(0.05)	3.03(0.07)
Nd	0.44(0.14)	0.37(0.17)	1.36(0.12)	1.87(0.11)
Eu	0.14(0.03)	0.19(0.05)	0.36(0.03)	0.40(0.03)
Dy	0.25(0.07)	0.27(0.11)	0.97(0.08)	1.22(0.09)
Ho	0.03(0.02)	0.06(0.03)	0.22(0.02)	0.26(0.02)
Er	0.05(0.04)	0.31(0.09)	0.69(0.07)	0.92(0.05)
Tm	0.02(0.02)	0.00(0.02)	0.09(0.01)	0.13(0.01)
Yb	0.24(0.06)	0.27(0.10)	0.69(0.05)	0.87(0.05)
Lu	0.05(0.02)	0.04(0.02)	0.11(0.01)	0.15(0.02)
Hf	10.82(0.45)	7.10(0.41)	5.01(0.16)	5.30(0.14)
Ta	0.20(0.04)	0.43(0.16)	1.63(0.07)	0.05(0.01)
Tl	2.36(0.17)	2.22(0.15)	0.88(0.05)	0.95(0.05)
Pb	3.20(0.19)	2.23(0.24)	2.27(0.09)	2.52(0.09)
Bi	0.15(0.03)	0.16(0.04)	0.11(0.02)	0.15(0.01)
Th	0.14(0.04)	0.13(0.05)	0.03(0.01)	0.25(0.02)
U	0.12(0.03)	0.10(0.04)	0.39(0.03)	0.51(0.03)

Table D.1: ICP-MS results (ppm, wt% oxide of Ti) of sample regions indicated in Figure 6.9.

Bibliography

Addadi L and Weiner S (1992) Control and design principles in biological mineralization. *Angewandte Chemie International Edition* 31: 153–169.

Addadi L, Raz S, and Weiner S (2003) Taking advantage of disorder: amorphous calcium carbonate and its roles in biomineralization. *Advanced Materials* 15: 959–970.

Aiken B, Hsu WP, and Matijević E (1988) Preparation of monodispersed colloidal particles of lanthanide compounds: III, yttrium(III) and mixed yttrium(III)/cerium(III) systems. *Journal of the American Ceramic Society* 71: 845–853.

Aizenberg J, Addadi L, Weiner S, and Lambert G (1996) Stabilization of amorphous calcium carbonate by specialized macromolecules in biological and synthetic precipitates. *Advanced Materials* 8: 222–226.

Akagi T and Kono Y (1995) Inhibiting effects of lanthanum ion on calcite formation from $CaCl_2$-$NaHCO_3$ solutions at 25°C. *Aquatic Geochemistry* 1: 231–239.

Alam M, DebRoy T, and Roy R (1990) Laser-induced calcite-aragonite transition. *Journal of the American Chemical Society* 73: 733–735.

Allamandola LJ, Banford SA, and Wopenka B (1987) Interstellar polycyclic aromatic hydrocarbons and carbon in interplanetary dust particles and meteorites. *Science* 56-59.

Allwood AC, Walter MR, Kamber BS, Marshall CP, and Burch IW (2006) Stromatolite reef from the early Archean era of Australia. *Nature* 441: 714–7118.

Altermann W (2004) Precambrian stromatolites: Problems in definition, classification, morphology and stratigraphy. In *The Precambrian Earth: Tempos and Events* (Edited by P Eriksson, W Altermann, D Nelson, W Mueller, and O Catuneanu), volume 12 of *Developments in Precambrian Geology*, pp. 564–574. Elsevier.

Altermann W and Kazmierczak J (2003) Archean microfossils: A reappraisal of early life on earth. *Research in Microbiology* 154: 611–617.

ALVAREZ R AND SPARKS DL (1985) Polymerization of silicate anions in solutions at low concentrations. *Nature* 318: 649–651.

ANDERSON RB (1984) *The Fischer-Tropsch synthesis*. Academic Press, Orlando, Florida.

ANOVITZ LM AND ESSENE EJ (1987) Phase equilibria in the system $CaCO_3$-$MgCO_3$-$FeCO_3$. *Journal of Petrology* 28: 389–414.

APPEL PWU, MOORBATH S, AND MYERS JS (2003) Isuasphaera isua (Pflug) revisited. *Precambrian Research* 126: 309–312.

ARMSTRONG HA AND BRASIER MD (2005) *Microfossils*. Blackwell Publishing, 2nd edition.

ARRHENIUS S (1896) On the influence of carbonic acid in the air upon the temperature of the ground. *Philosophical Magazine* 41: 237–276.

ARVIDSON RS AND MACKENZIE FT (1999) The dolomite problem: control of precipitation kinetics by temperature and saturation state. *American Journal of Science* 299: 257–288.

ATKIN R, CRAIG VSJ, AND BIGGS S (2000) Adsorption kinetics and structural arrangements of cationic surfactants on silica surfaces. *Langmuir* 16: 9374–9380.

ATKIN R, CRAIG VSJ, WANLESS EJ, AND BIGGS S (2003) Mechanism of cationic surfactant adsorption at the solid-aqueous interface. *Advances in Colloid and Interface Science* 103: 219–304.

ATTARD GS, GLYDE JC, AND GOLTNER CG (1995) Liquid-crystallilne phases as templates for the synthesis of mesoporous silica. *Nature* 378: 366–368.

AWRAMIK SM (2006) Respect for stromatolites. *Nature* 441: 700–701.

AWRAMIK SM, SCHOPF JW, AND WALTER MR (1983) Filamentous fossil bacteria from the Archean of Western Australia. *Precambrian Research* 20: 357–374.

AWRAMIK SM, SCHOPF JW, AND WALTER MR (1988) Carbonaceous filaments from the North Pole, Western Asutralia: Are they fossil bacteria in Archean stromatolites? A discussion. *Precambrian Research* 39: 303–309.

BADA JF, WANG XS, AND HAMILTON H (1999) Preservation of key biomolecules in the fossil record: Current knowledge and future challanges. *Philosophical Transactions of the Royal Society of London: Biological Sciences* 354: 77–87.

BAES CF AND MESMER RE (1986) *The hydrolysis of cations*. Wiley, 2nd edition.

BAIRD T, BRATERMAN PS, CHEN P, GARCÍA-RUIZ JM, PEACOCK RD, AND REID A (1992) Morphology of gel-grown barium carbonate aggregates-pH effect on control by a silicate-carbonate membrane. *Materials Research Bulletin* 27: 1031–1040.

BAKER PA AND KASTNER M (1981) Constraints on the formation of sedimentary dolomite. *Science* 213: 214–216.

BALDASARI A AND SPEER JA (1979) Witherite composition, physical properties, and genesis. *American Mineralogist* 64: 742–747.

BALL P (1999) *The self-made tapestry: pattern formaation in nature.* Oxford University Press, Oxford.

BANGE H AND UHER G (2005) Photochemical production of methane in natural waters: implications for its present and past oceanic source. *Chemosphere* 58: 177–183.

BAR H AND AIZENSHTAT Z (1991) Phenol-formaldehyde resins as a link to the understanding of the isothermal kinetic behaviour of geopolymers (kerogens and coals). *Journal of Analytical and Applied Pyrolysis* 19: 265–277.

BARGHOORN ES AND TYLER SA (1965) Microorganisms from the Gunflint Chert. *Science* 147: 563–577.

BARNICOAT A, HENDERSON I, KNIPE R, YARDLEY B, NAPIER R, FOX N, KENYON A, MUNTINGH D, STRYDOM D, WINKLER K, LAWRENCE S, AND CORNFORD C (1997) Hydrothermal gold mineralization in the Witwatersrand basin. *Nature* 386: 820–824.

BASKIN DK (1997) Atomic H/C ration of kerogen as an estimate of thermal maturity and organic matter conversion. *AAPG Bulletin* 81: 1437–1450.

BASS JL AND TURNER GL (1997) Anion distribution in sodium silicate solutions. Characterization by *mathrm(29)Si* NMR and infrared spectroscopies, and vapor phase osmometry. *Journal of Physical Chemistry B* 101: 10638–10644.

BECK JS, VARTULI JC, ROTH WJ, LEONOWICZ ME, KRESGE CT, SCHMITT KD, CHU CTW, OLSON DH, SHEPPARD EW, MCCULLEN SB, HIGGINS JB, AND SCHLENKER JL (1992) A new family of mesoporous molecular sieves prepared with liquid crystal templates. *Journal of the American Chemical Society* 114: 10834–10843.

BEHAR F, BEAUMONT V, AND DE B PENTADO HL (2001) Rock-Eval 6 technology: Preformances and developments. *Oil and Gas Science and Technology* 56: 111–134.

BEN-JACOB E (1997) From snowflake formation to growth of bacterial colonies II: Cooperative formation of complex colonial patterns. *Contemporary Physics* 38: 205–241.

Ben-Jacob E and Garik P (1991) The formation of patterns in non-equilibrium growth. *Nature* 343: 523–530.

Ben-Jacob E, Deutscher G, Garik P, Goldenfeld ND, and Lareah Y (1986) Formation of a dense branching morphology in interfacial growth. *Physical Review Letters* 57: 1903–1906.

Ben-Jacob E, Garik P, Mueller T, and Grier D (1988) Characterization of morphology transitions in diffudion-controlled systems. *Physical Review A* 38: 1370–1380.

Bennett P and Siegel DI (1987) Increased solubility of quartz in water due to complexing by organic compounds. *Nature* 326: 684–686.

Bennett PC (1991) Quartz dissolution in organic-rich aqueous systems. *Geochimica et Cosmochimica Acta* 55: 1781–1797.

Bennett PC, Melcer ME, Siegel DI, and Hassett JP (1988) The dissolution of quartz in dilute aqueous solutions of organic acids at 25°c. *Geochimica et Cosmochimica Acta* 52: 1521–1530.

Beny-Bassez C and Rouzaud JN (1985) Characterization of carbonaceous materials by correlated electron and optical microscopy and Raman microspectroscopy. *Scanning Electron Microscopy* 1985: 119–132.

Bergna HE (1994) Colloidal chemistry of silica: an overview. In *The colloid chemistry of silica* (Edited by HE Bergna), volume 234 of *Advances in Chemistry*, pp. 1–47. American Chemical Society.

Bermann A, Addadi L, and Weiner S (1988) Interactions of sea-urchin skeleton macromolecules with growing calcite crystals-a study of intracrystalline proteins. *Nature* 331: 546–548.

Berndt ME, Allen DE, and Seyfried Jr WE (1996) Reduction of CO_2 during serpentinization of olivine at 300 °c and 500 bar. *Geology* 24: 351–354.

Berner RA (1975) The role of magnesium in the crystal growth of calcite and aragonite from seawater. *Geochimica et Cosmochimica Acta* 39: 489–504.

Beyssac O, Goffé B, Chopin C, and Rouzaud JN (2002) Raman spectra of carbonaceous material in metasediments: A new geothermometer. *Journal of Metamorphic Geology* 20(9): 859–871.

Beyssac O, Goffé B, Petitet JP, Froigneux E, Moreau M, and Rouzaud JN (2003) On the characterization of disordered and heterogenous carbonaceous materials by Raman spectroscopy. *Spectrochimica Acta* 59(Part A): 2267–2276.

Bhattacharya S, Savarino J, and Thiemens M (2000) A new class of oxygen isotope fractionation in photodissociation of carbon dioxide: Potential implications for atmospheres of Mars and Earth. *Geophysical Research Letters* 27: 1459–1462.

Black LP, Gale NH, Moorbath S, Pankhurst RJ, and McGregor VR (1971) Isotopic dating of very early Precambrian amphibolite facies gneisses from the Godthaab district West Greenland. *Earth and Planetary Science Letters* 12: 245–259.

Boggs Jr S (2001) *Principles of sedimentology and stratigraphy*. Prentice Hall, New Jersey.

Bolis V, Fubini B, Marchese L, Martra G, and Costa D (1991) Hydrophilic and hydrophobic sites on dehydrated crystalline and amorphous silicas. *Journal of the Chemical Society. Faraday Transactions* 87: 497–505.

Boström K, Hanor J, Blankenburg J, and Glaccum R (1969) Some subsolidus phase relations in the system $BaCO_3$-$CaCO_3$-$PbCO_3$ at 500 °c. *Arkiv för Mineralogi och Geologi* 5: 47–53.

Bowring SA and Housh T (1995) The Earth's early evolution. *Science* 269(5230): 1535–1540.

Bowring SA and Williams IS (1999) Priscoan (4.00-4.03 ga) orthogneisses from northwestern Canada. *Contributions to Mineralogy and Petrology* 134: 3–16.

Bradley JP, Harvey RP, and Jr HYM (1997) No 'nanofossils' in martian meteorite. *Nature* 390: 454–454.

Braithwaite CJR (2005) *Carbonate sediments and rocks*. Whittles Publishing, Caithness, Scotland.

Brasier MD, Green OR, Jephcoat AP, Kleppe AK, Kranendonk MJV, Lindsay JF, Steele A, and Grassineau NV (2002) Questioning the evidence for Earth's oldest fossil. *Nature* 416: 76–81.

Brasier MD, Green OR, Lindsay JF, McLoughlin N, Steele A, and Stoakes C (2005) Critical testing of Earth's oldest putative fossil assemblage from the ~3.5 Ga Apex chert, Chinaman Creek, Western Australia. *Precambrian Research* .

Brigatti MF and Guggenheim S (2002) Mica crystal structure and the influence of pressure, temperature, and solid solution on atomistic models. In *Micas: crystal*

chemistry and metamorphic petrology (Edited by A Mottana, FP Sassi, JB Thompson Jr, and S Guggenheim), volume 46 of *Reviews in Mineralogy and Geochemistry*, pp. 1–97. Mineralogical Society of America.

Brinker CJ and Scherer GW (1990) *Sol-gel science: the physics and chemistry of sol-gel processing*. Academic Press, San Diego.

Brocks JJ and Summons RE (2004) Sedimentary hydrocarbons, biomarkers for early life. In *Biogeochemistry* (Edited by H Holland and K Turekian), volume 8 of *Treatise on Geochemistry*, pp. 63–115. Elsevier.

Brocks JJ, Logan GA, Buick R, and Summons RE (1999) Archean molecular fossils and the early rise of eukaryotes. *Science* 285: 1033–1036.

Brocks JJ, Logan R, and Summons RE (2003) Composition and syngeneity of molecular fossils from the 2.78 to 2.45 billion-year-old Mount Bruce Supergroup, Pilbara Craton, Western Australia. *Geochimica et Cosmochimica Acta* 67: 4289–4319.

Brown WH, Fyfe WS, and Turner FJ (1962) Aragonite in California glaucophane schists, and the kinetics of the aragonite-calcite transformation. *Journal of Petrology* 3: 566–582.

Buick R (1984) Carbonaceous filaments from the North Pole, Western Asutralia: Are they fossil bacteria in archean stromatolites? *Precambrian Research* 24: 157–172.

Buick R (1988) Carbonaceous filaments from the North Pole, Western Asutralia: Are they fossil bacteria in archean stromatolites? A reply. *Precambrian Research* 39: 311–317.

Buick R (1990) Microfossil recognition in Archean rocks: An appraisal of speroids and filaments from a 3500 m.y. old chert-barite unit at North Pole, Western Australia. *Palaios* 5: 441–459.

Buick R and Dunlop J (1990) Evaporitic sediments of Early Archaean age from the Warrawoona Group, North Pole, Western Australia. *Sedimentology* 37: 247–277.

Buick R, Dunlop JSR, and Groves DI (1981) Stromatolite recognition in ancient rocks: An appraisal of irregularly laminated structures in an early Archaean chert-barite unit from North Pole, Western Australia. *Alcheringa* 5: 161–181.

Buick R, Groves DI, and Dunlop JSR (1995) Abiological origin of described stromatolites older than 3.2 Ga: Comment. *Geology* 23: 191.

Burdon KL (1964) *Microbiology*. Macmillan, 5th edition.

Burkett SL and Davis ME (1994) Mechanism of structure direction in the synthesis of Si-ZSM-5: an investigation by intermolecular $^{1}H -^{2}$ 9Si CP MAS NMR. *Journal of Physical Chemistry* 98: 4647–4653.

Burns BP, Goh F, Allen M, and Neilan BA (2004) Microbial diversity of extant stromatolites in the hypersaline marine environment of Shark Bay, Western Australia. *Environmental Microbiology* 6: 1096–1101.

Burns JH and Bredig MA (1956) Transformation of calcite to aragonite by grinding. *Journal of Chemical Physics* 25: 1281–1281.

Busch S, Dolhaine H, DuChesne A, Heinz S, Hochrein O, Laeri F, Podebrad O, Vietze U, Weiland T, and Kniep R (1999) Biomimetic morphogenesis of fluoroapatite-gelatin composites: fractal growth, the question of intrinsic fields, core/shell assemblies, hollow spheres and reorganization of denaturated collagen. *European Journal of Inorganic Chemistry* 1999: 1643–1653.

Busenberg E and Plummer LN (1986) The solubility of $BaCO_3$(cr) (witherite) in $CO_2 - H_2O$ solutions between 0 and 90°c, evaluation of the association constants of $BaHCO_3^+$(aq) and $BaCO_3^0$(aq) between 5 and 80°c, and a preliminary evaluation of the thermodynamic properties of Ba^{2+}(aq). *Geochimica et Cosmochimica Acta* 50: 2225–2233.

Busenberg E, Plummer LN, and Parker VB (1984) The solubility of strontianite ($SrCO_3$) in $CO_2 - H_2O$ solutions between 2 and 91°c, the association constants of $SrHCO_3^+$(aq) bewteen 5 and 80 °c, and an evaluation of the thermodynamic properties of Sr^{2+}(aq) and $SrCO_3$(cr) at 25°c and 1 atm total pressure. *Geochimica et Cosmochimica Acta* 48: 2021–2035.

Cacace MG, Landau EM, and Ramsden JJ (1997) The Hofmeister series: salt and solvent effects on interfacial phenomena. *Quaterly Reviews of Biophysics* 30: 241–277.

Cady SL, Farmer JD, Grotzinger JP, Schopf JW, and Steele A (2003) Morphological biosignatures and the search for life on Mars. *Astrobiology* 3: 351–368.

Cameron EM (1982) Sulphate and sulphate reduction in early Precambrian oceans. *Nature* 296: 145–148.

Canfield D (1998) A new model for Preterozoic ocean chemistry. *Nature* 396: 450–453.

Canfield D (2004) The evolution of the Earth surface sulfur reservoir. *American Journal of Science* 304: 839–861.

CANFIELD D (2005) The early history of atmospheric oxygen: Homage to Robert M. Garrels. *Annual Review of Earth and Planetary Sciences* 33: 1–36.

CANFIELD D, HABICHT K, AND THAMDRUP B (2000) The Archean sulfur cycle and the early history of atmospheric oxygen. *Science* 2888: 658–661.

CARLSON WD (1980) The calcite-aragonite equilibrium: effects of sr substitution and anion orientational disorder. *American Mineralogist* 65: 1252–1262.

CARLSON WD (1983) The polymorphs of $CaCO_3$ and the aragonite-calcite transformation. In *Carbonates: Mineralogy and chemistry* (Edited by RJ Reeder), volume 11 of *Reviews in Mineralogy*, pp. 191–225. Mineralogical Society of America.

CARTWRIGHT JHE, GARCÍA-RUIZ JM, AND VILLACAMPA AI (1999) Pattern formation in crystal growth: Liesegang rings. *Computer Physics Communication* 121-122: 411–413.

CARTWRIGHT JHE, GARCÍA-RUIZ JM, NOVELLA ML, AND OTÄLORA F (2002) Formation of chemical gardens. *Journal of Colloid and Interface Science* 256: 351–359.

CARY LW, DE JONG BHWS, AND JR WED (1982) A (29)Si study of silica species in dilute aqueous solution. *Geochimica et Cosmochimica Acta* 46: 1317–1320.

CASTIGLIONI C, MAPELLI C, NEGRI F, AND ZERBI G (2001) Origin of the D line in Raman spectrum of graphite: A study based on Raman frequencies and intensities of polycyclic aromatic hydrocarbon molecules. *Journal of Chemical Physics* 114(2): 963–974.

CAVOSIE AJ, VALLEY JW, WILDE SA, AND E I M F (2005) Magmatic $\delta^{18}O$ in 4400-3900 Ma detrital zircons: A record of the alteration and recycling of crust in the Early Archean. *Earth and Planetary Science Letters* 235: 663–681.

CHANG LLY (1965) Subsolidus phase relations in the systems $BaCO_3 - SrCO_3$, $SrCO_3 - CaCO_3$ and $BaCO_3 - CaCO_3$. *Journal of Geology* 73: 346–368.

CHANG LLY AND BRICE WR (1972) Subsolidus phase relations in aragonite-type carboantes: II. the systems $CaCO_3$-$SrCO_3$-$PbCO_3$ and $CaCO_3$-$BaCO_3$-$PbCO_3$. *American Mineralogist* 57: 155–168.

CHANG LLY, HOWIE RA, AND ZUSSMAN J (1998) *Non-silicates: sulphates, carbonates, phosphates and halides*, volume 5b of *Rock-forming minerals*. The Geological Society, second edition.

CHE S, LIU Z, OHSUNA T, SAKAMOTO K, TERASAKI O, AND TATSUMI T (2004) Synthesis and characterization of chiral mesoporous silica. *Nature* 429: 281–284.

CHEN PC, CHENG GY, KOU MH, SHIA PY, AND CHUNG PO (2001) Nucleation and morphology of barium carbonate crystals in a semi-batch crystallizer. *Journal of Crystal Growth* 226: 458–472.

CHESTER R (1990) *Marine geochemistry*. Unwin Hyman, London, UK.

CHOI M, CHO HS, SRIVASTAVA R, VENKATESAN C, CHOI DH, AND RYOO R (2006) Amphiphilic organosilane-directed synthesis of crystalline zeolite with tunable mesoporosity. *Nature Materials* 5: 718–723.

CISAR JO, XI DQ, THOMPSON J, SWAIM W, HU L, AND KOPECKO DJ (2000) An alternative interpretation of nanobacteria-induced biomineralization. *Proceedings of the National Academy of Sciences* 97(21): 11511–11515.

CLEMMEY H AND BADHAM N (1982) Oxygen in the Precambrian atmosphere: An evaluation of the geological evidence. *Geology* 10: 141–146.

CLOUD P (1973a) Paleoecological significance of the banded iron-formation. *Economic Geology* 68: 1135–1143.

CLOUD P (1973b) Pseudofossils: A plea for caution. *Geology* 1: 123–127.

CLOUD JR P (1968) Atmospheric and hydrospheric evolution on the primitive Earth. *Science* 160: 729–736.

CLUNIES ROSS WJ (1910) Experiments with silicate of soda and observations thereon. *Journal and Proceedings of the Royal Society of New South Wales* 44: 583–592.

COATMAN RD, THOMAS NL, AND DOUBLE DD (1980) Studies of the growth of "silicate gardens" and related phenomena. *Journal of Materials Science* 15: 2017–2026.

COEY JMD, HINDS G, AND LYONS MEG (1999) Magnetic-field effects on fractal electrodeposits. *Europhysics Letters* 47: 267–272.

CÖLFEN H (2003) Precipitation of carbonates: recent progress in controlled production of complex shapes. *Current Opinion in Colloid and Interface Science* 8: 23–31.

CÖLFEN H AND QI L (2001) A systematic examination of the morphogenesis of calcium carbonate in teh presence of double-hydrophilic block copolymer. *Chemistry- A European Journal* 7: 106–116.

COLLINS C, ZHOU W, MACKAY AL, AND KLINOWSKI J (1998) The 'silica garden': a hierarcharcial nanostructure. *Chemical Physics Letters* 286: 88–92.

COLLINS C, ZHOU W, AND KLINOWSKI J (1999) A unique structure of $Cu_2(OH)_3NH_3$ crystals in the 'silica garden' and their degradation under electron beam irradiation. *Chemical Physics Letters* 306: 145–148.

COLLINS PJ AND HIRD M (1997) *Introduction to liquid crystals: chemistry and physics.* The liquid crystlas book series. Taylor & Francis, London.

COOPER G, KIMMICH N, BELISLE W, SARINANA J, BRABHAM K, AND GARREL L (2001) Carbonaceous meteorites as a source of sugar-related organic compounds for the early Earth. *Nature* 414: 879–883.

COWEN R (1995) *History of life.* Blackwell Scientific Publications, 2nd edition.

CRERAR DA, FISCHER AG, AND PLAZA CL (1980) *Metallogenium* and biogenic deposition of manganese from Precambrian to recent time. In *Geology and Geochemistry of Manganese* (Edited by IM Varentsov and G Grasselly), volume 3, pp. 285–303. Scweizerbart'sche Verlag, Stuttgart.

DACHILLE F AND ROY R (1960) High-pressure phase transformations in laboratory mechanical mixers and mortars. *Nature* 186: 34, 71.

DALTON R (2002) Squaring up over ancient life. *Nature* 417: 782–784.

DALTON R (2004) Fresh study questions oldest traces of life in Akilia rocks. *Nature* 429: 688.

DAUPHAS N, VAN ZUILEN M, WADHWA M, DAVIS AM, MARTY B, AND JANNEY PE (2004) Clues from Fe isotope variations on the origin of early Archean BIFs from Greenland. *Science* 306: 2077–2080.

DAVIDOVITCH B, FEIGENBAUM MJ, HENTSCHEL HGE, AND PROCACCIA I (2000) Conformal dynamics of fractal growth patterns without randomness. *Physical Review E* 62: 1706–1715.

DAVIS ME AND LOBO RF (1992) Zeolite and molecular sieve synthesis. *Chemistry of Materials* 4: 756–768.

DAWKINS R (1988) *The blind watchmaker.* Penguin Books.

DE LEEUW JW AND LARGEAU C (1993) A review of macromolecular organic compounds that comprise living organisms and their role in kerogen, coal, and petroleum formation. In *Organic Geochemistry: Principles and Applications* (Edited by MH Engel and SA Macko), pp. 23–72. Plenum Press, New York.

De Visscher A and Vanderdeelen J (2003) Estimation of the solubility constant of calcite, aragonite, and vaterite at 25°C based on primary data using the pitzer ion interaction approach. *Monatshefte für Chemie* 134: 769–775.

Di Renzo F, Cambon H, and Dutartre R (1997) A 28-year-old synthesis of micelle-templated mesoporous silica. *Microporous Materials* 10: 283–286.

Dominguez Bella S and García-Ruiz JM (1986) Textures in induced morphology crystal aggregates of $CaCO_3$: Sheaf of wheat morphologies. *Journal of Crystal Growth* 79: 236–240.

Dominguez Bella S and García-Ruiz JM (1987) Banding structures in induced morphology crystal aggregates of $CaCO_3$. *Journal of Materials Science* 22: 3095–3102.

Donnay G and Pawson DL (1969) X-ray diffraction studies of Echinoderm plates. *Science* 166: 1147–1150.

Dove PM and Craven CM (2005) Surface charge density on silica in alkali and alkaline earth chloride electrolyte solutions. *Geochimica et Cosmochimica Acta* 69: 4963–4970.

Dove PM and Nix CJ (1997) The influence of the alkaline earth cations, magnesium, calcium, and barium on the dissolution kinetics of quartz. *Geochimica et Cosmochimica Acta* 61: 3329–3340.

Dove PM and Rimstidt JD (1994) Silica-water interactions. In *Silica: physical behaviour, geochemistry and materials applications* (Edited by PJ Heaney, CT Prewitt, and GV Gibbs), volume 29 of *Reviews in Mineralogy*, pp. 259–301. Mineralogical Society of America.

Dresselhaus MS and Dresselhaus G (1982) Light scattering in graphite intercalation compounds. In *Light scattering in solids* (Edited by M Cardona and G Güntherodt), pp. 3–57. Springer Verlag, Berlin.

Driese S (2004) Pedogenic translocation of *mathrmFe* in modern and ancient vertisols and implications for interpretations of the Hekpoort paleosol (2.25 Ga). *Journal of Geology* 112: 543–560.

Duan W, Kitamura S, Uechi I, Katsuki A, and Tanimoto Y (2005) Three-dimensional morphological chirality induction using high magnetic fields in membrane tubes prepared by a silicate garden reaction. *Journal of Physical Chemistry B* 109: 13445–13450.

Dupont L, Portemer F, and Figlarz M (1997) Synthesis and study of a well crystallized $CaCO_3$ vaterite showing a new habitus. *Journal of Materials Chemistry* 7: 797–800.

DURAND B, (Editor) (1980a) *Kerogen-insoluble organic matter from sedimentary rocks.* Éditions Technip.

DURAND B (1980b) Sedimentary organic matter and kerogen. Definition and quantitative importance of kerogen. In *Kerogen-insoluble organic matter from sedimentary rocks* (Edited by B Durand), pp. 13–34. Éditions Technip.

DURAND B AND MONIN JC (1980) Elemental analysis of kerogens (C, H, O, S, Fe). In *Kerogen-insoluble organic matter from sedimentary rocks* (Edited by B Durand), pp. 113–142. Éditions Technip.

DYMEK RF, BOAK JL, AND KERR MT (1983) Green micas in the Archaean Isua and Malene supracrustal rocks, southern West Greenland, and the occurrence of a barian-chromian muscovite. *Grønlands Geologiske Undersøgelse* 112: 71–82.

EDLER KJ (2005) Current understanding of formation mechanisms in surfactant-templated materials. *Australian Journal of Chemistry* 58: 627–643.

EL SHAFEI GMS (2000) Silica surface chemical properties. In *Adsorption on silica surfaces* (Edited by E Papirer), volume 90 of *Surfactant Science Series*, pp. 35–62. Marcel Dekker, New York.

ELLIS AJ (1959) The solubility of calcite in carbon dioxide solutions. *American Journal of Science* 257: 354–365.

ENGEL MH AND MACKO SA (1993) *Organic Geochemistry: Principles and Applications.* Plenum Press.

ESCRIBANO R, SLOAN JJ, SIDDIQUE N, SZE N, AND DUDEV T (2001) Raman spectroscopy of carbon-containing particles. *Vibrational Spectroscopy* 26: 179–186.

EVANS DF AND WENNERSTRÖM H (1999) *The colloidal domain.* Wiley, New York, 2nd edition.

FALINI G, FERMANI S, GAZZANO M, AND RIPAMONTI A (1998) Structure and morphologyu of synthetic magnesium calcite. *Journal of Materials Science* 8(4): 1061–1065.

FAN Y AND WANG R (2005) Submicrometer-sized vaterite tubes formed through nanobubble-templated crystal growth. *Advanced Materials* 17: 2384–2388.

FARQUHAR J, BAO H, AND THIEMENS M (2000a) Atmospheric influence of Earth's earliest sulfur cycle. *Science* 289: 756–758.

FARQUHAR J, SAVARINO J, JACKSON T, AND THIEMENS M (2000b) Evidence of atmospheric sulphur in the martian regolith from sulphur isotopes in meteorites. *Nature* 404: 50–52.

FARQUHAR J, BAO H, AND THIEMENS M (2001a) Questions regarding Precambrian sulfur isotope fractionation: A response. *Science* 292: 1959a.

FARQUHAR J, SAVARINO J, AIRIEAU S, AND THIEMENS M (2001b) Observation of wavelength-sensitive mass-independent sulfur isotope effects during SO_2 photolysis: Implications for the early atmosphere. *Journal of Geophysical Research* 106: 32829–32839.

FEDO CM AND WHITEHOUSE MJ (2002) Metasomatic origin of quartz-pyroxene rock, Akilia, Greenland, and implications for Earth's earliest life. *Science* 296: 1448–1452.

FELMY AR, CHO H, RUSTAD JR, AND MASON MJ (2001) An aqueous thermodynamic model for polymerized silica species to high ionic strength. *Journal of Solution Chemistry* 30: 509–525.

FELMY AR, MASON MJ, AND ANS D E MCCREADY PLG (2003) The formation of Sr silicates at low temperature and the solubility product of tobermorite-like $Sr_5Si_6O_{16}(OH)_2 \cdot 5H_2O$. *American Mineralogist* 88: 73–79.

FENG A, MCCOY BJ, MUNIR ZA, AND CAGLIOSTRO DE (1996) Water adsorption and desorption kinetics on silica insulation. *Journal of Colloid and Interface Science* 180: 276–284.

FERRARI AC AND ROBERTSON J (2000) Interpretation of Raman spectra of disordered and amorphous carbon. *Physical Review B* 61(20): 14095–14107.

FLODSTRÖM K AND ALFREDSSON V (2003) influence of the block length of triblock copolymers on the formation of mesoporous silica. *Microporous and Mesoporous Materials* 59: 167–176.

FOLK RL (1993) SEM imaging of bacteria and nannobacteria in carbonate sediments and rocks. *Journal of Sedimentary Petrology* 63(5): 990–999.

FORIEL J, PHILIPPOT P, SUSINI J, DUMAS P, SOMOGYI A, SALOMÉ M, KHODJA H, MÉNEZ B, FOUQUET Y, MORIERA D, AND LÓPEZ-GARCÍA P (2004) High-resolution imaging of sulfur oxidation states, trace elements, and organic molecules distribution in individual microfossils and contemporary microbial filaments. *Geochimica et Cosmochimica Acta* 68: 1561–1569.

FRANCEY R, ALLISON C, ETHERIDGE D, TRUDINGER C, ENTING I, LEUENBERGER M, LANGENFELDS R, MICHEL E, AND STEELE L (1999) A 1000-year high precision record of $\delta^{13}C$ in atmospheric CO_2. *Tellus* 51B: 170–193.

FRANCK S, KOSSACKI K, VON BLOH W, AND BOUNAMA C (2002) Long-term evolution of teh global carbon cycle: historic minimum of global surface temperature at present. *Tellus* 54B: 325–343.

FRIMMEL H (2002) Genesis of the world's largest gold deposit. *Science* 297: 1815–1817.

FRYXELL GE (2006) The synthesis of functional mesoporous materials. *Inorganic Chemistry Communications* 9: 1141–1150.

GALSTIAN VD, OGANESSIAN EB, GRIGORIAN SA, SHAKHNAZARIAN FS, AND ZULUMIAN NO (1982) Investigation of the system $BaCl_2$-Na_2SiO_3-H_2O at 20 °c. *Armyanskii Khimicheskii Zhurnal* 35: 21–27.

GAO Y AND MARCUS R (2001) Strange and unconventional isotope effects in ozone formation. *Science* 293: 259–263.

GARCÍA-RUIZ JM (1993) Natural viscous fingering. In *Growth patterns in physical sciences and biology* (Edited by JM García-Ruiz, E Louis, P Meakin, and LM Sander), volume 304 of *NATO Science Series B*, pp. 183–189. Plenum Press, New York.

GARCÍA-RUIZ JM (1994) Inorganic self-organisation in Precambrian cherts. *Origins of Life and Evolution of the Biosphere* 24: 451–467.

GARCÍA-RUIZ JM (1998) Carbonate precipitation into alkaline silica-rich environments. *Geology* 26(9): 843–846.

GARCÍA-RUIZ JM (2000) Geochemical scenarios for the precipitation of biomimetic inorganic carbonates. In *Carbonate sedimentation and diagenesis in the evolving Precambrian world* (Edited by JP Grotzinger and NP James), volume 67, pp. 75–89. SEPM (Society for Sedimentary Geology) Special Publication.

GARCÍA-RUIZ JM AND AMARÓS JL (1981) Morphological aspects of some symmetrical crystal aggregates grown by silica gel technique. *Journal of Crystal Growth* 55: 379–383.

GARCÍA-RUIZ JM AND MORENO A (1985) On the formation of induced morphology crystal aggregates. *Journal of Crystal Growth* 73: 251–262.

García-Ruiz JM and Moreno A (1997) Growth behaviour of twisted ribbons of barium carbonate/silica self-assembled ceramics. *Anales de Quimica International Edition* 93: 1–2.

García-Ruiz JM, Louis E, Meakin P, and Sander LM, (Editors) (1993) *Growth patterns in physical sciences and biology*, volume 304 of *NATO Science Series B*. Plenum Press, New York.

García-Ruiz JM, Carnerup A, Christy AG, Welham NJ, and Hyde ST (2002) Morphology: An ambigous indicator of biogenicity. *Astrobiology* 2: 353–369.

García-Ruiz JM, Hyde ST, Carnerup AM, Christy AG, van Kranendonk MJ, and Welham NJ (2003) Self-assembled silica-carbonate structures and the detection of ancient microfossils. *Science* 302: 1194–1197.

Garrels R and Mackenzie F (1967) Origin of the chemical composition of some springs and lakes. In *Equilibrium concepts natural water systems*, volume 67 of *Advances in Chemistry*, pp. 222–242. American Chemical Society.

Gay A and Grandstaff D (1980) Chemistry and mineralogy of Precambrian paleosols at Elliot lake, Ontario, Canada. *Precambrian Research* 12: 349–373.

Gee H (2002) That's life? *Nature* 416: 28.

Golden DC, Ming DW, Morris RV, Brearley AJ, Jr HVL, Treiman AH, Zolensky ME, Schwandt CS, Lofgren GE, and McKay GA (2004) Evidence for exclusively inorganic formation of magnetite in martian meteorite ALH84001. *American Mineralogist* 89: 681–695.

Gower LA and Tirrell DA (1998) Calcium carbonate films and helices grown in solutions of poly(aspartate). *Journal of Crystal Growth* 191: 153–160.

Gower LB and Odom DJ (2000) Deposition of calcium carbonate films by a polymer-induced liquid-precursor (PILP) process. *Journal of Crystal Growth* 210: 719–734.

Graetsch H (1994) Structural characteristics of opaline and microcrystalline silica minerals. In *Silica: physical behaviour, geochemistry and materials applications* (Edited by PJ Heaney, CT Prewitt, and GV Gibbs), volume 29 of *Reviews in Mineralogy*, pp. 209–232. Mineralogical Society of America.

Grandstaff D (1980) Origin of uraniferous conglomerates at Elliot lake, Canada and Witwatersrand, South Africa: Implications for oxygen in the Precambrian atmosphere. *Precambrian Research* 13: 1–26.

GRATZ AJ AND HILLNER PE (1993) Poisoning of calcite growth viewed in the atomic force microscope (afm). *Journal of Crystal Growth* 129: 789–793.

GREENWOOD J, MOJZSIS S, AND COATH C (2000) Sulfur isotopic compositions of individual sulfides in martian meteorites ALH84001 and Nakhla: Implications for crust-regolith exchange on Mars. *Earth and Planetary Science Letters* 184: 23–35.

GROTZINGER J AND KASTING J (1993) New constraints on Precambrian ocean composition. *Journal of Geology* 101: 235–243.

GROTZINGER JP AND KNOLL AH (1999) Stromatolites in Precambrian carbonates: Evolutionary mileposts or environmental dipsticks? *Annual Review of Earth and Planetary Sciences* 27: 313–358.

GROTZINGER JP AND REED JF (1983) Evidence for primary aragonite precipitation, Lower Proterozoic (1.9 Ga) Rockport dolomite, Wopmay orogen, northwest Canada. *Geology* 11: 710–713.

GROTZINGER JP AND ROTHMAN DH (1996) An abiotic model for stromatolite morphogenisis. *Nature* 383: 423–425.

GUIDOTTI CV AND SASSI FP (1998) Miscellaneous isomorphous substitutions in Na-K white micas: a review with special emphasis to metamorphic micas. *Rend. Fis. Acc. Lincei* 9: 57–78.

GUTJAHR A, DABRINGHAUS H, AND LACMANN R (1996) Studies of the growth and dissolution kinetics of the $CaCO_3$ polymorphs calcite and aragonite ii. the influence of divalent cation additives on the growth and dissolution rates. *Journal of Crystal Growth* 158: 310–315.

HABICHT KS, GADE M, THAMDRUP B, BERG P, AND CANFIELD DE (2002) Calibration of sulfate levels in the Archean ocean. *Science* 298: 2372–2374.

HADDON AC (1895) *Evolution in art: As illustrated by the life-histories of designs.* Walter Scott.

HAMM CE, MERKEL R, SPRINGER O, JURKOJC P, MAIER C, PRECHTEL K, AND SMETACEK V (2003) Architecture and material properties of diatom shells provide effective mechanical protection. *Nature* 421: 841–843.

HAN TM AND RUNNEGAR B (1992) Megascopic eukaryotic algae from th e2.1-billion-year-old negaunee iron-formation, Michigan. *Science* 257: 232–235.

HARDIKAR VV AND MATIJEVIĆ E (2001) Influence of ionic and nonionic dextrans on the formation of calcium hydroxide and calcium carbonate particles. *Colloids and Surfaces A* 186: 23–31.

HARRIS RK, JONES J, KNIGHT CTG, AND PAWSON D (1980) Silicon-29 NMR studies of aqueous silicate solution. *Journal of Molecular Structure* 69: 95–103.

HARRIS RK, KNIGHT CTG, AND HULL WE (1981) Nature of species present in aqueous solution of potassium silicate. *Journal of the American Chemical Society* 103: 1577–1578.

HARTING P (1872a) On the artificial production of some of the principal organic calcareous formations. *Quaterly Journal of Microscopical Science* 12: 118–123.

HARTING P (1872b) *Recherches de morphologie synthétique sur la production artificielle de quelques formations calcaires organiques.* Verhandelingen der Koninklijke Akademie van Wetenschappen, Amsterdam.

HARTMAN P (1973) *Crystal growth: an introduction,* volume 1 of *North-Holland series in crystal growth.* North-Holland Publishig Company.

HAYES JM, KAPLAN IR, AND WEDEKING KW (1983) Precambrian organic geochemistry, preservation of the record. In *Earth's Earliest Biosphere* (Edited by JW Schopf), pp. 93–134. Princeton University Press, Princeton, New Jersey.

HAZEMANN JL, BERAR JF, AND MANCEAU A (1991) Rietveld studies of the aluminium-iron substitution in synthetic goethite. *Materials Science Forum* 79: 821–826.

HEANEY PJ (1994) Structure and chemistry of the low-pressure silica polymorphs. In *Silica: physical behaviour, geochemistry and materials applications* (Edited by PJ Heaney, CT Prewitt, and GV Gibbs), volume 29 of *Reviews in Mineralogy,* pp. 1–40. Mineralogical Society of America.

HEANEY PJ AND POST JE (1992) The widespread distribution of a novel silica polymorph in microcrystalline quartz varieties. *Science* 255: 441–443.

HELZ GR AND HOLLAND HD (1965) The solubility and geologic occurrence of strontianite. *Geochimica et Cosmochimica Acta* 29: 1303–1315.

HENISCH HK (1973) *Crystal growth in gels.* Dover Publications, 2nd edition.

HENISH HK (1970) *Crystal growth in gels.* Dover Publications.

HERRERA AL (1912) Importance biologique des colloides naturels inorganiques. *Mémoires Société Scientifique "Antonio Alzate"* 32: 345–369.

HESSLER A, LOWE D, JONES R, AND BIRD D (2004) A lower limit for atmospheric arbon dioxide levels 3.2 billion years ago. *Nature* 428: 736–738.

HETHERINGTON CJ, GIERÉ R, AND GRAESER S (2003) Composition of barium-rich micas from the Berisal Complex, Simplion region, Switzerland. *The Canadian Mineralogist* 41: 1281–1291.

HIEMENZ PC AND RAJAGOPALAN R (1997) *Priciples of colloid and surface chemistry.* Marcel Dekker, 3rd edition.

HOFMANN BA AND FARMER JD (2000) Filamentous fabrics in low-temperature mineral assemblages: Are they fossil biomarkers? Implications for the search for a subsurface fossil record on the early Earth and Mars. *Planetary and Space Science* 48: 1077–1086.

HOFMANN HJ (1973) Stromatolites: Characteristics and utility. *Earth-Science Reviews* 9: 339–373.

HOFMANN HJ (2004) Archean microfossils and abiomorphs. *Astrobiology* 4: 135–136.

HOFMANN HJ AND SCHOPF JW (1983) Early Proterozoic microfossils. In *Earth's Earliest Biosphere* (Edited by JW Schopf), pp. 321–360. Princeton University Press.

HOLLAND H (1973) The oceans: A possible source of iron in iron-formations. *Economic Geology* 68: 1169–1172.

HOLLAND H (1984) *The chemical evolution of the atmosphere and oceans.* Princeton University Press, Princeton, New Jersey.

HOLLAND H (2002) Volcanic gases, black smokers and the Great Oxidation Event. *Geochimica et Cosmochimica Acta* 66: 3811–3826.

HOLLAND H AND FEAKES C (1989) Paleosols and their relevance to Precambrian atmospheric composition: A discussion. *Journal of Geology* 97: 761–762.

HOLLAND H, RYE R, AND OHMOTO H (1997) Evidence in pre-2.2 Ga paleosols for the early evolution of atmospheric oxygen and terrestrial biota: Comment. *Geology* 25: 857–858.

HOLM NG AND CHARLOU JL (2001) Initial indications of abiotic formation of hydrocarbons in the Rainbow ultramafic hydrothermal system, Mid-Atlantic Ridge. *Earth and Planetary Science Letters* 191: 1–8.

HOLTZHÜTER G, NARAYANAN K, AND GERBER T (2003) Structure of silica in *equisetum arvense. Analytical and Bioanalytical Chemistry* 376: 512–517.

HOOD D AND PYTKOWICZ RM (1974) Chemical oceanography. In *Handbook of Marine Science*, volume 1, pp. 3–70. CRC Press, Cleveland, Ohio.

HORITA J AND BERNDT ME (1999) Abiogenic methane formation and isotopic fractionation under hydrothermal conditions. *Science* 285: 1055–1057.

HOUSE CH, SCHOPF JW, MCKEEGAN KD, COATH CD, HARRISON TM, AND STETTER KO (2000) Carbon isotopic composition of individual Precambrian microfossils. *Geology* 28: 707–710.

HUBER H, HOHN MJ, RACHEL R, FUCHS T, WIMMER VC, AND STETTER KO (2002) A new phylum of Archaea represented by a nanosized hyperthermophilic symbiont. *Nature* 417: 63–67.

HUNT JM (1979) *Petroleum geochemistry and geology*. W. H. Freeman and Company, San Fransisco, USA.

HUNT JM, LEWAN MD, AND HENNET RJC (1991) Modeling oil generation with time-temperature index graphs based on the Arrhenius equation. *The American Association of Petroleum Geologists Bulletin* 75(4): 795–807.

HUO Q, MARGOLESE DI, CIESLA U, FENG P, GIER TE, SIEGER P, LEON R, PETROFF PM, SCHÜTH F, AND STUCKY GD (1994) Generalized synthesis of periodic surfactant/inorganic composite materials. *Nature* 368: 317–321.

HYDE S, ANDERSSON S, LARSSON K, BLUM Z, LANDH T, LEDIN S, AND NINHAM BW (1997) *The language of shape - the role of curvature in condensed matter: physics, chemistry and biology*. Elsevier, Amsterdam, The Netherlands.

HYDE ST, CARNERUP AM, LARSSON AK, CHRISTY AG, AND GARCÍA-RUIZ JM (2004) Self-assembly of carbonate-silica colloids: between living and non-living form. *Physica A* 339: 24–33.

ICOPINI GA, BRANTLEY SL, AND HEANEY PJ (2005) Kinetics of silica oligomerization and nanocolloid formation as a function of pH and ionic strength at 25°c. *Geochimica et Cosmochimica Acta* 69: 293–303.

ILER RK (1979) *The chemistry of silica. Solubility, polymerization, colloid and surface properties, and biochemistry*. John Wiley & Sons, Inc, New York.

IMAI H, TERADA T, MIURA T, AND YAMABI S (2002) Self-organized formation of porous aragonite with silicate. *Journal of Crystal Growth* 244: 200–205.

IMAI H, TERADA T, AND YAMABI S (2003) Self-organized formation of hierarchical self-similar structure with calcium carbonate. *Chemical Communications* pp. 484–485.

JAMES H (1983) Distribution of banded iron-formation in space and time. In *Iron formation: Facts and problems* (Edited by A Trendall and R Morris), volume 6 of *Developments in Precambrian Geology*, pp. 471–490. Elsevier, Amstrdam, The Netherlands.

JAMES H AND TRENDALL A (1982) Banded iron formation: Distribution in time and paleoenvironmental significance. In *Mineral deposits and the evolution of the biosphere* (Edited by H Holland and M Schidlowski), pp. 199–218. Springer-Verlag, Berlin, Germany.

JAMES HL (1969) Comparison between Red Sea deposits and older ironstone and iron-formation. In *Hot brines and recent heavy metal deposit in the Red Sea* (Edited by ET Degens and DA Ross), pp. 525–532. Springer Verlag, New York.

JAVAUX EJ AND MARSHAL CP (2006) A new approach in deciphering early protist paleobiology and evolution: Combined microscopy and microchemistry of single proterozoic acritarchs. *Review of Palaeobotany and Palynology* 139: 1–15.

JAVAUX EJ, KNOLL AH, AND WALTER MR (2001) Morphological and ecological complexity in early eukaryotic ecosystems. *Nature* 412: 66–69.

JAVAUX EJ, KNOLL AH, AND WALTER MR (2003) Recognizing and interpreting the fossils of early eukaryotes. *Origins of Life and Evolution of the Biosphere* 33: 75–94.

JAVAUX EJ, KNOLL AH, AND WALTER MR (2004) TEM evidence for eukaryotic diversity in mid-Proterozoic oceans. *Geobiology* 2: 121–132.

JEHLIČKA J, URBAN O, AND POKORNÝ J (2003) Raman spectroscopy of carbon and solid bitumens in sedimentary and metamorphic rocks. *Spectrochimica Acta A* 59: 2341–2352.

JIN H, LIU Z, OHSUNA T, TERASAKI O, INOUE Y, SAKAMOTO K, NAKANISHI T, ARIGA K, AND CHE S (2006) Control of morphology and helicity of chiral mesoporous silica. *Advanced Materials* 18: 593–596.

JONES DEH AND WALTER U (1998) The silicate garden reaction in microgravity: A fluid interfacial instability. *Journal of Colloid and Interface Science* 203: 286–293.

KAJANDER EO AND ÇIFTÇIOGLU N (1998) Nanobacteria: An alternative mechanism for pathogenic intra- and extracellular calcification and stone formation. *Proceedings of the National Academy of Sciences* 95: 8274–8279.

KAJANDER EO, ÇIFTÇIOGLU N, AHO K, AND GARCIA-CUERPO E (2003) Chararacteristics of nanobacteria and their possible role in stone formation. *Urological Research* 31: 47–54.

KARLSSON M, CRAVEN C, DOVE PM, AND CASEY WH (2001) Surface charge concentrations on silica in different 1.0 M metal-chloride background electrolytes and implications for dissolution rates. *Aquatic Geochemistry* 7: 13–32.

KASTING J (1987) Theoretical constraints on oxygen and carbon dioxide concentrations in the Precambrian atmosphere. *Precambrian Research* 34: 205–229.

KASTING J (1993) Earth's early atmosphere. *Science* 259: 920–926.

KASTING J (2005) Methane and climate during the Precambrian era. *Precambrian Research* 137: 119–129.

KASTING J AND WALKER J (1981) Limits on oxygen concentration in the prebiological atmosphere and the rate of abiotic fixation of nitrogen. *Journal of Geophysical Research* 86: 1147–1158.

KASTING J, PAVLOV A, AND SIEFERT J (2001) A coupled ecosystem-climate model for predicting the methane concentration in the Archean atmosphere. *Origins of Life and Evolution of the Biosphere* 31: 271–285.

KATZ A, SASS E, STARINSKY A, AND HOLLAND HD (1972) Strontium behaviour in teh aragonite-calcite transformation: An experimental study at 40-98°c. *Geochimica et Cosmochimica Acta* 36: 481–496.

KAZMIERCZAK J, KEMPE S, AND ALTERMANN W (2004) Microbial orgin of Precambrian carbonates: Lessons from modern analogues. In *The Precambrian Earth: Tempos and Events* (Edited by P Eriksson, W Altermann, D Nelson, W Mueller, and O Catuneanu), Developments in Precambrian Geology, pp. 545–564. Elsevier, Amsterdam, The Netherlands.

KELLERMEIER M (2005) *Isocapillary gels and biomorphs as examples for equilibrium and non-equilibrium self-assembly.* Master's thesis, University of Regensburg.

KELLEY DS AND FRÜ-GREEN GL (1999) Abiogenic methane in deep-seated mid-ocean ridge environments: Insights from stable isotope analysis. *Journal of Geophysical Research* 104: 10439–10460.

KEMPE S AND DEGENS E (1985) An early soda ocean? *Chemical Geology* 53: 95–108.

KEMPE S AND KAŹMIERCZAK J (1994) The role of alkalinity in the evolution of ocean chemistry, organization ofliving systems, and biocalcification processes. *Bulletin de l'Intitut Océanographique, Monaco* spécial 13: 61–117.

KEMPE S AND KAZMIERCZAK J (2002) Biogenesis and early life on Earth and Europa: Favoured by an alkaline ocean? *Astrobiology* 2: 123–130.

KERR RA (1998) Requiem for life on Mars? Support for microbes fades. *Science* 282(5393): 1398–1400.

KERR RA (2002) Earliest signs of life just oddly shaped crud? *Science* 295: 1812–1813.

KERR RA (2003) Minerals cooked up in the laboratory call ancient microfossils into question. *Science* 302: 1134–1134.

KIPKEMBOI P, FOGDEN A, ALFREDSSON V, AND FLODSTRÖM K (2001) Triblock copolymers as templates in mesoporous silica formation: structural dependence on polymer chain length and synthesis temperature. *Langmuir* 17: 5398–5402.

KIRK J, RUIZ J, CHESLEY J, WALSHE J, AND ENGLAND G (2002) A major Archean, gold- and crust-forming event in the Kaapvaal Craton, South Africa. *Science* 297: 1856–1858.

KITANO Y AND HOOD DW (1965) The influence of organic material on th epolymorphic crystallization of calium carbonate. *Geochimica et Cosmochimica Acta* 29: 29–41.

KLEIN C (2002) *The manual of mineral science*. John Wiley & Sons, New York, 22nd edition.

KNAUTH L (1994) Petrogenesis of cherts. In *Silica: Physical Behavior, Geochemistry and Materials Applications* (Edited by P Heaney, C Prewitt, and G Gibbs), volume 29 of *Reviews in Mineralogy*. Mineralogical Society of America.

KNAUTH L AND LOWE D (2003) High Archean temperature inferred from oxygen isotope geochemistry of cherts in the 3.5 Ga Swaziland Supergroup, South Africa. *GSA Bulletin* 115: 566–580.

KNOLL AH (1985) Exceptional preservation of photosynthetic organisms in silicified carbonates and silicified peats. *Philosophical Transactions of the Royal Society of London. Series B* 311: 111–122.

KNOLL AH AND BARGHOORN ES (1976) A gunflint-type microbiota from the Duck Creek dolomite, Western Australia. *Origins of Life* 7: 417–423.

KNOLL AH AND BARGHOORN ES (1977) Archean microfossils showing cell division from the Swaziland System of South Africa. *Science* 198: 396–398.

Ko TH, Kuo WS, and Chang YH (2000) Raman study of the microstructure changes of phenolic resin during pyrolysis. *Polymer Composites* 21(5): 745–750.

Kotachi A, Miura T, and Imai H (2003) Formation of silicate-mediated $CaCO_3$ films. *Chemistry Letters* 32(9): 820–821.

Kotachi A, Miura T, and Imai H (2004) Formation of planar aragonite-type carbonate crystals consisting of iso-oriented subunits. *Crystal Growth and Design* 4(4): 725–729.

Kresge CT, Leonowicz ME, Roth WJ, Vartuli JC, and Beck JS (1992) Ordered mesoporous molecular sieves synthesized by a liquid-crystal template mechanism. *Nature* 359: 710–712.

Krüger G and Wieker W (1965) Untersuchungen im system $BaO - SiO_2 - H_2O$. *Zeitschrift fur anorganische und allgemeine Chemie* 340: 277–293.

Kudryavtsev AB, Schopf JW, Agresti DG, and Wdowiak TJ (2001) In situ laser-Raman imagery of Precambrian microscopic fossils. *Proceedings of the National Academy of Sciences of the Uniteed States of America* 98(3): 823–826.

Kump L, Kasting J, and Barley M (2001) Rise of atmospheric oxygen and the "upside-down" Archean mantle. *Geochemistry, Geophysics, Geosystems* 2.

Lafargue E, Marquis F, and Pillot D (1998) Rock-Eval 6 applications in hydrocarbon exploration, and soil contamination studies. *Oil and Gas Science and Technology* 53: 421–437.

Lancet MS and Anders E (1970) Carbon fractionation in the Fischer-Tropsch synthesis and in meteorites. *Science* 170: 980–982.

Lapidus DF (1990) *Collins dictionary of geology*. Harper Collins.

Large DJ, Christy AG, and Fallick AE (1994) Poorly crystalline carbonaceous matter in high grade metasediments-implications for graphitisation and metamorphic fluid compositions. *Contributions to Mineralogy and Petrology* 116: 108–116.

Lasaga A and Ohmoto H (2002) The oxygen geochemical cycle: Dynamics and stability. *Geochimica et Cosmochimica Acta* 66(3): 361–381.

Lee JH and Byrne RH (1992) Examination of comparative rare earth element complexation behaviour using linear free-energy relationships. *Geochimica et Cosmochimica Acta* 56: 1127–1137.

Lee W and Wdowiak TJ (1993) Origin of the hydrocarbon component of carbonaceous chondrites: the star-meteorite connection. *The Astrophysical Journal* L49-L51.

LEPLAND A, VAN ZUILEN MA, ARRHENIUS G, WHITEHOUSE MJ, AND FEDO CM (2005) Questioning the evidence for Earth's earliest life-Akilia revisited. *Geology* 33: 77–79.

LI CC AND JEAN JH (2002) Dissolution and dispersion behaviour of barium carbonate in aqueous solutions. *Journal of the American Ceramic Society* 85: 2977–2983.

LIEBSCH H AND DORNBERGER-SCHIFF K (1958) Zur structure des $BaSiO_3 \cdot 5.3H_2O$. *Acta Crystallographica* 11: 371–372.

LINDSAY JF, BRASIER MD, MCLOUGHLIN N, GREEN OR, FOGEL M, STEELE A, AND MERTZMAN SA (2005) The problem of deep carbon-An Archean paradox. *Precambrian Research* 143: 1–22.

LOAIZA-GIL A, FONTAL B, RUEDA F, MENDIALDUA J, AND CASANOVA R (1999) Oon carbonaceous deposit formation in carbon monoxide hydrogenation on a natural iron catalyst. *Applied Catalysis A* 177: 193–203.

LOMAS A (2006) Persoonal communication. URL `http://www.andylomas.com/`.

LOWE D AND TICE M (2004) Geologic evidence for Archean atmospheric and climatic evolution: Fluctuating levels of CO_2, CH_4 and O_2 with an overriding tectonic control. *Geology* 32: 493–496.

LOWE DR (1994) Abiological origin of described stromatolites older than 3.2 Ga. *Geology* 22: 387–390.

LOWE DR (1995) Abiological origin of described stromatolites older than 3.2 Ga:reply. *Geology* 23: 191–192.

LOWE DR AND GARY ERNST W (1992) The Archean geological record. In *The Proterozoic Biosphere: a multidisciplinary study* (Edited by JW Schopf and C Klein), pp. 13–19. Cambridge University Press.

LOWENSTAM HA AND WEINER S (1989) *On biomineralization*. Oxford University Press, Oxford.

MACKENZIE FT, BISCHOFF WD, BISHOP FC, LOIJENS M, SCHOONMAKER J, AND WOLLAST R (1983) Magnesian calcites: low temperature occurrence, solubility and solid-solution behaviour. In *Carbonates: Mineralogy and chemistry* (Edited by RJ Reeder), volume 11 of *Reviews in Mineralogy*, pp. 97–144. Mineralogical Society of America.

MACLEOD G, MCKEOWN C, HALL AJ, AND RUSSELL MJ (1994) Hydrothermal and oceanic pH conditions of possible relevance to the origin of life. *Origins of Life and Evolution of the Biosphere* 24: 19–41.

MADIGAN MT, MARTINKO JM, AND PARKER J (1996) *Brock biology of microorganisms*. Prentice Hall, USA, 8th edition.

MAISONNEUVE J (1982) The composition of the precambrian ocean waters. *Sedimentary Geology* 31: 1–11.

MAKI JS, TEBO BM, PALMER FE, NEALSON KH, AND STALEY JT (1987) The abundance and biological activity of manganese-oxidizing bacteria and *metallogenium*-like morphotypes in Lake Washington, USA. *FEMS Microbiology Ecology* 45: 21–29.

MALIVA RG, KNOLL AH, AND SIMONSON BM (2005) Secular change in the Precambrian silica cycle: Insights from chert petrology. *GSA Bulletin* 117(7/8): 835–845.

MANN S (2001) *Biomineralization: principles and concepts in bioinorganic chemistry*, volume 5 of *Oxford chemistry masters*. Oxford University Press, Oxford.

MANOLI F AND DALAS E (2000) Spontaneous precipitation of calcium carbonate in the presence of ethanol, isopropanol and diethylene glycol. *Journal of Crystal Growth* 218: 359–364.

MARAIS DJD (2001) Isotopic evolution of the biogeochemical carbon cycle during the Precambrian. In *Stable isotope geochemistry*, volume 43 of *Reviews in Mineralogy and Geochemistry*, pp. 555–578. Mineralogical Society of America.

MARSHALL CP, JAVAUX EJ, KNOLL AH, AND WALTER MR (2005) Combined micro-Fourier transform infrared (FTIR) spectroscopy and micro-Raman spectroscopy of Proterozoic acritarchs: A new approach to palaeobiology. *Precambrian Research* 138: 208–224.

MATTHEWS MJ, PIMENTA MA, DRESSELHAUS G, DRESSELHAUS MS, AND ENDO M (1999) Origin of dispersive effects of the Raman D band in carbon materials. *Physical Review B* 59(10): R6585–R6588.

MAYNARD J (1992) Chemistry of modern soils as a guide to interpreting Precambrian paleosols. *Journal of Geology* 100: 279–289.

MAYNARD J, RITGER S, AND SUTTON S (1991) Chemistry of sands from the modern Indus River and the Archean Witwatersrand basin: Implications for the composition of the Archean atmosphere. *Geology* 19: 265–268.

MCCOLLOM TM (2003) Formation of meteorite hydrocarbons from thermal decomposition of siderite ($FeCO_3$). *Geochimica et Cosmochimica Acta* 67(2): 311–317.

McCollom TM and Seewald JS (2006) Carbon isotope composition of organic compounds produced by abiotic synthesis under hydrothermal conditions. *Earth and Planetary Science Letters* 243: 74–84.

McCollom TM and Simoneit BRT (1999) Abiotic formation of hydrocarbons and oxygenated compounds during thermal decomposition of iron oxalate. *Origins of Life and Evolution in the Biosphere* 29: 167–186.

McCollom TM, Ritter G, and Simoneit BRT (1999) Lipid synthesis under hydrothermal conditions by Fischer-Tropsch-type reactions. *Origins of life and Evolution of the Biosphere* 29: 153–166.

McKay DS, Jr EKG, Thomas-Keprta KL, Vali H, Romanek CS, Clemett SJ, Chillier XDF, Maechling CR, and Zare RN (1996) Search for past life on Mars: Possible relic biogenic activity in martian meteorite ALH84001. *Science* 273(5277): 924–930.

Megson NJL (1958) *Phenolic resin chemistry*. Butterworths scientific publications.

Meldrum FC and Hyde ST (2001) Morphological influence of magnesium and organic additives on the precipitation of calcite. *Journal of Crystal Growth* 231: 544–558.

Meyer HJ (1960) Ueber Vaterit und seine Struktur. *Fortschritte der Mineralogie* 38: 186–187.

Miller JP (1952) A portion of the system calcium carbonate-carbon dioxide-water, with geological implications. *American Journal of Science* 250: 161–203.

Millero FJ (2001) *Physical chemistry of natural waters*. Wiley-Interscience Series in Geochemistry. Wiley-Interscience, New York.

Millero FJ and Pierrot D (1998) A chemical equilibrium model for natural waters. *Aquatic Geochemistry* 4: 153–199.

Millero FJ, Milne PJ, and Thurmond VL (1984) The solubility of calcite, strontianite and witherite in NaCl solutions at 25°c. *Geochimica et Cosmochimica Acta* 48: 1141–1143.

Mojzsis SJ and Harrison TM (2000) Vestiges of a beginning: Clues to the emergent biosphere recorded in the oldest known sedimentary rocks. *GSA Today* 10(4): 1–6.

Mojzsis SJ, Arrhenius G, McKeegan KD, Harrison TM, Nutman AP, and Friend CRL (1996) Evidence for life on Earth before 3,800 million years ago. *Nature* 384: 55–59.

MOJZSIS SJ, COATH CD, GREENWOOD JP, MCKEEGAN KD, AND HARRISON TM (2003) Mass-independent isotope effects in Archean (2.5 to 3.8 Ga) sedimentary sulfides determined by ion micro-probe analysis. *Geochimica et Cosmochimica Acta* 67: 1635–1658.

MONNIN C, JEANDEL C, CATTALDO T, AND DEHAIRS F (1999) The marine barite saturation state of the world's oceans. *Marine Chemistry* 65: 253–261.

MOORBATH S (2005) Dating earliest of life. *Nature* 434: 155.

MOORBATH S, O'NIONS RK, AND PANKHURST RJ (1973) Early Archean age for the Isua iron formation, West Greenland. *Nature* 245: 138–139.

MOORE B (1915) The production of growths or deposits in metastable inorganic hydrosols. *Proceedings of the Royal Society of London B* 89: 27–35.

MOORE B AND EVANS WG (1915) On forms of growth resembling living organisms and their products slowly deposited from metastable solutions of inorganic colloids. *Proceedings of the Royal Society of London B* 89: 17–27.

MOORE B AND WEBSTER TA (1913) Synthesis by sunlight in relationship to the origin of life. synthesis of formaldehyde from carbon dioxide and water by inorganic colloids acting as transformers of light energy. *Proceedings of the Royal Society of London B* 87: 163–176.

MOROWITZ HJ (1996) Past life on Mars? *Science* 273(5282): 1639–1640.

MORRIS D (1987) *The secret surrealist: the paintings of Desmond Morris.* Phaidon Press.

MORSE JW (1983) The kinetics of calcium carbonate dissolution and precipitation. In *Carbonates: Mineralogy and chemistry* (Edited by RJ Reeder), volume 11 of *Reviews in Mineralogy*, pp. 227–264. Mineralogical Society of America.

MUCCI A, CANUEL R, AND ZHONG S (1989) The solubility of calcite and aragonite in sulfate-free seawater and the seeded growth kinetics and composition of the precipitates at 25°c. *Chemical Geology* 74: 309–320.

NAKAMIZO M, KAMMERECK R, AND JR PLW (1974) Laser Raman studies on carbons. *Carbon* 12: 259–267.

NAWROCKI J (1997) The silanol group and its role in liquid chromatography. *Journal of Chromatography A* 779: 29–71.

NEALSON K (1999) Panel 2 - discussion. In *Size limits of very small microorgansims; Proceedings of a workshop*, pp. 39–42. National Academy of Science.

NEAMAN A, CHOROVER J, AND BRANTLEY S (2005) Element mobility patterns record organic ligands in soils on early Earth. *Geology* 33: 117–120.

NEDACHI Y, NEDACHI M, BENNETT G, AND OHMOTO H (2005) Geochemistry and mineralogy of the 2.45 Ga Pronto paleosols, Ontario, Canada. *Chemical geology* 214: 21–44.

NEMANICH RJ AND SOLIN SA (1979) First- and second-order Raman scattering from finite-size crystals of graphite. *Physical Review B* 20(2): 392–401.

NEWMAN M AND ROOD R (1977) Implications of solar evolution for the Earth's early atmosphere. *Science* 198: 1035–1037.

NGANTSOUE-HOC W, ZHANG Y, O'BRIAN RJ, LUO M, AND DAVIS BH (2002) Fischer-Tropsch synthesis: activity and selectivity for group i alkali promoted iron-based catalysts. *Applied Catalysis A* 236: 77–89.

NÍ MHÍOCHÁIN TR AND COEY JMD (2001) Adapted diffusion limited aggregation model for the effects of magnetic fields on fractal electrodeposits. *Journal of Magnetism and Magnetic Materials* 226-230: 1281–1283.

NIJMAN W, DE BRUIJNE KCH, AND VALKERING ME (1999) Growth fault control of Early Archaean cherts, barite mounds and chert-barite veins, North Pole Dome, Eastern Pilbara, Western Australia. *Precambrian Research* 95: 247–274.

NOLL F, SUMPER M, AND HAMPP N (2002) Nanostructure of diatom silica surfaces and of biomimetic analogues. *Nano Letters* 2: 91–95.

NUTMAN AP, MCGREGOR VR, FRIEND CRL, BENNETT VC, AND KINNY PD (1996) The Itsaq Gneiss Comples of southern West Greenland; The world's most extensive record of early crustal evolution (3900-3600 Ma). *Precambrian Research* 78: 1–39.

NUTMAN AP, FRIEND CRL, AND BENNETT VC (2001) Review of the oldest (4400-3600 Ma) geological and mineralogical record: Glimpses of the beginning. *Episodes* 24(2): 93–101.

NUTMAN AP, FRIEND CRL, BARKER SLL, AND MCGREGOR VR (2004) Inventory and assessment of Paleoarchaean gneiss terrains and detrital zircons in southern West Greenland. *Precambrian Research* 135: 281–314.

OEHLER DC AND SMITH JW (1977) Isotopic composition of reduced and oxidized carbon in early Archaean rocks from Isua, Greenland. *Precambrian Research* 5: 221–228.

OHMOTO H (1996) Evidence in pre-2.2 Ga paleosols for the early evolution of atmospheric oxygen and terrestrial biota. *Geology* 24: 1135–1138.

OHMOTO H (1997) Evidence in pre-2.2 Ga paleosols for the early evolution of atmospheric oxygen and terrestrial biota: Reply. *Geology* 25: 858–859.

OHMOTO H (2002) Banded iron formations as guides for the history of the lithosphere, atmosphere, and hydrosphere. *Abstract of The Geological Society of America Denver Annual Meeting* .

OHMOTO H (2003) Banded iron formations and the evolution of the atmosphere, hydrosphere, biosphere and lithosphere. *Applied Earth Science* 112: B161–B162.

OHMOTO H (2004) The Archaean atmosphere, hydrosphere and biosphere. In *The Precambrian Earth: Tempos and Events* (Edited by P Eriksson, W Altermann, D Nelson, W Mueller, and O Catuneanu), volume 12 of *Developments in Precambrian Geology*, pp. 361–388. Elsevier.

OHMOTO H AND WATANABE Y (2004) Palaeoclimatology: Archaean palaesols and Archaean air: a reply. *Nature* 432: 1–2.

OHMOTO H, YAMAGUCHI K, AND ONO S (2001) Questions regarding Precambrian sulfur isotope fractionation. *Science* 292: 1959a.

OHMOTO H, WATANABE Y, AND KUMAZAWA K (2004) Evidence from massive siderite beds for a CO_2-rich atmosphere before ~1.8 billion years ago. *Nature* 429: 395–399.

OHSUNA T, LIU Z, CHE S, AND TERASAKI O (2005) Characterization of chiral mesoporous materials by transmission electron microscopy. *Small* 1: 233–237.

OLIVIER S, OZIN GA, AND OZIN LA (1995) Skeletons in the cupboard: Rediscovery in science. *Advanced Materials* 7: 948–951.

ON DT AND KALIAGUINE S (2004) Zeolite/mesoporous molecular sieve composite materials. In *Nanoporous materials: science and engineering* (Edited by GQ Lu and XS Zhao), volume 4 of *Series on Chemical engineering*, pp. 47–100. Imperial College Press, London.

OZE C AND SHARMA M (2005) Have olivine, will gas: Serpentinization and the abiotic production of methane on Mars. *Geophysical Reasearch Letters* 32: L10203.

PALIŃSKA KA AND KRUMBEIN WE (1998) Patterns of growth in coccoid, aggregate forming cyanobacteria. *Annales Botanici Fennici* 35: 219–227.

PALMER D (2005) *CrystalMaker for Mac OS X, version 7.0.0.* CrystalMaker Software Limited, Oxfordshire.

PALMER J, PHILLIPS G, AND MCCARTHY T (1989a) Paleosols and their relevance to Precambrian atmospheric composition. *Journal of Geology* 97: 77–92.

PALMER J, PHILLIPS G, AND MCCARTHY T (1989b) Paleosols and their relevance to Precambrian atmospheric composition: A reply. *Journal of Geology* 97: 764–766.

PALMQVIST AEC (2003) Synthesis of ordered mesoporous materials using surfactant liquid crystals or micellar solutions. *Current Opinion in Colloid and Interface Science* 8: 145–155.

PARIDA SK, DASH S, PATEL S, AND MISHRA BK (2006) Adsorption of organic molecules on silica surface. *Advances in Colloid and Interface Science* 121: 77–110.

PASTERIS JD AND WOPENKA B (1991) Raman spectra of graphite as indicators of degree of metamorphism. *The Canadian Mineralogist* 29: 1–9.

PASTERIS JD AND WOPENKA B (2002) Images of the Earth's earliest fossils? *Nature* 420: 476–477.

PASTERIS JD AND WOPENKA B (2003) Necessary, but not sufficient: Raman identification of disordered carbon as a signature of ancient life. *Astrobiology* 3(4): 727–738.

PAVLOV A AND KASTING J (2002) Mass-independent fractionation of sulfur isotopes in Archean sediments: Strong evidence for an anoxic Archean atmosphere. *Astrobiology* 2: 27–41.

PAVLOV A, KASTING J, BROWN L, RAGES K, AND FREEDMAN R (2000) Greenhouse warming by CH_4 in the atmosphere of early Earth. *Journal of Geophysical Research* 105: 11981–11990.

PAVLOV A, BROWN L, AND KASTING J (2001a) UV shielding of NH_3 and $mathrmO_2$ by organic hazes in the Archean atmosphere. *Journal of geophysical research* 106: 1–21.

PAVLOV A, KASTING J, EIGENBRODE J, AND FREEMAN K (2001b) Organic haze in Earth's early atmosphere: Source of low-^{13}C Late Archean kerogens? *Geology* 29: 1003–1006.

PAVLOV A, HURTGEN M, KASTING J, AND ARTHUR M (2003) Methane-rich Proterozoic atmosphere. *Geology* 31: 87–90.

PERRY CC AND KEELING-TUCKER T (2000) Biosilicification: the role of organic matrix in structure control. *Journal of Biological Inorganic Chemistry* 5: 537–550.

PERRY CC AND LU Y (1992) Preparation of silicas from silicon complexes: role of cellulose in polymerisation and aggregation control. *Journal of the Chemical Society. Faraday Transactions* 88: 2915–2921.

PERRY JR EC AND AHMAD SN (1977) Carbon isotope composition of graphite and carbonate minerals from 3.8-ae metamorphosed sediments, Isukasia, Greenland. *Earth and Planetary Science Letters* 36: 280–284.

PERSELLO J (2000) Surface and interface structure of silicas. In *Adsorption on silica surfaces* (Edited by E Papirer), volume 90 of *Surfactant Science Series*, pp. 297–367. Marcel Dekker.

PETRICEK V, DUSEK M, AND PALATINUS L (2000) *Jana2000. The crystallographic computing system.* Institute of Physics, Praha, Czech republic.

PFLUG HD AND JAESCHKE-BOYER H (1979) Combined structural and chemical analysis of 3,800-Myr-old microfossils. *Nature* 280: 483–486.

PHILLIPS G, MYERS R, AND PALMER J (1987) Problems with the placer model for Witwatersrand gold. *Geology* 15: 1027–1030.

PINSENT BRW, PEARSON L, AND ROUGHTON FJW (1956) The kinetics of combination of carbon dioxide with hydroxide ions. *Transactions of the Faraday Society* 52: 1512–1520.

PITZER KS (1973) Thermodynamics of electrolytes. i. theoretical basis and general equations. *Journal of Physical Chemistry* 77: 268–277.

PLUMMER LN AND BUSENBERG E (1982) The solubilities of calcite, aragonite and vaterite in $CO_2 - H_2O$ solutions between 0 and 90°c, and an evaluation of the aqueous model for the system $CaCO_3 - CO - 2 - H_2O$. *Geochimica et Cosmochimica Acta* 46: 1011–1040.

POKROVSKIY OS AND SAVENKO VS (1995) The role of magnesium at homogeneous precipitation of calcium carbonate from seawater. *Oceanology* 34: 493–497.

POLITI Y, ARAD T, KLEIN E, WEINER S, AND ADDADI L (2004) Sea urchin spine calcite forms via a transient amorphous calcium carbonate phase. *Science* 306: 1161–1164.

POST JE (1999) Manganese oxide minerals: Crystal structures and economic and environmental significance. *Proceedings of National Academy of Science* 96: 3447–3454.

POULTON S, FRALICK P, AND CANFIELD D (2004) The transition to a sulphidic ocean ~1.84 billion years ago. *Nature* 431: 173–177.

PRASAD N AND ROSCOE S (1996) Evidence of anoxic to oxic atmospheric change during 2.45-2.22 Ga from lower and upper sub-Huronian paleosols, Canada. *Catena* 27: 105–121.

PRESCOTT LM, HARLEY JP, AND KLEIN DA (1996) *Microbiology*. Wm. C. Brown Publishers, Dubuque, 3rd edition.

PRIGOGINE I AND LEFEVER R (1968) Symmetry breaking in dissipative systems II. *The Journal of Chemical Physics* 48: 1695–1700.

PRIVMAN V, GOIA DV, PARK J, AND MATIJEVIĆ E (1999) Mechanism of formation of monodispersed colloids by aggregation of nanosized precursors. *Journal of Colloid and Interface Science* 213: 36–45.

QI L, MA J, CHENG H, AND ZHAO Z (1997) Reverse micelle based formation of $BaCO_3$ nanowires. *Journal of Physical Chemistry B* 101: 3460–3463.

QI L, LI J, AND MA J (2002) Biomimetic morphogenesis of calcium carbonate in mixed solutions of surfactants and double-hydrophilic block copolymers. *Advanced Materials* 14: 300–303.

RAIMONDI ME AND SEDDON JM (1999) Liquid crystal templating of porous materials. *Liquid Crystals* 26: 305–339.

RASMUSSEN B (2005) Evidence for pervasive petroleum generation and migration in 3.2 and 2.63 Ga shales. *Geology* 33: 497–500.

RASMUSSEN B AND BUICK R (1999) Redox state of the Archean atmosphere: Evidence from detrital heavy minerals in ca. 3250-2750 Ma sandstones from the Pilbara Craton, Australia. *Geology* 27: 115–118.

REDDY MM AND WANG KK (1980) Crystallization of calcium carbonate in the presence of metal ions i. inhibition by magnesium ion at ph 8.8 and 25 degree c. *Journal of Crystal Growth* 50: 470–480.

REEDER RJ (1983) Crystal chemistry of the rhombohedral carbonates. In *Carbonates: Mineralogy and chemistry* (Edited by RJ Reeder), volume 11 of *Reviews in Mineralogy*, pp. 1–47. Mineralogical Society of America.

REGO R, ADRIAENSENS P, CARLEER R, AND GELAN J (2004) Fully quantitative carbon-13 NMR characterisation of resol phenol- formaldehyde prepolymer resins. *Polymer* 45: 33–38.

RETALLACK G (1989) Paleosols and their relevance to Precambrian atmospheric composition: A discussion 2. *Journal of Geology* 97: 763–764.

REYES-GRAJEDA JP, JÁUREGUI-ZÚÑIGA D, BATINA N, SALMÓN-SALAZAR M, AND MORENO A (2002) Experimental simulations of the biomineralization phenomena in avian eggshells using $BaCO_3$ aggregates grown inside an alkaline silica matrix. *Journal of Crystal Growth* 234: 227–236.

RIDING R (1999) The term stromatolite: Towards an essential definition. *Lethaia* 32: 321–330.

RIDING R (2000) Microbial carbonates: The geological record of calcified bacterial-algal mats and biofilms. *Sedementology* 47: 179–214.

RIMSTIDT JD AND BARNES HL (1980) The kinetics of silica-water interactions. *Geochimica et Cosmochimica Acta* 44: 1683–1699.

ROBINSON A AND SPOONER E (1984) Can the Elliot Lake uraninite-bearing quartz pebble conglomerates be used to place limits on the oxygen content of the early Proterozoic atmosphere? *Journal of the Geological Society, London* 141: 221–228.

ROFER-DEPOORTER CK (1981) A comprahensive mechanism for the Fischer-Tropsch synthesis. *Chemical Reviews* 81: 447–474.

RÖPER M (1983) Fischer-Tropsch synthesis. In *Catalysis in* C_1 *chemistry* (Edited by W Keim), volume 4 of *Catalysis by metal comlpexes*, pp. 41–88. D. Reidel Publishing Company.

ROSING MT (1999) ^{13}C-depleted carbon microparticles in >3700-Ma sea-floor sedimentary rocks from West Greenland. *Science* 283: 674–676.

RUSSELL MJ AND HALL AJ (1997) The emergence of life from iron monosulphide bubbles at a submarine hydrothermal redox and pH front. *Journal of the Geological Society, London* 154: 377–402.

RYE R AND HOLLAND H (1998) Paleosols and the evolution of atmospheric oxygen: A critical review. *American Journal of Science* 298: 621–672.

RYE R AND HOLLAND H (2000a) Geology and geochemistry of paleosols developed on the Hekpoort basalt, Pretoria Group, South Africa. *American Journal of Science* 300: 85–141.

RYE R AND HOLLAND H (2000b) Life associated with a 2.76 Ga ephemeral pond?: Evidence from Mount Roe #2 paleosol. *Geology* 28: 483–486.

RYE R, KUO P, AND HOLLAND H (1995) Atmospheric carbon dioxide concentrations before 2.2 billion years ago. *Nature* 378: 603–605.

SAGAN C AND MULLEN G (1972) Earth and Mars: Evolution of atmospheres and surface temperatures. *Science* 177: 52–56.

SAKELLARIOU A, SAWKINS TJ, SENDEN TJ, AND LIMAYE A (2004) X-ray tomography for mesoscale physics applications. *Physica A* 339: 152–158.

SAMUELSSON J AND BUTTERFIELD NJ (2001) neoproterozoic fossils from the Franklin Mountains, northwestern Canada: stratigraphic and paleobiological implications. *Precambrian Research* 107: 235–251.

SANDER LM (1986) Fractal growth processes. *Nature* 322: 789–793.

SCHIDLOWSKI M (2001) Carbon isotopes as biogeochemical recorders of life over 3.8 Ga of Earth history: Evolution of a concept. *Precambrian Research* 106: 117–134.

SCHNEIDER DA, BICKFORD ME, CANNON WF, SCHULTZ KJ, AND HAMILTON MA (2002) Age of volcanic rocks and syndepositional iron formations, Marquette Range Supergroup: implications for the tectonic setting of Paleoproterozoic iron formations of the Lake Superior region. *Canadian Journal of Earth Science* 39: 999–1012.

SCHOENBERG R, KAMBER BS, CIOLLERSON KD, AND MOORBATH S (2002) Tungsten isotope evidence from ~3.8-Gyr metamorphosed sediments for early meteorite bombardment of the Earth. *Nature* 418: 403–405.

SCHOPF JW (1968) Microflora of the Bitter Springs formation, late Precambrian, central Australia. *Journal of Paleontology* 42(3): 651–688.

SCHOPF JW (1975) Precambrian paleobiology: Problems and perspectives. *Annual Review of Earth and Planetary Sciences* 3: 213–249.

SCHOPF JW (1992) Paleobiology of the Archean. In *The Proterozoic Biosphere: A multidisciplinary study* (Edited by J Schopf and C Klein), pp. 25–39. Cambridge University Press.

SCHOPF JW (1993) Microfossils of the early Archean Apex Chert: New evidence of the antiquity of life. *Science* 260: 640–646.

SCHOPF JW (1999a) *Cradle of life.* Princeton University Press, Princeton, New Jersey.

SCHOPF JW (1999b) Fossils and pseudofossils: lessons from the hunt for early life on Earth. In *Size limits of very small microorgansims; Proceedings of a workshop*, pp. 88–93. National Academy of Science.

SCHOPF JW (2004) Earth's earliest biosphere: Status of the hunt. In *The Precambrian Earth: Tempos and Events* (Edited by P Eriksson, W Altermann, D Nelson, W Mueller, and O Catuneanu), volume 12 of *Developments in Precambrian Geology*, pp. 516–539. Elsevier, 1 edition.

SCHOPF JW AND KUDRYAVTSEV AB (2005) Three-dimensional Raman imagery of Precambrian microscopic organisms. *Geobiology* 3: 1–12.

SCHOPF JW AND WALTER MR (1983) Archean microfossils: New evidence of ancient microbes. In *Earth's Earliest Biosphere* (Edited by J Schopf), pp. 214–239. Princeton University Press, Princeton, New Jersey.

SCHOPF JW, OEHLER DZ, HORODYSKI RJ, AND KVENNOLDEN KA (1971) Biogenicity and significance of the oldest known stromatolites. *Journal of Paleontology* 45: 477–485.

SCHOPF JW, KUDRYAVTSEV AB, AGRESTI DG, WDOWIAK TJ, AND CZAJA AD (2002a) Images of the Earth's earliest fossils? A reply. *Nature* 420: 477.

SCHOPF JW, KUDRYAVTSEV AB, AGRESTI DG, WDOWIAK TJ, AND CZAJA AD (2002b) Laser-Raman imagery of Earth's earliest fossils. *Nature* 416: 73–76.

SCHOPF JW, TRIPATHI AB, AND KUDRYAVTSEV AB (2006) Three-dimensional confocal optical imagery of Precambrian microscopic organisms. *Astrobiology* 6: 1–16.

SCHULZ HN, BRINKHOFF T, FERDELMAN TG, HERNÁNDEZ MARINÉ M, TESKE A, AND JØRGENSEN BB (1999) Dense populations of a giant sulfur bacterium in Namibian shelf sediments. *Science* 284: 493–495.

SEGNIT ER, HOLLAND HD, AND BISCARDI CJ (1962) The solubility of calcite in aqueous solutions i. the solubility of calcite in water between 75° and 200° at CO_2 pressures up to 60 atm. *Geochimica et Cosmochimica Acta* 26: 1301–1331.

SEINFELD J AND PANDIS S (1998) *Atmospheric chemistry and physics: From air pollution to climate change*. John Wiley & Sons, Inc.

SHANNON RD AND PREWITT CT (1969) Effective ionic radii in oxides and fluorides. *Acta Crystallographica* B25: 925–946.

SIEVER R (1957) The silica budget in the sedimentary cycle. *American Mineralogist* 42: 821–841.

SIEVER R (1992) The silica cycle in the Precambrian. *Geochimica et Cosmochimica Acta* 56: 3265–3272.

SIMONEIT BRT (1993) Aqueous high-temperature and high-pressure organic geochemistry of hydrothermal vent systems. *Geochimica et Cosmochimica Acta* pp. 3231–3243.

SIMONEIT BRT, LEIN AY, PERESYPKIN VI, AND OSIPOV GA (2004) Composition and origin of hydrothermal petroleum and associated lipids in the sulfide deposits of the Rainbow Field (Mid-Atlantic Ridge at 36°N. *Geochimica et Cosmochimica Acta* 68: 2275–2294.

SIMPSON P AND BOWLES J (1977) Uranium mineralization of the Witwatersrand and Dominion Reef systems. *Philosophical Transactions of the Royal Society of London. Series A* 286: 527–548.

SJÖBERG S (1996) Silica in aqueous environments. *Journal of Non-Crystalline Solids* 196: 51–57.

SMITH N AND MINTER W (1980) Sedimentological controls of gold and uranium in 2 Witwatersrand paleoplacers. *Economic Geology* 75: 1–14.

SOLER-ILLA GJAA, SANCHEZ C, LEBEAU B, AND PATARIN J (2002) Chemical strategies to design textured materials: from microporous and mesoporous oxides to nanonetworks and hierarchical structures. *Chemical Reviews* 102: 4093–4138.

SOLER-ILLA GJAA, CREPALDI EL, GROSSO D, AND SANCHEZ C (2003) Block copolymer-templated mesoporous oxides. *Current Opinion in Colloid and Interface Science* 8: 109–126.

SONDI I AND MATIJEVIC E (2001) Homogeneous precipitation of calcium carbonates by enzyme catalyzed reaction. *Journal of Colloid and Interface Science* 238: 208–214.

SONDI I AND MATIJEVIC E (2003) Homogeneous precipitation by enzyme-catalyzed reactions. 2. Strontium and barium carbonates. *Chemical Materials* 15: 1322–1326.

SPEER JA (1983) Crystal chemistry and phase realations of orthorombic carbonates. In *Carbonates: Mineralogy and chemistry* (Edited by RJ Reeder), volume 11 of *Reviews in Mineralogy*, pp. 145–190. Mineralogical Society of America.

STALEY JT (1999) Bacteria, their smallest representatives and subcellular structures, and the purported Precambrian fossil 'Metallogenium'. In *Size limits of very small microorgansims; Proceedings of a workshop*, pp. 62–67. National Academy of Science.

STÖBER W, FINK A, AND BOHN E (1968) Controlled growth of monodispersed silica spheres in the micron size range. *Journal of Colloid and Interface Science* 26: 62–69.

STONE DA AND GOLDSTEIN RE (2004) Tubular precipitation and redox gradients on a bubbling template. *Proceedings of the National Academy of Sciences* 101: 11537–11541.

STUMM W AND MORGAN JJ (1996) *Aquatic chemistry: chemical equilibria and rates in natural waters*. John Wiley & Sons, New York, 3rd edition.

SUÁREZ-ORDÚÑA R, RENDÓN-ANGELES JC, LÓPEZ-CUEVAS J, AND YANAGASIWA K (2004) The conversion of mineral celestite to strontianite under alkaline hydrothermal conditions. *Journal of Physics: Condensed Matter* 16: S1331–S1344.

SUDA J AND MATSUSHITA M (1995) Spiral crystal growth of potassium dichromate in gelatin. *Journal of the Physical Society of Japan* 64: 348–351.

SUDA J AND MATSUSHITA M (2004) Chirality change in helical crystals of potassium dichromate. *Journal of the Physical Society of Japan* 73: 300–302.

SUDA J, NAKAYAMA T, NAKAHARA A, AND MATSUSHITA M (1996) Morphological diversity in the crystal growth of potassium dichromate in gelatin gel. *Journal of the Physical Society of Japan* 65: 771–777.

SUDA J, NAKAYAMA T, AND MATSUSHITA M (1998) Influence of collagen macromolecular arrangement on the potassium dichromate spiral crystal growth. *Journal of the Physical Society of Japan* 67: 2981–2983.

SUGISAKI R AND MIMURA K (1994) Mantle hydrocarbons: Abiotic or biotic? *Geochimica et Cosmochimica Acta* 58: 2527–2542.

SUGITANI K (1992) Geochemical characteristics of Archean cherts and other sedimentary rocks in the Pilbara Block, Western Australia: evidence for Archean seawater enriched in hydrothermally-derived iron and silica. *Precambrian Research* 57: 21–47.

SUMMONS RE, JAHNKE LL, HOPE JM, AND LOGAN GA (1999) 2-Methylhopanoids as biomarkers for cyanobacterial oxygenic photosynthesis. *Nature* 400: 554–557.

SUMNER D AND GROTZINGER J (2000) Late Archean aragonite precipitation: petrography, facies associations, and environmental significance. In *Carbonate sedimentation and diagenisis in the evolving Precambrian world* (Edited by J Grotzinger and N James), volume 67, pp. 123–144. SEPM (Society for Sedimentary Geology) Special Publication.

SUMNER DY AND GROTZINGER JP (1996a) Herringbone calcite: petrography and eenvironmental significance. *Journal of Sedimentary Research* 66: 419–429.

SUMNER DY AND GROTZINGER JP (1996b) Were kinetics of Archean calcium carboante precipitation related to oxygen concentration? *Geology* 24: 119–122.

SUMPER M (2002) A phase separation model for the nanopatterning of diatom biosilica. *Science* 295: 2430–2433.

SVENSSON IL, SJÖBERG S, AND ÖHMAN LO (1986) Polysilicate equilibria in concentrated sodium silicate solutions. *Journal of the Chemical Society. Faraday Transactions 1* 82: 3635–3646.

SWADDLE TW, SALERNO J, AND TREGLOAN PA (1994) Aqueous aluminates, silicates, and aluminosilicates. *Chemical Society Reviews* 23: 319–325.

TADROS TF AND LYKLEMA J (1969) The electrical double layer on silica in the presence of bivalent counter-ions. *Journal of Electroanalytical Chemistry* 22: 1–7.

TERADA T, YAMABI S, AND IMAI H (2003) Formation process of helical forms consisting of strontium carbonate fibrous crystals with silicate. *Journal of Crystal Growth* 253: 435–444.

THIEMENS M (1999) Mass-independent isotope effects in planetary atmospheres and the early solar system. *Science* 283: 341–345.

THIEMENS M AND HEIDENREICH J (1983) The mass-independent fractionation of oxygen: A novel isotope effect and its possible cosmochemical implications. *Science* 219: 1073–1075.

THIEMENS M, SAVARINO J, FARQUHAR J, AND BAO H (2001) Mass-independent isotopic compositions in terrestrial and extraterrestrial solids and their applications. *Accounts of Chemical Research* 34: 645–652.

THOMAS-KEPRTA KL, BAZYLINSKI DA, KIRSCHVINK JL, CLEMETT SJ, MCKAY DS, WENTWORTH SJ, VALI H, GIBSON JR EK, AND ROMANEK CS (2000) Elongated prismatic magnetite crystals in ALH84001 carbonate globules: Potential martian magnetofossils. *Geochimica et Cosmochimica Acta* 64(23): 4049–4081.

THOMAS-KEPRTA KL, CLEMETT SJ, BAZYLINSKI DA, KIRSCHVINK JL, MCKAY DS, WENTWORTH SJ, VALI H, GIBSON JR EK, MCKAY MF, AND ROMANEK CS (2001) Truncated hexa-octahedral magnetite crystals in ALH84001: Presumptive biosignatures. *Proceedings of the National Academy of Sciences of the United States of America* 98(5): 2164–2169.

THOMAS-KEPRTA KL, CLEMETT SJ, BAZYLINSKI DA, KIRSCHVINK JL, MCKAY DS, WENTWORTH SJ, VALI H, GIBSON JR EK, AND ROMANEK CS (2002) Magnetofossils from ancient Mars: A robust biosignature in the martian meteorite ALH84001. *Applied and Environmental Microbiology* 68(8): 3663–3672.

THOUVENEL-ROMANS S AND STEINBOCK O (2003) Oscillatory growth of silica tubes in chemical gardens. *Journal of the American Chemical Society* 125: 4338–4341.

THOUVENEL-ROMANS S, VAN SAARLOOS W, AND STEINBOCK O (2004) Silica tubes in chemical gardens: Radius selection and its hydrodynamic origin. *Europhysics Letters* 67: 42–48.

THOUVENEL-ROMANS S, PAGANO JJ, AND STEINBOCK O (2005) Bubble guidance of tubular growth in reaction-precipitation systems. *Physical Chemistry Chemical Physics* 7: 2610–2615.

THUMBS J AND KOHLER HH (1996) Capillaries in alginate gels as an example of dissipative structure formation. *Chemical Physics* 208: 9–24.

TINGLE TN AND HOCHELLA JR MF (1993) Formation of reduced carbonaceous matter in basalts and xenoliths: Reaction of C-O-H gases on olivine crack surfaces. *Geochimica et Cosmochimica Acta* 57: 3245–3249.

TRÉGUER P, NELSON DM, VAN BENNEKOM AJ, DEMASTER DJ, LEYNAERT A, AND QUÉGUINER B (1995) The silica balance in the world ocean: A reestimate. *Science* 268: 375–379.

TREML H, WOELKI S, AND KOHLER HH (2003) Theory of capillary formation in alginate gels. *Chemical Physics* 293: 341–353.

TRENDALL A AND BLOCKLEY J (2004) Precambrian iron-formation. In *The Precambrian Earth: tempos and events* (Edited by P Eriksson, W Altermann, D Nelson, W Mueller, and O Catuneanu), volume 12 of *Developments in Precambrian Geology*, pp. 403–421. Elsevier, The Netherlands.

TRTACY RJ (1991) Ba-rich micas from the Franklin Marble, Lime Crest and Sterling Hill, New Jersey. *American Mineralogist* 76: 1683–1693.

TSUNO H, KAGI H, AND AKAGI T (2001) Effects of trace lanthanum ion on the stability of vaterite and transformation from vaterite to calcite in an aquatic system. *Bulletin of the Chemical Society of Japan* 74: 479–486.

TUINSTRA F AND KOENIG JL (1970) Raman spectrum of graphite. *The Journal of Chemical Physics* 53(3): 1126–1130.

UENO Y, ISOZAKI Y, YURIMOTO H, AND MARUYAMA S (2001) Carbon isotopic signatures of individual Archean microfossils(?) from Western Australia. *International Geology Review* 40: 196–212.

UENO Y, YRIMOTO H, YOSHIOKA H, KOMIYA T, AND MARUYAMA S (2002) Ion microprobe analysis of graphite from ca. 3.8 Ga metasediments, Isua supracrustal belt, West Greenland: Relationship between metamorphism and carbon isotopic composition. *Geochimica et Cosmochimica Acta* 66: 1257–1268.

UENO Y, YOSHIOKA Y, MARUYAMA S, AND ISOZAKI Y (2004) Carbon isotopes and petrography of kerogens in ~3.5-Ga hydrothermal silica dikes in the North Pole area, Western Australia. *Geochimica et Cosmochimica Acta* 68: 573–589.

UTSUNOMIYA S, MURAKAMI T, NAKADA M, AND KASAMA T (2003) Iron oxidation state of a 2.45-Byr-old paleosol developed on mafic volcanics. *Geochimica et Cosmochimica Acta* 67: 213–221.

VAN KRANENDONK MJ (2006) Volcanic degassing, hydrothermal circulation and the flourishing of early life on earth: A review of the evidence from c. 3490-3240 Ma rocks of th ePilbara Supergroup, Pilbara Craton, Western Australia. *Earth-Science Reviews* 74: 197–240.

VAN KRANENDONK MJ, WEBB GE, AND KAMBER BS (2003) Geological and trace element evidence for a marine sedimentary environment of deposition and biogenicity of 3.45 Ga stromatolitic carbonates in the Pilbara Craton, and support for a reducing Archaean ocean. *Geobiology* 1: 91–108.

VAN ZUILEN MA, LEPLAND A, AND ARRHENIUS G (2002) Reassessing the evidence for the earliset traces of life. *Nature* 418: 627–630.

VAN ZUILEN MA, LEPLAND A, TERANES J, FINARELLI J, WAHLEN M, AND ARRHENIUS G (2003) Graphite and carbonates in the 3.8 Ga old Isua Supracrustal Belt, southern West Greenland. *Precambrian Research* 126: 331–348.

VANDENBROUCKE M (2003) Kerogen: From types to models of chemical structure. *Oil and Gas Science and Technology* 58: 243–269.

VEIZER J (1982) Mantle buffering of the early ocean. *Naturwissenschaften* 69: 173–180.

VEIZER J (1983) Geologic evolution of the Archean-Early Proterozoic Earth. In *Earth's Earliest Biosphere* (Edited by JW Schopf), pp. 240–259. Princeton University Press, Princeton, New Jersey.

VEIZER J, HOEFS J, LOWE DR, AND THURSTON PC (1989a) Geochemistry of Precambrian carbonates: II. Archean greenstone belts and Archean seawater. *Geochimica et Cosmochimica Acta* 53: 859–871.

VEIZER J, HOEFS J, RIDLER RH, JENSEN LS, AND LOWE DR (1989b) Geochemistry of Precambrian carbonates: I. Archean hydrothermal systems. *Geochimica et Cosmochimica Acta* 53: 845–857.

VICSEK T (1989) *Fractal growth phenomena.* World Scientific, Singapore.

VICSEK T (1993) The fractal nature of common patterns. In *Growth patterns in physical sciences and biology* (Edited by JM García-Ruiz, E Louis, P Meakin, and LM Sander), volume 304 of *NATO Science Series B*, pp. 29–36. Plenum Press.

VIDANO R AND FISCHBACH DB (1978) New lines in the Raman spectra of carbons and graphite. *Journal of the American Ceramic Society* 61(1-2): 13–17.

VIDANO RP, FISCHBACH DB, WILLIS LJ, AND LOEHR TM (1981) Observations of Raman band shifting with excitation wavelength for carbons and graphites. *Solid State Communications* 39: 341–344.

VLASOV YA, ASTRATOV VN, KARIMOV OZ, AND KAPLYANSKII AA (1997) Existence of a photonic pseudogap for visable light in synthetic opals. *Physical Review B* 55: R13357–R13360.

VOGLESONGER KM, HOLLOWAY JR, DUNN EE, DALLA-BETTA PJ, AND O'DAY PA (2001) Experimental abiotic synthesis of methanol in seafloor hydrothermal systems during diking events. *Chemical Geology* 180: 129–139.

VOINESCU AE, KELLERMEIER M, CARNERUP AM, LARSSON AK, TOURAUD D, HYDE ST, AND KUNZ W (2006a) Co-precipitation of silica and alkaline-earth carbonates using TEOS as silica source. In preparation.

VOINESCU AE, KELLERMEIER M, CARNERUP AM, LARSSON AK, TOURAUD D, KIENLE L, PFITZNER A, AND HYDE ST (2006b) Self-assembly of silica-calcium carbonate biomorphs. Submitted.

WALKER J (1985) Carbon dioxide on the early Earth. *Origins of Life and Evolution of the Biosphere* 16: 117–127.

WALKER JCG (1983) Possible limits on the composition of the Archean ocean. *Nature* 302: 518–520.

WALSBY AE (1980) A square bacterium. *Nature* 283: 69–71.

WALSH MM (1992) Microfossils and possible microfossils from the Early Archean Onverwacht Group, Barberton Mountain Land, South Africa. *Precambrian Research* 54: 271–293.

Walsh MM and Lowe DR (1985) Filamentous microfossils from the 3,500-Myr-old Omverwacht Group, Barberton Mountain Land, South Africa. *Nature* 314: 530–532.

Walter MR (1976) Introduction. In *Stromatolites* (Edited by M Walter), volume 20 of *Developments in sedimentology*, pp. 1–3. Elsevier.

Walter MR, Buick R, and Dunlop JSR (1980) Stromatolites 3,400-3,500 Myr old from the North Pole area, Western Australia. *Nature* 284: 443–445.

Wang J, Wang W, Sun P, Yuan Z, Li B, Jin Q, Ding D, and Chen T (2006) Hierarchically helical mesostructures silica nanofibers templated by achiral cationic surfactant. *Journal of Materials Chemistry* DOI:10.1039/b609243h.

Wang L, Sondi I, and Matijevic E (1999) Preparation of uniform needle-like aragonite particles by homogeneous precipitation. *Journal of Colloid and Interface Science* 218: 545–553.

Wang Y, Alsmeyer DC, and McCreery RL (1990) Raman spectroscopy of carbon materials: Structural basis of observed spectra. *Chemistry of Materials* 2: 557–563.

Warren J (2000) Dolomite: occurrence, evolution and economically important associations. *Earth-Science Reviews* 52: 1–81.

Watson EB and Harrison TM (2005) Zircon thermometer reveals minimum melting conditions on earliest Earth. *Science* 308: 841–844.

Weinbruch S, Büttner H, and Rosenbauer M (1992) The orthorhombic-hexagonal phase transformation in the system $BaCO_3$-$SrCO_3$ to pressures of 7000 bar. *Physics and Chemistry of Minerals* 19: 289–297.

Westall F (1999) The nature of fossil bacteria: A guide to the search for extraterrestrial life. *Journal of Geophysical Research* 104(E7): 16437–16451.

Wilde SA, Valley JW, Peck WH, and Graham CM (2001) Evidence from detrital zircons for the existence of continental crust and oceans on the Earth 4.4 Gyr ago. *Nature* 409: 175–178.

Williams LB, Canfield B, Voglesonger KM, and Holloway JR (2005) Organic molecules formed in a "primordial womb". *Geology* 33: 913–916.

Witten TA and Sander LM (1983) Diffusion-limited aggregation. *Physical Review B* 27: 5686–5697.

Witten Jr TA and Sander LM (1981) Diffusion-limited aggregation, a kinetic critical phenomenon. *Physical Review Letters* 47: 1400–1403.

WOELKI S AND KOHLER HH (2003) Orientation of chain molecules in ionotropic gels: a Brownian dynamics model. *Chemical Physics* 293: 323–340.

WONG MS AND KNOWLES WV (2004) Surfactant-templated mesostructured materials: synthesis and compositional control. In *Nanoporous materials: science and engineering* (Edited by GQ Lu and XS Zhao), volume 4 of *Series on Chemical engineering*, pp. 125–164. Imperial College Press, London.

WOOD DA (1988) Relationships between thermal maturity indeces calculated using Arrhenius equation and lopatin method: Implications for petroleum exploration. *The American Association of Petroleum Geologists Bulletin* 72(2): 115–134.

WOPENKA B AND PASTERIS JD (1993) Structural characterization of kerogens to granulite-facies graphite: Applicability of Raman microprobe spectroscopy. *American Mineralogist* 78: 533–557.

WRAY JL AND DANIELS F (1957) Precipitation of calcite and aragonite. *Journal of the American Chemical Society* 79: 2031–2034.

YADAVA KL AND GHOSH S (1957) Studies in colloidal silicates. *Kolloid-Zeitschrift* 153: 166–168.

YANG W AND HOLLAND H (2003) The Hekpoort paleosol profile in strata 1 at Gaborone, Botswana: Soil formation during the Great Oxidation Event. *American Journal of Science* 303: 187–220.

YANG W, HOLLAND H, AND RYE R (2002) Evidence for low or no oxygen in the late Archean atmosphere from the ~2.76 Ga Mt. Roe #2 paleosol, Western Australia. *Geochimica et Cosmochimica Acta* 66: 3707–3718.

YOSHIDA A (1994) Silica nucleation, polymerization, and growth preparation of monodispersed sols. In *The colloid chemistry of silica* (Edited by HE Bergna), volume 234 of *Advances in Chemistry*, pp. 51–66. American Chemical Society.

YU SH, CÖLFEN H, HARTMANN J, AND ANTONIETTI M (2002) Biomimetic crystallization of calcium carbonate spherules with controlled surface structures and sizes by double-hydrophilic block copolymers. *Advanced Functional Materials* 12: 541–545.

YU SH, CÖLFEN H, AND ANTONIETTI M (2003) Polymer-controlled morphosynthesis and mineralization of metal carbonate superstructures. *Journal of Physical Chemistry B* 107: 7396–7405.

Yu SH, Cölfen H, tauer K, and Antonietti M (2004a) Tectonic arrangement of $BaCO_3$ nanocrystals into helices induced by a racemic block copolymer. *Nature Materials* 4: 51–55.

Yu SH, Cölfen H, Xu AW, and Dong W (2004b) Complex spherical $BaCO_3$ superstructures self-assembled by a facile mineralization process under control of simple polyelectrolytes. *Crystal Growth and Design* 4: 33–37.

Yue W, Park RJ, Kulak AN, and Meldrum FC (2006) Macroporous inorganic solids from a biomineral template. *Journal of Crystal Growth* 294: 69–77.

Yui TF, Huang E, and Xu J (1996) Raman spectrum of carbonaceous material: a possible metamorphic grade indicator for low-grade metamorphic rocks. *Journal of Metamorphic Geology* 14: 115–124.

Zang W and Walter MR (1992) *Late Proterozoic and Cambrian microfossils and biostratigraphy, Amadeus Basin, central Australia*, volume 12 of *Memoires*. Association of the Australasian Paleonologists.

Zeebe R and Wolf-Gladrow D (2001) CO_2 *in seawater: Equilibrium, kinetics, isotopes*, volume 65 of *Elsevier Oceanography Series*. Elsevier.

Zegers TE, de Wit MJ, Dann J, and White SH (1998) Vaalbara, Earth's oldest assembled continent? A combined structural, geochronological, and palaeomagnetic test. *Terra Nova* 10: 250–259.

Zhou GT and Zheng YF (1998) Synthesis of aragonite-type calcium carbonate by overgrowth technique at atmospheric pressure. *Journal of Materials Science Letters* 17: 905–908.